

Integral Field Spectroscopy of (U)LIRGs and PSQSOs: the role of mergers in galaxy evolution

Clara Cortijo Ferrero

Tesis doctoral

Universidad de Granada

Instituto de Astrofísica de Andalucía

Directora: Dra. Rosa M^a González Delgado



UNIVERSIDAD DE GRANADA

Tesis doctoral
Programa Oficial de Doctorado
en Física y Ciencias del Espacio
Noviembre 2015

Integral Field Spectroscopy of (U)LIRGs and Post-Starburst QSOs: the role of mergers in galaxy evolution

[PhD THESIS]

Clara Cortijo Ferrero
Instituto de Astrofísica de Andalucía (CSIC)

Memoria de Tesis
presentada en la Universidad de Granada
para optar al grado de Doctora en Física

Directora de tesis:
Rosa González Delgado

*A mi abuela, a mi hermana, y a mis padres,
por todo su amor y apoyo.*

*A mi perrita Lambru, que ya no está,
pero sigue viviendo en mi amor por ella.*

*Un día color de melocotón,
cuando todos seamos libres,
cuando las piedras se puedan comer
y ya nadie sea más que nadie,
canta por mí
si no estoy yo aquí.*

*Viene el día en que seremos puros
como un cielo de verano sobre el mar.
Cantaré por tí
si no estás tú aquí.*

- en *Canta por mí*, El Último de la Fila -

La doctoranda, Clara Cortijo Ferrero, y la directora de la tesis, Rosa M^a González Delgado, garantizamos, al firmar esta tesis doctoral, que el trabajo ha sido realizado por la doctoranda bajo la dirección de la directora de la tesis y hasta donde nuestro conocimiento alcanza, en la realización del trabajo, se han respetado los derechos de otros autores a ser citados, cuando se han utilizado sus resultados o publicaciones.

En Granada, a 23 de Octubre de 2015

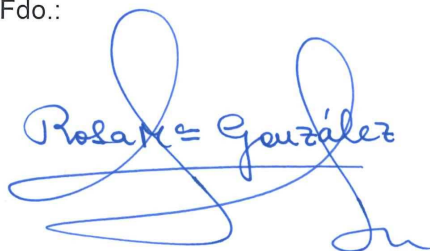
Director/es de la Tesis

Rosa M^a González Delgado

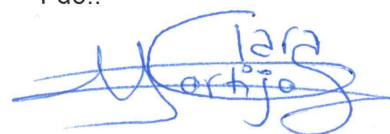
Doctorando

Clara Cortijo Ferrero

Fdo.:



Fdo.:



Agradecimientos

Bueno, no sé por donde empezar, técnicamente debería empezar agradeciendo a la Vía Láctea, porque sin ella yo no habría llegado hasta aquí, y no me refiero sólo a los átomos que me forman. Nacida y criada en Madrid, no vi un cielo estrellado libre de contaminación lumínica hasta los 18, justo un poco antes de la Selectividad. Eso fue en Castejón de Henares (Guadalajara), el pueblo de mi amiga Rita. Allí estaba la Vía Láctea en todo su esplendor, el cielo blanco de estrellas, y yo... totalmente fascinada, tanto, que ese día tuve clarísimo que estudiaría los astros. Y es curioso, porque no me gustaba especialmente la física, de hecho, barajaba otras muchas opciones: biología, matemáticas, química... claro, no contaba con el embrujo de la Milky Way.

Durante la carrera, sobre todo cuando empecé la especialidad, volvía a casa con los ojos brillantes, desbordada de pasión, y le contaba a mi madre todo lo que iba aprendiendo: los diferentes tipos de galaxias que existían, a qué se debía el color de las estrellas, cómo evolucionaban. Y esa pasión es también la que ha conseguido que llegue hasta aquí, a pesar de que el último año ha sido especialmente duro. Son muchas las personas a las que debo un sincero agradecimiento, ya que sin ellas este trabajo no hubiera sido posible.

En primer lugar, quiero agradecer a mi directora. Rosa, sabes bien que sin ti ésto no sería posible. Gracias por todo lo que me has enseñado, por haberme dado esta oportunidad de crecer intelectualmente, pero también, por todo el cariño, el apoyo, y la paciencia que has tenido conmigo, sobre todo en los últimos tiempos. Me siento muy afortunada de haber contado con una directora de tan enorme valía científica y humana.

Quiero hacer extensivo este agradecimiento a todo el grupo de trabajo, formado por investigadores excelentes y mejores personas: Enrique Pérez, Rubén García Benito, Roberto Cid Fernandes. Muchas gracias por todo lo que habéis compartido conmigo.

También a aquellos que ya no están en el IAA, pero que sí estaban en mis comienzos, haciendo de cada reunión de grupo un momento de aprendizaje: Montse Villar, Miguel Cerviño, Valentina Luridana y Jesús Maíz Apellániz.

Y más valía en todos los sentidos, la de Sebastián Sánchez, que me enseñó a reducir los datos empleados en mi tesis. Literalmente, sin él no habría podido ni empezar. Y bueno, a todo CALIFA, por los buenos momentos en las Busy Week y por todo lo que he aprendido.

A Paola Di Matteo, por su supervisión durante mi estancia en el Observatorio de París, y por ser tan amable, paciente, y linda conmigo.

Por supuesto, a mi hermano mayor de tesis, Víctor, a quien nunca le faltó tiempo para ayudarme, aun estando en los momentos más críticos de su tesis. Sabes lo mucho que significó eso para mí, agradecimiento total.

A mi hermano menor también, Rafa, muchas gracias por tus visitas a mi despacho, por los ánimos, y por el viaje a CAHA más divertido de mi vida.

También a William, André y Eduardo, por compartir ciencia y risas en más de una ocasión.

A dos amigas sin las cuales no habría podido ni mantenerme en pie en ciertas ocasiones, que no

me dejaron ni un segundo en los peores momentos: Yoli y Mónica.

A Mari Julis, por ese sentido maravilloso del humor capaz de subir el ánimo al más depresivo.

A Sandra y Juan Carlos, por su cariño y ayuda. Al pequeño Dani, por ser mi mayor alegría en Granada.

A Aythami, mi compañero de despacho durante mucho tiempo, desde el zulo hasta el final. Gracias por tus consejos de guitarra, y por las sesiones de terapia mutua para llevar mejor el final de tesis.

A Pablo, Marta, Carolina y Sara, que no se han separado de mí en los últimos tiempos, y sin cuya amistad y cariño todo hubiera sido infinitamente más difícil.

A Dominika, por transmitirme tanta energía y motivación.

A Guillermo, que desde que volvió a Granada ha sabido sacarme siempre una gran sonrisa.

A Naim, mi angelito, por su comprensión y apoyo en los momentos más bizarros.

A Javi Blasco, por vigilarme y acompañarme en mis altos vuelos descontrolados, y escuchar simultáneamente mis risas y lágrimas.

A Luis, una de las personas con más calidad humana que conozco, y por quien tengo un gran aprecio. Gracias por estar ahí.

A Ana de seguridad, por contagiarme su optimismo.

A Zaira, por los ánimos, y por haber sido capaz de hacerme reír hasta en los momentos más estresantes. A Rubén, porque sin el mirror de la ESO del ADS todavía estaría metiendo referencias en la tesis.

A todos los compis de comida con los que tantas risas y buenos momentos he compartido. Han sido muchos, vosotros sabéis quienes sois.

En general, quiero agradecer a todo el IAA, desde el personal de administración, como de seguridad, a los becarios, y al personal científico e investigador. Son muchas las personas que durante este tiempo me han transmitido cariño y apoyo.

Y fuera del IAA, gracias Vania, por ese año que convivimos juntas, y por no separarte de mí en los momentos duros. Ahí se ve a los amigos de verdad, y tu estás en un nivel superior ;).

A Nelleke, por ser una mujer valiente y sobre todo, inspiradora.

A mis amigas del barrio, por estar ahí siempre, independientemente de la distancia: Sara, Rita, el pequeño Aitor (mi alegría de vivir madrileña), Sandra, y Gisela. Bonitas.

Y a las de la universidad, que también han estado pendientes de mí, y me han mandado energía en los momentos precisos: Paz, Lidia, Paula y Lía. Gracias, niñas.

A Rocío, mi parisina favorita. Gracias por tus llamadas y por sacarme siempre una gran sonrisa.

Finalmente, mi mayor agradecimiento es para mi familia, especialmente para mis padres, Carmen y Jacinto, que no se han separado ni un momento de mí y que me han apoyado siempre, a pesar de todo, incondicionalmente. A mi hermana Isabel, por quererme tantísimo y ser un apoyo fundamental en mi vida. A mi abuela Josefa, que siempre ha estado pendiente de su nieta, a pesar de no gustarle que tuviera que irse lejos de Madrid. A mi perrita Lambru, que ahora descansa en paz, pero que ha curado con sus lametones todas mis lágrimas y ha sacado de mí el lado más dulce y tierno. Y por último a ti, que podrías tener cualquier nombre y cualquier cuerpo, pero eres y yo soy contigo, y eso basta para inspirarse en los momentos más necesarios.

¡Muchas gracias!.

Resumen

En esta tesis hemos caracterizado las historias de formación estelar, las poblaciones estelares, y las propiedades del gas ionizado en dos pequeñas muestras de galaxias en diferentes estadios a lo largo de la secuencia de fusión, tres LIRGs (las dos pre-coalescencia IC 1623 y NGC 6090, y la post-coalescencia NGC 2623) y nueve PSQSOs, analizando datos de Espectroscopía de Campo Integral en el rango óptico, 3700 - 7000 Å, e imagen de alta resolución del HST. Adicionalmente, para NGC 2623 disponemos de imagen en banda estrecha en H α y [NII] λ 6583, procedentes de los filtros sintonizables del instrumento OSIRIS@GTC, que nos han permitido estudiar las regiones externas de las colas de marea. Los resultados de las LIRGs y los PSQSOs han sido comparados con dos muestras de control formadas por espirales de tipo Sbc y Sc del cartografiado CALIFA. Para todos se ha seguido la misma metodología de análisis: síntesis del espectro completo empleando el código *Starlight* con una combinación de modelos de poblaciones estelares simples de la literatura.

Con nuestros datos encontramos una secuencia evolutiva consistente con simulaciones recientes. En los estadios iniciales (pre-coalescencia) la formación estelar (FE) inducida en los últimos 32 Maños es extendida, y está incrementada, en promedio, por un factor ~ 4 respecto a las espirales de control. Cuando resolvemos por regiones, encontramos que en IC 1623 W el incremento es igual en la zona central y en el disco (por un factor 7), mientras que para NGC 6090 NE el incremento es mayor en la zona central (un factor 9), aún significativo a un radio efectivo (un factor 5) y menos notable en el disco (un factor 1.5).

En fusiones más avanzadas, como NGC 2623, encontramos que la mayor parte de la FE reciente está concentrada en la zona central, aumentada por un factor 9 con respecto a las espirales. Sin embargo, también se ha producido FE con menos intensidad en las regiones externas (un factor $\lesssim 3$). Considerando el promedio de toda la galaxia, encontramos que se ha producido 3 veces más FE reciente que en las espirales. Además, en NGC 2623 detectamos emisión fósil extendida de un brote de formación estelar que tuvo lugar hace ~ 1.5 Gaños, probablemente cuando se encontraba en los estadios iniciales de la fusión. La masa estelar formada durante este primer episodio de FE es un factor 2 mayor (tanto en el centro como en las regiones externas) que la masa formada durante ese mismo periodo en espirales aisladas.

Promediando los resultados de los nueve PSQSOs, encontramos que, en términos de luz y masa, su historia de formación estelar es comparable a NGC 2623. Atendiendo a la edad promedio, encontramos que los PSQSOs son ~ 400 Maños más viejos que NGC 2623. Ésto podría indicar que están ligeramente más evolucionados, sin embargo, dadas las incertidumbres relacionadas con la base de modelos, y la heterogeneidad de la muestra, no podemos confirmar exactamente en qué grado. Resaltamos que ambos presentan una contribución significativa en masa de poblaciones estelares $\lesssim 1.5$ Gaños, que no está presente en ninguna de las dos LIRGs pre-coalescencia. Sin embargo, pensamos que el episodio activo de FE que acontece en las pre-coalescencia está, de hecho, formando la masa estelar en poblaciones de edad intermedia que se parecerá a NGC 2623 dentro de ~ 1.5 Gaños. La masa estelar en poblaciones de $\lesssim 1.5$ Gaños es $\sim 6.6 \times 10^9 M_{\odot}$ (Chabrier IMF) en NGC 2623 y $\sim 10^{10} M_{\odot}$ en los PSQSOs, por lo tanto, si las LIRGs pre-coalescencia siguen formando estrellas a su ritmo actual $\sim 16 M_{\odot}$ /año durante $\sim 400 - 600$ Maños, entonces serán capaces de formar las masas que se observan en NGC 2623 y los PSQSOs. Esta escala temporal es consistente con el límite superior de 500 Maños que se espera que dure la FE inducida según las simulaciones.

Con respecto a la evolución de NGC 2623 a PSQSO, resaltamos que en unos pocos 100 Maños, los vientos de algunas U/LIRGs son capaces de expulsar el gas molecular y el polvo del centro, dejando el AGN al descubierto, siendo ésto consistente con los ~ 400 Maños promedio de desfase que encontramos entre NGC 2623 y los PSQSOs.

Para concluir, dadas las masas estelares que medimos en nuestros objetos, la mayor parte de ellas $\lesssim 10^{11} M_{\odot}$, encontramos que formarán elípticas de masa intermedia ($\sim 10^{11} M_{\odot}$), o el núcleo de las futuras gigantes elípticas, de acuerdo con el modelo evolutivo de fusiones de espirales masivas ricas en gas.

Summary

In this thesis we have characterized and compared the star formation histories, average stellar population properties, and ionized gas properties in two small samples of galaxies in different stages across the merger sequence, three LIRGs (the two pre-mergers IC 1623 and NGC 6090, and the merger NGC 2623) and nine PSQSOs, by analysing high quality Integral Field Spectroscopy (IFS) data in the rest-frame optical range 3700 - 7000 Å, and high resolution HST imaging. Additionally, for NGC 2623 we have narrow band imaging in H α and [NII] λ 6583 from OSIRIS@GTC Tunable Filters, that allow us to study the outer parts of the tidal tails. The results from the LIRGs and PSQSOs have been compared with control Sbc and Sc galaxies from CALIFA survey. The methodology applied has been the same for all, a full spectral fitting analysis was performed using the *Starlight* code with a combination of single stellar population (SSP) models from the literature.

With our data we find a evolutionary sequence related to the merger progression that is in agreement with recent simulations. In the initial stages (pre-mergers) the induced star formation (SF) in the last 32 Myr, is extended, and enhanced, on average, by a factor ~ 4 with respect to the control spirals. When we resolve it spatially, we find that for IC 1623 W the enhancement is the same in the central region and in the disk (by a factor 7), while for NGC 6090 NE the enhancement is higher in the central region (by a factor 9), still significant at one half light radius (by a factor 5), and less significant in the "disk" (only enhanced by a factor 1.5). Attending to the importance of stellar populations ~ 300 Myr, we find that the merger-induced star formation started earlier in IC 1623 W than in NGC 6090 NE.

In more advanced mergers, as NGC 2623, we find that most of the young SF is concentrated in the central region, enhanced by a factor 9 with respect to control spirals. However, there exists also low level star formation in the outer parts, enhanced by $\lesssim 3$, in comparison to spirals. From the global average across the whole galaxy we find a factor ~ 3 higher than in spirals. In addition, in NGC 2623 we detect fossil emission of an extended merger-induced burst occurred ~ 1.5 Gyr ago, probably when it was at the pre-merger stage. The mass formed during this first burst is enhanced by a factor 2, both in the center and in the outer parts, with respect to the mass formed in the same period in isolated spirals.

From the average of the nine PSQSOs we find that, both in terms of light and mass, the SFH is comparable to NGC 2623. Attending to the average age, we found that PSQSOs are ~ 400 Myr older than NGC 2623. It seems that they are slightly more evolved, however, given the uncertainties related to the model base choice, and the heterogeneity of the sample, we can not confirm exactly to what degree. We note, however, that both present a significant contribution to mass of stellar populations younger than 1.5 Gyr, which is not present in the pre-merger LIRGs. However, we think that the current starburst seen in the pre-mergers is in fact forming this intermediate age mass that will look like NGC 2623 in $\lesssim 1.5$ Gyr. The stellar mass in SSPs younger than 1.5 Gyr is $\sim 6.6 \times 10^9 M_{\odot}$ (Chabrier IMF) in NGC 2623 and $\sim 10^{10} M_{\odot}$ in the PSQSOs, hence, we find that if the pre-merger LIRGs keep forming stars at the current rate $\sim 16 M_{\odot} \text{ yr}^{-1}$ during $\sim 400 - 600$ Myr, then they can account for the mass in NGC 2623 and PSQSOs. This time is approximately consistent with the 500 Myr upper limit expected for the duration of merger triggered starbursts from numerical simulations of mergers.

With respect to the evolution from NGC 2623 to PSQSO, we note that in few 100 Myr molecular outflows like the ones in some U/LIRGs would be able to remove dust from the core leaving the AGN uncovered. This is consistent with the average time delay of ~ 400 Myr found by us between NGC 2623 and the PSQSOs.

Finally, given the stellar masses measured in the LIRGs and in the PSQSOs, most of them $\lesssim 10^{11} M_{\odot}$, we find that they will form ellipticals of intermediate mass ($\sim 10^{11} M_{\odot}$), or the core of future giant ellipticals, in agreement with the major-merger evolutionary scenario.

Index

Acronyms	XXIII
1. Introduction	1
1.1. Galaxies	2
1.1.1. Morphological Classification	2
1.1.2. Bimodality in the Color-Magnitude Diagram	3
1.1.3. Two Families of Ellipticals	5
1.2. Nuclear activity in galaxies	6
1.2.1. Discovery of AGN/QSOs	7
1.2.2. Emission properties	7
1.2.3. The co-evolution of BH and galaxy growth	8
1.2.4. The influence of AGN on the evolution elliptical of galaxies	10
1.3. Formation and evolution of elliptical galaxies	13
1.3.1. Λ CDM Cosmology	13
1.3.2. Two-phase formation and dry merger growth for high mass-core Es	15
1.3.3. Major-merger scenario for low mass-coreless Es	16
1.4. (Ultra) Luminous Infrared Galaxies	19
1.4.1. Morphology	20
1.4.2. Power source: Starbursts or AGN	22
1.4.3. Merger-induced star formation	23
1.5. Post-Starburst QSOs	26
1.5.1. Properties	28
1.5.2. Evolutionary picture revisited and the Starburst / AGN timing	28
1.5.3. Other transition QSOs/AGNs	29
1.6. Thesis Overview	30
2. Data sample and observations	33
2.1. Integral Field Spectroscopy	33
2.1.1. Instrumentation	35
2.2. LIRGs observations	36
2.2.1. NGC 6090	37
2.2.2. IC 1623	38
2.2.3. NGC 2623	40

2.2.4. Arp 220	43
2.3. Post-Starburst QSOs data	45
3. Data reduction	55
3.1. PMAS data reduction	55
3.1.1. The raw data	55
3.1.2. Pre-reduction	56
3.1.3. Identification of the observation blocks and flexures correction	57
3.1.4. Spectra identification	57
3.1.5. Spectra extraction	59
3.1.6. Distorsion correction	59
3.1.7. Dispersion solution	62
3.1.8. Fiber-to-fiber transmission correction	64
3.1.9. Flux calibration	64
3.1.10. Sky subtraction	67
3.1.11. Creating datacubes and DAR correction	67
3.1.12. Mosaic construction	68
3.1.13. Absolute flux recalibration	69
3.2. VIMOS reduction	69
3.2.1. VIMOS raw data	70
3.2.2. Spectra identification	70
3.2.3. Spectra extraction	70
3.2.4. Wavelength calibration	72
3.2.5. Fiberflat correction	72
3.2.6. Flux calibration	72
3.2.7. Sky subtraction and DAR correction	72
3.3. OSIRIS data reduction	74
4. Tracing the evolution of galaxies with stellar population models	77
4.1. Introduction	77
4.2. Ingredients and uncertainties in the models	78
4.2.1. Initial Mass Function	78
4.2.2. Stellar tracks	80
4.2.3. Stellar libraries	81
4.3. Evolutionary synthesis models	82
4.3.1. Degeneracies	84
4.4. Spectral synthesis: the fossil method	85
5. Pre - Merger LIRGs: IC 1623 and NGC 6090	93
5.1. Introduction	93
5.2. Data	95
5.3. Star clusters photometry	97
5.3.1. Method	98

5.3.2.	Clusters ages	100
5.3.3.	Clusters mass	102
5.4.	Stellar populations	104
5.4.1.	Methodology	104
5.4.2.	Fit quality	108
5.4.3.	Stellar luminosity	108
5.4.4.	Stellar dust extinction	109
5.4.5.	Ages	112
5.4.6.	Metallicity	112
5.4.7.	Stellar mass surface density	115
5.4.8.	Stellar masses	115
5.4.9.	1D Star Formation Histories	117
5.4.10.	Contribution of young, intermediate and old populations	120
5.4.11.	NGC 6090 SW radial profiles from knot	126
5.4.12.	Comparison of results with base CB	126
5.5.	Ionized gas emission	128
5.5.1.	Methodology	128
5.5.2.	Ionized gas morphology	129
5.5.3.	Emission line ratios sensitive to gas density	134
5.5.4.	Ionized gas dust attenuation	134
5.5.5.	Emission line ratios sensitive to ionisation conditions	135
5.5.6.	Diagnostic diagrams	137
5.6.	Kinematics	141
5.6.1.	Velocity field of IC 1623 W	141
5.6.2.	Velocity field of NGC 6090	143
5.6.3.	Velocity dispersion	143
5.7.	Star formation rates	144
5.7.1.	Star formation rate densities	148
5.7.2.	IFS-base variations over Scalo's b parameter	150
5.8.	Summary and conclusions	154
6.	The merger LIRG NGC 2623	161
6.1.	Introduction	161
6.2.	Data	162
6.3.	Star clusters photometry	163
6.3.1.	Cluster distribution	163
6.3.2.	Cluster ages	164
6.3.3.	Clusters masses	165
6.4.	Stellar populations	167
6.4.1.	Methodology	167
6.4.2.	Fit quality	168
6.4.3.	Stellar luminosity	169
6.4.4.	Stellar dust extinction	169

6.4.5.	Age	172
6.4.6.	Metallicity	173
6.4.7.	Stellar mass surface density	176
6.4.8.	Stellar mass	176
6.4.9.	1D Star Formation Histories	176
6.4.10.	Contribution of young, intermediate and old populations	178
6.4.11.	Comparison of results with base CB	178
6.5.	Ionized gas emission	182
6.5.1.	Ionized gas morphology	182
6.5.2.	Emission line ratios sensitive to gas density	187
6.5.3.	Ionized gas dust attenuation	187
6.5.4.	Emission line ratios sensitive to ionisation source	188
6.5.5.	Diagnostic diagrams	190
6.5.6.	OSIRIS line emission at the edge of the SW tidal tail	192
6.6.	Kinematics	193
6.7.	Star formation rates	195
6.7.1.	Star formation rate densities	199
6.7.2.	IFS-base variations over Scalo's b parameter	199
6.8.	Discussion	202
6.8.1.	Cluster populations tracing the merger epochs	202
6.8.2.	Extended versus nuclear star formation in mergers	203
6.8.3.	Relative importance of extended and nuclear starbursts	204
6.8.4.	Ionized gas distribution in mergers	205
6.8.5.	Ionization mechanism in mergers	205
6.8.6.	Shock luminosity vs. input energy from star formation	205
6.8.7.	Tidal Dwarf Galaxy forming in NGC 2623?	206
6.9.	Summary and conclusions	207
7.	Post-Starburst QSOs	213
7.1.	Introduction	213
7.2.	Data	213
7.2.1.	PMAS/VIMOS IFS	213
7.2.2.	SDSS	214
7.3.	Stellar populations synthesis and AGN component modelling	214
7.3.1.	Comparison between constrained and unconstrained fits with a single A_V	217
7.3.2.	Comparison between constrained fits with $A_V^{AGN} = A_V^{stars}$ and $A_V^{AGN} \neq A_V^{stars}$	217
7.3.3.	Caveats about spectral modelling	222
7.4.	Emission line measurements	223
7.5.	AGN properties	226
7.5.1.	Black Hole Mass	226
7.5.2.	Eddington ratio	227
7.6.	Starburst properties	229
7.7.	Comparison between datasets	230

7.7.1. IFS central region vs SDSS	230
7.7.2. IFS Central vs IFS Integrated	234
7.7.3. SDSS vs C13 work	236
7.8. Results	237
7.8.1. BPT diagrams	237
7.8.2. Correlations of AGN versus Starburst properties	238
7.9. Conclusions	240
8. Overall comparison between Spirals, LIRGs and PSQSOs	243
8.1. Star formation histories of LIRGs	243
8.1.1. IC 1623 W	245
8.1.2. NGC 6090	247
8.1.3. NGC 2623	249
8.2. Comparison between CALIFA spirals and our LIRGs	251
8.2.1. Radial profiles of the stellar population properties	251
8.2.2. Central, outer, and global SFHs in light	255
8.2.3. SFHs in mass and mass growth	258
8.2.4. SFRs and specific SFRs	260
8.3. Comparison between LIRGs and PSQSOs	264
8.3.1. Global evolutionary picture	272
9. Conclusions	273
9.1. Pre-merger LIRGs IC 1623 and NGC 6090	273
9.2. Merger LIRG NGC 2623	277
9.3. PSQSOs	280
9.4. Global evolutionary picture	281
A. PSQSOs: Spectral synthesis results	283
B. PSQSOs: Emission line fits	313
References	321

Acronyms

A&AS	<i>Astronomy and Astrophysics</i>
A&A	<i>Astronomy and Astrophysics Supplement</i>
ACS	<i>Advanced Camera for Surveys</i>
AGB	<i>Asymptotic Giant Branch</i>
AGN	<i>Active Galactic Nucleus</i>
AJ	<i>Astronomical Journal</i>
ApJ	<i>Astrophysical Journal</i>
Ap&SS	<i>Astrophysics and Space Science</i>
ApJS	<i>Astrophysical Journal Supplement</i>
ApSSS	<i>Astrophysics and Space Science Supplement</i>
ARA&A	<i>Annual Review of Astronomy and Astrophysics</i>
BH	<i>Black Hole</i>
BLR	<i>Broad Line Region</i>
CALIFA	<i>Calar Alto Legacy Integral Field Area</i>
CCD	<i>Charged Couple Device</i>
CMD	<i>Color Magnitude Diagram</i>
ETG	<i>Early Type Galaxy</i>
FIR	<i>Far Infrared</i>
FoV	<i>Field of View</i>
FWHM	<i>Full Width at Half Maximum</i>
GTC	<i>Gran Telescopio de Canarias</i>
HLR	<i>Half Light Radius</i>
HST	<i>Hubble Space Telescope</i>
IFS	<i>Integral Field Spectroscopy</i>
IFU	<i>Integral Field Unit</i>
IMF	<i>Initial Mass Function</i>
IR	<i>Infrared</i>
IRAF	<i>Image Reduction and Analysis Facility</i>

IRAS	<i>Infrared Astronomical Satellite</i>
ISM	<i>Interstellar Medium</i>
ISP	<i>Intermediate-age Stellar Population</i>
LArr	<i>Lens Array</i>
LINER	<i>Low-Ionization Nuclear Emission-line Region</i>
LIRG	<i>Luminous Infrared Galaxy</i>
MNRAS	<i>Monthly Notices of the Royal Astronomical Society</i>
NICMOS	<i>Near Infrared Camera and Multi-Object Spectrometer</i>
NIR	<i>Near-Infrared</i>
NLR	<i>Narrow Line Region</i>
OSIRIS	<i>Optical System for Imaging and low-intermediate Resolution Integrated Spectroscopy</i>
OSP	<i>Old Stellar Population</i>
PAH	<i>Polycyclic Aromatic Hydrocarbon</i>
PASP	<i>Publications of the Astronomical Society of the Pacific</i>
PMAS	<i>Potsdam MultiAperture Spectrophotometer</i>
PPAK	<i>PMAS fibre PAcK</i>
PSF	<i>Point Spread Function</i>
PSQSO	<i>Post Starburst Quasar</i>
QSO	<i>Quasi Stellar Object</i>
SB	<i>Starburst</i>
SDSS	<i>Sloan Digital Sky Survey</i>
SED	<i>Spectral Energy Distribution</i>
SF	<i>Star Formation</i>
SFH	<i>Star Formation History</i>
SFR	<i>Star Formation Rate</i>
SMBH	<i>Super Massive Black Hole</i>
SSP	<i>Single Stellar Population</i>
SSC	<i>Super Star Cluster</i>
TDG	<i>Tidal Dwarf Galaxy</i>
ULIRG	<i>Ultraluminous Infrared Galaxy</i>
UV	<i>Ultraviolet</i>
VIMOS	<i>VIisible MultiObject Spectrograph</i>
VLT	<i>Very Large Telescope</i>
WFPC2	<i>Wide-Field Planetary Camera 2</i>
WR	<i>Wolf-Rayet</i>
YMC	<i>Young Massive Cluster</i>

YSP

Young Stellar Population

1

Introduction

Major gas-rich mergers are thought to be responsible of a dramatic evolution of galaxies. Attending to the changes in the morphology, [Kormendy & Sanders \(1992\)](#) propose that mergers of gas rich disks (U/LIRGs) lead to the formation of elliptical galaxies. Due to the large timescales needed to complete the merger, we can not study this process following the transformation of an individual system. Instead, we need to compare the properties of systems along the different stages of the merger sequence. However, identifying all the intermediate stages of a merger, and placing them in the right evolutionary order, it is not an easy task.

Morover, apart from the morphological changes, [Sanders et al. \(1988\)](#) proposed there is also a change in the ionizing mechanism along the merger sequence, from dusty starbursts in the initial stages (U/LIRGs) to unobscured QSO activity in the final ones. While it is quite clear that mergers lead to massive starburst activity, sometimes hidden by dust, and therefore, U/LIRGs ([Surace et al. 1998, 2000](#); [Veilleux et al. 2002](#); [Kim et al. 2013](#)), it is not so clear if the QSOs activity is merger-triggered and if so, when exactly during the merger it starts. The best approach is to find systems with intermediate properties in the proposed sequence, that is, galaxies hosting bright nuclear QSOs, showing morphological disturbance typical of a past merger and with an important post-starburst population, relics of the intense starburst activity triggered in the past. The best example of this kind of systems are post-starburst QSOs ([Brotherton et al., 1999](#)), which have been proposed to be the missing evolutionary link. They are, therefore, ideal laboratories to study connections between the starburst and AGN phenomenon.

In this chapter, I give the global astrophysical context of this PhD work. I start in Section [1.1](#) with a summary of the different types and properties of galaxies in the local Universe. In Section [1.2](#), I summarize our knowledge on AGN and how they affect the galaxy evolution. Section [1.3](#) presents the two main scenarios for the formation and evolution of elliptical galaxies. The characteristics of U/LIRGs and PSQSOs are summarized in Section [1.4](#) and Section [1.5](#), respectively. Finally, in Section [1.6](#), I describe the aims of my PhD work and the structure of this manuscript.

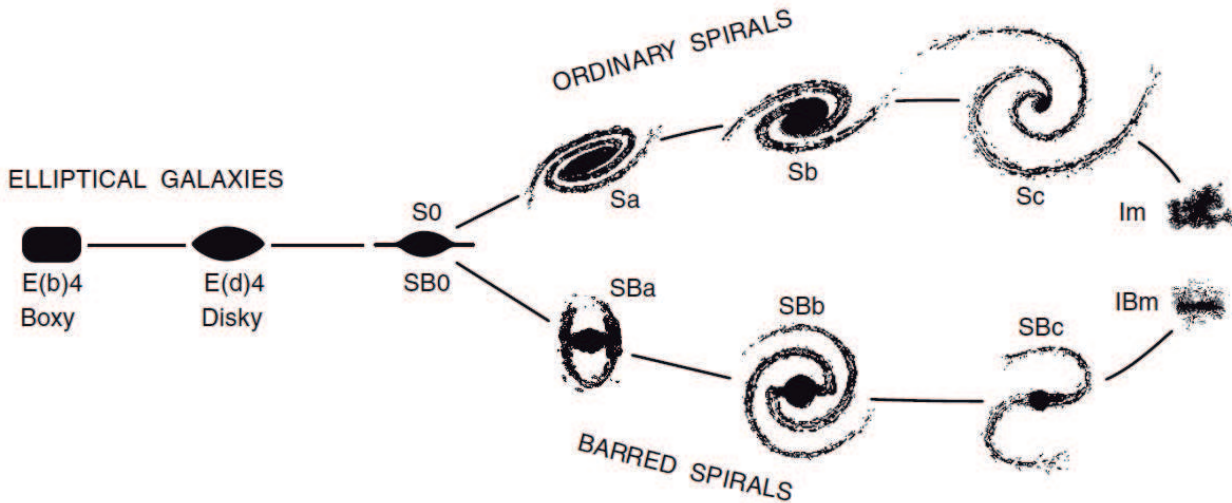


Figure 1.1 The Hubble Sequence of Galaxies as given by [Kormendy & Bender \(1996\)](#). Elliptical (early-type) galaxies are shown on the left, spiral (late-type) galaxies at the right.

1.1. Galaxies

Galaxies are gravitationally bound collections of stars, gas, dust, and dark matter. In our current understanding, these objects have been formed through the agglomeration of smaller clumps in a sort of dance governed by the gravitational properties of dark matter, in which all the visible components of the Universe are embedded. As the building blocks of the Universe, galaxies are one of the most important subjects of study in our effort to push the limits of our comprehension.

1.1.1. Morphological Classification

Galaxies can be divided in classes based on their morphology. The Hubble-Sequence was created and first published by Edwin Hubble in his monograph 'The Realms of the Nebulae' (1936) to put some order in the diversity of galaxy morphologies. It was later revised many times and described e.g. by [Kormendy & Bender \(1996\)](#) who (with others) added a few more types. See the classification in Figure 1.1. Most objects fall into one of two groups; spiral and elliptical galaxies.

Spiral galaxies (S) typically consist of a thin disk with spiral arms, a central bulge, and sometimes a bar. They are mainly supported against gravitational collapse by the rotation of stars in the disk. Some spiral galaxies are more disk-dominated (Sc type on the right-hand side of the Hubble diagram), while others are more bulge-dominated (Sa type). The relative significance of the disk and the bulge can be studied by measuring the surface-brightness profile of the galaxy. The surface brightness profile describes the stellar density distribution, which is more centrally concentrated in bulge-dominated galaxies. The surface brightness profile of a galaxy can be described with a Sérsic profile

$$I(r) = I_e \exp \left[-\beta_n \left(\left(\frac{r}{r_e} \right)^{1/n} - 1 \right) \right] \quad (1.1)$$

where β_n is chosen so that r_e , the effective radius, includes half of the light and $I_e = I(r_e)$. The Sérsic index n determines the curvature of the profile (Sérsic, 1963). The surface brightness profile of a disk typically has a Sérsic index $n = 1$, which is an exponential profile, while the bulge has a Sérsic index $n = 4$, known as the de Vaucouleurs profile (de Vaucouleurs, 1948). The profile of a spiral galaxy is usually a combination of these two.

Elliptical galaxies (E) have an apparently simple structure of a smooth, elliptical surface brightness distribution. They have no sign of a disk and are supported against gravitational collapse by the random motions of their stars. According to Driver et al. (2006), a typical Sérsic index for elliptical galaxies is $n = 4$, similarly to the bulge-dominated spiral galaxies. Elliptical galaxies are close to true ellipses, but there are small deviations from the simple axisymmetric form. Nowadays, we know that the old sub-classification of ellipticals (E0 to E7) is only a projection effect depending on the viewing angle of the observer. What is true is that elliptical galaxies do not have perfect elliptical isophotes, but they show typical deviations of a few %. Depending on the deviation, the classification was revised to distinguish between the two subclasses of ellipticals: *disky*, with peaked isophotes, and *boxy*, with box-shaped isophotes (Bender et al., 1988). Kormendy et al. (2009) showed that *disky* elliptical galaxies typically have low Sérsic indices, $n \sim 3 \pm 1$, while *boxy* ellipticals have large Sérsic indices, $n > 4$. More properties of both subtypes of ellipticals are described in Section 1.1.3.

1.1.2. Bimodality in the Color-Magnitude Diagram

The two main groups of ellipsoid-dominated and disk-dominated galaxies are often called *early-type* and *late-type* galaxies, respectively. These names refer to their places in the Hubble's sequence, where the E, S0, and Sa (= *early-types*) are plotted to the left and the spirals from Sb to Sd (= *late-types*) to the right. These expressions are of historical origin, when theorists thought that *late-type* galaxies are "late" in the sense of evolution history, so ellipticals evolve into spiral galaxies by the later formation of galactic substructure. Today this picture is known to be totally incorrect, but the terminology remained.

Besides morphology, galaxies can be divided in two distinct classes by their colors (Strateva et al. 2001, Baldry et al. 2004, 2006, Schawinski et al. 2014): the *blue cloud* and the *red sequence* (see Figure 1.2). The colors trace the physical properties of the systems, which are, in turn, connected to the morphology. The *blue cloud* is mainly formed by *late-type*, spiral galaxies which are gas-rich and star forming, while the *red sequence* is formed by gas poor *early-type* galaxies (ETGs) with quenched star formation and formed by old stars (Trager et al., 2000). This bimodality in the CMD of galaxies has been found to exist already at $z \leq 2.5$ (Franzetti et al. 2007; Brammer et al. 2009). However, the number of galaxies on the *red sequence*, and their stellar mass density, rose by about a factor of 2 from $z = 1$ to $z = 0$, whereas the number and stellar mass density of *blue* galaxies remained roughly constant (Arnouts et al., 2007). The intriguing aspect is that the stellar density corresponding to *blue cloud* galaxies (where new stars are expected to be formed) has barely been altered, and that most of that growth has been produced in the *red sequence*. This result has a strong implication: in order to reproduce the observed evolution in the color-stellar mass diagram, galaxies have to migrate from the *blue cloud* to the *red sequence* by means of a process in which the star formation (SF) in the galaxies is quenched (Bell et al. 2007; Walcher et al. 2008).

Galaxies in between, the so called *green valley*, have intermediate galaxy colours and were thought

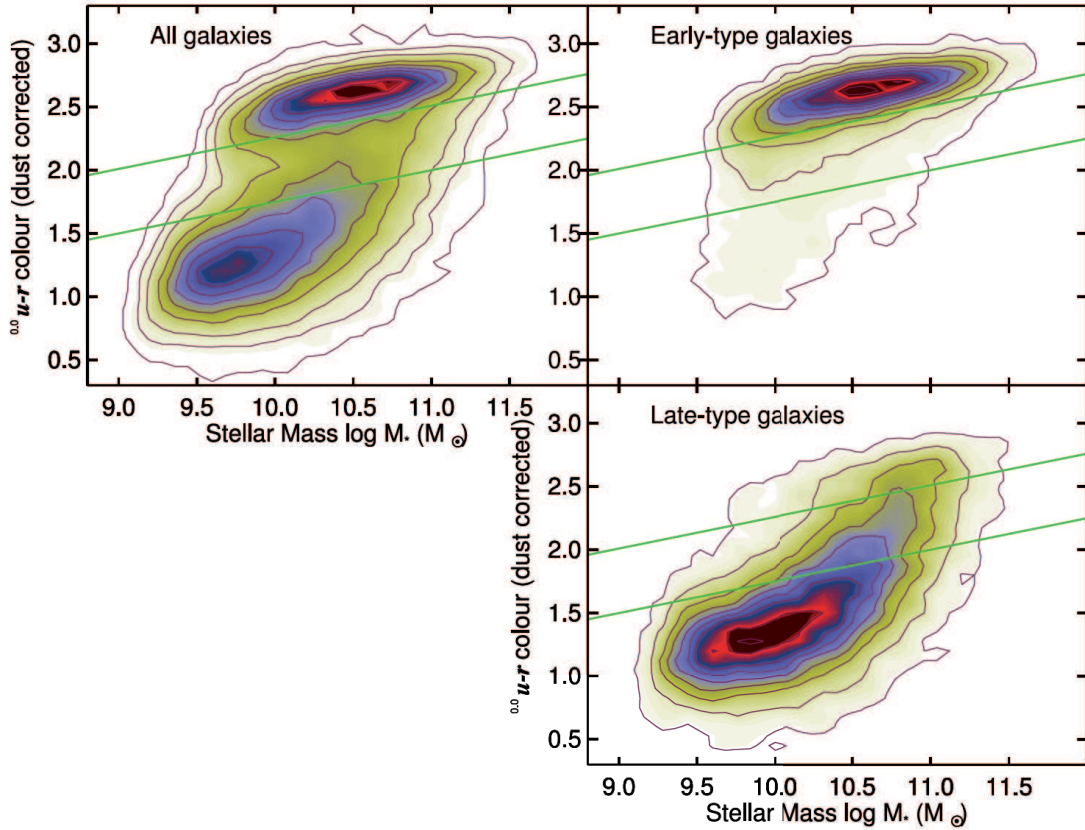


Figure 1.2 The $u-r$ color-mass diagram taken from [Schawinski et al. \(2014\)](#). In the top left all galaxies in their sample are shown. When representing only the early-type galaxies (top right) we found that they are distributed over the so-called red sequence. On the contrary, the location of the late-types (bottom right) is called blue cloud. The green lines show the green valley defined by the all-galaxy diagram.

to represent the transition population between the two aforementioned populations (e.g., [Faber et al. 2007](#); [Gonçalves et al. 2012](#)). However, we must be cautious, green valley is an heterogeneous group composed by galaxies of different morphologies that might evolve differently. In particular, green valley late-type galaxies are consistent with a scenario where the cosmic supply of gas is shut off, perhaps at a critical halo mass, followed by a slow exhaustion of the remaining gas over several Gyr, driven by secular and/or environmental processes. On the contrary, green valley early types require a scenario where the gas supply and gas reservoir are destroyed virtually instantaneously, with rapid quenching. Mergers of gas rich disk galaxies are invoked to be responsible ([Schawinski et al., 2014](#)). This major wet mergers are the quenching mode seen in local post-starburst galaxies. Post-starburst or K+A galaxies, discovered by [Dressler & Gunn \(1983\)](#), exhibit strong Balmer absorption lines, indicative of an intense star-formation epoch in the past billion years, and an absence of emission lines, a signature of a lack of ongoing star-formation. They are the results of mergers ([Bekki et al. 2005](#); [Snyder et al. 2011](#); [De Propris & Melnick 2014](#)) and reside in the low mass end ($M_{\star} \sim 10^{10}M_{\odot}$) of the green valley. If star formation has indeed ceased in these galaxies, they will contribute to the build-up of the low-mass end of the red sequence ([Wong et al., 2012](#)). Still, what happens with the high-mass end of this

red sequence? How is it formed? In Section 1.3 we describe in detail the two scenarios that explain the formation of both high and low mass ellipticals.

It is also important to note that most local AGN reside in the green valley (Martin et al. 2007; Salim et al. 2007). However, at high-Eddington ratios ($L/L_{Edd} > 0.1$) the only population with a substantial fraction of AGN are the low-mass green valley early-type galaxies (Schawinski et al., 2010). The high fraction of AGN hosts in the green valley, combined with the assumption that mergers are their main triggering mechanism, leads to a scenario in which AGN are the driver for the rapid migration of galaxies from the blue cloud to the red sequence due to AGN related quenching of star formation. The relevance of the AGN in galactic evolution will be explained in more detail in Section 1.2.4.

1.1.3. Two Families of Ellipticals

Elliptical galaxies range from the most luminous giant galaxies known today, with absolute blue magnitudes of $M_B \lesssim -22$, like M87 in Virgo Cluster, to faint dwarf elliptical galaxies (dE), like M32, with $M_B \gtrsim -18$. This corresponds to a range of possible stellar masses between $10^7 - 10^{13} M_\odot$. Despite this wide range of masses, all of them follow some regular trends. In particular, three simple but fundamental properties are related in all ellipticals (size R , mean surface brightness μ , and velocity dispersion σ) to form a three-dimensional scaling relation called "fundamental plane" (FP for short); $R \propto \sigma^a \mu^b$ (Djorgovski & Davis 1987, Dressler et al. 1987). In optical passbands, it has since consistently been found that the value of the coefficient "a" lies in the range 1 - 1.5, and "b" from 0.25 - 0.35.

Once believed as "simple" systems composed by old stars, with no cold gas or dust, non rotating, etc., in the last decade the results from integral field spectroscopy of a few nearby ETGs by SAURON survey (de Zeeuw et al., 2002) and a complete and statistically significant sample of 260 ETGs by ATLAS^{3D} survey (Cappellari et al., 2011) has revealed the full richness of these objects. From the two-dimensional nature of these unique data sets, the first striking finding was the separation of ETGs in two distinct kinematic families: fast and slow rotators (Emsellem et al., 2007, 2011). From ATLAS^{3D} sample, only a small fraction (12 per cent, 32/260) of the galaxies rotate slowly, with no indication of embedded disc components. In contrast, the majority (86 per cent, 224/260) of early-type galaxies show significant (disc-like) rotation with regular velocity fields. Fast rotators dominate the low- and intermediate-mass field population (Cappellari et al., 2011) and form a quite homogeneous family of flattened, oblate systems with regular velocity fields. Typical slow rotators dominate in high-density environments, are among the most massive and round galaxies, and have peculiar properties such as kinematic twists and kinematically decoupled components (Krajnović et al., 2011). The results from ATLAS^{3D} demonstrate the power of Integral Field Spectroscopy for fully characterizing the properties of early-type galaxies. A comprehensive summary of the current state, but without including integral field kinematics, can be found in Kormendy et al. (2009) and Kormendy & Ho (2013). Basically two families of ellipticals are found, with different properties:

Giant ellipticals ($M_V \lesssim -21.5$) are massive $M_\star \gtrsim 10^{11} M_\odot$, have cores in their nucleus, that is, central missing light with respect to an inward extrapolation of the outer Sérsic profile. They rotate slowly, so rotation is unimportant dynamically; therefore are moderately anisotropic and triaxial. They have boxy-distorted isophotes and Sérsic function outer profiles with $n > 4$; are mostly made up of very old stars that are enhanced in α elements. Often contain strong radio sources and X-ray

emitting gas.

Normal and dwarf ellipticals ($M_V \gtrsim -21.5$) have lower masses $M_* \lesssim 10^{11} M_\odot$ and are coreless, that is, they have central extra light with respect to an inward extrapolation of the outer Sérsic profile. They rotate rapidly, so rotation is dynamically important to their structure; are nearly isotropic and oblate spheroidal, with axial dispersions σ_z that are somewhat smaller than the dispersions σ_r, σ_ϕ in the equatorial plane. They have disky distorted isophotes and Sérsic function outer profiles with $n \lesssim 4$; are made of (still old but) younger stars with only modest or no α element enhancement. Rarely contain strong radio sources and X-ray emitting gas.

These new observational results have led to a large theoretical effort to understand how these two kinds of ellipticals form. In recent years, efforts have begun to converge, and two formation scenarios have been consolidated that can explain the dichotomy we observe in the properties thereof. In summary, normal low mass ellipticals are consistent with a formation through major gas rich mergers, while the giant massive ellipticals are consistent with a two phase formation scenario where the last mergers have been dry or dissipationless. Both scenarios are explained in detail in Section 1.3.

1.2. Nuclear activity in galaxies

The term Active Galactic Nuclei (AGN) refers to the existence of energetic phenomena in the nuclei or central regions of galaxies which cannot be attributed to stars. Their bolometric luminosities span a broad range of values, from 10^{42} to 10^{48} erg s⁻¹ for the most luminous AGN. A major breakthrough in the study of AGN is the realization that all massive galaxies in the universe, active and quiescent, contain a Super Massive Black Hole (SMBH) at the nucleus (Magorrian et al., 1998). This SMBH grows through mass accretion events. If there is fuel (gas and dust) surrounding a SMBH, it is attracted forming an accretion disk due to the conservation of angular momentum. Through viscous friction, the material in the disk can be heated to such high temperatures that it can be 100 - 1000 times more luminous than its host galaxy. This friction also provides a means for the innermost material to drop out of its stable circular orbit and spiral in towards the BH, feeding it. BHs that are actively accreting material are called AGN. Moreover, the strong time-variability observed in their optical/UV/X-ray emission implies that the spatial scale of the main engine of AGN is within the order of light days: a nucleus comparable to the size of the Solar System is emitting hundreds of times as much energy as an entire galaxy.

Furthermore, theoretical work now suggests that AGN activity has a profound influence on the evolution of its host galaxy. However, placing observational constraints on the influence of AGN on the evolution of galaxies remains an open area of research, with many outstanding questions. In this section we provide: (1) a (very) short history of the discovery of AGN; (2) a summary of the key properties and observations of AGN, (3) a brief review on the observational evidences of the co-evolution of BH and galaxy growth, and (4) the current research on the influence of AGN on the evolution of galaxies.

1.2.1. Discovery of AGN/QSOs

The first recorded observational evidence for the existence of (what are now referred to as) AGN came from Edward A. Fath who was obtaining spectra of star clusters and "spiral nebulae" at the Lick Observatory (Fath, 1909). Fath noted that the spectrum of the object called NGC 1068, which was not yet known to be extragalactic, showed unusually strong and broad high-excitation emission-line profiles. Twenty five years later, the seminal work of Carl Seyfert presented analyses on the spectra of six of the twelve galaxies that had been identified as having equivalent nuclear spectra to that of NGC 1068 (Seyfert, 1943). Consequently, similar objects are now called "Seyfert galaxies". Over the following three decades, the number of identified Seyfert galaxies increased dramatically and further study revealed the unusual nature of these objects: they have exceptionally compact and bright nuclear regions, and have a variable ultraviolet to optical continuum, in addition to their unusually strong and broad emission lines (an early review is given by Weedman 1977). All of these observations were suggestive of a very compact powerful energy source at the centre of these galaxies.

Independently of the optical studies discussed above, during the 1960s, radio astronomers discovered a class of extremely bright radio sources that appeared to be associated with optical point sources (e.g., Matthews & Sandage 1963). These "quasi stellar radio sources" (shortened to quasars), turned out to have very high redshifts (i.e., $z \gtrsim 0.1$; e.g., Schmidt 1963; Greenstein 1963). It is now common practice to use the term "quasar" or quasi-stellar-object (QSO) to refer to the most luminous AGN in the Universe (i.e., bolometric luminosities of $L_{AGN} \gtrsim 10^{45}$ erg s⁻¹) irrespective of their radio properties.

Therefore, both Seyferts and QSOs are AGN. The difference between them is just in the luminosity. The division was arbitrarily set at an absolute magnitude $M_B = -23$.

1.2.2. Emission properties

AGN are roughly divided into two spectral types regardless of their luminosity. The main features of the spectra include the continuum, narrow emission lines, and broad emission lines. Objects that exhibit all three of these features are known as type-1 AGN. The blue continuum of a type-1 AGN has typically a spectral slope $\alpha_\nu \approx -0.5$ (Vanden Berk et al. 2001; Richards et al. 2006) where $f_\nu \propto \nu^{\alpha_\nu}$. Narrow emission lines appear in forbidden transitions such as [OII] λ 3727, [OIII] λ 5007, [NII] λ 6548,6583 and [SII] λ 6716,6730. The emission line ratios are different from those of star forming regions and can be used to distinguish AGN from star forming galaxies (Baldwin et al., 1981). Broad emission lines appear most prominently in the Balmer series, Mg II λ 2796,2802, CIII λ 1909, CIV λ 1549, and Ly α . The broad emission lines can have widths on the order of thousands of km s⁻¹, indicating very high velocities. Type-2 AGN only show the narrow lines, with similar ratios as the type-1 objects, but the continuum and broad emission lines are not present in the spectra.

These different observational classes of AGN, have been unified using a single physical model (Antonucci 1993; Urry & Padovani 1995). According to this physical model the optical/UV continuum originates in the **accretion disk**. AGN accretion disks are relatively cool ($\sim 10^5 - 10^6$ K) producing the black body (BB) emission known as "big blue bump" which peaks between 1000 - 4000 Å. The UV photons produced at the accretion disk are thought to excite dense (i.e., electron densities $n_e \gtrsim 10^8$ cm⁻³; Osterbrock & Ferland 2006) high velocity gas clouds that are under the direct gravitational influence of the BH. This results in the production of extremely broad permitted emission lines

(typically FWHM $\sim 10^3 - 10^4 \text{ km s}^{-1}$). The region where these broad lines are produced is called the **broad-line region (BLR)** and has a size-scale of light-days to light-months (e.g., [Peterson et al. 2004](#)). Forbidden emission lines are not observed in this region due to these lines being collisionally de-excited before they can de-excite by the emission of a photon. Outside the BLR, at distance scales of few parsecs, there is a region of cold gas and dust with a toroidal geometry in a similar plane as the accretion disk, with its inner radius set by the dust sublimation temperature. This region is called the **obscuring torus**, although now it is widely thought to have a clumpy structure ([Hönig et al., 2006](#)). The dust heated by the nuclear emission is thought to be responsible for the MIR/FIR continuum emission. Ionising photons that escape the central regions of the AGN can ionise gas in low density regions that extend beyond the inner BLR (with electron densities $n_e \lesssim 10^6 \text{ cm}^{-3}$; [Osterbrock & Ferland 2006](#)). Here the emission lines produced have narrower widths (i.e., $250 \lesssim \text{FWHM} \lesssim 2000 \text{ km s}^{-1}$) and this region is referred to as the **narrow-line region (NLR)**. Unlike the BLR, both permitted and forbidden lines are produced in the NLR, which can extend over large scales (i.e., $\sim 10^2 - 10^4 \text{ pc}$). **Radio jets** may also be launched from close to the accretion disk.

The "unified model" of AGN implies that, along certain lines of sight, obscuration by the dusty torus will prevent the optical emission from the accretion disk and BLR from being observable. That is the reason for type 2 AGN not showing broad permitted emission lines. In contrast, observing emission from the NLR, torus and radio jets is less dependent on the line of sight.

1.2.3. The co-evolution of BH and galaxy growth

There are several observational results suggesting that BH growth and galaxy growth are intimately connected, which seems incredible because there are nine orders of magnitude difference in the physical size scale of a BH and its host galaxy. In this section we summarize the two most relevant: (1) the cosmic evolution of BH growth and star formation look very similar and (2) BH masses correlate with galaxy bulge mass and velocity dispersion.

Similar cosmic space density of BH growth and star formation

The cosmic space density of BH growth peaks at $z \sim 1 - 2$, as have been accurately calculated from X ray ([Aird et al., 2010](#)) and NIR ([Delvecchio et al., 2014](#)) observations of AGN, with the majority of BH growth occurring in AGN with luminosities of $L_{AGN} = 10^{44} - 10^{46} \text{ erg s}^{-1}$ (e.g., see review by [Alexander & Hickox 2012](#)). Similarly to AGN, the peak in the cosmic star formation rate density occurs at $z \sim 2$ ([Madau & Dickinson, 2014](#)). This result is shown in Figure 1.3, which shows the remarkably similar evolution with redshift of BH growth (i.e., AGN activity) and Star Formation (SF). In anycase, the fact that this two processes evolved in a similar manner, only provides indirect evidence that they might be causally connected.

BH masses are related to galaxy bulge properties

The most quoted pieces of observational evidence to argue that BH growth and galaxy growth are intimately connected, are probably the relationships between BH masses and the properties of their host galaxy bulges in local systems. BH masses are found to be proportional to the luminosities and therefore masses of their host galaxy bulges ([Magorrian et al., 1998](#)) and a tight relationship is also

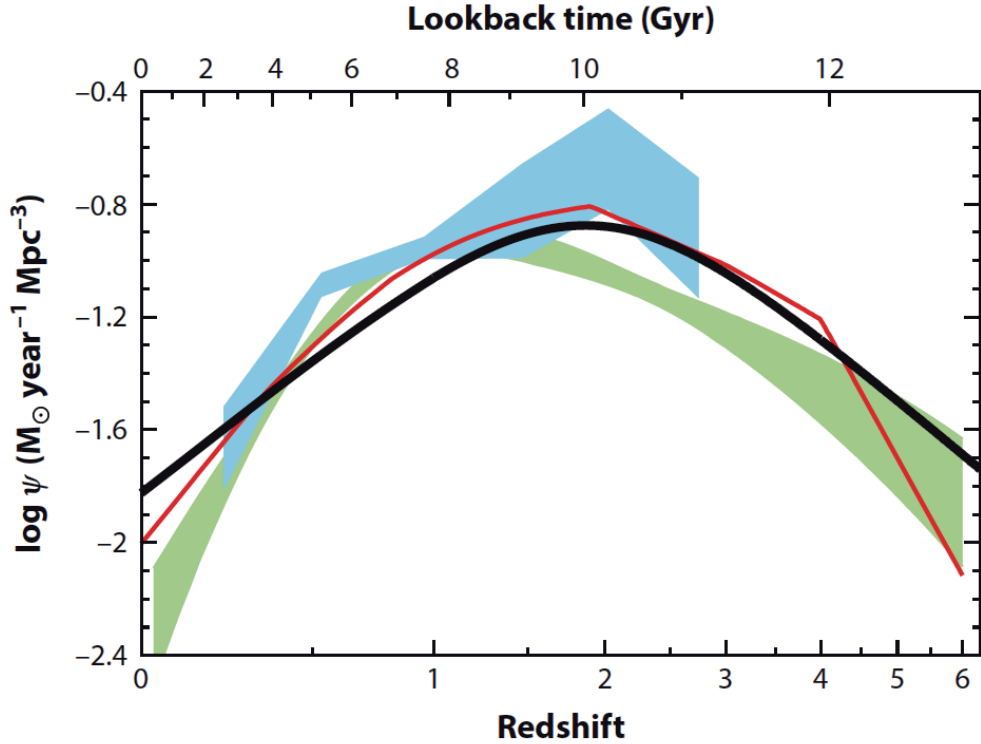


Figure 1.3 Comparison of the star-formation rate density (black solid curve) with the black hole accretion history from X-ray [red curve (Shankar et al., 2009); light green shading (Aird et al., 2010)] and infrared (light blue shading) (Delvecchio et al., 2014) data. The comoving rates of black hole accretion have been scaled up by a factor of 3300 to facilitate visual comparison to the star-formation history. The figure has been taken from Madau & Dickinson (2014).

found between BH masses and the velocity dispersion of the bulge (e.g., Ferrarese & Merritt 2000; Gebhardt et al. 2000; Gültekin et al. 2009). The term "bulge" here refers to both classical bulges and elliptical galaxies. It should be noted that, at least in the local Universe, BH masses do not appear to correlate well with pseudobulges or galaxy disks (Kormendy & Ho, 2013). Figure 1.4 shows the BH - bulge mass relationship, containing data on classical bulges and ellipticals compiled from the literature (Kormendy & Ho 2013 and references there-in). This relationship is almost linear, with BH masses (M_{BH}) containing around 0.2 - 0.8 % of the mass of their host bulges (M_{bulge}) and can be parametrised by their equation 10:

$$\frac{M_{BH}}{10^9 M_{\odot}} = (0.49^{+0.06}_{-0.05}) \left(\frac{M_{bulge}}{10^{11} M_{\odot}} \right)^{1.17 \pm 0.08} \quad (1.2)$$

These correlations were originally unexpected, since the black hole makes up less than a percent of the galaxy's mass and the volume of its gravitational influence is small compared to the galaxy's size. Why should stars across the galaxy have orbits that seemingly depend on the black holes mass? There must be a direct interplay between AGN activity (i.e., the build up of BH mass) and star formation (i.e., the build up of stellar mass).

This has been canonically answered with the idea that galaxies and their black holes both grow simultaneously from a common fuel supply. Because the matter accretion rate spans several orders

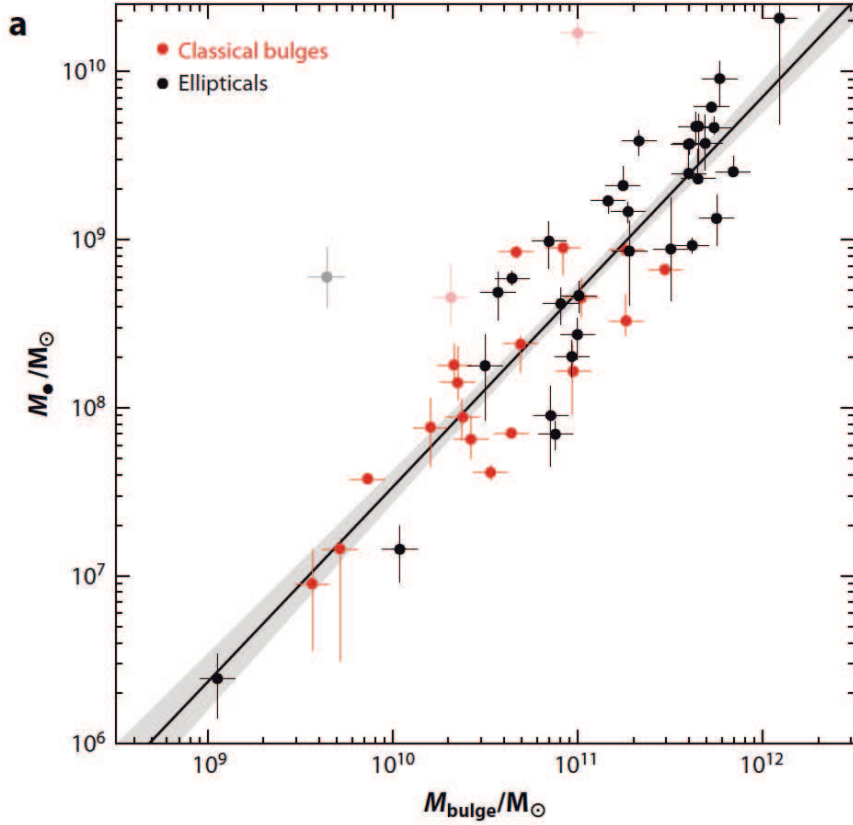


Figure 1.4 Correlation of M_{BH} with bulge mass for elliptical galaxies (black points) and classical bulges (red). Taken from [Kormendy & Ho \(2013\)](#).

of magnitude, various mechanisms are certainly allowed that provide the required fuel over the AGN duty cycle. While secular processes, such as large-scale bars and instabilities in disk galaxies, have been proposed to trigger low luminosity AGN, more violent triggering events may be required to achieve the high mass accretion rate for QSO activity. Major gas rich mergers appear as the best possible interpretation, because lots of gas is rapidly transported towards the nucleus as highlighted by numerical simulations (e.g [Barnes & Hernquist 1991](#); [Mihos & Hernquist 1996](#); [Hopkins et al. 2008a](#)).

Although mergers explain the simultaneous feed of the bulge and BH, some other mechanism is necessary to cut the gas supply of both components and set the observational correlations. The more coherent explanation comes from what have been called "feedback" processes from starburst, but specially from the AGN. AGN activity is known to be a source of high energy and momentum, due to radiation pressure and the expulsion of material through winds. If these winds are able to significantly suppress the supply of cold gas, they will cut off star formation and future black hole growth, fixing the M_{BH} - M_{Bulge} and M_{BH} - σ relations. This scenario has been successfully reproduced by numerical simulations ([Di Matteo et al. 2005](#), [Springel et al. 2005d](#))

1.2.4. The influence of AGN on the evolution elliptical of galaxies

As explained in previous sections, AGN are incredible energy sources. During the growth of a BH, huge amounts of energy can be liberated. For example, the energy released to build a BH with mass

$M_{BH} = 10^8 M_{\odot}$ (via mass accretion) would correspond to $E_{BH} \approx 10^{61}$ erg, assuming $E = 0.1 M_{BH} c^2$ (i.e., a mass-to-energy conversion of 10%). This total accretion energy is two-to-three orders of magnitude higher than the binding energy of the galaxy bulge in which this BH is likely to reside ($E_{BE} \approx 10^{58}$ erg¹) and is likely to be comparable to, or higher than, the thermal energy of the gas in the dark matter halo in which this galaxy resides (e.g., [Bower et al. 2008](#)). Therefore, if even a small fraction (0.1 - 1%) of the accretion energy could couple to the gas over 0.1 - 1000 kpc scales, growing BHs have the potential to regulate their own growth and the growth of their host galaxies, by preventing the supply of cold gas (i.e., by becoming a "feedback" mechanism) as well as impact upon the properties of the gas in the larger scale environment by injecting material and/or energy into this gas.

Theoretical work has shown that AGN feedback mechanisms are an integral part of the evolution of galaxies. They are necessary to successfully reproduce: (1) many of the fundamental properties of galaxies, the intergalactic medium (IGM; e.g., [Silk & Rees 1998](#); [McCarthy et al. 2010](#)), (2) the observed galaxy luminosity function and BH-bulge relations ([Benson et al. 2003](#); [Croton et al. 2006](#); [Di Matteo et al. 2005](#)), (3) the red elliptical remnants in agreement with the apparent colour bimodality ([Springel et al. 2005a](#); [Khalatyan et al. 2008](#)).

Next subsection provides an overview of some of the theoretical and observational research on AGN feedback and its implications for galaxy evolution (reviewed intensively in the last years by ([Alexander & Hickox, 2012](#); [McNamara & Nulsen, 2012](#); [Fabian, 2012](#); [Kormendy & Ho, 2013](#); [Heckman & Best, 2014](#)).

Feedback mechanisms from simulations

Simulations frequently adopt two different modes of AGN feedback, the so-called "quasar-mode" and "maintenance-mode" (see Figure 1.5):

- The "quasar-mode" or "superwind-mode" AGNs are triggered through major gas rich mergers of galaxies. This produces high-accretion rate, radiatively-efficient AGN that are able to expel gas from the central regions of the galaxy through high mass outflows which ultimately results in the rapid shut-down or suppression of future BH growth and star formation (e.g., [Di Matteo et al. 2005](#); [Springel et al. 2005d](#); [Alexander & Hickox 2012](#)).
- In the "maintenance-mode" or "radio-mode", energy is transferred by jets. Jets are radio luminous because of the synchrotron radiation from electrons that are accelerated in shocks. They originate in steady low-accretion rate AGN, located in the quasi-hydrostatic halos of massive galaxies that are able to accrete their hot halo gas. However, the cooling of this gas and therefore new star formation and AGN activity is almost suppressed or maintained at a very low level by the continuous heating from the mechanical feedback of the jet ([Cattaneo & Best, 2009](#)).

Of particular interest in this thesis, is the fact that these two different AGN feedback mechanisms are claimed to occur in the two kinds of ellipticals reported in Section 1.1.3. In **low- to moderate mass, coreless-rotating-disk elliptical galaxies** "quasar mode" feedback is responsible for establishing the $M_{BH}-\sigma$ relation and turning galaxies from the blue cloud to the red sequence. For

¹The binding energy $E_{BE} \approx 10^{58}$ erg is obtained assuming $M_{bulge} = 3 \times 10^{10} M_{\odot}$ and applying $E_{BE} \approx M_{bulge} \sigma^2$ with $\sigma \approx 200$ km/s

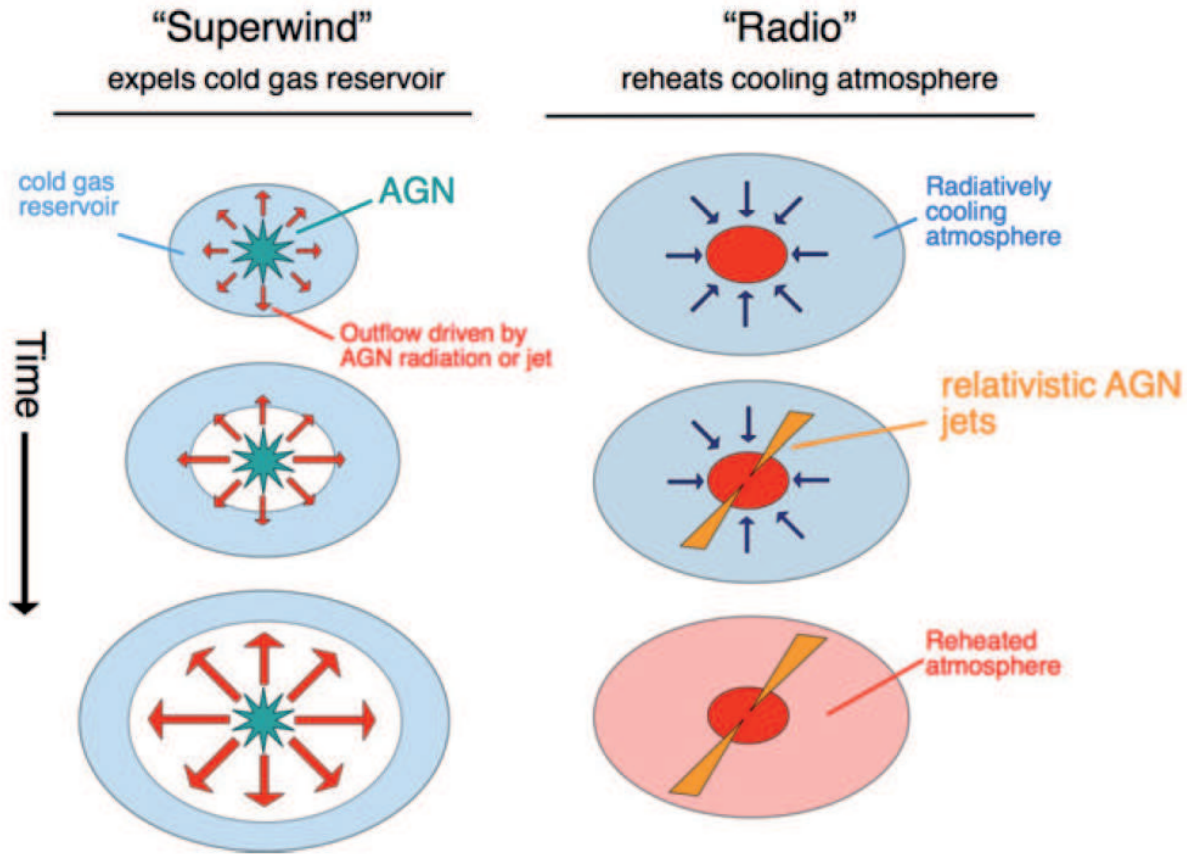


Figure 1.5 Schematic diagram to illustrate the two main modes of AGN feedback described in this thesis (taken from [Alexander & Hickox 2012](#)).

the **highest mass, core-nonrotating-boxy ellipticals** the $M_{BH}-\sigma$ relation was established at high redshift also through "quasar mode" feedback. However, nowadays, the "maintenance mode" feedback dominates. It helps to keep the hot gas hot and to prevent late star formation and BH accretion. Here the controlling factor is that these galaxies are massive enough to hold onto hot, X-ray-emitting gas ([Kormendy et al., 2009](#)). In Section 1.3, we will explain in detail the two scenarios that lead to the formation of these two different types of ellipticals.

Feedback mechanisms from observations

From the observational side, while there is ample evidence that star formation processes (stellar winds and supernovae) drive galaxy-wide outflows that are an integral part of galaxy evolution (e.g., [Heckman et al. 1990](#); [Rupke et al. 2005](#), see review in [Veilleux et al. 2005](#)), it is thought that AGN activity is required to drive the highest velocity outflows.

Recent Herschel velocity-resolved spectroscopic studies of U/LIRGs have discovered massive molecular outflows with velocities of over 1000 km/s and outflow rates of $\sim 1200 M_{\odot} \text{ yr}^{-1}$, several times larger than their star formation rates (SFRs). The fastest and most massive outflows are found in AGN-dominated U/LIRGs (according to MIR classification methods) suggesting that AGN are able to

expel the cold gas reservoirs from the center within a timescale of $10^6 - 10^8 M_{\odot} \text{ yr}^{-1}$. (e.g. [Fischer et al. 2010](#); [Sturm et al. 2011](#); [Veilleux et al. 2013](#)). In the closest quasar known, Mrk 231, the picture is similar. A giant molecular outflow is detected, with a rate of $700 M_{\odot} \text{ yr}^{-1}$, far larger than the on-going SFR in the host galaxy $200 M_{\odot} \text{ yr}^{-1}$ ([Feruglio et al., 2010](#)). Gemini/IFU observations have revealed that the Na ID outflow in Mrk 231 is not only spatially resolved on kpc scale but also wide-angled, thus driven by a QSO wind rather than a jet ([Rupke & Veilleux, 2011](#)). More kpc-scale outflows in low redshift AGN have been identified in ionised, atomic and molecular gas (e.g., [Westmoquette et al. 2012](#); [Rupke & Veilleux 2013a](#)). These are important results, as they could be the first observational evidence of the "quasar-mode" quenching.

Observational evidence for "maintenance-mode" heating the gas in massive halos, is found through combining X-ray and radio imaging of massive ellipticals and clusters, where cavities in the X-ray emitting gas (indicating the prevention of cooling) are observed to be spatially coincident with radio emission ([McNamara & Nulsen, 2012](#)).

To summarize the role of AGNs in galaxy evolution, quasars are triggered by major mergers of gas-rich galaxies, and they are responsible for expelling the gas, and thus terminating star formation and turning galaxies from the blue cloud to the red sequence. Radio galaxies, on the other hand, get active through a steady inflow of gas onto the black hole. Their jets provide mechanical feedback that warms the surrounding gas. This feedback process regulates the masses of old red galaxies.

1.3. Formation and evolution of elliptical galaxies

Early theorists suggest that ellipticals were formed in a single, early, rapid collapse of a gas cloud ([Larson, 1969, 1975](#)), often referred to as a "monolithic collapse". In this framework, galaxies originate from the collapse of a roughly spherical cloud of gas, forming stars in a rapid burst. Ellipticals would form mainly in non-rotating halos with relatively little angular momentum (e.g. [Chiosi & Carraro 2002](#)).

While conceptually simple, the monolithic collapse model has difficulties explaining the properties of low mass ellipticals: substantial net rotation, possibly embedded disks, stellar populations younger than the age of the Universe, dust lanes indicative of recent star formation or merger activity ([Kaviraj et al., 2012](#)) and relatively flat metallicity profiles ([González Delgado et al., 2015](#)). However, the main argument against monolithic collapse comes from the development of the cosmological model.

1.3.1. Λ CDM Cosmology

The experiments studying the redshift-distance relations from type Ia supernovae ([Riess et al., 1998](#); [Perlmutter et al., 1999](#)) have discovered the accelerated expansion of the universe. The responsible for this acceleration is thought to be some sort of dark energy or vacuum energy of space, which has the particularity of producing a negative pressure (see [Robaina & Cepa 2007](#) for a discussion of the systematic uncertainties). Moreover, the Cosmic Microwave Background (CMB) as observed by the Wilkinson Microwave Anisotropy Probe (WMAP, [Spergel et al. 2007](#)), reveal a flat Universe with a significant fraction of dark matter in a non-baryonic form. Every cosmology which takes into account the existence of dark energy (in whatever exotic form) and dark matter is usually labelled

as a Λ Cold Dark Matter (Λ CDM) cosmology. The main results from 7-years WMAP program infer that the total energy content of the universe is made up of $\sim 4\%$ baryonic matter, $\sim 23\%$ cold dark matter (CDM), with the remaining $\sim 73\%$ consisting of mysterious dark energy Λ (Komatsu et al., 2011; Jarosik et al., 2011). Here, dark matter is described as a collisionless particle, which interacts only gravitationally with baryonic matter. Presently, the nature of both dark matter and dark energy is unknown, but these components are essential for the Λ CDM model to correctly match observations of the large scale structure of the universe.

After cold dark matter became the widely accepted cosmological paradigm, numerical simulations like the Millennium simulation (Springel et al. 2005c) showed beyond the shadow of a doubt that massive halos assemble hierarchically, merging smaller halos and growing in mass and size. High mass halos partially grow through rather continuous mergers with a large number of smaller halos. When small halos merge with a much larger halo, they become subhalos of the main halo. The galaxies embedded in the subhalos then become satellites of the large central galaxy, with which they will eventually merge after suffering dynamical friction. These minor mergers (mass ratio $< 1/3$) result in a fairly smooth accretion of mass over time. Occasionally, a major merger (mass ratio $> 1/3$) between halos of similar mass will occur, resulting in an abrupt jump in the mass of the system. Such major mergers rapidly change the gravitational potential of the system, causing a total redistribution of the particle orbits through a process called violent relaxation.

Galaxies which are embedded within merging dark matter halos will also sometimes merge, but will obviously do so after their parent halos. This pushed the merger theory of elliptical galaxy formation into widespread acceptance. However, galaxy mergers are more difficult to simulate than halo mergers. They also have gas and are not only driven by gravitational forces. Hydrodynamical simulations provide a useful tool to study the baryonic processes that determine galaxy properties (Mihos & Hernquist, 1996; Di Matteo et al., 2007). The merger timescale, SF enhancement, and remnant properties of a galaxy merger, depend on several factors as: the mass ratio and morphologies of the progenitors, the availability of gas (gas-rich or gas-poor), and the orbital characteristics. Results from hydrodynamical merger simulations are described in detail in Section 1.4.3.

It has also been found that the halo mass of the galaxy is able to regulate its evolution. The stellar-to-halo mass (SHM) relation has a characteristic peak at $M_{DM}^{crit} \sim 10^{12} M_{\odot}$, where the stellar mass fraction reaches its maximum. At both lower and higher dark matter masses the stellar mass fraction declines steeply (see Figure 1.6). The physical interpretation of this behavior is the interplay between the various feedback processes that impact the star formation efficiency. Supernova feedback is more effective at reheating and expelling gas in low-mass halos, while AGN feedback is more effective in high mass halos (Moster et al., 2010). In this picture, M_{DM}^{crit} is the critical halo mass where the efficiency of these two processes crosses. Galaxies well above the M_{DM}^{crit} , like massive-core ellipticals, can retain X-ray-emitting gas (Cattaneo et al., 2006), and develop the "maintenance mode" feedback (see Section 1.2.4) that heats any cold gas and prevents new star formation. That is the reason why giant-boxy-core ellipticals grow dissipationlessly (see Section 1.3.2). In contrast, low mass-disky-extra-light ellipticals, and their merger progenitors, are too low in mass to hold onto hot X-ray gas (see Section 1.3.3).

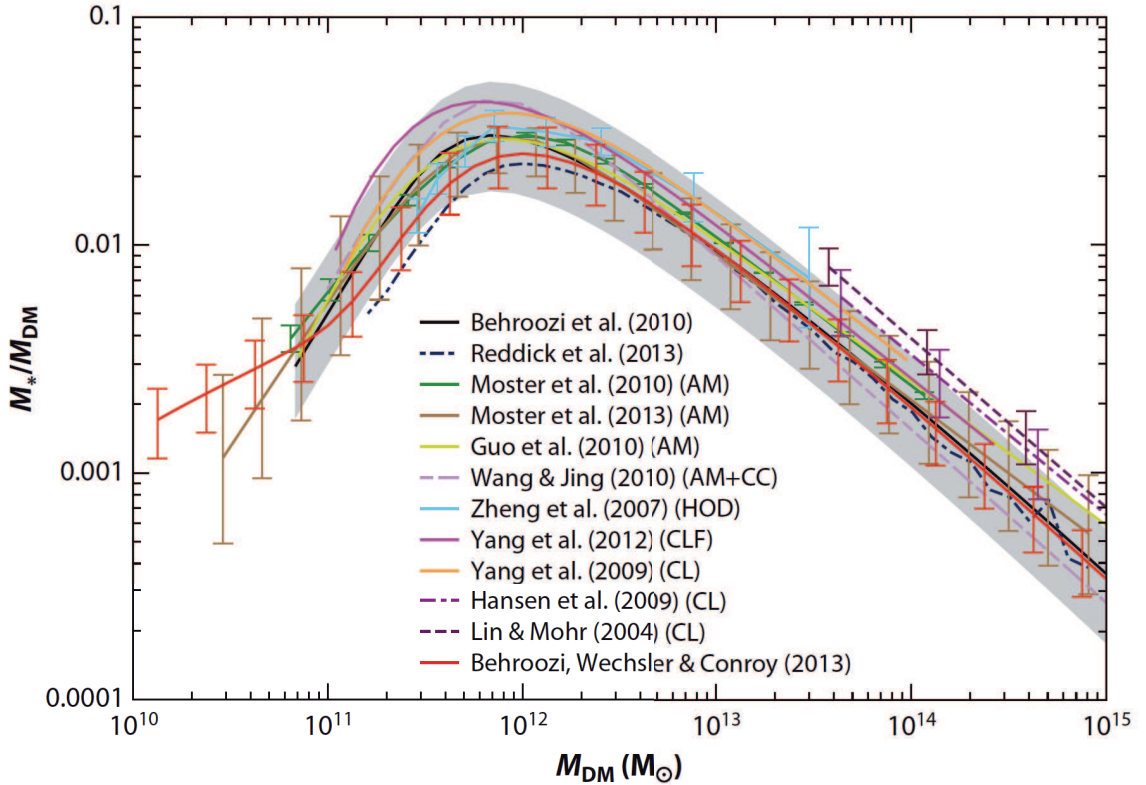


Figure 1.6 Summary of the stellar to halo mass relations as a function of dark matter halo mass obtained from different techniques (taken from [Kormendy & Ho 2013](#)). Note the characteristic peak at $M_{DM}^{crit} \sim 10^{12} M_{\odot}$, where the stellar mass fraction reaches its maximum.

1.3.2. Two-phase formation and dry merger growth for high mass-core Es

Both observations and cosmological simulations agree with a two phase formation scenario for giant E's, those with stellar masses $\gtrsim 10^{11} M_{\odot}$ ([Naab et al., 2009](#); [Kormendy et al., 2009](#); [Oser et al., 2012](#); [Toft et al., 2014](#)). It is schematized in Figure 1.7.

First, the central core is formed in a dissipative phase at high redshift ($2 < z < 6$). As long as it happens on a short timescale, this in situ star formation could be due to inflowing cold gas or mergers of extended gas dominated disks. This produces the massive and compact progenitor of present-day massive ellipticals, with sizes $r_{1/2} \leq 1$ kpc. This first phase has been observationally confirmed by [Toft et al. \(2014\)](#), who found that $z = 3 - 6$ SMGs are consistent with being the progenitors of $z = 2$ quiescent galaxies, matching their formation redshifts and their distributions of sizes, stellar masses, and internal velocities. The $z \gtrsim 3$ SMGs show multiple components or irregularities indicative of ongoing merging and/or clumpy structures with some of the most intense starbursts known and the quiescent galaxies at $z \sim 2$ host the densest conglomerations of stellar mass known. Also, they have a spectra typical of post starburst galaxies, with no emission lines and strong Balmer absorption lines, which suggests that they underwent major starbursts that were quenched 1 - 2 Gyr prior to the time of observation (i.e., $3 < z < 6$). The mean duty cycle of SMG starbursts is $t = 42_{-29}^{+40}$ Myr, which indicates that the bulk of stars in these massive galaxies were formed in a rapid surge of star formation. This, moreover, explains the alpha-enhancement observed in massive local ellipticals

ranging from m^* ² to giant Es. Whether or not major gas rich mergers are able to form ellipticals more massive than $\sim 10^{11} M_{\odot}$ is still an open question.

The whole updated evolution have been summarized by [Hopkins et al. \(2008\)](#). In this scenario (see Figure 1.8), the first phase (panels a & b) is a pair of isolated disk galaxies dominated by internal secular processes driven by internal structures such as spiral arms, bars and the halo. During the first close/strong encounter between them, turbulence, compression of the interstellar gas clouds and gas inflows due to gravitational torques result in an increase of star formation in the system. During this pre-merger phase, the nuclei of both progenitors are still separated (panel c). The merger evolves and for the final stage, when the two galaxies coalesce, the gas inflow rate is larger than during the initial merger stage, producing strong nuclear starburst activity and fueling of the SMBH, leading to AGN activity. However, together with the gas, the dust is also flowing to the central region, obscuring most of this activity in the UV-optical and re-emitting it into the infrared. At this stage, the system is a U/LIRG (panel d). Feedback processes, such as the energy and momentum released by the supernovae of massive stars and mainly by black hole activity can disperse the remaining gas (referred to as blowout phase, panel e) during short period of time. Once the dust is dispersed the systems appears as a traditional QSO (panel f). While the QSO dominates, the host morphology is difficult to observe. However, the spheroid is still characteristically blue/young. Star formation and AGN activity would be decreasing due to lack of fuel that was removed by the blowout. Also, the tidal features decay rapidly within a timescale of 200 - 400 Myr ([Lotz et al., 2010](#)). With time, the QSO luminosity also fades. Now the tidal features are only visible with deep observations. Stellar population of the merger remnant ages and shows post-starburst signature (K+A or E+A, panel g). From that, the system will finally relax and evolve into a passive elliptical with no star formation (panel h). The galaxy changes its color towards red rapidly, moving from blue cloud to red sequence in the galaxy CMD.

The typical merger timescale for a pair of massive galaxies is about a billion year, although large variations are possible for small impact parameters or high encounter velocities. This is barely larger than the rotation period of the outer disk of a spiral galaxy. Thus, stars (or gas clouds or dark matter particles) in an interacting and merging system undergo a variation in the mass distribution/gravitational potential that is relatively rapid compared to their own dynamical timescale.

The observational properties of low mass ellipticals are well match by this scenario ([Kormendy et al., 2009](#); [Kormendy & Ho, 2013](#)). The first observational support for this scenario starts in the 80's with the discovery and characterization of U/LIRGs (described in detail in Section 1.4). U/LIRGs are infrared bright mergers of gas-rich, disk galaxies sampling the entire Toomre merger sequence beyond the first peri-passage ([Veilleux et al., 2002](#)). [Kormendy & Sanders \(1992\)](#) were the first to propose that U/LIRGs evolve into ellipticals through merger induced dissipative collapse. They have large molecular gas concentrations in their central kpc regions ([Downes & Solomon, 1998](#)) with densities comparable to stellar densities in ellipticals. Their near infrared brightness profiles follow a de Vaucouleurs law $\propto R^{1/4}$ ([Wright et al., 1990](#); [Scoville et al., 2000](#); [Veilleux et al., 2006](#)), and they lie on the fundamental plane in the same region as intermediate mass ellipticals ([Genzel et al., 2001](#)). Moreover, until U/LIRGs discovery, QSOs were the only objects known to have bolometric luminosities greater than $10^{12} L_{\odot}$, so it was natural to speculate about a relation between them. [Sanders et al. \(1988\)](#) was

²A variety of methods have converged toward $m^* \sim 3 \times 10^{10} M_{\odot}$ ([Rothberg et al., 2013](#)).

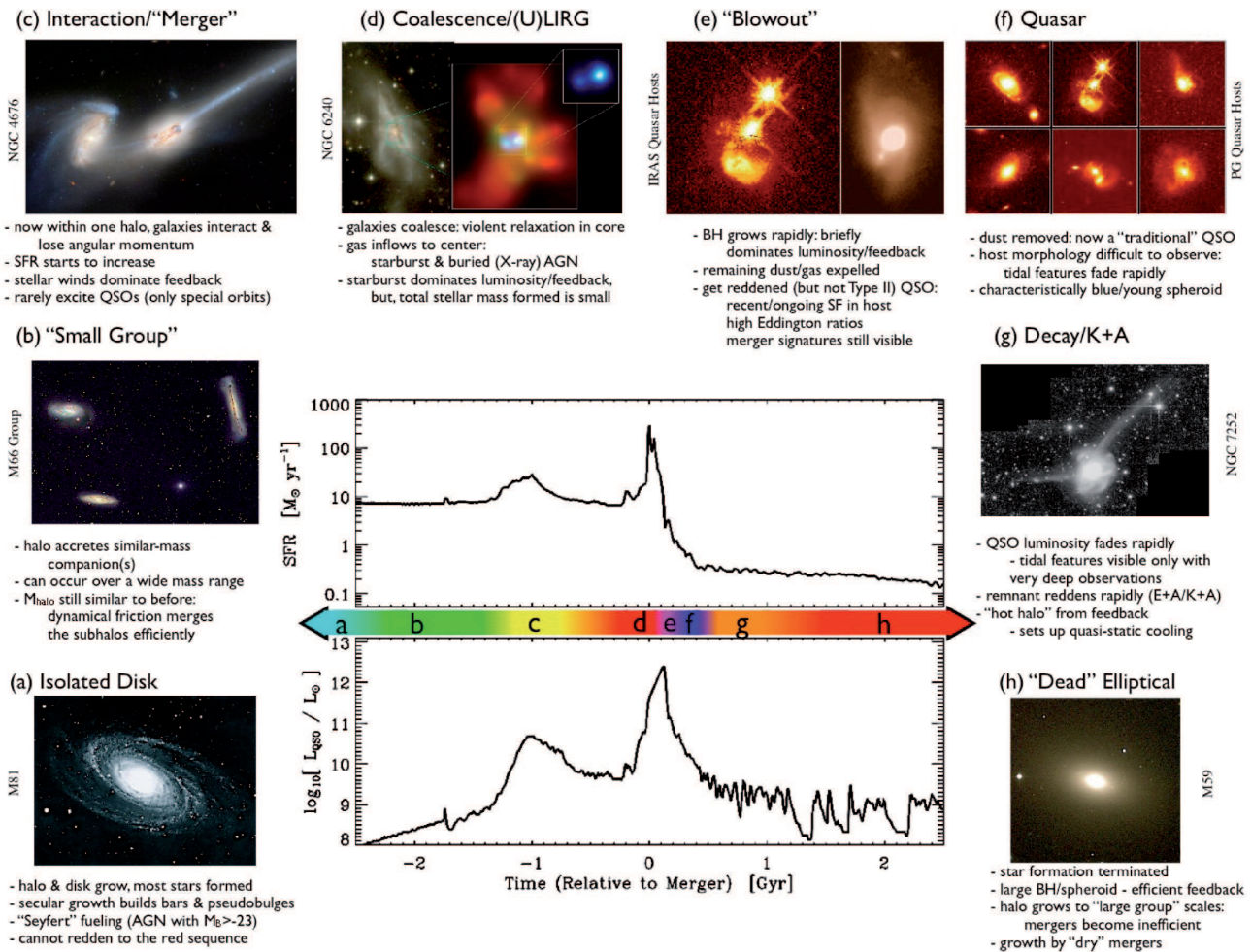


Figure 1.8 An example of the proposed theoretical framework for major gas-rich merger driven formation of low-intermediate mass elliptical galaxies by Hopkins et al. (2008). See text for an explanation.

the first to notice that U/LIRGs and QSOs also have similar space densities, that is, U/LIRGs were numerous enough to be the parent population of QSOs. Analyzing the SEDs of IRAS U/LIRGs, he separated them into "cool" and "warm" according to their 25/60 and 60/100 μm colours, and found the warm ones could be the progenitors of QSOs. The picture put forward was that U/LIRGs were the result of strong interactions and mergers which funneled gaseous material into the central regions of galaxies, fueling intense star formation and the QSO activity. U/LIRGs were then dust-enshrouded QSOs which, after blowing away the dust, became classical QSOs. Interestingly, deep imaging of luminous AGN/QSO hosts reveals that significant numbers appear to inhabit elliptical/disturbed systems consistent with a merger origin (Sánchez et al., 2004; Canalizo & Stockton, 2001; Zakamska et al., 2006; Bennert et al., 2008).

Observational tests to the proposed scenario using only U/LIRGs and traditional QSOs are challenging. In the former, their dusty nature difficult the determination of their power source (see Section 1.4.3), while the latter are so bright that the host can only be detected through deep imaging. The ideal approach would be to detect and characterize observationally all the possible transition stages in the sequence proposed by Hopkins. Determining and comparing the properties of their stellar populations, the dominating power source and the feedback mode (if present), would clarify if they are

evolutionarily linked.

However, post-merger evolution is quite fast and therefore is difficult to find systems in intermediate stages. Typical durations of the K+A phase as commonly defined are 0.1 - 0.3 Gyr (Snyder et al., 2011). Interestingly, Brotherton et al. (1999) found a particular class of QSOs (the so-called Post Starburst Quasars) whose characteristics reveal them as one of the best examples of transition between U/LIRGs and classical QSOs (they are described in detail in Section 1.5).

1.4. (Ultra) Luminous Infrared Galaxies

In 1983, the Infrared Astronomical Satellite (IRAS; Neugebauer et al. 1984) surveyed $\sim 96\%$ of the sky at near-IR (NIR) to far-IR (FIR) wavelengths. IRAS resulted in the discovery of a dusty population of galaxies which emit the bulk of their energy at infrared wavelengths (Houck et al., 1984; Soifer et al., 1984). They are the Luminous Infrared Galaxies LIRGs ($L_{IR} \sim 10^{11} - 10^{12} L_{\odot}$) and Ultra Luminous Infrared Galaxies ULIRGs ($L_{IR} \sim 10^{12} - 10^{13} L_{\odot}$). In these systems the extreme bursts of star formation and/or AGN activity are hidden by large amounts of dust, which absorb the UV radiation and re-emit it at longer wavelengths (in this case the FIR). The extinction in some cases is up to $A_V \sim 10$ mag or even higher depending on the observation (Lonsdale et al., 2006; Alonso-Herrero et al., 2006).

The L_{IR} is defined as the emission between 8 - 1000 μm , which can be determined for IRAS data from the equations:

$$L_{IR}(8 - 1000\mu\text{m}) = 4\pi D_L^2 F_{IR}(L_{\odot}) \quad (1.3)$$

$$F_{IR} = 1,8 \times 10^{-14}(13,48f_{12} + 5,16f_{25} + 2,58f_{60} + f_{100})Wm^{-2} \quad (1.4)$$

where D_L is the luminosity distance and f_{12} , f_{25} , f_{60} and f_{100} are the IRAS flux densities at 12, 25, 60 and 100 μm , respectively (Sanders & Mirabel, 1996).

Although they comprise the dominant population of extragalactic objects at $L_{bol} > 10^{11} L_{\odot}$ they are relatively scarce in the local Universe. With the advent of satellites and ground-based instruments working on the IR, millimeter and radio wavelengths, many high- z luminous infrared galaxies have been discovered. Using Spitzer observations, Magnelli et al. (2011) compare the LIRGs and ULIRGs space density with normal galaxies. In the local Universe, only 1 in 10000 is a LIRG. However, they were much more common at high redshift. Between $1 < z < 2$, LIRGs represent 1 in 300 galaxies. Moreover, they are so bright in the infrared that above $z > 1$, LIRGs are the major contributors (80 - 90%) of the co-moving star formation rate density of the Universe, and at $z \simeq 2$ ULIRGs have similar contributions (see Figure 1.9), and they account for at least half of the newly born stars by $z \sim 1.5$ (Pérez-González et al., 2005; Béthermin et al., 2011). These results imply that a large fraction of stars in present day galaxies would have formed during these evolutionary phases. However, given their faintness, it is difficult to characterize the properties of high redshift U/LIRGs. In that sense, local U/LIRGs can serve as a proxy. They are unique laboratories whose characteristics can be studied in detail, offering insight into the physical processes triggered by galaxy mergers (star formation, black hole growth).

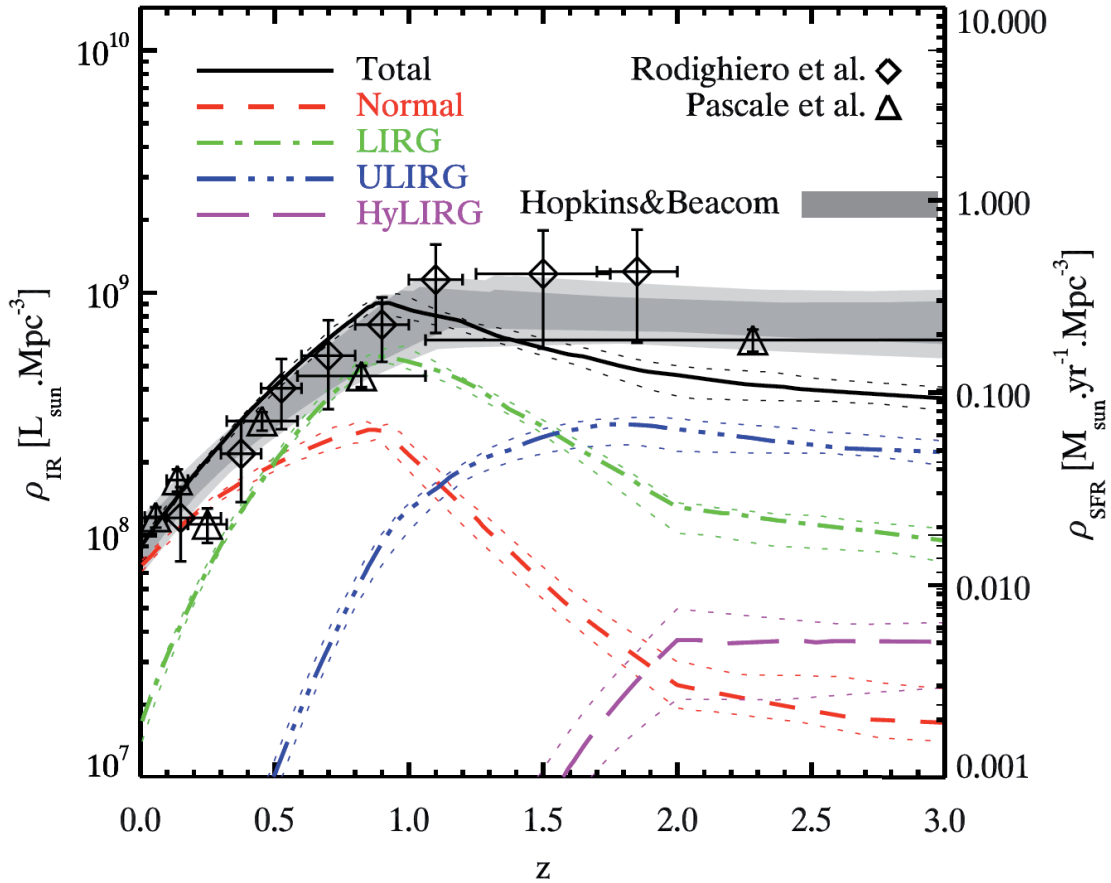


Figure 1.9 Evolution of the star formation rate density as a function of the redshift for sub-LIRG normal galaxies (red), LIRGs (green), ULIRGs (blue), HyLIRGs (magenta) and total (black). Taken from Béthermin et al. (2011).

1.4.1. Morphology

Studies of U/LIRGs in the local Universe have found that most of these systems, especially those with $L_{IR} \geq 10^{11.4} L_{\odot}$, were found to be interacting galaxies or mergers (Surace et al., 1998, 2000; Veilleux et al., 2002; Kim et al., 2013). The optical and NIR images show peculiar morphologies with tidal tails, bridges, shells, etc. Although some low-luminosity LIRGs are normal spirals, in this thesis we are only interested in merging U/LIRGs.

Using high-resolution NIR data, Haan et al. (2011) found that the projected separation between the progenitors nuclei is significantly smaller for ULIRGs (median value of 1.2 kpc) than for LIRGs (median value of 6.7 kpc), leading to the interpretation that ULIRGs represent more advanced merger stages, while LIRGs are earlier stages.

The interaction stage of a merger can be classified using the scheme first proposed by Surace et al. (1998) and described also in Veilleux et al. (2002). The main characteristics of each class are as follows (see Figure 1.10):

- Class I: First approach. This is the earliest stage of the interaction, prior to the first close passage of the galaxies, when the galaxy disks remain relatively unperturbed and separate.

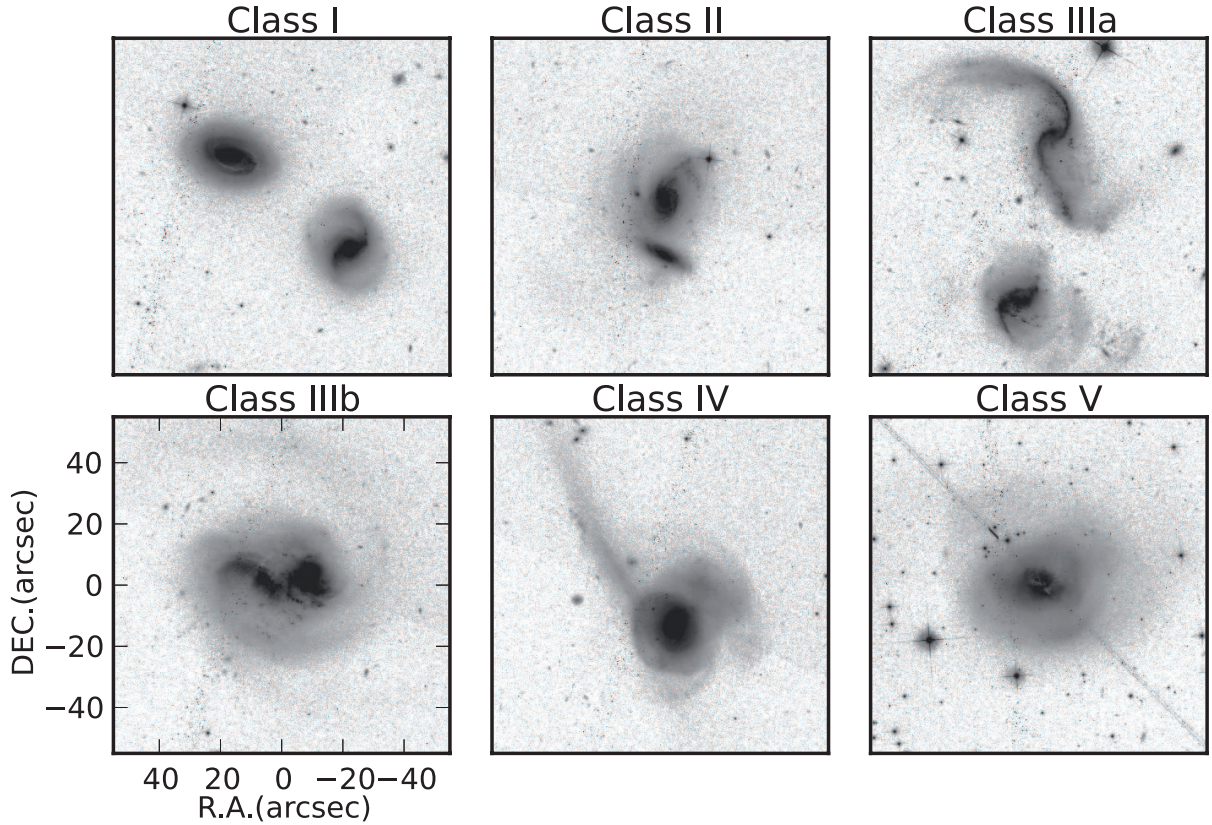


Figure 1.10 HST ACS(F814W) images of six U/LIRGs covering all the interaction stages. From class I to class V they are: MCG+05-06-036, ESO550-IG02, MCG-02-01-051, IC1623, NGC0034 and MCG+08-11-002. All axes are in arcsec, covering the same area and with North up and East to the left.

- Class II: First contact. At this stage, the disks overlap but strong bars and tidal tails have not yet formed.
- Class III: Pre-mergers. This stage is characterized by two identifiable nuclei with well-developed tidal tails and bridges. Within this category the systems were further divided into two subclasses based on their nuclei projected separations. IIIa are systems with apparent separation of > 10 kpc, while IIIb are systems with apparent separation of ≤ 10 kpc. Note that these subclasses are an approximation only to the merger phase since without detailed kinematic information for many of these systems, we cannot tell if the two galaxies are pre- or post-apgalacticon (farthest approach).
- Class IV: Mergers. This stage occurs after the nuclei have apparently coalesced. These systems have prominent tidal features, but only one nucleus can be detected at optical and near-infrared wavelengths. Additionally, the sole galaxy core is often noticeably extended and tends to be cut by many dust lanes.
- Class V: Old-mergers. These are systems which do not show signs of tidal tails, yet have disturbed central morphologies similar to those of the merger stage IV systems, showing the relaxed merger remnant core visible.

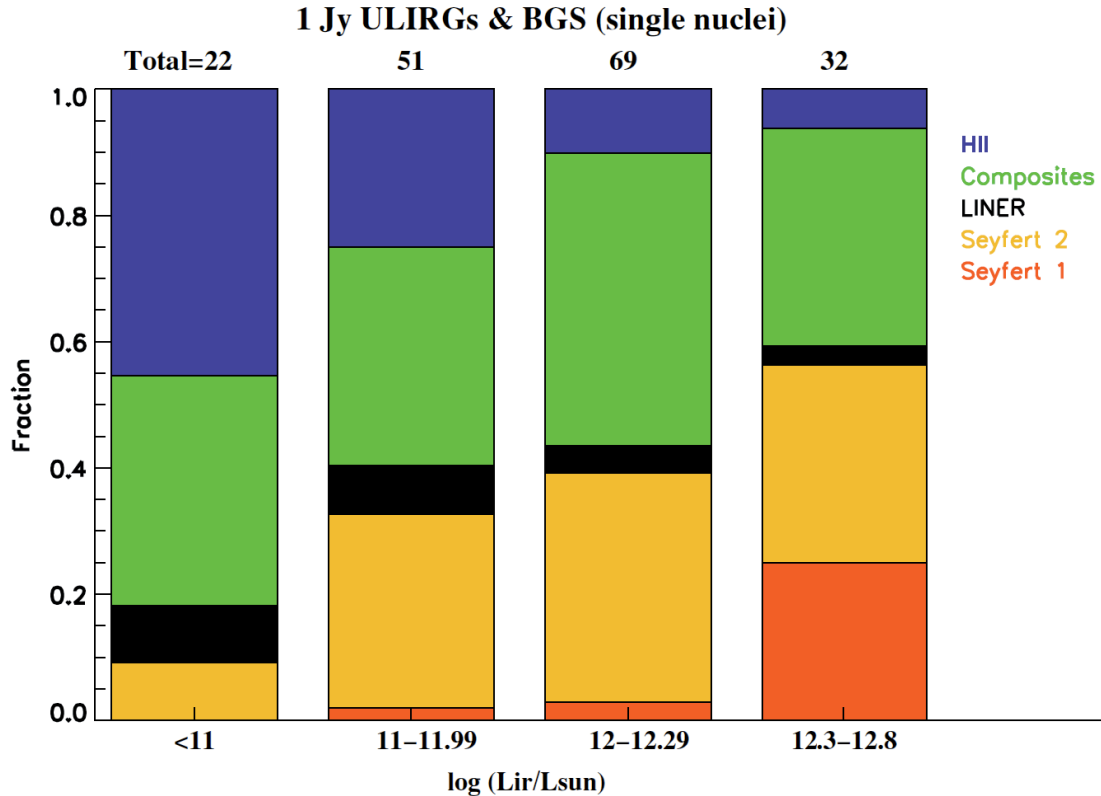


Figure 1.11 Spectral type as a function of L_{IR} for the 1 Jy ULIRG and the LIRGs in the BGS sample. The number of galaxies contained in each bin is marked on top of the histogram. The luminosity bins are labeled at the bottom. Blue is used for HII regions, green for composites, black for LINERs, yellow for Seyfert 2 galaxies, and orange for Seyfert 1 galaxies. Taken from [Yuan et al. \(2010\)](#).

1.4.2. Power source: Starbursts or AGN

Since their detection, the nature of the dominant power source in U/LIRGs has been one of the key questions and much effort has been devoted to resolve it. The dominating power source can be recognized spectroscopically by their optical emission line ratios. [Baldwin et al. \(1981\)](#) introduced the BPT (Baldwin, Phillips & Terlevich) diagram, where galaxies with emission lines can be divided in star-forming galaxies (SF), AGNs (Seyferts) and Low-Ionization Nuclear Emission-line Region (LINERs) based on two emission-line ratios. The photoionization sources causing the emission are: hot stars in SF, non-thermal continuum from AGN in Seyferts and shock excitation in LINERs. They lead to significantly different line ratios. Later on, the demarcation lines in the BPT diagram were modified by [Kewley et al. \(2001, 2006\)](#) to make a cleaner separation between different ionization conditions and to reduce ambiguity in the classification. This results in a fourth type of systems that are composite, their excitation being a combination of photoionization due to hot stars plus either ionization by a power-law radiation field associated with an AGN or shock excitation.

Following this approach, several works using IRAS 1 Jy survey and Bright Galaxy Sample (BGS) showed that the majority of U/LIRGs have optical spectra powered by starbursts (or composite), but with a systematic increase in the fraction of AGN dominated U/LIRGs with increasing IR luminosity ([Kim et al. 1998](#); [Veilleux et al. 1999a](#); [Yuan et al. 2010](#)). They found that Seyfert galaxies

systematically increased from $\sim 30\%$ at $L_{IR} = 10^{11-12} L_{\odot}$ to $\sim 55\%$ at $L_{IR} > 10^{12.3} L_{\odot}$ (see Figure 1.11).

Although optical spectroscopy can still be used to detect spectroscopic signatures of starbursts and AGN in objects with moderate obscuration, a multi-wavelength approach is the best manner in which to gain insight. Even in the mid-infrared, with greatly reduced extinction, only 20 - 30% of the U/LIRGs may be powered predominantly by an AGN (e.g., Genzel et al. 1998; Veilleux et al. 1999b; Petric et al. 2011). Again, the AGN fraction increases with increasing IR luminosity (reaching 50% at $L_{IR} > 10^{12.3} L_{\odot}$). This result are also consistent with hard X-ray emission from GOALS LIRGs sample (Koss et al., 2013). Moreover, not only the AGN fraction increases with IR luminosity, but also the AGN luminosity (Alonso-Herrero et al., 2012).

The conclusion is that starbursts are the dominant energy source of most U/LIRGs. However, an AGN may also be present, and even be the dominant energy source in a small percentage of the most luminous systems. LINER ionization has also been detected in this kind of systems and is thought to come out for the presence of galactic super-winds produced by strong starbursts or galaxy merging processes (Heckman et al., 1990; Colina et al., 2004; Monreal-Ibero et al., 2010).

1.4.3. Merger-induced star formation

Given the IR luminosities of LIRGs, they could reach SFRs as high as $\sim 170 M_{\odot} \text{ yr}^{-1}$, according to the relation between L_{FIR} and SFR provided by Kennicutt (1998, Salpeter IMF) This is very significant when compared to the SFR of the Milky Way, $1.9 \pm 0.4 M_{\odot} \text{ yr}^{-1}$ Chomiuk & Povich (2011, Kroupa IMF), even taking into account the differences due to the IMF.

Observationally, it is clear that mergers are able to trigger star formation both in the form of massive nuclear starbursts and as spatially extended star formation in the form of young stellar clusters, which have been identified in U/LIRGs in different merger stages, from pre-merger or separated progenitors (Wang et al., 2004; Elmegreen et al., 2006) to advanced or post coalesced systems (Evans et al., 2008; Wilson et al., 2006).

Traditionally, numerical merger simulations rely on two different star formation mechanisms: the **density dependent** (e.g., Schmidt 1959; Kennicutt 1998) and the **shock induced** (e.g., Scoville et al. 1986; Jog & Solomon 1992). The two star formation prescriptions differ in their predictions on the timing of the onset of SF during the merger and on the spatial distribution of star-forming regions.

The density dependent numerical simulations (Mihos & Hernquist, 1996), that parametrize the SFR as a function of the local gas density (Schmidt law), predict that most SF is strongly concentrated toward the central region of the merger remnant since the process of rapid gas funneling to the central region reduces the supply of gas needed to produce SF elsewhere. These simulations can reproduce the SFR enhancement of U/LIRGs central starbursts (by a factor 10 - 100 or more), although in general, the SFR enhancement in a random galaxy collision is lower than 5 (Di Matteo et al., 2008). We note that these density dependent models underestimate the spatially extended SF observed in many galaxy mergers.

The shock induced SF models (Barnes, 2004), that consider SF triggered by shocks, predict a wider spread, spatially-extended bursts of star formation. Shock-induced SF models respond promptly to external disturbances, while in density-dependent models the SF activity is delayed until sufficient gas density has build up. The larger spatial extent of SF in shock-induced models is, in part, a

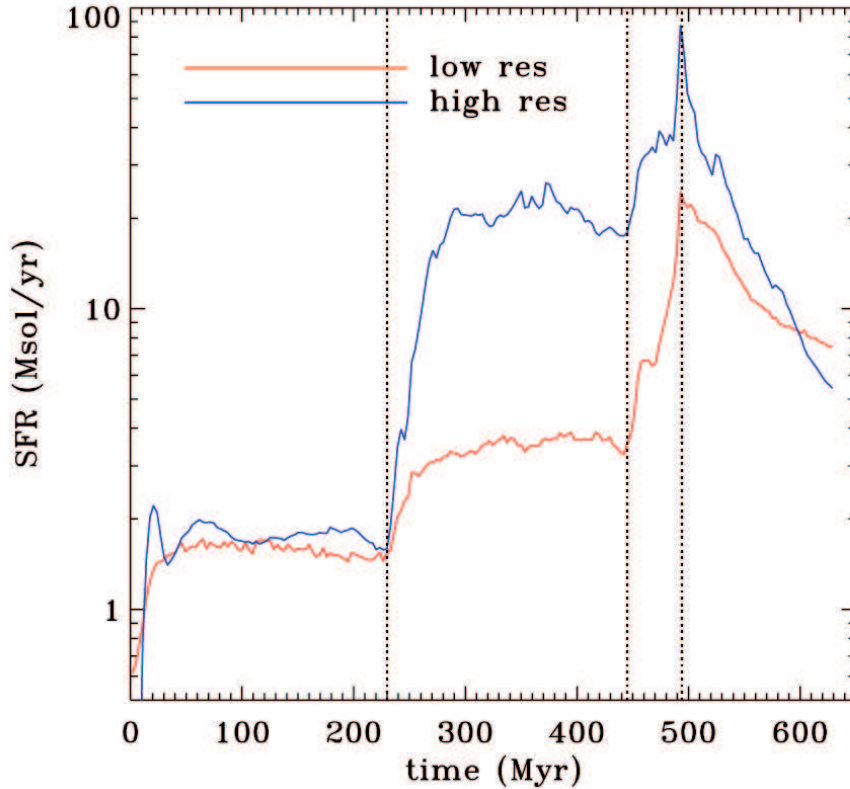


Figure 1.12 Star formation rate as a function of time of [Teyssier et al. \(2010\)](#) simulations for the low resolution (red) and high resolution (blue) runs. Times for the first pericenter, second pericenter, and final merger are indicated by vertical dotted lines.

consequence of the earlier onset of activity in such models, since the gas is more widely distributed at earlier times.

Current development in the field by [Teyssier et al. \(2010\)](#) and [Bournaud et al. \(2010\)](#), found that the extended starburst arise spontaneously without any prescription in high resolution hydrodynamic models capable of modeling gas below 300 K. They found that the extended starbursts are originated by the supersonic turbulence of the ISM, which is increased in galaxy mergers as a consequence of the tidal interaction itself. Traditional SPH simulations cannot explicitly treat this supersonic turbulence because, with their poor resolution, they cannot model the gas below 1000 - 10000 K. In these models, a merger-induced nuclear starburst is also present, but the timescale is substantially longer. Therefore, they conclude that the extended star formation is important in the early stages of the merger, while the nuclear starbursts will occur in advanced stages. In general, simulations expect many mergers result in two major epochs of star formation: one soon after first pericenter passage and one during final coalescence ([Mihos & Hernquist, 1996](#); [Cox et al., 2008](#)). In Figure 1.12, we show the Star Formation Rate (SFR) as a function of time predicted by [Teyssier et al. \(2010\)](#) low and high resolution simulations. Note how in the high resolution models the SFR enhancement occurs earlier and with more intensity than in the low resolution models.

Apart from the extension of the SF, the remnant properties and the SF enhancement of a galaxy merger depends on several factors as: the mass ratio and morphologies of the progenitors, the availa-

bility of gas (gas-rich or gas-poor), and the orbital characteristics. Some predictions from simulations:

- Mergers of "bulgeless" late-type galaxies are more prone to violent bar instability during an encounter, which drives the internal gas towards the galaxy center to trigger a nuclear starburst. On the contrary, the presence of a bulge can stabilize galaxy disks against bar formation, limiting the amplitude of the SF enhancement at the first close passage (Mihos & Hernquist, 1996).
- Major mergers of galaxies of comparable masses are the most efficient in triggering strong starbursts. Star formation decreases rapidly with increasing mass ratios (Cox et al., 2008).
- Retrograde encounters (when the galaxies spin is antiparallel) have larger star formation efficiency than direct encounters (when the galaxies spin is parallel). Moreover, direct encounters develop more pronounced asymmetries than retrograde ones, whose remnants are more compact (Di Matteo et al., 2007).
- The size of the tidal structures also depends on the orientations of the disc relative to the orbital plane. Zero inclination, planer orbits create two tidal arms, while polar orbits generally lead to the formation of just one arm (Howard et al., 1993).
- There is an anticorrelation between the amplitude of the SF burst in the final phases of the coalescence and the tidal forces exerted at the first close passage, which is due to the large amount of gas dragged outside the galaxy by tidal tails in strong interactions (Di Matteo et al., 2007).
- For galaxies with a gas content typical of Local or low-redshift galaxies (typically 15 % to 30 % of gas in the disk), the star formation rates are rarely enhanced by factors larger than 5 compared to isolated galaxies. However, strong starbursts with a relative efficiency higher than 5 are present in a 15 % of the major galaxy mergers, in agreement with local U/LIRGs (Di Matteo et al., 2008).

By studying the spatially resolved distribution of the stellar populations in U/LIRGs we can constrain and test the validity of the different merger simulations.

Young Massive Clusters in U/LIRGs

Large numbers of Young Massive Clusters (YMCs), also called Super Star Clusters (SSCs), are triggered in U/LIRGs. YMCs are nurseries to star formation and harbour the brightest and youngest stars (< 1 Gyr), with masses $> 5 \times 10^4 M_{\odot}$. As YMCs are formed in bursts, they can be considered as Single Stellar Populations (SSPs), meaning that the member stars of the cluster formed at the same time from a molecular cloud with the same chemical composition (metallicity). Evolutionary population synthesis models allow to age-date the YMCs from multi-band photometry or spectroscopy. They are useful tracers of the star formation history in merging galaxies, thus providing constraints to numerical simulations (Chien, 2010; Chien & Barnes, 2010).

One of the best-studied examples is the ongoing pre-merger NGC 4038/4039, the Antennae. The Antennae hosts a rich population of YMCs with ages: < 20 Myr, 100 Myr, 500 Myr, and a population of progenitor globular clusters indicating multiple periods of star formation since the merging process began (Renaud, 2010; Whitmore et al., 2010).

The YMC population in NGC 7252, a somewhat more advanced merger than the Antennae, has ages between 650 Myr and 750 Myr (Miller et al., 1997) and contains one of the most massive clusters detected so far $\sim 8 \times 10^7 M_{\odot}$ (Maraston et al., 2004). NGC 3256, a merger in an advanced stage but less complete than NGC 7252 (i.e., the progenitor nuclei in NGC 3256 have yet to coalesce), the clusters show a variety of ages, from a few Myr to 150 Myr (Trancho et al., 2007).

Using HST imaging, Miralles-Caballero et al. (2011) present a comprehensive characterization of the general properties (luminosity function, mass, size, age, etc.) of optically selected star forming knots in a representative sample of 32 low- z U/LIRGs. The galaxies in their sample represent different interaction phases (first approach, pre-merger, merger, and post-merger) and cover a wide luminosity range, $11.46 \leq \log(L_{IR}/L_{\odot}) \leq 12.54$. They found that the number of knots per system stays about the same (140 - 150) in the first three phases, and this number drops by a factor of four to five in the post-merger phase (34 knots per system). Some of the knots (15%) are so blue that their colors indicate a young (i.e., < 30 Myr) and almost extinction-free population. However, knots in post-mergers are on average (1.3 - 2 times) larger, more luminous (2 mag) in the I band and 0.5 mag redder than those in systems in earlier phases. They propose two possible scenarios to explain this: 1) the likely presence of relatively high extinction in the most advanced mergers and 2) the dissolution/disruption of the less massive clusters and/or their coalescence into more massive, evolved superclusters.

YMCs have also been detected in tidal tails, although not all tidal tails contain YMCs (Knierman et al. 2003; Mullan et al. 2011). It has been found that some of the star forming complexes in the tidal tails could lead to the formation of Tidal Dwarf Galaxies (TDGs). Miralles-Caballero et al. (2012) studied the likelihood survival of 22 star forming complexes in the tidal tails of 11 U/LIRGs and find that most of the complexes might be self-gravitating entities. By analysing the resistance to forces from the parent galaxy they conclude that 9 complexes show a high-medium or high likelihood of survival, their total mass likely being compatible with that of dwarf galaxies, being, therefore, defined as TDG candidates. They infer a TDG production rate of 0.3 candidates with the highest probabilities of survival per system for the (U)LIRGs class. This rate, though, might decrease to 0.1 after the systems in (U)LIRGs have evolved for 10 Gyr, for long-lived TDGs, which would imply that no more than 5 - 10% of the overall dwarf population could be of tidal origin.

When compared to the YMC population of the Milky Way, studies of these extragalactic YMCs shown several noticeable differences. On the one hand, the large number of YMCs observed in merging systems, which easily accumulate to a few hundred, compared to only a dozen YMCs that have so far been observed in the Milky Way. Also, the mass of clusters observed in these mergers are up to $10^7 M_{\odot}$ which easily exceeds the masses determined for YMCs in the Milky Way, which range between $10^3 - 10^5 M_{\odot}$ (see review from Portegies Zwart et al. 2010).

1.5. Post-Starburst QSOs

As mentioned at the end of Section 1.3.3, a key evolutionary phase in merger-driven evolutionary scenarios is the ignition of AGN activity that, through outflows, can inhibit both star formation and its own fueling. Such objects would be expected to have luminous quasar activity, starburst or post-starburst signatures, along with indications of a recent merger (e.g., companion, tidal tails, asymmetries, etc.).

One of the objects that more clearly meets all these requirements is called UN J1025-0040, the

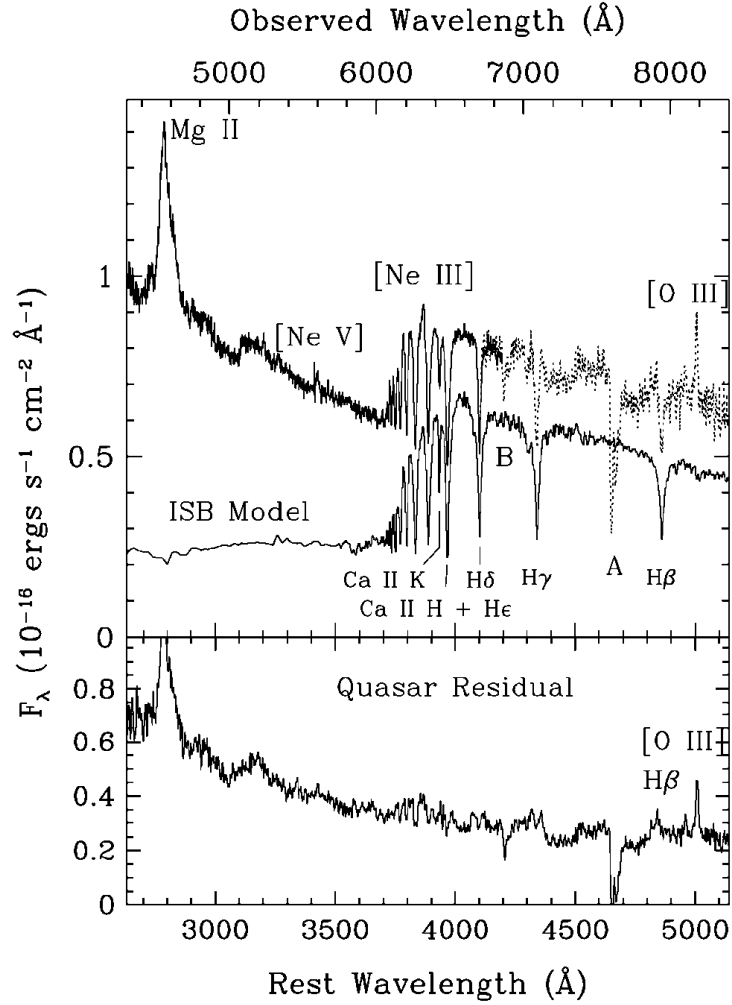


Figure 1.13 Optical spectrum of the PSQSO UN J1025-0040. An Instantaneous Starburst (ISB) model of 400 Myr old is also shown, matching the high order Balmer lines and H/K CaII. The bottom panel shows the residual quasar spectrum obtained by subtracting the ISB model from the UN J1025-0040 spectrum, revealing broad H β . Extracted from Brotherton et al. (1999).

most evident transition QSOs discovered in Sloan Digital Sky Survey (SDSS) data by Brotherton et al. (1999). Its optical spectrum shows simultaneously a strong blue continuum with broad H α and H β emission lines, typical of classical type 1 QSOs, and a red Balmer jump and high order Balmer lines in absorption, characteristic of a post-starburst population of ~ 400 Myr (see Figure 1.13). Attending to its spectral properties it was called Post Starburst QSO (PSQSO). Moreover, it is morphologically classified as a merger remnant (Brotherton et al., 2002), and has a companion galaxy in a post-starburst phase (Canalizo et al., 2000).

It is not an isolated case, in the SDSS data release 3 (DR3), ~ 600 PSQSOs were identified. It is important to note that, technically speaking, not all of them are QSO ($M_B < -23$), but a significant fraction are lower luminosity AGN ($M_B > -23$). In fact, in Cales et al. (2011) sample, only 1 out of 29 reaches the QSO luminosity.

1.5.1. Properties

The morphology of PSQSOs was analyzed by [Cales et al. \(2011\)](#) using HST images of a sample of 29 PSQSOs with redshifts between 0.25 and 0.4 ($z \sim 0.3$). They found a heterogeneous population with a variety of morphologies including host galaxies that are both early-type (13/29) and spiral (13/29). Disturbances such as tidal tails, shells, star-forming knots, and asymmetries are seen in 17/29 as signposts of interaction/merger, and are evenly distributed among early-type and spiral galaxies. Two of these systems are clearly merging with their companions.

Also, using optical spectroscopy, [Cales et al. \(2013\)](#) fully characterize PSQSOs properties. They model the spectra of 38 PSQSOs to determine ages and masses of the host stellar populations, and BH masses and Eddington fractions of the AGNs. They found PSQSOs have $M_{BH} = 10^{7.5-8.5} M_{\odot}$ and are accreting at a few percent ($\sim 1\% - 10\%$) of L_{Edd} . Hosts have stellar masses of around $10^{10-11} M_{\odot}$ and stellar populations with several hundred Myr to few Gyr old ($\sim 200 - 2000$ Myr). No clear correlations were found between ages/masses of the stellar populations and the AGNs properties when considering the sample as a whole. However, when sub-classifying in morphological types, they found early type galaxies have significantly higher AGN luminosities ($\langle L_{AGN} \rangle \sim 10^{43.82} \text{ erg s}^{-1}$) and younger starburst ages ($\langle SB_{age} \rangle \sim 960$ Myr) while the spiral hosts have a more complex and extended SFH ($\langle SB_{age} \rangle \sim 1.6$ Gyr) and lower luminosity AGN ($\langle L_{AGN} \rangle \sim 10^{43.51} \text{ erg s}^{-1}$). Using MIR spectra, [Wei et al. \(2013\)](#) found that PSQSOs in early-type host galaxies tend to have relatively strong AGN activities, while those in spiral hosts have stronger PAH emission, indicating more star formation.

[Cales et al. \(2013\)](#) hypothesize that early type PSQSOs are likely the result of a major merger and were likely LIRGs in the past. They may represent the low-redshift counterparts to the high-luminosity quasars much more common at $z = 2 - 3$. While spiral PSQSOs show more complex SFHs triggered by secular evolution or less dramatic events, as harassment or bars. Simulations also agree with two mechanisms responsible for mutual BH-bulge growth ([Hopkins & Hernquist, 2009](#)). The brightest AGN must be triggered in major mergers: the galactic supply of gas must lose angular momentum in less than a dynamical time to be converted to new bulge mass. However, lower luminosity AGN require little bulge growth and small gas supplies, and could be triggered in more common nonmerger events. For example, bars in spiral hosts may be sufficient to fuel the nuclear activity of Seyfert galaxies ([Jogee, 2006](#)).

1.5.2. Evolutionary picture revisited and the Starburst / AGN timing

In a recent work, [Cales & Brotherton \(2015\)](#) made a global comparison of their 38 PSQSOs sample with post-starburst galaxies and quasars at similar redshift ($z \sim 0.3$), and with similar luminosity ($M_r \sim -23$). They found that post-starburst galaxies have elliptical and disturbed / post-merger morphologies similar to those of the more luminous PSQSOs, display similar spectral properties, but also can have younger stellar populations for a given starburst mass (~ 400 Myr younger). Quasars at similar redshifts and luminosities around the Seyfert / quasar transition possess similar AGN characteristics, but do not appear to be hosted by galaxies with significant post-starburst populations. On the other hand, recent studies of more luminous quasars [Canalizo & Stockton \(2013\)](#) find hosts consistent with luminous PSQSOs. They proposed an scenario where the luminous / elliptical PSQSOs may be in transition between post-starburst galaxies and a more luminous quasar stage. The scenario proposed

by them is shown in their Figure 9. Basically, is the same as [Hopkins et al. \(2008\)](#) (see Figure 1.8) but including between (e) and (f) stages first the post-starburst galaxies and then the PSQSOs.

It seems that observationally and theoretically there is growing consensus regarding the AGN fuelling in the context of merger driven evolutionary scenarios; in which bursts of star formation happen early and coincide with the close approach passes of the two nuclei, while the AGN is triggered later on in the evolution of the merger around coalescence ([Wild et al., 2007](#); [Schawinski et al., 2010](#); [Alexander & Hickox, 2012](#); [Van Wassenhove et al., 2012](#); [Canalizo & Stockton, 2013](#)). At the sub-kpc scales, competing effects (e.g. inflow, outflow, star formation) cause the gas to pile up ([Alexander & Hickox, 2012](#); [Fathi et al., 2013](#)). At any rate, this suggests that getting fuel all the way down to the BH is not straightforward and takes time. Our current view of merger triggered AGN fuelling is one in which torques from the merger are efficient drivers for bringing gas down to a critical distance from the BH (~ 100 pc). Then a series of small-scale internal instabilities (stochastic fuelling) finally brings the gas to the BH, where the time it takes the gas to reach the BH may be comparable to or longer than the AGN duty cycle ($\sim 10^8$ yr).

1.5.3. Other transition QSOs/AGNs

Age dating the stellar populations in transition AGNs samples could be used as a constrain for the major merger driven scenario. If the proposed scenario is correct, the peak of star formation would occur while the AGN is still inactive / deeply buried, and therefore, by the time the AGN becomes visible in the optical, the stellar population would be detected as an ageing starburst of several hundred Myr to few Gyr.

This seem to be the case in the sample of transition QSOs at $z \sim 0.2$ (previously classified as passive ellipticals) of [Canalizo & Stockton \(2013\)](#), with important contributions of intermediate age post-starburst populations of 0.7 - 2.4 Gyr. Also, recently [Yesuf et al. \(2014\)](#) broaden the definition of post-starburst galaxies to include transiting systems possibly hosting AGN. The AGN fraction of these post-starbursts, as estimated from optical line ratios, is about 3 times higher than that of normal star-forming galaxies of the same mass. Moreover, these post-starburst AGN have mean stellar population ages between 350 - 700 Myr, and their spectral properties are analogous to previously discovered PSQSOs.

However, in other transition systems there is not a delay between star formation and the AGN activity, and both appear quasi-simultaneously ([Canalizo & Stockton, 2000, 2001](#); [Bessiere et al., 2014](#)). Some scatter in the delay between the starburst and the AGN activity is always expected, as the timescales of the different processes depend on the details of the merger: mass ratios and gas fractions of the progenitors, orbital configuration, etc. Moreover, the amount of dust in the nuclear region also determines the possibility of simultaneously detecting the SB and the AGN. If there is little dust, both phenomena could be seen simultaneously. If dusty, the AGN will not be visible until much later. According to the previous observational samples the scatter is really huge, ranging from 0 - 2 Gyr.

A detailed analysis of the stellar populations in greater statistical samples of transition objects is still needed to clear up this picture.

In anycase, post-starburst QSOs/AGNs as those found by [Brotherton et al. \(1999\)](#) and [Yesuf et al. \(2014\)](#) are ideal laboratories to study connections between the starburst and AGN phenomenon, as the properties of both could be derived simultaneously for each individual system.

1.6. Thesis Overview

The primary scientific objective of this thesis is to find new observational evidence that test the validity of the major gas rich merger scenario, in order to understand the genesis events that lead to the formation of quasar activity, and to place galaxies with nuclear activity in the context of the formation and evolution of galaxies. A significant contribution can be done to this field by studying and comparing the stellar populations and the extended ionized gas properties along the whole merger sequence from U/LIRGs to QSOs.

To approach this goal, we have characterized and compared the stellar populations and the ionized gas properties in two small samples of galaxies in different evolutionary stages: 4 U/LIRGs (2 pre-merger and 2 merger) and 9 PSQSOs. This study requires high quality optical data with resolved spatial and spectral information, like the one provided by Integral Field Spectroscopy (IFS). Our IFS covers the rest-frame optical range 3700 - 7000 Å, from which we can derive:

1. The spatial distribution of the stellar populations. The high-order Balmer lines, the CaII H and K, G band, Mgb and the Balmer break, together with our evolutionary synthesis models and spectral synthesis techniques, like *Starlight*, will be used to determine the average stellar population properties: age, metallicity, mass, stellar mass surface density and stellar extinction.
2. The spatially resolved SFHs in light and mass, and the SFR maps derived from the spectral synthesis.
3. The spatial distribution of the extended ionized gas by means of the most important emission lines, such as H α , H β , [NII] λ 6583, [OIII] λ 5007, [OII] λ 3727, [OI] λ 6300 and [SII] λ λ 6717,6732. The ionization conditions determined using the well-known and most updated forbidden-line diagnostics in the oxygen and nitrogen lines, used to distinguish between gas photoionized by the AGN or by young stellar components.
4. Ionized gas extinction maps will be used to deredden the observed H α maps and obtain extinction-corrected maps of the SFR.

We intend to test, for example, whether there is an evolution in the merger-induced star formation, the SFR and the ionization structure between U/LIRGs in different merger stages. Also, ages can be used as a clock to test if PSQSOs are part of the post-merger evolutionary sequence between U/LIRGs and normal elliptical galaxies. Another important goal is to found if the properties of the starbursts (age, mass) in the PSQSOs are somehow correlated with the BH properties (accretion rate, mass).

A brief outline of the content of each chapter in this thesis is as follows:

- **Chapter 2:** this chapter presents the data samples and the characteristics of the observations.
- **Chapter 3:** this chapter gives a summary of integral field spectroscopy (the major observational technique used in this thesis) and summarize the data reduction process.
- **Chapter 4:** this chapter gives a summary of the spectral synthesis methodology and models applied to study the stellar populations.
- **Chapter 5:** this chapter presents the results of the analysis of the two pre-merger (class IIIb) LIRGs IC 1623 and NGC 6090.

- **Chapter 6:** in this chapter the results of the merger (stage IV) LIRG NGC 2623 is presented. For this system, in addition to the IFS and HST data, we also have narrow band imaging from OSIRIS@GTC in $H\alpha$ and $[NII]\lambda 6583$, that complements the analysis.
- **Chapter 7:** this chapter presents the results of the PSQSOs. Because of the low signal to noise ratio of the data, at the end we could not conduct a spatially resolved study. However, we have been able to characterize the central and integrated spectra. In addition, we have also compared with nuclear SDSS spectra, for which we have followed the same methodology of analysis.
- **Chapter 8:** this chapter provides an overall discussion and comparison of the work presented in previous chapters with the results from a control sample of "normal" Sbc and Sc spiral galaxies from CALIFA survey.
- **Chapter 9:** the main conclusions are presented in this chapter.

2

Data sample and observations

In this thesis we studied in detail two small samples of systems with at least two representatives of different evolutionary stages along the merger sequence: 4 U/LIRGs (2 pre-merger and 2 merger) and 9 PSQSOs. In order to characterize the properties of the stellar populations and the ionized gas we have performed Integral Field Spectroscopy (IFS), that provides us with resolved spatial and spectral information. The U/LIRGs observations are from the Potsdam Multi-Aperture Spectrophotometer (PMAS) spectrograph (Roth et al., 2005) at the 3.5 m telescope of the Calar Alto Observatory (CAHA), either from the Lens Array (LArr) configuration or PPAK (PMAS fibre PAcK). On the other hand, the PSQSOs observations come from the VISIBLE Multi-Object Spectrograph (VIMOS) at the 8.2 m Very Large Telescope (VLT). Both datasets cover the rest-frame optical range 3700 - 7000 Å.

Apart from the IFS, we have downloaded from the Hubble Legacy Archive (HLA)¹ optical high resolution images from the Hubble Space Telescope (HST) for all the PSQSOs and U/LIRGs in order to have a better knowledge of the morphology of these systems. Moreover, in the case of the U/LIRGs we have also retrieved multiwavelength images in several broad band filters from FUV to NIR. We used them to study through photometry the stellar populations properties of the star clusters present in them. All these images were retrieved already pipeline reduced, astrometrically corrected and aligned North up, East left.

Finally, and just for NGC 2623, we have deep narrow band imaging in H α and [NII] λ 6583 from the Optical System for Imaging and low-intermediate Resolution Integrated Spectroscopy (OSIRIS) Tunable Filter instrument at Gran Telescopio de Canarias (GTC).

This chapter is organized as follows: in Section 2.1 I briefly summarize what is the IFS, and describe the instrumentation used in this thesis, in Section 2.2 I describe the LIRGs observations and in Section 2.3 the PSQSOs observations.

2.1. Integral Field Spectroscopy

The general term 3D-spectroscopy refers to those techniques that allow to obtain spatially-resolved spectra over a two dimensional field. In an extragalactic context, each point of the galaxy (α , δ) has

¹<http://hla.stsci.edu/>

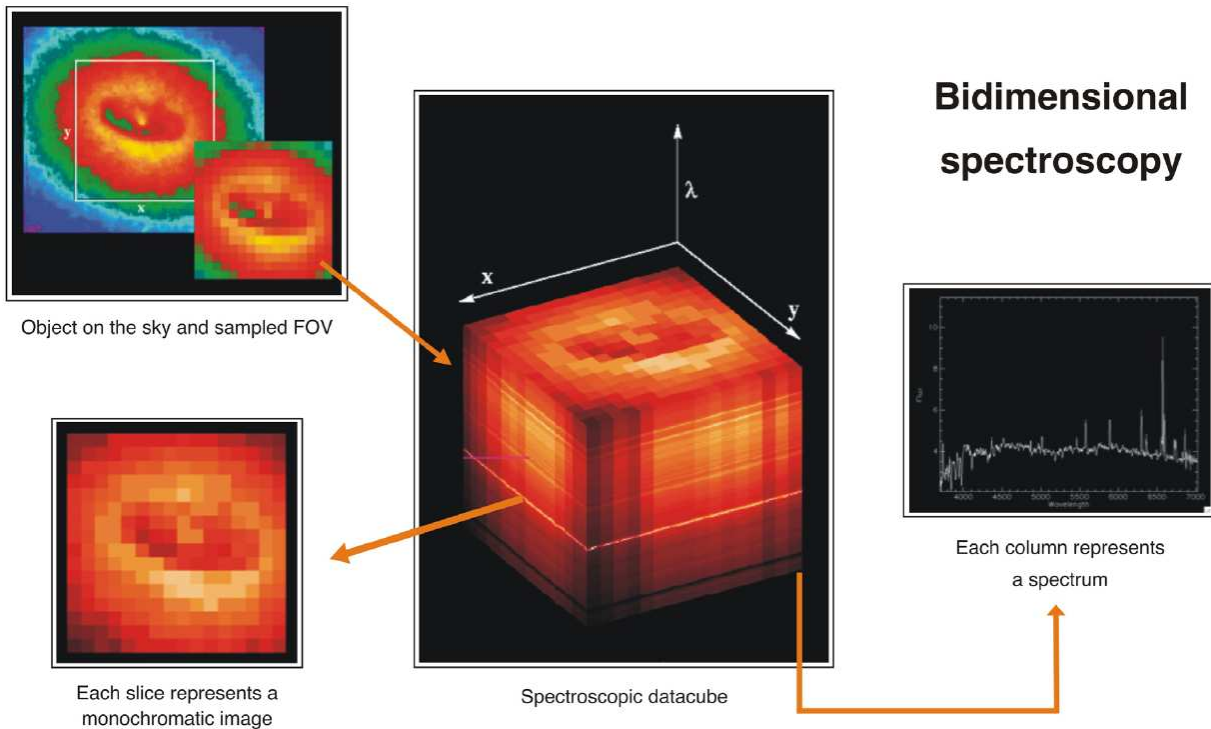


Figure 2.1 Diagram showing the principle of bidimensional spectroscopy. A reduced datacube can be thought as a series of monochromatic images along the spectral range, whereas each column represents an individual spectrum of a discrete spatial position. Figure extracted from Rosales-Ortega (2009), who adapted it from an original of M. Roth, <http://tinyurl.com/IFS-principle>.

associated a spectrum (λ), and all the information has to be stored in a two-dimensional detector. The Integral Field Spectroscopy (IFS) is one of the most widely used 3D-spectroscopy methods in which all the spectral and spatial information for a given telescope pointing is obtained simultaneously (Allington-Smith, 2007). This technique presents a good compromise between the exposure time, resolution, and homogeneity of the data, which is one of the fundamental advantages with respect to other 3D-spectroscopy methods. It also allows the spectra to be characterized and corrected for differential atmospheric refraction which can severely influence the classical sequential techniques, especially long-slit observations. Figure 2.1 shows the principle of Integral Field Spectroscopy. A two-dimensional field-of-view on the sky (white frame) is sampled into discrete spatial elements, which can have a round or (like in this example) square shape. These spatial elements are sometimes called spaxels in order to distinguish them from ordinary pixels of direct imaging instruments. The peculiar virtue of IFS consists in the ability to create an individual spectrum for each spaxel simultaneously over the whole field-of-view. After data reduction, the set of generated spectra can be rearranged in a computer to form a 3-dimensional data cube of two spatial, and one wavelength coordinates. Alternatively, it is possible to create monochromatic images or co-added quasi-broadband images from slices of the datacube. This figure is extracted from Rosales-Ortega (2009), who adapted it from an original of M. Roth, <http://tinyurl.com/IFS-principle>.

Since the '80s several instruments have been designed using different IFS techniques. [Allington-Smith \(2007\)](#) gives a review of the most popular present and future IFUs. All these techniques are based on dividing the light coming from the source and dispersing each of the subdivisions to obtain its spectrum. The data for this thesis were taken using either fiber arrays or their combination with lenslets as integral field unit (see the second row of panels in their Figure 1).

- **Fiber Array:** In this case, a fiber array is used to subdivide the FoV in the focal plane of the telescope. The fibers are then reordered forming a pseudo-slit and the information dispersed by a conventional spectrograph. The low cross-talk derived from the reordering of the fibers and the large spectral coverage represent the best advantages of this configuration. However, this configuration has two main disadvantages: round fibers cannot fill a two-dimensional region completely, and the light beam is widened as it travels across the fiber (focal degradation). The PMAS PPAK instrument uses this technique.
- **Lenslets+Fiber:** Some disadvantages associated to the pure fiber-based IFU (e.g., flux losses and focal degradation) can be avoided by coupling them to a lens array at the focal plane. This way, the spatial coverage is optimal, and the small pupil created at the entrance of the fiber core avoids light losses and minimizes the focal ratio degradation. However, in general these systems need for additional optical mechanisms that can lead to a decrease of the system efficiency. Among others, PMAS LArr and VIMOS ([Le Fèvre et al., 2003](#)) instruments make use of this technique.

2.1.1. Instrumentation

The two instrumental requirements for the specific science case of this thesis were: 1) to cover the whole surface area of our galaxies and 2) to cover the whole optical range from 3700 - 7000 Å. For this purpose, the best options result to be PMAS and VIMOS instruments.

The Potsdam Multi-Aperture Spectrophotometer (PMAS) is an integral-field instrument, developed and built at the Astrophysical Institute Potsdam (AIP) covering the optical wavelength regime of 3500 - 10000 Å ([Roth et al., 2005](#)). PMAS is available as a common-user instrument at the German Spanish Calar Alto (CAHA) observatory, mounted at the Cassegrain focal station of the 3.5 m telescope. The instrument was later equipped with an additional IFU, featuring a wider field and higher light collecting power per spaxel. This second unit (called PPAK-IFU, [Kelz et al. 2006](#)) is placed 60 off-axis, to by-pass the fore-optics and lens array IFU. It consists of a focal reducer lens and a densely-packed bare fibre-bundle, that connects to the same spectrograph. The PPAK FoV spans 64 x 74 arcsec, and is one of the world's largest integral field unit.

The Visible MultiObject Spectrograph (VIMOS) is an optical (3600 - 10000 Å) wide field imager and multi-object spectrograph mounted on the UT3 Melipal Very Large Telescope (VLT) in Chile. VIMOS operates in three different modes: 1) Imaging (IMG); 2) Multi-Object Spectroscopy (MOS); and 3) Integral Field Unit (IFU). For the IFU configuration, VIMOS incorporates 6400 fibres (80 x 80) coupled with microlenses. The total aperture of the FoV ranges between 13 x 13 and 54 x 54 arcsec, with element sizes of 0.33 - 0.67 arcsec per fibre depending on spectral resolution and spatial

Table 2.1. U/LIRGs sample properties

Galaxy	RA	DEC	Interaction stage	z [Mpc]	Distance	$\log(L_{IR}[L_{\odot}])$
(1)	(2)	(3)	(4)	(5)	(6)	(7)
NGC 6090	16 11 40.8	+52 27 27	3	0.029304	127.7	11.51
IC 1623	01 07 46.3	-17 30 32	3	0.020067	86.8	11.65
NGC 2623	08 38 23.8	+25 45 17	4	0.018509	80.0	11.54
Arp 220	15 34 57.1	+23 30 10	4	0.018126	78.3	12.21

Note. — Columns from left to right are: (1) Common name, (2) and (3) Right Ascension and Declination from Equinox J2000 extracted from [Sanders et al. \(2003\)](#), (4) Interaction Stage according to [Veilleux et al. \(2002\)](#) classification based on the optical morphologies, (5) Redshift extracted from NED webpage, (6) Distance in Mpc calculated assuming a flat cosmology with $\Omega_M = 0.272$, $\Omega_{\Lambda} = 0.728$ and $H_0 = 70.4 \text{ km s}^{-1} \text{ Mpc}^{-1}$ (WMAP, seven years results) and (7) Infrared luminosities $L_{IR} = L(8-1000)\mu\text{m}$ from IRAS fluxes extracted from [Sanders et al. \(2003\)](#). They are in logarithm and in units of solar bolometric luminosity, $L_{\odot} = 3.83 \times 10^{33} \text{ erg s}^{-1}$.

magnification.

2.2. LIRGs observations

Four merging U/LIRGs were selected from IRAS Bright Galaxy Survey ([Sanders et al., 2003](#)), two of them in the pre-merger interaction stage (IC 1623 and NGC 6090) and two mergers (NGC 2623 and Arp 220). In Table 2.1 we summarize the main properties of our U/LIRGs sample.

All the IFS observations were taken with PMAS either in LArr mode or PPAK:

- PMAS in LArr mode:** IC 1623, NGC 2623 and NGC 6090 were observed with the Lens Array Mode (LArr) configuration, which is made of a 16×16 array of microlenses coupled with fibers. The observations were taken with the same instrument set-up. We have used a spatial magnification of $0.75''/\text{lens}$, covering a $12'' \times 12''$ FoV. To determine the spatial resolution we have measured the Full Width at Half Maximum (FWHM) of the Point Spread Function (PSF) using the standard stars and correcting by the seeing measured from CAHA seeing monitor in each of the observing nights. We found $\text{FWHM}_{PSF} = 1.3'' - 2''$. This range is larger but similar to the one derived by [Sandin et al. \(2008\)](#) with the LArr $0.5''$ sampling configuration, $1.4'' - 1.8''$.

The V300 grating was used, providing a $3.2 \text{ \AA}/\text{pixel}$ dispersion and covering a wavelength range between $3700 - 7100 \text{ \AA}$ with a resolution of 7.1 \AA FWHM (velocity resolution $\sigma \sim 170 \text{ km/s}$). With this configuration, the high-order Balmer lines, metallic lines, and the Balmer break are covered allowing to study the stellar populations. We can also detect some of the most important optical emission lines to trace the nebular emission ionized by the youngest stellar components.

- CALIFA, PMAS in PPAK mode:** NGC 2623 and Arp 220 have been observed by Calar Alto Integral Field Area (CALIFA) survey project ([Sánchez et al., 2012](#)). CALIFA is a survey

Table 2.2. U/LIRGs IFS observations

Galaxy	Instrument	Grating	Total exposure time [s]	Observation date
NGC 6090	LArr	V300	3h (3 x 1800s + 3 x 1800s)	31/03/2008
IC 1623 W	LArr	V300	1.75h (3 x 1200s + 3 x 900s)	01/09/2008
NGC 2623	LArr	V300	2.5h (3 x 1200s + 3 x 1800s)	31/03/2008
NGC 2623	PPAK-CALIFA	V500	0.75h (3 x 900s)	20/01/2012
Arp 220	PPAK-CALIFA	V500	0.75h (3 x 900s)	02/07/2011

aiming to carry out statistically complete IFS of ~ 600 galaxies in the local Universe, distributed uniformly across the entire color-magnitude diagram and of any morphological type. The observations were conducted using PMAS in its PPAK mode. A new CCD was installed in PMAS in 2010 (Roth et al., 2010) which is being used for the entire survey. Fibers in the PPAK bundle have a projected diameter on the sky of $2.7''$, 331 out of 382 of the fibers form a hexagonal area covering a field of view of $64'' \times 74''$. The remaining 51 fibers are dedicated to sky background (36 fibers) or used to obtain exposures of calibration lamps (15 fibers). The whole optical extension of the galaxies is covered (up to at least 2.5 HLR). The spatial resolution of CALIFA data has been determined by García-Benito et al. (2015) measuring the FWHM of the calibration stars, $\text{FWHM}_{PSF} = 2.39 \pm 0.26$ arcsec.

Observations were performed using two overlapping grating setups (V500 and V1200) with resolutions of 6.3 \AA and 2.3 \AA (FWHM) and wavelength ranges of $3650 - 7500 \text{ \AA}$ and $3650 - 4840 \text{ \AA}$ respectively (average velocity resolutions of $\sigma \sim 140 \text{ km/s}$ and 70 km/s). The raw data have been processed through an automatic pipeline, and the reduced data cubes are already publicly available for the community (Husemann et al., 2013). In our case, we have analysed the V500 data (combined with the V1200 to improve the signal in the blue side). The data analyzed in this paper were reduced using the CALIFA Pipeline version 1.3c. The main reduction steps and properties of the reduced data are similar to the ones summarized in Sánchez et al. (2012), based on version 1.2. A list of the differences and improvements with respect to this earlier version are presented in Husemann et al. (2013). Afterwards, the datacubes have gone through a series of pre-processing steps to feed them into *Starlight* spectral synthesis code. The methodology we followed is described in detail in Cid Fernandes et al. (2013) and in Section 5.4.1.

The characteristics of the IFS observations of the U/LIRGs are summarized in Table 2.2.

2.2.1. NGC 6090

NGC 6090 (Mrk 496 = UGC 10267; $L_{IR} = 3.2 \times 10^{11} L_{\odot}$; e.g., Sanders et al. 2003) is a luminous infrared pair of interacting galaxies located in the constellation of Draco, the Dragon, about 127.7 Mpc away from Earth. At optical wavelengths, NGC 6090 appears as a double nucleus system, with a projected separation between them of 3.2 kpc. This is consistent with an interaction stage III. The observations for this galaxy were performed on 31st of March 2008. Two pointings were taken, covering the nuclear regions of both galaxies. We obtained three science frames of 1800 s exposure time in each pointing position. In the left panel of Figure 2.2 we show the HST ACS F435W image of NGC 6090.

Table 2.3. Summary of HST data for NGC 6090

Filter	Instrument	Detector/ Camera	Plate Scale (arcsec pixel ⁻¹)	Observation Date	t_{exp} (s)	Proposal ID, PI
F140LP	ACS	SBC	0.025	2008-08-09	2648.0	11110, S. McCandliss
F330W	ACS	HRC	0.025	2005-11-12	800.0	10575, G. Ostlin
F435W	ACS	WFC	0.05	2005-09-18	1380.0	10592, A. Evans
F814W	ACS	WFC	0.05	2005-09-18	800.0	10592, A. Evans
F110W	NICMOS	NIC2	0.075	1997-11-10	383.6	7219, N. Scoville
F160W	NICMOS	NIC2	0.075	2003-12-01	599.4	9726, R. Maiolino

This image reveals the two galaxies are roughly equal size, with a pair of tidal tails with a full extent of ~ 50 kpc. While the northeastern galaxy (NGC 6090 NE) has a clear distorted spiral structure viewed face-on, the southwestern nucleus (NGC 6090 SW) is seen edge-on with an amorphous morphology and no spiral arms visible. The most striking feature of NGC 6090 is the abundance of luminous blue and red bright knots of newborn stars along the overlapping region, in the western side of NGC 6090 NE. The black rectangles indicate the positions where we have obtained the IFS. On the right panel we show the observed PMAS LArr continuum flux at 5110 \AA rest-frame (obtained by averaging the continuum from 5050 to 5170 \AA), in logarithmic scale. We have superimposed in contours the HST F435W image, smoothed to match the spatial resolution of the IFS (~ 1.7 arcsec). The distorted spiral morphology of the NE component can be appreciated. The nucleus is marked with a black dot. To its west, there is the region of multiple star clusters formation. Far and near UV spectroscopy shows that the NE nucleus is also dominated by a young starburst (González Delgado, 2008). The luminosity maximum of the map falls between them. In the SW component we have indicated the luminosity maximum of the cube with a black dot. The star symbol indicate the position of the brightest point source in this galaxy seen in the (not smoothed) HST images. This knot is also present in NICMOS images, and was previously reported by Dinshaw et al. (1999). However, the radio emission peak is not coincident with the knot, leading Dinshaw et al. (1999) to suggest that this bright point source is not likely the nucleus of NGC 6090 SW and that it may actually be a foreground star. However, with the IFS, we have confirmed that it is not a foreground star, and we can not discard it as the nucleus of the SW galaxy. As the exact position of the nucleus of this component is not clear, in Chapter 5, Section 5.4.11, we have checked if the radial profiles of the derived stellar population properties change when centering in the cube luminosity peak or in the knot.

We have also retrieved the HST images of NGC 6090 in six broad band filters from ACS and NICMOS instruments (2 in UV, 2 in the optical and 2 in NIR). They are shown in Figure 2.3 and their characteristics are summarized in Table 2.3.

2.2.2. IC 1623

IC 1623 (VV 114 = Mrk 236; $L_{IR} = 4.5 \times 10^{11} L_{\odot}$; e.g., Sanders et al. 2003) is another pair of luminous infrared interacting galaxies. It is located in the constellation of Cetus, the Whale, 86.8 Mpc away from Earth. It is in stage III of interaction, with a projected separation between the two nuclei of 6 kpc. The western component, IC 1623 W, is very bright in the UV and optical, with a lot of star

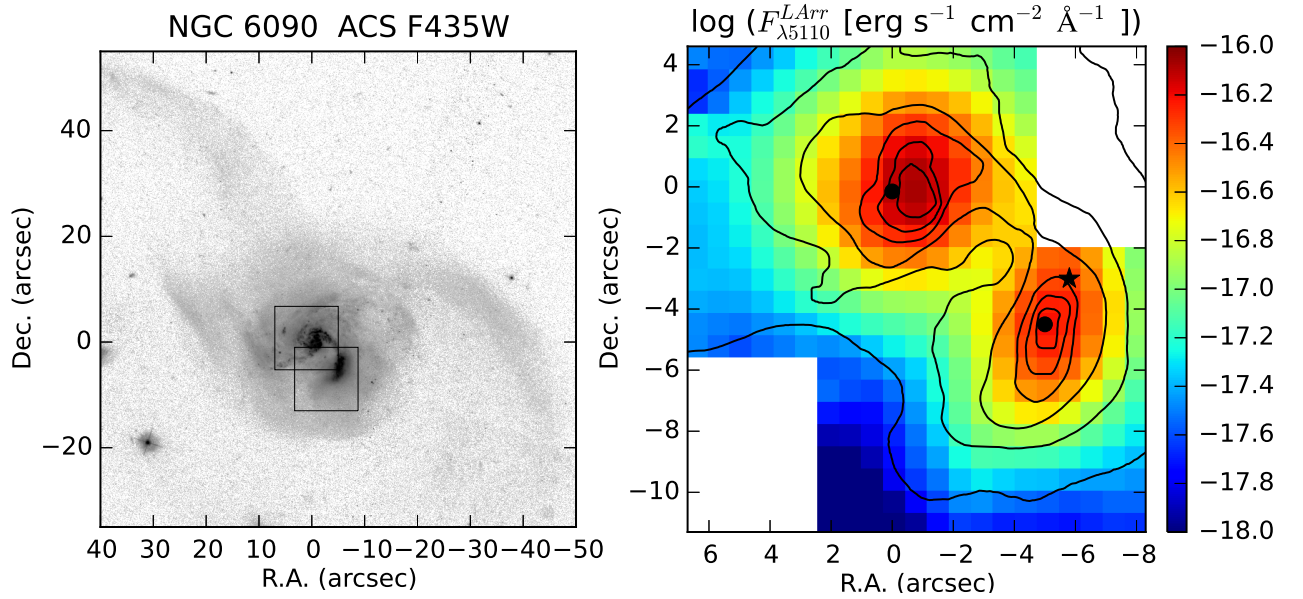


Figure 2.2 Left: HST ACS F435W image of NGC 6090. The black rectangles indicate the positions where we have obtained the IFS. Right: PMAS LArr data continuum flux at 5110 Å rest-frame (obtained by averaging the continuum from 5050 to 5170 Å), in logarithmic scale. Contours are from HST ACS435W image smoothed to PMAS LArr resolution.

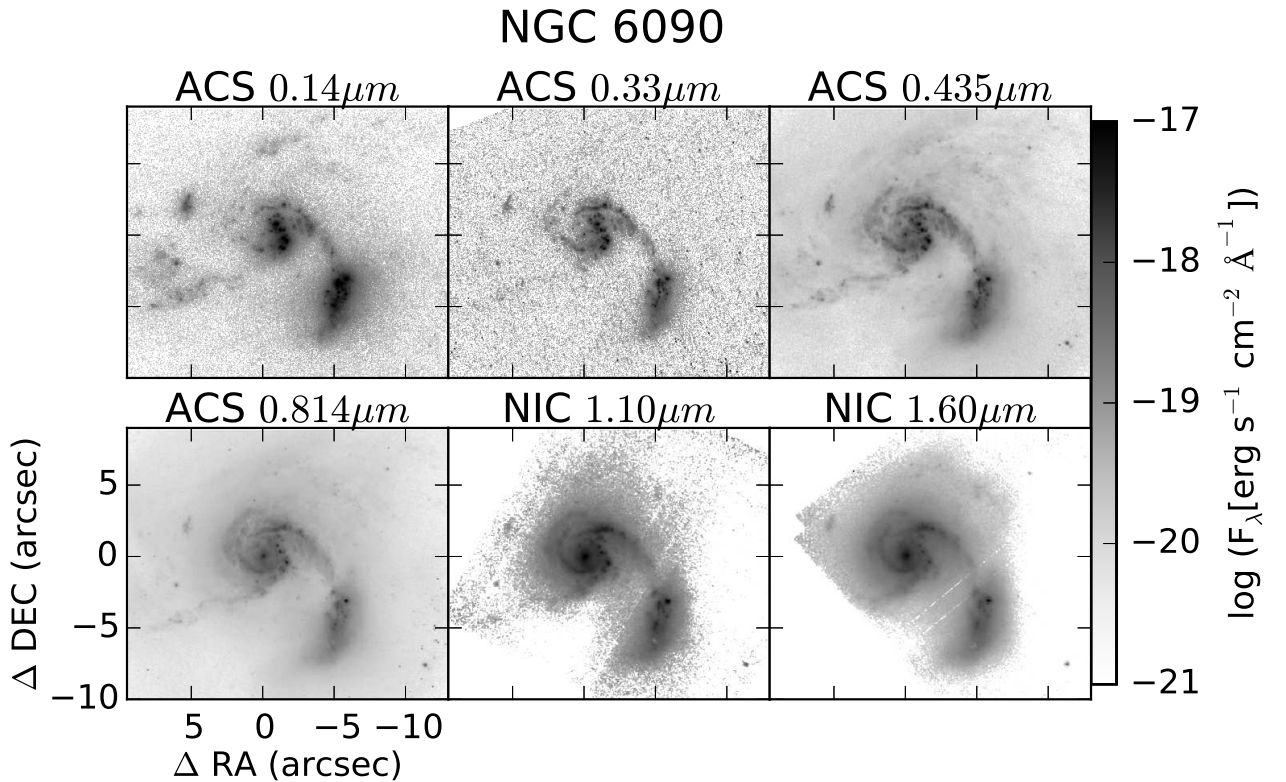


Figure 2.3 HST multiwavelength images NGC 6090. From top left to bottom right: ACS FUV 1400 Å, ACS NUV 3300 Å, ACS optical 4350 Å and 8140 Å and NICMOS NIR 1.1 μm and 1.6 μm.

Table 2.4. Summary of HST data for IC 1623

Filter	Instrument	Detector/ Camera	Plate Scale (arcsec pixel ⁻¹)	Observation Date	t_{exp} (s)	Proposal ID, PI
F25SRF2	STIS	FUV-MAMA	0.025	2000-12-25	2371.0	8201, G. Meurer
F25QTZ	STIS	NUV-MAMA	0.025	2000-12-25	750.0	8201, G. Meurer
F435W	ACS	WFC	0.05	2006-07-12	1260.0	10592, A. Evans
F814W	ACS	WFC	0.05	2006-07-12	720.0	10592, A. Evans
F110W	NICMOS	NIC2	0.075	1998-08-03	223.8	7219, N. Scoville
F160W	NICMOS	NIC2	0.075	1998-08-03	223.8	7219, N. Scoville

clusters detected in HST images. Its properties are very similar to the cosmological Lyman Break galaxies, and it is considered as the nearest Lyman Break Analog (Grimes et al., 2006). On the other hand, IC 1623 E is optically obscured but very infrared-bright. It has a substantial amount of warm and dense gas. This is also found in the overlap region connecting the two nuclei. This system was observed on 1st September 2008. Two pointings were taken covering only IC 1623 W. Three science frames per pointing were taken of 1200 s and 900 s, respectively. In the left panel of Figure 2.4 we show the HST ACS F435W image of IC 1623. The black rectangles indicate the positions where we have obtained the IFS. On the right panel we show the PMAS LArr continuum flux at 5110 Å rest-frame (obtained by averaging between 5050 to 5170 Å).

For this system we have also analysed HST broad band imaging from UV to NIR, in order to obtain some information about the stellar population content in IC 1623 E, not covered by our spectroscopic data. The six HST images analysed are shown in Figure 2.5 and their characteristics are summarized in Table 2.4.

2.2.3. NGC 2623

NGC 2623 (UGC 04509 = Arp 243; $L_{IR} = 3.5 \times 10^{11} L_{\odot}$; e.g., Sanders et al. 2003) is an infrared luminous merger of galaxies located at 80.0 Mpc from Earth in the constellation of Cancer (the Crab). It is an advanced merger, in stage 4, and the progenitors nuclei have already coalesced. Its nucleus is extended and quite obscured in UV and optical, and becomes very bright and point-like in infrared images. Moreover, this galaxy has two long and fairly simetrical tidal tails, extending up to 20 kpc away from the main body. The nucleus of this system was observed with LArr on 31 March 2008. Six science frames were taken, 3 of 1200 s exposure time and 3 of 1800 s. On 20th January 2012 it was observed by CALIFA survey. A three-pointing dithering scheme was used to sample the whole optical extent. Each pointing was observed for a total of 900 s for the V500 filter and 600 s for V1200 filter. In the upper panel of Figure 2.6 upper panel we show the HST ACS F555W image of NGC 2623. The black rectangle indicates the position where we have obtained the LArr IFS, while the black hexagon indicates the position of CALIFA IFS. The lower left panel show the continuum flux at 5110 Å rest-frame, $F_{\lambda 5110}$, for the CALIFA data. While the lower right panel show $F_{\lambda 5110}$ for LArr data.

We have also analysed multiwavelength HST broad-band imaging in seven broad band filters from ACS and NICMOS instruments. Their characteristics are summarized in Table 2.5. The images are shown in Figure 2.7. As can be seen the multiwavelength information is spatially limited to the

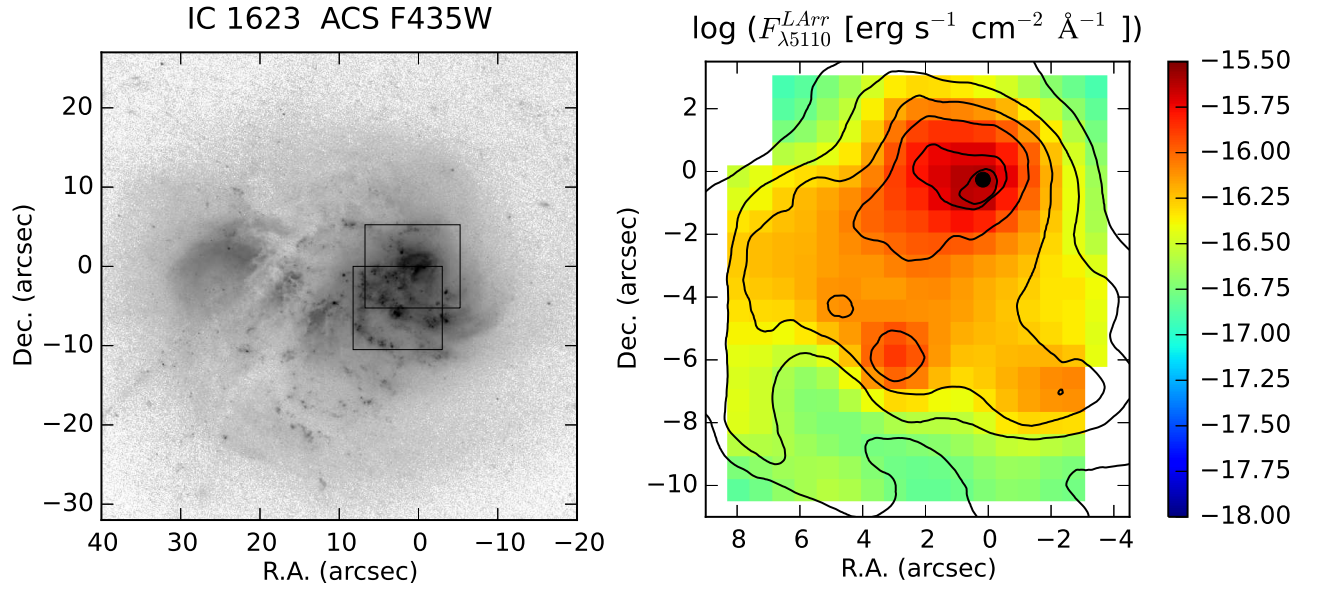


Figure 2.4 Left: HST ACS F435W image of IC 1623. The black rectangles indicate the positions where we have obtained the IFS. Right: PMAS LArr data continuum flux at 5110 Å rest-frame (obtained by averaging the continuum from 5050 to 5170 Å), in logarithmic scale. Contours are from HST ACS435W image smoothed to PMAS LArr resolution.

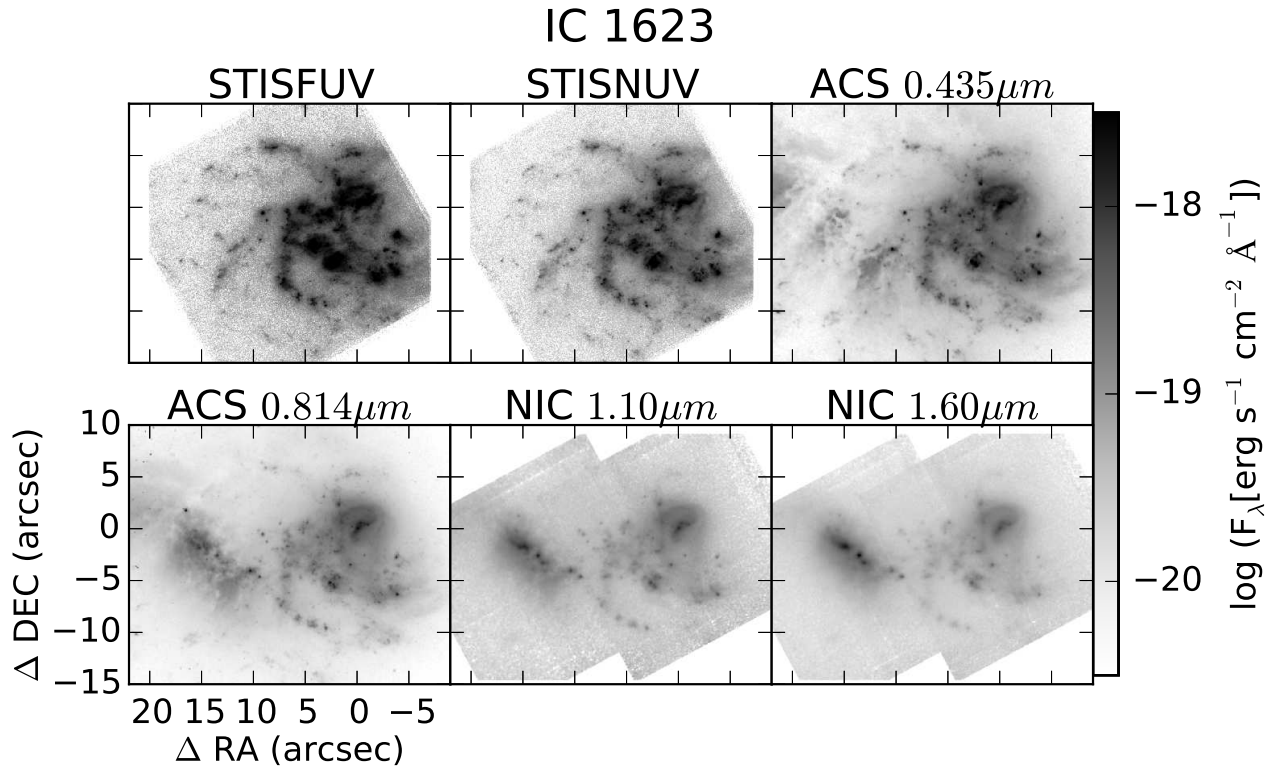


Figure 2.5 HST multiwavelength images IC 1623. From top left to bottom right: STIS FUV, STIS NUV, ACS 4350 Å, ACS 8140 Å and NICMOS NIR 1.1 μm and 1.6 μm.

Table 2.5. Summary of HST data for NGC 2623

Filter	Instrument	Detector/ Camera	Plate Scale (arcsec pixel ⁻¹)	Observation Date	t_{exp} (s)	Proposal ID, PI
F140LP	ACS	SBC	0.025	2008-10-30	2520	11196, A. evans
F330W	ACS	HRC	0.025	2004-12-28	5465	9735, B. Whitmore
F435W	ACS	WFC	0.05	2004-02-06	3729.9	9735, B. Whitmore
F435W	ACS	WFC	0.05	2005-11-29	1275	10592, A. evans
F555W	ACS	WFC	0.05	2004-02-06	1206	9735, B. Whitmore
F814W	ACS	WFC	0.05	2004-02-06	2460	9735, B. Whitmore
F814W	ACS	WFC	0.05	2005-11-29	730	10592, A. evans
F110W	NICMOS	NIC3	0.2	2004-01-13	2559.76	9735, B. Whitmore
F160W	NICMOS	NIC3	0.2	2004-01-13	2559.74	9735, B. Whitmore

FoV of UV images, $\sim 40'' \times 40''$. Several bright clusters are distributed throughout the nuclear and circumnuclear region. There exists also a prominent concentration of bright clusters located ~ 6 kpc south of the nucleus in an arc-shape nebulosity.

OSIRIS observations

In the particular case of NGC 2623, we have additional data from OSIRIS Tunable Filter instrument. OSIRIS is an imager and spectrograph for the optical wavelength range, located in the Nasmyth-B focus of GTC. Tunable Filters allow to obtain deep narrow band imaging specifying custom bandpasses by their central wavelength and FWHM.

The OSIRIS observations were carried out in service mode, on 13th January 2010, using TF imaging mode with a seeing $\sim 0.9''$. A FoV of 260×520 arcsec square was covered with a pixel scale of $0.254''/\text{pixel}$. The red TF in scanning mode was used, covering $H\alpha$ and $[\text{NII}]\lambda 6583$ lines plus the adjacent continuums. Filters were centered at $\lambda_0 = 6640, 6700, 6705, 6720, 6725$ and 6760 \AA , with a $\text{FWHM} = 14 \text{ \AA}$. These are the wavelength values at the optical centre. The optical centre for OSIRIS TF is placed approximately at pixel (1059,983) respect to pixel (1,1) at CCD1, just in the gap between both CCDs. The wavelength tuning is not uniform over the full FoV of OSIRIS. There is a progressive increasing shift to the blue of the central wavelength (λ_0) as the distance to the optical centre (r) increase. The wavelength (in \AA) observed with the red TF relative to the optical center changes following the law reported by [González et al. \(2014\)](#):

$$\lambda = \lambda_0 - 5,04 \times r(\text{arcmin})^2 \quad (2.1)$$

where $r(\text{arcmin})$ is the distance in arcminutes between the optical centre and the CCD position where we want to calculate the wavelength. Because of this effect, the target and the calibration star were positioned at the same distance from the optical centre and on the same CCD chip. We obtained three science frames per filter of 300 s of exposure time each. For the standard spectrophotometric star, Feige 34, one frame per filter of 5 s of exposure time.

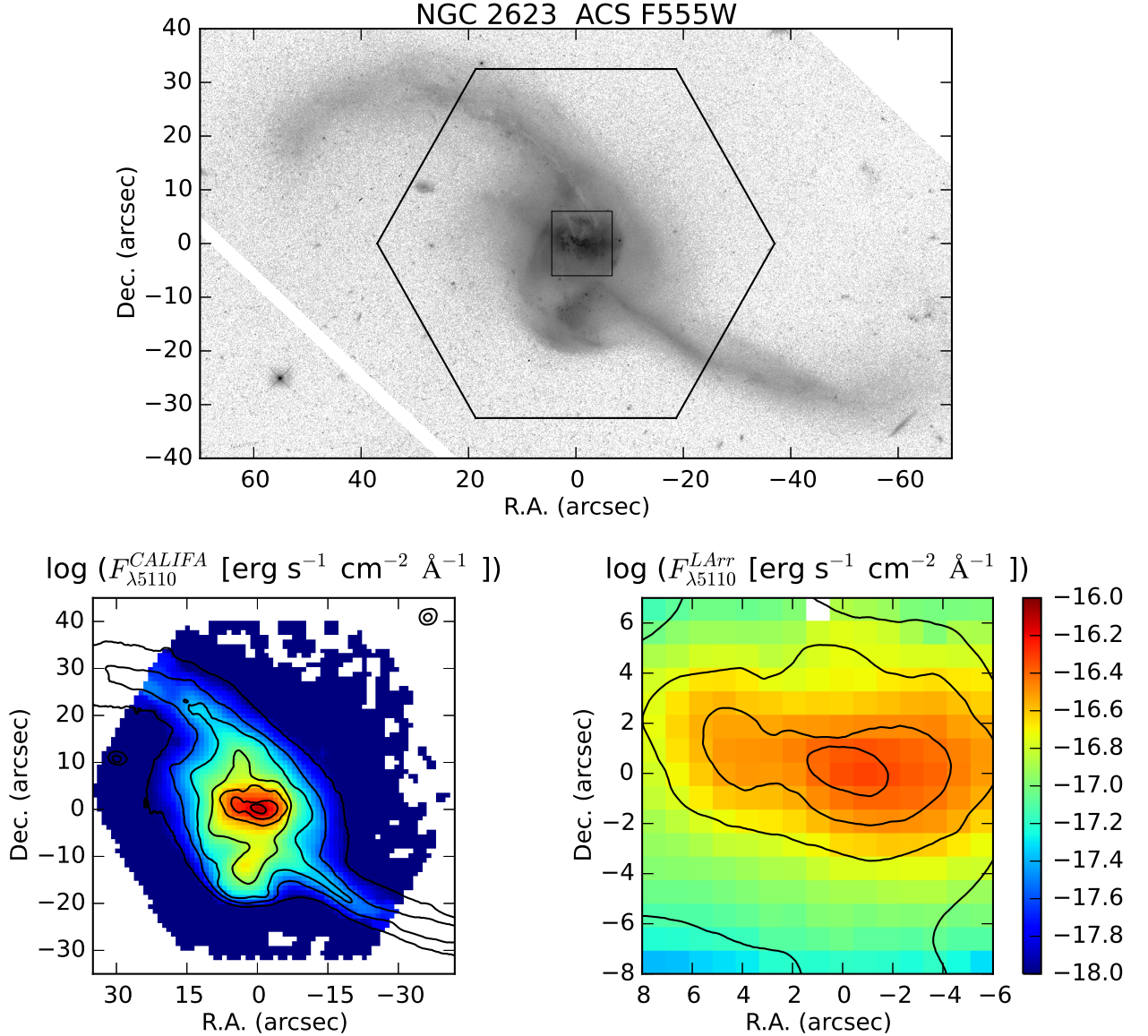


Figure 2.6 Top: HST ACS F555W image of NGC2623. The black rectangle indicate the positions where we have obtained the LArr IFS, while the black hexagon indicate the position of PPaK CALIFA IFS. Lower left: continuum flux at 5110 Å rest-frame, $F_{\lambda 5110}$, for the CALIFA data. Lower right: $F_{\lambda 5110}$ continuum for LArr data.

2.2.4. Arp 220

Arp 220 (UGC9913 = VV540; $L_{IR} = 1.6 \times 10^{12} L_{\odot}$; e.g., Sanders et al. 2003) is the brightest and closest example of an ultraluminous infrared galaxy (Soifer et al. 1984b, Sanders et al. 1988a). It is located about 78.3 Mpc away in the constellation of Serpens, the Serpent. HST observations of Arp 220 revealed more than 200 huge star clusters in the central part of the galaxy, together with dense dust lanes. Arp 220 has faint tidal tails and distortions seen in both optical and HI emission in the outer parts of the galaxy (Joseph & Wright, 1985; Hibbard et al., 2000) and twin nuclei separated by

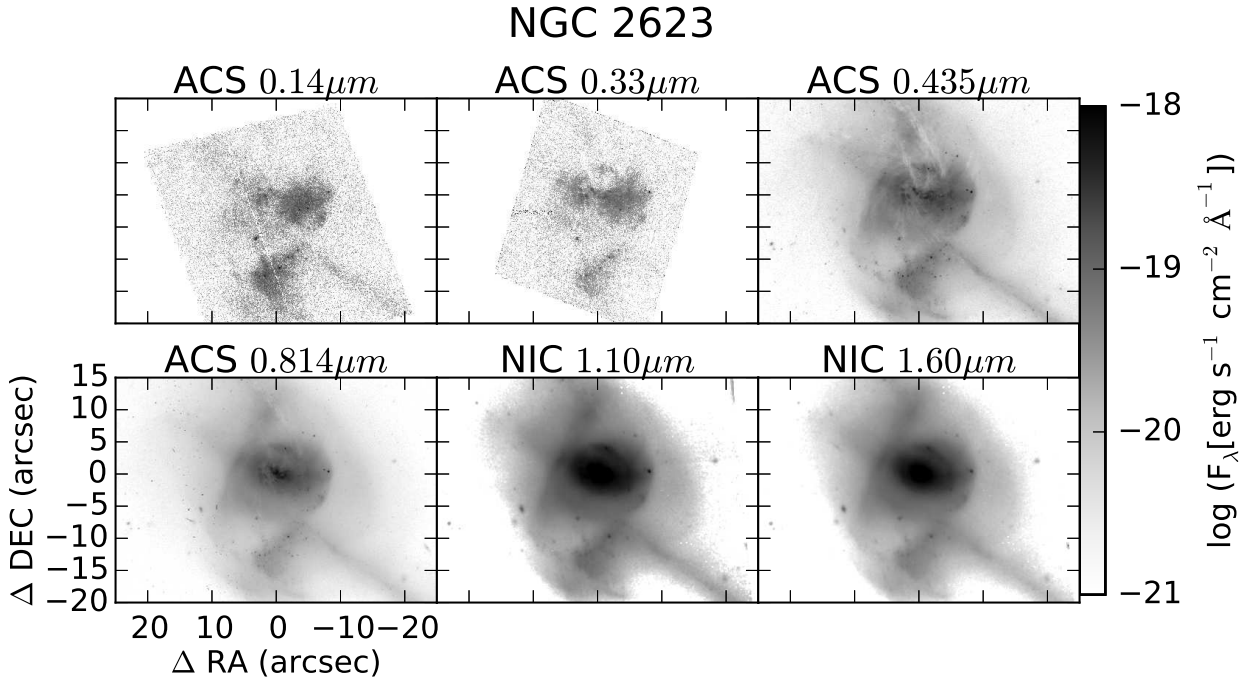


Figure 2.7 HST multiwavelength images of NGC 2623. From top left to bottom right: ACS FUV 1400 Å, ACS NUV 3300 Å, ACS optical 4350 Å and 8140 Å and NICMOS NIR 1.1 μm and 1.6 μm .

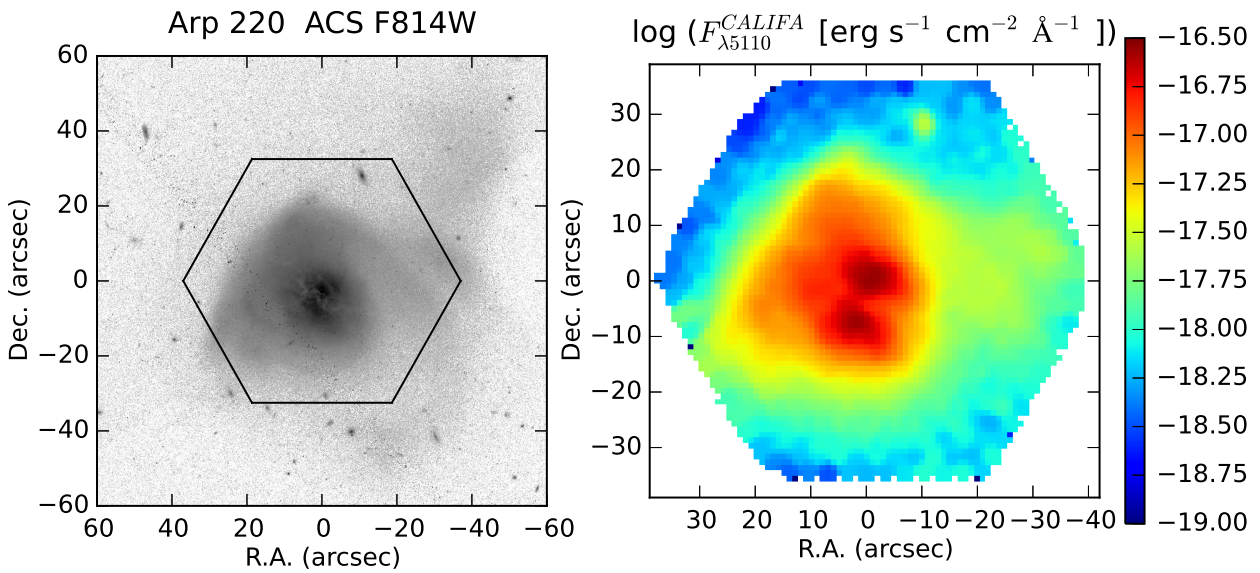


Figure 2.8 Left: HST ACS F814W image of Arp 220. The black hexagon indicate the position of PPAK CALIFA IFS. The right panel show the continuum flux at 5110 Å rest-frame, $F_{\lambda 5110}$, for the CALIFA data.

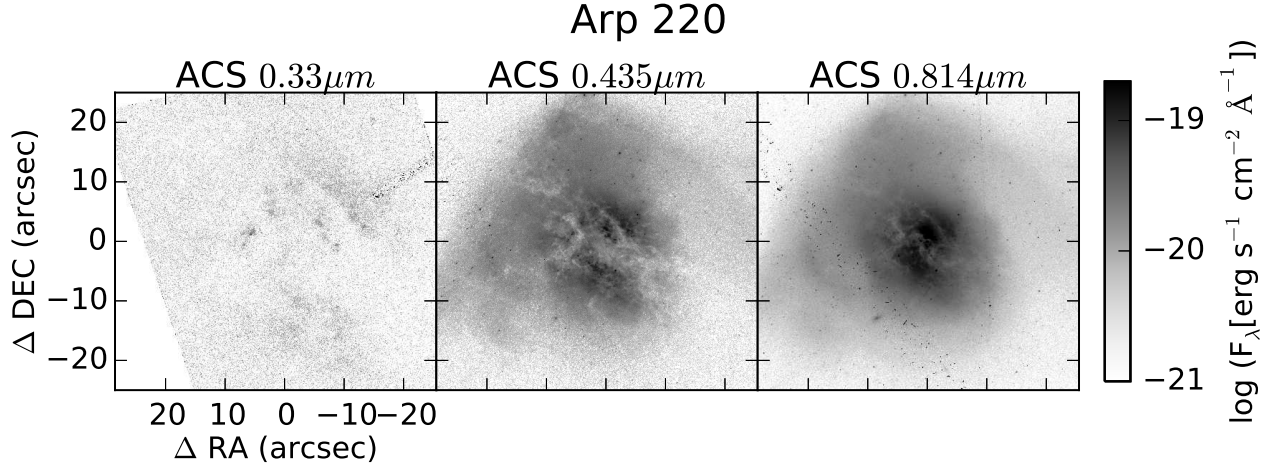


Figure 2.9 HST multiwavelength images of Arp 220. From left to right: ACS NUV 3300 Å, ACS optical 4350 Å and 8140 Å.

only ~ 360 pc (Scoville et al., 1998). It was observed the 2nd July 2011 by CALIFA survey. The same three pointing dithering scheme as for NGC 2623 was employed. In left panel of Figure 2.8 we show the HST ACS F814W image of Arp 220. The black hexagon indicates the position where CALIFA IFS was taken. On right panel we show the continuum flux at 5110 Å rest-frame, $F_{\lambda 5110}$. In Figure 2.9 we show HST images of Arp 220 in UV and optical filters. Its emission is almost totally obscured in the UV, and even in the red filter the amount of obscuration is significant.

During the thesis we have not had time to fully analyze this system, and therefore, it remains as a pending future work, together with the global comparison with other mergers observed by CALIFA.

2.3. Post-Starburst QSOs data

The SDSS survey has revealed that the PSQSO UN J1025-0040 is not an unique case. Brotherton et al. (2007) constructed a catalog of approximately 600 PSQSOs, spectroscopically selected from SDSS DR3, constituting several percent of low-redshift broad-lined AGNs. Their selection criteria require that the spectra display both the broad emission lines of luminous AGNs (Seyfert galaxies or quasars) and the Balmer jumps and high-order Balmer absorption lines of massive stellar populations of several hundreds Myrs. Moreover, Brotherton et al. (2008) report the results of a Hubble Space Telescope snapshot survey of 29 PSQSOs (HST proposal ID10588) at redshifts between 0.25 and 0.4. The broadband F606W ACS images resolve morphological details in nearly all targets and indicate that interactions and merger activity are common for this class. Some spectacular images include double nuclei, starbursting ring systems, and nuclear dust rings (Cales et al., 2011).

Our PSQSOs sample consists of 9 out of these 29 PSQSOs, which were selected for IFS follow up. Their main properties are summarized in Table 2.6. In the text, we will refer to them using the first four numbers in their SDSS name.

The sample is very heterogeneous, composed by systems with different morphologies and different interaction stages:

Table 2.6. PSQSOs properties

SDSS Name	z	M_{F606W}^{PSF}	M_{F606W}^{HOST}	Activity Class	Morphology
(1)	(2)	(3)	(4)	(5)	(6)
J023700.30-010130.5	0.344	-20.6	-22.3	?	S
J123043.41+614821.8	0.324	-21.0	-22.1	AGN	?
J124833.52+563507.4	0.266	-21.4	-23.0	AGN	E
J145658.15+593202.3	0.326	-19.8	-22.2	Sy 1	S?
J170046.95+622056.3	0.276	-20.0	-21.9	Sy 1	S
J233430.89+140649.7	0.363	-21.4	-22.9	AGN	E
J020258.94-002807.5	0.339	-20.0	-22.6	Sy 1	?
J212843.42+002435.6	0.346	-21.5	-21.9	AGN	E
J231055.50-090107.6	0.364	-20.8	-23.8	AGN	S

Note. — Column 1: SDSS name. Column 2: redshift from NED. Column 3 and 4: integrated Galactic dereddened K-corrected absolute ST magnitude in the F606W filter of the PSF and the host, respectively. Taken from [Cales et al. \(2011\)](#). Column 5: activity class from NED, taken from [Véron-Cetty & Véron \(2006\)](#). Column 6: Morphology classification taken from [Cales et al. \(2011\)](#). S represents spiral, S? probable spiral, E elliptical and ? indeterminate host morphology. The first six PSQSOs are the ones observed by PMAS and the last three by VIMOS.

- Two pre-merger spiral PSQSOs, similar in morphology to our pre-merger LIRGs: J1456 and J2310.
- Undefined pre-merger system where the morphology of the main galaxy is not clear: J1230
- Three post-merger elliptical systems: J2334, J1248 and J2128. J2128 has, in turn, another close companion of elliptical type that could end in another merger.
- Apparently isolated but distorted spirals due to past minor merging or maybe another processes: J0202, J0237, J1700.

The observations come from two different fiber-fed integral field spectrographs:

- Six PSQSOs, J0237, J1230, J1248, J1456, J1700, J2334, were observed with PMAS in LArr mode. As for the LIRGs, we have used a spatial resolution of $0.75''/\text{lens}$, covering a $12'' \times 12''$ FoV with a spatial resolution of $\text{FWHM}_{PSF} = 1.3'' - 2''$, maintaining the same telescope and instrument set up for all the target galaxies. The V300 grating was used, providing a $3.2 \text{ \AA}/\text{pixel}$ dispersion and covering a wavelength range between $3700 - 7100 \text{ \AA}$ ($\sim 2900 - 5500 \text{ \AA}$ rest-frame) with a spectral resolution of $R = 747$, 7.1 \AA FWHM at 5300 \AA (velocity resolution $\sigma \sim 170 \text{ km/s}$).

$H\alpha$ line could not be covered with the V300 grating as for the LIRGs due to the higher redshift values ($z \sim 0.3$). In order to obtain the rest-frame red optical spectra of the PSQSOs, including $H\alpha$, the R600 grating was used. This grating has a dispersion value of $1.6 \text{ \AA}/\text{pixel}$, covering a

Table 2.7. PSQSOs IFS observations

SDSS Name	Instrument	Grating	Total exposure time [s]	Observation date
J023700.30-010130.5	LArr	V300	2.5h (5 x 1800s)	02/09/2008
J023700.30-010130.5	LArr	R600	2h (6 x 1200 s)	04/09/2008
J123043.41+614821.8	LArr	V300	3.5h (4 x 1800s + 3 x 1800s)	02-03/04/2008
J123043.41+614821.8	LArr	R600	1.33h (4 x 1200s)	28/04/2008
J124833.52+563507.4	LArr	V300	5h (10 x 1800s)	03/04/2008
J124833.52+563507.4	LArr	R600	1.33h (4 x 1200s)	28/04/2008
J145658.15+593202.3	LArr	V300	9h (8 x 1800s + 10 x 1800s)	01-02/04/2008
J145658.15+593202.3	LArr	R600	3h (4 x 1200s + 5 x 1200s)	28/04/2008 + 03/07/2008
J170046.95+622056.3	LArr	V300	4.5h (6 x 1800s + 3 x 1800 s)	01-02/09/2008
J170046.95+622056.3	LArr	R600	2h (6 x 1200 s)	04/09/2008
J233430.89+140649.7	LArr	V300	4.5h (3 x 1800s + 6 x 1800s)	01-02/09/2008
J233430.89+140649.7	LArr	R600	2.67 h (8 x 1200 s)	04/09/2008
J020258.94-002807.5	VIMOS-IFU	MR	5h (10 x 1800s)	02-08-09-10/08/2008
J212843.42+002435.6	VIMOS-IFU	MR	5h (10 x 1800s)	03/05/2008 + 06-07-11-13-14/06/2008
J231055.50-090107.6	VIMOS-IFU	MR	6h (12 x 1800s)	14/06/2008 + 03-26-30/07/2008

wavelength range between 7700 - 9200 Å (\sim 5900 - 7100 Å rest-frame) with a resolution of $R = 2311$, 3.7 Å FWHM at 8500 Å, corresponding to a velocity resolution $\sigma \sim 130$ km/s.

- Three PSQSOs, J0202, J2128 and J2310, were observed by VIMOS in service mode. These observations cover a 27" x 27" FoV (matching well the angular size of the PSQSOs), using 40 x 40 fibres with a spatial scale of 0.67"/fibre. The medium resolution grating ($R = 720$) were used, with 2.5 Å/pixel dispersion, covering from 4900 - 10150 Å (3770 - 7800 Å rest-frame) with a spectral resolution of 10.4 Å FWHM at 7500 Å, corresponding to a velocity resolution $\sigma \sim 177$ km/s. The exposure time was split into 10 - 12 frames of 1800s each. A 4 pointing dithering scheme was used in order to correct for dead fibres within the FoV. VIMOS observations include both the higher order Balmer lines and H α line in the same spectrum.

Our IFS observations of the PSQSOs are summarized in Table 2.7. In Figure 2.10 we show the images of the six PSQSOs observed with PMAS LArr. The left panels show the HST ACS F606W image of the PSQSO. The middle panels show the continuum flux at 5110 Å rest-frame, $F_{\lambda 5110}$ in logarithmic scale, extracted from the IFS. The right panels show the signal-to-noise ratio (SNR) maps at 5110 Å rest-frame. Analogously, in Figure 2.11 we show the images of the three PSQSOs observed with VIMOS.

Although initially our idea was to study the spatially resolved (spaxel by spaxel) stellar populations of the PSQSOs, finally it has not been possible due to the low SNR of the data. The spectral synthesis require $\text{SNR} \gtrsim 20$, and in our data only a few spaxels in the nuclear region satisfy this requirement, while the spaxels in the external regions have lower SNR (see the right panels in Figure 2.10 and 2.11). We eventually approached their study analyzing:

1. The spectra of the central regions. We have extracted them in an aperture radius of 1.5 arcsec, identical to the fiber aperture radius of SDSS spectroscopy, with which we have compared.
2. The integrated spectra. They have been extracted in variable apertures (all of them above the Petrosian radius aperture given by SDSS DR7), in a way that they include the whole optical

extension of each PSQSOs in ACS F606W image. The companion galaxies (when present) have not been included.

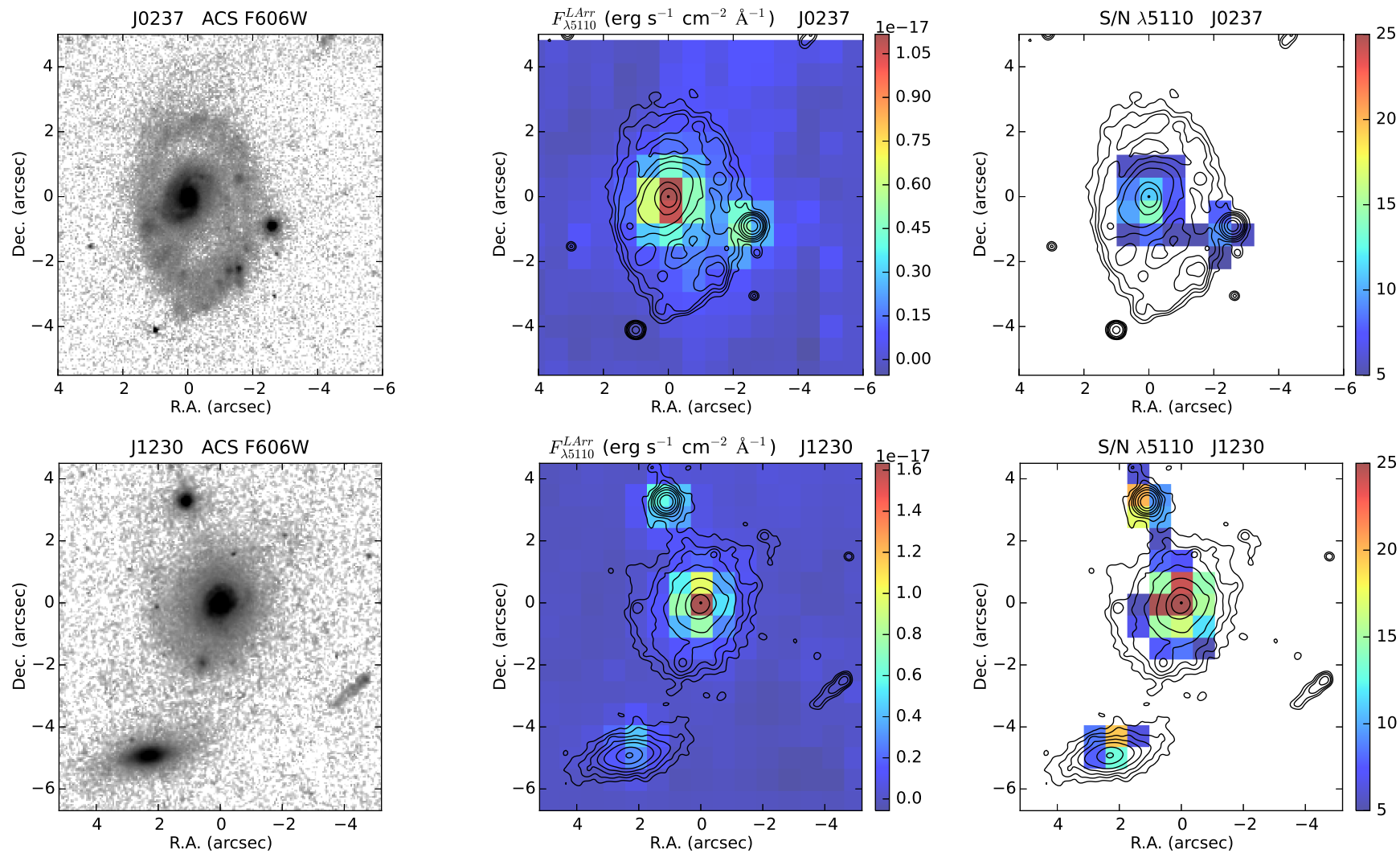


Figure 2.10 PMAS Larr PSQSOs observations. Left: HST ACS F606W image of the PSQSO. Middle: Continuum flux at 5110 Å rest-frame, $F_{\lambda 5110}$, in logarithmic scale, extracted from the IFS. Right: SNR map at 5110 Å rest-frame.

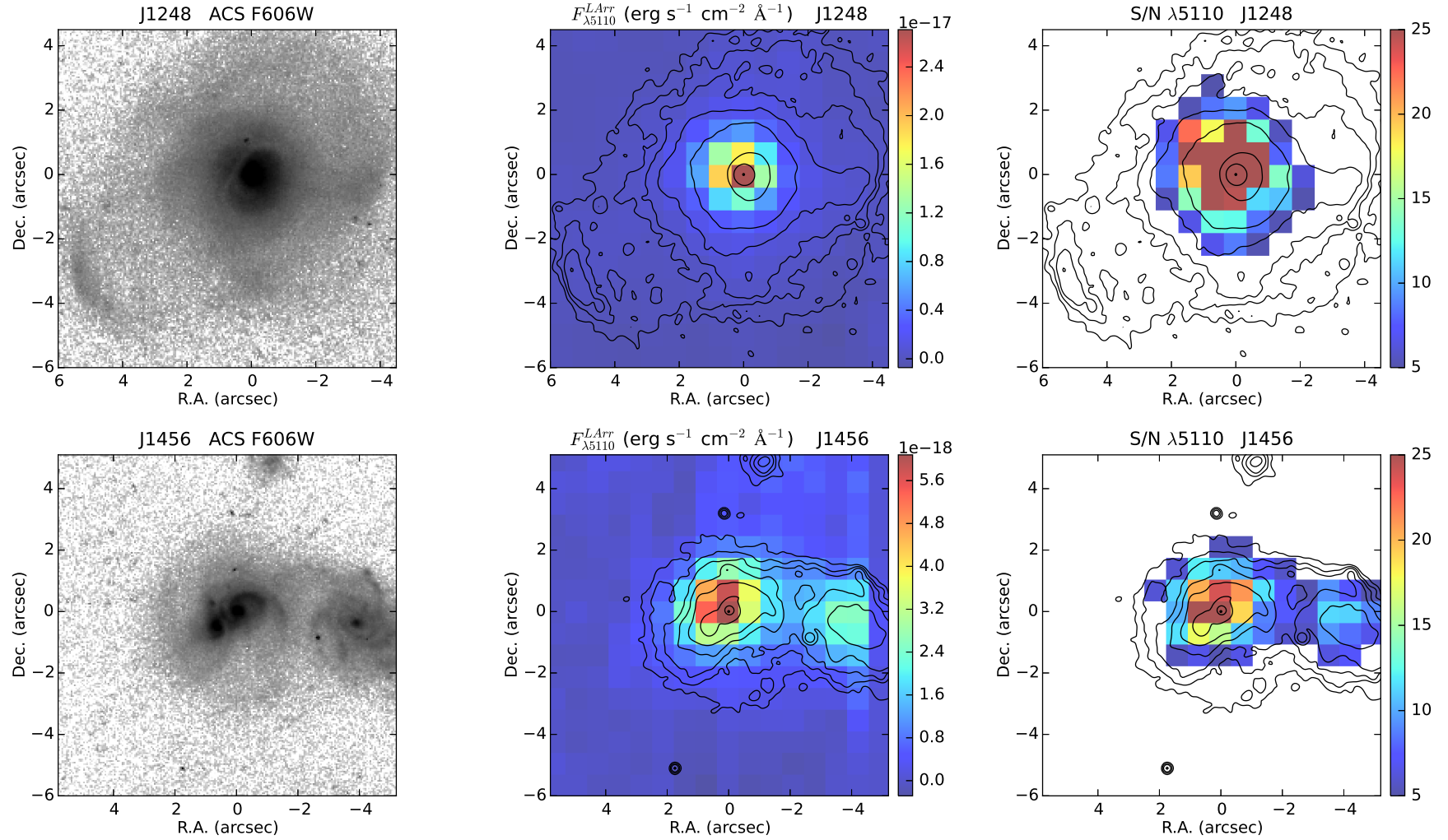


Figure 2.10 PMAS LArr PSQSOs observations. Left: HST ACS F606W image of the PSQSO. Middle: Continuum flux at 5110 Å rest-frame, $F_{\lambda 5110}$, in logarithmic scale, extracted from the IFS. Right: SNR map at 5110 Å rest-frame.

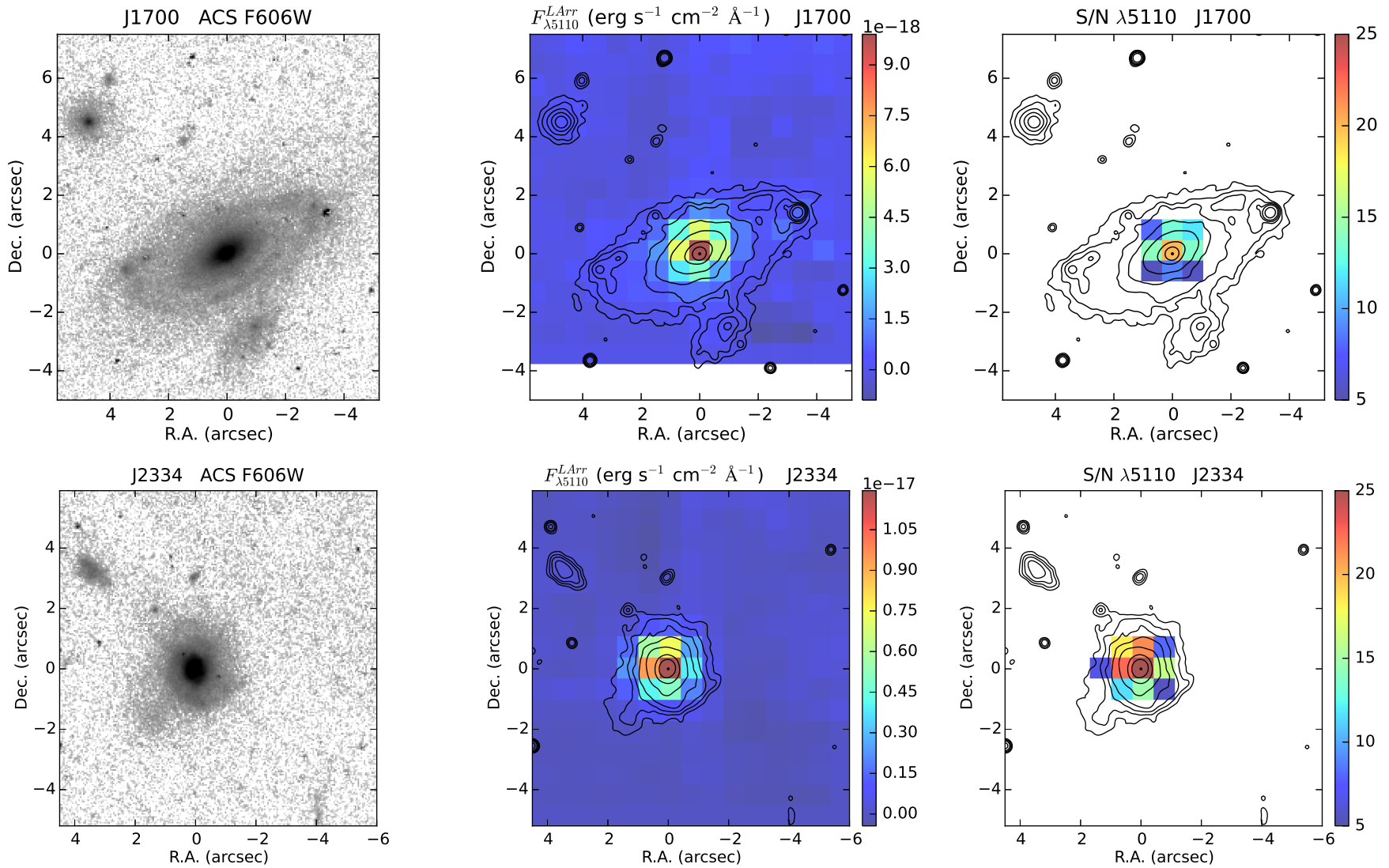


Figure 2.10 PMAS Larr PSQSOs observations. Left: HST ACS F606W image of the PSQSO. Middle: Continuum flux at 5110 Å rest-frame, $F_{\lambda 5110}$, in logarithmic scale, extracted from the IFS. Right: SNR map at 5110 Å rest-frame.

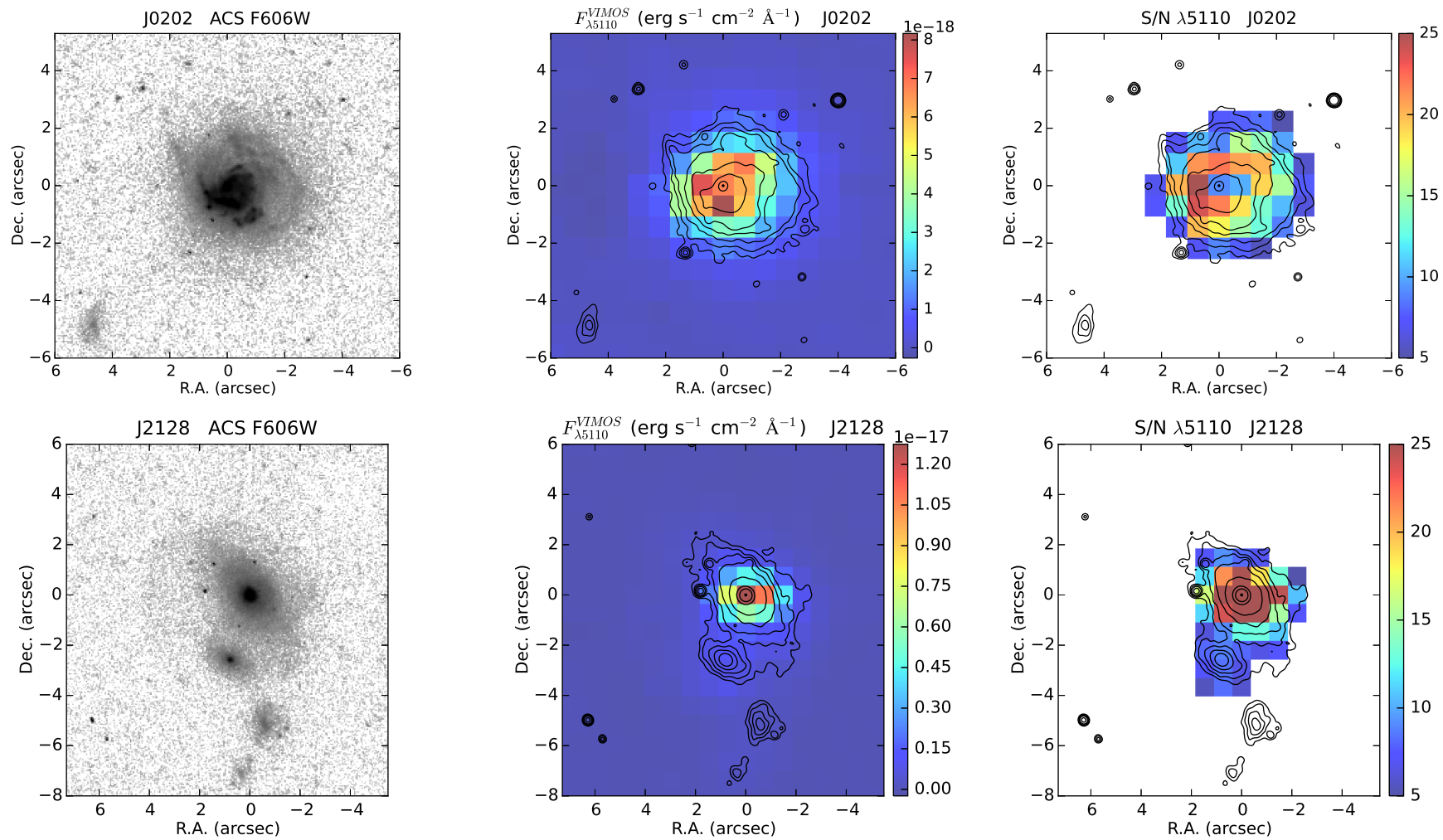


Figure 2.11 VIMOS PSQSOs observations. Left: HST ACS F606W image of the PSQSO. Middle: Continuum flux at 5110 Å rest-frame, $F_{\lambda 5110}$, in logarithmic scale, extracted from the IFS. Right: SNR map at 5110 Å rest-frame.

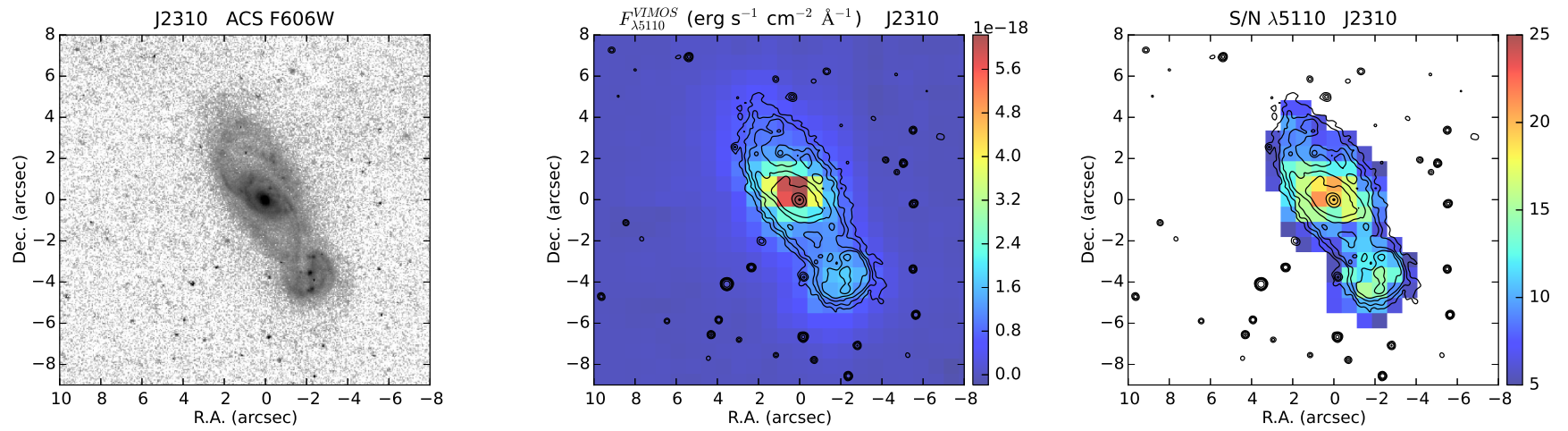


Figure 2.11 VIMOS PSQSOs observations. Left: HST ACS F606W image of the PSQSO. Middle: Continuum flux at 5110 Å rest-frame, $F_{\lambda 5110}$, in logarithmic scale, extracted from the IFS. Right: SNR map at 5110 Å rest-frame.

3

Data reduction

We devote this chapter to explain the reduction process of our IFS and OSIRIS TF observations. In the case of the IFS, a single observation contains several hundred spectra of different regions in the sky. The reduction of such a vast amount of information is a complex process. The general fiber-fed IFS data reduction process is already described in detailed in the literature ([Sánchez, 2006](#)). However, each instrument has its own particularities and specificities.

3.1. PMAS data reduction

Here, I describe in detail the steps followed to reduce our PMAS observations. A considerable amount of time was invested in understanding, applying and improving each of the individual reduction steps. We have used a combination of existing software packages specially designed for fibre-fed and IFS data, as R3D ([Sánchez, 2006](#)) and E3D ([Sánchez, 2004](#)), together with IRAF routines, and our own Python scripts, developed for easily repeating common tasks in an homogeneous and consistent way, and to speed up/automate certain reduction steps.

3.1.1. The raw data

In most cases, the raw data of fiber-fed spectrographs consist of a collection of spectra distributed along a certain axis of a 2D frame. Figure 3.1 shows a section of our PMAS raw data of IC 1623 W. Each spectrum is distributed in x-axis with wavelength, along the so-called dispersion axis. For each wavelength, the spectrum is spread over a certain number of pixels along the y-axis (cross-dispersion axis or spatial axis), following a characteristic profile of finite width, which may be considered Gaussian in the simplest approximation.

Depending of the pointing position of the telescope, the fibers suffer from different amounts of flexures and tensions which causes the projected spectra in the CCD to change and a variable spectral dispersion from fiber-to-fiber. Note the misalignment of the spectra along the dispersion axis with respect to the CCD frame in Figure 3.1. These are the so-called flexure effects. To be able to properly reduce an IFS observation, it is necessary to take several calibration frames immediately after each science exposure, at least an arc lamp for performing wavelength calibration and a continuum lamp for spectra extraction. This ensures that the flexure pattern of the calibration and science frames is

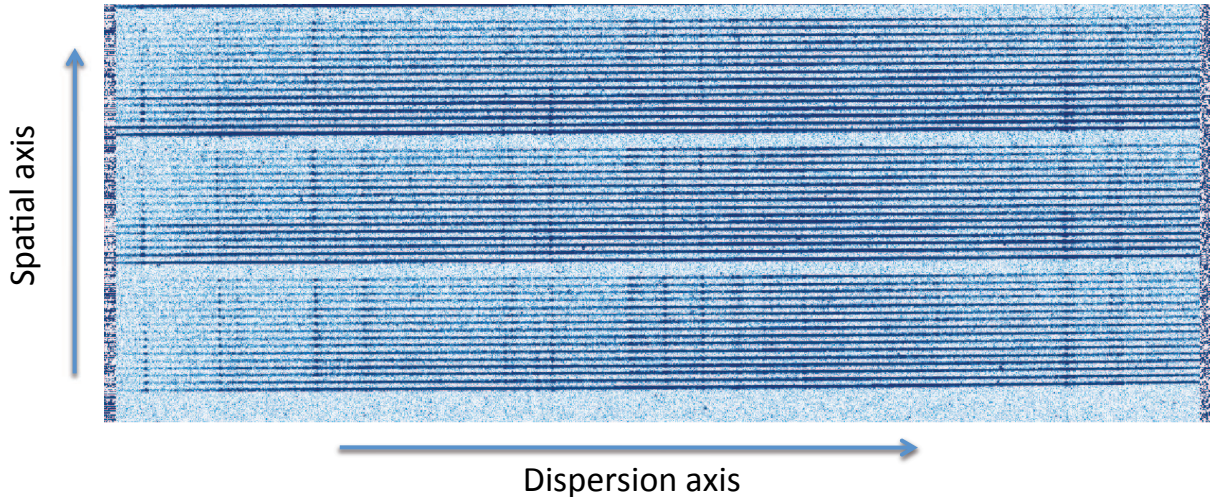


Figure 3.1 Section of PMAS raw data of IC 1623 W. Each dark line corresponds to the projection of a spectrum along the dispersion axis.

the same and, therefore, it is possible to trace and extract the projected spectra and calibrate them in wavelength properly. As the flexure pattern varies with the pointing position, we have taken as much calibration frames as science pointings. However, even maintaining the same pointing position, the flexure pattern also changes with time. The variation due to time-related flexures is less than 0.2 pixels during 1.5 h in the case of PMAS. Moreover, the amplitude of the flexures is small before the culmination of the targets and gets stronger while targets are setting.

3.1.2. Pre-reduction

Before starting with the specific reduction steps of IFS, a general pre-reduction scheme was performed. The pre-reduction consisted of all the corrections that are common to any CCD-based data:

- a) Bias correction: The bias frames acquired during each observing night were visually inspected and then combined to create a master bias frame, which has been subtracted to all the raw images.
- b) Flat-field correction: A flat-field correction is also necessary to remove artifacts in the raw images caused by variations in the pixel-to-pixel sensitivity of the detector. With the CCD used during our observing runs, these variations are around $\pm 1\%$ of the average for most of the field. We have divided our bias-corrected data for the master CCD flat provided by the Calar Alto observatory. It has been created using long exposures of scattered light (in PMAS it is not possible to illuminate the CCD without passing through the fibers and the spectrograph).
- c) Cosmic rays rejection: When only one or two science exposures in a certain pointing position were available, the cosmic rays rejection was performed using the L.A.Cosmic algorithm (van Dokkum, 2001). When we had three or more science exposures, the cosmic rays were removed later, during their combination, after the sky subtraction (see Section 3.1.11).

3.1.3. Identification of the observation blocks and flexures correction

As explained above, each IFS observation block consist in:

- Science frames (one or more exposures, could be the science targets, standard stars, twilight sky or adjacent sky exposures).
- Continuum lamp frame, for spectra extraction.
- Arc lamp frame, for wavelength calibration.

The first step in the data reduction consisted in identifying the observation blocks, by cheking the logfile and confirming in the data headers the time at which the observations were acquired and the telescope azimuth and elevation in that moment. Once identified, we checked if the science and calibration frames were affected by the same flexure pattern. This is crucial to be able to extract the spectra and perform the right wavelength calibration. In most of our cases we found the flexure pattern of the calibrations and science frames was the same. However, in a few cases, we found small linear offsets between the science and the calibration frames that were corrected by applying a linear shift (with IRAF `imshift` task) to align them.

At this stage we did not combined the science exposures of the same pointing, when more than one were available. All of them were reduced independently and then combined at the end, after sky subtraction. In this way we avoid increasing the uncertainties in the reduction due to differences in the airmass and atmospheric extinction values from one exposure to another.

3.1.4. Spectra identification

Once corrected the flexure pattern misalignments, the next step of the IFS reduction was to trace the location of all the spectra along the dispersion axis of the CCD to, later on, extract its corresponding flux. The tracing procedure must be applied over well illuminated continuum exposures, with enough signal-to-noise through all the fibers at every wavelength. That is why the continuum exposures are needed. Two steps were followed:

1. First, we identified the fiber peaks for the central column of the CCD. The location of the spectra was found by comparing the intensity at each row along the cross-dispersion axis with those of its adjacent pixels, checking for those pixels that verify the maximum criteria. The `peak_find` R3D task has been used for this purpose.¹ The process is visually crosschecked by a graphical output, shown in Figure 3.2. In the left panel we show a continuum exposure. The black vertical line indicates the cut along the spatial axis corresponding to the central column, where we have obtained the spatial profile for peak-searching. In the right panel we show the profile of intensities along the mentioned central column. The red dots mark the location of the pixels where the program has found a peak, using the parameters defined by the command line. The blue dots mark the location of the centroid of these peaks, calculated through a hyperbolic fit of the peak pixel and the two adjacent ones. All these values were stored in an output file.

¹The input parameters needed by this and another R3D tasks to run are explained in detail in the R3D user guide. Moreover, it includes specific examples of the best parameter choice in the case of PMAS LArr data reduction.

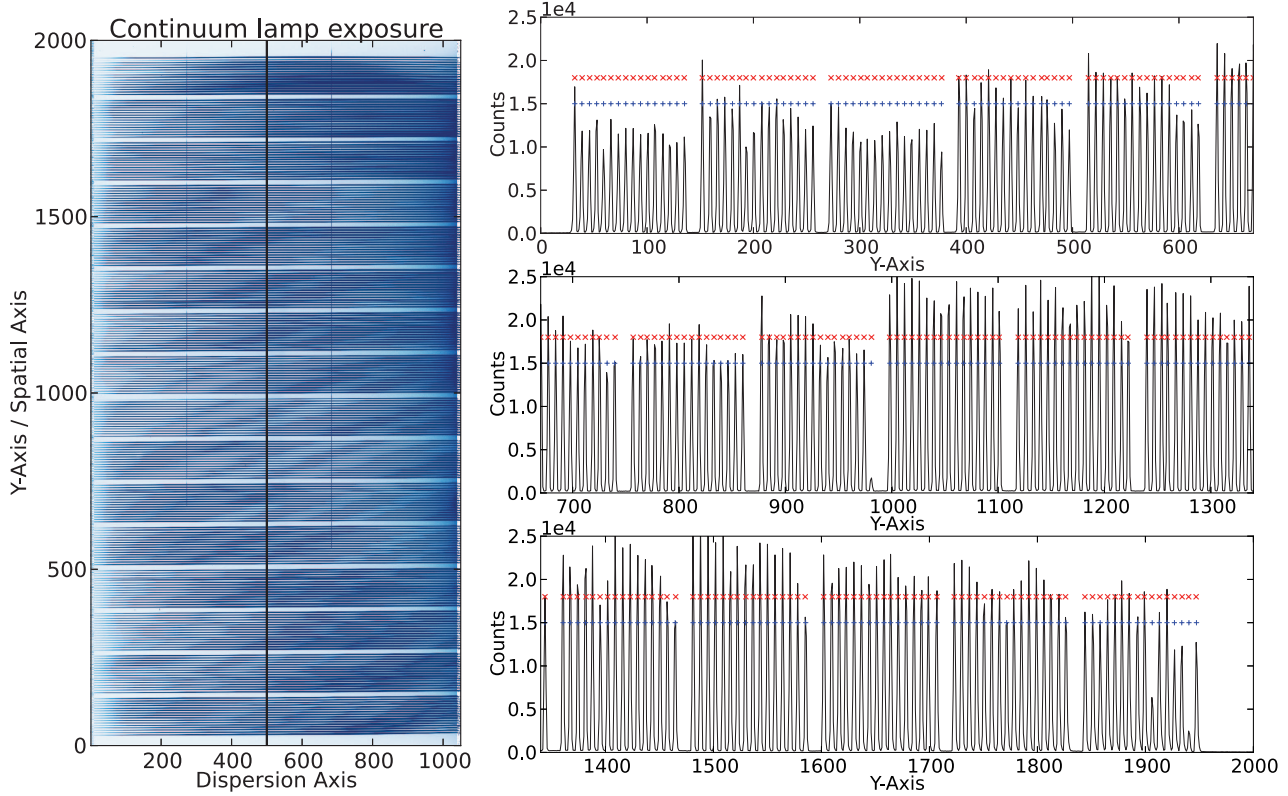


Figure 3.2 Schema of the fibers peaks identification. Left: continuum lamp exposure. The black vertical line indicates the cut along the spatial axis corresponding to the central column, whose spatial profile has been used for peak-searching. Right: spatial profile of intensities along the mentioned central column. The red dots mark the location of the pixels where the program has found a peak, using the parameters defined by the command line. The blue dots mark the location of the centroid of these peaks, calculated through a hyperbolic fit of the peak pixel and the two adjacent ones.

2. The second step, once we knew the location of the fibers for the central column of the CCD was to trace their locations for the remaining columns, that is, along the whole dispersion axis. This was performed by the `trace_peak_recursive` task. Within a predefined window for a certain column in the dispersion axis, this routine finds the fibers peaks, looking for maxima in the intensity profile, taking as a first guess the position found in the central column. The process was iterative, starting from the central column and continuing to the end and to the beginning of the CCD. If no maximum is found within the predefined window for a certain column, the location of the spectra on the previous column is used assuming a smooth behavior of the trace along the dispersion axis. This method solves the possible problems of bad columns, low sensitivity pixels, and/or cosmic rays. The result was stored as a 2D image, where the X-axis corresponds to the original dispersion axis and the Y-axis indicates the traced spectrum number, from 1 to 256 in the case of PMAS LArr. The stored value at each pixel is the location of the peak centroid in the original frame, the analogous to the blue crosses in the right panel of Figure 3.2, but extended to every pixel in the spectral direction. This file is called the trace, and an example of it is shown in Figure 3.3.

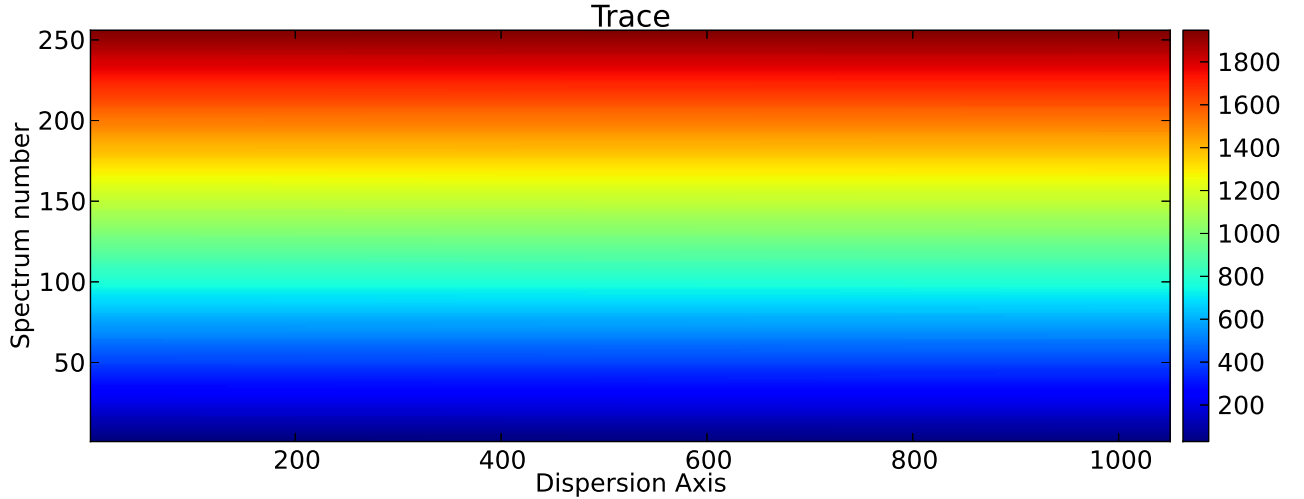


Figure 3.3 Trace for spectra extraction. The stored value at each pixel is the location of the peak centroid in the original frame, the analogous to the blue crosses in the right panel of Figure 3.2, but extended to every pixel in the spectral direction.

3.1.5. Spectra extraction

The next step was to extract the flux corresponding to the different spectra at each pixel along the dispersion axis, for both science and arc lamp exposures. We have used the trace file obtained in the previous section. By construction, the projected spectrum of each fiber in the CCD contaminates the adjacent ones in an amount that depends on the distance between adjacent spectra and the width of the projected profiles along the cross-dispersion. This effect is known as cross-talk, and may produce a wrong interpretation of the data, as the adjacent spectra on the plane of the CCD may not correspond to nearby locations in the FoV. In many instruments, like PMAS in the Larr mode, it is not important (less than 1%), while in others, like VIMOS, may be critical (see Section 3.2.3)

As for these observations cross-talk is not important, the spectra have been extracted by co-adding the flux within a 5 pixels aperture around the trace position. This procedure is called aperture extraction, and it has been implemented in R3D, with the `extract_aper` task. The extracted spectra are represented in a 2D image. The X-axis of the resulting image corresponds to the original dispersion axis, while the Y-axis corresponds to different extracted spectra, as they were ordered along the pseudo-slit. This is the so-called row-stacked spectra representation, RSS (Sánchez, 2004). In Figure 3.4 we show the extracted spectra for the arc lamp (top panel) and NGC 2623 science data (bottom panel). Once extracted, the PMAS data were ready for the next reduction step.

3.1.6. Distorsion correction

Most grating spectrographs do not disperse the light homogeneously along the cross-dispersion axis. The dispersion is distorted, being larger at the edges of the slit than in the center. This is the so-called C distortion. When the spectrographs are fed with fibres, additional distortions are produced due to the placing of the fibers in the pseudo-slit. In both panels of Figure 3.4 the curvature and distortions are clearly seen. These distortions must be corrected fiber-to-fiber before finding a common

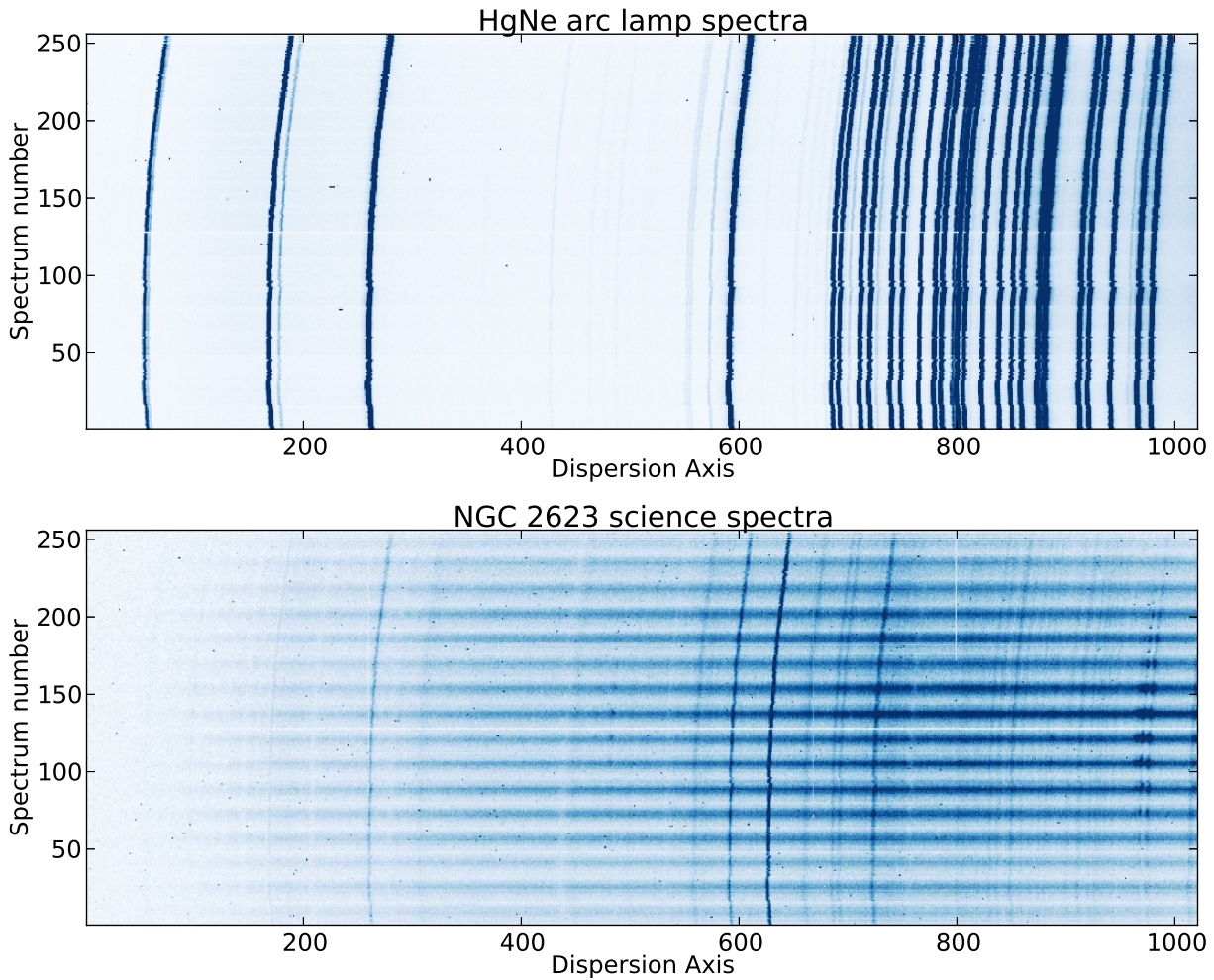


Figure 3.4 RSS of the HgNe arc lamp (top panel) and NGC 2623 science frame (bottom panel). The X-axis is the dispersion axis (in pixels), while the Y-axis corresponds to different extracted spectra, as they were ordered along the pseudo-slit.

wavelength solution. The correction was performed with R3D using the RSS arc lamp exposures (like the one shown in upper panel of Figure 3.4), extracted as indicated in the previous section.

First, the peak intensity of a single emission line was traced along the cross-dispersion axis, and shifted to a common reference, by a linear shift. This was done by the program `dist_cor`, and the process is shown in Figure 3.5. In the top left panel we show the HgNe arc lamp RSS, before distortion correction. The spectral line around pixel 593 in the dispersion axis has been taken as a reference. The red stars indicate the position of the peak intensity along the cross-dispersion axis. A zoom into this region is shown in the top right panel. In lower left panel we have applied the first order distortion correction, by shifting every spectrum in wavelength until the line profile is centered around pixel 593, which is shown with white stars. Note the difference with respect to the uncorrected one (red stars).

Although the first order transformation corrects significantly the distortion, there are still small misalignments in other emission lines, which are specially evident at the edges of the frame (note the lines at the edges of bottom left panel of Figure 3.5). To correct them, we traced the intensity

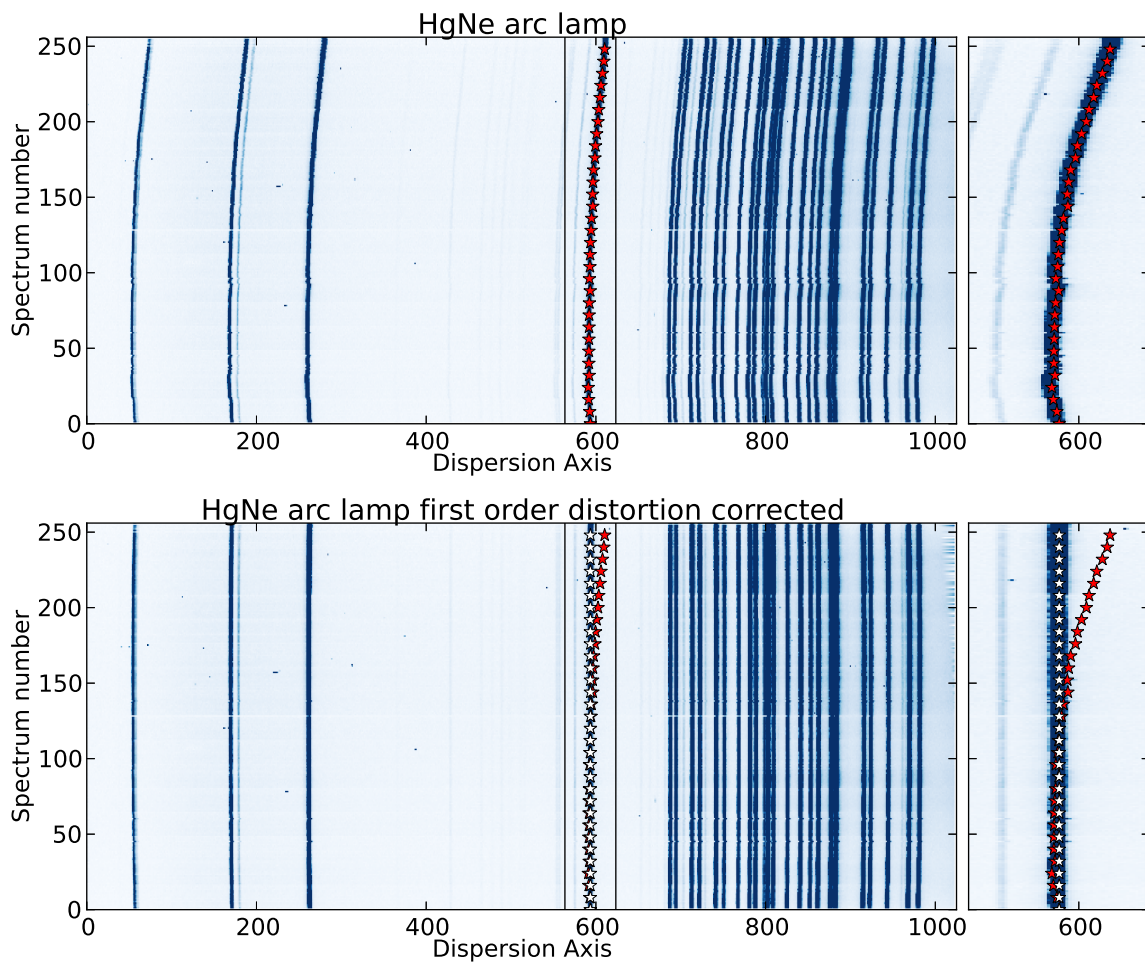


Figure 3.5 Top left panel: HgNe arc lamp RSS before distortion correction. Spectral line around pixel 593 in the dispersion axis was taken as a reference. Red stars indicate the position of the intensity peak along the cross-dispersion axis. A zoom into this region is shown in the top right panel. Bottom left panel: first order distortion corrected image, all the profile has been shifted around pixel 593, which is shown with white stars. Note the difference with respect to the uncorrected profile (red stars).

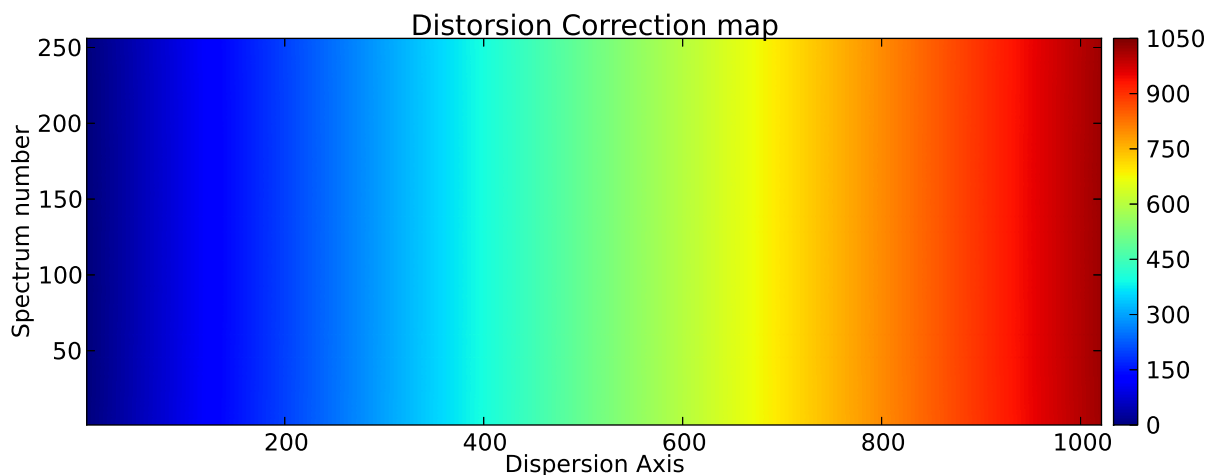


Figure 3.6 Distortion correction map. The stored value at each pixel is the position in the dispersion axis where the actual position should be moved in order to correct the distortion.

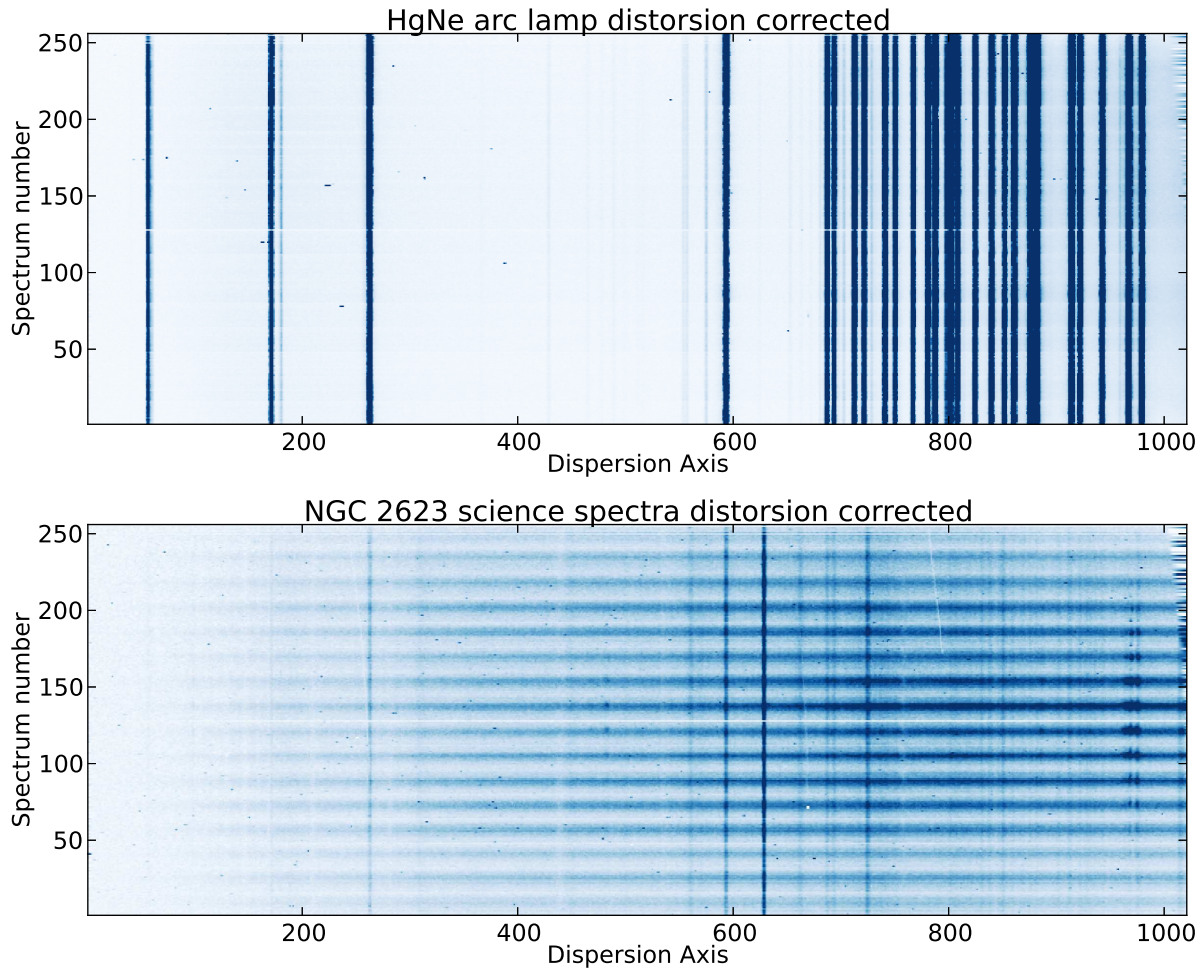


Figure 3.7 Distorsion corrected RSS of the HgNe arc lamp (top panel) and NGC 2623 science frame (bottom panel). Note the differences between them and the uncorrected ones in Figure 3.4.

peak of a set of selected emission lines, well distributed along the whole dispersion axis, to find a polynomial transformation that recenter all the lines to a common reference. This was done using the task `mdist_cor_sp.pl`, that allow to interactively select the lines that will be used. Both PMAS and VIMOS are well-behaved instruments in terms of distortion and, therefore, just a low-order polynomial function (order $\sim 4 - 5$) was needed, by using around 15 bright emission lines. The distortion correction map is given as an output, an example is shown in Figure 3.6. This is the map to be applied to the science exposures to get them distortion corrected. The R3D routine used was `mdist_cor_external.pl`. The resulting distortion corrected maps are shown in Figure 3.7. Note the differences with respect to the uncorrected ones in Figure 3.4.

3.1.7. Dispersion solution

The wavelength solution was determined by identifying the emission lines in the distortion-corrected arc lamps exposures, as the one in the top panel of Figure 3.7. The arc lamps used were HgNe for V300 grating, and ThAr for R600. The correspondence between pixels and wavelength was

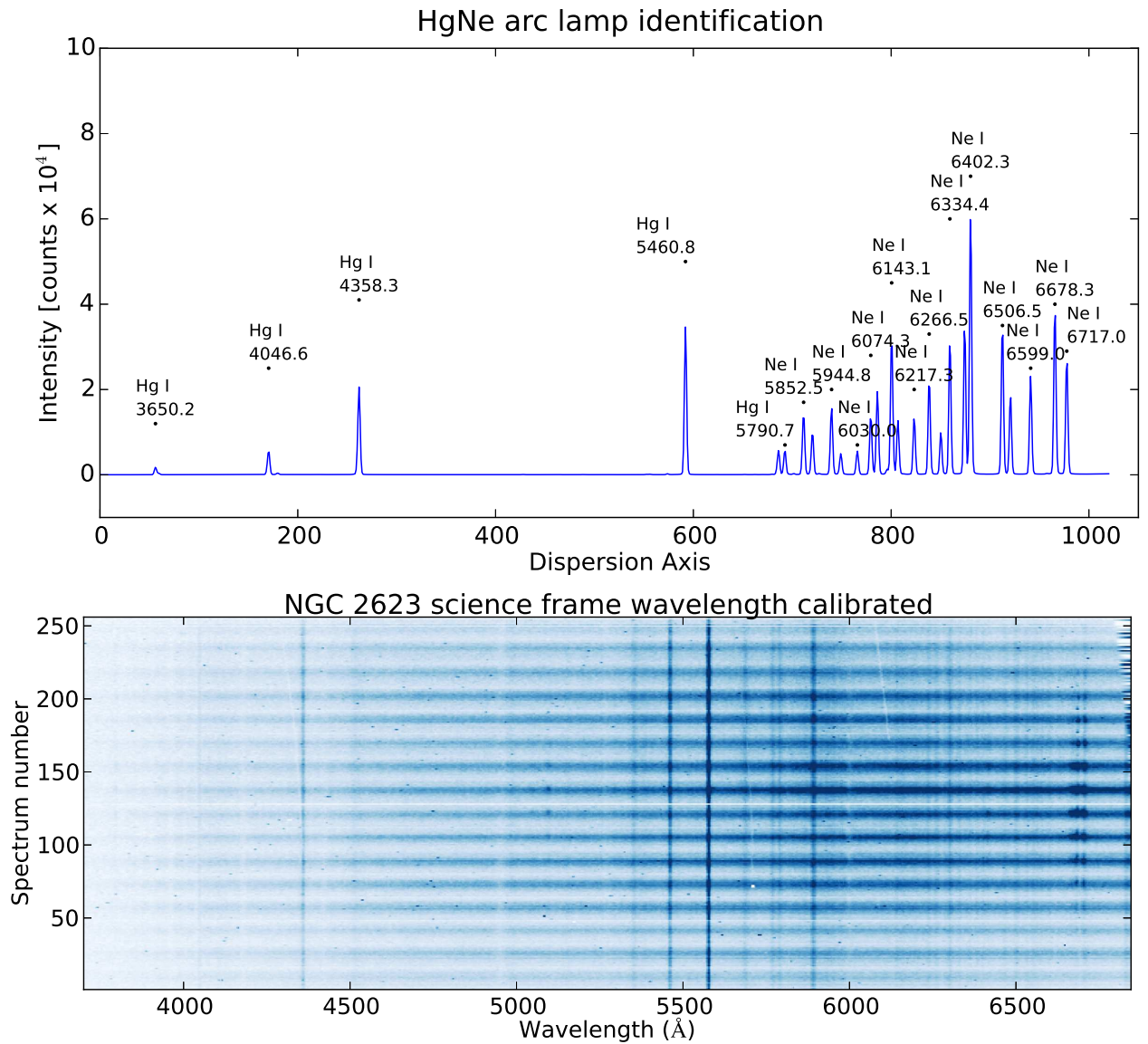


Figure 3.8 Top panel: Identification of the main emission lines in HgNe arc lamp spectra. Bottom panel: NGC 2623 science frame wavelength calibrated.

made using the identification charts provided by the CAHA webpage. See top panel of Figure 3.8 for an example of identification of HgNe lines. The interactive routine `disp_cor.pl` transformed the pixel coordinate system into a linear wavelength coordinate system through a polynomial transformation. The required transformation was stored in an ASCII file to be applied over the science data, using the `disp_cor_external` task.

The final accuracy of the wavelength calibration was estimated by comparing the central wavelength of the sky emission lines with their nominal values. It depends on the selected order of the polynomial function, the number of identified lines, and the coverage of emission lines along the wavelength range. For example, for PMAS in the LArr mode, using V300 grating, we find an agreement within a range of ~ 0.38 Å, identifying between 18 - 20 emission lines, and using a polynomial function

of order 4 - 5. For R600 grating, we have reached an accuracy of $\sim 0.25 \text{ \AA}$ using between 12 - 14 lines. In bottom panel of Figure 3.8 we show the wavelength calibrated science data.

3.1.8. Fiber-to-fiber transmission correction

The fibers of most fiber-fed IFUs, although done with the same material, have slightly different transmissions one-to-other, with a clear wavelength dependency. To correct for this effect is required to obtain an exposure of a continuous, well-illuminated and flat uniform source. In the case of PMAS LArr observations, we acquired twilight skyflat exposures in each observing night, that have been reduced following the same procedure as the science frames. The reduced twilight skyflat frame is shown in top panel of Figure 3.9. Note the differences between the spectra as a consequence of fiber-to-fiber differential transmission.

To normalize the transmission of all the fibers to the median one we used R3D `fiberflat.pl` task. This task calculates the median spectrum of all the spectra in the skyflat frame, and then divide each spectrum by this median one. The result is stored in a file (the so-called FiberFlat, see middle panel of Figure 3.9) that could be used to correct from the differential transmission fiber-to-fiber, simply dividing the science frames by it. Moreover, in bottom panel of Figure 3.9, we show the relative transmission of some of the fibers along the wavelength range. They are plotted in different colors to illustrate the differences in the transmission fiber-to-fiber at each particular wavelength. When dividing the science frames by the fiberflat the transmission of all the fibers is normalized to the median transmission.

3.1.9. Flux calibration

The flux calibration of IFS is analogous to other spectroscopic techniques, like longslit or aperture spectroscopy. We have observed at least one standard spectrophotometric star each night for performing the relative flux calibration. In Table 3.1 we indicate the standard stars observed, the date and Universal Time (UT) of observation, the airmass, the local optical extinction A_V from CAHA extinction monitor, and the exposure time. Their data have also been reduced following all the steps described in previous sections.

In order to obtain the calibration sensitivity function from a standard star, a 1D spectrum must be extracted from it. This uncalibrated spectrum was obtained as follows. First, we have converted the RSS standard frame into a datacube, using `rss2cube.pl`. This task uses the fibers position table to assign each spectra in the RSS the right spatial location in the FoV. In Figure 3.10 we show an example of the intensity maps (in counts) of BD+28D4211 in different wavelengths ranges. As can be seen, the intensity peak position changes with wavelength. The star is centered in pixel [8,7] at blue wavelengths, and at [7,6] in red wavelengths. This is due to the prismatic effect the atmosphere has on the incoming light beam. Blue wavelengths are refracted more strongly than red wavelengths. This effect is called differential atmospheric refraction (DAR), and it is necessary to correct it before extracting any spectra from the datacube, for assure we are not missing flux in any spectral range (Filippenko, 1982). To perform this correction we used `DAR_det_cube.pl` task. Taking the star position at 5500 \AA as a reference, this task looks for any shift in this centroid along the wavelength range within a box of 5×5 spaxels. Once the shift is determined, a polynomial fitting of order 3 is applied to smooth the correction, and the shift is applied wavelength to wavelength, recentering the cube and

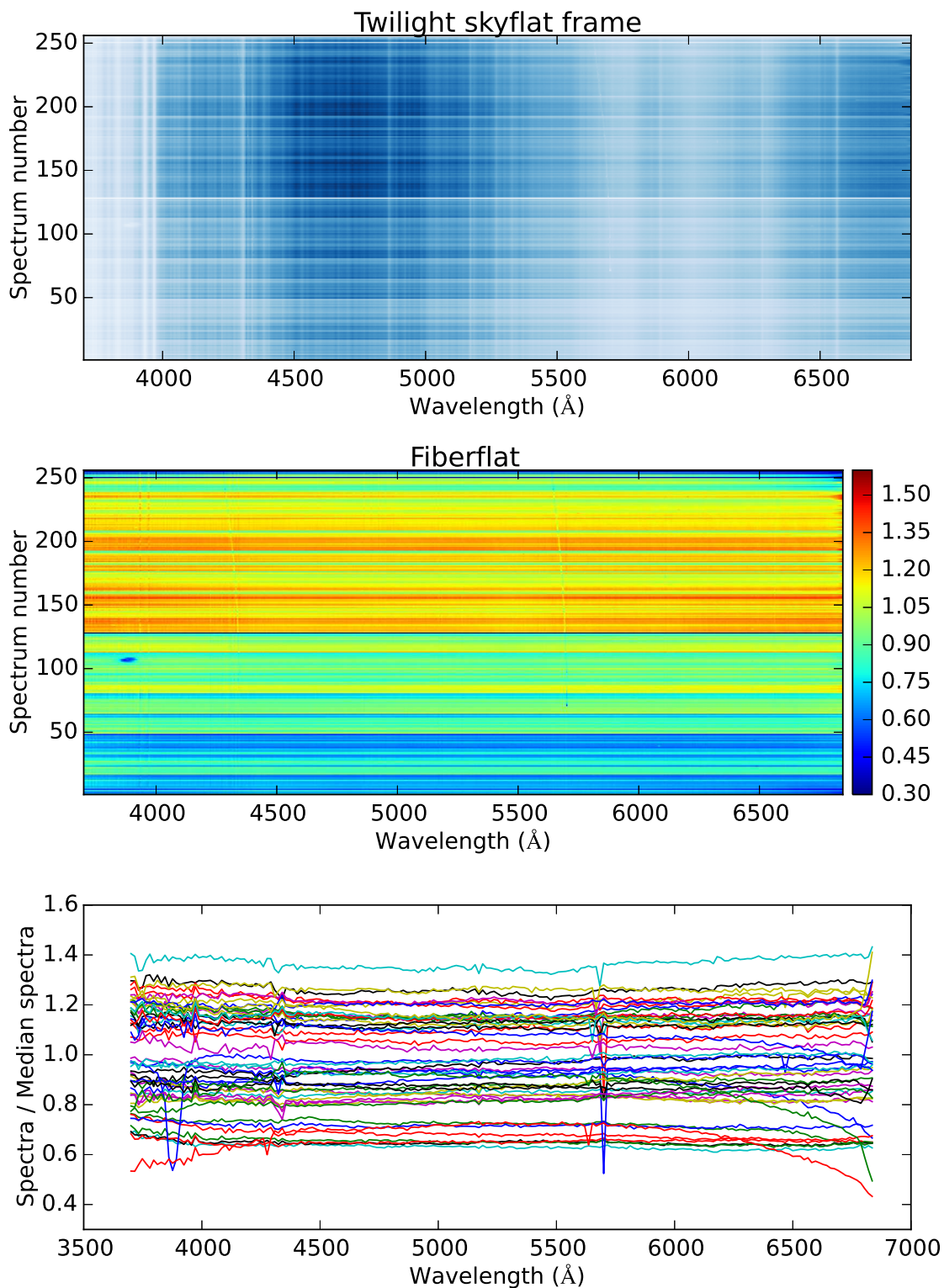


Figure 3.9 Top panel: Twilight skyflat. Note the differences between the spectra as a consequence of fiber-to-fiber differential transmission. Middle panel: Fiberflat. Bottom panel: Relative transmission of some fibers along the wavelength range. They are plotted in different colors to illustrate the differences in the transmission fiber-to-fiber at each particular wavelength.

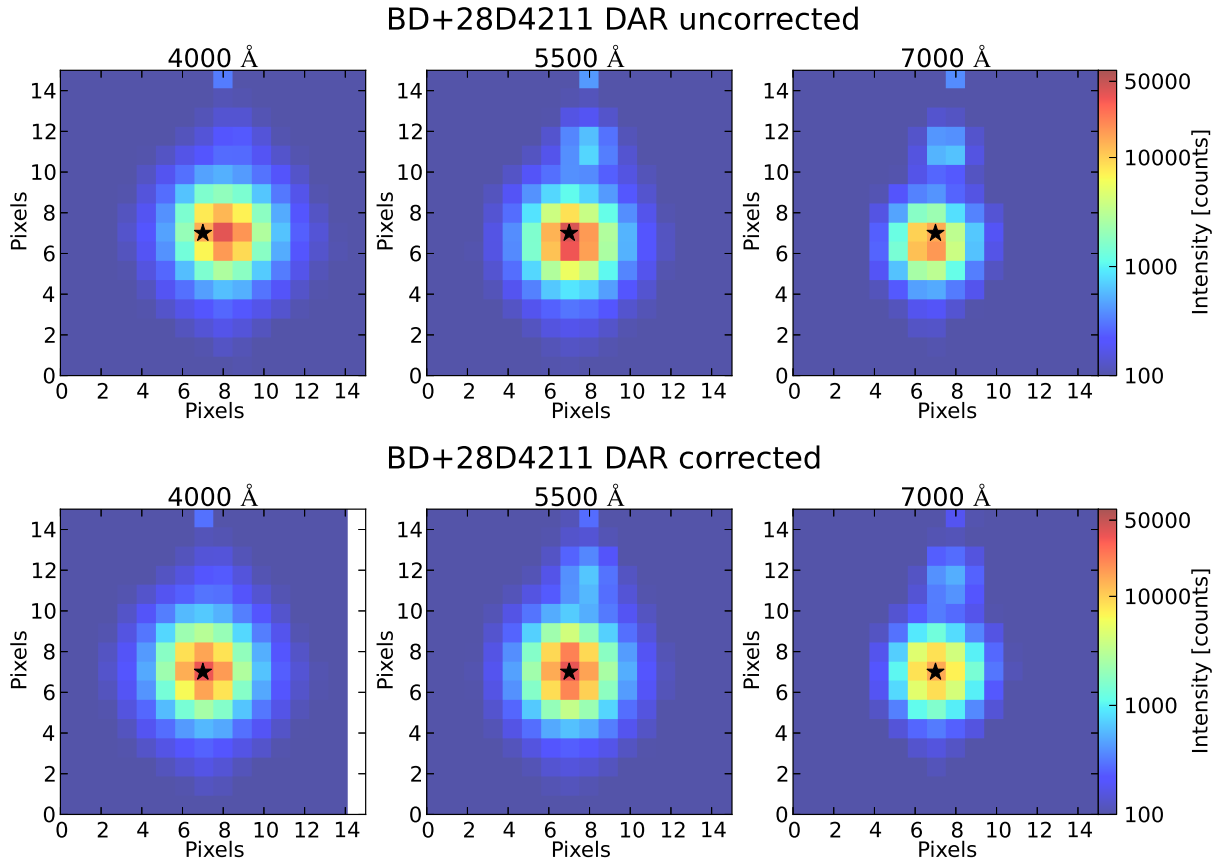


Figure 3.10 Top panels: Intensity maps (in counts) of BD+28D4211 in different wavelengths without correcting for DAR. As can be seen, the intensity peak position changes with wavelength. The star is centered in pixel [8,7] at blue wavelengths, and at [7,6] in red wavelengths, due to the prismatic effect the atmosphere has on the incoming light beam. The star symbol represents the position where the standard star is centered in the V band, at $\sim 5500 \text{ \AA}$, which corresponds to pixel [7,7]. Bottom panels: Same as top panel but after correcting the DAR. Now the star is centered at pixel [7,7] at all wavelengths.

correcting for the DAR. The DAR corrected cube is shown in the bottom panel of Figure 3.10. Now, the intensity peak of the star is the same at all wavelengths.

Using E3D we have extracted the uncalibrated spectra of the standards, by previously subtracting the sky. A night sensitivity curve as a function of wavelength was obtained for each night by comparing the observed flux with the calibrated spectrophotometric standard spectrum obtained from [Oke \(1990\)](#) catalogue. IRAF routines for longslit flux calibration (`STANDARD`, `SENSFUNC`) were used. The sensitivity function was then applied to the science frames observed during that night (IRAF `CALIBRATE` task), taking into account the airmass, exposure time and local extinction of each individual pointing. Using CAHA V-band extinction monitor (CAVEX), we have taken into account the atmospheric extinction value of the standard star and the science targets, at the time they were observed. Analogously to what found for CALIFA data ([Sánchez et al., 2012](#)), we find that, on average, the relative flux calibration shows a dispersion of $\sim 2 - 3\%$ for wavelengths redder than of 3850 \AA . At shorter wavelengths, the error in the accuracy of the relative flux calibration becomes worse, being about $\sim 7 - 10\%$ from 3700

Table 3.1. Standard stars observed for PMAS LArr dataset

Name	Obs. date	UT	Airmass	$A_V(mag)$	$t_{exp}(s)$
Feige34	31 March 2008	19:26	1.18	0.18	180
Feige34	1 April 2008	19:38	1.14	0.14	180
Feige34	2 April 2008	19:15	1.19	0.10	180
Feige34	3 April 2008	19:37	1.13	0.10	180
Hz 44	3 April 2008	04:35	1.43	0.11	180
Feige66	28 April 2008	22:56	1.03	0.18	180
Hz 44	3 July 2008	20:27	1.07	0.17	180
BD+28D4211	1 Sept 2008	19:48	1.39	0.24	300
BD+28D4211	2 Sept 2008	19:34	1.44	0.20	300
BD+28D4211	4 Sept 2008	19:16	1.49	0.18	300

- 3750 Å.

Note that this method yields a relative flux calibration, an absolute spectrophotometry can only be achieved using additional information, like the comparison with broad-band photometry, as described in Section 3.1.13.

3.1.10. Sky subtraction

One of the most difficult steps in the data reduction is the subtraction of the night sky emission spectrum. The emission from the atmosphere contributes significantly to the detected signal and the sky emission lines can be easily identified in the RSS frames as bright vertical lines (as the ones seen in bottom panel of Figure 3.8).

For the LIRGs, we have taken one nearby blank sky exposure to properly subtract it from the science frames. They were also reduced following the previously described steps. In top panel of Figure 3.11 the sky frame of NGC 2623 is shown. However, given their short exposure times, they have a low signal to noise ratio, and they will worsen the signal to noise of our science frames if we directly subtract them to it. To improve our sky subtraction we created a new sky frame which is the median of all the spectra in the original sky frame. We used `median_spec.pl` task. See the result in bottom panel of Figure 3.11, and note how the signal to noise ratio of the sky spectra has increased.

For the PSQSOs, we have obtained the sky directly from the science frames, using several blank spaxels far from the target emission to calculate the median sky spectra.

3.1.11. Creating datacubes and DAR correction

Once we had all the individual frames for the same pointing position flux calibrated and sky-subtracted they were combined and cosmic rays rejected, using IRAF `IMCOMBINE` task. Then, we used `rss2cube.pl` task, described in Section 3.1.9, to create datacubes from the RSS frames. As for the standards, our science targets must be corrected from DAR. For that, it is important to use as a reference a bright point-like source. In the case of the PSQSOs they already satisfy this requirement.

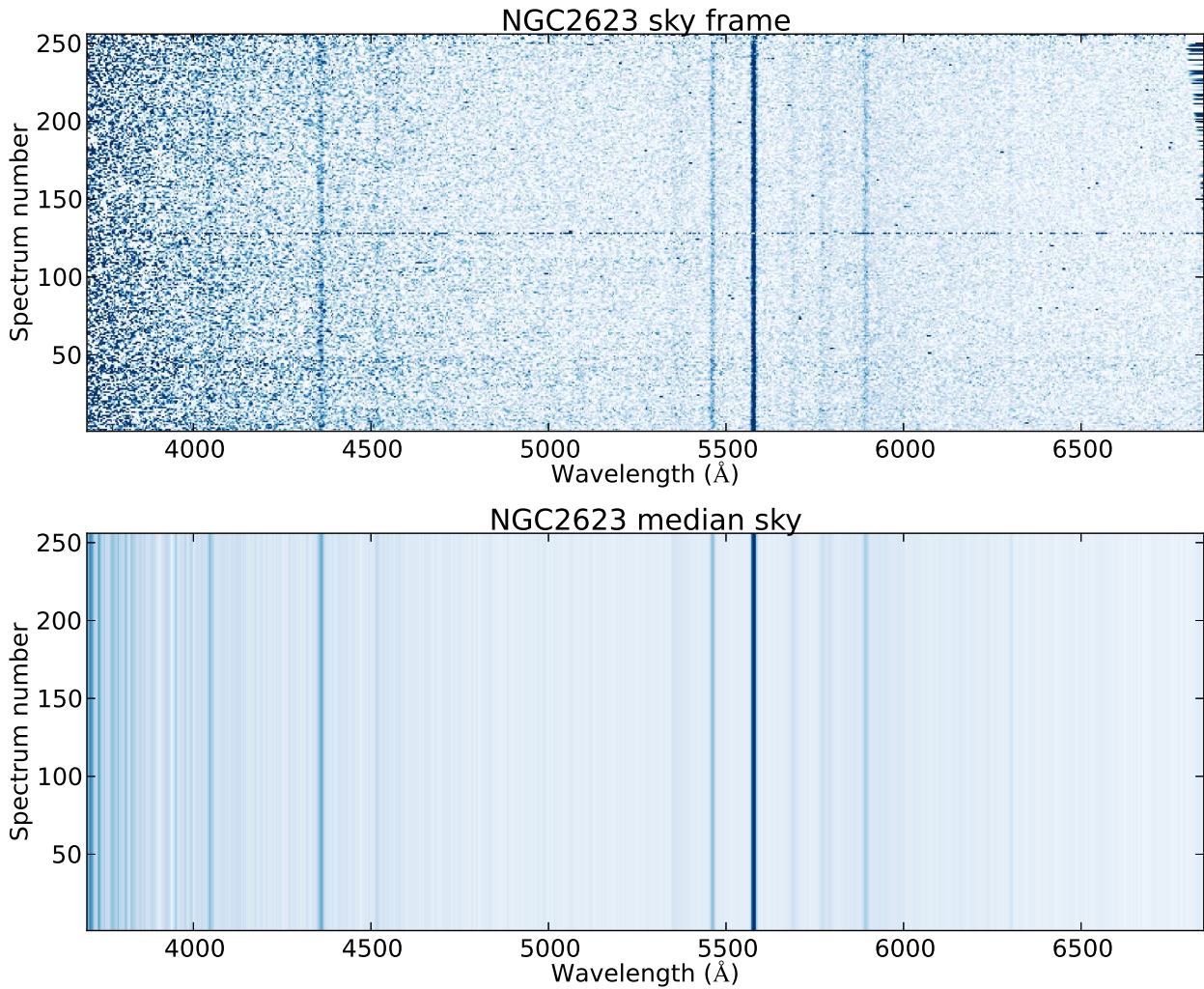


Figure 3.11 Top panel: NGC 2623 reduced sky frame. Bottom panel: NGC 2623 median sky frame that has been subtracted to the science data.

For the LIRGs we use as a reference their nucleus, or, in the case of IC 1623 W, the bright star cluster located south of the nucleus.

3.1.12. Mosaic construction

For the LIRGs we had two exposures, taken at different locations on the targets, that were joined together in a mosaic. First, we transformed the individual DAR corrected cubes again into RSS, using `cube2rss.pl`. Then, we used `R3D Mosaic_rss_overlap.pl`. This task creates the mosaic, taking one of the images as a reference, and using the information given in a configuration file, which consists of an ASCII table listing: the name of the individual RSS frames that are going to be mosaicked, their position tables, and the X and Y offset with respect to the reference.

Table 3.2. Flux recalibration factors for the LIRGs and the PSQSOs in different SDSS and HST filters.

Galaxy	SDSS g	SDSS r	SDSS i	WFC F435W	WFC F606W
IC 1623 W	-	-	-	0.85	-
NGC 2623	1.14	1.1	-	1.14	-
NGC 6090	1.16	1.18	-	1.15	-
J1700	1.27	0.99	-	-	1.19
J2334	1.1	0.9	-	-	1.04
J0237	0.87	0.87	-	-	0.93
J1230	0.7	0.84	-	-	0.99
J1248	0.82	0.88	-	-	1.11
J1456	0.96	1.01	-	-	1.21
J0202	0.73	0.76	0.73	-	0.83
J2128	0.54	0.54	0.57	-	0.69
J2310	-	0.79	0.71	-	0.86

3.1.13. Absolute flux recalibration

For those galaxies with suitable multi-band photometric data publicly available, a flux re-calibration was performed. This additional correction is intended to provide the closest absolute flux calibration by finding the difference in the flux level (i.e. a scale factor that should be applied to spectra in the datacubes), between spectroscopy and photometry.

The broad band photometry was extracted from HST and SDSS data, and compared to the photometry extracted from the IFS in the same region. For that, each spectrum in the mosaic was multiplied by the transmission curve of the corresponding broad-band filters, in order to extract a similar flux based on the IFS data. Table 3.2 shows the ratios found between the broad-band aperture photometry and the IFS derived photometry. See an example in Figure 3.12, where we show the IFS of the nuclear region of NGC 2623 (extracted in a $4.5''$ aperture) in comparison with the photometry from SDSS and HST images in the same aperture. In the case of the LIRGs, the spectra and photometry were extracted in a $4.5''$ aperture. For the PSQSOs, we have compared with photometry both the central and the integrated spectra. The numbers shown in Table 3.2 correspond to the central spectra. However, we note that they do not change significantly in the case of the integrated spectra.

Moreover, we note that in all cases there is no color effect or is almost insignificant, and therefore, the flux recalibration is not altering the shape of the individual spectra.

3.2. VIMOS reduction

We employed the IFU mode of the VIMOS instrument (Le Fèvre et al., 2003) to perform optical 3D spectroscopy of three PSQSOs (J0202, J2128 and J2310). As for PMAS LArr data, arc lamp and continuum lamp exposures were acquired for each configuration, directly after the target exposures, for calibration purposes. Standard star exposures were taken for each night according to the instrumental

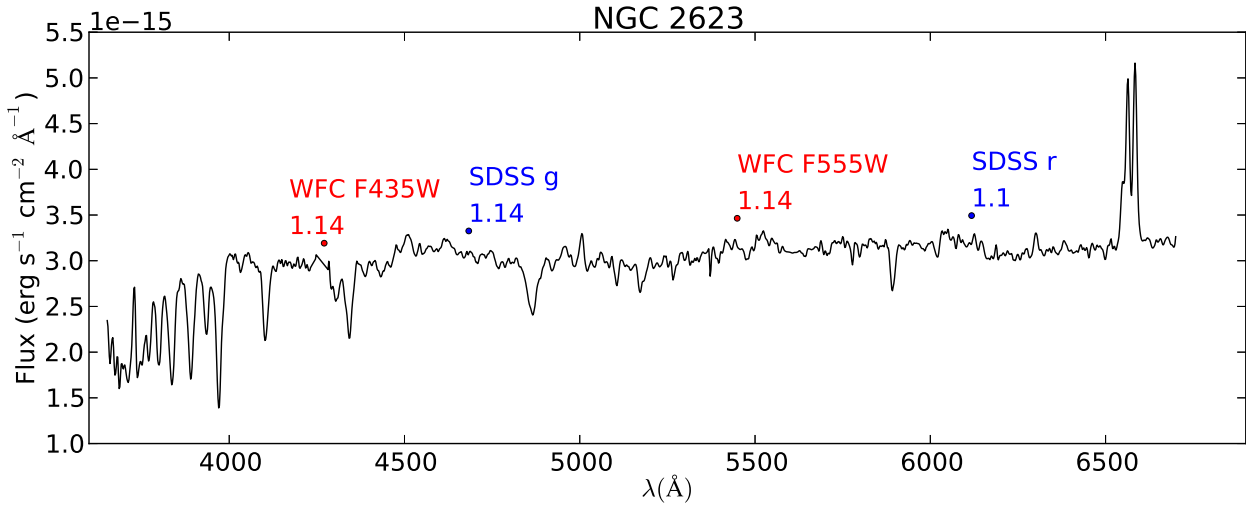


Figure 3.12 PMAS LArr spectrum of NGC 2623 extracted in a central $4.5''$ radius aperture. SDSS photometry extracted in the same region is shown with blue points, and HST one in red. The numbers indicate the flux recalibration factor by which the IFS datacube should be multiplied to match the broad-band photometry. Note that there is no significant color effect.

setup. As mentioned, each instrument has its own peculiarities in the reduction process. In this section I will describe the main differences with respect to the PMAS reduction.

3.2.1. VIMOS raw data

The VIMOS instrument is a complex IFU with 1600 operating fibres in the medium-resolution mode. They are split up into 4 bundles of 400 fibres densely projected onto each of the 4 spectrograph CCDs. Then, VIMOS raw data exposures are formed by 4 frames, each from a different CCD. In Figure 3.13 we show an example of the 4 raw frames of one of the exposures of SDSS J231055.50-090107.6. Until spectra extraction, the reduction was performed independently for each of the 4 frames, but after that, they were glued together, to apply the remaining reduction steps in all of them simultaneously.

3.2.2. Spectra identification

As explain in Section 3.1.4, the fiber peaks need to be identified and traced in the continuum exposures to be able to extract the spectra. In the case of VIMOS, `peak_find` task did not work well in the spectra identification, due to the large number of broken or low-transmission fibers, resulting in an underestimation of the total number of fibers. Instead, we have used a manually configured ASCII file, provided by S. F. Sánchez, containing the location of the spectra on the CCD, at each column, and for each individual quadrant of VIMOS data. For the broken fibers, R3D calculate their theoretical position by interpolating between adjacent, well-behaved fibers.

3.2.3. Spectra extraction

In VIMOS data, the cross-talk between fibers is important, and we could not perform a simple aperture extraction (see Section 3.1.5 for an explanation). To reduce the cross-talk effect, we adopted a

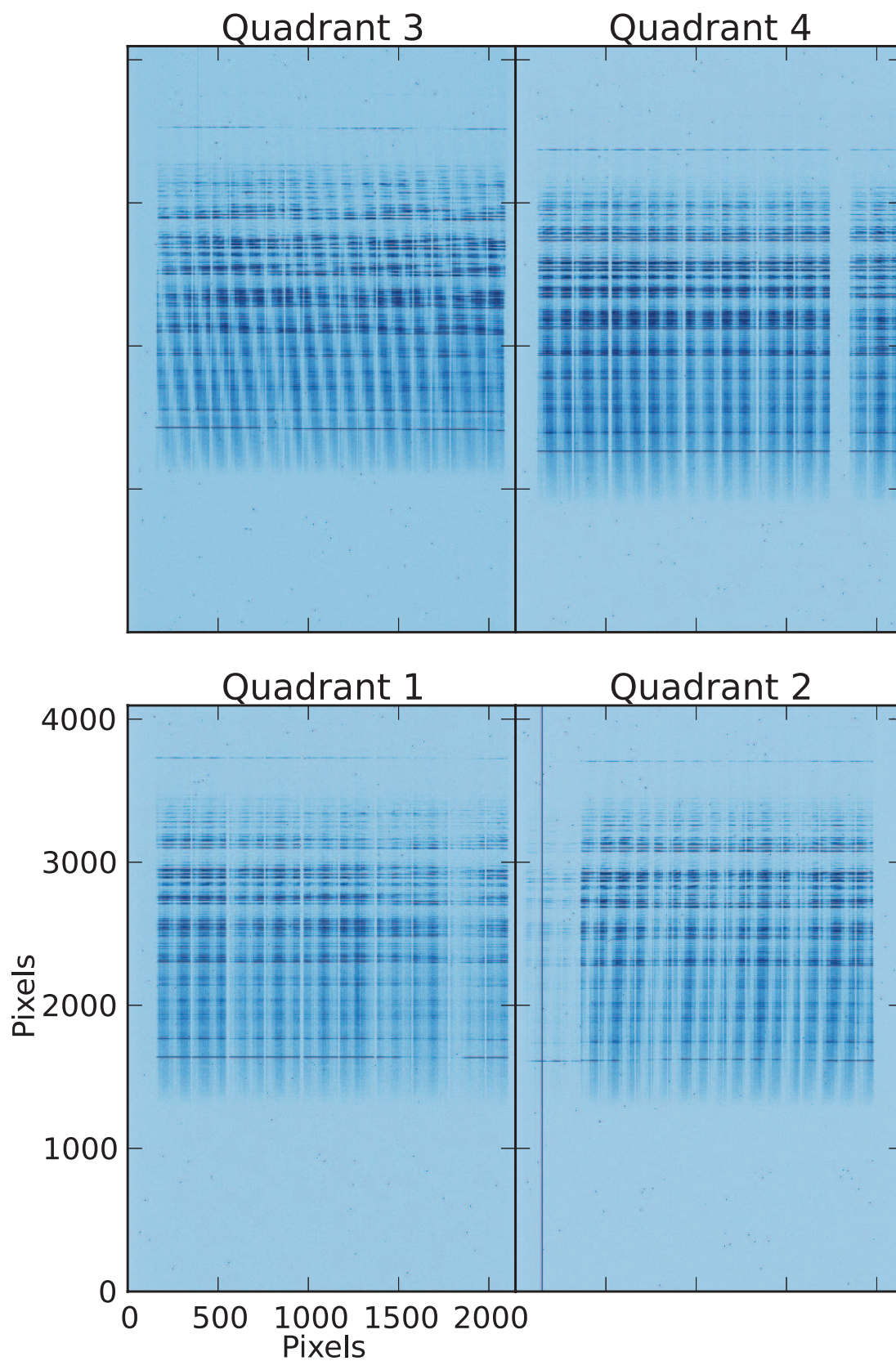


Figure 3.13 VIMOS raw data from a single pointing of SDSS J231055.50-090107.6.

modified version of the Gaussian-suppression (Sánchez, 2006), first used in the reduction of the PINGS data (Rosales-Ortega et al., 2010), and described in detail in Sánchez et al. (2011). The new technique assumes a Gaussian profile for the projection of each fibre spectrum along the cross-dispersion axis. It basically performs a Gaussian fitting to each of the fibres after subtracting the contribution of the adjacent fibres in an iterative process. The cross-talk is reduced to less than 1% when adopting this new method. The R3D task doing this is `extract_gauss_simple`.

Once we have extracted the RSS of the 4 quadrants, they were glued together into an unique frame of 1600 spectra, to perform simultaneously the following reduction steps. This allow us to save reduction time. An example of the glued spectra is shown in top panel of Figure 3.14.

3.2.4. Wavelength calibration

The wavelength calibration procedure is analogous to that performed for PMAS data. See Sections 3.1.6 and 3.1.7 for more information. In this case, the HeAr lamps were used as calibrators, and an accuracy of 0.2 Å has been obtained identifying 15 emission lines, and using a polynomial function of order 4. See in bottom panel of Figure 3.14 an example of SDSS J231055.50-090107.6 frame after wavelength calibration.

3.2.5. Fiberflat correction

The main difference with PMAS data, is that in this case we have used the domeflat continuum exposures to create the fiberflat, because we did not acquired twilight flat exposures. However, this is enough for our purposes.

3.2.6. Flux calibration

Flux calibration was performed following the same steps as in PMAS LArr data. See Section 3.1.9 for more details. For VIMOS observations we do not have information about the V-band atmospheric extinction of the standards and the science targets, so we assumed it was the same. However, we have taken into account the differences in the airmasses. The standard stars used for this dataset are summarized in Table 3.3.

3.2.7. Sky subtraction and DAR correction

For each PSQSO, an adjacent blank sky exposure has been taken to properly subtract it from the science frames. The sky exposures were also reduced following all the previously described steps.

To improve the sky subtraction we have created a new sky frame where in each quadrant the sky is calculated as the median of all the sky spectra in that quadrant. In this way the SNR of the sky spectra is increased.

Once sky subtracted, each of the individual frames has been DAR corrected. Combining the dithered exposures we were able to correct for dead fibres within the FoV. As for PMAS, the final datacubes were re-calibrated in flux to match the SDSS and HST photometry (last 3 rows in Table 3.2).

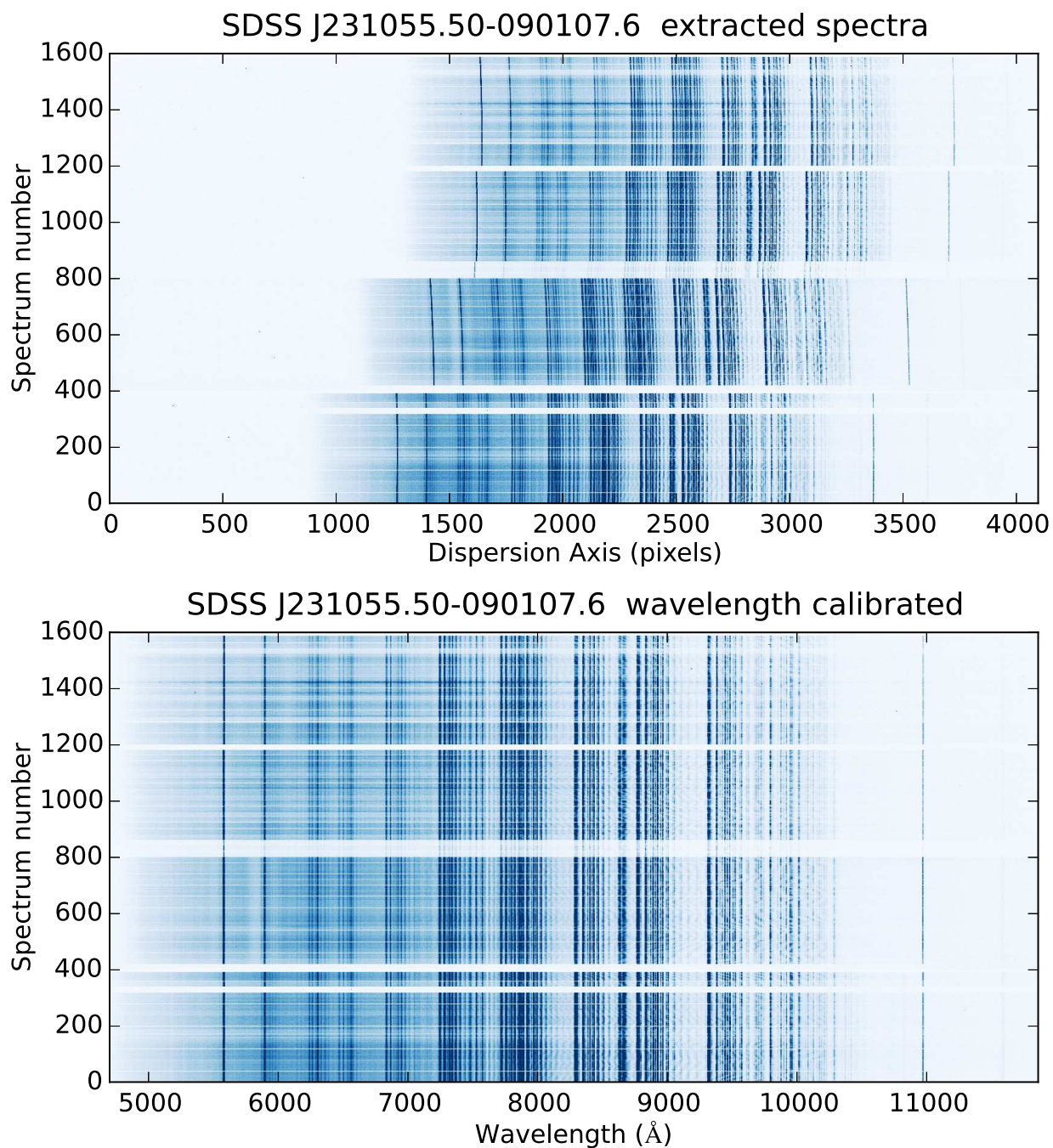


Figure 3.14 Top panel: Extracted spectra of the PSQSO J2310 after pasting together the four quadrants in a 1600 spectra fits file. Lower panel: top panel after applying the wavelength calibration.

Table 3.3. Standard stars observed for VIMOS dataset

Name	Obs. Date	UT	Airmass	t_{exp} (s)
LTT-7987	03 May 2008	09:40	1.01	41
G-93-48	06 June 2008	09:57	1.13	66
LTT-7379	11 June 2008	06:27	1.07	3
LTT-9239	13 June 2008	10:14	1.00	22
LTT-7987	14 June 2008	07:23	1.01	41
Feige-56	03 July 2008	23:29	1.34	14
Feige-110	26 July 2008	10:07	1.29	30
LTT-9239	30 July 2008	06:10	1.03	22
LTT-7379	02 August 2008	03:25	1.08	3
LTT-9239	08 August 2008	06:17	1.00	22
EG-21	09 August 2008	10:34	1.39	20

3.3. OSIRIS data reduction

The data were reduced using standard procedures for CCD imaging within the IRAF package (`IMRED.CCDRED.CCDPROC`). The bias frames acquired during the night were visually inspected and then combined to create a master bias frame, which has been subtracted to all the raw images. Due to the high dark level in the OSIRIS CCDs, a series of dark images with the same exposure time as the science data were taken (5s darks for the spectrophotometric standard and 300s for the science observations). After dark subtraction, we perform the flat-field correction, dividing the dark-corrected images by the normalized flat frames. The 3 science exposures per filter were combined using `IMCOMBINE` task, and the cosmic rays rejected during the combination. The same procedure has been applied to NGC 2623 data, and to the spectrophotometric standard star, Feige 34.

In the left panel of Figure 3.15, we show the blue continuum frame of NGC 2623 after the combination. Note the presence of several sky emission rings at the left edges of the image. We have subtracted this background emission by developing a simple Python script, that generate an artificial background map from the original images. First, we replaced the target emission by background emission adjacent to it, and then we smooth this image enough to generate the sky frame we will subtract (shown in middle panel of Figure 3.15). The blue continuum map of NGC 2623 subtracted from this sky background frame is shown in the right panel of Figure 3.15. Note how the sky emission rings have almost disappear.

Finally, a relative flux calibration has been performed for each filter by comparing the aperture photometry of Feige 34 measured in OSIRIS data, with the theoretical value obtained from Oke (1990) calibrated spectra. These theoretical values have been obtained integrating the calibrated spectra flux within the normalized transmission profiles of the tunable filters. For each filter, we found the scaling factor that transforms the flux units from counts s^{-1} to $\text{erg s}^{-1} \text{cm}^{-2} \text{\AA}^{-1}$.

Once we had all the science images reduced, a mean continuum map was obtained by averaging the blue (6640 Å) and red (6760 Å) continuums. Analogously, we have obtained a mean H α +continuum

and [NII]+continuum maps by averaging the 6700 Å and 6705 Å, and 6720 Å and 6725 Å filters, respectively. By subtracting the mean continuum map to the latters, we have obtained the pure H α and [NII] emission line maps shown in Section 6.5.

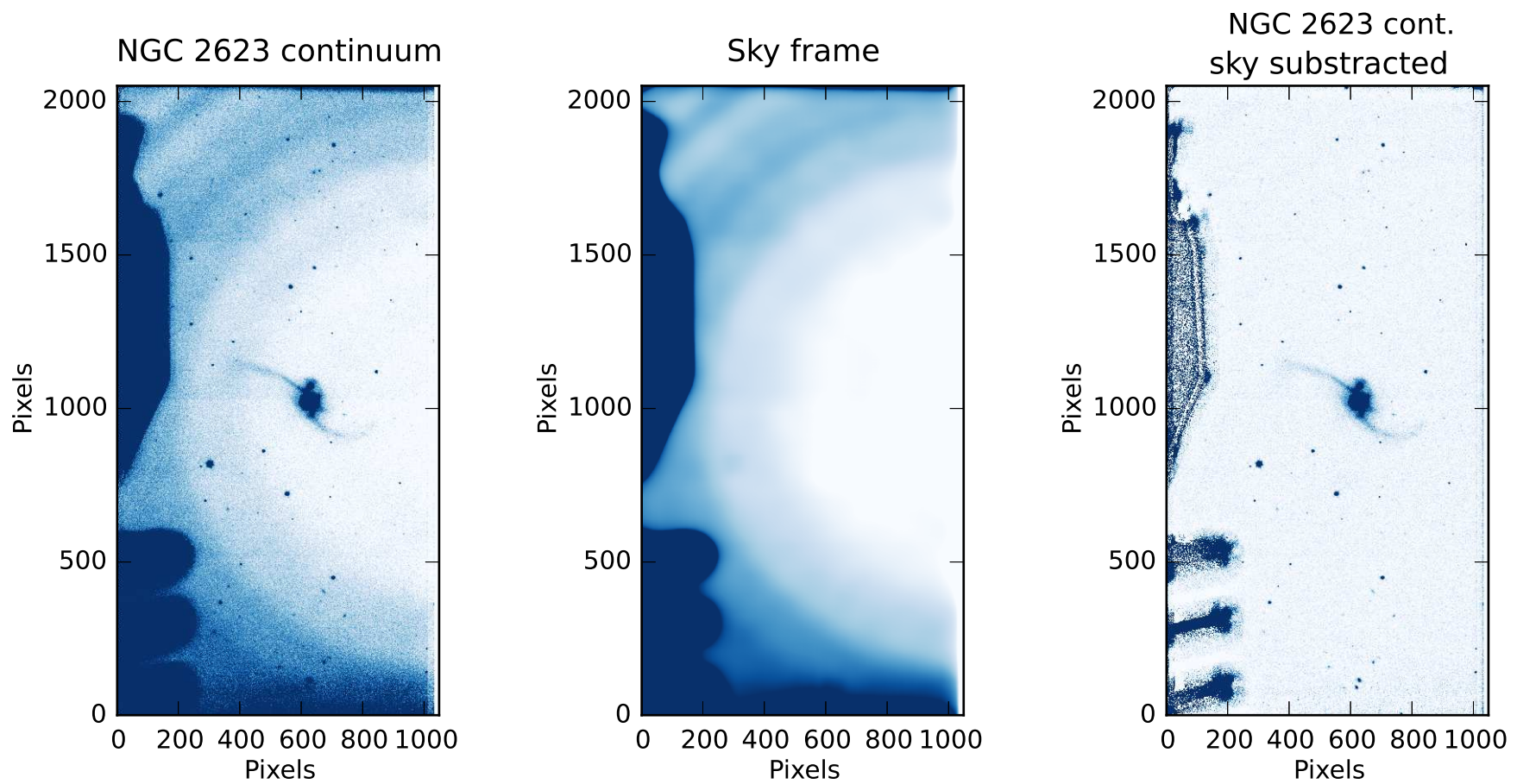


Figure 3.15 OSIRIS sky subtraction procedure. Left panel: NGC 2623 blue continuum image prior to sky subtraction. Note the sky rings emission at the left corners of the image. Medium panel: sky emission obtained from the previous image by replacing the pixels with important target emission by sky emission from adjacent pixels, and smoothing. Right panel: sky subtracted NGC 2623 continuum image. Notice how the sky rings have been removed.

4

Tracing the evolution of galaxies with stellar population models

4.1. Introduction

Single stellar population (SSP) synthesis models are the crucial tool to interpret the spectroscopy/photometry of galaxies, and to infer their star formation and mass assembly histories, unveiling the different stellar populations that have ever born there.

A SSP model is a theoretical spectrum of a group of stars with the same age (= born at the same time, t) and having the same initial element composition (or metallicity, Z). In nature, the best examples of SSPs are star clusters, that is, groups of stars that were born simultaneously from the same molecular cloud. Star clusters are one of the main modes of star formation in galaxies, specially in starbursts. They have been used to test the most modern evolutionary synthesis models, finding very good agreement. Accuracies of about 0.1 dex in age and 0.3 dex in metallicity can be achieved as long as the models are not extrapolated beyond their expected range of validity ([González Delgado & Cid Fernandes, 2010](#)).

Galaxies are certainly not SSPs, because their stars are born in different environments and times. However, a complex population like a galaxy can always be expanded in a series of SSPs. Each SSP inhabiting a galaxy has a particular spectrum, according to its age and metallicity, and leaves its imprint in the whole galaxy spectrum, like the lines in a barcode. Thus, a galaxy spectrum can be seen as a fossil record of its history, containing rich information about all its stellar generations, and allowing us to know the different stages through which the galaxy evolved.

Much progress has been obtained in this decade through the extensive photometric and spectroscopic surveys on the local Universe, like the Sloan Digital Sky Survey (SDSS). As I mentioned in Chapter 1, SDSS allowed to discover the bimodality in the galaxy colour-magnitude diagrams ([Strateva et al., 2001](#)), and provided us with thousands of high quality spectra. From the stellar population analysis of them, it has been found that the blue cloud galaxies are younger and less massive than the red-sequence galaxies ([Mateus et al., 2006](#)). These results indicate that massive galaxies as seen nowadays have stellar populations formed at early times (result known as "downsizing").

The stellar population studies are therefore relevant to constrain the galaxy formation models.

Because different formation scenarios leave distinct imprints in the stellar content of galaxies, by deriving the stellar population properties in different samples of galaxies, we can estimate when and how the galaxies formed and evolved (for example from the blue cloud to the red sequence).

Evolutionary synthesis modelling was introduced more than forty years ago by [Tinsley \(1968\)](#). This technique allows to predict the synthetic spectrum of a stellar population relying on three ingredients: (1) the initial mass function, (2) the stellar evolutionary tracks, and (3) the stellar libraries, either empirical or synthetic. Many advances have been made since the work of Tinsley due to improvements in our knowledge of the stellar evolutionary tracks, of the stellar atmosphere models used to compute synthetic stellar libraries, and in our ability to obtain homogeneous sets of observed stellar spectra at intermediate or high spectral resolution, and covering a wide range of stellar parameters (effective temperature, gravity and metallicity).

The aim of this chapter is to summarize the recent advances and main uncertainties associated to evolutionary synthesis models, and how they affect to the determinations of the stellar population properties. In [Section 4.2](#) I describe the main ingredients of the stellar population models. In [Section 4.3](#) I summarize some of the models available in the literature. The degeneracies affecting the models are explained in [Section 4.3.1](#). In [Section 4.4](#) I describe the spectral synthesis methods.

4.2. Ingredients and uncertainties in the models

4.2.1. Initial Mass Function

The initial mass function (IMF) describes the distribution of stellar masses in a newly formed population (i.e. none of the stars have had a chance to lose mass or undergo supernova). It was first derived by [Salpeter \(1955\)](#) from the stars in the Solar neighborhood. He obtained:

$$\xi(M) = \xi_0 M^{-2.35} \quad (4.1)$$

where ξ_0 is a constant which sets the local stellar density. To determine the total number of stars, N , formed with masses between M_1 and M_2 , we just have to integrate the IMF between these limits:

$$N = \int_{M_1}^{M_2} \xi(M) dM = \xi_0 \int_{M_1}^{M_2} M^{-2.35} dM \quad (4.2)$$

Similarly, to determine the total mass in stars M_\star born with $M_1 < M < M_2$, we just multiply by the mass:

$$M_\star = \int_{M_1}^{M_2} M \xi(M) dM = \xi_0 \int_{M_1}^{M_2} M^{-1.35} dM \quad (4.3)$$

It is important to note that most of the stars formed are low mass stars. That is why usually most of the mass in galaxies resides in low mass stars, they significantly outnumber massive stars.

In most codes, above $1 M_\odot$, the IMF is assumed to be a power-law of Salpeter index. However, for masses below $1 M_\odot$, there are other parametrizations of the IMF, like the log-normal of [Chabrier \(2003\)](#), or the shallower power-law of [Kroupa \(2001\)](#) with an index of $\alpha = -1.3$. For even lower masses, below $0.08 M_\odot$, the power-law could be even shallower. [Figure 4.1](#) (taken from [Bastian et al. 2010](#)) shows the different behaviour of the IMF as parametrized by the Γ index. The IMF shape below and around $1 M_\odot$ is very uncertain, and this mass range is very critical for galaxies at ages older than 1

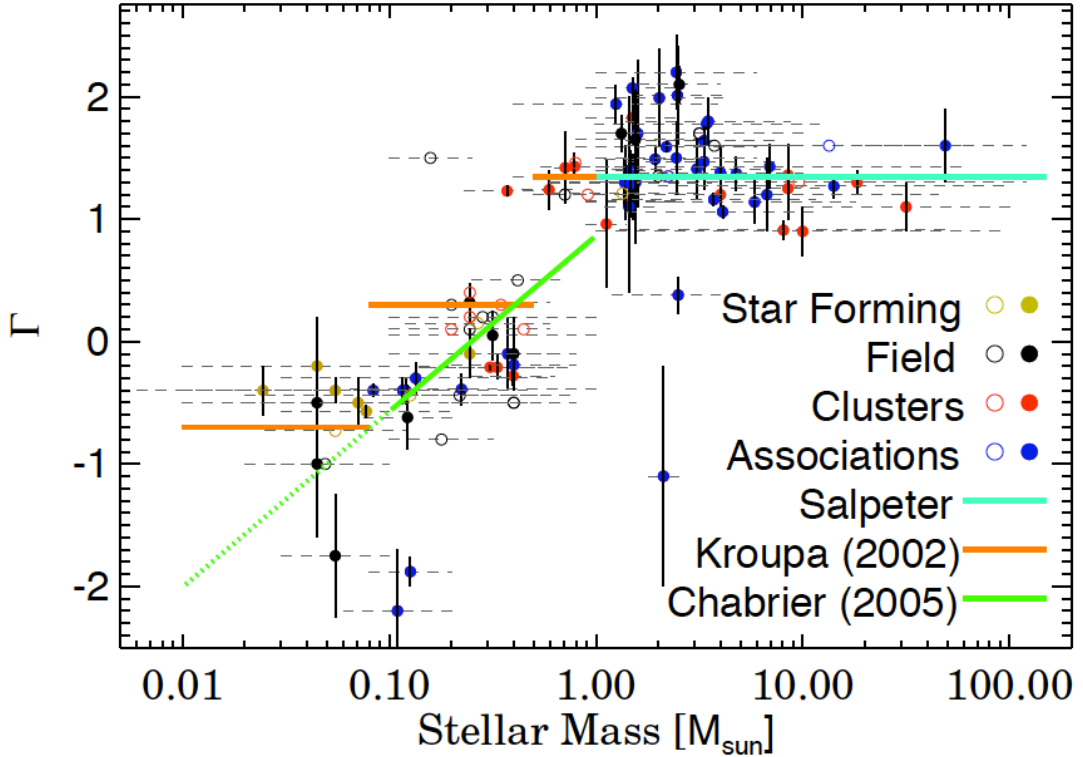


Figure 4.1 Comparison between different IMFs parametrized by the Γ index. This figure has been extracted from [Bastian et al. \(2010\)](#).

Gyr, because the main-sequence turnoff of these populations is located $\sim 1 M_{\odot}$. Using photometry, the IMF uncertainty induces a shift in the mass-to-light ratio in some bands up to a factor 2, and can even change the color evolution of a galaxy by 0.1 mag in V-K at intermediate ages ([Conroy et al., 2009](#)).

The IMF has a direct impact on all the models calculations. The uncertainties in the slope, and in the upper and lower mass limits of the IMF, have a significant impact on the predicted mass, luminosity, and star formation rates, and have to be taken into account when results from different IMFs are compared.

The origin of the IMF is the most important unsolved problem in star formation. Observationally, it is known that dense cores in molecular clouds have a power-law mass function, rather similar to the IMF. So the IMF may be determined, in part, by how such cores form from turbulent molecular gas.

Another topic of discussion is the universality of the IMF. Theory predicts that fragmentation is easier if the gas can cool, so primordial gas without any metals (cannot cool) should form more massive stars. However, observationally, there is no clear evidence that the IMF varies strongly and systematically with the initial conditions and/or environment after the first generations of stars (see the review by [Bastian et al. 2010](#)).

In this work we use SSPs with Salpeter and Chabrier IMFs. As Salpeter IMF predicts a larger number of low mass stars than Chabrier IMF, we expect to derive larger stellar masses by a factor of 1.84 ([González Delgado et al., 2015](#)), that will be taken into account in comparisons.

4.2.2. Stellar tracks

Along its evolution, the stars vary in brightness and temperature, changing their position in the Hertzsprung-Russell diagram (HR). The evolution of a star depends primarily on its mass. The most massive stars rapidly consume their nuclear fuel and explode as a supernova, to finally transform into a black hole. All this can happen as fast as in ~ 10 Myr for a $100 M_{\odot}$ star. On the other hand, solar mass stars spend much more time on the main sequence (~ 10 Gyr), and then transformed into a red giant (RGB) and ultimately expel its atmosphere as a planetary nebula and become a white dwarf.

Stellar tracks tell us how is the temporal evolution in brightness and temperature of a star, according to its mass. The Geneva and Padova groups have reached during many years the state of the art of stellar evolution modeling, and they have released complete sets of stellar tracks.

There are, however, several phases in the stellar evolution that are difficult to model, either because the physics that leads to the stars there is unknown, or either because their evolution is very fast or variable in time. Some of these are: massive stars, thermally pulsating asymptotic giant branch (TP-AGBs), Horizontal Branch (HB) and Post-AGBs. Here, I focus on the first two (massive stars and TP-AGBs), since are those that could affect the kind of galaxies studied in this thesis. I briefly summarize how they affect the results from stellar population models.

Massive stars

Uncertainties associated with the evolution of massive stars have a relevant impact on galaxies with on-going star formation, in particular at wavelengths like the rest-frame ultraviolet that is dominated by O and B stars. Some of the things to be considered are: rotation, magnetic fields, mass loss-rates, and binarity. In particular, rotation is common in massive stars and play an important role in its evolution, although most of the evolutionary stellar models are now beginning to take it into account. Rotation induce instabilities that produce the transport of angular momentum and chemical elements to the outer radiative envelope. These rotationally induced mixing processes widen the main sequence (MS), and increase the core hydrogen-burning lifetime, similar to the effects of convective overshooting. It can also significantly increase the luminosity and the effective temperature, making MS stars bluer and more luminous (Heger & Langer, 2000). Moreover, the Wolf Rayet (WR) phase is also longer, and starts earlier in the evolution.

Leitherer et al. (2014) have computed two sets of models; one with zero rotation velocity, and the other with a rotation velocity corresponding to 40% of the break-up velocity of a star on the zero-age main-sequence. These two values are considered the boundary cases, and should bracket the actual situation in the observations. The young SSPs for models with rotation are bluer in optical and UV, and emit a harder ionizing spectrum. This has important consequences when determining stellar population properties. The models with rotation lead to older ages (as the same luminosity can be reached with less massive stars), higher reddening (as the predicted SED is bluer), lower star cluster masses (as the theoretical L/M is higher), or a combination of all these parameters.

Thermally pulsating asymptotic giant branch

TP-AGB phase is a very short-lived period at the end of the AGB phase that happens when the main energy source comes from a double burning shell: an outer shell of hydrogen surrounding the

helium core. The fact that the fusion shell changes in time (switching from He to H every 10^4 to 10^5 years) in a quite explosive manner, produces the thermal pulses and mass-loss in this type of stars.

During the thermal pulses, material from the core region may be mixed into the outer layers in a process referred to as dredge-up, that can change the surface composition. Several or strong dredge-ups can lead to the formation of carbon rich TP-AGBs, whose spectroscopy is significantly different from oxygen rich TP-AGBs (Lançon & Mouhcine, 2002). The variability makes it difficult to model the TP-AGBs, as their position in the HR diagram vary with time.

The spectral signature of stars in the TP-AGB phase appears around ~ 1 Gyr, which is the time period when they are important contributors to the SSPs spectra. While the optical part of the spectra is not significantly affected by the TP-AGBs, their emission dominates the NIR bands, and produces a significant uncertainty in the K band luminosity and therefore, in the stellar masses derived from it. In Figure 14 of Maraston (2005) it can be appreciated how different is the NIR spectra of a SSP of 0.8 Gyr with or without including TP-AGBs. Moreover, different treatment in the models also lead to a factor 2 of difference in the derived stellar masses between Bruzual & Charlot (2003) and Maraston (2005). However, the latest Charlot & Bruzual (2007, unpublished) predict 60% more flux at K band than their previous models, being in better agreement with Maraston (2005).

Here we use two sets of isochrones from Padova group (Fagotto et al. 1994 a,b, Girardi et al. 2000) and for young SSPs (those younger than 4 Myr) the Geneva group tracks (Schaerer et al. 1993 a,b, Charbonnel et al. 1993) without rotation.

4.2.3. Stellar libraries

The stellar libraries are another main ingredient in evolutionary synthesis models. The libraries must be formed by a set of stellar spectra covering an homogeneous range of effective temperature (T_{eff}), gravity (g), and metallicity (Z). These libraries can be empirical (based on observations of stellar spectra) or synthetic (based on theoretical spectra obtained with stellar atmosphere models). In terms of spectral range, spectral resolution, and homogeneity in the parameter ranges, the stellar libraries have improved significantly in this decade. An extensive discussion of the main stellar libraries (at optical wavelengths) obtained in the last two decades is provided by González Delgado (2009).

Spectral libraries, whether empirical or theoretical, have their own limitations, as explained by Martins & Coelho (2007). Many aspects are important when considering a library for stellar population synthesis, and parameter coverage is one of the main issues. A good parameter coverage is not trivial for empirical libraries, which are limited to whatever is possible to obtain given observational constraints (resolution, wavelength coverage, exposure time, etc.). They have to cover not only a good wavelength range (which limits the spectral resolution), but also cover from cool to hot stars, dwarfs and giants, and different chemical abundances.

Synthetic libraries overcome limitations of empirical libraries, for instance, their inability to cover the whole space in atmospheric parameters, and particular abundance patterns that differ from that of the solar neighbourhood. However, synthetic libraries alone can not safely replace empiricals, as they are based on model atmospheres and, therefore, are limited to the approximations adopted in the computations. Ideally, one would like to generate models that account for all the effects taking place across the HR diagram: non-local thermodynamic equilibrium (LTE), line blanketing, sphericity, expansion, non-radiative heating, convection, etc. Such an approach is unfeasible at present time. The

hardest stars to reproduce in this sense are the very hot and very cool stars, where extreme scenarios take place (e.g. non-LTE effects for very hot stars, and sphericity for cool giants). Additionally, computing reliable high-resolution synthetic spectra is a very challenging task, since it requires building an extensive and accurate list of atomic and molecular line opacities.

Therefore, the best approach is to join empirical and synthetic libraries whose characteristics are optimized to the science you want to do. Here, I highlight the characteristics of the stellar libraries used in this thesis: MILES (Sánchez-Blázquez et al., 2006), and Granada (Martins et al. 2005, González Delgado et al. 2005) libraries.

- **MILES** contains 985 stars spanning a large range of stellar parameters. The spectra were obtained at the INT in the Roque de Los Muchachos Observatory in La Palma, and they cover from 3500 to 7500 Å with a spectral resolution of 2.3 Å FWHM. The spectra are very well flux calibrated. This library represents a significant improvement with respect to previous empirical libraries. However, the library has still only a small number of hot stars (over 15000 K).
- **Granada** library contains 1654 high-resolution stellar spectra with a sampling of 0.3 Å covering from 3000 to 7000 Å. The library was computed using the latest improvements in stellar atmospheres, non-LTE line-blanketed models for hot stars $T_{eff} \geq 27500$ K (Lanz & Hubeny, 2003), ATLAS (Kurucz, 1993) for stars with T_{eff} between 4500 K and 25000 K, and PHOENIX line blanketed models (Hauschildt et al., 1999) for cool stars ($3000 \text{ K} \leq T_{eff} \leq 4500 \text{ K}$). The gravity ranges from $\log g = -0.5$ to 5.5, and the models are computed for five metallicities from twice solar to 1/20 solar ($Z = 0.04; 0.02; 0.005; 0.002$ and 0.001). The full set of synthetic spectra are available in <http://www.iaa.es/~rosa>.

The widely used Bruzual & Charlot (2003) (BC03 hereafter) models are based on the STELIB library (Le Borgne et al., 2003), a major advance in its days, but limited to 249 stars, some of which have severe spectral gaps. Its relatively poor coverage of the stellar parameter space propagates to the predicted SSP spectra, with collateral effects on the results of a spectral synthesis analysis. For instance, Koleva et al. (2008) noticed that because of the lack of truly very metal-rich stars in the library, BC03 spectra for 2.5 Z_{\odot} SSPs behave like $\sim Z_{\odot}$ models of an older age. Moreover, using well known star clusters from the literature, with ages and metallicity determinations from S-CMD methods, González Delgado & Cid Fernandes (2010) found that new generation of models using the Granada and MILES libraries are superior to STELIB-based models, both in terms of spectral fit quality, and regarding the accuracy with which age and metallicity are retrieved.

The SSP models used in this thesis are based on MILES and Granada libraries.

4.3. Evolutionary synthesis models

In this section I describe the characteristics of the two bases of stellar population synthesis models used in this thesis, the so called base GM and base CB. They have been previously described in detail in Cid Fernandes et al. (2014), and used in the stellar population analysis of the CALIFA sample (González Delgado et al. 2014, 2015).

- **Base GM** is a combination of publicly available SSP spectra from Vazdekis et al. (2010), which start at an age of 63 Myr, with the González Delgado et al. (2005) models for younger ages. The

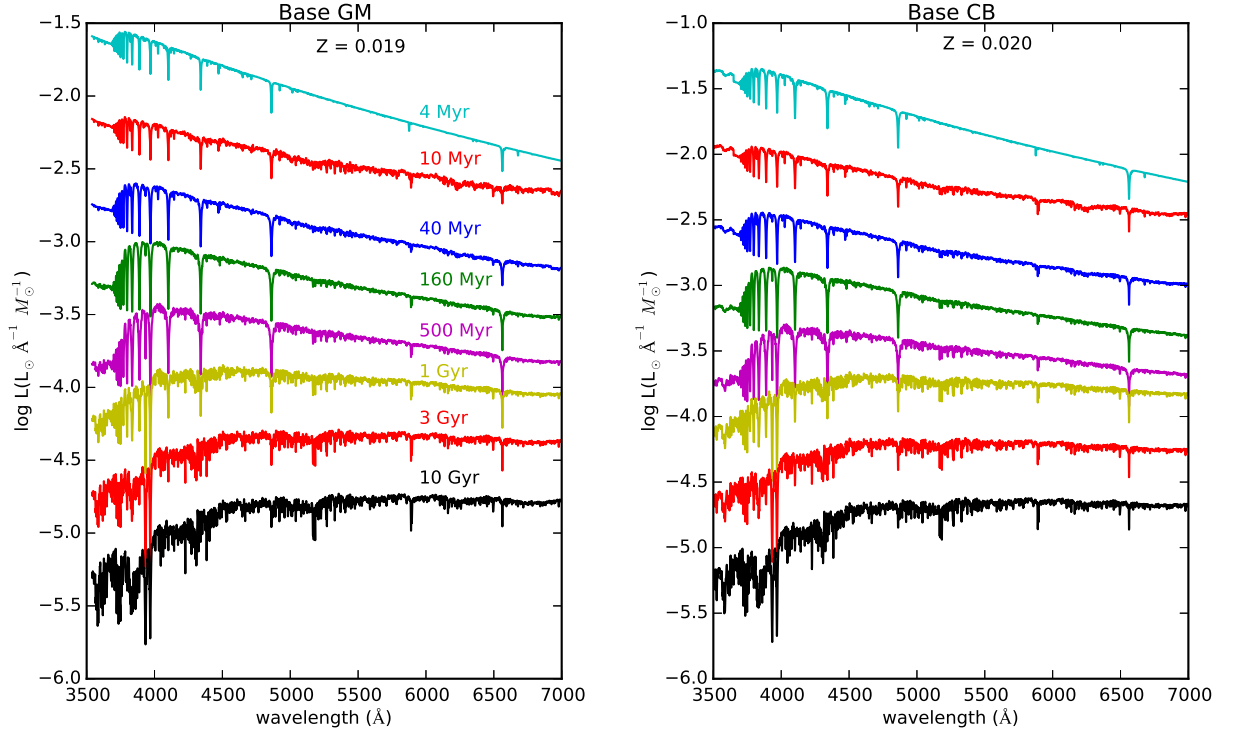


Figure 4.2 Spectral evolution of base GM SSPs (left) and base CB SSPs (right) for solar metallicity and 8 ages from top to bottom 4 Myr, 10 Myr, 40 Myr, 160 Myr, 500 Myr, 1 Gyr, 3 Gyr and 10 Gyr.

former are based on stars from the MILES library, while the latter relies on the synthetic stellar spectra from the Granada library. Only minor adjustments were needed to match these two sets of models. First, we smoothed the Granada models to the spectral resolution of MILES (2.3 Å FWHM), and then multiplied them by a factor of 1.05, estimated from a direct comparison of the predicted spectra in the 63 Myr to 1 Gyr range, where these models agree very well in both continuum shape and absorption features. These independently derived SSP spectra complement each other, providing a base suitable for spectral fitting analysis of galaxies of all types. The evolutionary tracks in base GM are those of Padova 2000, except for the youngest ages (1 and 3 Myr), which are based on Geneva tracks. This base is formed by 156 elements, the specific subset of SSPs used in the spectral fits comprises 39 ages between 1 Myr and 14 Gyr and four metallicities: $Z = 0.2, 0.4, 1,$ and 1.5 solar Z_{\odot} . They are based on the Salpeter IMF.

- **Base CB** is an updated version of the BC03 models (Charlot & Bruzual 2007, unpublished), replacing STELIB by MILES and Granada libraries. The IMF is that of Chabrier, and the evolutionary tracks are those collectively labeled as Padova 1994 by BC03. The base is formed by 160 SSPs comprising 40 ages in the 1 Myr to 14 Gyr range and four metallicities (0.2, 0.4, 1, and $2.5 Z_{\odot}$) were chosen for the spectral fits.

These two bases cover the same age range, and have the same number of metallicities. Both start at $Z = 0.2 Z_{\odot}$, but GM stops at $1.5 Z_{\odot}$, while CB extend to $2.5 Z_{\odot}$. Because MILES is based on stars not far from the Sun, it does not contain many stars as metal-rich as $2.5 Z_{\odot}$, hence the latter models

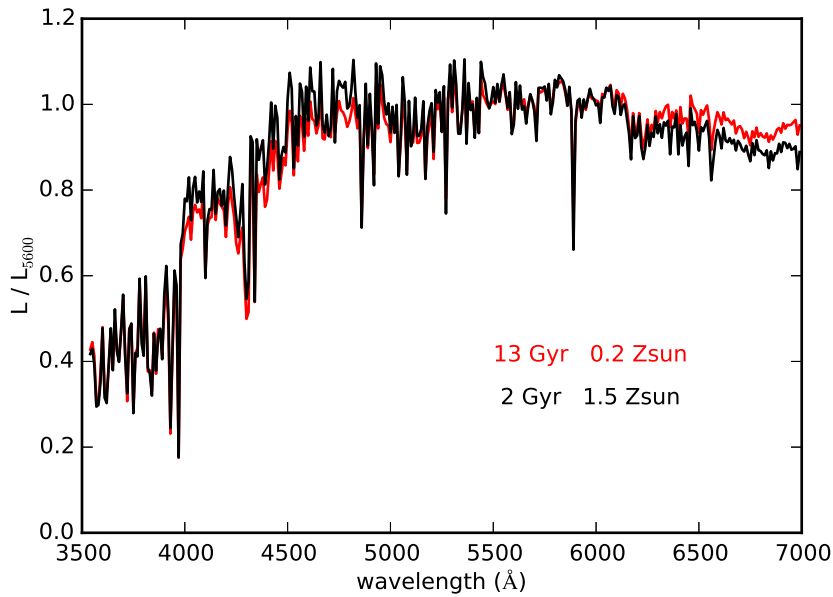


Figure 4.3 Comparison between two SSPs from base GM affected by age-metallicity degeneracy. In red we show a SSP of 13 Gyr and $0.2 Z_{\odot}$ while in black we show the SSP of 2 Gyr and $1.5 Z_{\odot}$. Both are normalized at 5600 \AA .

should be interpreted with care. In principle, we note that we do not expect such high metallicities in the systems analyzed in this thesis. In fact, the oxygen abundances of LIRGs have been found to be a factor 2 smaller than local emission line galaxies of similar luminosity and mass, as a consequence of merger-induced gas inflows that move low metallicity gas into the nuclear region whose initial abundance was higher (Rupke et al., 2008).

In Figure 4.2 we show the spectral evolution of GM SSPs (left) and CB SSPs (right) for solar metallicity and 8 ages from top to bottom: 4 Myr, 10 Myr, 40 Myr, 160 Myr, 500 Myr, 1 Gyr, 3 Gyr and 10 Gyr.

4.3.1. Degeneracies

The spectral synthesis is a degenerate problem. A given SSP will be redder due to several causes: by having an older age, or a higher metallicity, or if it is affected by a higher extinction. On the other hand, a SSP will be bluer if it has younger ages, or lower metallicities, or if it is not affected by extinction or only by low values.

Depending on the type of galaxies where we want to apply the spectral synthesis, we must know the kind of degeneracies we face and which is the best methodology to break them. In the case of elliptical galaxies, which are, on average, older than a few Gyr, and where the extinction is generally low, the main problem is the age-metallicity degeneracy. In Figure 4.3 we compare two extreme cases to illustrate this problem. In red we show a SSP of 13 Gyr and $0.2 Z_{\odot}$ while in black we show the SSP of 2 Gyr and $1.5 Z_{\odot}$. Both are normalized at 5600 \AA . In terms of the continuum shape they are almost indistinguishable.

On the other hand, in the type of galaxies studied in this thesis, with young and intermediate-age

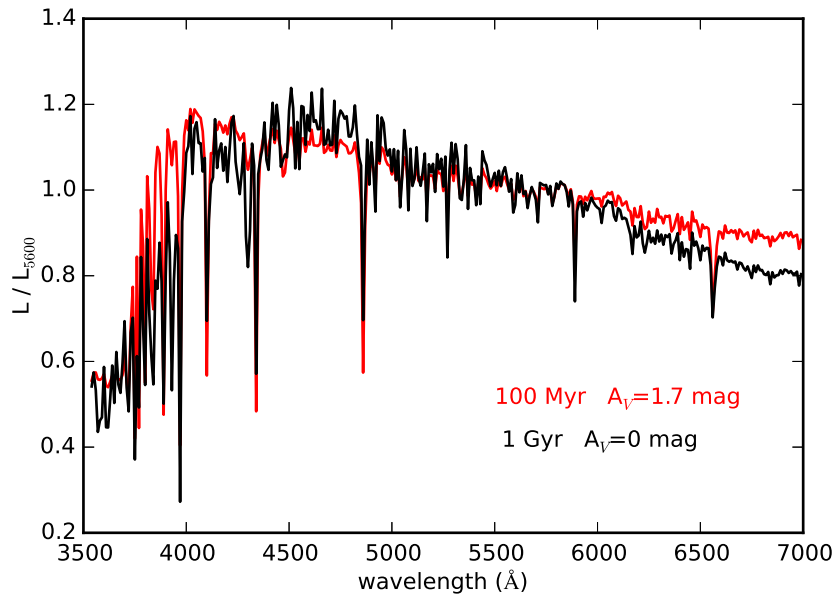


Figure 4.4 Comparison between two SSPs from base GM affected by age-extinction degeneracy. In black we show a SSP of 1 Gyr not affected by extinction and in red we show a SSP of 100 Myr and affected by 1.7 mag of extinction following [Calzetti et al. \(2000\)](#) law. Both are normalized at 5600 Å and in both the metallicity is fixed to solar.

stellar populations, and where dust obscuration is important, the stellar continuum could be affected by the age-extinction degeneracy. In Figure 4.4 we compare in black a SSP of 1 Gyr not affected by extinction, and in red a SSP of 100 Myr affected by 1.7 mag of extinction following [Calzetti et al. \(2000\)](#) law. Both are normalized at 5600 Å and in both the metallicity is fixed to solar. They are also quite similar with some differences at the beginning and at the end of the spectra.

Whatever it is, the best option to break the degeneracy is to have spectroscopy. Through photometry it is more complicated, although possible in case it covers a very large spectral range from UV to IR. Similarly, with spectroscopy, the greater the spectral range the better the possibilities to break degeneracies.

4.4. Spectral synthesis: the fossil method

There are two methods of analyzing spectra to constrain the stellar population properties. One of them is through the stellar indices, and the second one is through the spectral synthesis. The indices method is very useful to decouple the effect of age and metallicity, by combining the strength of lines which are mainly sensitive to the main sequence turn-off temperature, or age sensitive, like Balmer lines ($H\beta$), with metallic lines which are sensitive to the temperature of the giant branch, which depends on metallicity (Mg and Fe lines, or combined indices). The problem with this method is that the Balmer lines may be affected by the emission of gas if any in the galaxy, and as a consequence older ages will be derived in case of not taking it into account. That is why the indices method is especially useful for the study of stellar populations in elliptical galaxies with little gas.

Here, I will focus on the full spectral synthesis, or fossil method, which uses the SSPs models to make a detailed λ -by- λ fit of the whole spectrum. This method is preferred to the stellar indices for the galaxies studied in this thesis, and in general, for young stellar systems where the Balmer lines can be contaminated by nebular emission. Moreover, for a sample of disc galaxies, [Sánchez-Blázquez et al. \(2011\)](#) found that the spectral synthesis allows to break the age - Z - A_V degeneracies better than with the indices method.

There are several codes available to perform the synthesis. However, here I summarize the code *Starlight*, developed by [Cid Fernandes et al. \(2005\)](#), because it has been used extensively to fit galaxy spectra, and it has been proved to give results in very good agreement with those produced by other codes such as MOPED ([Heavens et al., 2000](#)) or STECMAP ([Ocvirk et al., 2006](#)).

Starlight fits the observed spectrum using a combination of several SSPs from high/intermediate spectral resolution evolutionary synthesis models, in our case the GM and CB bases. The extinction is modeled by a foreground dust screen, and parameterized by the V-band extinction A_V .

The strategy is to consider that the integrated light from a galaxy is the sum of single stellar populations, each with its ages and metallicities; thus, the best model of the galaxy luminosity is calculated as:

$$M_\lambda = \sum_{j=1}^{N_*} x_j \gamma_{j,\lambda}^{SSP}(t, Z) 10^{-0.4A_V(q_\lambda - q_{\lambda_0})} \quad (4.4)$$

where x_j is the scaling factor that gives the fractional contribution to light of each SSP, $q_\lambda = A_\lambda/A_V$ is the reddening curve, and

$$\gamma_{j,\lambda}^{SSP}(t, Z) = \frac{L_\lambda^{SSP}(t, Z)}{L_{\lambda_0}^{SSP}(t, Z)} \otimes G(v_*, \sigma_*) \quad (4.5)$$

gives the spectrum of an SSP of age t and metallicity Z normalized at λ_0 and convolved with a gaussian filter centered at velocity v_* and with dispersion σ_* . The $L_\lambda^{SSP}(t, Z)$ are taken directly from the evolutionary synthesis models.

The fit searches for the minimum χ^2 between the observations and the combined models:

$$\chi^2 = \sum_{\lambda} \frac{(O_\lambda - M_\lambda)^2}{e_\lambda^2} \quad (4.6)$$

where O_λ is the observed spectrum we are fitting and e_λ is the error spectrum. Normally, e_λ comes from error propagation during the data reduction. That is the case for CALIFA data, for which the reduced cubes already contained carefully derived errors and bad-pixel flags that were implemented in the pipeline (see [Husemann et al. 2013](#), for details). However, for LArr data we did not propagate errors during the reduction, and we needed to estimate them a posteriori, in an iterative way. The procedure we have followed is explained in detail in Section 5.4.1.

From the χ^2 minimization, *Starlight* finds the population vector (x_j), that is, the fractional contribution to light of each SSP at the normalization wavelength, that better reproduces the observations. The *Starlight* output of each fitted spectrum is a plain ASCII file storing all the synthesis information. All these quantities are well documented in the user manual.

In Figures 4.5, 4.6, 4.7, and 4.8, we show as examples the *Starlight* fits of the nuclear spaxel of IC 1623 W, NGC 6090 NE, NGC 6090 SW, and NGC 2623, respectively. All these spectra are from LArr, except for NGC 2623, where we show the CALIFA spectrum. The top panel shows the observed

nuclear spectrum (O_λ) in black solid line, together with the error spectrum in light grey. The best fit model (M_λ) from GM base is shown in red and the residual spectrum ($O_\lambda - M_\lambda$) is shown in green solid line. The bottom left panel shows the contribution in percentage to the total light of the SSPs with different ages. The results are shown in red for GM base, and in black for CB base. On the other hand, the bottom right panel shows the contribution, in percentage, to the total mass of the SSPs with different metallicities in red for GM base and in black for CB base.

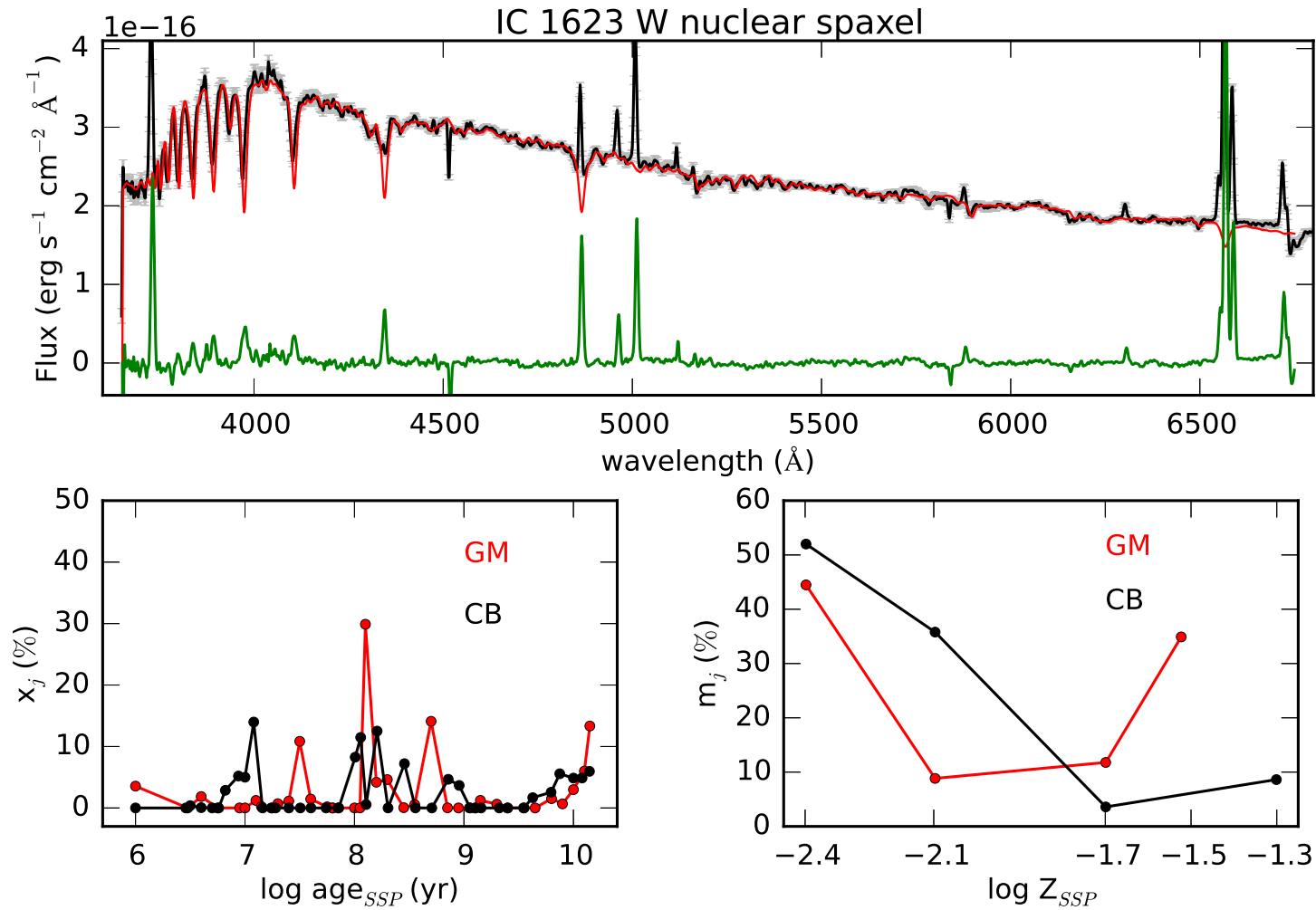


Figure 4.5 *Starlight* fit of the nuclear spectrum of IC 1623 W with base GM. The top panel shows the observed nuclear spectrum (O_λ) in black solid line, together with the error spectrum in light grey. The best fit model (M_λ) from GM base is shown in red and the residual spectrum ($O_\lambda - M_\lambda$) is shown in green solid line. The bottom left panel shows the contribution in percentage to the total light of the SSPs with different ages in red for GM base and black for CB base. The bottom right panel shows the contribution in percentage to the total mass of the SSPs with different metallicities in red for GM base and black for CB base.

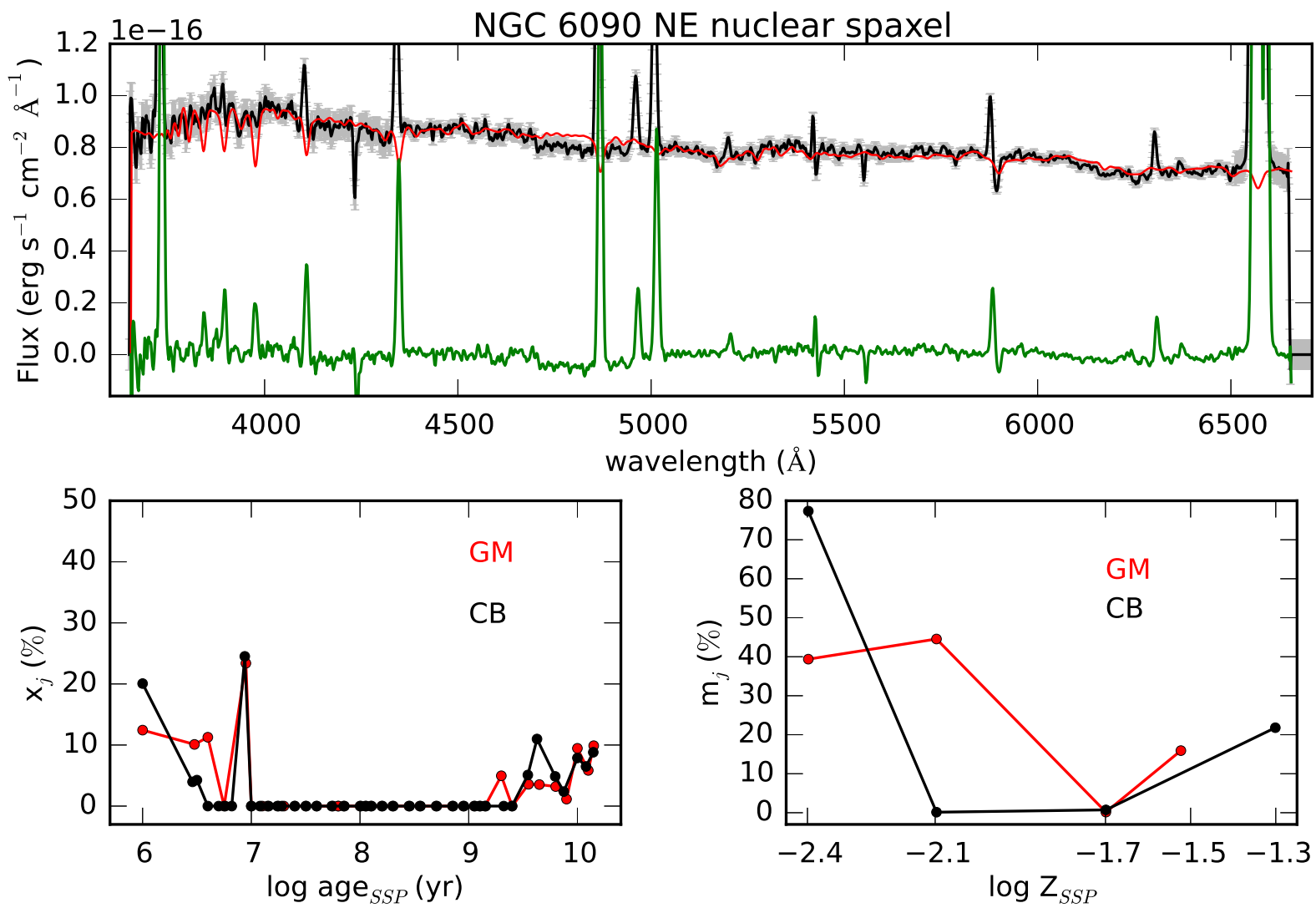


Figure 4.6 *Starlight* fit of the nuclear spectrum of NGC 6090 NE with base GM. The panel distribution is the same as in Figure 4.5.

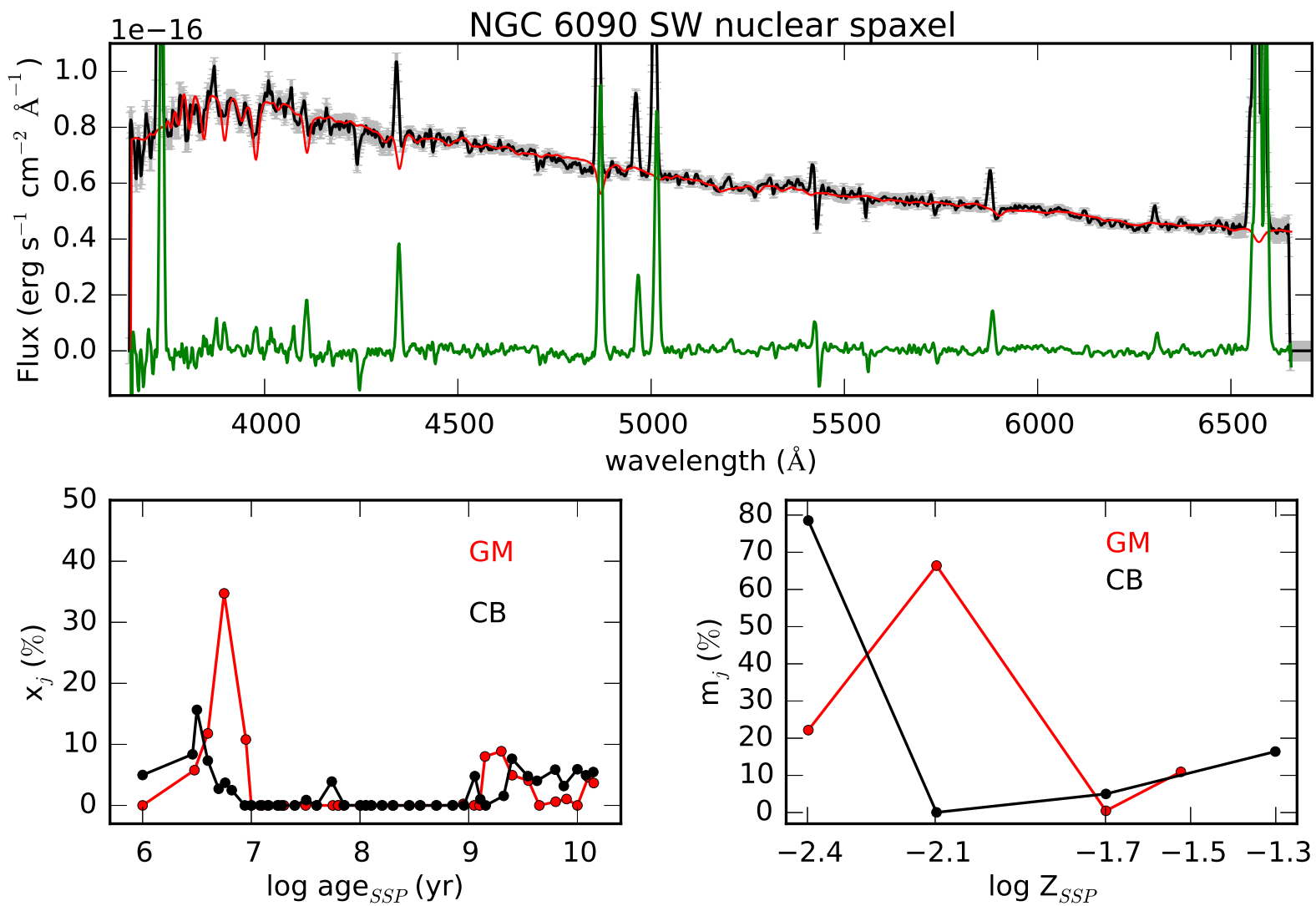


Figure 4.7 *Starlight* fit of the nuclear spectrum of NGC 6090 SW with base GM. The panel distribution is the same as in Figure 4.5.

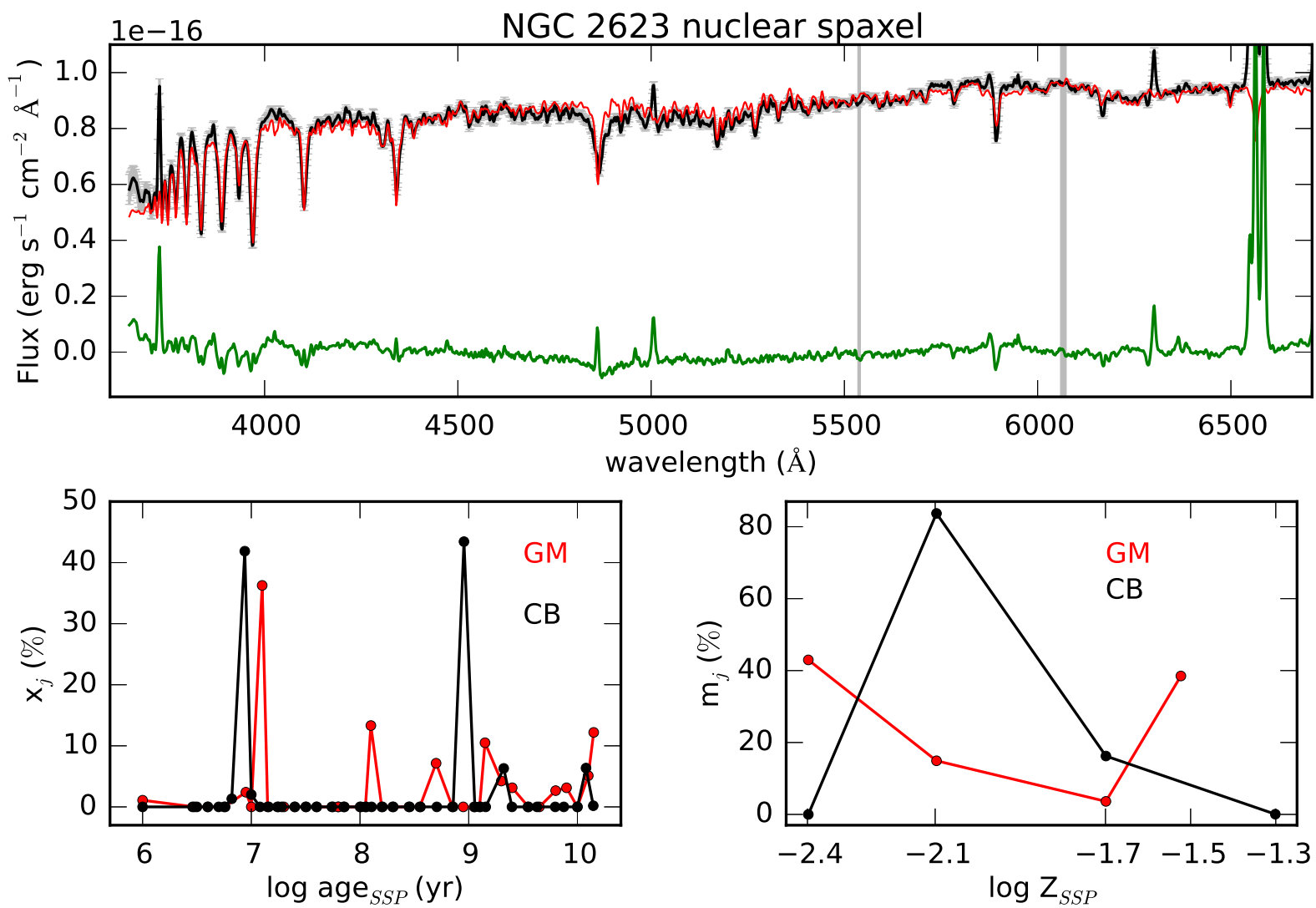


Figure 4.8 *Starlight* fit of the nuclear spectrum of NGC 2623 (from CALIFA) with base GM. The panel distribution is the same as in Figure 4.5.

Pre - Merger LIRGs: IC 1623 and NGC 6090

5.1. Introduction

To understand the role of major mergers in galaxy evolution we are characterizing the spatially resolved stellar population properties and ionization mechanism in several interacting systems in different stages of the merger process. In this chapter we present the results of the pre-merger LIRGs IC 1623 and NGC 6090.

IC 1623 (also commonly referred to as VV 114 or IRAS 01053-1746) is a gas-rich ($M_{H_2}=5.1 \times 10^{10} M_{\odot}$; Yun et al. 1994) nearby ($D=86.8$ Mpc; $1''=420$ pc) interacting system with high-infrared luminosity ($L_{IR}=4.7 \times 10^{11} L_{\odot}$; Armus et al. 2009). It consists of two galaxies: IC 1623 W and IC 1623 E. The western component resembles a distorted spiral with multiple, widespread HII regions. The eastern galaxy is nearly invisible in the optical due to heavy obscuration, but becomes progressively brighter than the western galaxy at NIR and longer wavelengths. There are two $2.2 \mu\text{m}$ emission peaks in IC 1623 E, separated by ~ 800 pc. Moreover, they coincide with the two sites of emission at 8.4 GHz, suggesting a double core (Knop et al., 1994). If they represent galactic nuclei, IC 1623 E itself might be an advanced merger, interacting with a third galaxy IC 1623 W. The projected nuclear separation between IC 1623 W and IC 1623 E is about 6 kpc, consistent with a IIIb interaction stage or close binary according to Veilleux et al. (2002) classification.

Frayser et al. (1999) found a large amount of dust ($M_{dust}=1.2 \times 10^8 M_{\odot}$) distributed across the system with a dust temperature of 20 - 25 K. Submillimeter emission is extended over $30''$ (12 kpc). A good correlation exists between the spatial distribution of the submillimeter and CO emission, indicating that gas and dust are spatially coincident. Their peak is located near the suspected dynamical center of the merger remnant, between IC 1623 W and IC 1623 E nuclei. However, radio and NIR peaks trace star forming regions, which are not spatially correlated with CO and submillimeter emission. This displacement indicates that the gas collapses before the stars and explains the cool temperature of the dust. About half of the warmer dust traced in the mid-IR is associated with the eastern galaxy, where both compact (nuclear region) and extended emission is found (Le Floch et al., 2002). Evidence for wide-spread star formation activity and shocks across the entire system is found in the UV, optical, and mid-IR (Knop et al., 1994; Goldader et al., 2002; Rich et al., 2011). Analysing Far UV and X ray data, Grimes et al. (2006) found a galactic superwind in IC 1623. This outflow of

material is moving at 300 - 400 km s⁻¹. Also, assuming that the hard X-ray emission is tracing high mass X-ray binaries (HMXBs) and is not contaminated by an AGN, they derive the SFR for the two galaxy components which is roughly equal with $\sim 28 M_{\odot} \text{yr}^{-1}$ for IC 1623 E and $\sim 33 M_{\odot} \text{yr}^{-1}$ for IC 1623 W. With respect to the existence of an active galactic nucleus in this system, [Iono et al. \(2013\)](#) identified a highly obscured AGN (with $\leq 4 \times 10^8 M_{\odot}$) in IC 1623 E using sub-arcsecond resolution ALMA cycle 0 observations of HCN (4-3) and HCO⁺ (4-3) emission, suggesting that both starburst and AGN activities might have been triggered by the ongoing merger.

NGC 6090 is an IR luminous ($L_{IR} = 3.2 \times 10^{11} L_{\odot}$; [Sanders et al. 2003](#)) galaxy merger viewed face-on. The optical images of NGC 6090 show two galaxies of roughly equal size that are almost completely overlapping, and a pair of tidal tails that extend at least 65 kpc to the southwest and 50 kpc northeast. At optical and NIR the separation of the nuclei is ~ 3.2 kpc ([Dinshaw et al., 1999](#)). While the southwestern nucleus (NGC 6090 SW) appears amorphous, the northeastern galaxy (NGC 6090 NE) clearly has distorted spiral structure. The most striking feature of NGC 6090 NE is the abundance of luminous blue and red knots along the western arm and the paucity of similar clusters on its eastern spiral arms. NGC 6090 SW also shows a similar abundance of blue knots along the eastern side, and one extremely luminous knot at the northern end.

The molecular gas has a single component that peaks between the two galactic nuclei ([Bryant & Scoville, 1999](#)), suggesting that the gas responds to the interaction faster than the stars. Although the two galaxies show strong H α emission at their nuclei, the H α emission appears to be brighter on the companion-facing side of each galaxy ([Hattori et al., 2004](#)). [Arribas et al. \(2004\)](#) found an irregular morphology in the innermost regions around the nuclei (1 - 2 kpc), where a "bridge" connects the northern part of these two regions. A common envelope extends up to about 7 kpc. There is considerable evidence for starburst activity, but no evidence at optical or radio wavelengths for a compact AGN. [Wang et al. \(2004\)](#) found the dense molecular gas peaks in the overlap region. Weak radio continuum in overlap region indicates that the history of star formation there may not be very long (in agreement with [González Delgado et al. 1998](#)). Otherwise, supernovae after the starbursts would have produced comparable radio continuum emission as in the two nuclei. The weak radio continuum and weak CO (3-2) emission in NGC 6090 SW suggest that there is much less star formation activity than in NGC 6090 NE. From optical IFS, [Sugai et al. \(2004\)](#) found that the fraction of heavy elements is currently increasing in the kiloparsec-scale star forming region to the West of NE nucleus. Young starbursts and starburst related outflow were previously reported in NGC 6090 using UV ([González Delgado et al., 1998](#)).

The aim of this study of IC 1623 and NGC 6090 is to combine high quality IFS from PMAS@LArr at CAHA with previous high resolution HST imaging to investigate the physical processes that occur during the early stages of major mergers. In Section 5.2 we summarize the data and observations. In Section 5.3 we present the results of the star clusters photometry detected in the HST images. The stellar population properties derived from the IFS are described in Section 5.4. In Section 5.5 we show the ionized gas distribution, dust attenuation, and the emission line ratios tracing the ionization source. The gas kinematics is described in Section 5.6. The analysis of the Star Formation Rates is shown in Section 5.7.

Throughout the chapter we assume a flat cosmology with $\Omega_M = 0.272$, $\Omega_{\Lambda} = 0.728$ and $H_0 = 70.4$ km s⁻¹ Mpc⁻¹ (WMAP, seven years results). For IC 1623 redshift ($z=0.020067$) this results in a distance of 86.8 Mpc. At this distance 1" corresponds to 0.421 kpc. For NGC 6090 ($z=0.029304$), the

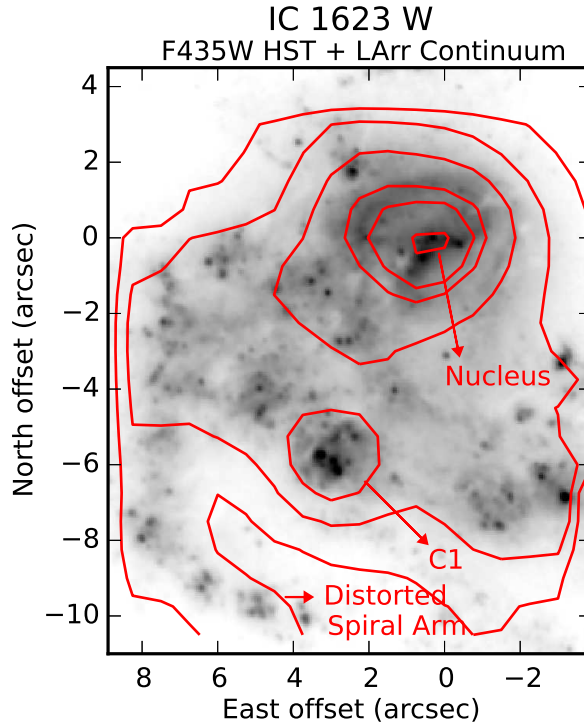


Figure 5.1 In greyscale we show the HST F435W continuum image of IC 1623 W. The average continuum of the IFS in our spectral range is superimposed with red contours. We note some characteristic regions of this galaxy. The nucleus corresponds with the peak at $2 \mu\text{m}$ in NIR and was determined by [Knop et al. \(1994\)](#). At bluer wavelengths, another important emission peak appears that corresponds with the giant star forming region labeled by us as C1 in the figure. The distorted spiral arm is also covered by our datacube.

distance is 127.7 Mpc, $1''$ corresponds to 0.619 kpc.

5.2. Data

For both galaxies we have the PMAS LArr IFS and HST imaging. Detailed information on the characteristics of the data and their reduction procedure is given in Chapters 2 and 3.

In the case of **IC 1623**, because of the extensive dust lane that covers almost all IC 1623 E, our optical IFS observations cover only the star formation in the western galaxy. In Figure 5.1 we show the HST F435W continuum image of IC 1623 W in the region where we have taken the IFS. The average continuum of the IFS in our spectral range is superimposed with red contours. We note some characteristic regions of this galaxy. The nucleus corresponds with the peak at $2 \mu\text{m}$ in NIR and was determined by [Knop et al. \(1994\)](#). At bluer wavelengths, another important emission peak appears that corresponds with the giant star forming region labeled by us as C1 in the Figure. The distorted spiral arm is also covered by our datacube.

In the case of **NGC 6090**, our IFS covers the main body of the system, including both nuclei. In Figure 5.2 we show the HST F435W continuum image of NGC 6090 in the region where we have taken the IFS. The average continuum of the IFS in our spectral range is superimposed with red

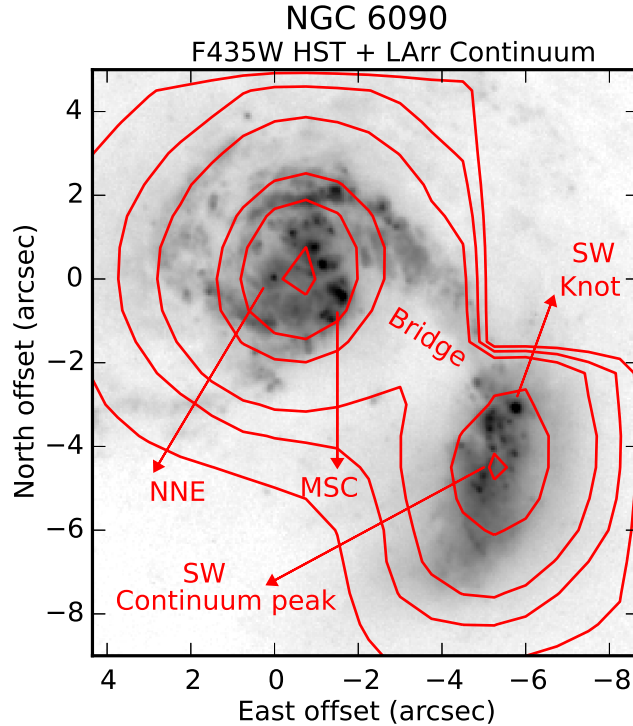


Figure 5.2 In greyscale we show the HST F435W continuum image of NGC 6090. The average continuum of the IFS in our spectral range is superimposed with red contours. In the NE component the most striking feature is the increased star formation with abundant luminous blue and red knots along the western arm. We have defined this region of multiple star clusters formation as MSC. The position of NGC 6090 NE nucleus is noted in the figure as NNE. As can be seen, the luminosity maximum of the IFS continuum falls between NNE and MSC. The position of SW nucleus is not clear. In this work, we have considered as SW nucleus the continuum peak of the IFS, where the luminosity reaches its maximum. However, there exist one extremely luminous knot at the northern end of the SW component (also indicated in the figure), that we can not discard as a possible nucleus.

contours. In the NE component the most striking feature is the abundance of star forming regions along the western arm (in the side of the galaxy closest to NGC 6090 SW). We have defined this region of multiple star clusters formation as MSC. From now on, we will refer to it as MSC in the text. The position of NGC 6090 NE nucleus is noted in the Figure as NNE. As can be seen, the luminosity maximum of the IFS continuum falls between NNE and MSC. With respect to NGC 6090 SW, it also shows a similar abundance of blue knots along the eastern side. As explained in Section 2.2.1, the position of SW nucleus is not clear. In subsequent analysis, we have considered as SW nucleus the continuum peak of the IFS, where the luminosity reaches its maximum. We have labeled it in the Figure. Our SW nucleus will be indicated with a black dot in NGC 6090 maps in Section 5.4 and thereafter. However, there exists one extremely luminous knot at the northern end of the SW component (also indicated in the Figure), that we can not discard as a possible nucleus. This is the brightest point source in NGC 6090 SW in optical and NIR HST images, and was previously reported by [Dinshaw et al. \(1999\)](#). Given the mismatch between the radio emission peak and this knot, [Dinshaw et al. \(1999\)](#) suggest that it may not be the nucleus of SW component but actually a foreground star. We have confirmed with our spectroscopy that it is not a foreground star because the

main absorption lines are at the redshift of the galaxy. Therefore, we can not discard it as the nucleus of the SW galaxy. The position of this bright knot in following NGC 6090 maps will be indicated with a star symbol. Just for comparison, in Section 5.4.11, we will discuss how the radial profiles of the derived stellar population properties change when centering in our selected nucleus or in the knot.

Also, for both IC 1623 and NGC 6090 we have high resolution HST multiwavelength imaging from UV to NIR covering the main bodies of both systems, from which we will derive, in the following section, the star clusters photometry.

5.3. Star clusters photometry

During the last decade a significant population of extragalactic massive ($> 5 \times 10^4 M_{\odot}$), young (< 1 Gyr) clusters have been detected in many environments: in the LMC (Elson & Fall, 1985), in normal spirals (Larsen, 2004), in starburst galaxies (e.g., in M82; de Grijs et al. 2005), in ongoing mergers (e.g., in the Antennae; Whitmore et al. 1999) and in merger remnants (e.g., in NGC 7252; Maraston et al. 2001). These objects are known as young massive clusters YMC or super star clusters SSC.

The HST caused a revolution in the field of extragalactic clusters. Its high angular resolution first allowed to establish an upper limit to the size on young extragalactic clusters. They did indeed have sizes (1 - 20 pc) comparable to globular clusters in our Galaxy (e.g., Whitmore et al. 1999).

The first environments that were discovered to contain copious amounts of massive star clusters were those of galaxy mergers. Holtzman et al. (1992) studied the recent galaxy merger NGC 1275, and found a population of blue point-like sources, with ages of less than 300 Myr old and masses between $10^5 - 10^8 M_{\odot}$. These young massive clusters were also found in the prototypical merger remnant NGC 7252, with ages ranging from 34 to 500 Myr, consistent with having been formed during the interaction process (Whitmore et al., 1993). Many more examples soon followed, like those in NGC 3597 (Holtzman et al., 1996), in NGC 3256 (Zepf et al., 1999), in the Antennae NGC 4038/4039 (Whitmore et al., 1999, 2010; Bastian et al., 2006), and in Arp 284 (Peterson et al., 2009), among others.

YMC found in mergers are an intriguing mode of star formation in the present-day universe. They have many of the same properties as the galactic globular clusters, namely size and mass (and hence stellar density). On the other hand, their ages, metallicities, and mass functions are much more similar to those in galactic open clusters. This mixture of properties has led to their designation as young globular clusters, implying that they are the same as the old globular clusters in our Galaxy (only younger) and that any differences between these populations are simply due to evolutionary effects.

In this section we will use HST photometry to characterize the stellar population properties of the SSCs in IC 1623 and NGC 6090, to determine how are they related with the interaction process. Although with less accuracy than with spectroscopy, we can estimate the stellar population properties using photometry. According to Alvensleben (2004), a long wavelength basis from U band through NIR is necessary to determine the SPs properties of star clusters in a reliable way, where the availability of U band photometry is crucial. In this section we have used the HST images from FUV to NIR. By comparing the colors and magnitudes of IC 1623 and NGC 6090 clusters with stellar population synthesis models we have derived their main properties: ages, masses, and the amount of dust obscuration.

5.3.1. Method

The first step was to detect the star clusters present in HST images. For that, we registered and resampled all the HST images to a common pixel scale, using GEOMAP/GEOTRAN IRAF tasks. In the cases where more than one image per filter was available they were combined using the IRAF imcombine task with the reject option set to `crreject` to eliminate cosmic-ray events. For the detection we used a combination of the optical images in F435W and F814W filters. For that, we removed large-scale background variations in this optical image in two steps. First, it was smoothed with a 9×9 box median filter, and then, the smoothed image was subtracted from the original. The input object list for photometry was obtained by running DAOFIND task in DAOPHOT package on this background-subtracted image. This procedure is similar to that followed by [Larsen & Brodie \(2000\)](#). As an additional selection criterion, only clusters with $S/N \geq 5$ in optical filters were considered for subsequent photometry.

In Figure 5.3 we show F814W images of IC 1623 (top panel) and NGC 6090 (bottom panel). The detected clusters are marked with apertures of different colors given by their F435W - F814W color as:

1. **Blue clusters:** $F435W - F814W \leq -1$
2. **Green clusters:** $-1 < F435W - F814W \leq 0$
3. **Red clusters:** $F435W - F814W > 0$

A total of 228 and 156 clusters were detected in IC 1623 and NGC 6090, respectively, with a SNR > 5 in FUV, F435W and F814W filters. Analogously, 225 and 117 clusters were detected in IC 1623 and NGC 6090 with a SNR > 5 in F435W, F814W, and F160W filters.

In IC 1623, the blue clusters are located in the western component while the red ones in the eastern component. Strong dust lanes can be seen in IC 1623 E in HST V and B band images. Most of the green clusters are located in IC 1623 W, a few in the spiral arms but preferentially around the nucleus. In NGC 6090 almost all clusters are green or blue, with most of the blue ones located in NGC 6090 SW and in the West side of NGC 6090 NE, in the region of multiple star clusters MSC. It is important to note that this enhancement of the star formation is occurring in the side of NGC 6090 NE facing towards the SW component. Only 6 red clusters are identified, one of them being NGC 6090 NE nucleus, and the others located at a distance of ~ 1.4 kpc, simetrically with respect to the nucleus, 2 of them to the NE and the other 3 to the SW.

Differences in cluster colors could be due to real differences in the stellar population properties and/or different levels of dust extinction affecting the clusters depending on their location. A cluster could be redder due to a high amount of extinction or an older stellar population, or a combination of both. This is the so-called age-extinction degeneracy. In the following section we will use our multiwavelength information to break this age-extinction degeneracy and estimate the SP properties of the clusters.

Photometry was obtained using the phot task in APPHOT. It gives us the fluxes of the clusters in all the filters, by specifying the aperture radius, and the position and width of the sky ring for background determination. We have followed the recommendations of the reference guide to IRAF/APPHOT package (Lindsey E. Davis), chosing an aperture radius of $\sim FWHM_{PSF}$, and \sim

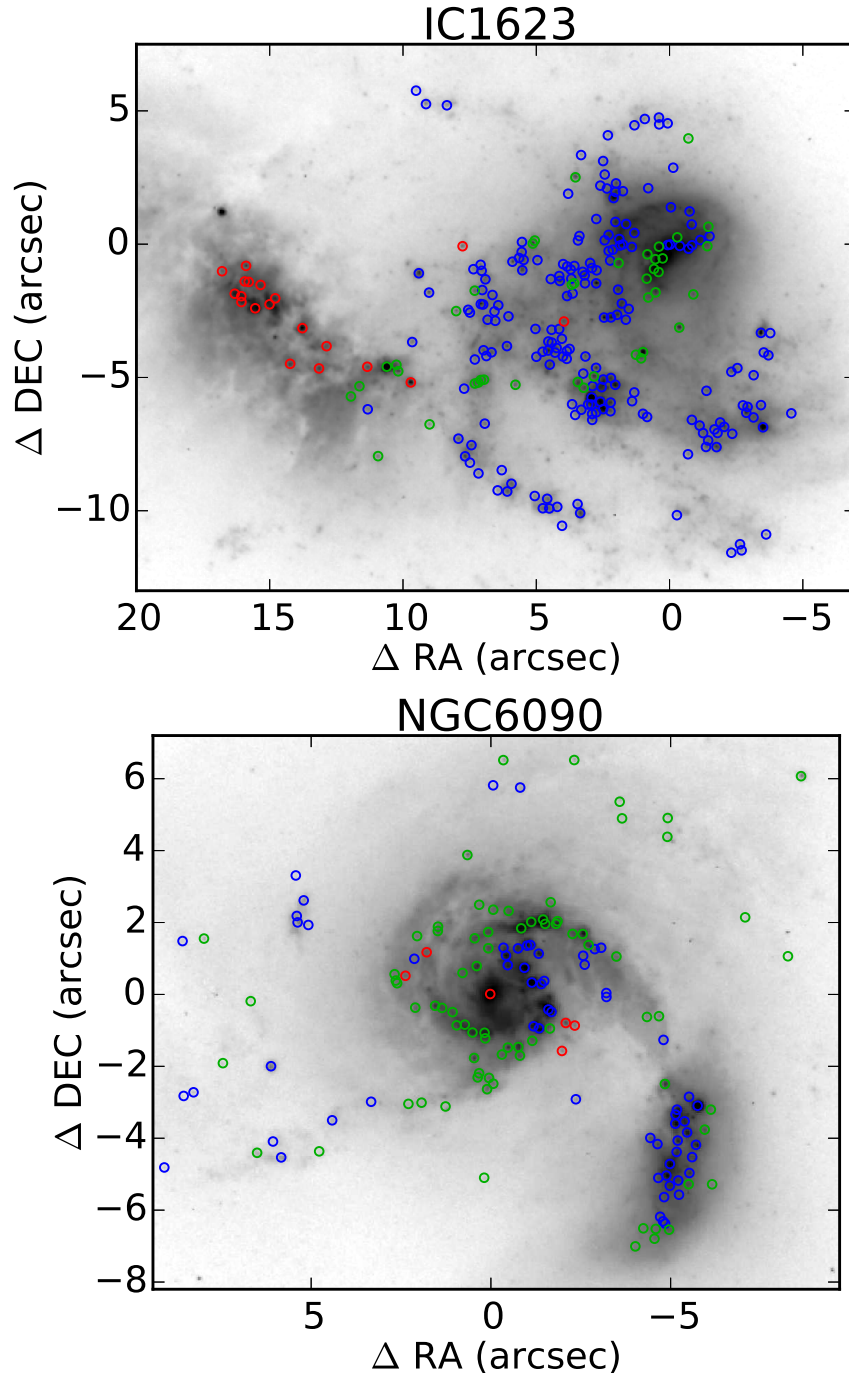


Figure 5.3 F814W images of IC 1623 (top panel) and NGC 6090 (bottom panel). North is up, East to left. The detected clusters are marked with circles of different colors given by their $F_{435W} - F_{814W}$ color as: 1) blue clusters those with $F_{435W} - F_{814W} \leq -1$; 2), green clusters if $-1 < F_{435W} - F_{814W} \leq 0$ and 3), red clusters if $F_{435W} - F_{814W} > 0$. In IC 1623 the blue clusters are located in the western component while the red ones in the eastern component. Strong dust lanes can be seen in IC 1623 E in HST V and B band images. Most of the green clusters are located in IC 1623 W, a few in the spiral arms but preferentially around the nucleus. In NGC 6090 almost all clusters are green or blue, with most of the blue ones located in NGC 6090 SW and in the West side of NGC 6090 NE in MSC region. Only 6 red clusters are identified, one of them being NGC 6090 NE nucleus, and the others located at a distance of ~ 1.4 kpc, symmetrically with respect to the nucleus, 2 of them to the NE and the other 3 to the SW.

$4 \times \text{FWHM}_{PSF}$ for the sky ring inner radius and width. The aperture photometry of sources requires the correction for the light lost due to the finite size of the aperture used, that is called the aperture correction. The best way to determine aperture corrections is from real point sources (stars) on the images. However, isolated bright stars to obtain a meaningful correction were only present in optical images, but not in UV neither in NIR. Thus, aperture corrections were determined from analytically generated point sources using Tiny Tim software (Krist et al., 2011).

We have converted these fluxes into STMAG magnitudes, using equation (6) in Sirianni et al. (2005). The errors have been calculated through error propagation:

$$\Delta F = \sqrt{F + n_{aper} \times (sky + \sigma_{RO}^2) \times \left(1 + \frac{n_{aper}}{n_{sky}}\right)} \quad (5.1)$$

where F is the star cluster flux within the aperture, n_{aper} is the number of pixels in the aperture, sky is the sky background value per pixel, measured in the sky annulus around the cluster, n_{sky} is the number of pixels in the background annulus, and σ_{RO} is the readout noise of the CCD. Analogously, the magnitude errors:

$$\Delta mag = 1,0857 \frac{\Delta F}{F} \quad (5.2)$$

5.3.2. Clusters ages

We have compared the colors and magnitudes of IC 1623 and NGC 6090 clusters with those of Charlot & Bruzual SSPs models (2007, unpublished) in a range of ages between 1 Myr to 13 Gyr. These models are analogous to those in Bruzual & Charlot (2003), but replacing STELIB (Le Borgne et al., 2003) by a combination of the MILES (Sánchez-Blázquez et al., 2006) and GRANADA (Martins et al., 2005) libraries. Chabrier IMF and Padova 1994 evolutionary tracks were used. Model colors have been computed using STSDAS.SYNPHOT software. Using Calzetti et al. (2000) extinction law we have computed also the colours of the models reddened by up to 6 mag. Despite the recent improvements in modelling techniques, it is very difficult from photometry to estimate metallicity on individual clusters. From the spectroscopy we found that the average value for the metallicity in these systems is $\sim 0.6 Z_{\odot}$ (see Section 5.4.6). Taking this into account, we have used solar metallicity SSP models ($1 Z_{\odot}$) in this analysis.

Comparing the position of the clusters in color - color diagrams with respect to the model positions we can estimate the range of cluster ages. In Figure 5.4 we show the FUV - F435W vs F435W - F814W diagram for IC 1623 (top panel) and NGC 6090 (bottom panel), which is the best for breaking the age - A_V degeneracy. The color coding is the same as in Figure 5.3, but only those clusters with SNR ≥ 5 in FUV, F435W, and F814W filters are included in the plots. The black solid line is the path described by SSP models from 1 Myr to 13 Gyr, Z_{\odot} , and $A_V = 0$ mag. The greyscale lines are the paths for the same models reddened by 1 to 3 mag, with the lighter shades tracing the more reddened models.

IC 1623. The vast majority of IC 1623 W clusters (blue ones) are very young (< 200 Myr) and affected by very low to almost no foreground extinction (< 1 mag). If we considered they are not obscured at all, then they could have ages up to 200 Myr. If they are affected by some extinction 0.5 - 1.0 mag, then they could be even younger than 10 Myr. The green clusters are affected by slightly larger average extinctions, above 0.5 mag and up to 2 mag. However, they also have ages below 200

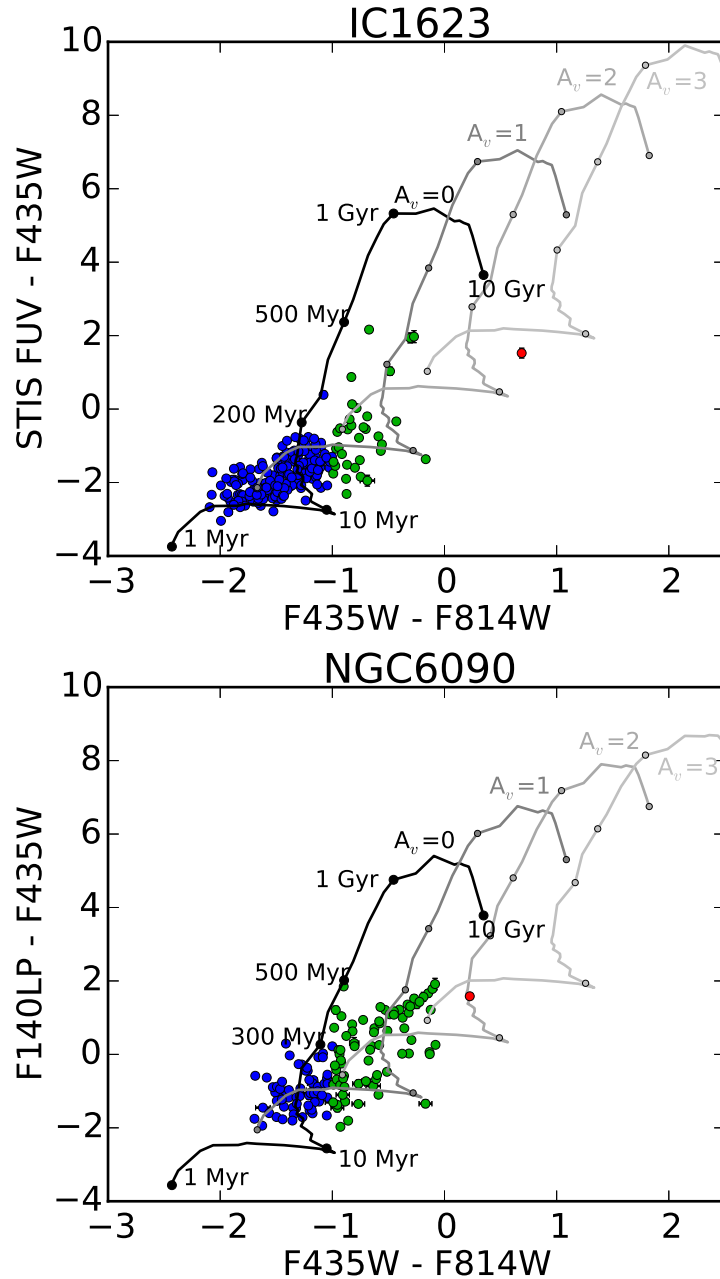


Figure 5.4 FUV - F435W vs F435W - F814W diagram for IC 1623 clusters (top panel) and NGC 6090 clusters (bottom panel). The color coding is the same as in Figure 5.3, but only those clusters with SNR > 5 in FUV, F435W, and F814W filters are included in the plots. The black solid line is the path described by SSP from 1 Myr to 13 Gyr, Z_{\odot} , and $A_V=0$ mag. The greyscale lines are the paths for the same models reddened by 1 to 3 mag, with the lighter shades tracing the more extinguished models. For both systems the blue and most of the green clusters are consistent with ages younger than 200 - 300 Myr, assuming very low to almost no foreground extinction. If affected by some extinction 0.5 - 1.0 mag, they could be even younger than 10 Myr. In the top panel, the only red cluster is located in IC 1623 E component and is consistent with an extinction between 2 - 3 mag and with an age below 10 Myr. This might suggest that, although hidden under large amounts of dust, some clusters in IC 1623 E are as young as IC 1623 W clusters. In the bottom panel, the red cluster is the nucleus of NGC 6090 NE, compatible with ages below 50 Myr and a $A_V = 2 - 3$ mag. In any case it seems that the nucleus itself is rejuvenating as a consequence of the merger process.

Myr. Only 3 of them could be older, up to 500 Myr. Also, only one red cluster (located in IC 1623 E) has enough SNR in FUV filter to appear in this diagram. It is consistent with an extinction between 2 - 3 mag and with an age below 10 Myr. This might suggest that, although hidden under large amounts of dust, some clusters in IC 1623 E are as young or more than IC 1623 W clusters.

NGC 6090. In the case of NGC 6090 (bottom panel) we found something similar. The blue clusters are very young (< 300 Myr) and affected by very low to almost no foreground extinction (< 1 mag). If we considered they are not obscured at all, then they could have ages between 50 - 300 Myr. If they are affected by some extinction 0.5 - 1.0 mag, then they could also be younger than 10 Myr. The scatter is much higher for green clusters, allowing them to be affected by 0 - 2 mag of extinction and having ages up to ~ 300 Myr. The only red cluster that has enough SNR in FUV band to appear in this diagram is the nucleus of NGC 6090 NE. Given the age-extinction degeneracy, it is possible that it has around 50 Myr affected by 2 mag of dust extinction, or being younger than 10 Myr if affected by 3 mag. In any case it seems that the nucleus has rejuvenated as a consequence of the merger process.

Analogously, in Figure 5.5 we show the F435W - F814W vs F814W - F160W diagram for IC 1623 (top panel) and NGC 6090 (bottom panel). This diagram allows to estimate the range of extinction affecting the clusters which are obscured in the FUV. Only clusters with $\text{SNR} \geq 5$ in F435W, F814W, and F160W filters are shown. Again, the black solid line is the path described by SSPs from 1 Myr to 13 Gyr, Z_{\odot} , and $A_V = 0$ mag. The greyscale lines are the paths for the same models reddened by up to 6 mag, with the lighter shades tracing the more extinguished models.

IC 1623. We found that IC 1623 E clusters (the red points in the Figure) are affected by very high values of extinction, between 2 - 6 mag. Except for the < 10 Myr cluster that appears in top panel of Figure 5.4, we can not estimate the ages of the remaining clusters in IC 1623 E, as they are not bright enough in the UV and this diagram does not allow us to break the age-extinction degeneracy.

NGC 6090. Analogously, for the few red clusters in NGC 6090 (bottom panel) we found that they are not so severely extinguished, with much lower values of the extinction around 1 - 2 magnitudes. We note that while in NGC 6090 the difference in the values of extinction between the two components is small (~ 1 mag more of extinction in NGC 6090 NE than in NGC 6090 SW) for IC 1623 the contrast between both components is much higher, possibly up to 4 - 6 mag.

5.3.3. Clusters mass

We found that NICMOS 1.6 μm band is the most sensitive to mass variations. We will estimate the mass range of the star clusters, by comparing their 1.6 μm absolute magnitude with the absolute magnitude of SSPs models of masses ranging from 10^5 to $10^9 M_{\odot}$. The results are shown in Figure 5.6 for IC 1623 (top panel) and NGC 6090 (bottom panel). This is a NIR 1.6 μm absolute magnitude vs F814W - F160W diagram. The paths from models of 10^5 , 10^6 , 10^7 , 10^8 and $10^9 M_{\odot}$ are shown as solid and dashed lines. The models have been cut between 1 - 500 Myr, as we know from the previous section that these are the older ages our clusters can have.

IC 1623. For the western component of IC 1623 we found the clusters have masses between 10^5 - $10^7 M_{\odot}$. However, IC 1623 E clusters have larger masses, between 10^7 - $10^8 M_{\odot}$. There are two of them with masses possibly up to $10^9 M_{\odot}$. In fact, they are no "normal" clusters, but very close or spatially coincident with the two nuclei in IC 1623 E reported by (Knop et al., 1994).

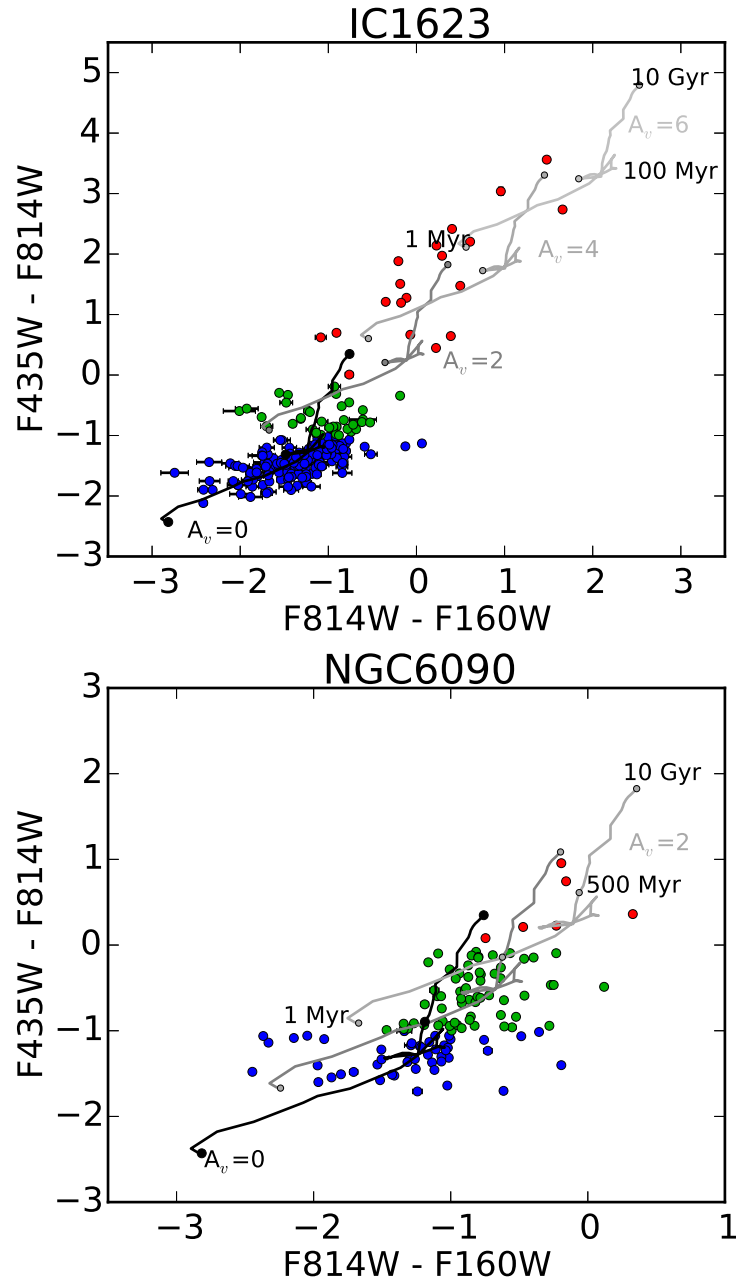


Figure 5.5 $F435W - F814W$ vs $F814W - F160W$ diagram for IC 1623 clusters (top panel) and NGC 6090 (bottom panel). Only clusters with $\text{SNR} > 5$ in $F435W$, $F814W$, and $F160W$ filters are shown. The black solid line is the path described by SSPs from 1 Myr to 13 Gyr, Z_{\odot} , and $A_V=0$ mag. The greyscale lines are the paths for the same models but reddened by 1, 2, 4 and 6 mag. From top panel we found that IC 1623 E clusters (the red points in the figure) are affected by very high values of extinction, between 2 - 6 mag. We can not estimate their ages as they are not bright enough in the UV and this diagram does not allow us to break the age-extinction degeneracy. Analogously, for the few red clusters in NGC 6090 (bottom panel) we found that they are not so severely extinguished, with much lower values of the extinction around 1 - 2 magnitudes. While in NGC 6090 the difference in the values of extinction between the two components is small (~ 1 mag more of extinction in NGC 6090 NE than in NGC 6090 SW) for IC 1623 the contrast between both components is much higher, possibly up to 4 - 6 mag.

NGC 6090. Also, in NGC 6090 most clusters have masses between $10^5 - 10^7 M_{\odot}$. The two "clusters" with higher $1.6 \mu\text{m}$ luminosity (above $10^4 L_{\odot}$) and therefore, higher masses (around $10^7 - 10^8 M_{\odot}$) are NGC 6090 E nucleus (the red one) and NGC 6090 W nucleus (the blue one).

We have performed a rough estimate of the total mass in clusters in these systems, by assigning a certain average mass for the clusters in each luminosity $L_{1.6\mu\text{m}}$ range. In particular, we have separated the clusters in four possible luminosity ranges: from $0.9 < \log L_{1.6\mu\text{m}} < 1.5$ we assign a mass of $\sim 10^5 M_{\odot}$, if $1.5 < \log L_{1.6\mu\text{m}} < 2.65$ then $\sim 10^6 M_{\odot}$, if $2.65 < \log L_{1.6\mu\text{m}} < 3.5$ then $\sim 10^7 M_{\odot}$ and above $\log L_{1.6\mu\text{m}} > 3.5$ we assign $\sim 10^8 M_{\odot}$. In the case of IC 1623 W we have 0, 143, 62 and 1 clusters in each range, leading to a clusters mass $M_{IC1623W}^{clus} \sim 9 \times 10^8 M_{\odot}$. In NGC 6090 we have 0, 19, 79, 19 clusters in each luminosity range, leading to $M_{NGC6090}^{clus} \sim 2 \times 10^9 M_{\odot}$. As we will discuss in Section 5.4.10 these masses are in agreement with the ones derived from the spectroscopy for IC 1623 W, and also for NGC 6090 considering the uncertainties.

5.4. Stellar populations

The stellar content of a galaxy can be approximated as the combination of many SSPs. As explained in Section 4.1, a SSP is a group of stars that formed at the same time and under the same initial chemical composition, and has a particular spectra according to them. Every SSP within a galaxy leaves its imprint on the whole galaxy spectra, like the lines in a barcode. When comparing galaxy spectroscopy or photometry with stellar population synthesis models, we can estimate the star formation history (SFH) of galaxies, unveiling the different stellar populations that have ever born there.

In this section we use the stellar continuum shape to characterize the spatially resolved stellar population properties and constrain the star formation history of IC 1623 and NGC 6090.

5.4.1. Methodology

As explained in Section 4.4, there are two ways to determine the stellar populations using spectroscopic data. In this thesis we apply the full spectral synthesis method, that consists in fitting the full galaxy spectra using stellar population synthesis models. This technique has been extensively tested and applied (Cid Fernandes & González Delgado, 2010; Cid Fernandes et al., 2013, 2014; González Delgado & Cid Fernandes, 2010; González Delgado et al., 2014) and it has been proven to reduce the age-metallicity degeneracy (Sánchez-Blázquez et al., 2011). It is also worth pointing out that despite the diversity of spectral synthesis methods, substantial changes in the results are more likely to come from revisions in the input data and from updates in the base models, the single most important ingredient in any spectral synthesis analysis.

A general consensus in the field is that uncertainties in the results for individual objects average out for large statistical samples (Panter et al., 2007). With IFS, each galaxy is a statistical sample per se, hence, even if the results for single spaxels (or zones) are not iron-clad, the overall trends should be robust. Cid Fernandes et al. (2014) present an analysis of the errors caused by use of different spectral synthesis models and spectrophotometric calibration, applied to the CALIFA data. They find that noise and shape-related errors at the level expected for CALIFA lead to uncertainties of 0.10 - 0.15 dex in stellar masses, light-weighted mean ages and metallicities, with larger uncertainties on star

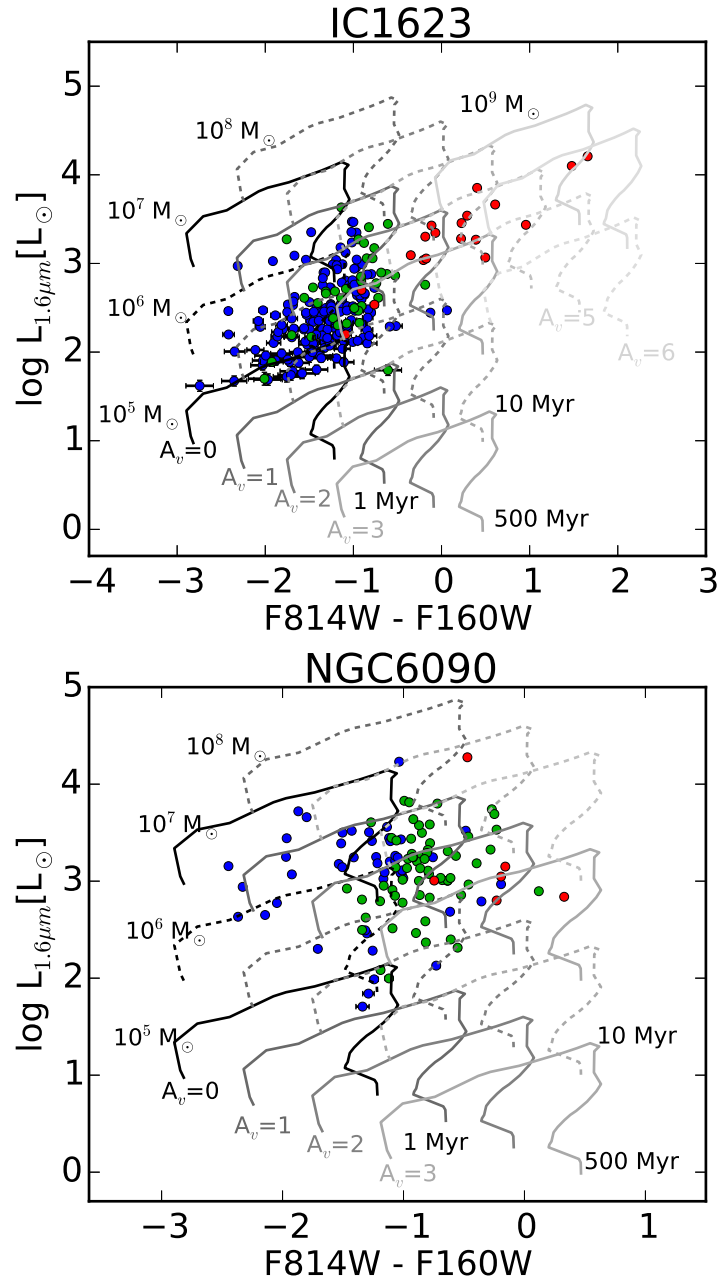


Figure 5.6 Absolute NIR $1.6\mu\text{m}$ magnitude vs F814W - F160W diagram for IC1623 clusters (top panel) and NGC 6090 clusters (bottom panel). Only clusters with SNR > 5 in F435W, F814W and F160W filters are shown. The colors of the clusters are the same as in Figure 5.3. The paths from models of 10^5 , 10^6 , 10^7 , 10^8 and $10^9 M_{\odot}$ have been shown as solid and dashed lines. The models have been cut between 1 - 500 Myr, as we known from previous diagrams that the clusters are not older than 500 Myr in these two pre-merger LIRGs. The greyscale coding represents the variation in stellar extinction as in previous figures. Top panel: IC 1623 W have clusters with masses between $10^5 - 10^7 M_{\odot}$. However, IC 1623 E clusters are more massive, between $10^7 - 10^8 M_{\odot}$, and two of them with mass possibly up to $10^9 M_{\odot}$. In fact, they are no "normal" clusters, but very close or spatially coincident with the two nuclei in IC 1623 E reported by (Knop et al., 1994). Bottom panel: In NGC 6090 most of the clusters have masses between $10^5 - 10^7 M_{\odot}$. The most massive, with $1.6\mu\text{m}$ luminosity above $10^4 L_{\odot}$, and mass $\sim 10^7 - 10^8 M_{\odot}$, are located in NGC 6090 NE nucleus (the red one) and NGC 6090 SW nucleus (the blue one).

formation histories and therefore on mass-weighted quantities. There are even larger uncertainties associated with the choice of population synthesis model, at the level 0.2 - 0.3 dex.

In this thesis we have used the *Starlight* code (see Section 4.4), but before being able to apply it to our IFS data, a series of pre-processing steps were performed to prepare the datacubes for the stellar population analysis. Adequate signal-to-noise ratio in the stellar continuum is vital to extract robust ages, metallicities and star formation histories from continuum spectra in which we observe the integrated light of multiple stellar populations. For CALIFA data a Voronoi binning algorithm was used to combine the spectra in neighbouring spaxels until a combined spectrum of sufficient SNR (> 20 at 5650 Å) was obtained. In the case of CALIFA data all the process of analysis is described in detail in [Cid Fernandes et al. \(2013\)](#).

For our LArr data we follow the same steps as in the CALIFA survey, but with some differences. First, they were corrected by Galactic extinction using [Schlegel et al. \(1998\)](#) maps and the extinction law of [Cardelli et al. \(1989\)](#) with $R_V = 3.1$. Then, they were rest-framed using the redshift provided by NED and spectrally resampled in steps of 2 Å from 3650 - 7000 Å. To ensure the quality of the fits, *Starlight* needs as inputs an error $e_{i,j,\lambda}$ spectrum, indicating the error of the flux for each spectral pixel, and a flag spectrum, $b_{i,j,\lambda}$, that indicates which are the pixels with unreliable flux entries, that we do not want to fit. For CALIFA the reduced cubes already contained carefully derived errors and bad-pixel flags that were implemented in the pipeline (see [Husemann et al. 2013](#), for details). However, for LArr data we did not propagate errors during the reduction, and we need to estimate them a posteriori, in an iterative way.

First, we perform a quick *Starlight* fit to all the spectra, using a simplified spectral base and a mask for the spectral regions we do not want to fit. This includes both the main emission lines ([OII]λλ 3727, 3729, Hε, Hδ, Hγ, Hβ, [OIII]λ4959, [OIII]λ5007, [OI]λ6300, Hα, [NII]λ6548 and [NII]λ6583), and regions with no reliable continuum due to the subtraction of strong sky lines, mainly HgI 4358 Å, HgI 5461 Å and NaI D (around 5890 Å). From *Starlight* output, we obtain the theoretical spectra of the best model fit, $M_{i,j,\lambda}$, and the weights vector, $w_{i,j,\lambda}$, which is zero for the masked pixels, >0 for the fitted ones, and -1 for the clipped pixels. The clipped pixels are those that verify:

$$|O_{i,j,\lambda} - M_{i,j,\lambda}| > 5 \times RMS(O_{i,j,\lambda} - M_{i,j,\lambda}) \quad (5.3)$$

over all (non-masked) pixels. $O_{i,j,\lambda}$ are the observed input spectra and RMS are the initials of Root Mean Square. This is a good first choice when $e_{i,j,\lambda}$ is still not available. To calculate it, we used the residuals of the fit $R_{i,j,\lambda} = O_{i,j,\lambda} - M_{i,j,\lambda}$. For each spectral pixel in $R_{i,j,\lambda}$, $e_{i,j,\lambda}$ is calculated as the standard deviation of the nearest 100 pixels that satisfy ($w_{i,j,\lambda} > 0$). On the other hand, the flag array, $b_{i,j,\lambda}$ is defined as 0 (good pixels) when $w_{i,j,\lambda} \geq 0$, and as 9 (bad pixels) when $w_{i,j,\lambda} = -1$ and for its neighbouring pixels. During this step we visually checked that *Starlight* was clipping the right points.

Finally, we discard from the analysis all the spaxels with $S/N < 5$. For consistency with CALIFA data (which will be used in the next chapter for the merger LIRG NGC 2623), the S/N were calculated in the rest-framed window between 5590 and 5680 Å. In Figure 5.7 we show the S/N ratio maps for IC 1623 (left panel) and NGC 6090 (right panel). Color scale is the same in both maps and goes from 5 to 75. Superimposed in contours are the HST F435W images, smoothed to match the spatial resolution of our LArr data which is ~ 1.7 arcsec (see Section 2.2). The black dots indicate the position of the

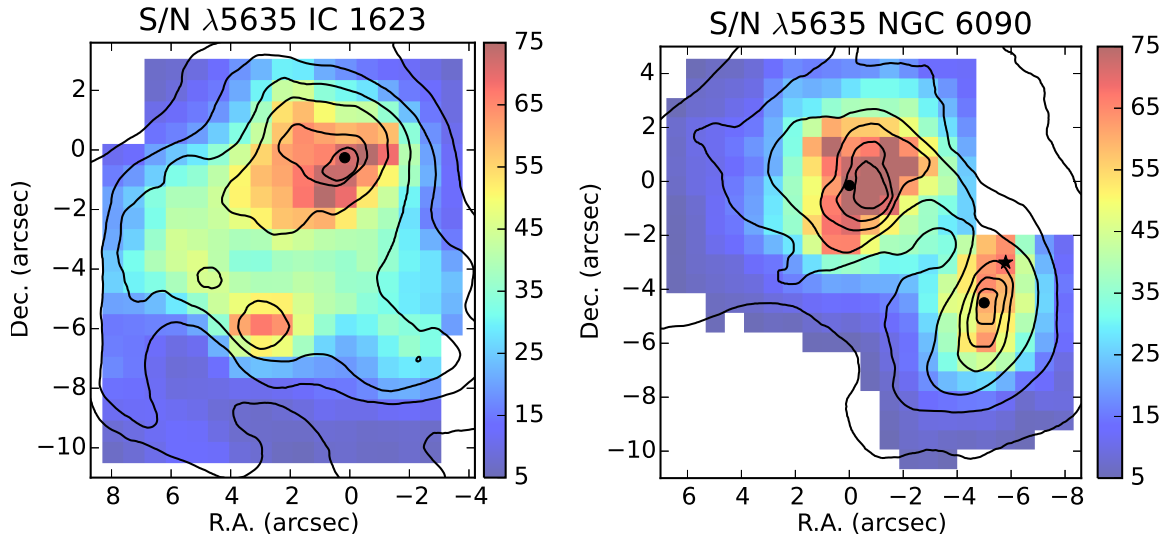


Figure 5.7 S/N ratio maps calculated in $5635 \pm 45 \text{ \AA}$ interval for IC 1623 (left panel) and NGC 6090 (right panel). Color scale is the same in both maps and goes from 5 to 75. Superimposed in contours are HST F435W images, smoothed to match the spatial resolution of our LArr data. The black dots indicate the optical position of the nuclei. In the case of NGC 6090 SW the black star indicate the position of the brightest knot.

optical nuclei.

Now, we are ready to apply *Starlight*. As explained in Section 4.4, *Starlight* is a spectral synthesis method which combines the spectra from a base of SSPs to match an observed spectrum by minimizing the χ^2 of the fit. As a result, it finds the fractional contribution (x_j) of each of the elements in the spectral base to the total flux at the normalization wavelength.

The results reported in this chapter rely on the GM base of models, whose characteristics are explained in detail in Section 4.3. This base combines the Granada models of González Delgado et al. (2005) for $t < 63 \text{ Myr}$ with those of Vazdekis et al. (2010). They are based on the Salpeter IMF. It contains 156 SSPs, comprising four metallicities, $Z = 0.2, 0.4, 1, \text{ and } 1.7 Z_{\odot}$, and 39 ages between $t = 10^6$ and $1.4 \times 10^{10} \text{ yr}$.

For comparison purposes, we have performed the spectral synthesis using also the model base called CB (see Section 4.3), which is built from an update of the Bruzual & Charlot (2003) models, replacing STELIB by a combination of the MILES and GRANADA spectral libraries (the same ones used in base GM). The IMF is that of Chabrier (2003) and it comprises 160 SSPs of four metallicities, $Z = 0.2, 0.4, 1, \text{ and } 2.5 Z_{\odot}$, and 40 ages between $t = 10^6$ and $1.4 \times 10^{10} \text{ yr}$.

The fits were carried out in the $3800 - 6850 \text{ \AA}$ interval. Reddening was modelled with the Calzetti et al. (2000) curve with $R_V = 4.5$, which has been shown to be the more appropriate for starburst galaxies. The main emission lines were masked, as well as the NaI D doublet (because its sensitivity to the ISM absorption) and some residuals from the sky subtraction.

The *Starlight* output of each fitted spectrum is a plain ASCII file storing all the synthesis information. All these quantities are documented in the user manual. For our purposes we focused on: the $\bar{\Delta}$ Figure of merit, the V-band stellar extinction (A_V), the total stellar mass and luminosity, and the population vector, expressed in terms of light (x_j) and mass (m_j) fractions. For LArr data we have

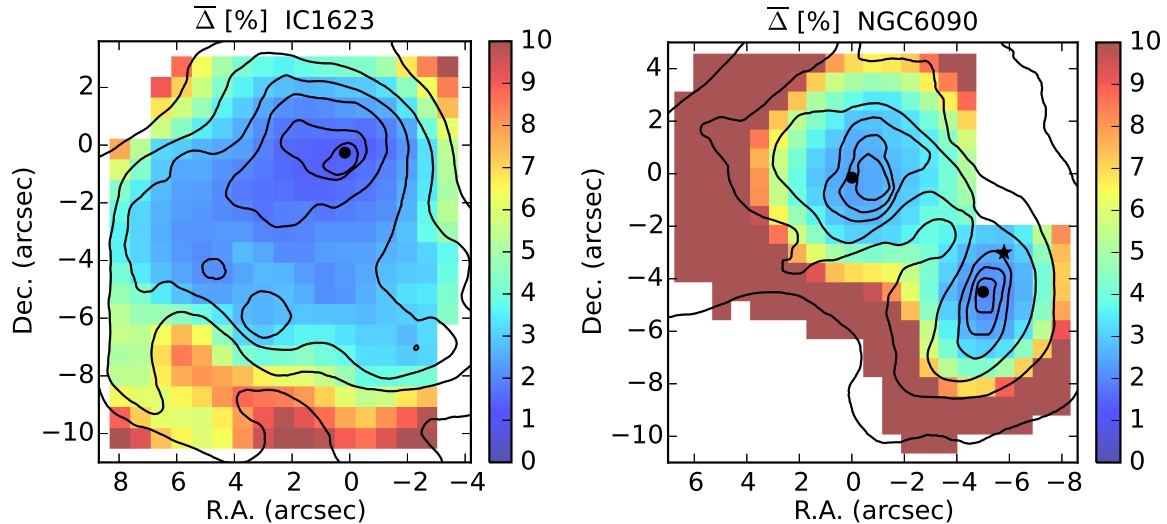


Figure 5.8 Mean relative deviation maps $\overline{\Delta}$, tracing the quality of the fits for IC 1623 (left panel) and NGC 6090 (right panel). Color scale is the same in both maps and goes from 0 to 10. Contours are HST F435W images, smoothed to match the spatial resolution of LArr data. Only spaxels with $\overline{\Delta} < 10\%$ are reliable to be considered in the analysis.

developed our own Python macros to handle the synthesis results.

5.4.2. Fit quality

The quality of the spectral fits should be examined before proceeding to interpretation of the results. The fit quality indicator:

$$\overline{\Delta} = \frac{1}{N_{\lambda}^{eff}} \sum_{\lambda} \frac{|O_{\lambda} - M_{\lambda}|}{M_{\lambda}} \quad (5.4)$$

has been proposed in [Cid Fernandes et al. \(2013\)](#) (CF2013 hereafter) as the best Figure of merit to trace the quality of the fits (see their Section 5.1). Again, O_{λ} and M_{λ} are the observed and model spectra, respectively, and the sum is carried over the N_{λ}^{eff} wavelengths actually used in the fit, i.e., discarding masked, flagged, and clipped pixels. $\overline{\Delta} = 10\%$ is a reasonable quality-control limit.

In Figure 5.8 we show the $\overline{\Delta}$ maps for IC 1623 (left) and NGC 6090 (right) data. The color scale in both maps is the same, and goes from 0 to 10. As can be seen, the larger residuals ($\overline{\Delta} > 10\%$) are located in the outer regions, specially for NGC 6090. We visualize the fits and found the $S/N = 5$ limit too low for the spectral synthesis. Generally, $\overline{\Delta} < 10\%$ when $S/N > 20$. From now on, only the spaxels with $\overline{\Delta} < 10\%$ are shown in the maps and considered in the analysis.

5.4.3. Stellar luminosity

In Figure 5.9 we show the observed surface brightness maps at 5635 \AA (not dust-attenuation corrected) for IC 1623 W (upper left panel) and NGC 6090 (upper right panel). Azimuthal averaging of the maps is another option to compress these results for easier comparison. *PyCASSO* code provides circular convolution tensors to obtain the radial profiles as a function of radius in kiloparsecs. The lower panel shows the radial profile of the surface brightness densities for NGC 6090 NE in red,

NGC 6090 SW in green, and IC 1623 W in blue. The light red, green, and blue points are the values from every spectra in the datacubes as a function of radius.

For **IC 1623 W** we found that the stellar luminosity decreases from $0.4 L_{\odot} \text{ pc}^{-2} \text{ \AA}^{-1}$ in the nucleus to $0.08 L_{\odot} \text{ pc}^{-2} \text{ \AA}^{-1}$ at 2.2 kpc. Between 2.2 kpc and 4.5 kpc, the luminosity density remains approximately constant around $0.08 L_{\odot} \text{ pc}^{-2} \text{ \AA}^{-1}$. Beyond 4.5 kpc it decreases again down to $0.04 L_{\odot} \text{ pc}^{-2} \text{ \AA}^{-1}$ at 6 kpc from the nucleus.

NGC 6090 NE and NGC 6090 SW have a similar profile in the luminosity density, but the NE component is 0.2 dex more luminous. For NGC 6090 NE it ranges from $0.2 L_{\odot} \text{ pc}^{-2} \text{ \AA}^{-1}$ in the nucleus to $0.05 L_{\odot} \text{ pc}^{-2} \text{ \AA}^{-1}$ at 2.7 kpc. For NGC 6090 SW it goes from $0.13 L_{\odot} \text{ pc}^{-2} \text{ \AA}^{-1}$ in the nucleus to $0.03 L_{\odot} \text{ pc}^{-2} \text{ \AA}^{-1}$ at 2.7 kpc.

Comparing the surface brightness profiles of our pre-mergers with CALIFA spirals from [Marino et al. \(2015\)](#), we found that in the nuclear regions pre-mergers are not consistent with having a bulge component, because at the cores of IC 1623 W and NGC 6090 the surface brightness profiles grow linearly or flatten rather than keep growing faster as expected if a bulge were present. The inner parts ($< 2 - 3$ kpc) of IC 1623 W and NGC 6090 are more compatible with pure disk profiles, resembling to some Sc to Sdm in [Marino et al. \(2015\)](#). However, we have to consider that the surface brightness profiles are altered in these systems due to star formation induced by the interaction. In the case of IC 1623 W this is seen in the flattening of the profile above 2.5 kpc, coinciding with the star-forming region C1. In both components of NGC 6090 the profiles flatten in the nucleus as a consequence of the merger-induced star formation in the nuclear regions. For a perfect disk, the surface brightness profile should keep growing linearly in the nucleus (see Figure 2 of [Sánchez-Blázquez et al. 2009](#)) rather than flattening.

5.4.4. Stellar dust extinction

The stellar extinction maps are shown in Figure 5.10. Panels are as in Figure 5.9. The upper left panel is IC 1623 W stellar extinction map and the upper right panel is NGC 6090. The lower panel shows the radial profile of the stellar dust extinction as a function of the radial distance in kpc, in red for NGC 6090 NE, green for NGC 6090 SW and blue for IC 1623 W.

IC 1623 W (upper left) has very little reddening, with $A_V < 0.4$ mag nearly everywhere. From the radial profile, we found a slight but nonuniform increase of the average extinction from 0.06 mag in the nucleus to 0.4 mag at 5 kpc. Between 5 - 6 kpc it decreases again. The regions most affected by extinction are located "behind" areas where a lot of HII regions accumulate. The most extreme case is to the South of the cluster concentration C1 at (3 East,-6 South), where the extinction reaches 1.2 mag. To checked that the increase in A_V is real, we have compared the observed and fitted spectra of the dusty spaxels with several spaxels in their surroundings. Although all are dominated by the emission lines, we find that the underlying continuum is significantly redder in the spaxels where *Starlight* derives high extinction, while in the not-so-extincted spaxels the continuum is significantly bluer. Therefore, we conclude that the observed distribution in A_V is real. As an explanation we suggest that the enhancement of A_V could be due to the accumulation of dust swept the supernovae in the star forming regions, at least in some spaxels. Another possibility is that the interaction itself has led to the accumulation of dust in these regions.

In **NGC 6090** (upper right) we found that in most spaxels in the NE component the extinction

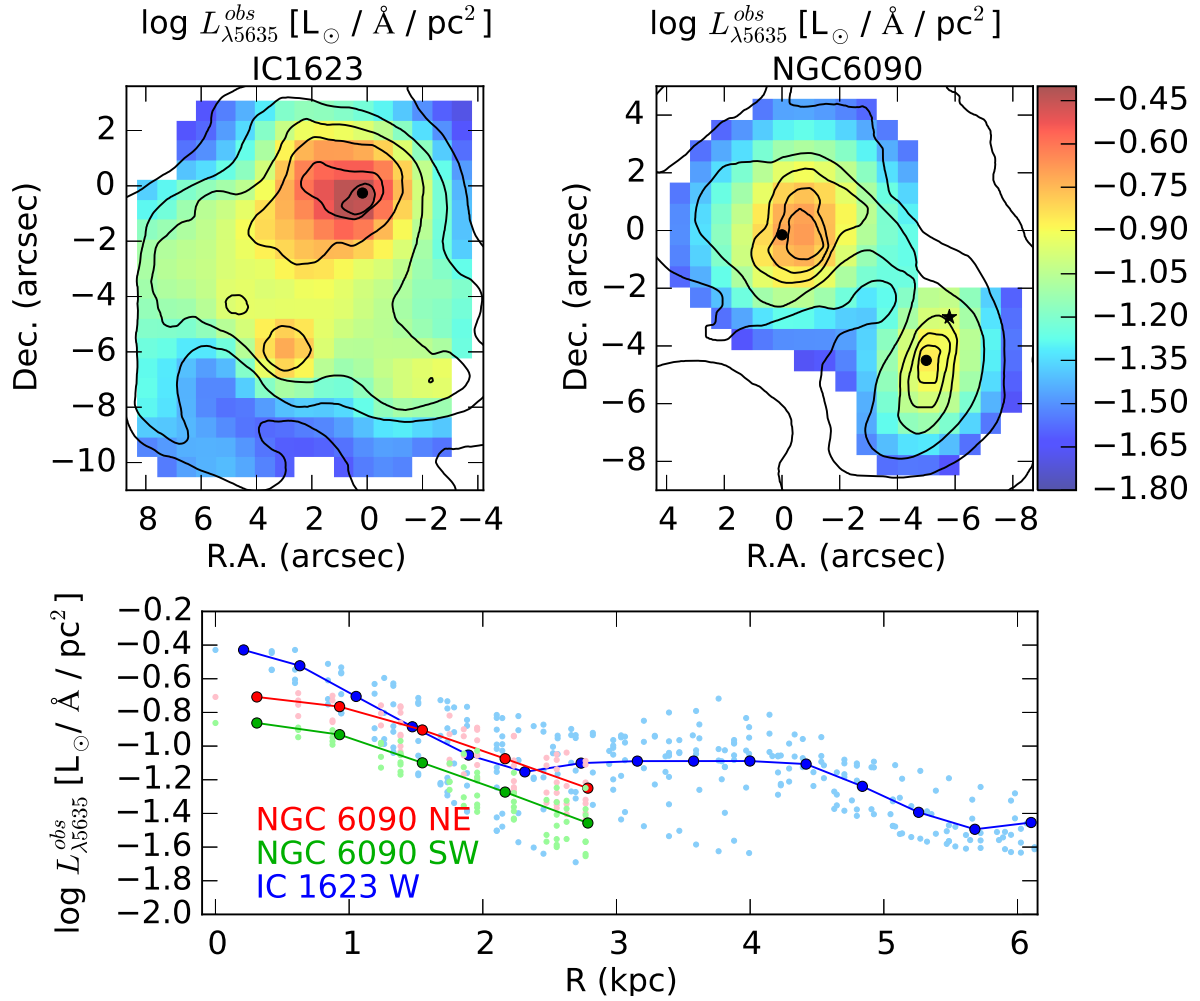


Figure 5.9 Observed surface brightness at 5635 \AA (not corrected for $A_{V,*}$) in logarithmic scale for IC 1623 (upper left) and NGC 6090 (upper right). The color scale is the same for both maps. The contours correspond to the smoothed HST F435W images. Lower panel: mean radial profile of the observed surface brightness as a function of the radial distance in kiloparsecs, in red for NGC 6090 NE, green for NGC 6090 SW and blue for IC 1623 W. The light red, green and blue points are the values measured for every individual spectra in the datacubes. For IC 1623 W we found that the stellar luminosity decreases from $0.4 L_{\odot} \text{ pc}^{-2} \text{ \AA}^{-1}$ in the nucleus to $0.04 L_{\odot} \text{ pc}^{-2} \text{ \AA}^{-1}$ at 6 kpc from the nucleus. In NGC 6090 NE it ranges from $0.2 L_{\odot} \text{ pc}^{-2} \text{ \AA}^{-1}$ in the nucleus to $0.05 L_{\odot} \text{ pc}^{-2} \text{ \AA}^{-1}$ at 2.7 kpc away from the nucleus. NGC 6090 SW has a similar profile in the luminosity density to NGC 6090 NE, but ~ 0.2 dex less luminous.

ranges between 1.2 - 1.6 mag. On the other hand, in the SW component we found values ranging from 0.6 mag in the North to about 0.2 mag in the South. To the West of NGC 6090 NE and in the bridge between the two galaxies the dust extinction has intermediate values of 0.8 - 0.9 mag. There is approximately 1 mag difference in the stellar dust extinction between the two components. When averaging (lower panel), we do not find significant gradients of the dust distribution across the main bodies of the individual galaxies, reflected in the nearly flat radial profiles. We found average values of ~ 1.2 mag and 0.5 mag along NGC 6090 NE and NGC 6090 SW, respectively. Finally, we note

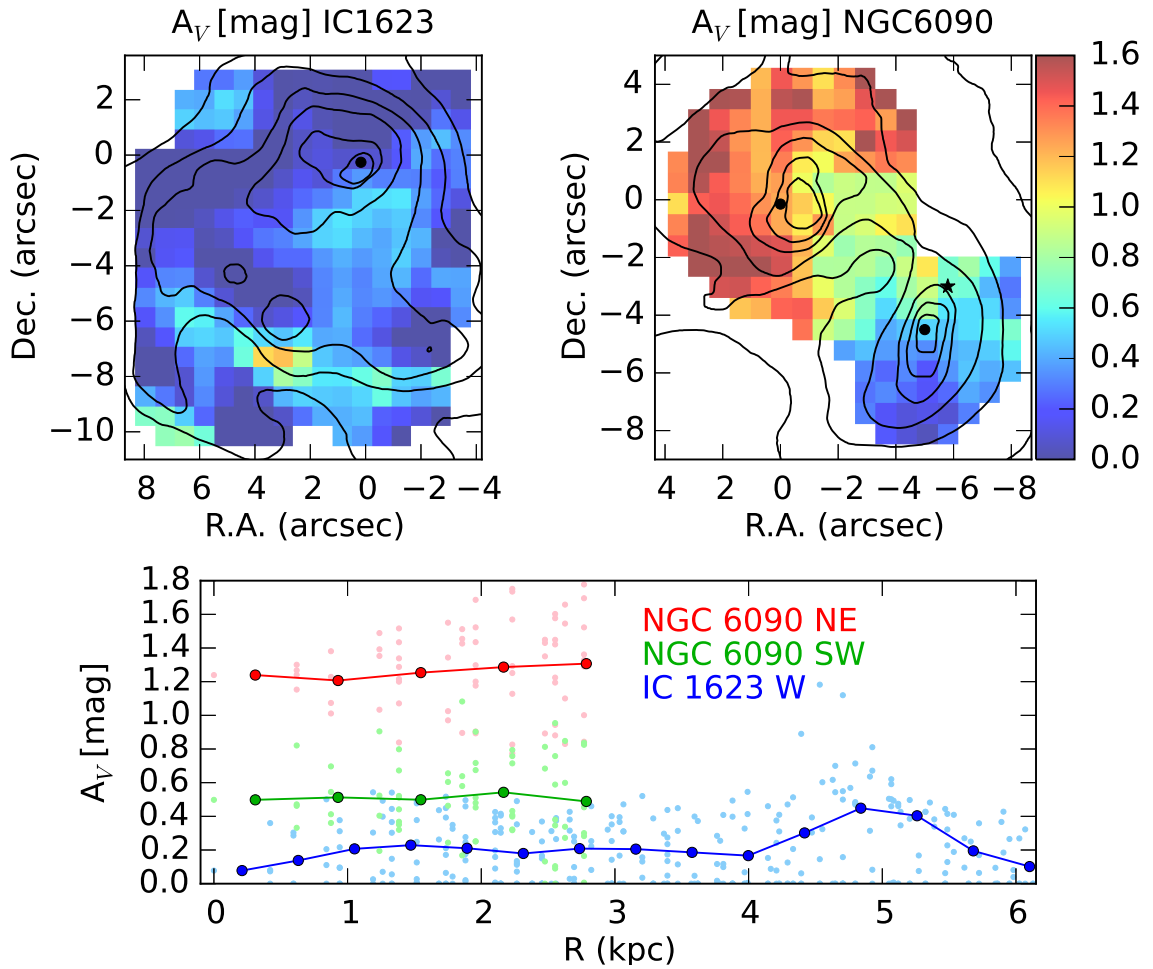


Figure 5.10 Stellar dust extinction maps for IC 1623 (upper left panel) and NGC 6090 (upper right panel). The color scale is the same for both maps from 0 to 1.6 mag. The contours correspond to the smoothed HST F435W images. Lower panel: radial profile of the stellar dust extinction as a function of the radial distance in kiloparsecs, in red for NGC 6090 NE, green for NGC 6090 SW, and blue for IC 1623 W. The light red, green, and blue points are the values measured for every individual spectra in the datacubes. In the case of IC 1623 W (upper left) it is almost not reddened, with A_V below 0.4 mag nearly everywhere. From the radial profile, we found a slight but nonuniform increase of the average extinction from 0.06 mag in the nucleus itself to 0.4 mag at 5 kpc. Between 5 - 6 kpc it decreases again. The regions most affected by extinction are located "behind" areas where a lot of HII regions accumulate. The most extreme case is to the South of the cluster concentration C1 at (3 East, -6 South), where the extinction reaches 1.2 mag. In NGC 6090 (upper right) we found that in most spaxels in the NE component the extinction ranges from 1.2 to 1.6 mag. To the West of this component and in the bridge between the two galaxies the dust extinction is 0.8 - 0.9 mag. On the other hand, in the SW component we found values ranging from 0.6 mag in the North to about 0.2 mag in the South. There is ~ 1 mag difference in the stellar dust extinction between the two components. When averaging (lower panel), we do not find significant gradients of extinction across the main bodies of the individual galaxies, reflected in the nearly flat radial profiles. We found average values of ~ 1.2 mag and 0.5 mag along NGC 6090 NE and NGC 6090 SW, respectively.

that in these pre-merger systems one of the components is significantly more obscured than the other. In these cases it is the eastern component which is more obscured, although the difference is higher for IC 1623 than for NGC 6090. The radial variations of A_V in IC 1623, and NGC 6090, are flat, very different to typical spiral galaxies, which show a negative radial gradient independently of the morphology (González Delgado et al. 2015, GD2015 hereafter).

5.4.5. Ages

The simplest way to quantify the SFH of a system is to compress the age distribution encoded in the light population vectors to their first moments. For this purpose we will use the following definition:

$$\langle \log age \rangle_L = \sum_{t,Z} x_{t,Z} \log t \quad (5.5)$$

where $x_{t,Z}$ is the fraction of light at the normalization wavelength (5635 Å) due to the base population with age t and metallicity Z .

The mean stellar age maps are shown in Figure 5.11. The scale is the same for both maps to facilitate the comparison and goes from $\langle \log age \rangle_L = 6.0$ to 9.0.

In **IC 1623 W** the nuclear regions are clearly older than the outer parts. From the radial profile we find a negative trend of the mean age with distance; from ~ 300 Myr in the nucleus to ~ 30 Myr 3 kpc away. From 3 to 6 kpc the age remains approximately constant between 15 - 40 Myr.

In **NGC 6090** the older spaxels are located in the outskirts for both components, but specially for the SW galaxy, where they reach ages up to ~ 300 Myr. The youngest spaxels (~ 50 Myr) are located in the bridge. When averaging we found that both components have the same mean ages, between 50 - 100 Myr. Moreover, there are no significant variations across the face of the galaxies, with an almost flat trend of ages with distance (see lower panel of Figure 5.11).

In both pre-merger systems the age profiles are significantly flatter than in Sb to Sc galaxies (GD2015). Even for IC 1623 W, where we find a negative gradient, the absolute variation of the ages from the nucleus to the outskirts is ~ 280 Myr, while for Sbs and Scs the variation in the inner 1HLR is ~ 3 Gyr and ~ 620 Myr, respectively.

5.4.6. Metallicity

The mean metallicity has been obtained like the mean ages, but weighing by the mass. That is, collapsing the metallicity distribution to their first moments, using the mass population vectors:

$$\langle \log Z_* \rangle_M = \sum_{t,Z} \mu_{t,Z} \log Z \quad (5.6)$$

where $\mu_{t,Z}$ is the mass fraction at the normalization wavelength due to the base population with age t and metallicity Z . For comparison purposes, this is the same definition adopted in GD2015.

The mass-weighted metallicity maps are shown in Figure 5.12. The scale range in both maps is the same, and goes in log from -0.7 to 0.23 (0.2 to 1.7 Z_\odot).

In **IC 1623 W** (upper left panel) we found that the metallicity is higher in the outskirts than in the nuclear region. From the radial profile (lower panel) we found that the metallicity really increases

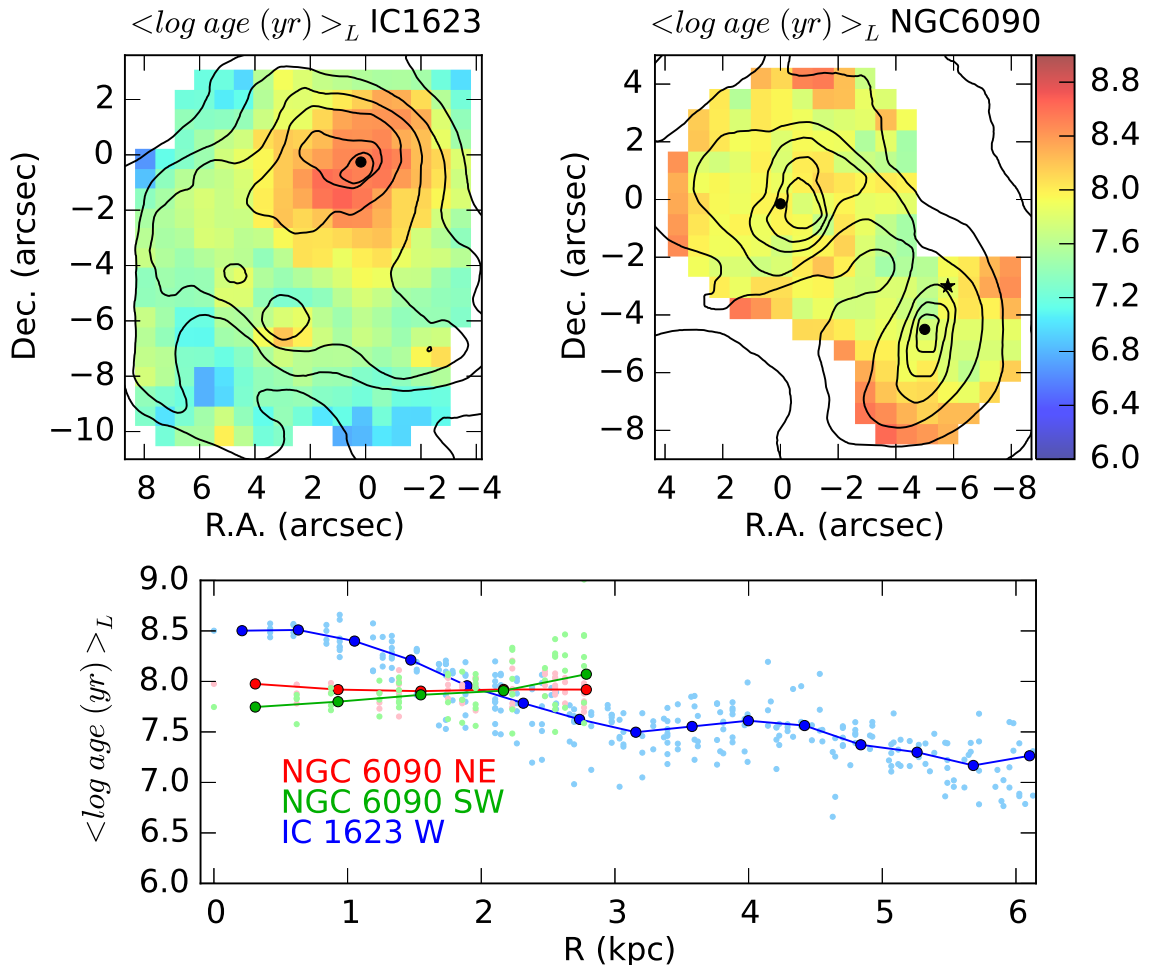


Figure 5.11 Mean stellar age maps (in logarithmic scale) for IC 1623 (upper left panel) and NGC 6090 (upper right panel). The color scale is the same for both maps and ranges from 6 to 9. The contours correspond to the smoothed HST F435W images. Lower panel: radial profile of the mean stellar age as a function of the radial distance in kiloparsecs, in red for NGC 6090 NE, green for NGC 6090 SW and blue for IC 1623 W. The light red, green and blue points are the values measured for every individual spectra in the datacubes. In IC 1623 W the nuclear regions are clearly older than the outer parts. From the radial profile we find a negative trend of the mean age with distance; from ~ 300 Myr in the nucleus to ~ 30 Myr at 3 kpc away from it. From 3 to 6 kpc the age remains approximately constant between 15 - 40 Myr. However, in NGC 6090 it seems to happen the contrary, the older spaxels are located in the outskirts for both components, but specially for the SW galaxy, where they reach ages up to ~ 300 Myr. The youngest spaxels (~ 50 Myr) are located in the bridge. When averaging we found that both components have the same mean ages, between 50 - 100 Myr. Moreover, there are not significant variations across the face of the galaxies with an almost flat trend of ages with distance.

outwards; from around -0.5 to -0.3 ($0.3 - 0.5 Z_{\odot}$) around the nucleus to -0.2 ($0.6 Z_{\odot}$) between 1.5 and 4.5 kpc away, and up to 0 ($1.0 Z_{\odot}$) between 4.5 and 6 kpc.

In **NGC 6090** (upper right) we found several regions with high metallicity values; to the East of NE nucleus ($Z_{\star} \sim 1.6 Z_{\odot}$), in the bridge between components and south of NGC 6090 SW, with Z_{\star}

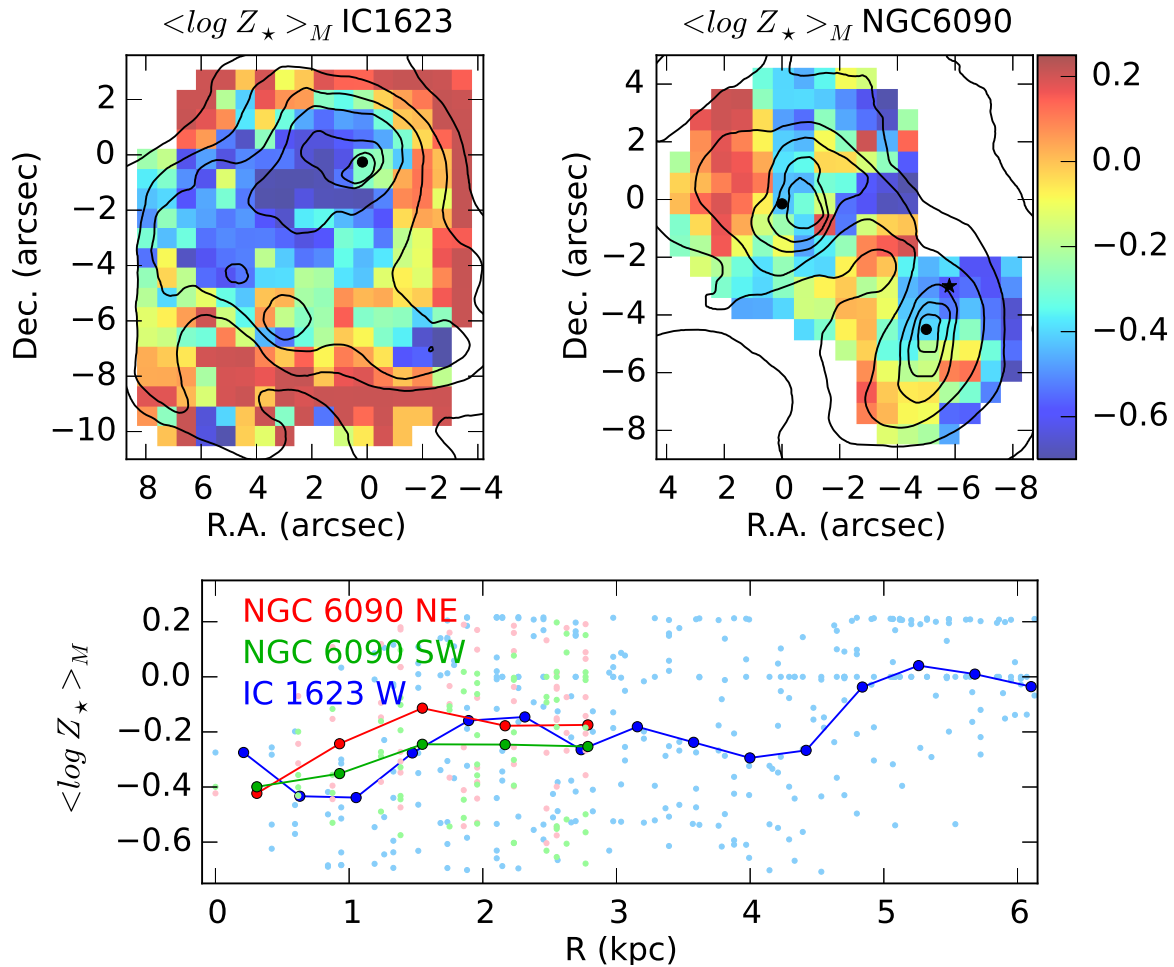


Figure 5.12 Mean stellar metallicity maps for IC 1623 (upper left) and NGC 6090 (upper right). The color scale is the same for both maps and goes from -0.7 to 0.25. Lower panel: radial profile of the mean stellar metallicity as a function of the radial distance in kiloparsecs, in red for NGC 6090 NE, green for NGC 6090 SW, and blue for IC 1623 W. The light red, green, and blue points are the values measured for every individual spectra in the datacubes. Given the uncertainties, from this figure we can conclude that both pre-merger LIRGs have global mean metallicities $\sim 0.6 Z_{\odot}$. The metallicity radial profiles, at least in the inner 3 kpc of these three galaxies, are either slightly positive or flat, that is, metallicity increases or remains constant with distance.

ranging from $\sim 0.8 - 1.6 Z_{\odot}$ depending on the spaxel. From the radial profile we found that in the NE component the metallicity ranges from -0.4 in the nucleus to -0.1 at 1.5 kpc away ($0.4 - 0.8 Z_{\odot}$). Above 1.5 kpc the metallicity stabilizes at $\sim 0.7 Z_{\odot}$. In the SW component the metallicity also increases from -0.4 in the nucleus to -0.25 at 1.5 kpc away ($0.4 - 0.6 Z_{\odot}$). Above 1.5 kpc it also stabilizes at $\sim 0.6 Z_{\odot}$. Both profiles are fairly similar, with NGC 6090 NE being ~ 0.1 dex more metallic than NGC 6090 SW.

However, as can be seen in the lower panel, the scatter is large. Metallicity in one of the most difficult quantities to constrain. The fact that sometimes age and Z grow in the opposite sense, as in IC 1623 W, could suggest that the results are affected by the age-metallicity degeneracy. Due to

this, we will take the metallicity results with caution. Focusing on the mean value, it seems that all of them IC 1623 W, NGC 6090 NE, and NGC 6090 SW have global mean metallicities around $\sim 0.6 Z_{\odot}$.

The metallicity radial profiles in the inner 3 kpc of these three galaxies are approximately flat. That is, metallicity remains constant or even slightly increases with distance in these pre-merger systems, contrary to what happens in spirals earlier than Sc, which show a negative gradient (GD2015). In anycase, this kind of inverted/flat metallicity gradients were previously found in the gas metallicity of mergers where significant gas inflows have occurred (Rich et al., 2012; Kewley et al., 2010). Given the above mentioned degeneracies and the large scatter in the results, the stellar metallicity should be interpreted with caution.

5.4.7. Stellar mass surface density

In Figure 5.13 we show the stellar mass surface density ($\log \mu_{\star}$) maps for IC 1623 W (upper left panel) and NGC 6090 (upper right panel), and the radial profiles for both systems (lower panel).

In **IC 1623 W** nucleus and in the cluster concentration C1 is where the highest values of the mass surface density are reached, with a logarithmic value of around 3.7. From the radial profile we found a negative gradient with distance, going from $\log \mu_{\star} = 3.7 M_{\odot} \text{ pc}^{-2}$ in the nucleus itself to 2.8 at 3 kpc; it increases again up to $\log \mu_{\star} = 3.0$ at 4.5 kpc, and decreases sharply to $\log \mu_{\star} \sim 2.2$ at 6 kpc.

For **NGC 6090** we found that the stellar mass surface density is significantly higher in the NE component than in the SW. The region with the highest value of the mass surface density ($\log \mu_{\star} \sim 3.8$) is located to the South East of NGC 6090 NE nucleus. In NGC 6090 SW, $\log \mu_{\star}$ is higher in the North of the component than in the South. From the radial profile, we also found a negative gradient of the stellar mass density with distance, but not as steep as for IC 1623 W; $\log \mu_{\star}$ goes from 3.8 to 3.2 for NGC 6090 NE and from 3.0 to 2.7 for NGC 6090 SW.

The central density in IC 1623 W and NGC 6090 NE is similar to the central density of Sbc galaxies, and NGC 6090 SW is more similar to Sc, but their radial profiles are different because they are much flatter than in spirals (GD2015).

5.4.8. Stellar masses

Another important *Starlight* output is the stellar mass, which is calculated from the stellar luminosity and taking into account the mass to light ratio of the different SSPs. The total stellar mass obtained from the sum of all spaxels is $M = 3.9 \times 10^{10} M_{\odot}$ and $6.8 \times 10^{10} M_{\odot}$ for IC 1623 W and NGC 6090, respectively. This is the mass locked in stars today. Counting also the mass returned by stars to the interstellar medium $M' = 5.5 \times 10^{10} M_{\odot}$ and $9.6 \times 10^{10} M_{\odot}$ were involved in star formation for IC 1623 W and NGC 6090, respectively.

Since in LIRGs the light is dominated by young stellar populations and the extinction may be important in some regions, we could be underestimating the stellar mass from old stars. To check this, we have alternatively determined the old stellar mass using MIR data from Spitzer at 3.6 and 4.5 μm following the approach proposed by Meidt et al. (2014). Using Independent Component Analysis they found that, when isolating the contribution from old stars, the [3.6] - [4.5] color ranges from -0.15 to -0.02. However, in the presence of "contaminants" (hot dust, PAH emission, intermediate age

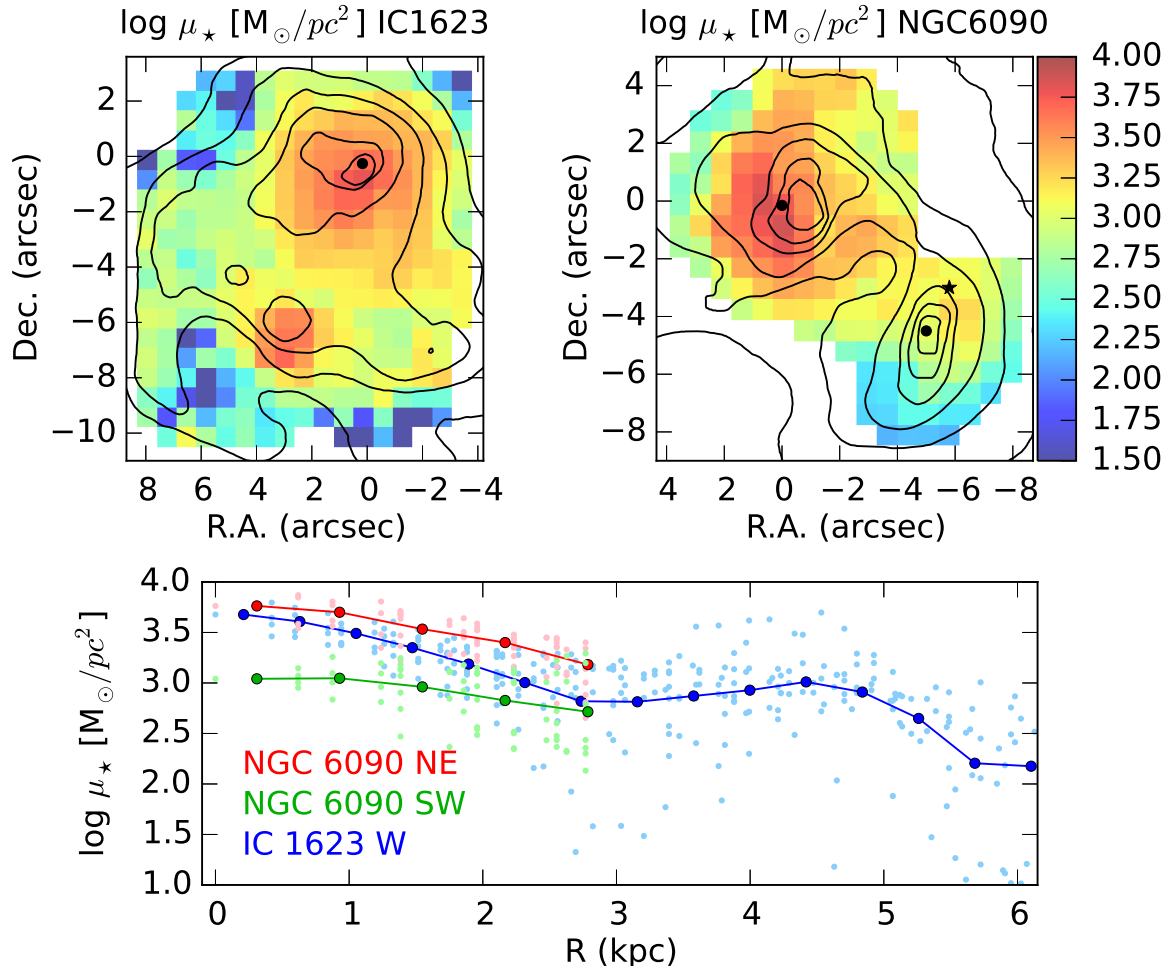


Figure 5.13 Stellar mass density maps for IC 1623 (upper left) and NGC 6090 (upper right). The color scale is the same for both maps and goes from $\log \mu_{\star} = 1.5$ to 4. Contours correspond to the smoothed HST F435W images. Lower panel: radial profile of the stellar mass density as a function of the radial distance in kiloparsecs, in red for NGC 6090 NE, green for NGC 6090 SW, and blue for IC 1623 W. The light red, green, and blue points are the values measured for every individual spectra in the datacubes. In IC 1623 W nucleus and in the cluster concentration C1 is where the highest values of the mass surface density are reached, with a logarithmic value of around 3.7. From the radial profile we found a negative gradient with distance, going from $\log \mu_{\star} = 3.7 \text{ M}_{\odot} \text{ pc}^{-2}$ in the nucleus itself to 2.8 at 3 kpc; it increases again up to $\log \mu_{\star} = 3.0$ at 4.5 kpc, and decreases sharply to $\log \mu_{\star} \sim 2.2$ at 6 kpc. For NGC 6090 we found that the stellar mass surface density is significantly higher in the NE component than in the SW. The region with the highest value of the mass surface density ($\log \mu_{\star} \sim 3.8$) is located to the South East of NGC 6090 NE nucleus. In NGC 6090 SW, $\log \mu_{\star}$ is higher in the North of the component than in the South. From the radial profile, we also found a negative gradient of the stellar mass density with distance, but not as steep as for IC 1623 W; $\log \mu_{\star}$ goes from 3.8 for NGC 6090 NE and from 3.0 to 2.7 for NGC 6090 SW.

Red Super Giants (RSG), and AGB stars) this color is much redder $[3.6] - [4.5] \gtrsim 0.3$, Meidt et al. (2012). The latter is the case of our two galaxies whose average $[3.6] - [4.5]$ color are 0.27 and 0.20 for IC 1623 W and NGC 6090, respectively. This indicates that "contaminants", probably dust emission, are important in our LIRGs.

In this case, we can estimate the stellar masses from the global mass to light ratio at $3.6\mu\text{m}$ ($\zeta_{3,6}^d$), calibrated by Jarrett et al. (2013):

$$\log \zeta_{3,6}^d(M_{\odot}/L_{\odot}) = -0.22 + 3.42([3,6] - [4,5]) \quad (5.7)$$

where $[3.6]$ and $[4.5]$ are the magnitudes measured at 3.6 and 4.5 μm bands. This expression is calculated under several assumptions that we have to take into account. On the one hand, it considers the SSPs of Bruzual & Charlot (2003) with a Chabrier IMF that is optimal for early type galaxies. On the other hand, it considers that the average mass to light ratio for strictly old stars is $\log \zeta_{3,6} = -0.23 \pm 0.1$ dex. This was determined by Meidt et al. (2012, 2014), and is valid in the range of metallicities covered by our models. The global mass to light ratio can also be expressed as:

$$\zeta_{3,6}^d = \frac{M_{\star}}{L_{3,6}^{\text{tot}}} \quad (5.8)$$

where M_{\star} is the total stellar mass and $L_{3,6}^{\text{tot}}$ is the total luminosity at 3.6 μm . From it, we can calculate the total stellar mass.

With this procedure we found that the old stellar mass derived from the MIR is $3.4 \times 10^{10} M_{\odot}$ and $4.4 \times 10^{10} M_{\odot}$ for IC 1623 W and NGC 6090, respectively. Given that equation 5.7 is valid for early type galaxies, when comparing with our optical estimates, we consider only the stellar mass in populations with ages greater than 1.4 Gyr, which is $5.3 \times 10^{10} M_{\odot}$ and $8.8 \times 10^{10} M_{\odot}$ for IC 1623 W and NGC 6090, respectively. The masses derived with our optical spectroscopy are a factor 1.5 - 2 higher than the masses calculated with the MIR photometry. However, this factor is explained by the difference in the IMF. Our optical analysis uses a Salpeter IMF (results from GM base of models), and these masses should be on average a factor 1.84 larger than when compared with Chabrier IMF, as calculated by González Delgado et al. (2015). In fact, from *Starlight* results with the base CB, which uses Chabrier, we found an old (> 1.4 Gyr) stellar mass of $2.6 \times 10^{10} M_{\odot}$ and $5.9 \times 10^{10} M_{\odot}$ for IC 1623 W and NGC 6090, respectively.

This remarkable agreement between mass estimations from optical spectra and MIR imaging confirms that for IC 1623 W and NGC 6090 we are not underestimating the stellar masses with *Starlight*, and also ensures that the extinction estimates are approximately correct.

5.4.9. 1D Star Formation Histories

The 1D SFHs are obtained by collapsing the spatial information, summing the SFH of every single spaxel in the datacubes, keeping the whole age range used in the spectral fitting so we can get a detailed idea of when the bursts of star formation started and how many of them occurred.

In Figure 5.14 we present the total 1D SFH in light for IC 1623 W (top panel) and NGC 6090 (bottom panel). They x axis represents the ages of the SSPs included in our base, while the y axis represents the relative light fraction calculated over all spaxels in the cubes, for a given age.

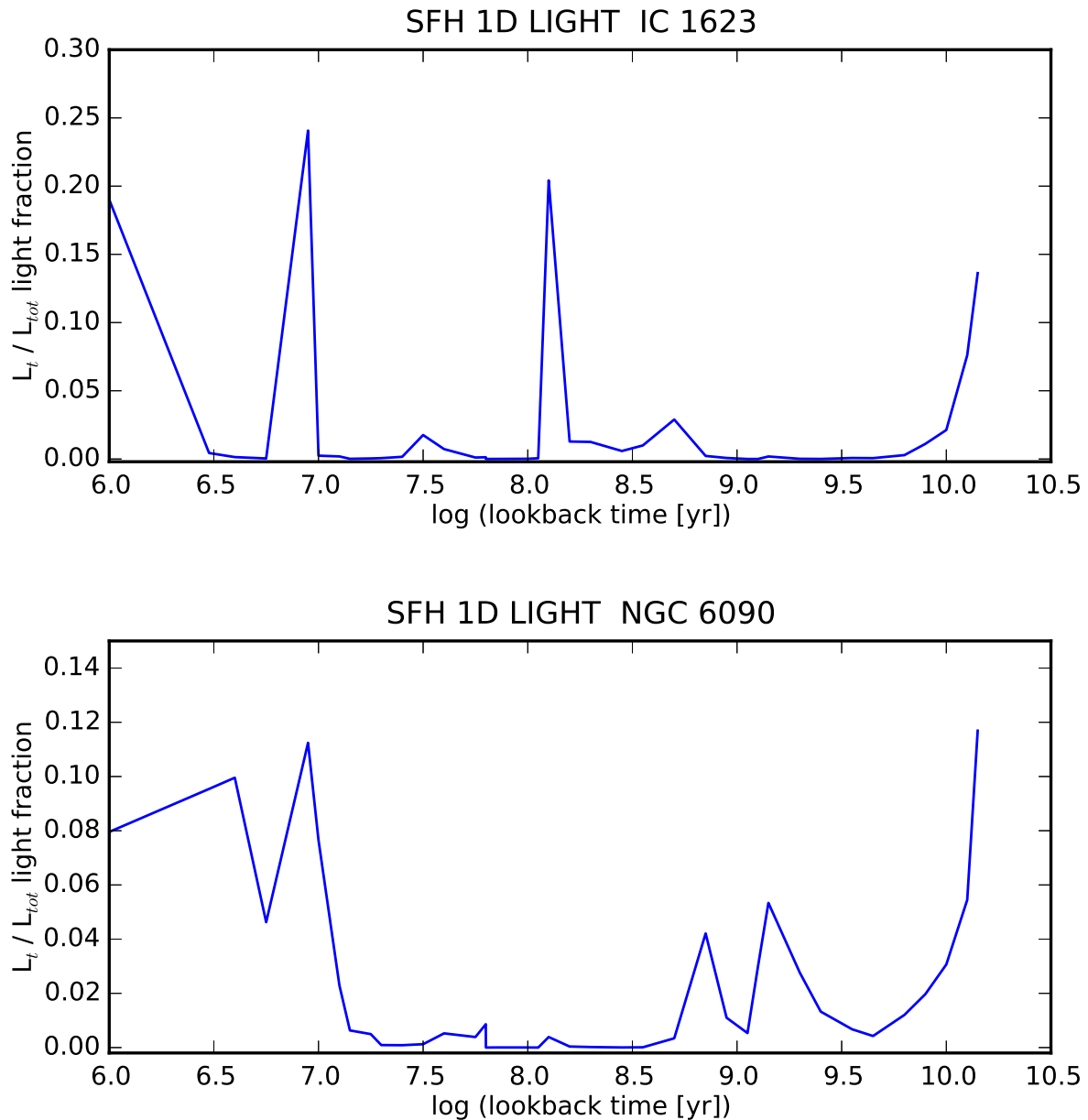


Figure 5.14 Total 1D SFHs in light for IC 1623 W (top panel) and NGC 6090 (bottom panel). The x axis represents the ages of the SSPs included in our base, while the y axis represents the relative light fraction calculated over all spaxels in the cubes, for a given age. For IC 1623 W we found that there could have been two relevant "young" bursts, in the last 1 Myr and 8 Myr. However, the spectral differences between these two SSPs are not enough to distinguish (within our temporal resolution) if they were individual bursts or something more "continuous". In anycase the young components may be younger than 10 Myr. Within the intermediate age range we found that star formation took place between 500 to 140 Myr ago with the more intense peak located at 140 Myr. The old populations formed between 14 Gyr and 6 Gyr ago for IC 1623 W. In the case of NGC 6090, most of the young star formation started in the last 20 Myr and seems to have been continuous since. Two relevant intermediate age bursts may have occurred in NGC 6090, one at 1.4 Gyr and another peaking around 600 Myr. The old populations formed between 14 Gyr and 5 Gyr ago for this system.

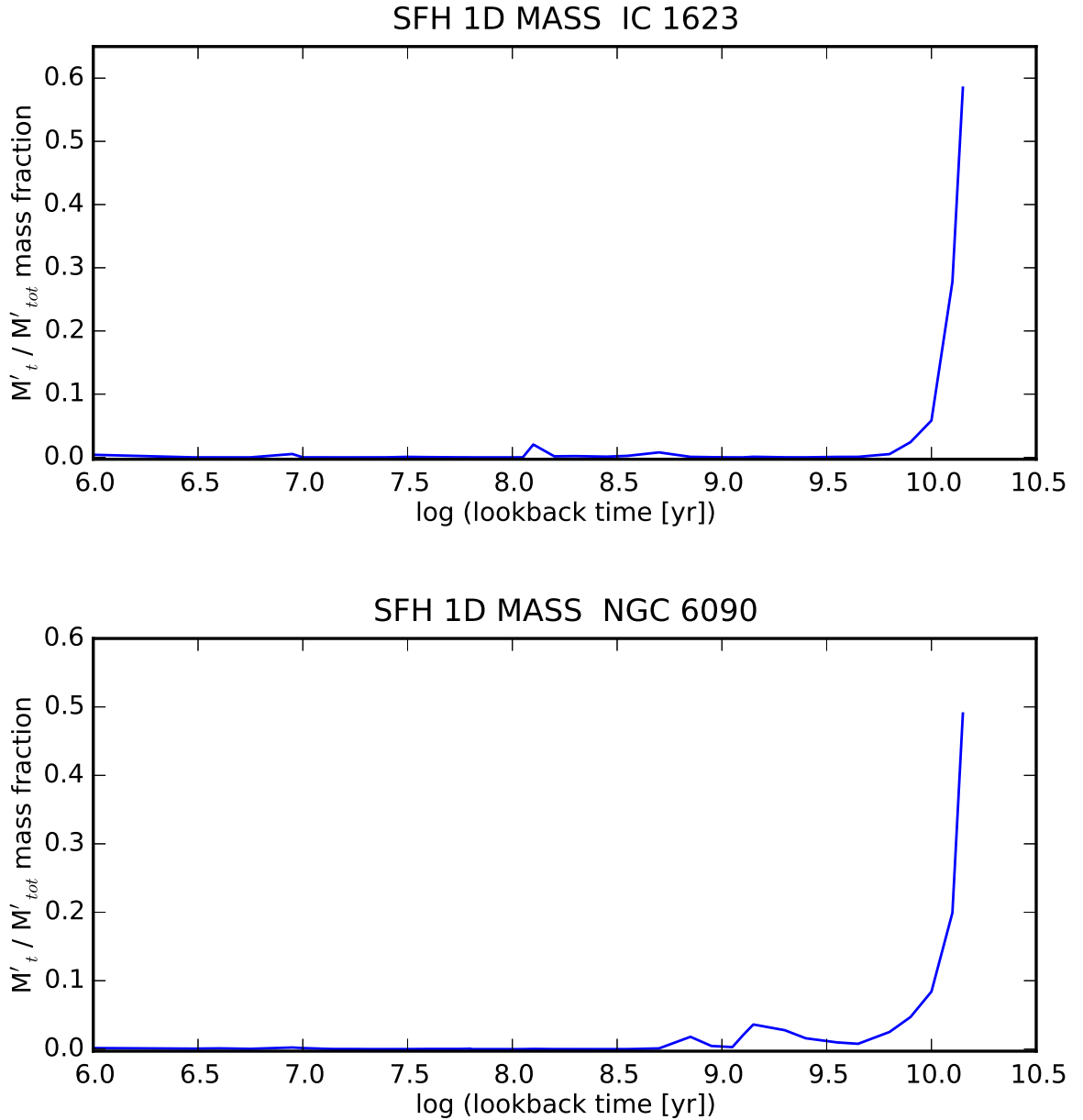


Figure 5.15 Total 1D SFHs in mass for IC 1623 W (top panel) and NGC 6090 (bottom panel). The x axis represents the ages of the SSPs included in our base, while the y axis represents the relative mass fraction calculated over all spaxels in the cubes, for a given age. As usual, due to the highly non-linear relation between light and mass in stars, the young populations that show up so well in light practically disappear when seen in mass. For both galaxies, more than 90% of the mass is in stellar populations older than 1.4 Gyr.

For **IC 1623 W** we found that there could have been two relevant "young" bursts, in the last 1 Myr and 8 Myr. However, the spectral differences between these two SSPs are not enough to distinguish (within our temporal resolution) if they were individual bursts or something more "continuous". In anycase, the young components may be younger than 10 Myr. Within the intermediate age range we

found that star formation took place between 500 to 140 Myr ago, with the more intense peak located at 140 Myr. The old populations formed between 14 Gyr and 6 Gyr ago for IC 1623 W.

In the case of **NGC 6090**, most of the young star formation started in the last 20 Myr and seems to have been continuous since. Two relevant intermediate age bursts may have occurred in NGC 6090, one at 1.4 Gyr and another peaking around 600 Myr. The old populations formed between 14 Gyr and 5 Gyr ago for this system.

As usual, due to the highly non-linear relation between light and mass in stars, the young populations that show up so well in light practically disappear when seen in mass. This can be seen in Figure 5.15, where we present the total 1D SFH in mass for IC 1623 W (top panel) and NGC 6090 (bottom panel). Now, the y axis represents the relative mass fraction calculated over all spaxels in the cubes, for a given age. As can be seen, in both cases more than 90 % of the mass is in stellar populations older than 1.4 Gyr.

The SFHs of IC 1623 and NGC 6090 are analyzed in much more detail in Sections 8.1.1 and 8.1.2.

5.4.10. Contribution of young, intermediate and old populations

Population synthesis studies in the past found that a useful way to summarize the SFH is to condense the age distribution encoded in the population vector into age ranges. This strategy comes from a time when the analysis was based on equivalent widths and colors (Bica et al., 1988; Fernandes et al., 2003), but it was also applied to full spectral fits (González Delgado et al., 2004). We divide into: young stellar populations (YSP, SSPs ≤ 140 Myr), intermediate age stellar populations (ISP, $140 \text{ Myr} < \text{SSPs} \leq 1.4 \text{ Gyr}$), and old stellar populations (OSP, SSPs $> 1.4 \text{ Gyr}$). We select these three age bins to correspond to the main sequence lifetimes of stars with distinctly different optical line and continuum features.

Figure 5.16 presents maps of the light fraction due to YSP, ISP, and OSP (x_Y , x_I , and x_O). IC 1623 W is shown in the top panels, and NGC 6090 in the bottom panels.

We find that both pre-merger systems are clearly dominated by young stellar populations widespread across the whole observed extension.

In **IC 1623 W** we found that the contribution of the YSP to light is around 90 % everywhere except in the nucleus, where the contribution is around 50 %. Only in the nucleus the ISP have a significant contribution, between 30 - 40 %. The contribution of OSP is everywhere below 20 % in IC 1623 W.

In **NGC 6090** we found that almost all spaxels have YSP contribution above 70 %, except for some spaxels located at the easternmost end of NGC 6090 NE and at the south edge of NGC 6090 SW. In these regions the contribution of ISP and OSP are also important.

In Figure 5.17 we show the radial averages of the contributions to light of YSP, ISP and OSP in blue, green, and red colors, respectively. IC 1623 W is shown in the top panel, and NGC 6090 in the bottom panel. NGC 6090 NE profile is drawn with solid lines and NGC 6090 SW with dashed lines.

For **IC 1623 W** we found that the contribution of the YSP increases from 50 % in the nucleus to 95 % at 2.7 kpc. Above it and up to 6 kpc the contribution remains constant around 95 %. In the case of the ISP they range from 36 % in the nucleus to not contributing at all, above 2.7 kpc. And for the OSP they contribute to 15 % of the light in the nucleus and only 5 - 7 % in the outskirts.

In **NGC 6090** we found that the contribution of YSP is ~ 75 % for both components up to 1.5

kpc. Above it, they contribute 10 % more in NGC 6090 NE than in NGC 6090 SW, 80 % vs 70 % respectively at 3 kpc. The average contribution of ISP is very small, below 10 % for both components, but being a bit more important in the outskirts of the SW galaxy. The OSP contribute to 25 % of the light of both components in the nucleus, and decreases to 15 % (20 %) in the outskirts of NGC 6090 NE (SW).

Analogously, in Figures 5.18 and 5.19 we present maps of the mass contribution in percentage due to young, intermediate and old populations (m_Y , m_I and m_O) and their radial profiles for IC 1623 W (top panels) and NGC 6090 (lower panels). For both systems we found that most of the mass is provided by the old stellar populations.

For **IC 1623 W** this is true everywhere, except for some spaxels in the outer regions, which are completely dominated by young components. From the radial profile we found that the mass contribution of the OSP and YSP evolve inversely. In a non uniform way, the OSP contribution decreases from 80 % in the nucleus to 40 % in the outskirts at 6 kpc. Conversely, the mass in YSP grow from 5 % in the nucleus to 60 % in the outskirts at 6 kpc. In the case of the mass in ISP they range from 15 % in the nucleus to not contribution at all above 2.7 kpc.

The same happens with **NGC 6090**, the OSP dominate the mass everywhere except in the easternmost end of NGC 6090 NE, in some spaxels to the North West of NGC 6090 NE nucleus and to the South of NGC 6090 SW, where the contributions of ISPs are also important, between 50 % - 80 %, and up to 90 % in some spaxels. From the radial profile we found that for both components the OSP have more than 85 % of the mass, and this is true up to 3 kpc from the nuclei of the galaxies. The fraction of stellar mass contributed by stars younger than 140 Myr is less than 7 % everywhere. The contribution of ISPs reaches values up to of 12 % around 1.0 - 1.5 kpc of NGC 6090 NE and 1.5 - 2.2 kpc of NGC 6090 SW.

IC 1623 W. When summing the total mass in each age bin, we found that from the total $M' = 5.5 \times 10^{10} M_\odot$ in IC 1623 W, the mass in young $M'(Y)$, intermediate age $M'(I)$ and old $M'(O)$ stellar populations is $1.8 \times 10^9 M_\odot$ (3 %), $8.2 \times 10^8 M_\odot$ (1 %) and $5.3 \times 10^{10} M_\odot$ (96 %), respectively.

NGC 6090. Analogously, from the total $M' = 9.6 \times 10^{10} M_\odot$ in NGC 6090, the mass contained in young $M'(Y)$, intermediate age $M'(I)$ and old $M'(O)$ stellar populations is $1.0 \times 10^9 M_\odot$ (1 %), $6.6 \times 10^9 M_\odot$ (7 %) and $8.8 \times 10^{10} M_\odot$ (92 %), respectively.

For both systems we found that the mass in young stellar components SSPs < 140 Myr represents less than a 3 % of the total stellar mass. Moreover, we have compared the mass in YSP with the mass in clusters derived in Section 5.3.3. In the case of IC 1623 W, the mass in young components derived through the IFS is comparable (only a factor ~ 1.3 less) to the mass in star clusters derived roughly from the photometry, which is $M_{clus}^{IC1623W} \sim 9 \times 10^8 M_\odot$. This would agree with the idea that the vast majority of stars form in clusters rather than in isolation. However, in NGC 6090, the mass in star clusters, $M_{clus}^{NGC6090} \sim 2 \times 10^9 M_\odot$, is a factor ~ 4 higher than the mass in SSPs < 300 Myr from the spectroscopy. This is within the error expected from the uncertainties in the exact ages of the clusters. From the photometry we found an upper limit for the ages of ≤ 300 Myr, while from the spectroscopy we find that the young components are in fact younger than 30 Myr. The ratio of the mass-to-light ratios for these populations at Z_\odot is approximately $\frac{(M/L)_{300Myr}}{(M/L)_{30Myr}} \sim 3.6$. Therefore, the age uncertainty with the photometry could lead to mass uncertainties of up to a factor ~ 4 .

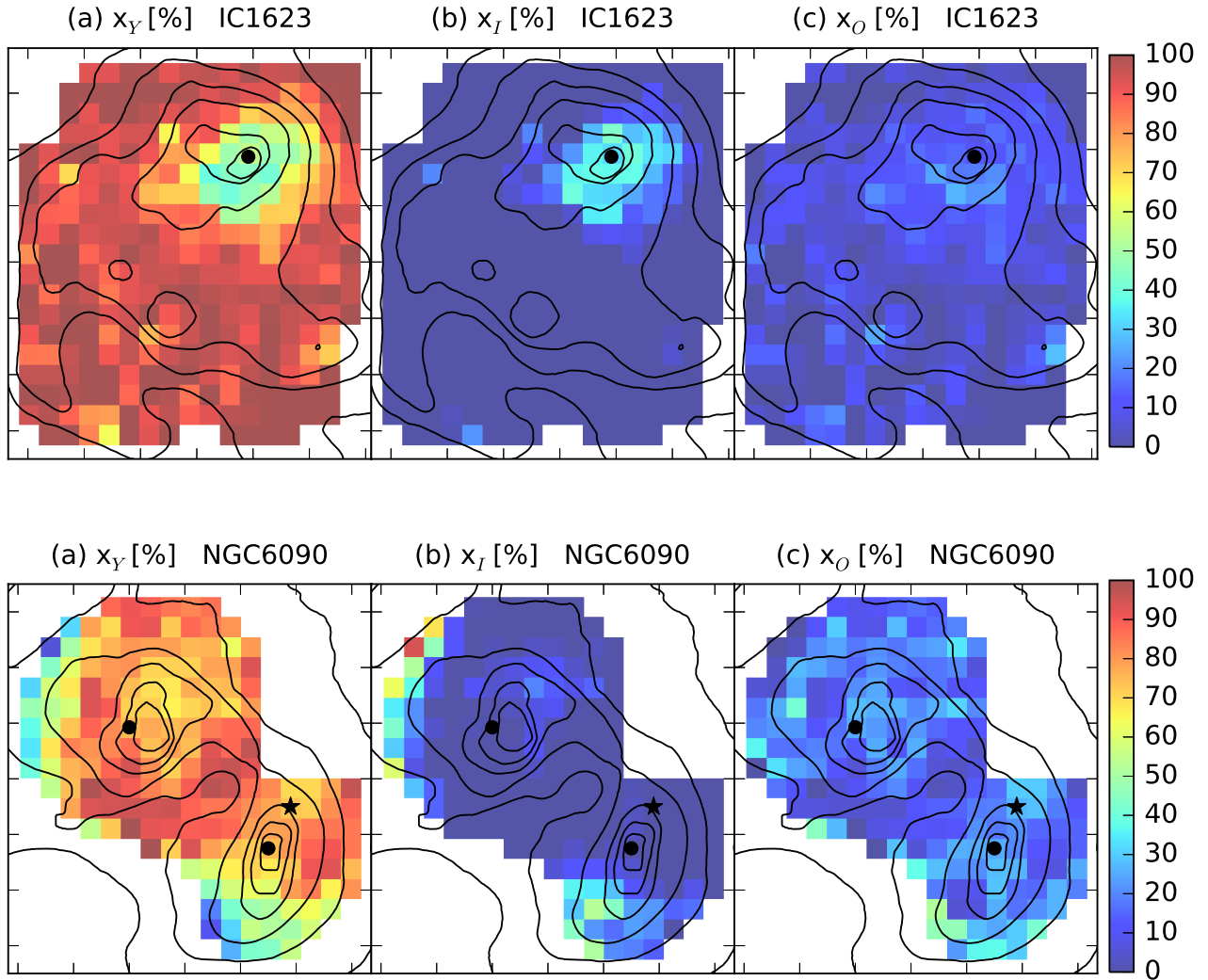


Figure 5.16 From left to right: Maps of contribution in percentage of young (a) $t < 140$ Myr , (b) intermediate ($140 \text{ Myr} < t < 1.4 \text{ Gyr}$) and old (c) $t > 1.4 \text{ Gyr}$ stellar populations to the observed light at 5635 \AA . Top panels: IC 1623 W. Bottom panels: NGC 6090. Contours represent the smoothed HST F435W image. We find that both pre-merger systems are clearly dominated by young stellar populations widespread across the whole observed extension. In IC 1623 W we found contribution of the young stellar populations to light is around 90% everywhere except in the nucleus, where the contribution is around 50%. Only in the nucleus the intermediate age stellar populations have a significant contribution, between 30 - 40%. The contribution of old stellar population is everywhere below 20% in IC 1623 W. In NGC 6090 we found that almost all spaxels have YSP contribution above 70%, except some spaxels located at the easternmost end of NGC 6090 NE and at the south edge of NGC 6090 SW. In these regions the contribution of ISP and OSP are also important.

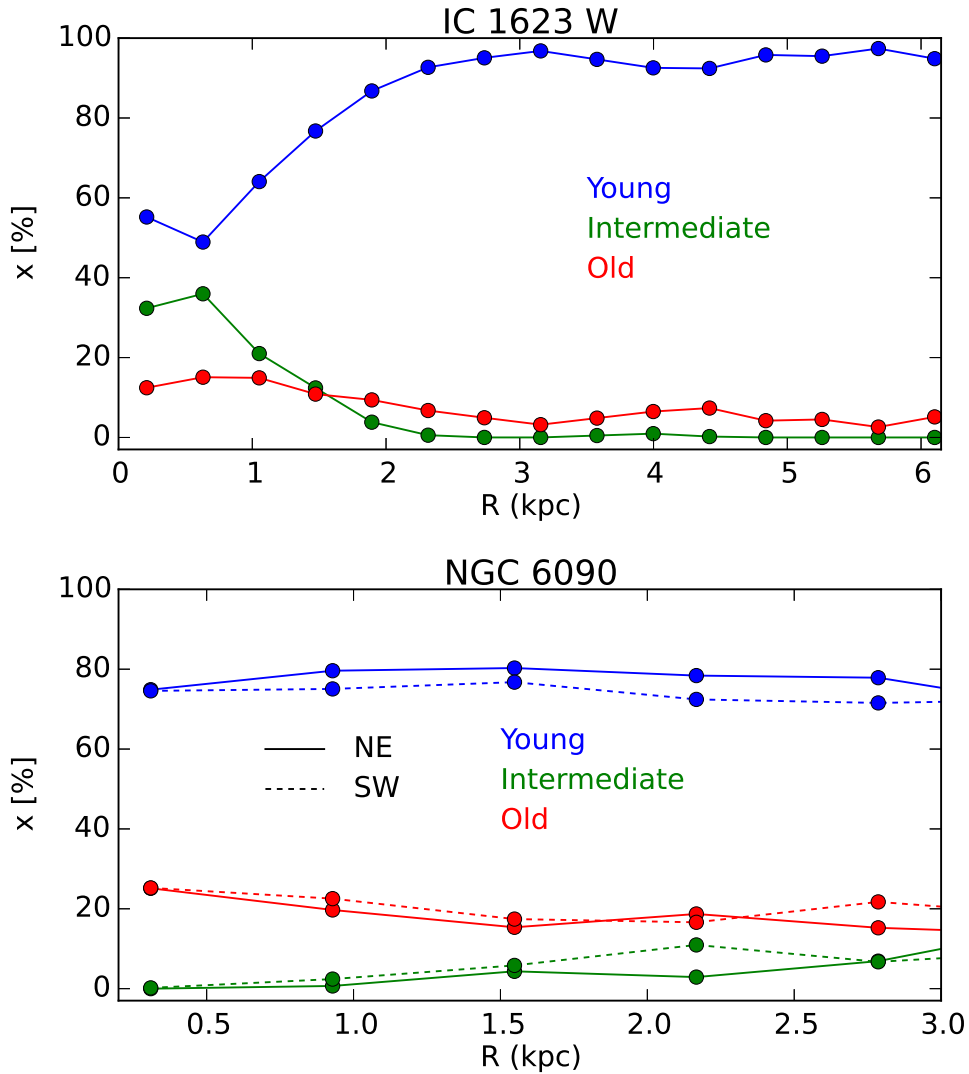


Figure 5.17 Radial profiles of the light contributions from (a) young x_Y (blue), (b) intermediate x_I (green) and (c) old populations x_O (red) with the radial distance in kiloparsec. Top panel: IC 1623 W. Bottom panel: NGC 6090. The NE component profile is shown with solid lines, while the SW component with dashed lines. For IC 1623 W we found that the contribution of the YSP increases from 50% in the nucleus to 95% at 2.7 kpc. Above it and up to 6 kpc the contribution remains constant around 95%. In the case of the ISP they range from 36% in the nucleus to not contributing at all, above 2.7 kpc. And for the OSP they contribute to 15% of the light in the nucleus and only 5 - 7% in the outskirts. In NGC 6090 we found that the contribution of YSP is $\sim 75\%$ for both components up to 1.5 kpc. Above it, they contribute 10% more in NGC 6090 NE than in NGC 6090 SW, 80% vs 70% respectively at 3 kpc. The average contribution of ISP is very small, below 10% for both components, but being a bit more important in the outskirts of the SW galaxy. The OSP contribute to 25% of the light of both components in the nucleus, and decreases to 15% (20%) in the outskirts of NGC 6090 NE (SW).

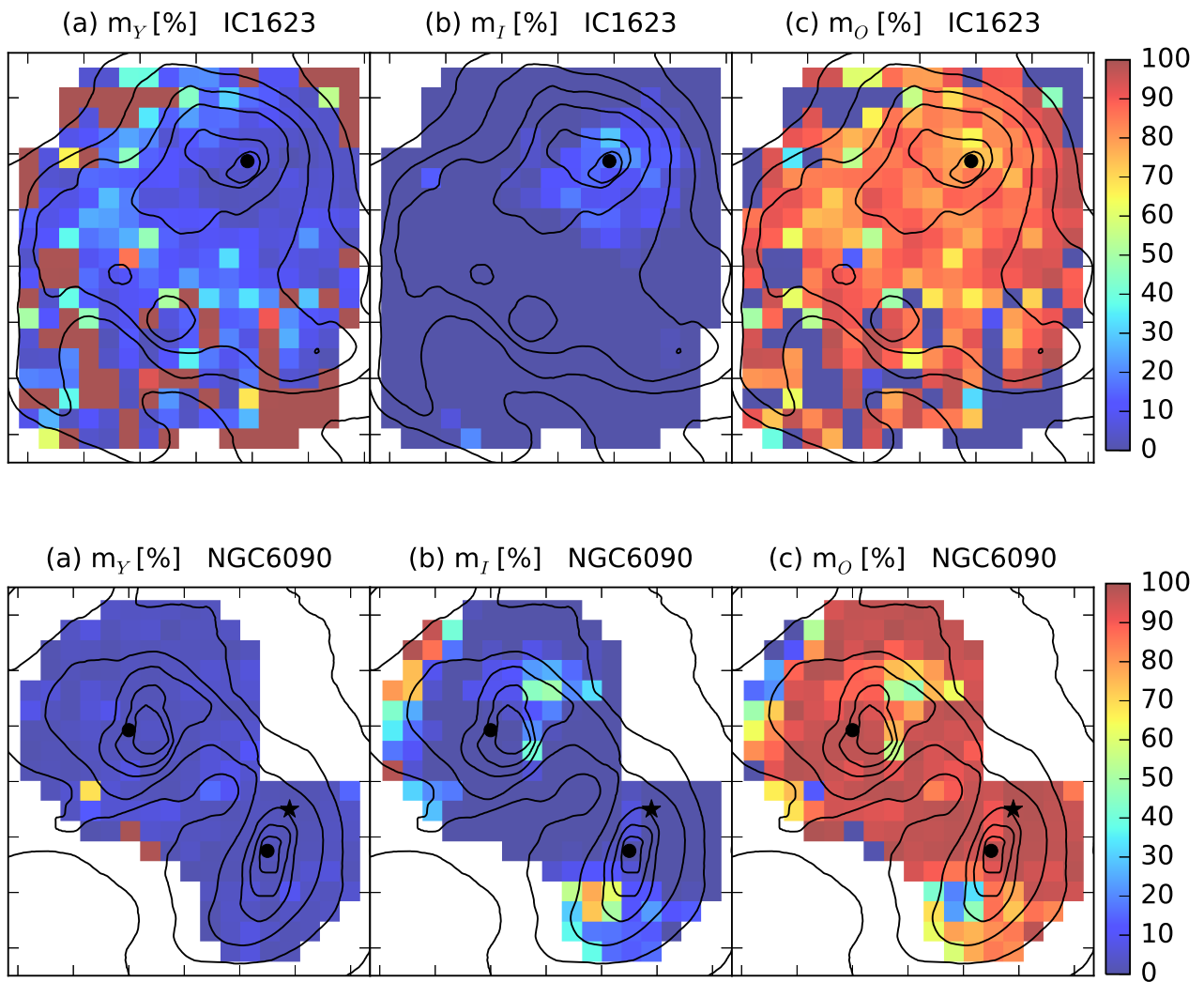


Figure 5.18 From left to right: Maps of the contribution in percentage of young (a) $t < 140$ Myr , (b) intermediate ($140 \text{ Myr} < t < 1.4 \text{ Gyr}$), and old (c) $t > 1.4 \text{ Gyr}$ stellar populations to the total stellar mass. Top panels: IC 1623 W. Bottom panels: NGC 6090. Contours represent the smoothed HST F435W images. For both systems we found that most of the mass is contained is old stellar populations. For IC 1623 W this is true everywhere, except for some spaxels in the outer regions, which are completely dominated by young components. The same happens with NGC 6090, the OSPs dominate the mass everywhere except in the easternmost end of NGC 6090 NE, in some spaxels to the North West of NGC 6090 NE nucleus and to the South of NGC 6090 SW, where the contributions of ISPs are also important, between 50 % - 80 %, and up to 90 % in some spaxels.

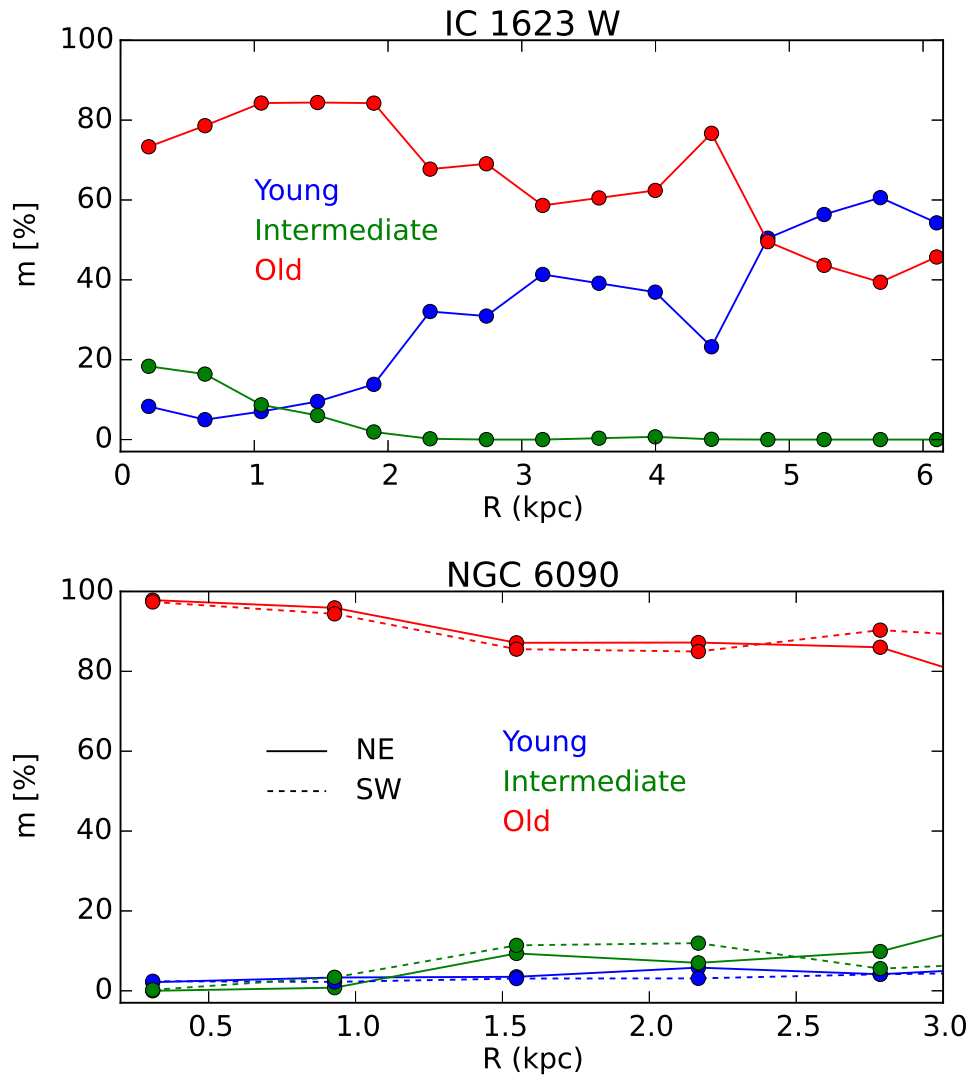


Figure 5.19 Radial profiles of the mass contributions from (a) young x_Y (blue), (b) intermediate x_I (green), and (c) old populations x_O (red) with the radial distance in kiloparsec for IC 1623 W (top panels) and NGC 6090 (bottom panels). For IC 1623 W we found that the mass contribution of the OSP and YSP evolve inversely. In a non uniform way, the OSP contribution decreases from 80% in the nucleus to 40% in the outskirts at 6 kpc. Conversely, the mass in YSPs grow from 5% in the nucleus to 60% in the outskirts at 6 kpc. In the case of the mass in ISP they range from 15% in the nucleus to not contribution at all above 2.7 kpc. In NGC 6090 we found that for both components the OSPs have more than 85% of the mass, and this is true up to 3 kpc from the nuclei of the galaxies. The fraction of stellar mass contributed by stars younger than 140 Myr is less than 7% everywhere. The contribution of ISPs reaches values up to of 12% around 1.0 - 1.5 kpc of NGC 6090 NE and 1.5 - 2.2 kpc of NGC 6090 SW.

5.4.11. NGC 6090 SW radial profiles from knot

As commented in Section 5.2, the exact position of NGC 6090 SW nucleus is not clear. In the radial profiles shown in previous sections, we consider as nucleus the luminosity peak in the cube continuum, marked as a black dot in the maps. However, there exists the possibility that the real nucleus is the bright knot located to the North West of this component, which is indicated with a star symbol in the maps. As a sanity check we have repeated the radial profiles of the stellar population properties taking the knot position as origin. The only property for which the radial profile changes is the metallicity. The trend is the same, metallicity grows with distance from the core, but the gradient is steeper from the knot than from our nucleus. From the knot it goes from -0.6 to -0.15 ($0.25 - 0.7 Z_{\odot}$), while for our nucleus it goes from -0.4 to -0.25 ($0.4 - 0.6 Z_{\odot}$). For the other properties the profiles are very similar and the differences are not significant.

5.4.12. Comparison of results with base CB

As mentioned at the end of Section 5.4.1, we performed two sets of *Starlight* fits using different model bases, the so-called GM and CB. So far, we have presented the results with GM base. Here we will describe the main differences in the derived stellar population properties if we consider the base CB.

In Figure 5.20 we compare the radial profiles of IC 1623 W: (a) stellar dust attenuation, (b) ages, (c) metallicities, and (d) stellar mass surface densities; for GM base of models in color blue and CB base in red. In IC 1623 the differences between them are:

- **Dust extinction** is very similar with both bases, with GM returning slightly higher extinctions than CB. Averaging at all distances, the difference between GM and CB is 0.02 ± 0.02 mag. Therefore, they can be considered equal.
- **Stellar ages** derived by GM are older than CB, by 0.26 ± 0.06 dex.
- **Stellar metallicity** is slightly higher with GM base than with CB by 0.08 ± 0.07 dex. Given the dispersion, they can be considered approximately equal.
- **Stellar mass surface density** is 0.66 ± 0.25 dex higher with GM than with CB base when averaging at all distances. Simply taking into account the difference in the IMFs we expect GM to have 0.26 dex more mass surface density than CB. The difference between bases increases in the outermost regions, above ~ 4.5 kpc. Given the low SNR (~ 5) of the outer spaxels of the datacube, we have found that even small variations in the stellar population properties translate into big relative differences in the mass to light ratios, translating in mass differences of ~ 0.5 dex.

Analogously, in Figure 5.21 we make the same comparison for NGC 6090. Now, to distinguish between the NE and SW components, we have used blue solid line for GM base and NE, red for CB and NE, black for GM and SW, and green for CB and SW. The differences between them in NGC 6090 are:

- **Dust extinction** is very similar with both bases, with GM returning slightly higher extinctions than CB. For NGC 6090 NE, the difference between bases is 0.19 ± 0.03 mag on average. In

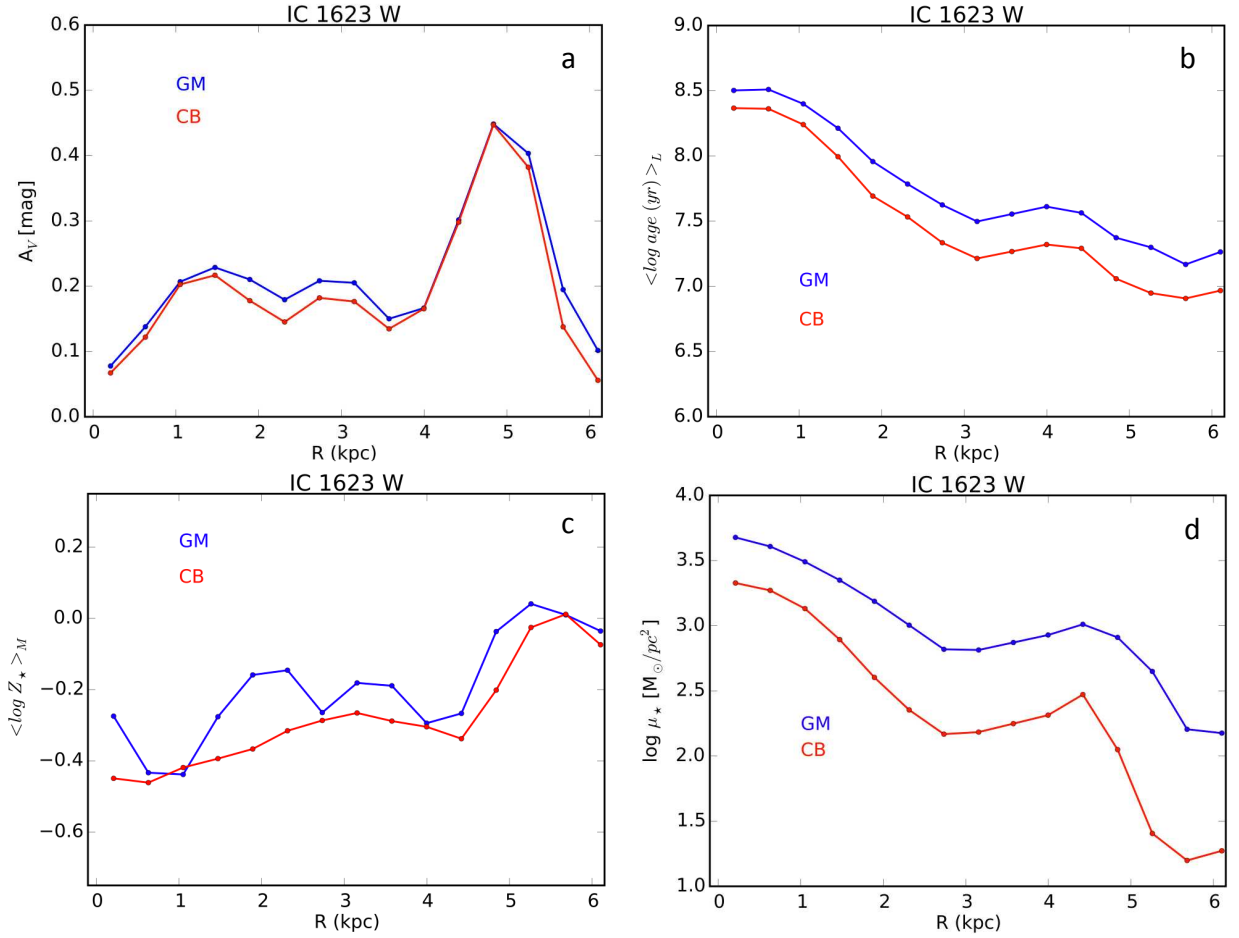


Figure 5.20 Comparison of the radial profiles of the stellar population properties of IC 1623 W for GM base (blue lines) and CB base (red lines). From top left to bottom right we show: (a) stellar dust attenuation, (b) ages, (c) metallicities and (d) stellar mass surface densities.

the case of NGC 6090 SW, the difference between GM and CB is smaller, less than 0.1 mag at all distances. On average, 0.07 ± 0.02 mag.

- **Stellar ages** derived by GM are younger than CB in the case of NGC 6090 NE, by -0.17 ± 0.03 dex. For NGC 6090 SW we can not conclude the same. In its nuclear region GM base derives ages 0.5 dex younger than CB. At 1.5 kpc the radial profile of CB inverts to match or slightly pass the GM radial profile. Averaging at all distances the difference between GM and CB is -0.08 ± 0.18 dex.
- **Stellar metallicity** of NGC 6090 NE is 0.4 dex higher for GM than CB at the middle of the radial profile (~ 1.5 kpc). However, when averaging at all distances we found 0.16 ± 0.13 dex. For NGC 6090 SW, the difference between GM and CB is 0.07 ± 0.05 dex.
- **Stellar mass surface densities** are higher with GM than with CB base for both NGC 6090 components. For NGC 6090 NE we found an average difference of 0.36 ± 0.06 dex, while for NGC 6090 SW, 0.28 ± 0.13 dex. Simply taking into account the difference in the IMFs we

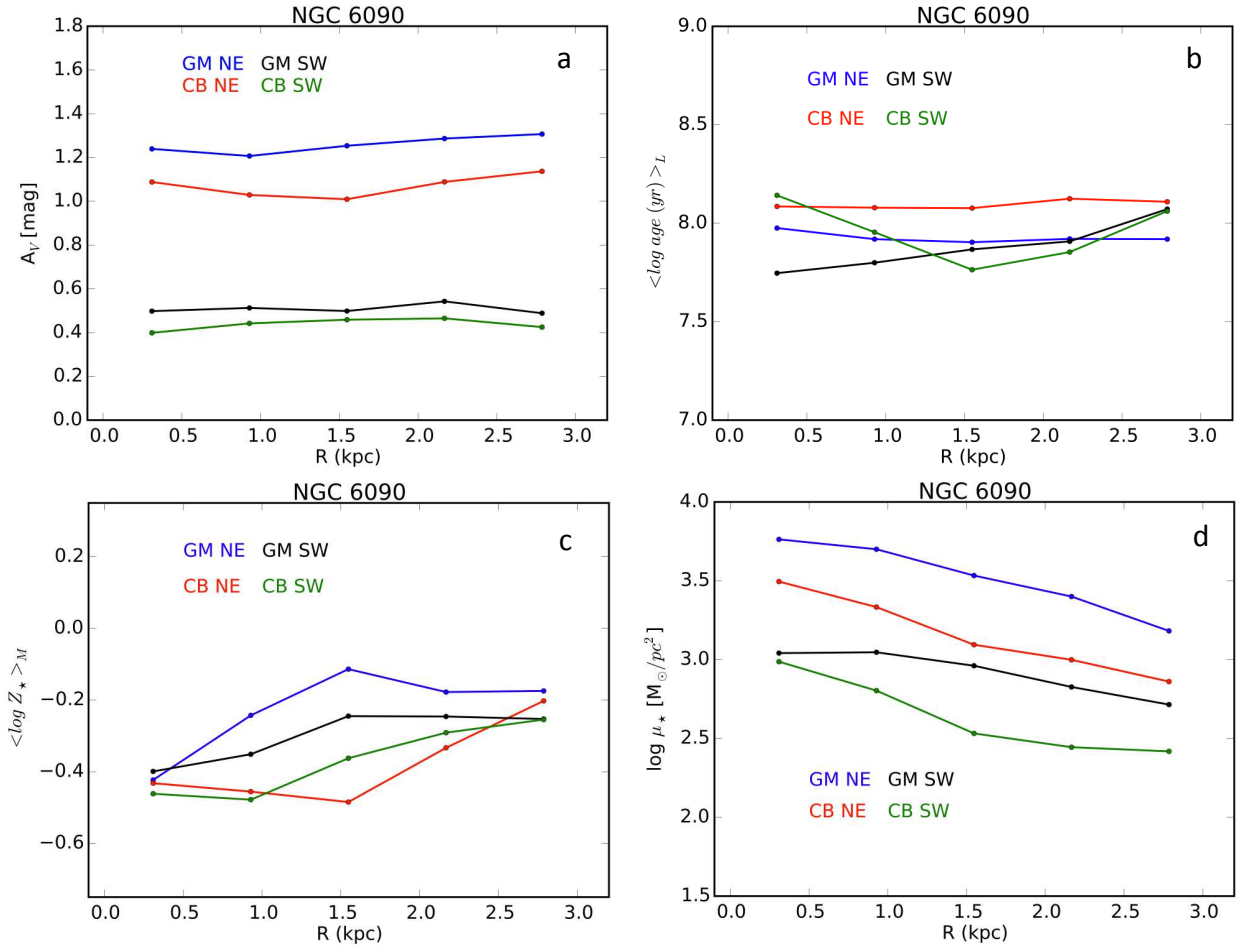


Figure 5.21 Comparison of the radial profiles of the stellar population properties of NGC 6090 for GM base (blue lines for NE component and black lines for SW one) and CB base (red lines for NE and green lines for SW). From top left to bottom right we show: (a) stellar dust attenuation, (b) ages, (c) metallicities and (d) stellar mass surface densities.

expect GM to have 0.26 dex more mass surface density than CB. The remaining differences are small and can be explained by the dissimilarities in the other properties.

5.5. Ionized gas emission

The *Starlight* best fits were subtracted from the observed spectra to obtain 3D cubes with the pure nebular emission line spectra. These emission spectra contain information relative to the ionised gas properties. In this section we present maps of key line ratios sensitive to the ionization mechanism, together with $H\alpha$ luminosity and ionized gas dust attenuation.

5.5.1. Methodology

We have measured the line fluxes of some prominent emission lines: $[\text{OII}]\lambda 3727$, $H\beta$, $[\text{OIII}]\lambda 5007$, $[\text{OI}]\lambda 6300$, $H\alpha$, $[\text{NII}]\lambda 6583$ and $[\text{SII}]\lambda, \lambda 6716, 6731$ when present in the emission line spectra.

First, a local continuum is estimated around each line by using a few pixels located at both sides of the emission. This local continuum is subtracted to account for small mismatches between the *Starlight* best fitted model continuum and the real galaxy continuum. Then, the emission line fluxes in each spaxel are calculated by fitting the lines with Gaussian profiles. Nearby, blended lines (e.g. [NII] and H α) are fitted simultaneously using multiple Gaussian profiles. The Python `scipy.optimize.leastsq` task perform the fits by computing the minimization of the reduced χ^2 . Emission-line intensity maps are thus created for each individual line.

The statistical uncertainty in the measurement of the line fluxes was calculated from the product between the standard deviation of the adjacent continuum, σ_c , and the FWHM of the emission line. However, this statistical uncertainty does not account for systematic uncertainty in the data reduction or stellar continuum fitting. In order to avoid spurious weak line measurements, we imposed two criteria to discriminate between real features and noise: (1) only spaxels with line fluxes with relative error < 0.4 and (2) only spaxels with S/N > 5 are included in the maps, where the noise has been calculated as the standard deviation of a blank region in the outskirts of the map (when possible).

5.5.2. Ionized gas morphology

IC 1623 W. Figure 5.22 shows the observed H α (left panel) and H β (right panel) emission flux for IC 1623 W, that traces the distribution of the ionised gas. They are in units of 10^{-16} erg s $^{-1}$ cm $^{-2}$ and in logarithmic scale to enhance the contrast. As these maps show, ionized gas is extended across the galaxy. The morphology is identical in both, with H α being brighter than H β . The brightest regions are those that correspond to aggregates of SSCs and star forming regions along the distorted spiral arm. To get a better idea of the overall morphology of IC 1623 W, in Figure 5.23 we have superimposed in red contours the LArr H α emission over the HST F435W continuum image. We can see that H α emission is concentrated in the distorted spiral arm and SSCs aggregates (of which we have labeled C1 and C2 in the image). Furthermore, in the nuclear area we detected a cylindrical structure, C3, which seems to leave or enter the nucleus. Due to its morphology, at first we thought it might be a gas inflow / outflow. Yet we see in the HST image that this emission has also a stellar counterpart with several SSCs along it. Moreover, we will see in Sections 5.5.5 and 5.5.6 that in C3 the photoionization is also due to star formation.

NGC 6090. Analogously, in Figure 5.24 we show the observed H α (left panel) and H β (right panel) emission flux for NGC 6090. They are in units of 10^{-16} erg s $^{-1}$ cm $^{-2}$ and in logarithmic scale to enhance the contrast. The ionised gas distribution is extended across both components in a more uniform and less clumpy way than in IC 1623 W. The NE component is more luminous than the SW one. The two black points indicate the position of the nuclei of the two galaxies. In Figure 5.25 we show the HST F435W continuum image of NGC 6090. The red contours represent the LArr H α emission. In the NE component, the H α peak is offset to the West of the nucleus. As expected, it is spatially coincident with the MSC region. For the SW component, H α peaks in the northern half where most of the star forming regions accumulate.

For IC 1623 W the remaining emission line maps are shown in Figure 5.26. From top left to bottom right: [OII] λ 3727, [OIII] λ 5007, [OI] λ 6300, [NII] λ 6583, [SII] λ 6716 + [SII] λ 6731, and [SII] λ 6716/[SII] λ 6731, which is a tracer of the electron density. All panels, except the last one which is a ratio, are in logarithmic scale and in units of 10^{-16} erg s $^{-1}$ cm $^{-2}$. The scale range is different for each map to maximize

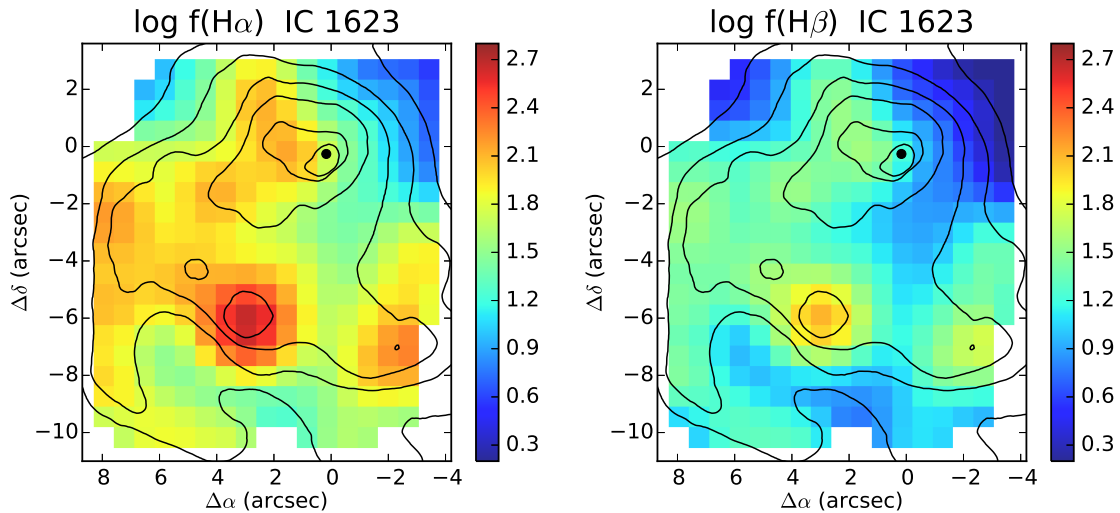


Figure 5.22 $H\alpha$ emission line flux (left panel) and $H\beta$ emission line flux (right panel) for IC 1623 W. They are in units of $10^{-16} \text{ erg s}^{-1} \text{ cm}^{-2}$ and in logarithmic scale to enhance the contrast, ranging from 0.2 to 2.8. The smoothed HST F435W continuum image is superimposed in contours. Ionized gas is extended across the galaxy. The brightest regions correspond to aggregates of SSCs and star forming regions along the distorted spiral arm.

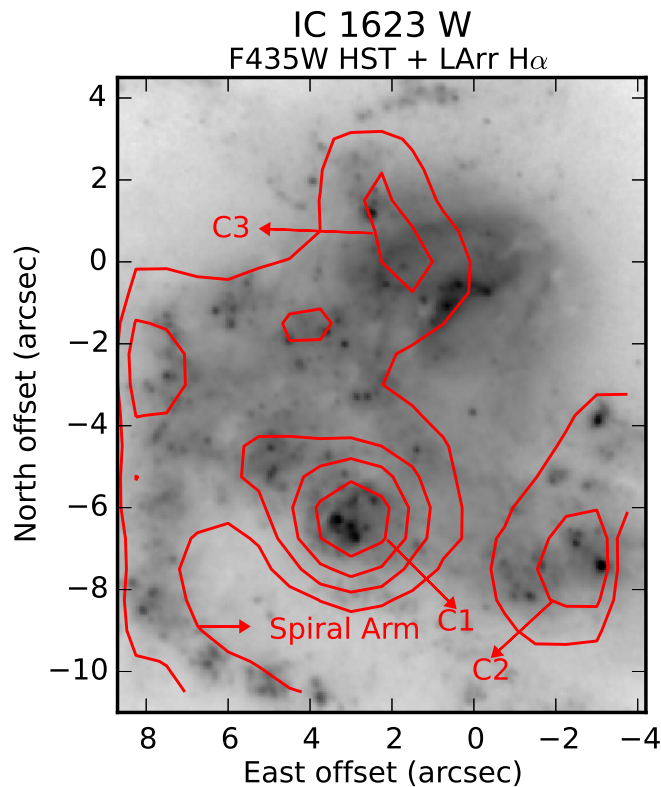


Figure 5.23 IC 1623 W HST F435W continuum image together with LArr $H\alpha$ line emission in red contours. We see that $H\alpha$ emission is concentrated in the distorted spiral arm and SSCs aggregates (we have labeled C1 and C2 in the image). Furthermore, in the nuclear area we detected a cylindrical structure that also coincides to several SSCs. We have labeled it as C3 in this figure.

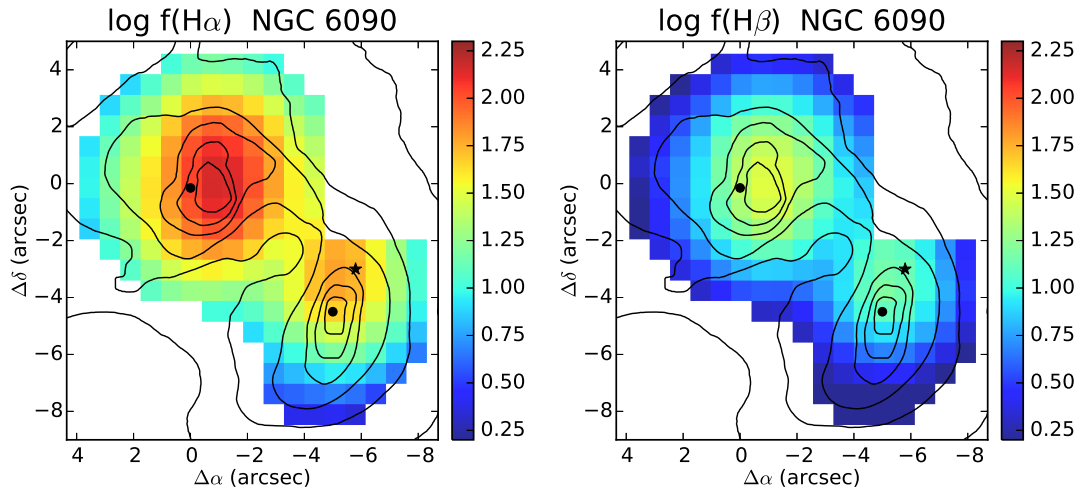


Figure 5.24 NGC 6090 H α emission line flux (left panel) and H β emission line flux (right panel). Both are in units of 10^{-16} erg s $^{-1}$ cm $^{-2}$ and in logarithmic scale ranging from 0.2 to 2.3. The smoothed HST F435W continuum image is superimposed in contours. The ionised gas distribution is extended across both components in a more uniform and less clumpy way than in IC 1623 W. The NE component is more luminous than the SW one. The two black points indicate the position of the nuclei of the two galaxies.

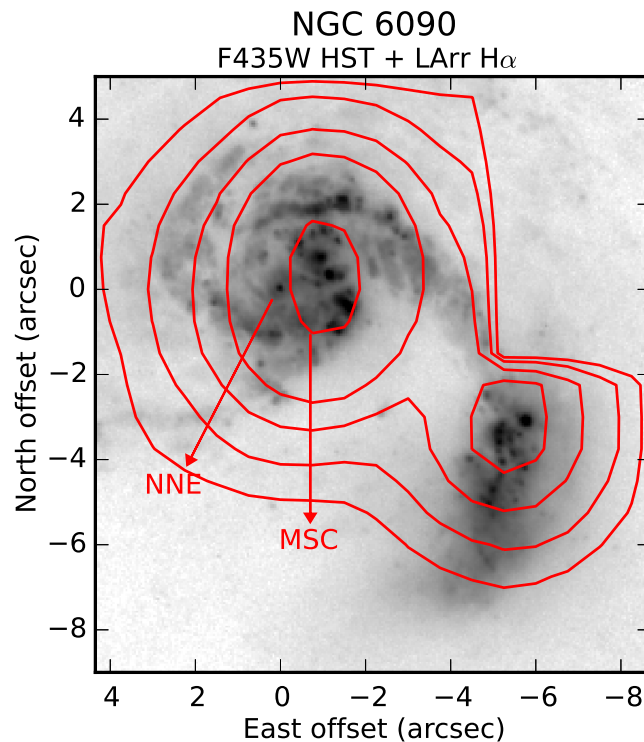


Figure 5.25 NGC 6090 HST F435W continuum image together with LArr H α line emission in red contours. In the NE component, the H α peak is offsetted to the West with respect to the nucleus. As expected, it is spatially coincident with the MSC region. For the SW component, H α peaks in the northern half where most of the star forming regions accumulate.

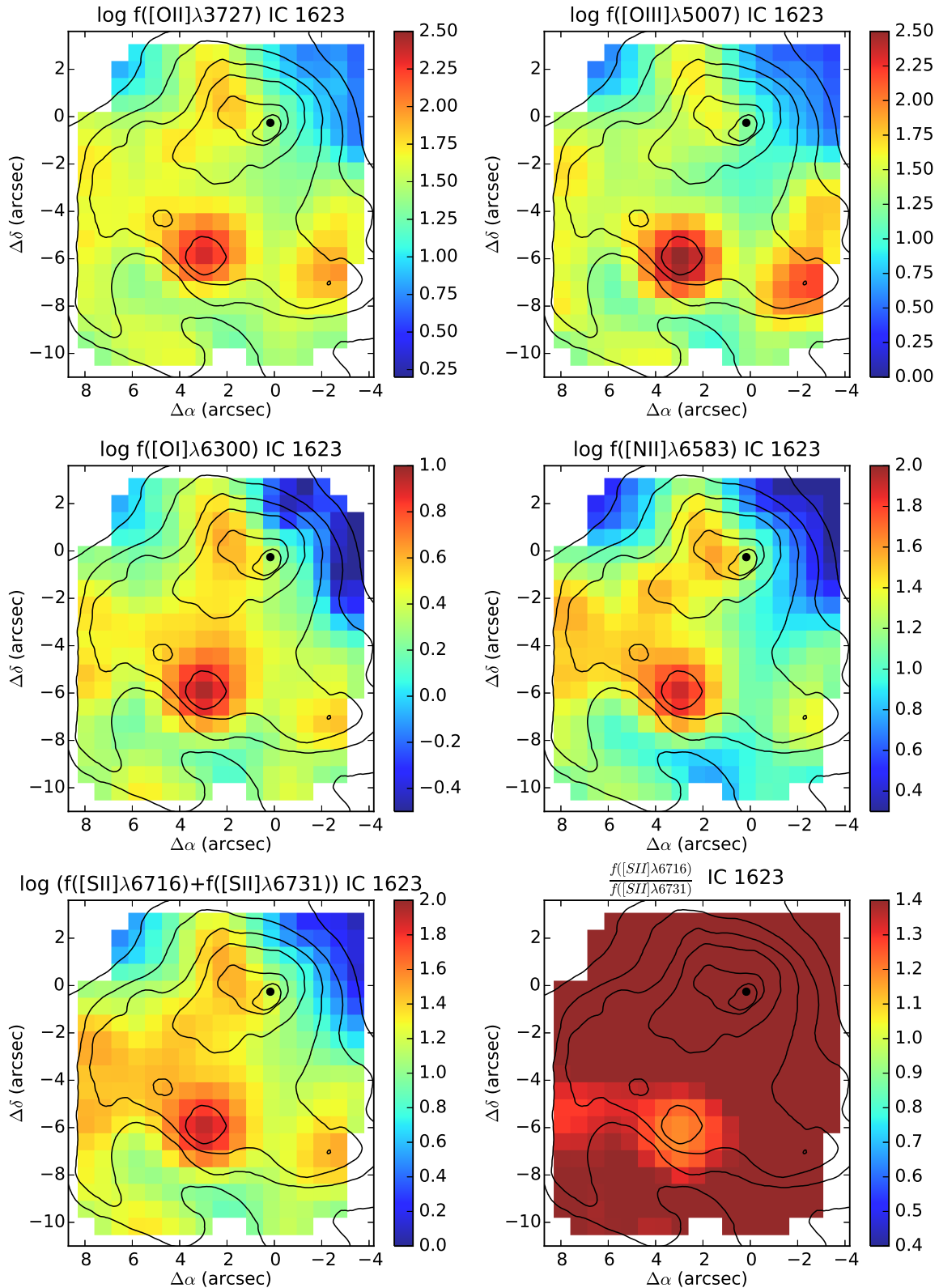


Figure 5.26 Emission line maps of IC 1623 W. From top left corner to bottom right: $[\text{OII}]\lambda 3727$, $[\text{OIII}]\lambda 5007$, $[\text{OI}]\lambda 6300$, $[\text{NII}]\lambda 6583$, $[\text{SII}]\lambda 6716 + [\text{SII}]\lambda 6731$ and $[\text{SII}]\lambda 6716/[\text{SII}]\lambda 6731$, which is a tracer of the electron density of the emitting gas (n_e). All panels, except the last one which is a ratio, are in logarithmic scale and in units of 10^{-16} erg s^{-1} cm^{-2} . The scale range is different for each map to maximize the contrast. In the case of the $[\text{SII}]\lambda 6716/[\text{SII}]\lambda 6731$ panel the range is between 0.4 to 1.4, which are the limits within which the ratio is sensitive to density variations. The smoothed continuum HST F435W image is superimposed in contours. The morphology is the same for $\text{H}\alpha$ and $\text{H}\beta$ and does not change significantly with the ionization degree of the gas. There are only changes in the relative intensity between regions.

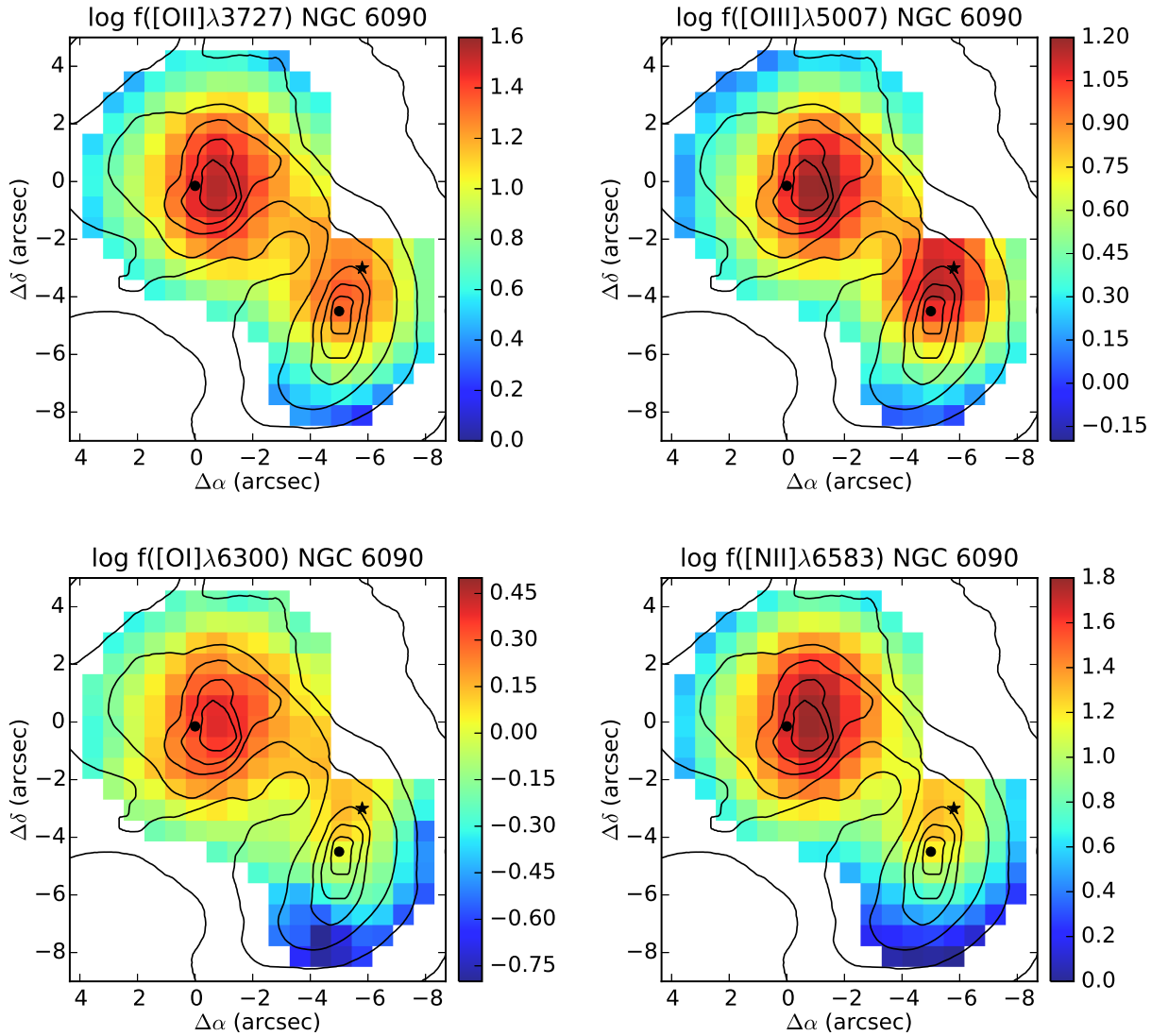


Figure 5.27 Emission line maps of NGC 6090. From top left corner to bottom right: $[\text{OII}]\lambda 3727$, $[\text{OIII}]\lambda 5007$, $[\text{OI}]\lambda 6300$ and $[\text{NII}]\lambda 6583$. In NGC 6090, $[\text{SII}]$ lines are not covered by our spectra due to its higher redshift. All panels are in units of $10^{-16} \text{ erg s}^{-1} \text{ cm}^{-2}$ and in logarithmic scale. The morphology is the same for $\text{H}\alpha$ and $\text{H}\beta$ and does not change significantly with the ionization degree of the gas. There are only changes in the relative intensity between regions; i.e., NGC 6090 SW $[\text{NII}]\lambda 6583$ intensity is much lower than that of NGC 6090 NE in the same map. However, their intensities are more similar to each other in the $[\text{OIII}]\lambda 5007$ map.

the contrast.

The continuum HST F435W image is superimposed in contours, smoothed to match the spatial resolution of LArr data. Analogously, in Figure 5.27 we show the emission line maps for NGC 6090. The order is the same, except the $[\text{SII}]$ lines, which are not covered by our spectra of NGC 6090 due to its higher redshift. For both LIRGs, the morphology of these lines is similar to $\text{H}\alpha$ and $\text{H}\beta$, and does not change significantly with the ionization degree of the gas. There are only changes in the relative

intensity between regions; i.e, in IC 1623 W the [NII] λ 6583 emission of C2 with respect to C1 is much less than in the [OIII] λ 5007 map, where their intensities are more similar. The same happens for NGC 6090 SW, whose intensity is much lower than that of NGC 6090 NE in the [NII] λ 6583 map, but more similar to each other in the [OIII] λ 5007 one. These relative differences are indicative of variations in the ionization conditions and will be treated in Sections 5.5.5 and 5.5.6.

5.5.3. Emission line ratios sensitive to gas density

IC 1623 W. The [SII] λ 6716/[SII] λ 6731 doublet ratio is primarily sensitive to the electron density of the emitting gas (n_e), and it is shown in the bottom-right panel of Figure 5.26. It traces variations in density between 10^5 to 10^2 cm^{-3} (at $T_e = 10^4$ K, Osterbrock & Ferland 2006), that correspond to values of the ratio between 0.4 to 1.4. Outside these limits the ratio is no longer sensitive to density variations. In IC 1623 W, the ratio reaches its minimum around the star forming region C1 with values ~ 1.2 , equivalent to an electron density of ~ 260 cm^{-3} . Everywhere else the ratio is above the low density limit (> 1.4), indicating that densities are below 100 cm^{-3} .

NGC 6090. This estimation is not available for this galaxy as the [SII] lines are not included in the spectrum.

5.5.4. Ionized gas dust attenuation

The observed ratio of $H\alpha$ to $H\beta$ emission lines provides an estimate of the ionized gas dust attenuation, A_V , along the line of sight through a galaxy. The effect of reddening on the ratio $F(H\alpha)/F(H\beta)$ can be written as:

$$c(H\beta) = \frac{\log \frac{F(H\alpha)}{F(H\beta)} - \log \frac{I(H\alpha)}{I(H\beta)}}{f(H\alpha)} \quad (5.9)$$

where $c(H\beta)$ is the logarithmic extinction coefficient, $I(H\alpha)$ and $I(H\beta)$ are the dereddened fluxes, $F(H\alpha)$ and $F(H\beta)$ are the observed fluxes, and $f(H\alpha)$ is the reddening function for a given extinction curve at 6563\AA . We assume an intrinsic ratio of $I(H\alpha)/I(H\beta)=2.86$, valid for case B recombination with $T = 10000$ K and electron density 10^2 cm^{-3} (Osterbrock & Ferland, 2006).

In turn, $c(H\beta)$ relates to the extinction at different wavelengths from the expression:

$$A_\lambda = 2,5 c(H\beta) (1 + f_\lambda) \quad (5.10)$$

We have used the Calzetti et al. (2000) reddening function, as it has been proven to work better for starburst galaxies. At V band the function takes a value of $f_V = - 0.12$.

Finally, the dereddened fluxes can be obtained from:

$$I_\lambda = F_\lambda 10^{c(H\beta)[1+f(\lambda)]} \quad (5.11)$$

In Figure 5.28 we show the line attenuation at 5500\AA (left panels) and the dereddened $H\alpha$ emission line (right panels) for IC 1623 W (top) and NGC 6090 (bottom).

In **IC 1623 W** the mean extinction is ~ 0.8 mag. As we already found from the stellar extinction map (upper left panel of Figure 5.10), the regions most affected by extinction are located behind areas where a lot of HII regions accumulate. For example, behind C1 cluster at (3 East, -6 South) the

extinction reaches its maximum value of around 2.5 mag at (3 East, -8 South). The same happens behind C2, with values up to 1.6 mag. Also, values between 1.3 - 1.6 mag are found in the distorted spiral arm, and between 1.0 - 1.3 mag to the South-East of the nucleus and along the cylindrical structure C3. Everywhere else, the extinction is below 1 mag. Given the generally low values of extinction, the main morphology of the dereddened $H\alpha$ map (top right panel) is very similar to the $H\alpha$ reddened emission (see left panel of Figure 5.22).

In **NGC 6090**, the average extinction of the NE component is 1.8 mag, however, it ranges between 1.5 mag in the nucleus of the galaxy, to values around 2 mag in the North, and up to 2.5 mag in a few spaxels in the South. For the SW component we found an average value around 0.8 mag, but it also varies across the galaxy from 0.5 mag in the South to 1 mag in the North. We found an average difference of ~ 1 mag between components, as also happens with the stellar extinction (see upper right panel of Figure 5.10). In the overlapping / bridge region the extinction have values $\sim 1.3 - 1.4$ mag. Although the extinction in NGC 6090 NE is quite high, the morphology of the dereddened $H\alpha$ map (bottom right panel) is also very similar to the $H\alpha$ reddened emission (see left panel of Figure 5.24).

There is a good spatial correlation between the extended $H\alpha$ emission and the regions where the YSP are contributing to $\geq 70\%$ to the total light (see left panels of Figure 5.16 for comparison).

Moreover, we have compared the ratio between ionized gas extinction to stellar extinction, considering as reliable spaxels those with extinctions above 0.15 mag. For IC 1623 we found $\langle \frac{A_{V,gas}}{A_{V,stars}} \rangle = 2.1 \pm 1.1$, while for NGC 6090 $\langle \frac{A_{V,gas}}{A_{V,stars}} \rangle = 1.6 \pm 0.6$. Analysing UV and optical spectra of 39 starburst galaxies, [Calzetti et al. \(1994\)](#) found $\langle \frac{A_{V,gas}}{A_{V,stars}} \rangle = 2.0 \pm 0.4$, which is compatible with the results from our pre-merger LIRGs. This discrepancy could be a consequence of the fact that the hot ionizing stars (the ones contributing to the emission lines) are associated with dustier regions than the cold stellar populations which contribute most of the optical continuum.

5.5.5. Emission line ratios sensitive to ionisation conditions

Standard line ratios sensitive to the shape of the ionising spectrum have been calculated. First, we focus on those ratios where lines are close enough in wavelength space to not be strongly affected by dust attenuation. In Figure 5.29 we show the $[NII]\lambda 6583/H\alpha$ (left panels), $[OI]\lambda 6300/H\alpha$ (right panels) line ratio maps for IC 1623 W (top) and NGC 6090 (bottom). The scale is the same for both and goes from 0 to 0.5 for $[NII]\lambda 6583/H\alpha$ and from 0 to 0.15 for $[OI]\lambda 6300/H\alpha$.

- **$[NII]\lambda 6583/H\alpha$ map of IC 1623 W:** the lowest value of this ratio (~ 0.15) is located in the clusters regions C1 and C2, followed by the spiral arm and region C3 with 0.20 - 0.25. The region with the highest value of the ratio (0.35 - 0.40) forms a strip originating above C1 and ending at the top right corner of the map.
- **$[NII]\lambda 6583/H\alpha$ map of NGC 6090:** we found average values of this ratio of ~ 0.45 and ~ 0.35 for the NE and SW components, respectively. No significant variations are observed across the faces of the galaxies.

According to [Kauffmann et al. \(2003\)](#) regions with $[NII]\lambda 6583/H\alpha \leq 0.56$ are compatible with being high-metallicity star forming regions, which is the case **everywhere** in our two pre-merger LIRGs.

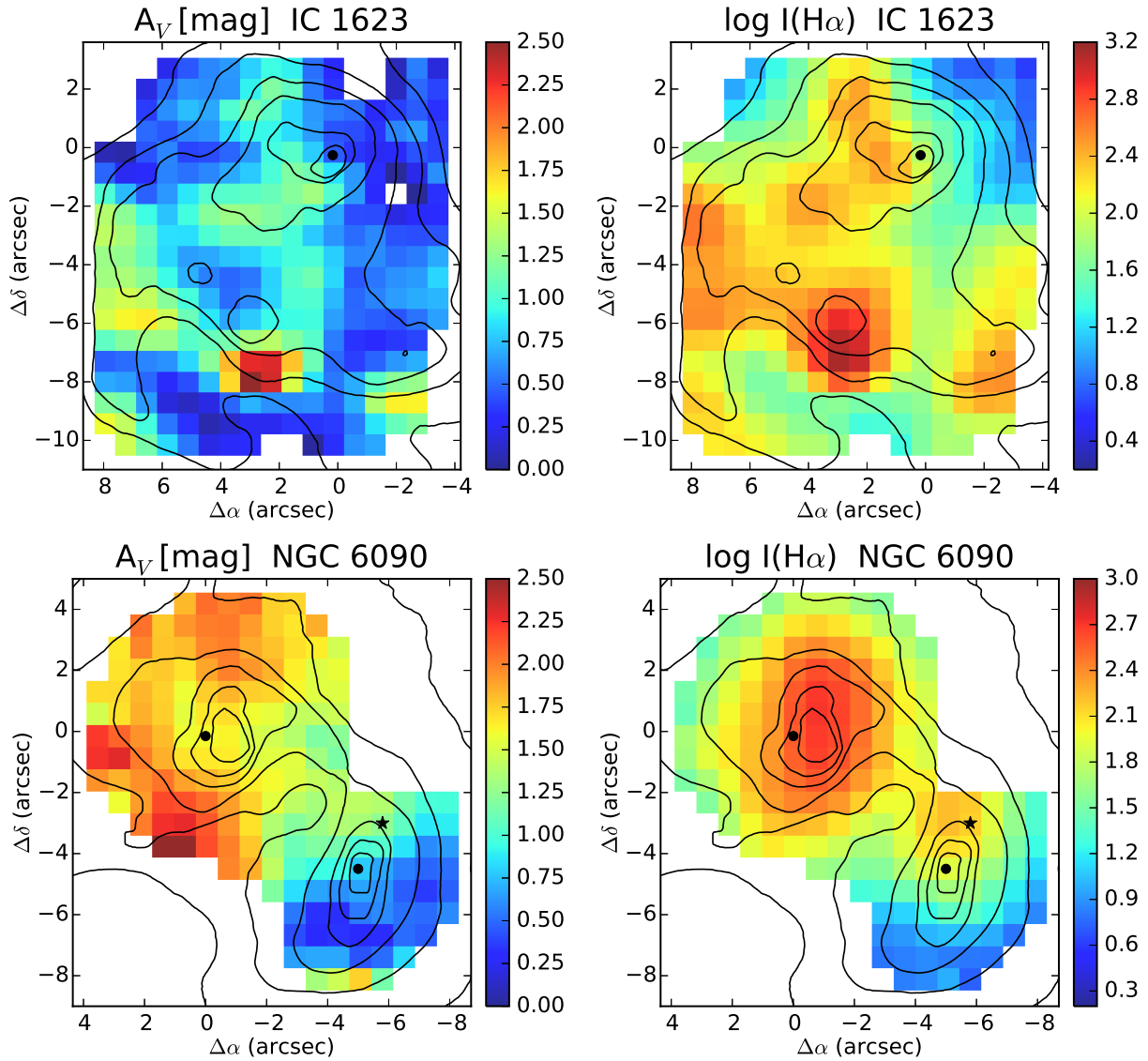


Figure 5.28 Line attenuation at 5500 \AA (left panels), calculated from the $\text{H}\alpha/\text{H}\beta$ emission line ratio assuming a Calzetti like dust attenuation curve and dereddened $\text{H}\alpha$ emission line (right panels) for IC 1623 W (top) and NGC 6090 (bottom). In IC 1623 W the regions most affected by extinction are located behind areas where a lot of HII regions accumulate. For example, behind C1 cluster located approximately at (3 East, -6 South) the extinction reaches its maximum value of around 2.5 mag at (3 East, -8 South). The same happens behind C2, with values up to 1.6 mag. Also, values between 1.3 - 1.6 mag are found in the distorted spiral arm, and between 1.0 - 1.3 mag to the South-East of the nucleus and along the cylindrical structure C3. For NGC 6090 we found an average difference of ~ 1 mag between components. For the NE component the average extinction is 1.75 mag, however it ranges between 1.5 mag in the nucleus of the galaxy, to values around 2 mag in the North and higher values up to 2.5 mag in a few spaxels in the South. For the SW component we found an average value around 0.8 mag, but it also varies across the galaxy from 0.5 mag in the South to 1 mag in the North. In the overlapping / bridge region the extinction have values $\sim 1.3 - 1.4$ mag. From the dereddened $\text{H}\alpha$ maps (right panels), we found that the main morphology does not change significantly. There is a good spatial correlation between the extended $\text{H}\alpha$ emission and the regions where the young stellar populations are contributing to $\geq 70\%$ to the total light.

- **[OI] λ 6300/ $H\alpha$ map of IC 1623 W:** the nucleus, spiral arm, C1 and C2 have ratios below 0.03. Values between 0.06 - 0.08 are found in the outskirts and in the strip that extends approximately from above C1 to the top right corner of the map, which also presented enhancement in [NII]/ $H\alpha$. Only two spaxels in the top corners of the map present values around 0.11, which is the highest value of the ratio in IC 1623 W.
- **[OI] λ 6300/ $H\alpha$ map of NGC 6090:** this ratio ranges from < 0.03 in the nuclear regions of both NE and SW components, to ~ 0.07 in the outer regions traced by our data. There is also a single spaxel in the South of the SW component with a value of ~ 0.11 .

According to Heckman et al. (1990) the [OI] λ 6300/ $H\alpha$ ratio for pure HII regions is below 0.03. In addition, the range of this ratio for starburst-related LINERs is 0.08 - 0.16. This is an important subclass of LINERs in which the main source of ionization is associated with the diffuse radiation field of metal-rich dusty starbursts (Heckman et al., 1996).

Therefore, in our pre-merger LIRGs we found (except for 3 spaxels) ratios below the LINER definition. We expect them to be dominated by stellar photoionization or at best for something composite between star formation and LINER emission.

In the particular case of IC 1623 W, the fact that the two LINER spaxels are located at the edge of the map, is in agreement with Rich et al. (2011) results. They performed IFS of IC 1623 W covering a FoV significantly larger than us and with better spectral resolution, which allows them to fit several components in some regions. They found that the core of IC 1623 W is dominated by starbursts, while in the outskirts the emission is dominated by shocks (= LINER). We note that in the region in common with them (the core of IC 1623 W) our results are in total agreement with them, in the sense that the line ratios are starburst dominated. In the region traced by us, and with the spectral resolution of V300 grating, the line profiles do not show more than one velocity component.

Finally, in Figure 5.30 we show [OIII] λ 5007/ $H\beta$ line ratio maps for IC 1623 W (left) and NGC 6090 (right). The scale is the same for both and goes from 0 to 3.

- In IC 1623 W this ratio is below 2.0 everywhere except in the cluster regions C1 and C2, where values up to 3 can be found.
- In NGC 6090 the ratio is below 1 for the NE component and ~ 1.2 for the SW component, with some spaxels in its South reaching values around 2.

Both [OIII] λ 5007/ $H\beta$ ratio maps are everywhere below 3. Ratios above 3.2 would be expected for Seyfert emission (Heckman et al., 1987; Veilleux et al., 1995), which can be discarded in our two pre-merger LIRGs, even in the nuclei.

5.5.6. Diagnostic diagrams

In the left panels of Figure 5.31 we show the [NII] λ 6583/ $H\alpha$ vs [OIII] λ 5007/ $H\beta$ diagnostic diagrams for IC 1623 W (top panels) and NGC 6090 (bottom panels). Line ratios from individual spaxels are plotted as filled circles. Overplotted as black lines are empirically and theoretically derived separations between LINERs/Seyferts and HII regions. Dotted line is from Kauffmann et al. (2003), a conservative demarcation line to separate pure star formation ionization from other ionization mechanisms; solid

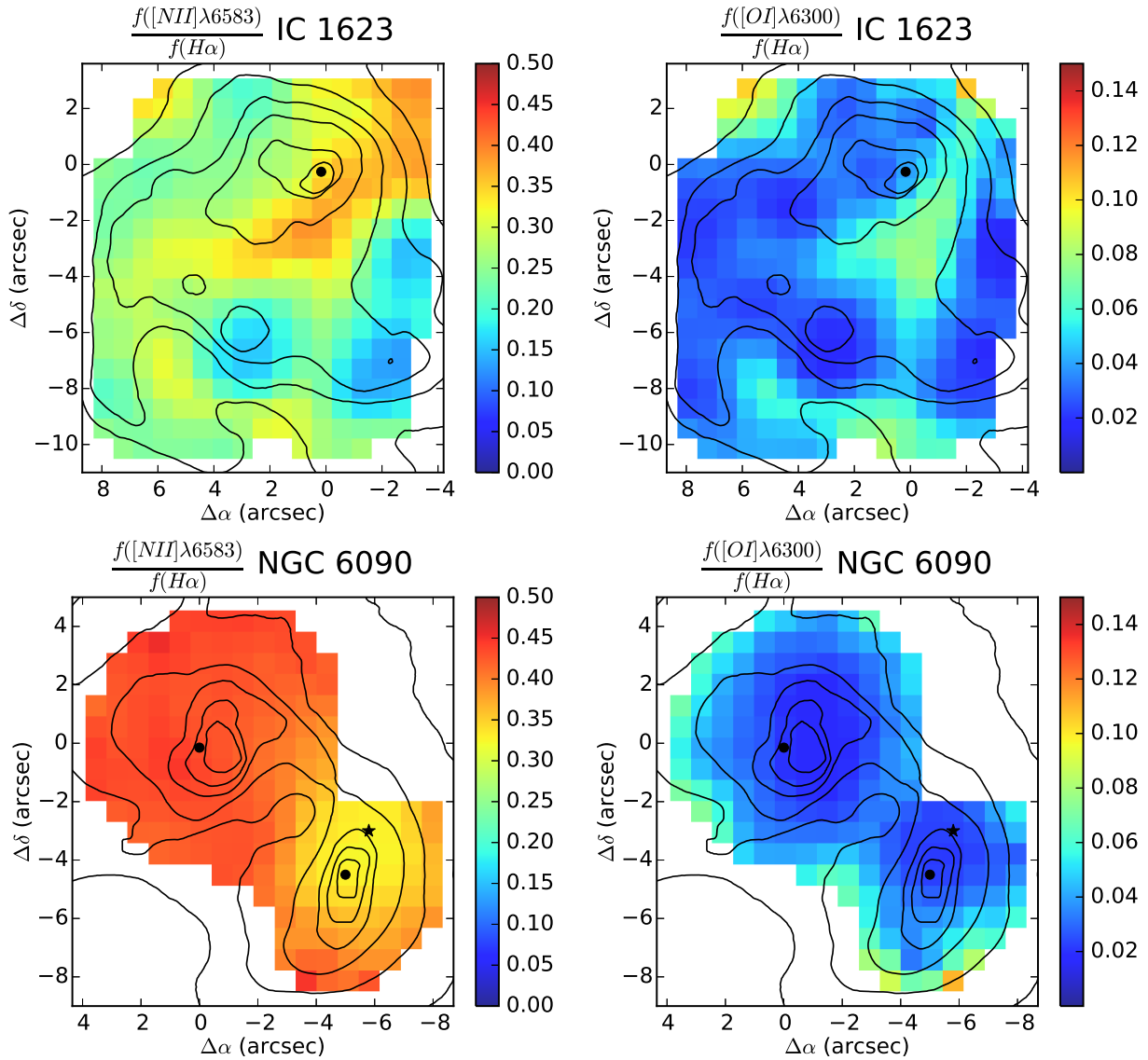


Figure 5.29 [NII] λ 6583/ $H\alpha$ (left panels) and [OI] λ 6300/ $H\alpha$ (right panels) emission line ratio maps for IC 1623 W (top panels) and NGC 6090 (bottom panels). The scales go from 0 to 0.5 for the nitrogen ratios and from 0 to 0.15 for the oxygen ratios. Every spaxel in our two pre-merger LIRGs shows [NII] λ 6583/ $H\alpha$ \leq 0.56, compatible with star formation ionization according to [Kauffmann et al. \(2003\)](#). Also, [OI] λ 6300/ $H\alpha$ = 0.03 for pure HII regions ([Heckman et al., 1990](#)), and between 0.08-0.16 for starburst-related LINERs. In our two pre-merger LIRGs we found (except for 3 spaxels) ratios below the LINER definition. We expect them to be dominated by stellar photoionization or at best for something composite between star formation and LINER emission.

line is [Kewley et al. \(2001\)](#), which represents regions of composite ionization mechanisms, normally starbursts and shocks. Finally, the dashed-dotted line is [Cid Fernandes et al. \(2010\)](#), that separates Seyferts from LINERs. Spaxels consistent with pure star formation ionization are plotted in colour blue and the composite in colour green. In the right panels, we show where the different ionization mechanisms are located within each system.

We found that for both galaxies the dominating ionization mechanism is star formation, at least

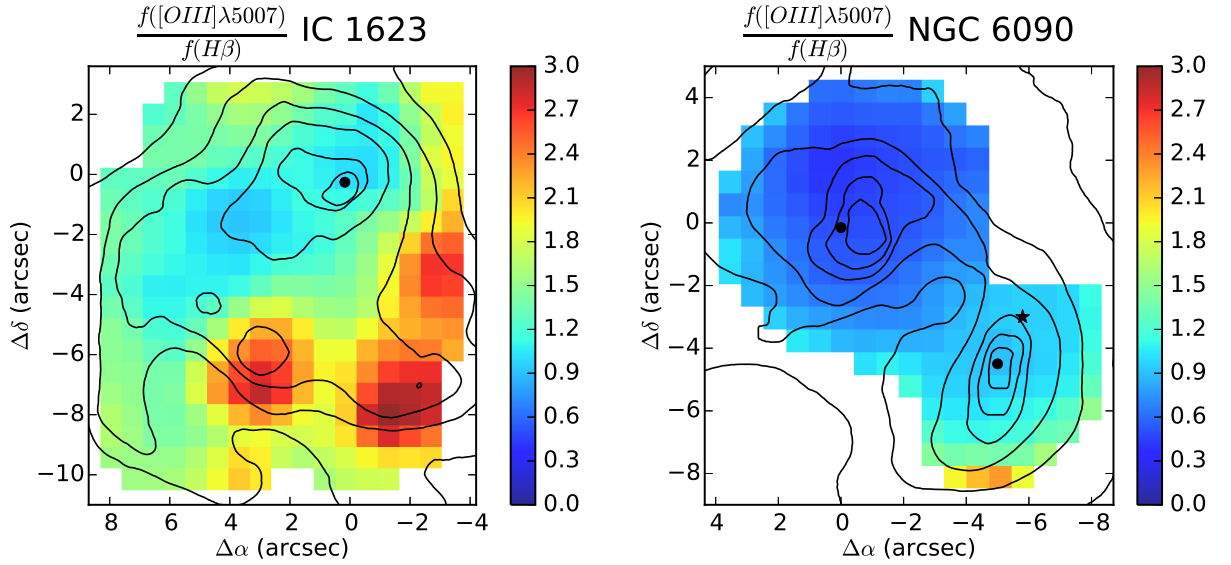


Figure 5.30 $[\text{OIII}]\lambda 5007/\text{H}\beta$ line ratio maps for IC 1623 W (left panel) and NGC 6090 (right panel). The scale is the same for both and goes from 0 to 3. In IC 1623 W the found values of this ratio are below 2.0 everywhere, except in the cluster regions C1 and C2 where values up to 3 can be found. In NGC 6090 the $[\text{OIII}]\lambda 5007/\text{H}\beta$ ratio is below 1 for the NE component and ~ 1.2 for the SW component, with some spaxels in its South reaching values around 2. Both $[\text{OIII}]\lambda 5007/\text{H}\beta$ ratio maps are everywhere below 3. Ratios above 3.2 would be expected for Seyfert emission (Heckman et al., 1987; Veilleux et al., 1995), which can be discarded in our two pre-merger LIRGs.

in the region mapped by us. However, there are some spaxels in the "composite" emission region, between Kauffmann et al. (2003) and Kewley et al. (2001) demarcation lines. In IC 1623 W they are located in the strip extending from above C1 to the upper right corner of the map, and four spaxels at the southern end of this component. In NGC 6090 they are located in the outskirts of the map, above $2'' - 3''$ from the nuclei.

Given the proximity of the vast majority of the "composite" spaxels to the Kauffmann demarcation line, we do not think that the ionization source is different for them, and is therefore quite possible that they are also star forming regions. In addition, recently Sánchez et al. (2015) found that some of the HII regions ($\sim 14\%$) detected in the CALIFA sample are also over the Kauffmann demarcation line.

However, for a few spaxels we can not discard a truly composite photoionization. The nature of the composite emission have been proposed to be a combination of hot stars plus either ionization by a power-law radiation field associated with an AGN or shock excitation where the shock may result from such processes as cooling flows or superwind activity (Kewley et al., 2001). Given the position of the composite emission in our pre-merger LIRGs, we can rule out the AGN as a possible origin. We think it can also be due to ISM shocks that would occur naturally as a result of the increase of the supersonic turbulence in mergers (Bournaud et al., 2010).

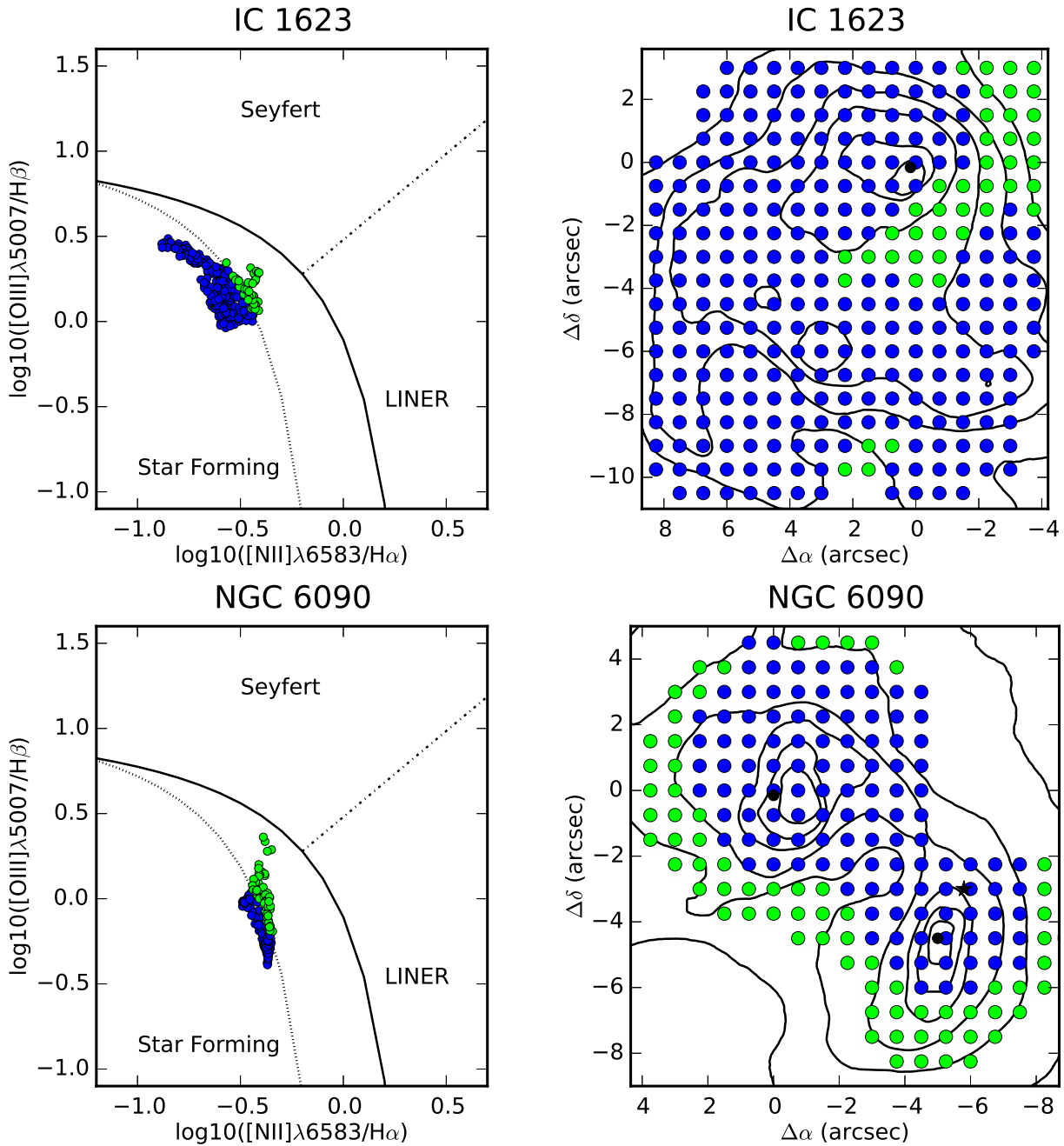


Figure 5.31 $[\text{NII}]\lambda 6583/\text{H}\alpha$ vs $[\text{OIII}]\lambda 5007/\text{H}\beta$ line ratio diagnostic diagrams (left panels) and distribution of the ionization (right panels) for IC 1623 W (top panels) and NGC 6090 (bottom panels). In the left panels, overplotted as black lines are empirically and theoretically derived separations between LINERs/Seyferts and HII regions. Dotted line is [Kauffmann et al. \(2003\)](#), solid line is [Kewley et al. \(2001\)](#), and the dashed-dotted line is [Cid Fernandes et al. \(2010\)](#), that separates Seyferts from LINERs. Spaxels consistent with pure star formation ionization are plotted in colour blue and the composite ones in colour green. We found that for both galaxies the dominating ionization mechanism is star formation, at least in the region mapped by us. In IC 1623 W the only "composite" spaxels are the ones located in the strip extending from above C1 to the upper right corner of the map, and four spaxels at the southern end of this component. In NGC 6090 they are located in the outskirts of the map, above $2'' - 3''$ from the nuclei. Given the proximity of the vast majority of the "composite" spaxels to the Kauffmann demarcation line, we do not think that the ionization source is different for them, and is therefore quite possible that they are also star forming regions. However, we can not totally discard some contribution from ISM shocks which would naturally occur as a result of the increase of the supersonic turbulence in merger.

5.6. Kinematics

We have determined both the stellar and gas kinematics of NGC 6090 and IC 1623 W, when possible. *Starlight* fits the stellar kinematics using the absorption lines. It determines the position of the lines $v_{0,*}$, and their width $v_{d,*}$, which are the shift and broadening applied to the base models to match the observed spectra. *Starlight* usually does a very good job in measuring the stellar kinematics, but sometimes (e.g., HII galaxies) a spectrum has few absorption lines where to anchor $v_{0,*}$ and $v_{d,*}$ estimates, which may then go wild, since all there is to fit in this case is the continuum shape. This is the case with our galaxies, except in the nucleus of IC 1623 W which is dominated by absorption lines, in the remaining spaxels of IC 1623 W and in NGC 6090, $v_{d,*}$ is too broad and non realistic. Therefore, we will not rely on the stellar kinematics and pay attention only to the gas kinematics.

The ionized gas kinematics is much more reliable for these systems, as it is derived from the prominent emission lines, in this case from H α . For each emission line we fit a single Gaussian profile. When several lines are blended, as for H α and the [NII] $\lambda\lambda 6548, 6583$ we fit simultaneously three Gaussians, constraining the position of the nitrogen lines with respect to H α . The position in wavelength of the center of the Gaussian (λ) can be converted to velocity using:

$$v_{0,H\alpha} = \frac{\lambda - \lambda_0}{\lambda_0} c \quad (5.12)$$

where λ_0 is the rest-frame wavelength of the line, ~ 6562.8 for H α , and c is the speed of light. Analogously, the velocity dispersion can be calculated as:

$$\sigma_{H\alpha} = \frac{\sigma_{pix}}{\lambda_0} c \quad (5.13)$$

where σ_{pix} is the width in \AA of the fitted Gaussian.

To obtain the final velocity dispersion, we have subtracted the instrumental resolution (σ_{inst}) in quadrature:

$$\sigma_{H\alpha} = \sqrt{\sigma_{H\alpha}^2 - \sigma_{inst}^2} \quad (5.14)$$

where σ_{inst} at H α is $\sim 140 \text{ km s}^{-1}$.

5.6.1. Velocity field of IC 1623 W

In left panel of Figure 5.32 we show the ionized gas velocity field map for IC 1623 W. A distorted rotation pattern is seen, with the NW side receding from us and the SE approaching us. We performed a simple estimate of the kinematical properties of this system. First, we found that the kinematic minor axis which symmetrizes the velocity field, is formed by spaxels whose velocities range from 70 - 100 km/s. In the Figure we have indicated with black dots the spaxels whose velocities in the original map were $v_{0,H\alpha} = 100 \pm 10 \text{ km/s}$. This is the velocity we have subtracted to our velocity field to have a symmetric rotation between the approaching and receding sides. This also indicates that our redshift correction considering NED value was insufficient. Moreover, the black solid line crossing the black dots is our finally chosen kinematic minor axis. It has a position angle of $PA = 69^\circ$. In the Figure we also show the kinematic minor axis we would have obtained if we had chosen as velocity reference $70 \pm 10 \text{ km/s}$ instead of $100 \pm 10 \text{ km/s}$. It is indicated with a black dashed line and it has a $PA = 70^\circ$,

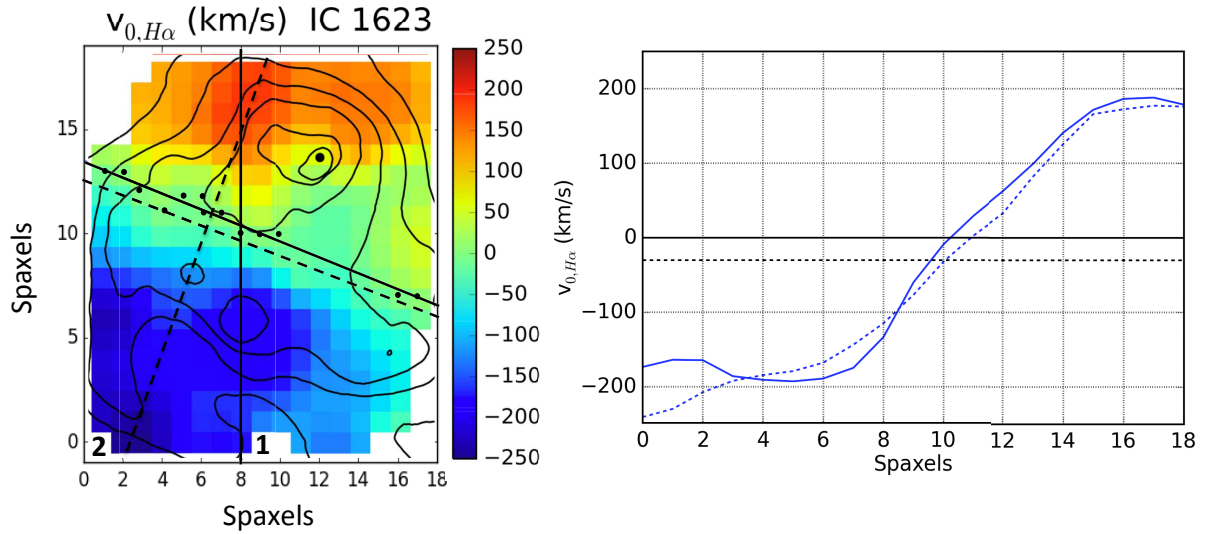


Figure 5.32 Left: Ionized gas velocity field of IC 1623 W. A distorted rotation pattern is seen, with the NW side receding from us and the SE approaching us. The kinematic minor axis which symmetrizes the velocity field is formed by spaxels whose velocities range from 70 - 100 km/s. We have indicated with black dots the spaxels whose velocities in the original map were $v_{0,H\alpha} = 100 \pm 10$ km/s. The black solid line crossing the black dots is our finally chosen kinematic minor axis, with a PA = 69° . We also show the kinematic minor axis we obtain if we choose as velocity reference 70 ± 10 km/s instead of 100 ± 10 km/s. It is indicated with a black dashed line and it has a PA = 70° . Right: velocity curves along the two kinematic major axes, labeled as 1 (solid line) and 2 (dashed line) in the left panel.

almost parallel to our chosen kinematics minor axis.

With respect to the kinematic major axis, we have tried to find the direction along which the velocity range of the rotation curve is maximized. There are two possibilities, labeled as 1 (solid line) and 2 (dashed line) in the Figure. In the right panel of Figure 5.32 we show the rotation curves along both possible kinematic major axes, with solid blue line for 1 and dashed blue line for 2. As explained before, we have corrected our velocity field for a reference velocity of 100 km/s. According to this, the major axis 1 is more symmetric, oscillating from -190 to 190 km/s. However, we note that it is not exactly perpendicular to the kinematic minor axis. This is common in mergers where the rotation is disturbed. On the other hand, the velocity range traced is larger using the kinematic major axis 2. In this case, the velocities oscillate between -240 to 180 km/s. This curve would be symmetrical if we had considered a velocity offset of ~ 70 km/s (whose kinematics minor axis is also shown in the velocity map with dashed line). Moreover, in this case kinematic major and minor axes are perpendicular.

Given the intersection between both pairs of kinematics axes 1 and 2, we found two possible kinematic centers in this galaxy, (8,10) and (6,10), respectively. It is important to note that these kinematic centers do not coincide with the photometric one.

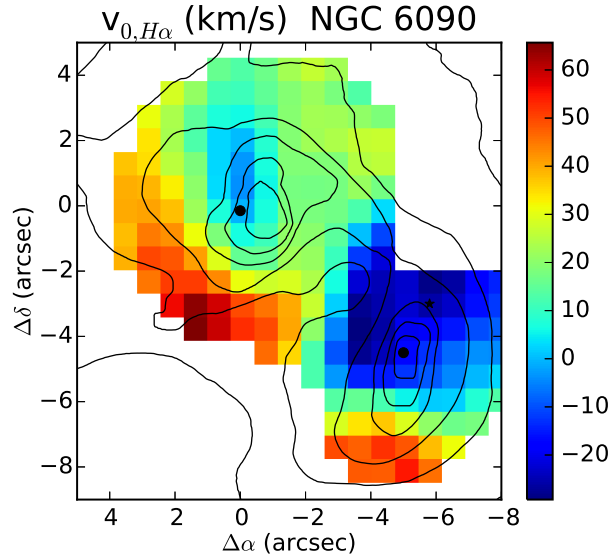


Figure 5.33 Ionized gas velocity field of NGC 6090. The NE component is a face on spiral, so we do not expect to find significant rotation, as we are only seeing the movements of gas perpendicular to the disk. The velocity range is small and oscillates between -5 to 65 km/s. The only region of NGC 6090 NE approaching us is the nucleus. With our spectral resolution we can not confirm if it could be an outflow. To the South, there is gas receding from us at ~ 65 km/s, probably due to the interaction. On the other hand, NGC 6090 SW seems to retain traces of the rotation, but very distorted. Its velocity field ranges from -35 km/s to the North to $+50$ km/s to the South of this component.

5.6.2. Velocity field of NGC 6090

The ionized gas velocity field map of NGC 6090 is shown in Figure 5.33. The NE component is a face on spiral, so we do not expect to find significant rotation, as we are only seeing the movements of gas perpendicular to the disk. The velocity range is small and oscillates between -5 to 65 km/s. The only region of NGC 6090 NE approaching us is the nucleus. We hypothesize that there could be an outflow, however, we can not resolve it with our spectral resolution. To the South, there is gas receding from us at ~ 65 km/s, probably due to the interaction. On the other hand, NGC 6090 SW seems to retain traces of the rotation, but very distorted. Its velocity field ranges from -35 km/s to the North to $+50$ km/s to the South of this component. The morphology of NGC 6090 reminds us of the Antennae. Hydrodynamical simulations of the Antennae suggest that $500 - 600$ Myr have passed since the first pericenter passage. If a similar time has passed for NGC 6090, then ~ 500 Myr would be enough to significantly distort the original rotation.

5.6.3. Velocity dispersion

Figure 5.34 shows the ionized gas velocity dispersion maps for IC 1623 W (left) and NGC 6090 (right).

In **IC 1623 W** the velocity dispersion is low in the star forming regions and in the distorted spiral arms, with $\sigma_{H\alpha} < 120$ km/s. However, $\sigma_{H\alpha} > 120$ km/s in several outermost spaxels, with a region to the NW of the nucleus where $\sigma_{H\alpha}$ reaches up to 170 km/s. We interpret this result as a consequence

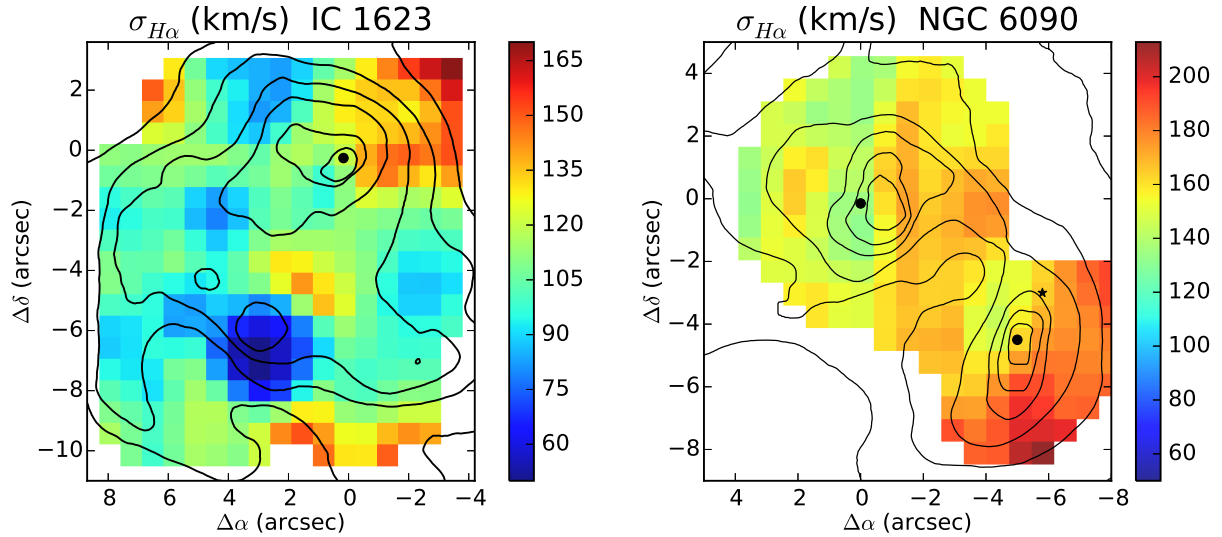


Figure 5.34 Ionized gas velocity dispersion map for IC 1623 W (left panel) and NGC 6090 (right panel). In IC 1623 W, the velocity dispersion is low in the star forming regions and in the distorted spiral arms, with $\sigma_{H\alpha} < 120$ km/s. However, $\sigma_{H\alpha} > 120$ km/s in several outermost spaxels, with a region to the North West of the nucleus where $\sigma_{H\alpha}$ reaches up to 170 km/s. We interpret this result as a consequence of shocks being more important there, producing a broadening of the emission lines. In NGC 6090 there exist a gradual increase in the velocity dispersion from $\sim 140 - 150$ km/s to the East side of NE component, to 170 km/s in the bridge between components, and up to 190 km/s to the South West of the SW component. The increase of the velocity dispersion in the bridge between components could be due to the shocks produced by the interaction itself. In the case of the higher values to the South of the SW component there also exist the possibility that we are simultaneously observing several gas components moving at different velocities as a consequence of the interaction.

of shocks being more important there, producing a broadening of the emission lines. This is again in agreement with Rich et al. (2011), who found widespread shocks in the outskirts of IC 1623, beyond the region traced by us.

In **NGC 6090** there exists a gradual increase in the velocity dispersion from $\sim 140 - 150$ km/s to the East side of NE component, to 170 km/s in the bridge between components, and up to 190 km/s to the SW of the SW component. The increase of the velocity dispersion in the bridge between components could be due to the shocks produced by the interaction itself. In the case of the higher values to the South of the SW component there exists also the possibility that we are simultaneously observing several gas components moving at different velocities as a consequence of the interaction.

5.7. Star formation rates

In this section we have derived the Star Formation Rates (SFRs) of IC 1623 W and NGC 6090 using multiwavelength data from UV, optical IFS, and MIR.

First, from our IFS there are two ways to estimate the SFRs. On the one hand, for the spaxels of the galaxies where the gas is photoionised by light from stars, we can measure the SFR from the dust attenuation corrected $H\alpha$ line luminosity. We use the conversion to star formation rate provided by

Lacerda et al. (private communication), calculated for the average metallicity of our galaxies $\sim 0.7 Z_{\odot}$ and for [Bruzual & Charlot \(2003\)](#) models with both Salpeter

$$SFR(M_{\odot}yr^{-1}) = 7,4 \times 10^{-42} L(H\alpha)_{corr} \text{ (erg s}^{-1}\text{)} \quad (5.15)$$

and Chabrier IMF:

$$SFR(M_{\odot}yr^{-1}) = 4,4 \times 10^{-42} L(H\alpha)_{corr} \text{ (erg s}^{-1}\text{)} \quad (5.16)$$

The first calibration is remarkably similar to the standard calibration of [Kennicutt \(1998\)a](#), calculated for solar metallicity models with Salpeter IMF (0.1 - 100 M_{\odot}). While the second one is more similar to the [Calzetti \(2013\)](#) calibration also for solar metallicity and Kroupa IMF. We note that variations over the constant in this relation are present and mainly due to differences in the stellar IMF assumption and in general, to the stellar population models used to derive it.

We have computed the results from both the spatially resolved information (summing over all spaxels in the datacubes) and also using the integrated spectra. Also, we compare between the two model bases, that is, GM which uses Salpeter IMF and CB which uses Chabrier's. The $H\alpha$ dust-attenuation corrected luminosity is shown in Table 5.1. The corresponding SFRs are reported in Table 5.2.

On the other hand, we can also use the stellar continuum. Its decomposition provides an independent estimate of star formation rate, uncontaminated by non-stellar photoionisation sources. However, the errors on the spectral decomposition are more difficult to quantify. The SFR can be obtained by summing all the stellar mass formed since a lookback time t_{SF} and performing a mass-over-time average:

$$\overline{SFR}(t_{SF}) = \frac{1}{t_{SF}} \sum_{t < t_{SF}} M'_t \quad (5.17)$$

where M'_t is the total mass of stars formed at lookback time t . This gives the mean SFR since $t=t_{SF}$. One can tune t_{SF} to reach different depths in the past, but as t_{SF} increases this estimator becomes increasingly useless, converging to the mass density divided by $t_{\infty}=14$ Gyr (the largest age in the base). For comparison purposes we estimate it for $t_{SF}=30$ Myr, which is approximately the lifetime of the ionizing populations also emitting in $H\alpha$, that is O and early B stars, and also for $t_{SF}=140$ Myr which is more comparable to the FUV emission, tracing stellar populations dominated by up to A0 stars.

Additionally, we have used GALEX FUV and NUV imaging to determine the SFR. First, we have measured the observed fluxes and converted them into magnitudes to calculate the extinction in the FUV, using equation (2) in [Catalán-Torrecilla et al. \(2015\)](#):

$$A_{FUV} = 0,556 + 2,292 \times (FUV - NUV) \quad (5.18)$$

The SFR has been calculated from the dust attenuation corrected FUV luminosity, using the calibration provided by López-Fernandez et al. (private communication), derived by using CB base of models. For $Z \sim 0.7 Z_{\odot}$ this calibration is:

$$SFR(M_{\odot}yr^{-1}) = 3,8 \times 10^{-44} L(FUV)_{corr} \text{ (erg s}^{-1}\text{)} \quad (5.19)$$

For solar metallicity this equation is compatible with the one derived by [Calzetti \(2013\)](#) with Kroupa IMF.

Finally, we have used a hybrid calibration including the Spitzer MIPS 24 μm flux to check if there is star formation completely obscured from view in the optical, which is not accounted for by the Balmer decrement attenuation correction. The calibration for a Salpeter IMF is:

$$SFR(M_{\odot}\text{yr}^{-1}) = 7,4 \times 10^{-42} [L(H\alpha)_{obs} + 0,020 L(24)] \text{ (erg s}^{-1}\text{)} \quad (5.20)$$

For a Chabrier IMF:

$$SFR(M_{\odot}\text{yr}^{-1}) = 4,4 \times 10^{-42} [L(H\alpha)_{obs} + 0,020 L(24)] \text{ (erg s}^{-1}\text{)} \quad (5.21)$$

where $L(H\alpha)_{obs}$ is the observed $H\alpha$ luminosity and $L(24) = \lambda L_{\lambda}$ at $24\mu\text{m}$. Again, all the luminosities and resulting SFRs are reported in Tables 5.1 and 5.2, respectively.

First, we note that in both IC 1623 W and NGC 6090 there are no significant differences between the spatially resolved SFRs and the SFRs derived from the integrated spectra.

In both IC 1623 W and NGC 6090

$$SFR(30\text{Myr}) \sim SFR(H\alpha)$$

$$SFR(140\text{Myr}) \sim SFR(FUV)$$

this makes sense precisely because $H\alpha$ ionizing stars usually have ≤ 30 Myr. This includes O and early B stars, for later spectral types the number of ionizing photons emitted declines drastically. However, the UV is emitted by up to A0 stars with lifetimes ~ 100 Myr.

In the case of IC 1623 W for Salpeter IMF, SFR ($H\alpha$) is a factor 1.6 higher than SFR (30 Myr), but they are remarkably similar for Chabrier IMF. Most of the SFR in IC 1623 W is happening in the distorted disk and probably a Chabrier IMF is more appropriated in this case. In NGC 6090, the SFR results agree for both IMFs.

The average SFR from the very young stellar populations and $H\alpha$ is $14 \pm 1 M_{\odot} \text{ yr}^{-1}$ for IC 1623 W and $20 \pm 3 M_{\odot} \text{ yr}^{-1}$ for NGC 6090 (with Chabrier IMF). For the populations below 140 Myr and FUV, the SFR = $5 \pm 1 M_{\odot} \text{ yr}^{-1}$ for both systems (also, with Chabrier IMF), a factor of 3 - 4 smaller than the one for the very young components (< 30 Myr) and $H\alpha$. This difference indicates that recent SFR is more concentrated in instantaneous bursts occurred in the last 10 Myr rather than as a continuum SFR (see Figure 5.14).

Also, with the continuum, the SFRs derived with Salpeter IMF are a factor 1.5 ± 0.3 larger than the Chabrier ones. For $H\alpha$ we found something similar, 1.69 ± 0.03 .

When including the MIR, we found hybrid SFR = $15 M_{\odot} \text{ yr}^{-1}$ and $17 M_{\odot} \text{ yr}^{-1}$ for IC 1623 W and NGC 6090, respectively. They are very similar to the ones derived from dust-attenuation corrected $H\alpha$ and SFR(30 Myr). We can conclude that for IC 1623 W and NGC 6090 there is no substantial star formation which is not accounted for by the Balmer decrement attenuation correction.

Finally, we note that in the Milky Way, $\langle SFR \rangle = 1.9 \pm 0.4 M_{\odot} \text{ yr}^{-1}$ ([Chomiuk & Povich, 2011](#)). This calculation is based on the Kroupa IMF. However, they note that the Chabrier IMF yields total stellar masses that are practically identical to the Kroupa IMF, implying that the SFR

Table 5.1. Multiwavelength luminosities of IC 1623 W and NGC 6090.

Luminosities (erg s ⁻¹)	IC 1623 W spatially resolved	IC 1623 W integrated	NGC 6090 spatially resolved	NGC 6090 integrated
L(H α) _{obs}	1.69×10^{42}	1.69×10^{42}	1.31×10^{42}	1.31×10^{42}
L(H α) _{corr}	3.47×10^{42}	3.40×10^{42}	4.95×10^{42}	4.96×10^{42}
L(FUV) _{obs}	5.93×10^{43}		2.66×10^{43}	
L(FUV) _{corr}	1.45×10^{44}		1.47×10^{44}	
L(24)	8.35×10^{43}		1.23×10^{44}	

Note. — All the luminosities are in units of erg s⁻¹.

Table 5.2. Multiwavelength Star Formation Rates for IC 1623 W and NGC 6090.

SFR (M _⊙ yr ⁻¹)	IC 1623 W spatially resolved	IC 1623 W integrated	NGC 6090 spatially resolved	NGC 6090 integrated
Base GM Salpeter $\star < 30$ Myr	18	15	30	36
Base BC03 Salpeter H α _{corr}	26	25	37	37
Base CB Chabrier $\star < 30$ Myr	14	12	16	21
Base BC03 Chabrier H α _{corr}	15	15	22	22
Base CB Chabrier $\star < 140$ Myr	5	4	4	5
Base CB Chabrier GALEX FUV		6		6
Hybrid Salpeter H α _{obs} + 24 μ m		25		28
Hybrid Chabrier H α _{obs} + 24 μ m		15		17

Note. — All the SFR are in units of M_⊙ yr⁻¹. The SFR derived from our optical IFS is computed for spatially resolved and for integrated spectra. The first 4 rows in the table compare the continuum ($\star < 30$ Myr) and H α emission for the different model bases, using different IMFs. The next two rows compare the continuum ($\star < 140$ Myr) and the FUV estimates. Finally, the last two rows are the hybrid H α _{obs} + 24 μ m estimate including the MIR.

calculated in their work should also represent SFR assuming a Chabrier IMF. Under this assumption, we found that the average SFR in our two pre-merger LIRGs is enhanced by a factor 8 - 9 with respect to the Milky Way.

5.7.1. Star formation rate densities

Using H α and the stellar continuum in the last 30 Myr we also calculate the star formation rate densities (SFR per unit area):

- In **IC 1623 W**, we cover a total area of 30 kpc², which leads to $\langle \Sigma \text{SFR}(30\text{Myr}) \rangle \sim 0.47 \text{ M}_{\odot} \text{ yr}^{-1} \text{ kpc}^{-2}$ and $\langle \Sigma \text{SFR}(\text{H}\alpha) \rangle \sim 0.5 \text{ M}_{\odot} \text{ yr}^{-1} \text{ kpc}^{-2}$.
- In **NGC 6090** the total area covered is 40 kpc², leading to $\langle \Sigma \text{SFR}(30\text{Myr}) \rangle \sim 0.4 \text{ M}_{\odot} \text{ yr}^{-1} \text{ kpc}^{-2}$ and $\langle \Sigma \text{SFR}(\text{H}\alpha) \rangle \sim 0.55 \text{ M}_{\odot} \text{ yr}^{-1} \text{ kpc}^{-2}$.
- The **Milky Way** disk has a radius of active star formation of 13.5 kpc, that implies $\langle \Sigma \text{SFR} \rangle = 3.3 \times 10^{-3} \text{ M}_{\odot} \text{ yr}^{-1} \text{ kpc}^{-2}$ (Kennicutt & Evans, 2012).

The star formation rate densities of our pre-merger LIRGs are 120 - 170 times higher than in the Milky Way.

In Figure 5.35 we show the star formation rate densities (in logarithmic scale) estimated from H α (left panels) and from the stellar continuum in the last 30 Myr (right panels) for IC 1623 W (top panels) and NGC 6090 (lower panels). Comparing the left and right panels we note some similarities and differences.

In **IC 1623 W** the $\Sigma \text{SFR}(\text{H}\alpha)$ follows the morphology seen in the ionised gas, while $\Sigma \text{SFR}(30\text{Myr})$ is more uniform, that is, there is less contrast between regions. In both plots, we can identify the enhanced SFR surface densities in the nucleus of IC 1623 W and in the star forming regions C1 and C2. However, in C1 and C2 the H α derived star formation rate density is a factor ~ 6 higher than that derived from the continuum. This happens also in some spaxels along the spiral arm and in some spaxels near the nucleus with factors between 3 - 5. On the contrary, in the top left and specially in the top right corners, the opposite happens; $\Sigma \text{SFR}(30\text{Myr})$ is a factor 3 - 8 higher than $\Sigma \text{SFR}(\text{H}\alpha)$. Despite this, for the vast majority of the spaxels the match is quite good. When averaging in the maps we found $\langle \log \Sigma \text{SFR}(30 \text{ Myr}) \rangle = -0.23 \pm 0.19$ and $\langle \log \Sigma \text{SFR}(\text{H}\alpha) \rangle = -0.28 \pm 0.48$.

For **NGC 6090** both maps are remarkably similar. In some spaxels in the MSC region and in the outskirts the $\Sigma \text{SFR}(\text{H}\alpha)$ is a factor between 2 - 4 greater than the derived from the continuum. On the contrary, in the South of NGC 6090 SW the $\Sigma \text{SFR}(30\text{Myr})$ is a factor 3 greater than $\Sigma \text{SFR}(\text{H}\alpha)$. This also happens East side of NGC 6090 NE nucleus, with a factor 1.4 difference. The overall agreement is very good. When averaging in the maps we found $\langle \log \Sigma \text{SFR}(30 \text{ Myr}) \rangle = -0.32 \pm 0.47$ and $\langle \log \Sigma \text{SFR}(\text{H}\alpha) \rangle = -0.32 \pm 0.49$.

The conclusion is that ultimately, both methods provide a similar and satisfactorily robust measurement of the star formation rate. It is important to note that these are quite "simple" systems, in the sense that the dominating ionization mechanism is clearly star formation and the extinction is relatively low, so we do not expect substantial star formation completely obscured from view in the optical, i.e. star formation that is not accounted for by the Balmer decrement attenuation correction. This is not always the case, in fact, in the merger LIRG NGC 2623 studied in Chapter 6 we found a

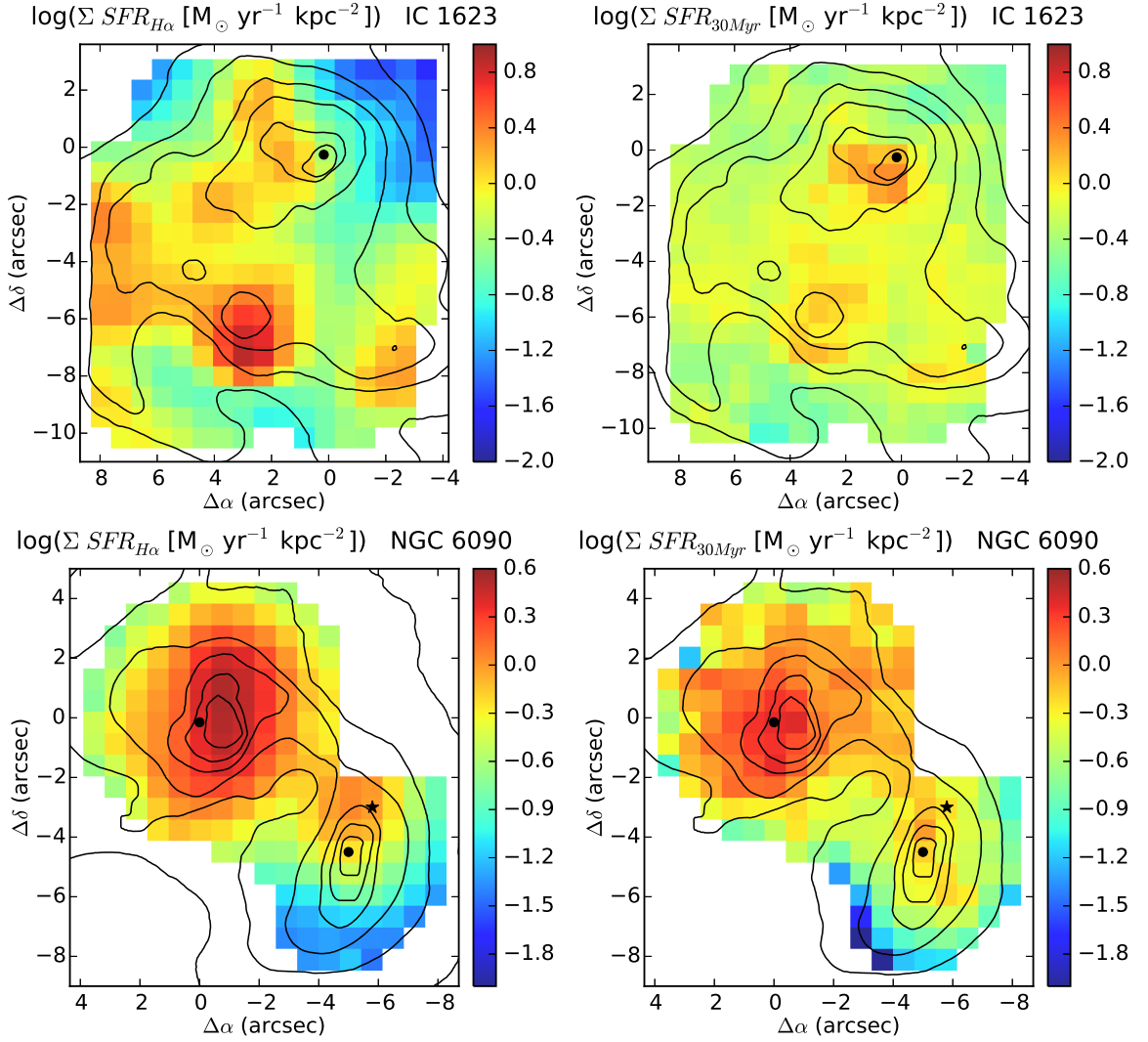


Figure 5.35 SFR density estimated from dust-attenuation corrected H α (left panels) and SFR density averaged over the last 30 Myr, measured from the decomposition of the stellar continuum (right panels) for IC 1623 W (top panels) and NGC 6090 (bottom panels). We only plot spaxels with $\Sigma_{SFR} > 10^{-2} M_{\odot} \text{ yr}^{-1} \text{ kpc}^{-2}$. In IC 1623 W the $\Sigma \text{ SFR}(\text{H}\alpha)$ follows the morphology seen in the ionised gas, while $\Sigma \text{ SFR}(30\text{Myr})$ is more uniform. In both plots, we can identify the enhanced SFR surface densities in the nucleus of IC 1623 W and in the star forming regions C1 and C2. However, in C1 and C2 the H α derived star formation rate density is a factor between ~ 6 greater than the derived from the continuum. Despite this, for the vast majority of the spaxels the match is quite good. When averaging in the maps we found $\langle \log \Sigma \text{ SFR}(30 \text{ Myr}) \rangle = -0.23 \pm 0.19$ and $\langle \log \Sigma \text{ SFR}(\text{H}\alpha) \rangle = -0.28 \pm 0.48$. For NGC 6090 both maps are remarkably similar. In some spaxels in the MSC region and in the outskirts the $\Sigma \text{ SFR}(\text{H}\alpha)$ is a factor between 2 - 4 greater than the derived from the continuum. On the contrary, in the South of NGC 6090 SW the $\Sigma \text{ SFR}(30\text{Myr})$ is a factor 3 greater than $\Sigma \text{ SFR}(\text{H}\alpha)$. The overall agreement is very good. When averaging in the maps we found $\langle \log \Sigma \text{ SFR}(30 \text{ Myr}) \rangle = -0.32 \pm 0.47$ and $\langle \log \Sigma \text{ SFR}(\text{H}\alpha) \rangle = -0.32 \pm 0.49$.

more complex ionization structure and higher extinction, requiring multiwavelength SFR to verify the results.

5.7.2. IFS-base variations over Scalo's b parameter

As stated in CF2013, it is often useful to consider SFRs in relation to some fiducial value instead of absolute units. The classical example is Scalo's birthrate parameter, defined by us as b^{loc} , which measures the SFR in the recent past ($t < t_{SF}$) with respect to its average over the whole lifetime of the system. It is obtained dividing the star formation rate surface density since $t=t_{SF}$, $\overline{SFR}_{xy}(t_{SF})$, by its asymptotic value (see also equation 12 of CF2013):

$$b_{xy}^{loc}(t_{SF}) = \frac{\overline{SFR}_{xy}(t_{SF})}{\overline{SFR}_{xy}(t_{\infty})} \quad (5.22)$$

The superscript "loc" is to emphasize that the reference lifetime average SFR is that of the same spatial location xy . One should recall that while young stars in a spaxel were probably born there (or near it), old ones may have migrated from different regions. Thus, despite the identical definitions, the physical meaning of b_{xy}^{loc} is not really the same as for galaxies as a whole. The IFS data allow for other definitions. For instance, one might prefer to compare $\overline{SFR}_{xy}(t_{SF})$ to $\overline{SFR}_{gal}(t_{\infty})$ of the galaxy as a whole. This variation measures the "present" ($t < t_{SF}$) "here" (at xy) to the "past" ($t < t_{\infty}$) average in the whole galaxy. We defined it as b^{gal} and its mathematical expression is

$$b_{xy}^{gal}(t_{SF}) = \frac{\overline{SFR}_{xy}(t_{SF})}{\overline{SFR}_{gal}(t_{\infty})} \quad (5.23)$$

See also equation 13 of CF2013. A formally similar but conceptually different definition is obtained using for the reference value in the denominator the SFR surface density within the same time scale but evaluated in the whole galaxy, i.e., to compare not "now versus then" but "now here versus now there". We defined this property as c^{gal} and obtained it through equation 14 of CF2013, or:

$$c_{xy}^{gal}(t_{SF}) = \frac{\overline{SFR}_{xy}(t_{SF})}{\overline{SFR}_{gal}(t_{SF})} \quad (5.24)$$

These three definitions cover the different combinations of time and space enabled by the application of fossil methods to IFS data.

In Figure 5.36 we show maps of b^{loc} (left panels), b^{gal} (middle panels), and c^{gal} (right panels) for three values of t_{SF} : 30 Myr (top), 140 Myr (middle), and 1400 Myr (bottom) for IC 1623 W. All panels are in logarithmic scale to highlight regions where $\overline{SFR}(t_{SF})$ is larger than the chosen reference value; the dynamical range of the images goes from 1 to 50 (0 to 1.7 in log). The same is shown in Figure 5.37 for NGC 6090.

We are going to discuss both systems simultaneously:

- **The first column of panels (a, d, g) shows the regions where the recent star formation on the different timescales (30 Myr, 140 Myr, 1400 Myr) is enhanced with respect to the average of these same regions over their whole lifetime:** Before starting the description of the various panels we emphasize that this first column is the most difficult for

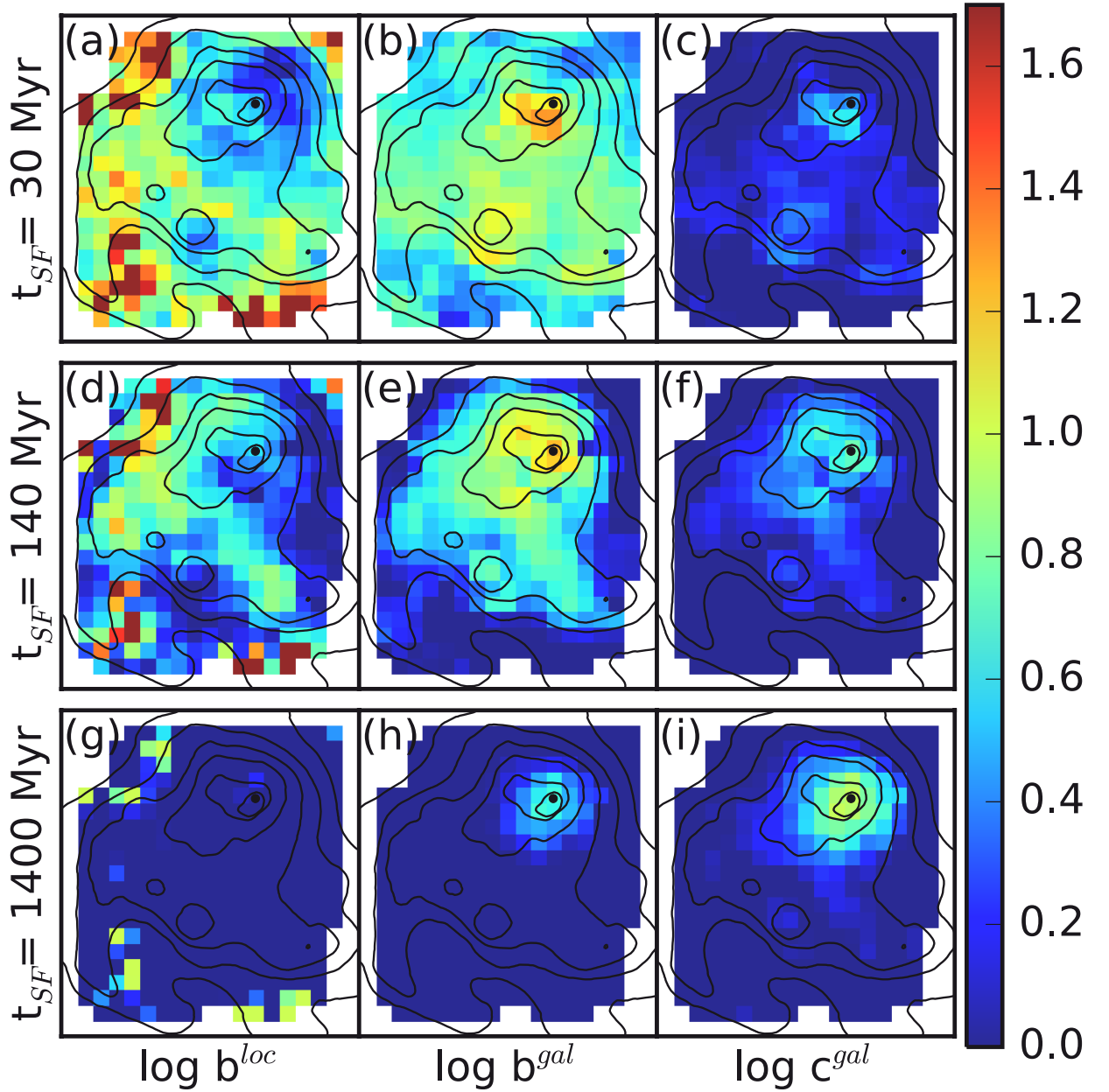


Figure 5.36 Spatially resolved SFR surface density on the last $t_{SF} = 30 \text{ Myr}$ (top), 140 Myr (middle) and 1400 Myr (bottom) in units of different reference values for IC 1623 W. The left panels compare $\overline{SFR}_{xy}(t_{SF})$ to $\overline{SFR}_{xy}(t_{\infty})$ i.e., the all-times average at xy , thus providing a local version of Scalo's b parameter. Middle panels compare the local $\overline{SFR}_{xy}(t_{SF})$ to the all-times average over the whole galaxy $\overline{SFR}_{gal}(t_{\infty})$. Panels on the right compare $\overline{SFR}_{xy}(t_{SF})$ to that of the galaxy as a whole over the same time scale $\overline{SFR}_{gal}(t_{SF})$. All images are on log scale from $\log 1$ to $\log 50$, such that only $\overline{SFR}_{xy}(t_{SF})$ values above the corresponding reference value are visible. See in the text in Section 5.7.2 a detailed description of each map.

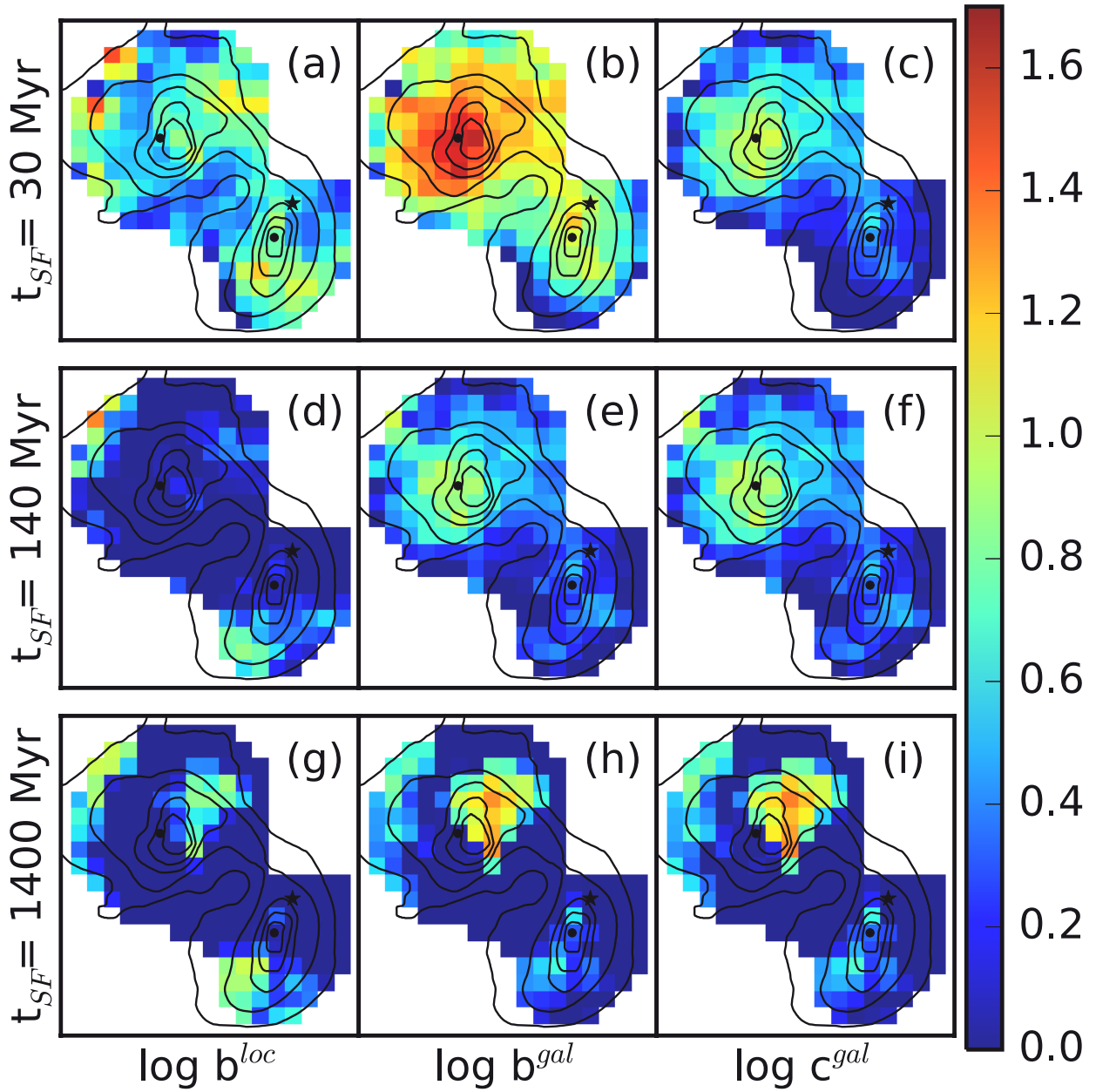


Figure 5.37 Spatially resolved SFR surface density on the last $t_{SF} = 30$ Myr (top), 140 Myr (middle) and 1400 Myr (bottom) in units the same reference values as Figure 5.36, but for NGC 6090. All images are on log scale from $\log 1$ to $\log 50$, such that only $\overline{SFR}_{xy}(t_{SF})$ values above the corresponding reference value are visible. See in the text in Section 5.7.2 a detailed description of each map.

us to interpretate, given that the stellar populations inhabiting each spaxel/region have not remained static in that position throughout the whole lifetime of the system, but have changed with the dynamics of the galaxy.

IC 1623 W. In panel a, we see that the SFR is enhanced everywhere except in the nucleus itself. The larger b^{loc} are located in the outskirts (it increases outwards) and specially to the East of the nucleus. We consider that this could be due to the interaction with IC 1623 E. Considering the past 140 Myr (panel d) the enhancement is located again to the East of the nucleus and also near C2. On the longest time scale considered (panel g) almost none spaxel has been more active than their lifelong average, with very few exceptions. This confirms what we found in Figure 5.14 and in top middle panel of Figure 5.16, there are no relevant intermediate-old stellar populations in IC 1623 W.

NGC 6090. In panel a we found that almost everywhere across the galaxies the SFR in the last 30 Myr have been larger than in the past average, specially to the North West of NE component and to the South of SW component. Considering the past 140 Myr (panel d), only a few spaxels at the East edge of NE component and to the South of SW component have a SFR enhanced with respect to their past average. On the contrary, in the past 1.4 Gyr (panel g) only some spaxels to the North West of the NE component, in a region partially coincident with MSC region, in the eastern edge of this same component and in the southern edge of SW component have been more active than their lifelong average.

- **In the middle column of panels (b, e, h) we can see the regions where the recent star formation on the different timescales (30 Myr, 140 Myr, 1400 Myr) is enhanced with respect to the average of the galaxy over its whole lifetime:**

IC 1623 W. From the longest timescale (h) to the shortest (b) we found that the region where the SFR is enhanced goes from only the nucleus to widespread across the system. The 140 Myr timescale (panel e) show something intermediate. This distribution is consistent with an inside-out formation in the last 1.4 Gyr.

NGC 6090. In NGC 6090 NE we found something analogous to IC 1623 W. From the longest timescale (h) to the shortest (b) we found that the region where the SFR is enhanced goes from concentrated in the MSC region to widespread across the system. In NGC 6090 SW the enhancement of the SFR is only relevant in the last 30 Myr, but significantly less than in the NE component.

- **The right column of panels (c, f, i) shows the regions where the recent star formation on the different timescales (30 Myr, 140 Myr, 1400 Myr) is enhanced with respect to the average of the galaxy in the same timescales. They show the location of the recent star formation in the galaxy for each timescale, so to speak:**

IC 1623 W. At all timescales, the only region with relevant enhancement of the SFR with respect to the galaxy at this same time is the nuclear region.

NGC 6090. We found a distribution in the enhancement of the SFR very similar to its middle column of panels, except for the shortest timescale (panel c), where the relative ratio is lower.

In summary, both pre-merger LIRGs show an enhancement of the SFR at the central part (nuclei or close) in the three timescales chosen (30 Myr, 140 Myr and 1.4 Gyr) in comparison with the average SFR occurred along the Hubble time in the galaxies and the SFR occurred in the galaxies in the same time periods.

5.8. Summary and conclusions

In this chapter we have fully characterized two pre-merger LIRGs: IC 1623 W and NGC 6090. Using HST multiwavelength imaging and PMAS LArr IFS with V300 grating, we have analyzed the star clusters properties, the stellar population properties, the ionized gas distribution and properties, the ionization mechanism, the kinematics, and the star formation rates.

Our main results are:

1. *Star clusters properties: IC 1623.* IC 1623 W clusters are very young (< 200 Myr) and affected by very low to almost no foreground extinction (< 1 mag). On the contrary, the clusters in IC 1623 E are affected by 2 - 6 mag of extinction. For the only IC 1623 E cluster emitting in FUV, we derive an age below 10 Myr, and $A_V = 2 - 3$ mag. This might suggest that, although hidden under large amounts of dust, some clusters in IC 1623 E are as young or more than IC 1623 W clusters. Moreover, IC 1623 W clusters have masses between $10^5 - 10^7 M_\odot$, while in IC 1623 E they are more massive $\sim 10^7 - 10^8 M_\odot$. A rough estimate of the total mass in clusters in IC 1623 W is $\sim 9 \times 10^8 M_\odot$, which represents 3% of the total stellar mass.

NGC 6090. Most NGC 6090 SW clusters and NGC 6090 NE clusters in MSC region are also young (< 300 Myr) and affected by very low to almost no foreground extinction (< 1 mag). The rest of clusters in NGC 6090 NE are also consistent with ages $\lesssim 300$ Myr and A_V up to 2 mag. The only red "cluster" emitting in FUV is NGC 6090 NE nucleus. It has ages between 10 - 50 Myr and is affected by 2 - 3 mag. It seems that in this case the nucleus is rejuvenating as a consequence of the merger process. In general, NGC 6090 clusters have masses between $10^5 - 10^7 M_\odot$. The two "clusters" with higher masses (around $10^7 - 10^8 M_\odot$) are NGC 6090 NE nucleus and NGC 6090 SW nucleus. The total stellar mass in clusters in NGC 6090 is approximately $\sim 2 \times 10^9 M_\odot$, which represents 4% of the total stellar mass.

When comparing the mass in clusters with the mass in YSP from the spectroscopy, we found that in IC 1623 W both are comparable to each other within a factor of ~ 1.3 , in agreement with the idea that the vast majority of stars form in clusters rather than in isolation. However, in NGC 6090, the mass in star clusters is a factor ~ 4 higher than the mass in YSP, probably due to the uncertainties in the determination of cluster ages through photometry.

2. *Stellar luminosities:* In **IC 1623 W** the observed (not dust-attenuation corrected) stellar luminosity decreases from $0.4 L_\odot \text{ pc}^{-2} \text{ \AA}^{-1}$ in the nucleus to $0.08 L_\odot \text{ pc}^{-2} \text{ \AA}^{-1}$ at 2.2 kpc. Between 2.2 kpc and 4.5 kpc, the luminosity density remains approximately constant around $0.08 L_\odot \text{ pc}^{-2} \text{ \AA}^{-1}$. Above 4.5 kpc it decreases again down to $0.04 L_\odot \text{ pc}^{-2} \text{ \AA}^{-1}$ at 6 kpc.

NGC 6090 NE and NGC 6090 SW have a similar gradient in the luminosity density, but with the NE component being 0.2 dex more luminous. For NGC 6090 NE it ranges from $0.2 L_\odot \text{ pc}^{-2} \text{ \AA}^{-1}$ in the nucleus to $0.05 L_\odot \text{ pc}^{-2} \text{ \AA}^{-1}$ at 2.7 kpc. Analogously, for NGC 6090 SW it goes from $0.13 L_\odot \text{ pc}^{-2} \text{ \AA}^{-1}$ in the nucleus to $0.03 L_\odot \text{ pc}^{-2} \text{ \AA}^{-1}$ at 2.7 kpc.

3. *Stellar dust extinction:* **IC 1623 W** has little extinction, with A_V below 0.4 mag nearly everywhere. The regions most affected by extinction are located "behind" areas where a lot of HII regions accumulate, as C1, where the extinction reaches values up to 1.2 mag. As an explanation we suggest that the enhancement of A_V could be due to the accumulation of dust swept by the supernovae of the star forming regions, at least in some spaxels. Another possibility is that the interaction itself has led to the accumulation of dust in these regions.
In **NGC 6090 NE** the extinction ranges from 1.2 - 1.6 mag, while in NGC 6090 SW from 0.6 mag in the North to about 0.2 mag in the South. To the West of NGC 6090 NE and in the bridge between the two galaxies the dust extinction has an intermediate value of 0.8 - 0.9 mag. There is approximately 1 mag difference in the stellar dust extinction between the two components. We note that in these two pre-merger systems one of the components is significantly more obscured than the other. In these cases it coincides that is the eastern component which is more obscured, although the difference is higher for IC 1623 than for NGC 6090.
4. *Stellar ages:* In **IC 1623 W** the nuclear regions are clearly older than the outer parts. From the radial profile we find a negative trend of the mean age with distance; from ~ 300 Myr in the nucleus to ~ 30 Myr at 3 kpc away from it. From 3 to 6 kpc the age remains approximately constant between 15 - 40 Myr.
In **NGC 6090** it happens the contrary, the older spaxels are located in the outskirts, specially for the SW galaxy, where they reach ages up to ~ 300 Myr. The youngest region is the bridge between components with ~ 50 Myr. When averaging, both components have the same mean ages between 50 - 100 Myr and almost flat trends of the age profiles with distance.
5. *Stellar metallicities:* We found that metallicity is one of the most difficult quantities to constrain. Focusing on the mean values, it seems that all of them IC 1623 W, NGC 6090 NE SW have global mean metallicities around $\sim 0.6 Z_\odot$. The metallicity radial profiles in these three galaxies (at least in the inner 3 kpc) are approximately flat, that is, metallicity remains constant with distance. This is in agreement with the inverted metallicity gradients which are found in the ionized gas metallicity of mergers where significant gas inflows have occurred ([Kewley et al., 2010](#); [Rich et al., 2012](#)).
6. *Stellar mass surface densities:* In **IC 1623 W** the highest values of the mass surface density are reached in the nucleus and in C1, with a logarithmic value of around 3.7. From the radial profile we found a negative gradient with distance, going from 3.7 in the nucleus itself to 2.8 at 3 kpc. Above it, it increases again slightly up to 3.0 at 4.5 kpc.
For **NGC 6090** we found that the stellar mass surface density is significantly higher in the NE component than in the SW. The region with the highest value of the mass surface density ($\log \mu_\star \sim 3.8$) is located to the South East of NGC 6090 NE nucleus. In NGC 6090 SW, $\log \mu_\star$ is higher in the North of the component than in the South. From the radial profile, we also found a negative gradient of the stellar mass density with distance, but not as steep as for IC 1623 W. $\log \mu_\star$ goes from 3.8 to 3.2 for NGC 6090 NE and from 3.0 to 2.7 for NGC 6090 SW.
7. *Stellar masses:* From the spectral synthesis the total stellar mass obtained is $M = 3.9 \times 10^{10} M_\odot$ and $6.8 \times 10^{10} M_\odot$ for IC 1623 W and NGC 6090, respectively (for Salpeter IMF). This is the present day mass locked in stars. Counting also the mass returned by stars to the interstellar

medium $M' = 5.5 \times 10^{10} M_{\odot}$ and $9.6 \times 10^{10} M_{\odot}$ were involved in star formation for IC 1623 W and NGC 6090, respectively.

Stellar masses from Spitzer 3.6 μm : We have derived the mass in old stellar populations from the MIR at 3.6 μm , which is $3.4 \times 10^{10} M_{\odot}$ and $4.4 \times 10^{10} M_{\odot}$ for IC 1623 W and NGC 6090, respectively. From spectral synthesis we found that the masses in SSPs > 1.4 Gyr are $5.3 \times 10^{10} M_{\odot}$ and $8.8 \times 10^{10} M_{\odot}$ for IC 1623 W and NGC 6090, respectively.

The masses derived with our optical spectroscopy are a factor 1.5 - 2 bigger than the masses calculated with the MIR photometry. However, this factor is explained by the difference in the IMF. Our optical spectral synthesis analysis uses a Salpeter IMF (results from GM base of models), and these masses should be on average a factor 1.84 larger than when compared with Chabrier IMF (González Delgado et al., 2015). Taking this into account, the agreement between optical and MIR estimations is remarkable and confirms that for IC 1623 W and NGC 6090 we are not underestimating the stellar masses with optical spectral synthesis, also ensuring that the extinction estimates are approximately correct.

8. *Star Formation Histories:* We calculate and compare both the time resolved 1D SFHs and the spatially resolved SFHs, condensing the population vector into three age ranges, namely young (YSP, SSPs ≤ 140 Myr), intermediate (ISP, $140 \text{ Myr} < \text{SSPs} \leq 1.4$ Gyr), and old populations (OSP, SSPs > 1.4 Gyr).

IC 1623 W

- From the time resolved 1D SFH we get a more detailed idea of when the bursts of star formation started and how many of them occurred. We found that the young components may be younger than 10 Myr. Within the intermediate age range we found that star formation took place between 500 to 140 Myr ago with the more intense peak located at 140 Myr. The old populations formed between 14 Gyr and 6 Gyr ago for IC 1623 W.
- The contribution of YSP to light is around 90 % everywhere except in the nucleus, where the contribution is around 50 %. Only in the nucleus the ISP have a significant contribution, between 30 - 40 %. The contribution of OSP is everywhere below 20 % in IC 1623 W.
- When summing the total mass in each age bin, we found that from the total $M' = 5.5 \times 10^{10} M_{\odot}$ in IC 1623 W, the mass in young $M'(Y)$, intermediate age $M'(I)$ and old $M'(O)$ stellar populations is $1.8 \times 10^9 M_{\odot}$ (3 %), $8.2 \times 10^8 M_{\odot}$ (1 %), and $5.3 \times 10^{10} M_{\odot}$ (96 %), respectively.

NGC 6090

- From the time resolved 1D SFH we found that most of the young star formation started in the last 20 Myr and seems to have been continuous since. Two relevant intermediate age bursts may have occurred in NGC 6090, one at 1.4 Gyr and another peaking around 600 Myr. The old populations formed between 14 Gyr and 5 Gyr ago for this system.
- Almost all spaxels have YSP contribution above 70 %, except for some spaxels located at the easternmost end of NGC 6090 NE and at the South edge of NGC 6090 SW. In these regions the contribution of ISP and OSP is also important. The average contribution of ISP is very small, below 10 % for both components, but being a bit more important in the

outskirts of the SW galaxy. The OSP contribute to 25 % of the light of both components in the nucleus, and decreases to 15 % (20 %) in the outskirts of NGC 6090 NE (SW).

- From the total $M' = 9.6 \times 10^{10} M_{\odot}$ in NGC 6090, the mass contained in young $M'(Y)$, intermediate age $M'(I)$ and old $M'(O)$ stellar populations is $1.0 \times 10^9 M_{\odot}$ (1 %), $6.6 \times 10^9 M_{\odot}$ (7 %) and $8.8 \times 10^{10} M_{\odot}$ (92 %), respectively.

The general conclusion is that the light of both pre-merger systems is clearly dominated by the young stellar populations, widespread across the whole observed extensions. However, in terms of mass, the YSP represent less than a 3 % of the total stellar mass. Most of the stellar mass (80 - 100 %) is provided by the OSP.

9. *Ionized gas morphology:* In **IC 1623 W** the $H\alpha$ emission is concentrated in the distorted spiral arm and SSCs aggregates C1 and C2. Furthermore, in the nuclear area we detected a cylindrical structure, C3, which seems to leave or enter the nucleus. Due to its morphology, at first we thought it might be a gas inflow / outflow. Yet we see in the HST image that this emission has also a stellar counterpart with several SSCs along it.

NGC 6090. The $H\alpha$ is extended across both components in a more uniform and less clumpy way than in IC 1623 W. The NE component is more luminous than the SW one. In the NE component, the $H\alpha$ peak is offsetted to the West with respect to the nucleus, spatially coincident with the multiple star clusters MSC region. For the SW component, $H\alpha$ peaks in the northern half where most of the star forming regions accumulate. In both cases, there is a good spatial correlation between the extended $H\alpha$ emission and the regions where the young stellar populations are contributing to $\geq 70\%$ to the total light.

10. *Ionized gas electron density:* Using $[SII]\lambda 6716 / [SII]\lambda 6731$ doublet ratio we have determined the electron density in **IC 1623 W**. The ratio reaches its minimum around the star forming region C1 with values ~ 1.2 , equivalent to an electron density of $\sim 260 \text{ cm}^{-3}$. Everywhere else the ratio is above the low density limit (> 1.4), densities are below 100 cm^{-3} . This estimation is not available for **NGC 6090** as the $[SII]$ lines are not included in the spectrum.
11. *Ionized gas dust extinction:* In **IC 1623 W** the average A_V is ~ 0.8 mag. As for the stellar extinction, the regions most affected by extinction are located behind areas where a lot of HII regions accumulate. Behind C1 the extinction reaches its maximum value of around 2.5 mag. The same happens behind C2, with values up to 1.6 mag. Also, values between 1.3 - 1.6 mag are found in the distorted spiral arm, and between 1.0 - 1.3 mag to the South-East of the nucleus and along the cylindrical structure C3. Everywhere else, the extinction is below 1 mag. The ratio between ionized gas and stellar extinctions in IC 1623 W is $\langle \frac{A_{V,gas}}{A_{V,stars}} \rangle = 2.1 \pm 1.1$. In **NGC 6090**, the average extinction of the NE component is 1.8 mag, however it ranges between 1.5 mag in the nucleus of the galaxy, to values around 2 mag in the North and higher values up to 2.5 mag in a few spaxels in the South. For the SW component we found an average value around 0.8 mag, but it also varies across the galaxy from 0.5 mag in the South to 1 mag in the North. We found an average difference of ~ 1 mag between components, as also happens with the stellar extinction. In the overlapping / bridge region the extinction have values in between, $\sim 1.3 - 1.4$ mag. In NGC 6090, the ratio between ionized gas and stellar extinctions is $\langle \frac{A_{V,gas}}{A_{V,stars}} \rangle = 1.6 \pm 0.6$.

12. *Emission line ratios sensitive to ionisation source:* $[\text{NII}]\lambda 6583/\text{H}\alpha$ and $[\text{OI}]\lambda 6300/\text{H}\alpha$ line ratios are consistent with both IC 1623 W and NGC 6090 being dominated by young stars photoionization or in some spaxels by something composite between star formation and LINER emission. Only in a few spaxels (~ 3) in the outskirts of the maps, the ratios are consistent with starburst-related LINERs. In the case of IC 1623 W, this is in agreement with Rich et al. (2011) results. Like us, they found that the core of IC 1623 W is dominated by starbursts. However, they cover a larger FoV and found that in the outskirts the emission is dominated by shocks (= LINER).
13. *Diagnostic diagrams:* We found that for both IC 1623 W and NGC 6090 the dominating ionization mechanism is star formation, at least in the regions mapped by us. However, there are some spaxels in the "composite" emission region, between Kauffmann et al. (2003) and Kewley et al. (2001) demarcation lines. In **IC 1623 W** they are located in the strip extending from above C1 to the upper right corner of the map, and four spaxels at the southern end of this component. In **NGC 6090** they are located in the outskirts of the map. Given the proximity of the vast majority of the "composite" spaxels to the Kauffmann demarcation line, we do not believe that the ionization source is different for them, and is therefore quite possible that they are also star forming regions. However, for a few spaxels we can not discard a truly composite photoionization which we believe it should be due to ISM shocks that would occur naturally as a result of the increase of the supersonic turbulence in mergers (Bournaud et al., 2010).
14. *Ionized gas velocity field:* The velocity field of **IC 1623 W** shows a distorted rotation pattern, with the NW side receding from us and the SE approaching us. We estimate two pairs of possible kinematic minor and major axes. The position angle of the kinematic minor axis is $\text{PA} \sim 69 - 70^\circ$. The kinematic major axis is almost but not necessarily/exactly perpendicular to the minor one, due to the distortion in the velocity field caused by the interaction. Approximately, the velocities range from -200 to 200 km/s. We found that the kinematic center of IC 1623 W does not coincide with the photometric one.
NGC 6090 NE is a face on spiral, so we are only seeing the movements of gas perpendicular to the disk. No rotation is found and the velocity range is small and oscillates between -5 to 65 km/s. The only region of NGC 6090 NE approaching us is the nucleus. We hypothesize that there could be an outflow, however, we can not resolve it with our spectral resolution. To the South, there is gas receding from us at ~ 65 km/s, probably due to the interaction. On the other hand, **NGC 6090 SW** seems to retain traces of the rotation, but very distorted. Its velocity field ranges from -35 km/s to the North to +50 km/s to the South of this component. If this system is similar to the Antennae, then ~ 500 Myr would be enough to significantly distort the original rotation.
15. *Ionized gas velocity dispersion:* In **IC 1623 W** the velocity dispersion is low in the star forming regions and in the distorted spiral arms, with $\sigma_{\text{H}\alpha} < 120$ km/s. However, $\sigma_{\text{H}\alpha} > 120$ km/s in several outermost spaxels, with a region to the North West of the nucleus where $\sigma_{\text{H}\alpha}$ reaches up to 170 km/s. We interpret this result as a consequence of shocks being more important in the outskirts, producing a broadening of the emission lines. This is again in agreement with Rich et al. (2011), who found widespread shocks in the outskirts of IC 1623, beyond the region traced by us. In **NGC 6090** there exists a gradual increase in the velocity dispersion from ~ 140

- 150 km/s to the East of NE component, to 170 km/s in the bridge between components, and up to 190 km/s to the South West of the SW component. The increase of the velocity dispersion in the bridge between components could be due to the shocks produced by the interaction itself. In the case of the higher values to the South of the SW component there also exists the possibility that we are simultaneously observing several gas components moving at different velocities as a consequence of the interaction.

16. *Star Formation Rates:* We have derived the SFRs using multiwavelength data from UV, optical IFS (continuum and lines) and MIR.

- In both IC 1623 W and NGC 6090 we found that $\text{SFR}(30 \text{ Myr}) \sim \text{SFR}(\text{H}\alpha)$ and $\text{SFR}(140 \text{ Myr}) \sim \text{SFR}(\text{FUV})$, which makes sense precisely because $\text{H}\alpha$ ionizing stars usually have $\leq 30 \text{ Myr}$. This includes O and early B stars, for later spectral types the number of ionizing photons emitted declines drastically. However, the UV is emitted for up to A0 stars with lifetimes $\sim 100 \text{ Myr}$.
- The average SFR from the very young stellar populations and $\text{H}\alpha$ is $14 \pm 1 \text{ M}_{\odot} \text{ yr}^{-1}$ for IC 1623 W and $20 \pm 3 \text{ M}_{\odot} \text{ yr}^{-1}$ for NGC 6090 (with Chabrier IMF). For the populations below 140 Myr and FUV, the $\text{SFR} = 5 \pm 1 \text{ M}_{\odot} \text{ yr}^{-1}$ for both systems (also, with Chabrier IMF), a factor of 3 - 4 smaller than the one for the very young components ($< 30 \text{ Myr}$) and $\text{H}\alpha$. This difference indicates that recent SFR is more concentrated in instantaneous bursts occurred in the last 10 Myr rather than as a continuum SFR.
- The SFRs derived with Salpeter IMF are a factor 1.5 ± 0.3 larger than the Chabrier ones. For $\text{H}\alpha$ we found something similar 1.69 ± 0.03 .
- When including the MIR, we found hybrid $\text{SFR} = 15 \text{ M}_{\odot} \text{ yr}^{-1}$ and $17 \text{ M}_{\odot} \text{ yr}^{-1}$ for IC 1623 W and NGC 6090, respectively. They are very similar to the ones derived from dust-attenuation corrected $\text{H}\alpha$ and $\text{SFR}(30 \text{ Myr})$. We can conclude that for IC 1623 W and NGC 6090 there is no substantial star formation which is not accounted for by the Balmer decrement attenuation correction.
- The average SFR in our two pre-merger LIRGs is enhanced by a factor 8 - 9 with respect to the Milky Way.

17. *Star Formation Rate Densities:* We have compared the star formation rate densities estimated from $\text{H}\alpha$ and from the stellar continuum in the last 30 Myr for IC 1623 W and NGC 6090. Both methods (continuum and lines) provide a similar and satisfactorily robust measurement of the star formation rate density. Moreover, when averaging we found

- In **IC 1623 W**, we cover a total area of 30 kpc^2 , that leads to $\langle \Sigma \text{SFR}(30\text{Myr}) \rangle \sim 0.47 \text{ M}_{\odot} \text{ yr}^{-1} \text{ kpc}^{-2}$ and $\langle \Sigma \text{SFR}(\text{H}\alpha) \rangle \sim 0.5 \text{ M}_{\odot} \text{ yr}^{-1} \text{ kpc}^{-2}$.
- In **NGC 6090** the total area covered is 40 kpc^2 , leading to $\langle \Sigma \text{SFR}(30\text{Myr}) \rangle \sim 0.4 \text{ M}_{\odot} \text{ yr}^{-1} \text{ kpc}^{-2}$ and $\langle \Sigma \text{SFR}(\text{H}\alpha) \rangle \sim 0.55 \text{ M}_{\odot} \text{ yr}^{-1} \text{ kpc}^{-2}$.
- Compared with the $\langle \Sigma \text{SFR} \rangle = 3.3 \times 10^{-3} \text{ M}_{\odot} \text{ yr}^{-1} \text{ kpc}^{-2}$ of the Milky Way, the star formation rate densities of our pre-merger LIRGs are 120 - 170 times higher than it.

18. *IFS-base variations over Scalo's b parameter*: Both pre-merger LIRGs show an enhancement of the SFR at the central part (nuclei or close) in the three timescales chosen (30 Myr, 140 Myr and 1.4 Gyr) in comparison with the average SFR occurred along the Hubble time in the galaxies and the SFR occurred in the galaxies in the same time periods.

6

The merger LIRG NGC 2623

6.1. Introduction

To understand the role of major mergers in galaxy evolution we are characterizing the spatially resolved stellar population properties and ionization mechanism in several interacting systems in different stages of the merger process. In this chapter we present the results of the evolved merger LIRG NGC 2623.

NGC 2623 (Arp 243, UGC 4509, IRAS 08354 2555) is a nearby luminous IR galaxy ($z \sim 0.01850$, $L_{IR}[8 - 1000 \mu\text{m}] \sim 3.56 \times 10^{11} L_{\odot}$), which is the result of a major merger between two gas-rich galaxies (Toomre, 1977). It shows a single nucleus, indicating that it is an advanced, post coalescence merger, interaction stage 4 in Veilleux et al. (2002) classification. It also shows a blue star forming region south of the main body and two extended tidal tails. The NIR surface brightness profile in the nuclear regions follows a $r^{1/4}$ law, consistent with a system evolving into an elliptical galaxy (Wright et al., 1990; Rothberg & Joseph, 2004). A substantial post starburst population dominates in the circumnuclear region of NGC 2623 (Joy & Harvey, 1987; Armus et al., 1989; Liu & Kennicutt, 1995; Shier et al., 1996), while a young nuclear starburst is also present (Bernloehr, 1993; Shier et al., 1996). Evans et al. (2008) reported that the blue, UV bright star forming region located 5 kpc south of the nucleus, is formed by ~ 100 stellar clusters with ages between 1 - 100 Myr. This region could be either part of a loop of material associated with the northern tidal tail, or nuclear tidal debris created during one of the final passages of the progenitor nuclei prior to their coalescence. However, the bulk of infrared luminosity comes from the obscured nuclear regions, and the off-nuclear starburst only represents 1% of the total star formation in NGC 2623. The ionization process in the nucleus of NGC 2623 is a combination of a dusty starburst and shock heating due to an starburst related outflow (Lípari et al., 2004). The outflow has an aperture angle $\theta = 100^{\circ} \pm 5^{\circ}$ and reaches a distance of 3.2 kpc from the nucleus and a velocity of $V_{OF} = (-405 \pm 35) \text{ km s}^{-1}$. The merger core hosts an AGN as determined from the hard X-ray spectrum (Maiolino et al., 2003) and the presence of the [NeV] 14.3 μm line (Evans et al., 2008; Petric et al., 2011). However the energetics of the system are dominated by star formation.

The aim of this study of NGC 2623 is to combine high quality IFS from CALIFA survey and PMAS at CAHA with previous high resolution HST imaging and with narrow band filter imaging from

Tunable Filters@OSIRIS to present the most complete picture of the physical processes that occur during the final stages of a major merger. In Section 6.2 we summarize the data and observations. In Section 6.3 we present the results of the star clusters photometry detected in the HST images. The stellar population properties derived from the IFS is described in Section 6.4. In Section 6.5 we show the ionized gas distribution, dust attenuation, and the emission line ratios tracing the ionization source. The gas kinematics is described in Section 6.6. A multiwavelength analysis of the Star Formation Rate in NGC 2623 is shown in Section 6.7. Section 6.8 is the discussion of the results, and Section 6.9 is the summary and conclusions.

Throughout the chapter we assume a flat cosmology with $\Omega_M = 0.272$, $\Omega_\Lambda = 0.728$ and $H_0 = 70.4$ km s⁻¹ Mpc⁻¹ (WMAP, seven years results). For NGC 2623 redshift ($z=0.018509$), this results in a distance of 80.0 Mpc. At this distance 1'' corresponds to 0.390 kpc.

6.2. Data

For this galaxy we have the PMAS Larr IFS from the nuclear region along with CALIFA PPAK IFS covering the main body of NGC 2623, that is, virtually the entire extension of the system, except the outermost parts of the tidal tails. Also, we have HST high resolution imaging from UV to NIR covering the main body of NGC 2623, from which we will derive the star clusters photometry. Moreover, we have Tunable Filters OSIRIS@GTC narrow line imaging of H α and [NII] λ 6583, covering

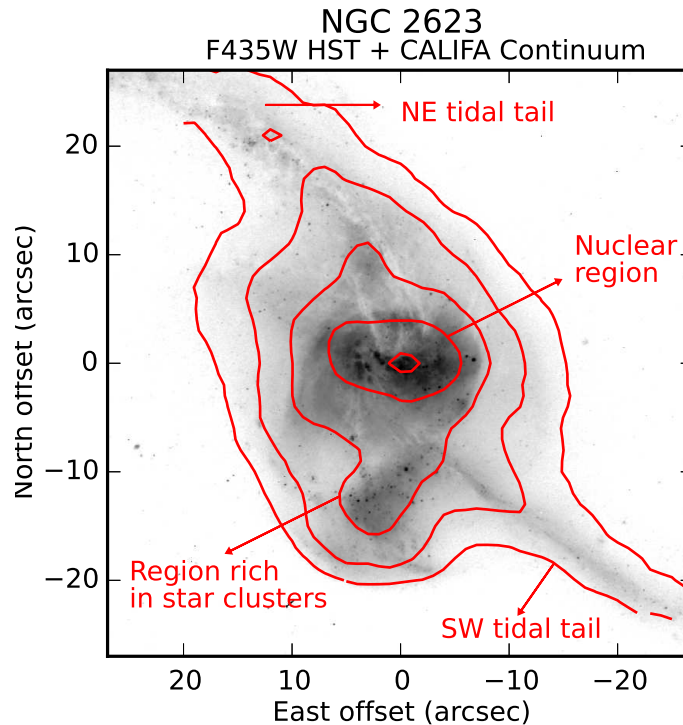


Figure 6.1 In greyscale we show the HST F435W continuum image of NGC 2623 in the region covered by CALIFA IFS. The average continuum from the IFS is superimposed with red contours. We note some characteristic regions of this galaxy as the SW and NE tidal tails and the region rich in star clusters located 10 arcsec to the south of the nucleus.

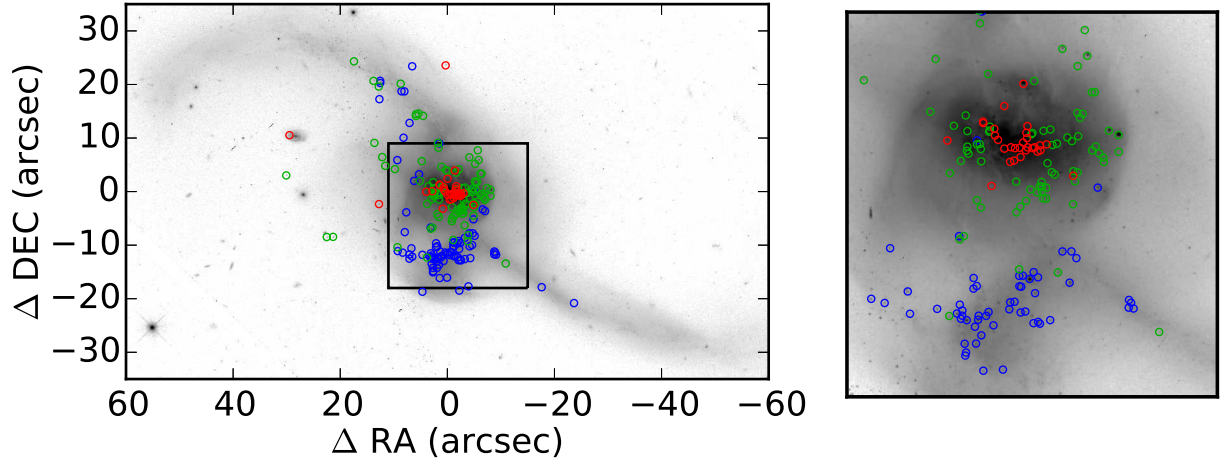


Figure 6.2 F814W image of NGC 2623. North is up, East to left. The detected clusters are marked with apertures of different colors given by their $F435W - F814W$ color as: 1) blue clusters those with $F435W - F814W \leq -1$, 2) green clusters if $-1 < F435W - F814W \leq 0$, and 3) red clusters if $F435W - F814W > 0$. In the left panel the whole galaxy is shown, where the black rectangle indicates the region simultaneously covered by all the filters from UV to NIR. A zoom into this region is shown in the right panel.

the full extent of NGC 2623. For a complete information on the characteristics of the data and their reduction procedure see Chapters 2 and 3.

In Figure 6.1 we show the HST F435W continuum image of NGC 2623 in the region covered by CALIFA IFS. The average continuum from the IFS is superimposed with red contours. We note some of the characteristic regions of this galaxy as the SW and NE tidal tails and the region rich in star clusters located 10 arcsec to the south of the nucleus.

6.3. Star clusters photometry

As explained in Section 5.3, galaxy mergers were the first environments discovered to contain copious amounts of young massive star clusters. They are an intriguing mode of star formation in the present-day universe. Using HST photometry we can characterize the stellar population properties of the SSCs in NGC 2623, to determine how are they related with the interaction process. By comparing the colors and magnitudes of NGC 2623 clusters with stellar population synthesis models we have derived their main properties: age, mass, and the amount of dust extinction. The methodology of the analysis, how we have detected the clusters, and performed aperture photometry is explained in detail in Section 5.3.1.

6.3.1. Cluster distribution

In Figure 6.2 we show the F814W image of NGC 2623. The detected clusters are marked with apertures of different colors given by their $F435W - F814W$ color as: 1) blue clusters are those with $F435W - F814W \leq -1$; 2) green clusters if $-1 < F435W - F814W \leq 0$ and 3) red clusters if

$F435W - F814W > 0$. In the left panel the whole galaxy is shown, where the black rectangle indicates the region simultaneously covered by all the filters from UV to NIR. A zoom into this region is shown in the right panel. A total of 156 clusters were detected with $\text{SNR} > 5$ in FUV, F435W, and F814W, in the region in common for all filters. Analogously, 203 clusters were detected with $\text{SNR} > 5$ in F435W, F814W, and F160W. In NGC 2623 the blue clusters are located in the concentration south of the nucleus, while the red ones are located in the highly obscured nuclear region. Strong dust lanes can be seen in the nucleus of NGC 2623 in HST B and V band images.

Differences in cluster color could be due to real differences in the stellar population properties and/or different levels of dust extinction affecting the clusters depending on their location. A cluster could be redder due to a high amount of extinction or an older stellar population, or a combination of both. In the following section we will use our multiwavelength information to break this age-extinction degeneracy and estimate the SP properties of the clusters.

6.3.2. Cluster ages

We have compared the colors and magnitudes of NGC 2623 clusters with those of Charlot & Bruzual SSP models (2007, unpublished) in a range of ages between 1 Myr to 13 Gyr. Despite the recent improvements in modelling techniques, it is very difficult from photometry to estimate metallicity of individual clusters. From the spectroscopy we obtain an average value for the metallicity inside 2 HLR of $\sim 0.5 Z_{\odot}$ (see Section 6.4.6). Taking this into account, we have used the $0.4 Z_{\odot}$ SSP models as a proxy in this analysis.

Comparing the position of the clusters in color-color diagrams with respect to the model positions we can estimate the cluster ages. In Figure 6.3 we show the FUV - F435W vs F435W - F814W diagram, which is the best for breaking the age - A_V degeneracy. The color coding is the same as in Figure 6.2, but only those clusters with $\text{SNR} \geq 5$ in FUV, F435W, and F814W filters are included in the plots. The black solid line is the path described by SSP models from 1 Myr to 13 Gyr, $0.4 Z_{\odot}$, and $A_V = 0$ mag. The greyscale lines are the paths for the same models reddened by 1 to 3 mag, with the lighter shades tracing the more reddened models. From this plot we found that the concentration of clusters south of the nucleus (the blue points in the Figure) is consistent with not being affected by foreground extinction. They have ages ranging from 100 - 500 Myr, with an average around ~ 300 Myr. Only a few of them could be younger if we consider they are affected by some extinction. Using only optical colors, Evans et al. (2008) derived cluster ages younger than us, between 1 - 100 Myr. This result totally agrees with the obtained by us using their same color-color diagram. However, we found that including the UV we can constrain better the cluster ages. We have also confirmed this result spectroscopically. This cluster-rich region in the south has mean ages between 200 - 300 Myr, and the light in this region is dominated by intermediate age stellar populations between 140 Myr - 1 Gyr (see Sections 6.4.5 and 6.4.8). This reinforces the inclusion of UV bands in photometric analysis to break the age-extinction degeneracy.

Analogously, in Figure 6.4 we show the F435W - F814W vs F814W - F160W diagram. Only clusters with $\text{SNR} \geq 5$ in F435W, F814W, and F160W filters are shown. Again, the black solid line is the path described by SSPs from 1 Myr to 13 Gyr, $0.4 Z_{\odot}$, and $A_V = 0$ mag. The greyscale lines are the paths for the same models reddened by up to 6 mag, with the lighter shades tracing the more extinguished models. From it, we found that NGC 2623 nuclear clusters (the red points in the Figure) are

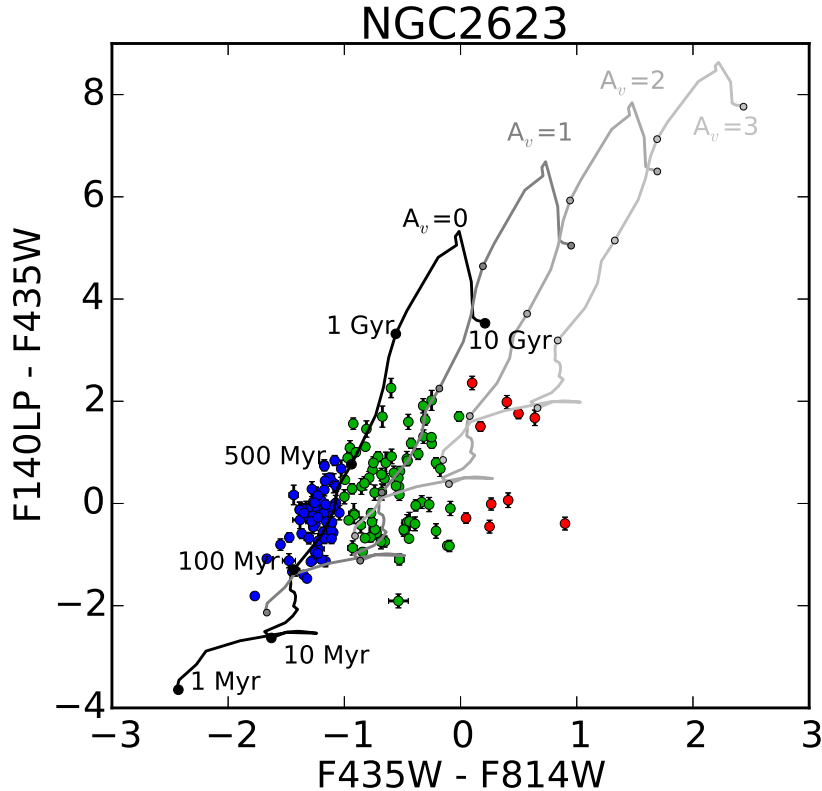


Figure 6.3 FUV - F435W vs F435W - F814W diagram for NGC 2623 clusters. The color coding is the same as in Figure 6.2, but only those clusters with SNR > 5 in FUV, F435W, and F814W filters are included in the plots. The black solid line is the path described by SSPs from 1 Myr to 13 Gyr, 0.4 Z_{\odot} , and $A_V=0$ mag. The greyscale lines are the paths for the same models reddened by 1 to 3 mag, with the lighter shades tracing the more extinguished models.

affected by high values of extinction, between 2 - 4 mag. However, given the location of some of these clusters in the diagram of Figure 6.3, the less affected by extinction, we found they are younger than the off-nuclear ones (the blue ones), with ages younger than 50 Myr. This suggests that the nuclear region of NGC 2623 is slightly younger than its surroundings.

The greater scatter is in the circumnuclear clusters, that is, the green ones. They are consistent with an average extinction of around 1 mag. Given their spread in the diagrams they are compatible with having ages ranging from 1 - 500 Myr.

6.3.3. Clusters masses

We found that NICMOS 1.6 μm band is the most sensitive to mass variations. We will estimate the mass range of the star clusters, by comparing their 1.6 μm absolute magnitude with the absolute magnitude of SSP models of masses ranging from 10^4 to $10^8 M_{\odot}$. The results are shown in Figure 6.5. This is an optical color-color vs NIR 1.6 μm absolute magnitude diagram. The paths from models of 10^4 , 10^5 , 10^6 , 10^7 , and $10^8 M_{\odot}$ are shown as solid and dashed lines. The models have been cut between 1 - 500 Myr, as we know from the previous section that these are the older ages our clusters can have.

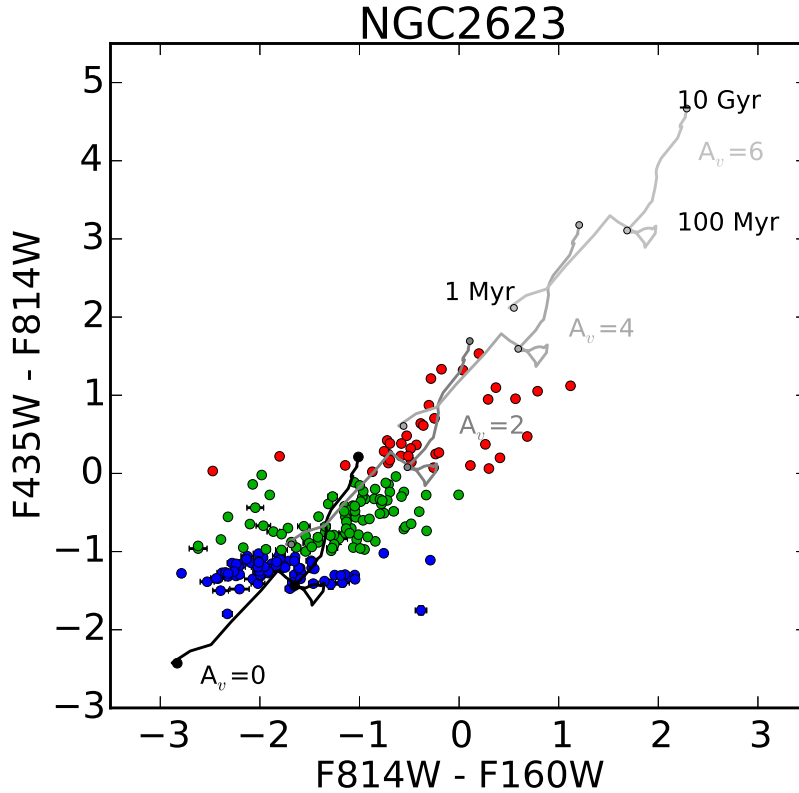


Figure 6.4 F435W - F814W vs F814W - F160W diagram for NGC 2623 clusters. Only clusters with SNR > 5 in F435W, F814W, and F160W filters are shown. The black solid line is the path described by SSPs from 1 Myr to 13 Gyr, $0.4 Z_{\odot}$, and $A_V=0$ mag. The greyscale lines are the paths for the same models but reddened by 2, 4, and 6 mag.

We found a large range of masses in the clusters of NGC 2623. The intermediate-age clusters in the region south of the nucleus (the blue ones) have masses from $10^4 - 10^5 M_{\odot}$. For the circumnuclear (green ones) the spread is larger $10^4 - 10^7 M_{\odot}$. On the other hand, the vast majority of the inner nuclear clusters (red ones) are consistent with masses between $10^6 - 10^8 M_{\odot}$. These impressively large masses are comparable to the most massive globular clusters seen in giant elliptical galaxies and the massive, intermediate-age clusters seen in NGC 7252 and NGC 1316 (Maraston et al., 2004; Bastian et al., 2006), and some YMC in Arp 220 (Wilson et al., 2006). Of course, their masses are expected to decrease over the next 500 Myr due to the combined effects of stellar mass loss, supernova-driven winds, and tidal trimming in the central galaxy potential.

We have performed a rough estimate of the total mass in clusters in NGC 2623, by assigning a certain average mass for the clusters in each luminosity $L_{1.6\mu m}$ range. In particular, we have separated the clusters in five possible luminosity ranges: if $\log L_{1.6\mu m} < 0.9$ we assign a mass of $\sim 10^4 M_{\odot}$, from $0.9 < \log L_{1.6\mu m} < 1.5$ we assign a mass of $\sim 10^5 M_{\odot}$, if $1.5 < \log L_{1.6\mu m} < 2.65$ then $\sim 10^6 M_{\odot}$, if $2.65 < \log L_{1.6\mu m} < 3.5$ then $\sim 10^7 M_{\odot}$, and above $\log L_{1.6\mu m} > 3.5$ we assign $\sim 10^8 M_{\odot}$. In the case of NGC 2623 we have 39, 64, 75, 22, and 3 clusters in each range, leading to a total cluster mass of $M_{NGC2623}^{clus} \sim 6 \times 10^8 M_{\odot}$. As we will discuss in Section 6.4.10, this mass is in agreement with the one we derived from the spectroscopy for the young-intermediate stellar components.

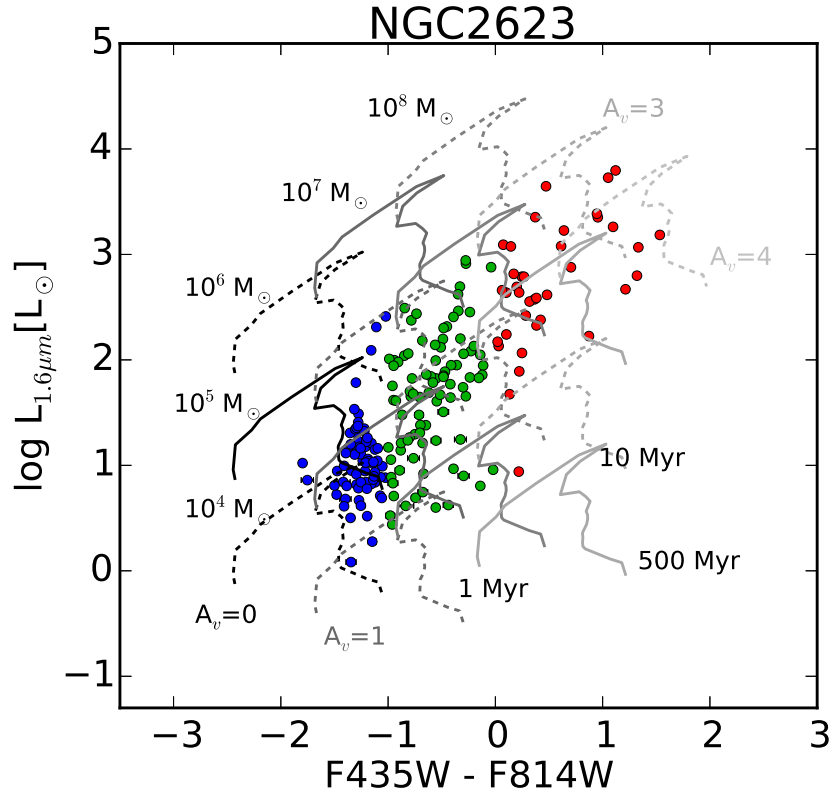


Figure 6.5 Right: NIC 1.6 μm absolute magnitude vs F435W - F814W diagram. Only clusters with SNR > 5 in F435W, F814W and F160W filters are shown. The solid and dashed lines are the path of SSPs from 1 Myr to 500 Myr and with masses from 10^5 to $10^8 M_{\odot}$. The greyscale coding represents the variation in stellar extinction as in previous figures.

6.4. Stellar populations

In this section we use the stellar continuum shape to characterize the spatially resolved stellar population properties and constrain the star formation history of NGC 2623. We investigate how widespread the star formation was, and if it continues to the present time.

6.4.1. Methodology

Adequate signal-to-noise ratio in the stellar continuum is vital to extract robust ages, metallicities and star formation histories from continuum spectra in which we observe the integrated light of multiple stellar populations. For CALIFA data a Voronoi binning algorithm was used to combine the spectra in neighbouring spaxels until a combined spectrum of sufficient S/N (> 20 at 5650 \AA) was obtained. For consistency with CALIFA data, the S/N was calculated in the rest-framed window between 5590 and 5680 \AA . All spaxels with $S/N < 5$ were discarded from the analysis. In Figure 6.6 we show the S/N maps of NGC 2623 for CALIFA and LArr data, calculated in $5635 \pm 45 \text{ \AA}$. Color scale is the same in both maps and goes from 5 to 75. Superimposed in contours is the HST F555W image, smoothed to a spatial resolution of ~ 2.0 arcsec, intermediate between LArr data (~ 1.7 arcsec) and

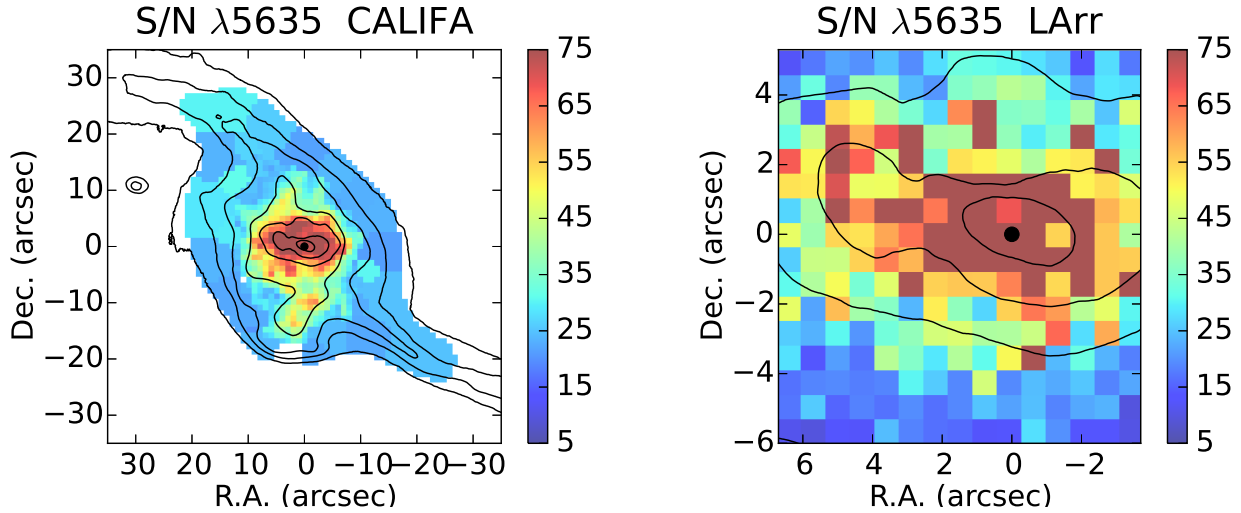


Figure 6.6 S/N ratio maps calculated in $5635 \pm 45 \text{ \AA}$ interval. Color scale is the same for both maps and goes from 5 to 75. The HST F555W image is superimposed in contours, smoothed to approximately match the spatial resolution of our IFS. Left panel: CALIFA data, already in Voronoi zones. In this case every spaxel/zone has $S/N > 20$. Right panel: LArr data for the nuclear region of NGC 2623.

CALIFA data ($\sim 2.4 \text{ arcsec}$) spatial resolutions.

In the case of CALIFA data all the process of analysis is described in detail in [Cid Fernandes et al. \(2013, 2014\)](#). For the LArr data the main steps are the same, with several differences. The methodology of the analysis is explained in detail in Section 5.4.1. As in previous chapter, we have used the same two model bases to perform the spectral synthesis, the so called GM base and CB base. Although the maps and results shown rely on the GM base, in Section 6.4.11 we will describe how the results would change with CB base.

We used *PyCASSO* code ([Amorim et al. in prep.](#)) to handle the synthesis results for CALIFA data and our own Python macros in the case of LArr data.

6.4.2. Fit quality

The quality of the spectral fits should be examined before proceeding to interpretation of the results. The fit quality indicator $\overline{\Delta}$ defined by [Cid Fernandes et al. \(2013\)](#) is explained in Section 5.4.2. Experiments with the whole CALIFA data set suggest that $\overline{\Delta} = 10\%$ is a reasonable quality-control limit.

In Figure 6.7 we show the $\overline{\Delta}$ maps for NGC 2623 CALIFA (left) and LArr (right) data. The color scale in both maps is the same, and goes from 0 to 10. As can be seen, the larger residuals ($\overline{\Delta} > 10\%$) are located in the outer regions. For CALIFA data it only happens in a few, while for LArr this number is greater. We visualize the fits and found the $S/N = 5$ limit used in our LArr data too low for the spectral synthesis. Generally, $\overline{\Delta} < 10\%$ when $S/N > 20$. From now on, only the spaxels with $\overline{\Delta} < 10\%$ are shown in the maps and considered in the analysis.

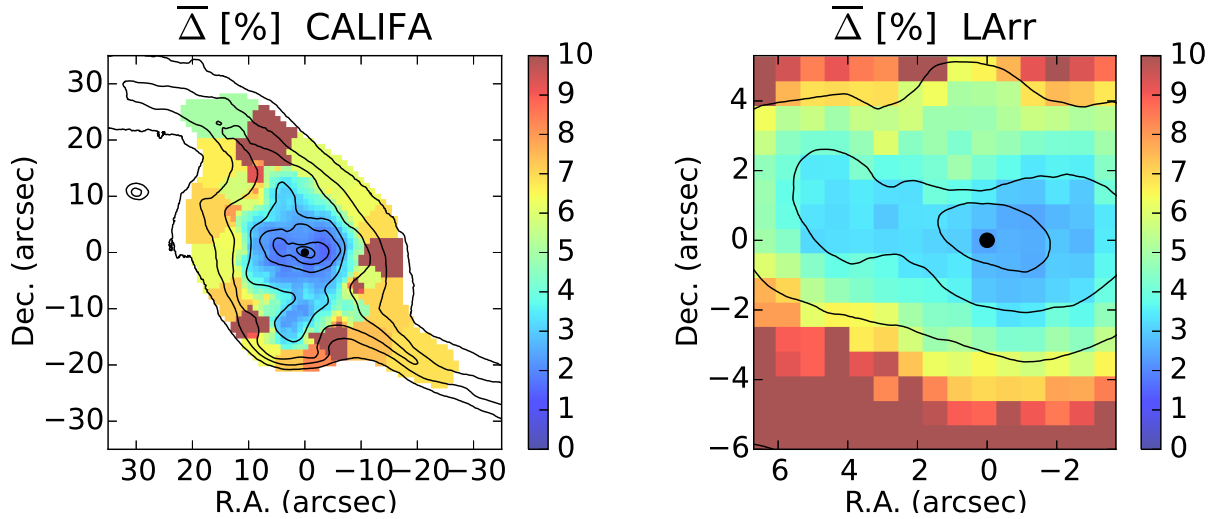


Figure 6.7 Mean relative deviation maps $\bar{\Delta}$, tracing the quality of the fits. Only spaxels/zones with $\bar{\Delta} < 10\%$ are considered in the analysis. Contours represent the smoothed HST F555W emission. Left panel: CALIFA data. Right panel: LArr data.

6.4.3. Stellar luminosity

In Figure 6.8 we show the observed surface brightness map at 5635 \AA (not dust-attenuation corrected) for CALIFA and LArr data, and the radial profiles for both datasets. The upper left panel is the total CALIFA map. The white dashed lines indicate the position of 1, 2, and 3 Half Light Radius (HLR). In this case 1 HLR is equivalent to 3.3 kpc in physical distance. The upper right panels are the LArr map and a zoom of the CALIFA map in the same region covered by LArr data. Azimuthal averaging of the maps is another option to compress this result in a easier to compare way. *PyCASSO* code provides circular convolution tensors to obtain the radial profiles of the CALIFA and LArr 2D maps as a function of radius in units of kiloparsecs or HLR. The lower panel shows the radial profile of the surface brightness density as a function of the radial distance in HLR, in red for LArr and black for CALIFA. The light-red and grey points are the values from all the spectra we have at each radius. As it can be seen in the lower panel, there exists a good agreement in the measured surface brightness density from the two datasets. The stellar luminosity at 5635 \AA decreases uniformly from $0.1 L_{\odot} \text{ pc}^{-2} \text{ \AA}^{-1}$ in the nucleus of NGC 2623 to $0.003 L_{\odot} \text{ pc}^{-2} \text{ \AA}^{-1}$ in the outskirts.

6.4.4. Stellar dust extinction

Another important *Starlight* output is the stellar extinction. While the effects of the Voronoi binning are present in all panels, they are much more salient in the maps of intensive properties, as the A_V map. This is because the extensive properties maps (luminosity and mass) were "dezonified" by scaling the value at each xy spaxel by its fractional contribution to the total flux in a zone (z). For example, for the luminosity surface density in the previous section we have applied:

$$L_{xy} = \frac{L_{xy}}{A_{xy}} = \frac{L_z}{A_z} \times w_{xyz} \quad (6.1)$$

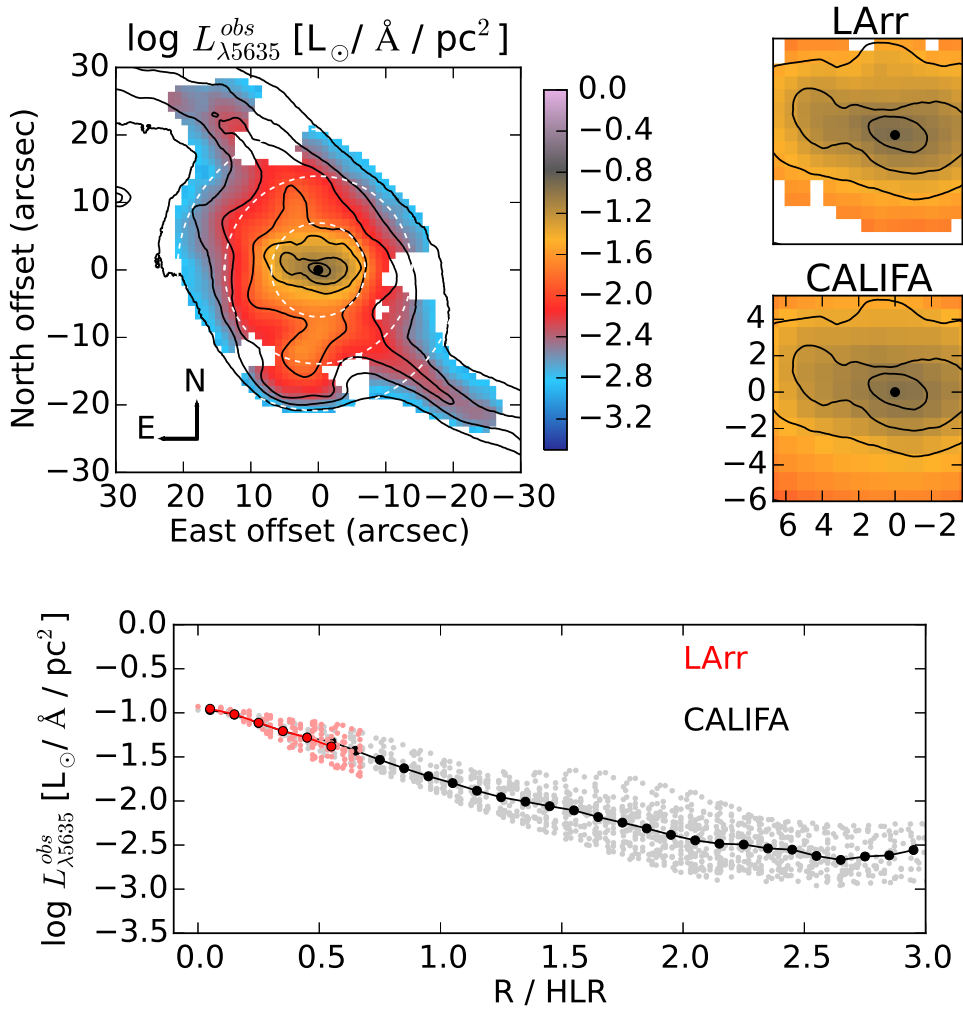


Figure 6.8 Upper left: Observed surface brightness CALIFA map in logarithmic scale (at 5635\AA). The white dashed lines indicate the position of 1, 2, and 3 Half Light Radius (HLR). 1 HLR is equivalent to 3.3 kpc in physical distance. The contours correspond to the smoothed HST F555W image. Upper right: observed surface brightness LArr map in logarithmic scale (at 5635\AA). Same color scale as the CALIFA map. Below it is a zoom of the CALIFA map in the nuclear region, to match the region covered by LArr map. Lower panel: radial profile of the observed surface brightness as a function of the radial distance in HLR, in red for LArr and black for CALIFA. The light-red and grey points are the values measured for all the spectra in the datacubes.

where A_{xy} (A_z) denotes the area in a spaxel (zone), and

$$w_{xyz} = \frac{F_{xy}}{\sum_{xyz} F_{xy}} \quad (6.2)$$

with F_{xy} being the mean flux at $5635 \pm 45 \text{\AA}$ region (for more details and the analogous equations for mass surface density see Section 5.2 of [Cid Fernandes et al. 2013](#)). This operation was applied to luminosity and mass related quantities, producing somewhat smoother images than obtained with $w_{xyz}=1$. Intensive properties like A_V , mean ages, and metallicities, however, cannot be dezonified.

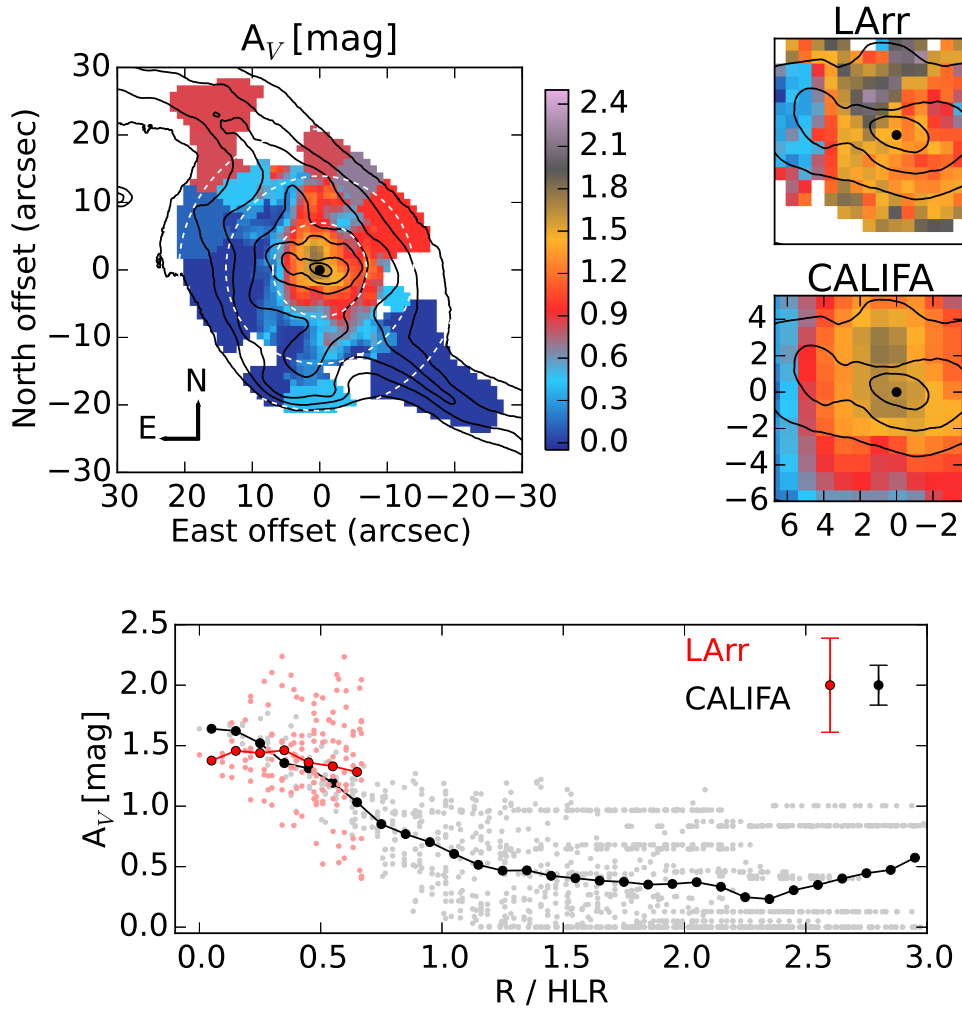


Figure 6.9 Upper left: CALIFA map of the stellar dust extinction. The white dashed lines indicate the position of 1, 2, and 3 Half Light Radius (HLR). 1 HLR is equivalent to 3.3 kpc in physical distance. The contours correspond to the smoothed HST F555W image. Upper right: LArr map of stellar dust extinction. Same color scale as the CALIFA map. Below it is a zoom of the CALIFA map in the nuclear region, to match the region covered by LArr map. Lower panel: radial profile of the stellar dust extinction as a function of the radial distance in HLR, in red for LArr and black for CALIFA. The light-red and grey points are the values measured for all the spectra in the datacubes. The dispersion of the data at 0.5 HLR are shown with a black (red) errorbars for PPAK (LArr).

The stellar extinction maps are shown in Figure 6.9. The Figure distribution is the same as in Figure 6.8. The upper left panel is the total CALIFA map. The upper right panels are the LArr map and a zoom of the CALIFA map in the same region covered by LArr data. The lower panel shows the radial profile of the dust extinction as a function of the radial distance in HLR, in red for LArr and black for CALIFA. In the CALIFA map we found significant variations in the dust distribution, with most of the dust located in the central (inner kpc) regions, reaching values up to 2 mag. The dust content is decreasing with distance to the nucleus to < 1 mag outside the inner 0.8 HLR (~ 2.6 kpc). Moreover, we found that the north tidal tail is affected by ~ 1 mag, while the south tidal tail

is almost no dust obscured. The global average is $A_V \sim 0.5$ mag.

In the innermost nuclear regions (≤ 0.6 HLR), we have data from both CALIFA and LArr datasets. At 0.5 ± 0.1 HLR, we found $A_V^{LArr} = 1.37 \pm 0.33$ mag and $A_V^{PPAK} = 1.29 \pm 0.20$ mag. Considering the dispersion of both datasets, above 0.2 HLR they are indistinguishable from each other. In the lower panel of Figure 6.9 we show the dispersion at 0.5 HLR with a black errorbar for PPAK and a red errorbar for LArr. Only in the nucleus itself (inner to 0.2 HLR) we derive slightly lower extinctions from LArr (~ 1.4 mag) than from CALIFA (~ 1.6 mag). As explained in next section, we believe the nuclear differences in the stellar population properties derived with PPAK and LArr are due to a combination of differences in the PSFs of PPAK and LArr, and also, to the age-extinction degeneracy.

NGC 2623 shows a negative gradient in A_V , as also happens in Sb to Sc spirals in CALIFA sample (GD2015). However, in NGC 2623 the profile flattens in the center, instead of keep growing like in spirals. Moreover, in Sb to Sc the absolute variation of A_V in the inner 1HLR is ~ 0.3 mag, while in NGC 2623 the variation is approximately three times larger, ~ 0.9 mag. We believe that this is due to the accumulation of gas and dust in the central regions which occurs in the final stages of mergers.

6.4.5. Age

The mean stellar ages have been obtained applying equation 5.5, as explained at the beginning of Section 5.4.5. The mean stellar age maps are shown in Figure 6.10. The scale in CALIFA and LArr maps is the same to facilitate the comparison and goes from $\langle \log age[yr] \rangle_L = 7.5$ to 9.5. From the CALIFA map we found that the younger regions are the nucleus, the region rich in star clusters located south of the nucleus, and the north tidal tail, with mean ages around 250 Myr. On the other hand, the south tidal tail, and the eastern region of the main body, are older, with ages around 1 Gyr. In the circumnuclear regions we find a positive trend of the ages with distance, from ~ 200 Myr in the nucleus itself to ~ 500 Myr at 1 HLR. This positive trend of age with distance is expected in advanced mergers where the gas inflows into the nuclear regions, triggering new star formation episodes that rejuvenates them. It is also interesting to note that everywhere in this system the mean stellar ages range between 140 Myr to 1.4 Gyr.

Again, when comparing both datasets, we found that above 0.2 HLR they are indistinguishable from each other, considering the dispersions. At 0.5 ± 0.1 HLR, we found $\langle \log age \rangle_L^{LArr} = 8.74 \pm 0.29$ mag and $\langle \log age \rangle_L^{PPAK} = 8.58 \pm 0.12$ mag. The dispersions at 0.5 HLR have been shown in the lower panel of Figure 6.10 with a black errorbar for PPAK and a red errorbar for LArr. Inner to 0.2 HLR, the ages derived from LArr are 360 - 570 Myr older than CALIFA.

There are two possible origins to the differences between the stellar ages and extinctions derived in the nucleus with PPAK and LArr. On the one hand, the spatial resolution of LArr (~ 1.7 arcsec) is better than CALIFA (~ 2.4 arcsec) and, as a consequence, small scale variations are softer for the latter. On the other hand, the nuclear region is very dusty, and as we have mentioned before, we have an age-extinction degeneracy. While the shape of the spectra of both datasets is almost identical, with LArr data we derive older ages and smaller extinctions (810 Myr, 1.43 mag), while for CALIFA data we estimate younger ages but higher extinctions (240 Myr, 1.65 mag). There is a maximum variation of the properties of 0.5 dex in the ages and 0.2 mag in A_V . These variations give us an idea of the uncertainties with which we can derive the different properties in the particular case of the obscured nuclear region.

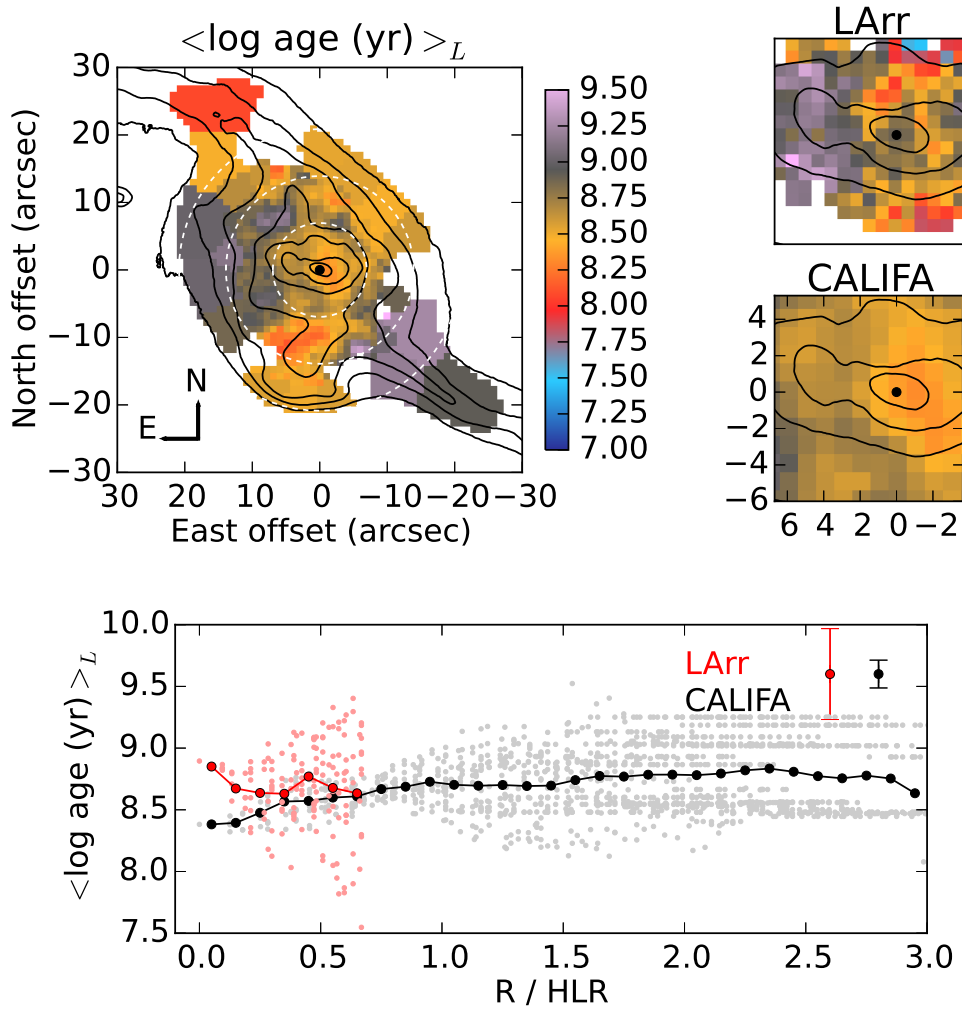


Figure 6.10 Upper left: CALIFA map of the mean stellar ages. The white dashed lines indicate the position of 1, 2, and 3 Half Light Radius (HLR). 1 HLR is equivalent to 3.3 kpc in physical distance. The contours correspond to the smoothed HST F555W image. Upper right: LArr map of the mean stellar ages. Same color scale as the CALIFA map. Below it is a zoom of the CALIFA map in the nuclear region, to match the region covered by LArr map. Lower panel: radial profile of the mean stellar ages as a function of the radial distance in HLR, in red for LArr and black for CALIFA. The light-red and grey points are the values measured for all the spectra in the datacubes. The dispersion of the data at 0.5 HLR are shown with a black (red) errorbars for PPAK (LArr).

From both LArr and PPAK results we found that the age radial profile of NGC 2623 is much flatter than in isolated spiral galaxies, which show a decreasing radial profile (GD2015). Moreover, the nuclear ages in spirals are older than 1 Gyr, in contrast with NGC 2623, whose average nuclear age is less than 1 Gyr.

6.4.6. Metallicity

The mean metallicities were obtained by applying the equation 5.6, as explained at the beginning of Section 5.4.6. The mass-weighted metallicity maps are shown in Figure 6.11. The scale range in

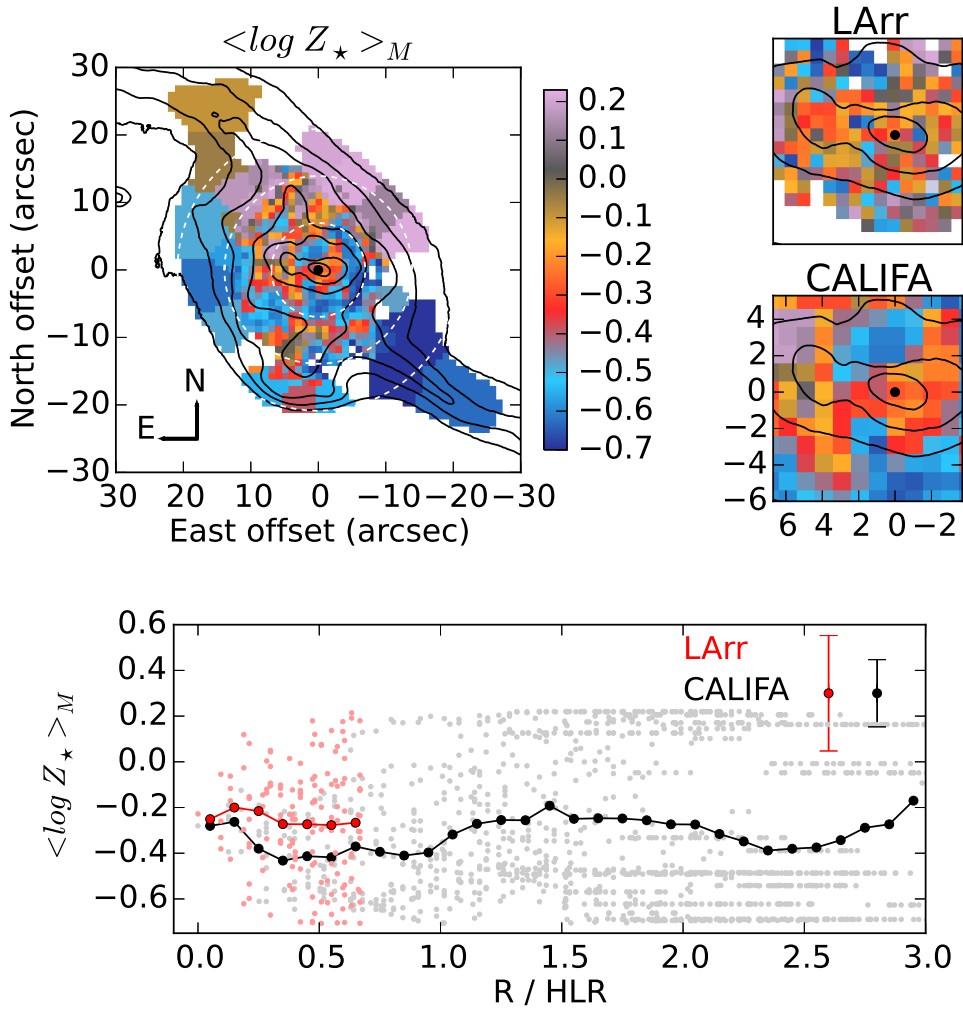


Figure 6.11 Upper left: CALIFA map of the mean stellar metallicity. The white dashed lines indicate the position of 1, 2, and 3 Half Light Radius (HLR). 1 HLR is equivalent to 3.3 kpc in physical distance. The contours correspond to the smoothed HST F555W image. Upper right: LArr map of the mean stellar metallicity. Same color scale as the CALIFA map. Below it is a zoom of the CALIFA map in the nuclear region, to match the region covered by LArr map. Lower panel: radial profile of the mean stellar metallicity as a function of the radial distance in HLR, in red for LArr and black for CALIFA. The light-red and grey points are the values measured for all the spectra in the datacubes. The dispersion of the data at 0.5 HLR are shown with a black (red) errorbars for PPAK (LArr).

both maps is the same, and goes from $\langle \log Z_{\star} \rangle_M = -0.7$ to 0.23 (0.2 to 1.7 Z_{\odot}). Unlike what happens with age and extinction, CALIFA and LArr mean metallicities are almost equal below 0.2 HLR. Above 0.2 HLR, $\langle \log Z_{\star} \rangle_M^{LArr}$ is 0.2 dex higher than $\langle \log Z_{\star} \rangle_M^{CALIFA}$. However, given the dispersion at 0.5 HLR, 0.14 dex for CALIFA and 0.23 dex for LArr, they can be considered equal.

Metallicity in one of the most difficult quantities to constrain. The fact that sometimes age and Z grow in the opposite sense, as in the tails of NGC 2623, could suggest that the results are affected by the age-metallicity degeneracy. The north tail is young (300 Myr) and metal rich (1.5 Z_{\odot}), while the south tail is old (1.4 Gyr) and metal poor (0.25 Z_{\odot}). Due to this, we will take the metallicity results

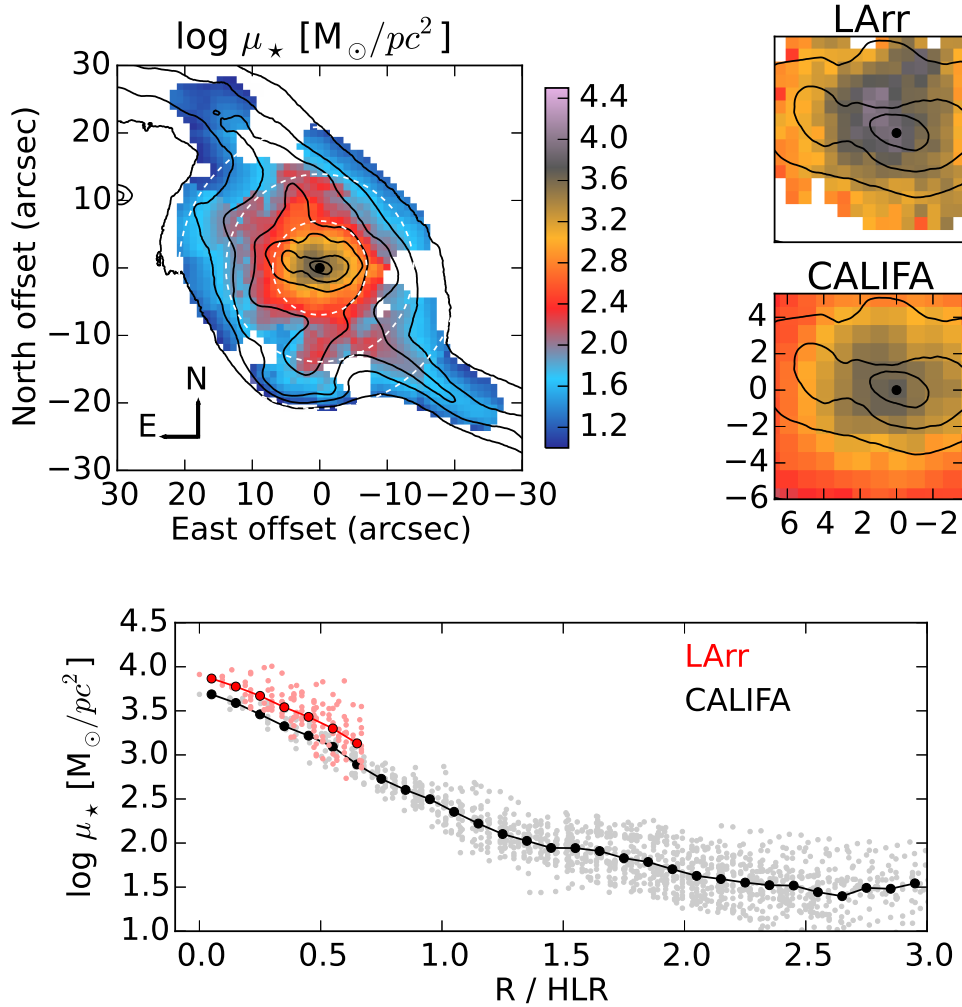


Figure 6.12 Upper left: CALIFA map of the stellar mass density. The white dashed lines indicate the position of 1, 2, and 3 Half Light Radius (HLR). 1 HLR is equivalent to 3.3 kpc in physical distance. The contours correspond to the smoothed HST F555W image. Upper right: LArr map of the stellar mass density. Same color scale as the CALIFA map. Below it is a zoom of the CALIFA map in the nuclear region, to match the region covered by LArr map. Lower panel: radial profile of the stellar mass density as a function of the radial distance in HLR, in red for LArr and black for CALIFA. The light-red and grey points are the values measured for all the spectra in the datacubes.

with caution. Moreover, as can be seen in the lower panel, the scatter is really large.

Focusing on the mean value it seems that NGC 2623 has a mean metallicity of $\sim 0.5 Z_{\odot}$. Moreover, the metallicity radial profile is fairly flat, as would be expected for an advanced merger where significant gas inflows have occurred (Rich et al., 2012; Kewley et al., 2010). This flat radial behaviour in the metallicity of NGC 2623, contrast with the negative radial gradient of spirals indicative of the inside-out growth of disks (GD2015).

6.4.7. Stellar mass surface density

In Figure 6.12 we show the stellar mass surface density maps, $\log \mu_*$, for CALIFA and LArr data, and the radial profiles for both datasets. We found a negative trend of $\log \mu_*$ with distance. From the CALIFA map we found that it decreases from $\log \mu_* \sim 3.7$ in the nucleus itself to $\log \mu_* \sim 1.5$ in the outer parts at 3 HLR. Stellar mass surface densities from LArr data are 0.2 dex larger than CALIFA, due to the differences in the other stellar population properties.

The stellar mass central density in NGC 2623 vary from $\log \mu_* \sim 3.7$ in the nucleus to $\log \mu_* \sim 2.6$ at 1 HLR, which involves 1.1 dex change. This behaviour is a bit flatter but comparable to Sbc galaxies in CALIFA sample, whose stellar mass central density vary from $\log \mu_* \sim 3.8$ in the nuclei to $\log \mu_* \sim 2.4$ at 1 HLR, with a total variation of 1.4 dex (GD2015).

6.4.8. Stellar mass

Another important *Starlight* output is the stellar mass, calculated from the stellar luminosity and taking into account the mass to light ratio of the different SSPs. The total stellar mass obtained summing the mass of each zone is $M = 4.5 \times 10^{10} M_\odot$. This is the mass locked in stars nowadays. Counting also the mass returned by stars to the interstellar medium $M' = 6.3 \times 10^{10} M_\odot$ were involved in star formation. These are the results for GM base of models, with Salpeter IMF. With CB base (Chabrier IMF) we found $M' = 4.4 \times 10^{10} M_\odot$ and $M = 2.4 \times 10^{10} M_\odot$. The last one being very similar to the photometric mass from SDSS derived by the CALIFA collaboration, using BC03 models $M_{phot} \sim 2.8 \times 10^{10} M_\odot$.

Moreover, we know the dynamical mass from [Privon et al. \(2013\)](#); $M_{dyn} \sim 6 \times 10^{10} M_\odot$. Since it is the same order as our stellar mass, we believe we are not underestimating the masses with the optical spectral synthesis.

6.4.9. 1D Star Formation Histories

The 1D Star Formation Histories are obtained by collapsing the spatial information, summing the SFH of every single spaxel in the datacube, keeping the whole age range used in the spectral fitting so we can get a detailed idea of when the bursts of star formation started and how many of them occurred.

In Figure 6.13 we present the total 1D SFHs in light (upper panel) and mass (lower panel) of NGC 2623. They x axis represent the ages of the SSPs included in our base, while the y axis represents the average light (or mass) fraction calculated over all spaxels in the cubes, for a given age. From the top panel we found that there could have been two relevant "young" bursts between 5 Myr to 13 Myr ago. However, the spectral differences between these 2 SSPs are not enough to distinguish (within our temporal resolution) if they were individual bursts or something more "continuous". Within the intermediate/intermediate-old age range we found that two bursts may have occurred, the less intense peaking at 1.4 Gyr and the more intense peaking around 500 Myr but ranging from 300 Myr to 1 Gyr. The old populations formed between 14 Gyr and 4 Gyr ago for NGC 2623. The lower panel show the mass fraction formed in NGC 2623 as a function of time. As usual, due to the highly non-linear relation between light and mass in stars, the young populations that show up so well in light practically disappear when seen in mass. However, the intermediate age stellar population are clearly

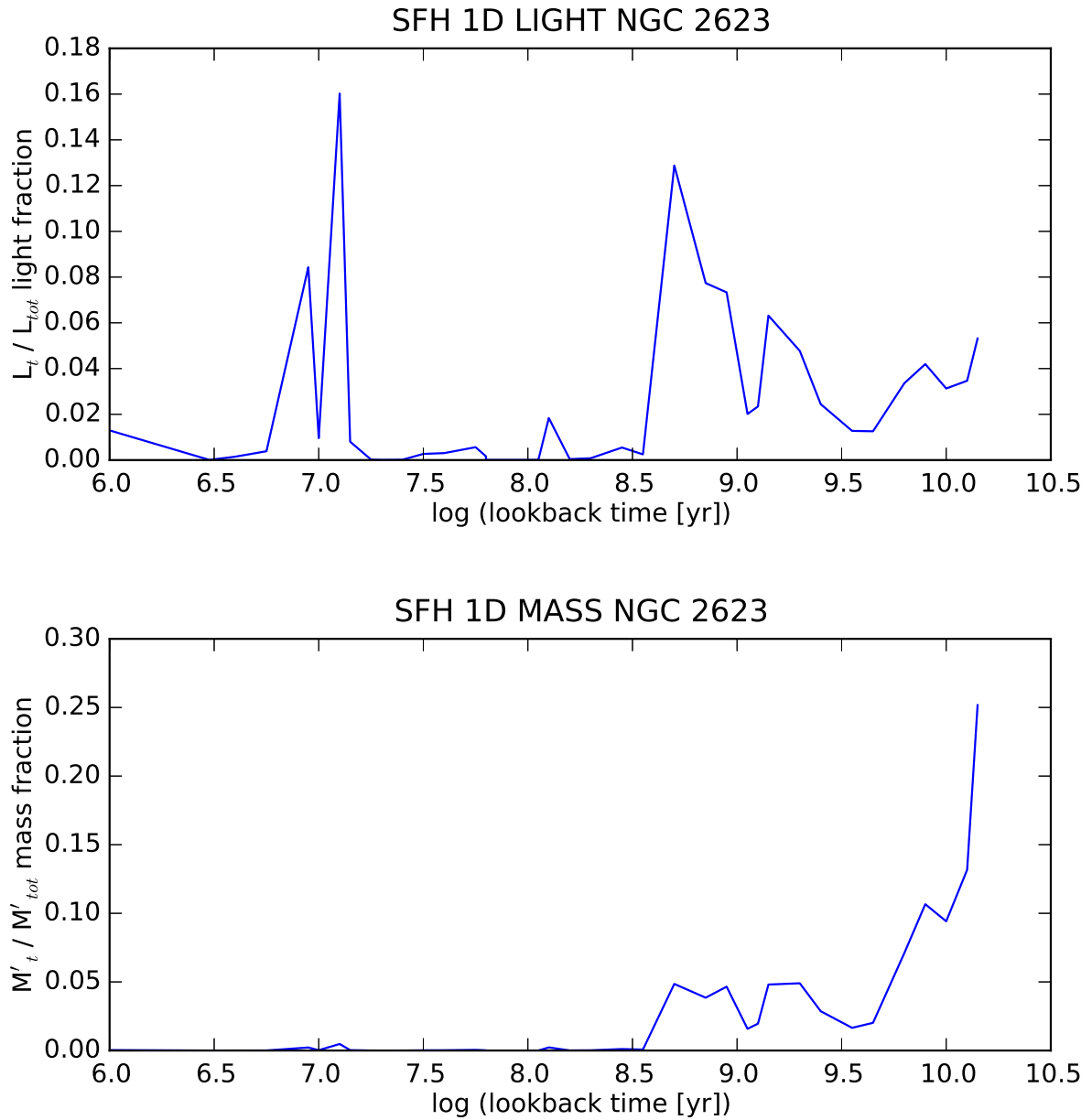


Figure 6.13 Total 1D Star Formation Histories in light (upper panel) and mass (lower panel). The x axis represents the ages of the SSPs included in our base, while the y axis represents the total luminosity (or mass) summed over all spaxels in NGC 2623, for a given age. In the top panel, the two periods of increased star formation can be seen around 10 Myr and 500 Myr. The lower panel shows the total stellar mass formed in NGC 2623 as a function of time. As usual, due to the highly non-linear relation between light and mass in stars, the young populations that show up so well in light practically disappear when seen in mass.

seen in mass, confirming that their contribution to the total mass of the system is not negligible.

The SFH of NGC 2623 is analyzed in much more detail in Section 8.1.3.

6.4.10. Contribution of young, intermediate and old populations

As in Section 5.4.10, here we study the spatially resolved SFH, by condensing the age distribution encoded in the population vector into three age ranges: the so called young stellar populations (YSP, SSPs ≤ 140 Myr), intermediate age stellar populations (ISP, $140 \text{ Myr} < \text{SSPs} \leq 1.4 \text{ Gyr}$), and old stellar populations (OSP, SSPs $> 1.4 \text{ Gyr}$). We select these three age bins to correspond to the main sequence lifetimes of stars with distinctly different optical line and continuum features.

In Figure 6.14 we present the images of the light fraction due to YSP, ISP, and OSP (x_Y , x_I , and x_O). We found that YSP are only important in the nuclear region, the north tidal tail and the region rich in star clusters located south of the nucleus, with contributions to total light between 40 - 70 % (left panel Figure 6.14). The ISP dominates the light almost everywhere (60 %, middle panel Figure 6.14), except in the nucleus itself and the south tidal tail. It is interesting to note the presence of this widespread ISP in this merger. On the other hand, the only region which is clearly dominated by OSP is the south tidal tail, with a contribution to light of ~ 70 %. They are also responsible of 30 % of the nuclear light (right panel Figure 6.14).

In Figure 6.15 we show the radial profiles of the contributions to light of young x_Y , intermediate x_I , and old x_O populations in blue, green, and red colors, respectively. We found that below 1.5 kpc (0.6 HLR) the light is dominated by YSP, with contributions between 35 - 60 %. Above 1.5 kpc and up to 9 kpc the light is clearly dominated by ISP, also with contributions between 35 - 60 %.

Analogously, in Figures 6.16 and 6.17, we present maps of the mass contribution in percentage due to young, intermediate, and old populations (m_Y , m_I , and m_O) and their radial profiles. The fraction of stellar mass contributed by YSP is less than 5 % everywhere, except maybe in the north tidal tail, where it can be up to 30 %. Most of the mass is contained in OSP. In particular, they dominate the mass contribution below 4 kpc (1.5 HLR), as can be seen in Figure 6.17. Above it, the mass contribution of the ISP is also significant, between 40 - 60 %, similar to the old stars contribution.

When summing the total mass in each age bin, we found that from the total $M' = 6.3 \times 10^{10} M_\odot$ in NGC 2623, the mass in young $M'(Y)$, intermediate age $M'(I)$ and old $M'(O)$ stellar populations is $8.1 \times 10^8 M_\odot$ (1 %), $1.4 \times 10^{10} M_\odot$ (22 %), and $4.8 \times 10^{10} M_\odot$ (77 %), respectively.

The mass in young components (of $\lesssim 300$ Myr) derived through the IFS is comparable (only a factor ~ 1.5 less) to the mass in star clusters derived roughly from the photometry, which is $M_{clus}^{NGC2623} \sim 6 \times 10^8 M_\odot$ (see Section 6.3.3). This would agree with the hypothesis that the vast majority of stars form in clusters rather than in isolation.

6.4.11. Comparison of results with base CB

As mentioned at the end of Section 6.4.1, we performed two sets of *Starlight* fits using the so-called GM and CB bases. So far, we have presented the results with GM base. Focusing only on CALIFA data, here we will describe the main differences in the derived stellar population properties if we consider the base CB.

Cid Fernandes et al. (2014) calculate the uncertainties in the stellar population properties due to the choice of model base (GM or CB) for CALIFA data, and also for the noise and shape-related

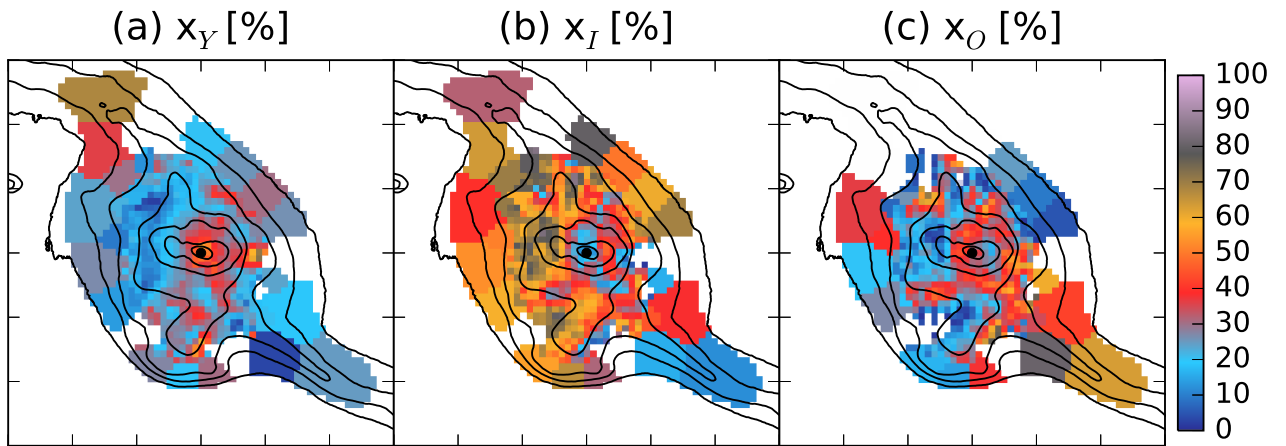


Figure 6.14 From left to right: Maps of the contribution in percentage of young (a) $t < 140$ Myr , (b) intermediate ($140 \text{ Myr} < t < 1.4 \text{ Gyr}$), and old (c) $t > 1.4 \text{ Gyr}$ stellar populations to the observed light at 5635 \AA . Contours represent the smoothed HST F555W image. We found that the young stellar components are concentrated in the nuclear region, the north tidal tail and the region rich in star clusters located south of the nucleus, with contributions to total light between 40-70 %. The intermediate age stellar populations dominate the light almost everywhere (60 %), except in the nucleus itself and the south tidal tail. On the other hand, the only region which is clearly dominated by old SPs is the south tidal tail, with a contribution to light of ~ 70 %. They are also responsible of 30 % of the nuclear light.

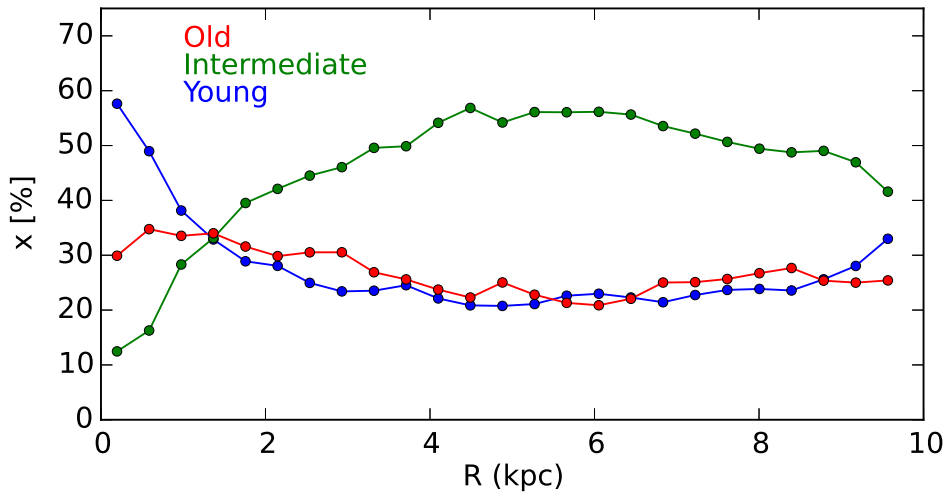


Figure 6.15 Radial profiles of the light contributions from (a) young x_Y (blue), (b) intermediate x_I (green) and (c) old populations x_O (red) with the radial distance in kiloparsec. As can be seen, young stellar populations are dominating the light below 1.5 kpc, while above it, light is clearly dominated by intermediate age stellar populations.

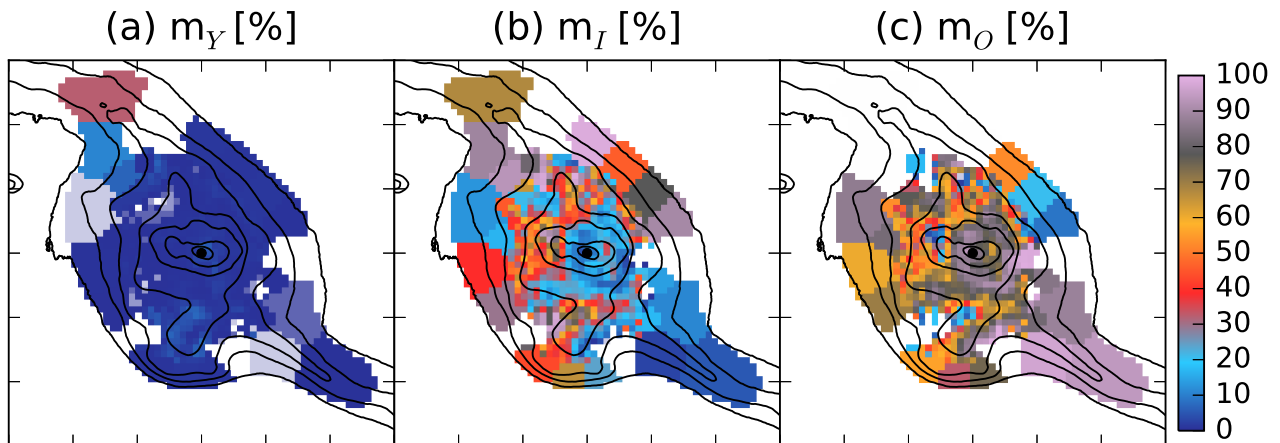


Figure 6.16 From left to right: Maps of the contribution in percentage of young (a) $t < 140$ Myr, (b) intermediate ($140 \text{ Myr} < t < 1.4 \text{ Gyr}$), and old (c) $t > 1.4 \text{ Gyr}$ stellar populations to the total stellar mass. Contours represent the smoothed HST F555W image. The fraction of stellar mass contributed by stars younger than 140 Myr is less than 5% everywhere, except maybe in the north tidal tail, where it can be up to 30%. Most of the mass is contained in old stellar populations.

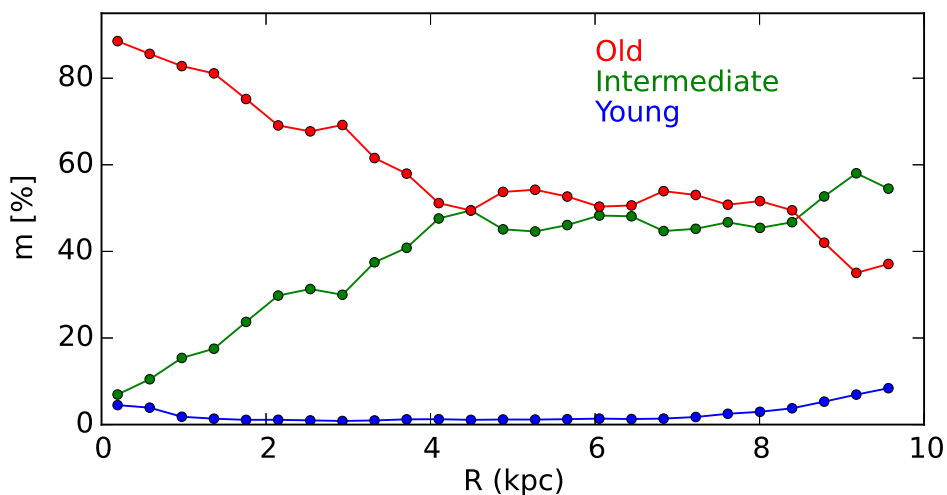


Figure 6.17 Radial profiles of the mass contributions from (a) young x_Y (blue), (b) intermediate x_I (green), and (c) old populations x_O (red) with the radial distance in kiloparsec. The old populations dominate the mass below 4 kpc (1.5 HLR). Beyond it, the mass contribution of the intermediate age stellar population is also significant, between 40 - 60%, similar to the old stars contribution.

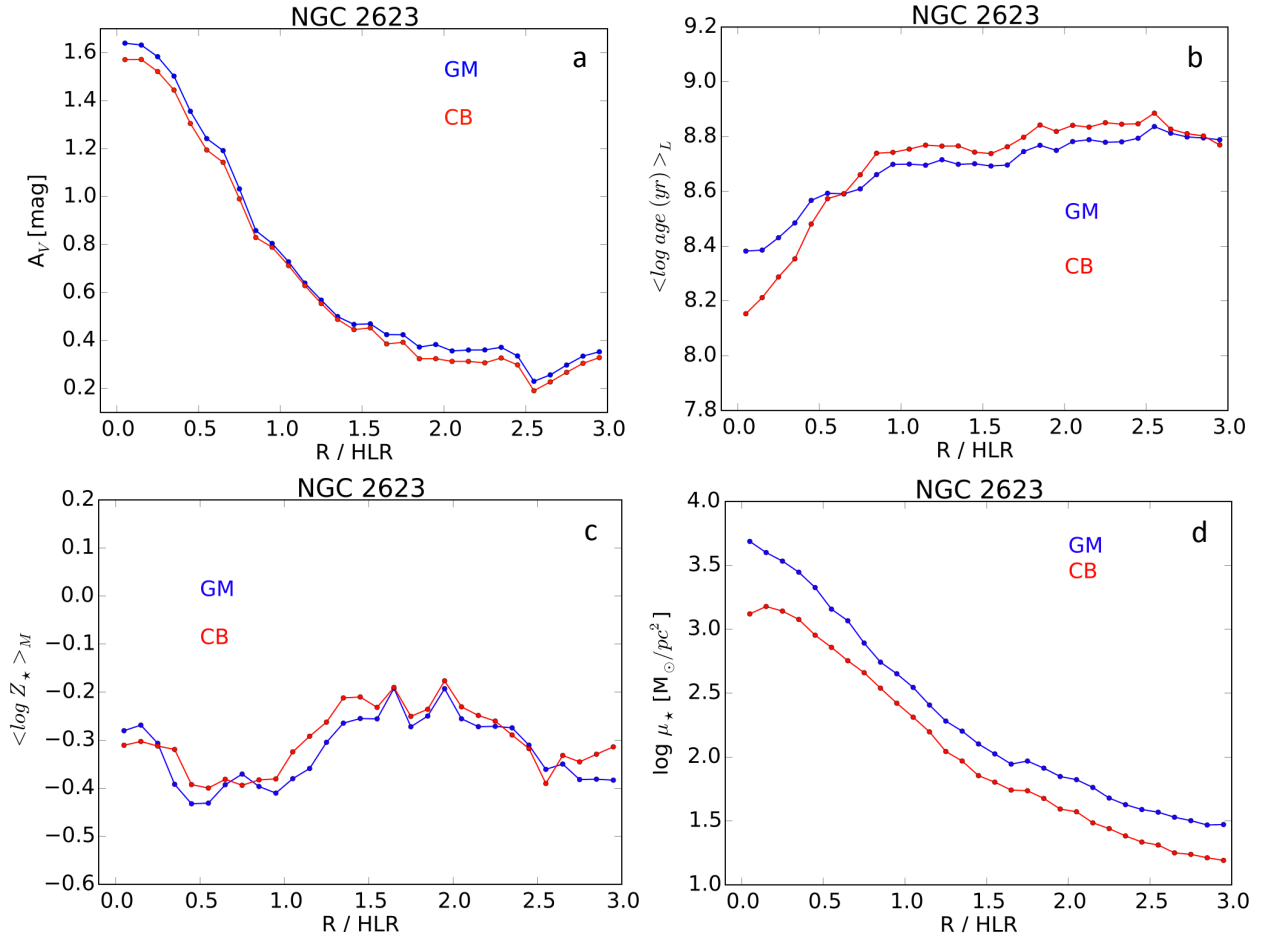


Figure 6.18 Comparison of the radial profiles of the stellar population properties of NGC 2623 for GM base (blue lines) and CB base (red lines). From top left to bottom right we show: (a) stellar dust attenuation, (b) age, (c) metallicity, and (d) stellar mass surface density.

errors. They found that the uncertainties related to the choice of base models are larger than those associated with data and method, with one- σ differences in $\langle \log \text{age} \rangle_L$, A_V , and $\langle \log Z_* \rangle_L$ of ~ 0.15 , 0.08 , and 0.18 dex.

In Figure 6.18 we compare the radial profiles of NGC 2623: (a) stellar dust attenuation, (b) ages, (c) metallicities, and (d) stellar mass surface densities; for GM base of models in color blue and CB base in red. The differences between them are:

- **Dust extinction** is very similar with both bases, with GM returning slightly higher extinctions than CB. Averaging at all distances, GM is 0.04 ± 0.02 mag higher than CB. The difference is less than that found by [Cid Fernandes et al. \(2014\)](#). For A_V they found 0.08 mag due to the base choice and up to 0.16 mag for spectral shape errors.
- **Stellar age.** We found that above 0.6 HLR, CB returns stellar ages ~ 0.1 dex older than GM. This is also within the 0.15 dex error expected from the base choice. Below 0.6 HLR, the trend between bases is reversed, with GM deriving older ages than CB. In the nucleus (inner to 0.2

HLR) the difference reaches up to 0.25 dex. The average difference at all distances is -0.01 ± 0.08 dex.

- **Stellar metallicity** is -0.02 ± 0.03 dex lower with GM than with CB base when averaging at all distances. This difference is not significant given the dispersion. Therefore, they can be considered equal.
- **Stellar mass surface density** is 0.28 ± 0.08 dex higher with GM than with CB base when averaging at all distances. This is due to a combination of the differences in the IMF (~ 0.26 dex, GD2015) and in the other stellar population properties.

6.5. Ionized gas emission

The *Starlight* best fits were subtracted from the observed spectra to obtain 3D cubes with the pure nebular emission line spectra. These emission spectra contain information relative to the ionised gas properties. In this section we present maps of key line ratios sensitive to the ionization mechanism, together with $H\alpha$ luminosity and ionized gas dust attenuation. Hereafter, we focus only in the CALIFA IFS. The methodology we have followed to measure emission line fluxes is described in Section 5.5.1. Moreover, the OSIRIS data will be used to complement these results, we have the $H\alpha$ and $[NII]\lambda 6583$ emission line maps with high spatial resolution.

6.5.1. Ionized gas morphology

Figure 6.19 shows the observed $H\alpha$ emission flux from OSIRIS data (left panel) and CALIFA (right panel), that traces the distribution of ionised gas. They are in units of 10^{-16} erg s $^{-1}$ cm $^{-2}$ and in logarithmic scale to enhance the contrast. As can be seen, OSIRIS emission is more compact than CALIFA. We think this is mainly due to the better spatial resolution of OSIRIS ($\sim 1''$) than CALIFA ($\sim 2.4''$). Moreover, the CALIFA $H\alpha$ emission has been corrected from stellar absorption, while this was not possible in OSIRIS data. We believe these are the reasons why the ionized gas seems to be more compact in OSIRIS than in CALIFA map. In NGC 2623, the vast majority of the ionized gas emission comes from the nuclear regions. Outside the nuclear regions, we also found three star forming knots south of the nucleus, and fainter $H\alpha$ emission in the north tidal tail, detected in both CALIFA and OSIRIS maps.

Lípari et al. (2004) (L04 hereafter), reported the existence of an outflow due to a nuclear dusty starburst in this system, forming a cone-shaped nebulae, with an aperture angle of $\theta \sim 100^\circ$. The orientation and location of the outflow, as reported by L04, is shown with black solid lines in this Figure. This outflowing cone-nebulae fits perfectly the OSIRIS $H\alpha$ emission. In both cases, the emission is quite compact. Attending to CALIFA $H\alpha$ emission, we found that the outflowing nebulae could be in fact more extended than reported by L04. Analogously, in Figure 6.20 we show the observed $[NII]\lambda 6583$ emission flux from OSIRIS data (left panel) and CALIFA (right panel). Its distribution and morphology is very similar to $H\alpha$.

With respect to the morphology, and given the highest spatial resolution of the OSIRIS map, we are able to distinguish several substructures within the cone-nebulae, that are unresolved in the CALIFA and L04 maps. Figure 6.21 zooms into the nuclear regions of OSIRIS $H\alpha$ and $[NII]\lambda 6583$

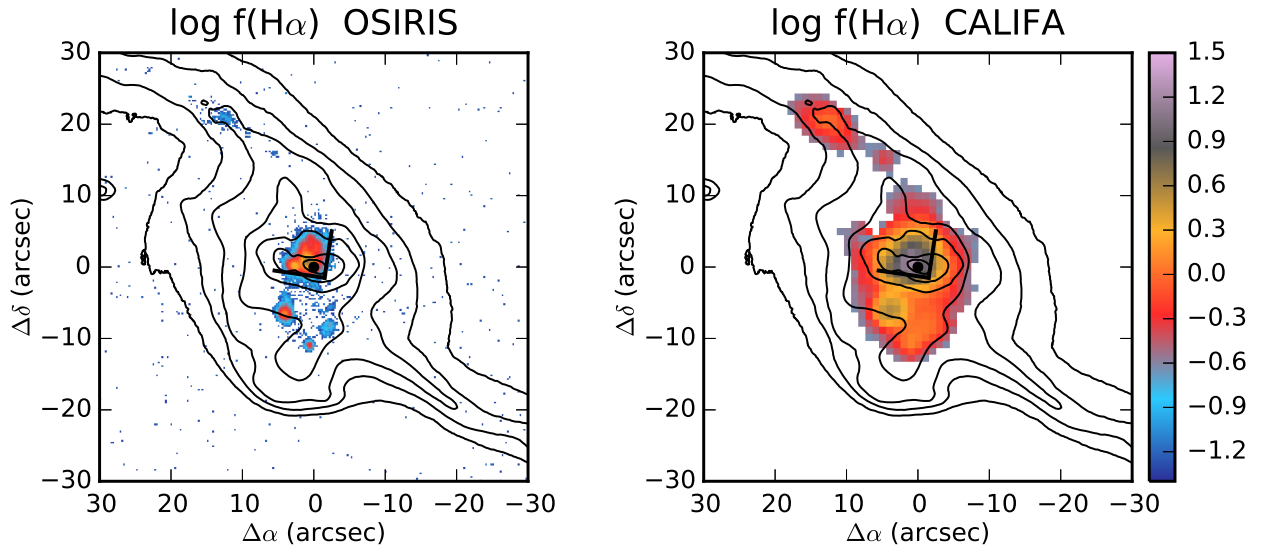


Figure 6.19 OSIRIS $H\alpha$ (left) and CALIFA $H\alpha$ (right) emission line fluxes. They are in units of 10^{-16} $\text{erg s}^{-1} \text{cm}^{-2}$ and in logarithmic scale to enhance the contrast. The black cone delimits the nuclear outflowing nebula reported by [Lípari et al. \(2004\)](#). Outside the nuclear regions, we also found 3 star forming knots south of the nucleus and fainter $H\alpha$ emission in the north tidal tail, detected in both CALIFA and OSIRIS maps. HST F555W image is shown in contours, smoothed to approximately match the spatial resolution of our IFS.

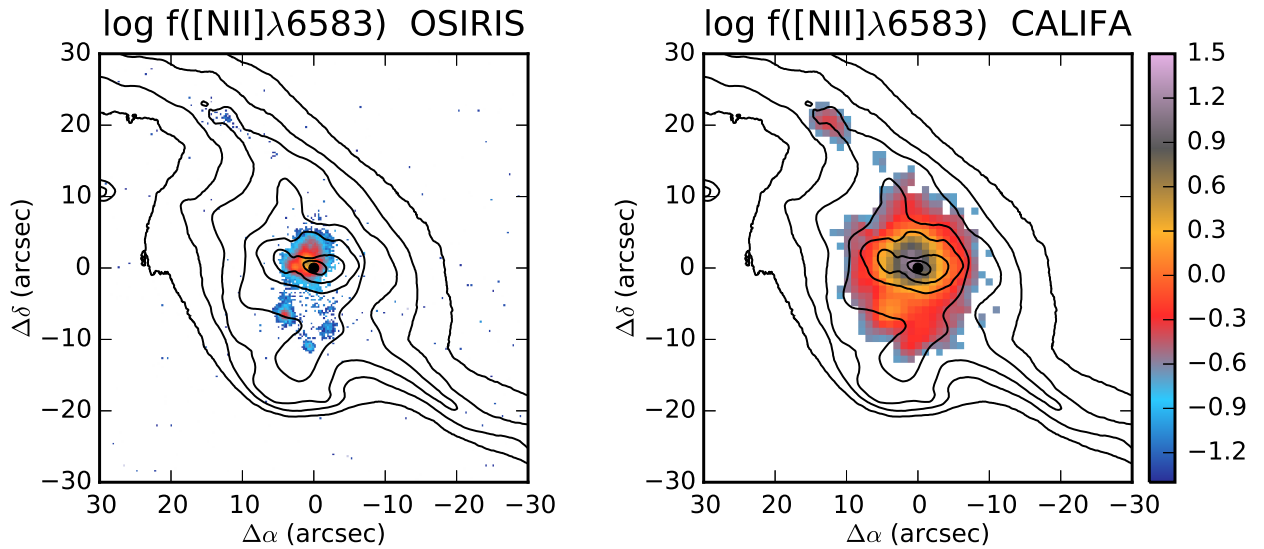


Figure 6.20 Left: OSIRIS $[\text{NII}]\lambda 6583$ emission line flux in units of 10^{-16} $\text{erg s}^{-1} \text{cm}^{-2}$ and in logarithmic scale to enhance the contrast. The smoothed HST F555W image is shown in contours. Right: CALIFA $[\text{NII}]\lambda 6583$ emission line flux.

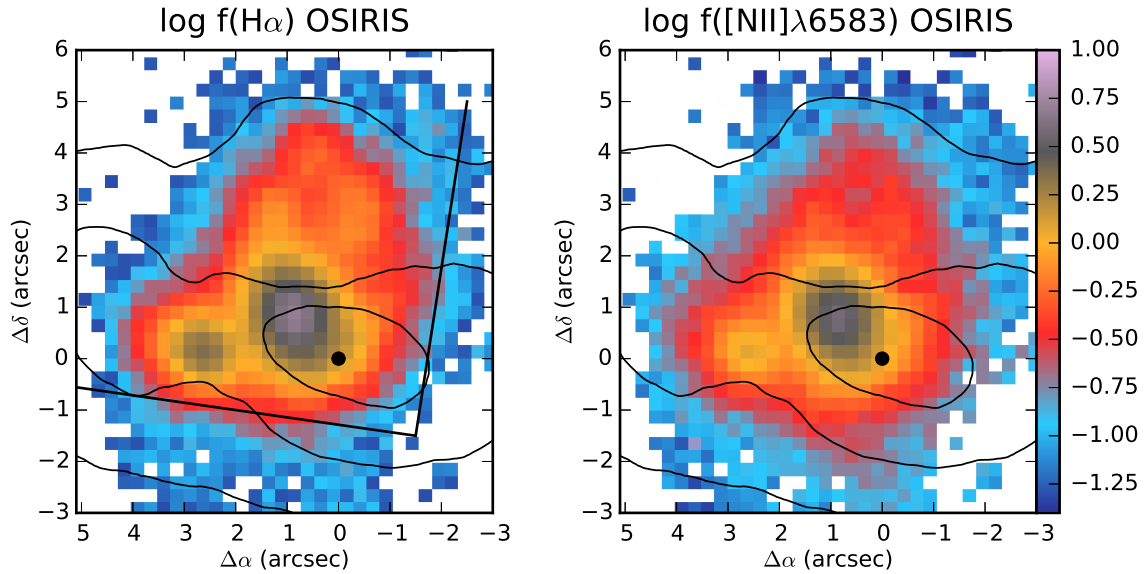


Figure 6.21 OSIRIS $H\alpha$ (left) and $[NII]\lambda 6583$ emission (right) zoom into the nuclear region of NGC 2623. Given the high spatial resolution of OSIRIS we can differentiate several substructures. On one hand, there is a point-like source offset with respect to the nucleus by $(2.7''E, 0.1''N)$. Its morphology is consistent with a star forming knot. On the other hand, there is an extended, lobular-like emission with bow-shaped, clumpy ends that seems to emerge from the nucleus. This kind of morphology is typical from shocked regions.

maps. We notice two different structures. On one hand, there is a point-like source offset with respect to the nucleus by $(2.7''E, 0.1''N)$, label A in Figure 6.22). Its morphology is consistent with a star forming knot. This is confirmed by the line-ratios, with $[NII]/H\alpha \sim 0.5$ (see Section 6.5.4). On the other hand, there is an extended, lobular-like emission with bow-shaped, clumpy ends that seems to emerge from the nucleus (the lobe in Figure 6.22). This kind of morphology is typical from shocked regions.

To get a better idea of the overall morphology of the cone nebulae, in Figure 6.22 we have superimposed in red contours the OSIRIS $H\alpha$ emission over the HST F555W continuum image. Within the cone nebulae, we distinguish the stellar origin of eastern source, labelled as A in the image. Inside the lobe, we find that the brightest $H\alpha$ emission also corresponds to several cluster aggregations, labelled as B. Most of the extended $H\alpha$ emission is spatially coincident with highly obscured regions. Some bright clusters appear at the tip of the lobe (at the "edges" of the outflow), whose formation could have been induced by it. It seems like the "outflow" is in the process of removing/sweeping some of the highly obscured nuclear gas. Finally, the three HII regions south of the nucleus C1, C2, and C3 are also indicated in the Figure. Although weak, their stellar counterpart is appreciated.

The remaining emission lines maps are shown in Figure 6.23. From top left to bottom right: $[OII]\lambda 3727$, $[OI]\lambda 6300$, $H\beta$, $[OIII]\lambda 5007$, $[SII]\lambda 6716 + [SII]\lambda 6731$, and $[SII]\lambda 6716/[SII]\lambda 6731$, which is a tracer of the electron density. All panels, except the last one which is a ratio, are in logarithmic scale and in units of $10^{-16} \text{ erg s}^{-1} \text{ cm}^{-2}$. The scale range is different for each map to maximize the contrast. The continuum HST F555W image is superimposed in contours, smoothed to approximately match the spatial resolution of the IFS.

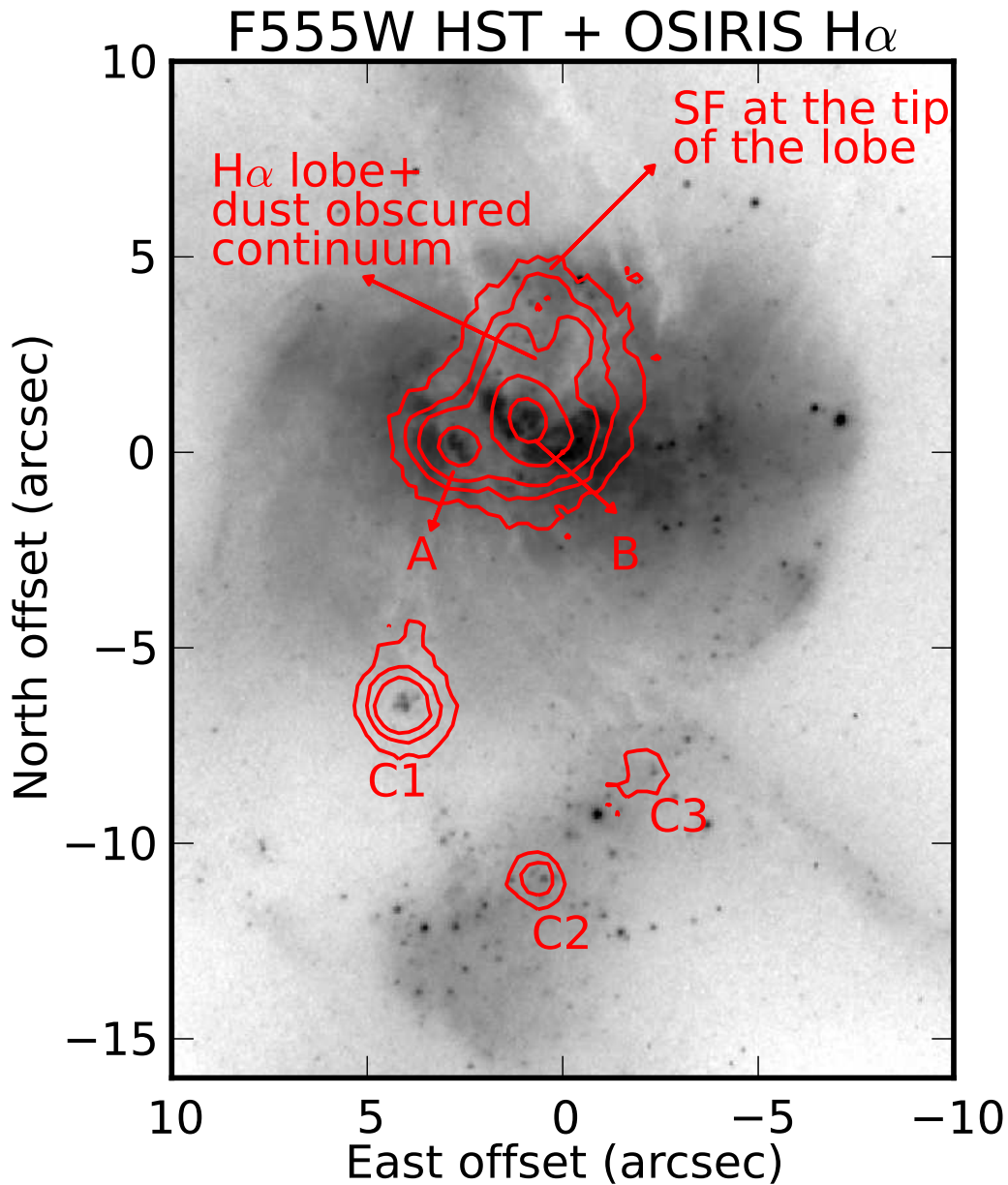


Figure 6.22 HST F555W continuum image of the nuclear region of NGC 2623 together with OSIRIS $H\alpha$ line emission in red contours. Within L04 cone nebulae, we distinguish the stellar origin of eastern source, labelled as A in the image. Inside the lobe, we find that the brightest $H\alpha$ emission also correspond to several cluster agregations, labelled as B. Most of the extended $H\alpha$ emission is spatially coincident with highly dust obscured regions. Some bright clusters appear at the tip of the lobe (at the "edges" of the outflow), whose formation could have been induced by it. It seems like the "outflow" is in the process of removing/sweeping some of the highly obscured nuclear gas. Finally, the three HII regions south of the nucleus C1, C2, and C3 are also indicated in the figure. Although weak, their stellar counterpart is appreciated.

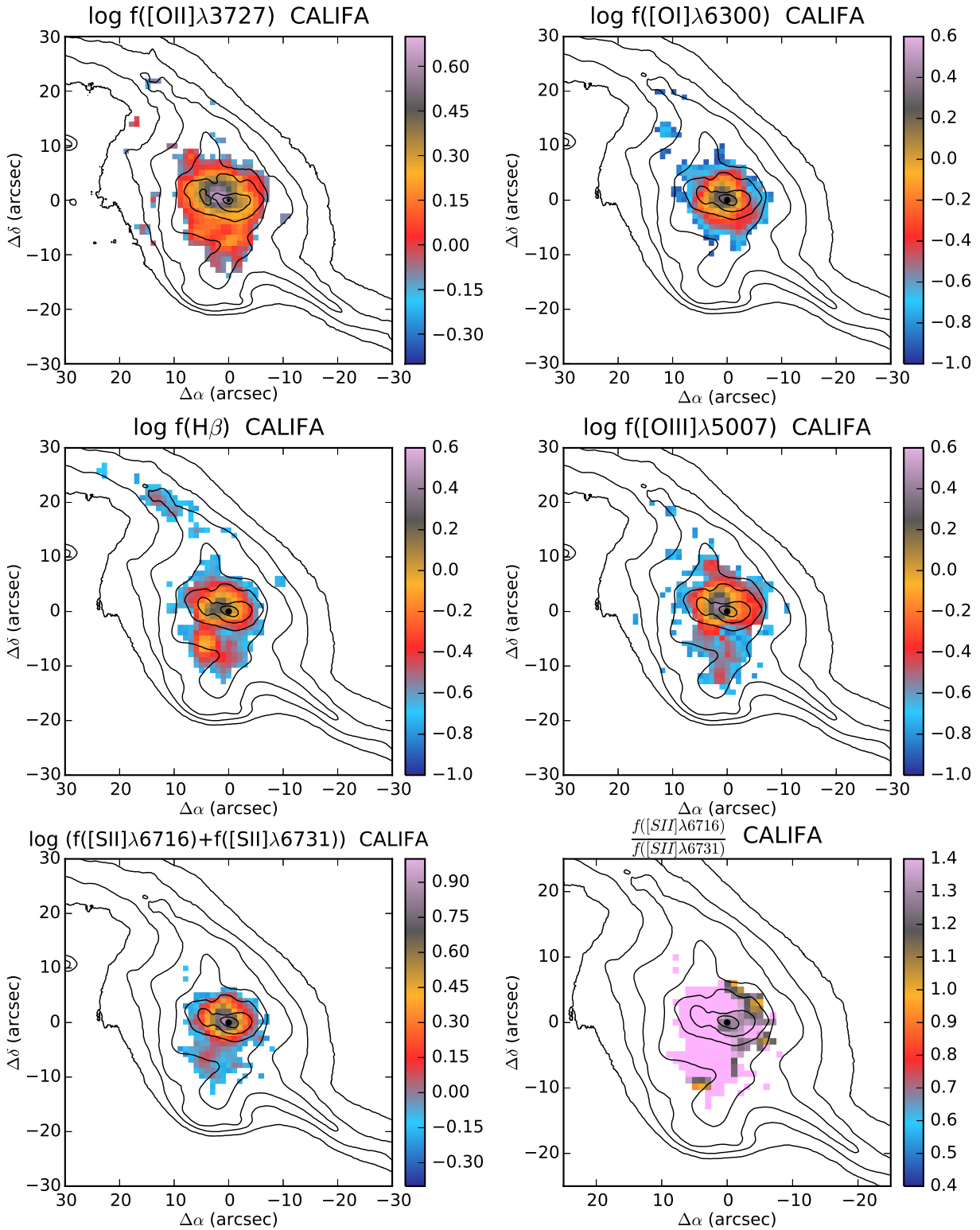


Figure 6.23 From top left to bottom right: emission line maps of $[\text{OII}]\lambda 3727$, $[\text{OI}]\lambda 6300$, $\text{H}\beta$, $[\text{OIII}]\lambda 5007$, $[\text{SII}]\lambda 6716 + [\text{SII}]\lambda 6731$ and $[\text{SII}]\lambda 6716/[\text{SII}]\lambda 6731$ (a tracer of the electron density). All panels, except the last one which is a ratio, are in logarithmic scale and in units of $10^{-16} \text{ erg s}^{-1} \text{ cm}^{-2}$. The scale range is different for each map to maximize the contrast. The smoothed continuum HST F555W image is superimposed in contours.

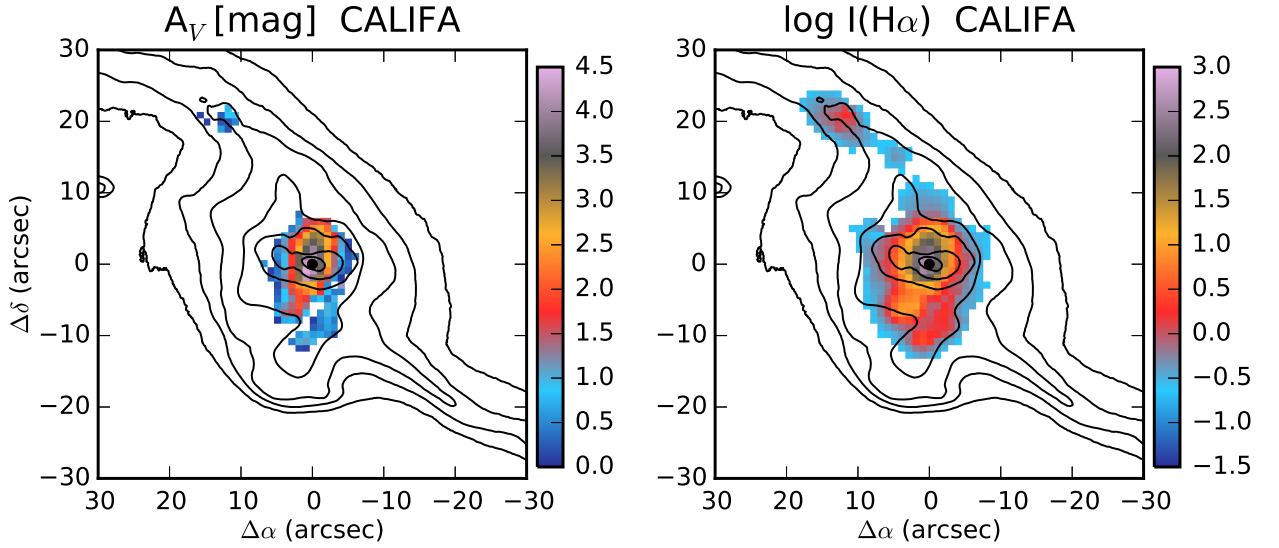


Figure 6.24 Left: Emission line attenuation at 5500 \AA , calculated from the $H\alpha/H\beta$ emission line ratio assuming a Calzetti like dust attenuation curve. Right: CALIFA dereddened $H\alpha$ emission line. The spaxels in which we have $H\alpha$ emission but no attenuation measurements are plotted with the same values as in right panel of Figure 6.19. The nuclear region is very dusty, with up to 4.5 magnitudes of extinction at 5500 \AA . However, the ionized gas in the north tidal tail and in the cluster-rich region south of the nucleus has $A_V \leq 1 \text{ mag}$. The global average is $A_V \sim 1.4 \text{ mag}$. From the dereddened $H\alpha$ map, we find that the distribution of ionized hydrogen in NGC 2623 is in fact rather centrally concentrated.

6.5.2. Emission line ratios sensitive to gas density

As shown in the previous chapter, the $[SII]\lambda 6716/[SII]\lambda 6731$ doublet ratio is primarily sensitive to the electron density of the emitting gas (n_e). This ratio varies from 0.4 to 1.4 for densities between 10^5 to 10^2 cm^{-3} (at $T_e = 10^4 \text{ K}$, Osterbrock & Ferland 2006). From bottom-right panel of Figure 6.23 we found that in NGC 2623 nucleus the ratio has values around 1.25, equivalent to an electron density of $\sim 200 \text{ cm}^{-3}$. To the west of the nucleus and in several spaxels to the south east we found regions with higher densities, up to $\sim 600 \text{ cm}^{-3}$ (ratios up to 1.0). Everywhere else the ratio is above 1.4, implying densities below 100 cm^{-3} .

6.5.3. Ionized gas dust attenuation

Using the observed $F(H\alpha)$ and $F(H\beta)$ fluxes, assuming an intrinsic ratio of 2.86, and a Calzetti et al. (2000) reddening function, we have derived the dust attenuation A_V and the dereddened $I(H\alpha)$ flux using the equations reported in Section 5.5.4.

In Figure 6.24 the attenuation map (A_V) and dereddened $H\alpha$ emission flux are shown. The highest extinction is found in the nuclear regions with up to 4.5 magnitudes. This level of extinction implies that a dust screen with high covering fraction lies in front of the central region of the galaxy, consistent with the dust lanes visible in HST images. However, the ionized gas in the north tidal tail and in the clusters south of the nucleus has $A_V \leq 1 \text{ mag}$. The global average is $A_V \sim 1.4 \text{ mag}$.

We compared the ratio between ionized gas and stellar extinction, considering as reliable spaxels

those with extinction above 0.15 mag, and found an average of $\langle \frac{A_{V,gas}}{A_{V,stars}} \rangle = 1.9 \pm 1.1$. This result is in agreement with Calzetti et al. (1994) who obtained $\langle \frac{A_{V,gas}}{A_{V,stars}} \rangle = 2.0 \pm 0.4$ for a sample of 39 starburst galaxies. We think that this discrepancy between stellar and ionized gas extinction could be a consequence of the fact that the hot ionizing stars (the ones contributing to the line emission) are associated with dustier regions than the cold stellar populations which contribute most of the optical continuum.

From the dereddened H α map, we find that the distribution of ionized hydrogen in NGC 2623 is in fact rather centrally concentrated. The H α bright regions are approximately coincident with the regions where the YSP are contributing 40 - 60 % to the total light (see Section 6.4.10).

6.5.4. Emission line ratios sensitive to ionisation source

Standard line ratios sensitive to the shape of the ionising spectrum have been calculated. First, we focus on those ratios where lines are close enough in wavelength space to not be strongly affected by dust attenuation.

In Figure 6.25 we show the [NII] λ 6583/H α maps for OSIRIS data (left) and CALIFA data (right). Regions with [NII] λ 6583/H α ≤ 0.56 are compatible with being high-metallicity star forming regions (Kauffmann et al., 2003). From the CALIFA map this is the case for the star formation in the north tidal tail and the three emission knots south of the nucleus (C1, C2, and C3). The CALIFA ratios are consistent with the OSIRIS ones, but less sensitive to small-scale variations due to its poorer spatial resolution. With the greater spatial resolution of OSIRIS we see finer details of the ionization

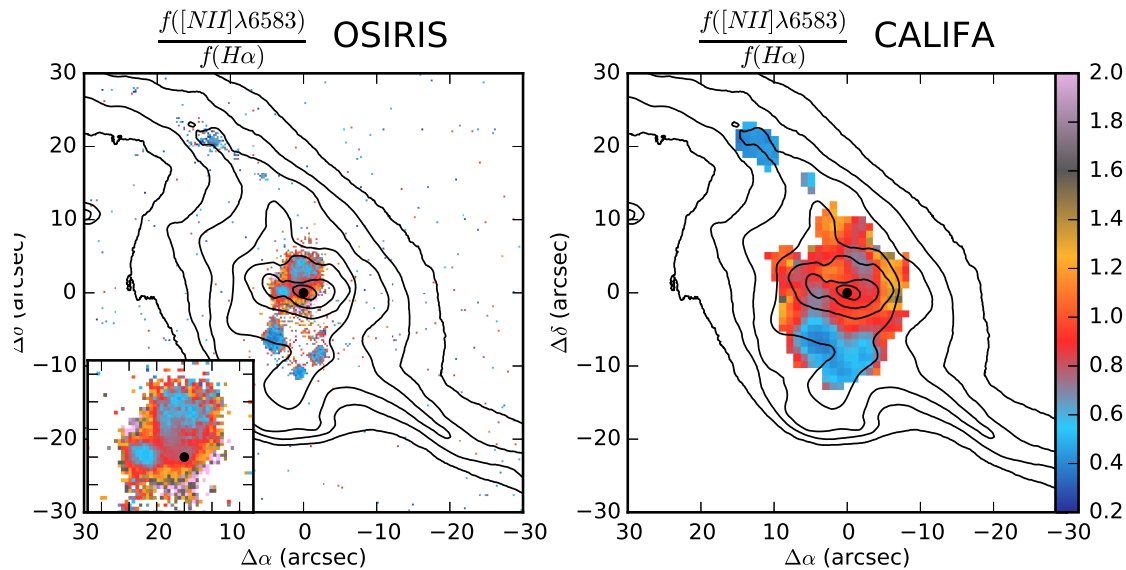


Figure 6.25 Emission line ratio map of [NII] λ 6583/H α for OSIRIS and CALIFA, in left and right panel respectively. In CALIFA map we see ionization due to star formation in the north tidal tail and in the three emission knots south of the nucleus (C1, C2, and C3). With the greater spatial resolution of OSIRIS we see that inside L04 cone nebula, the nuclear knot (A) and some pixels at the clumpy ends of the lobe, are also consistent with high metallicity star formation. For the spaxels at the edges of the cone nebulae, the [NII] λ 6583/H α is much larger, between 1 - 2 and mainly associated with the effects of large-scale shocks.

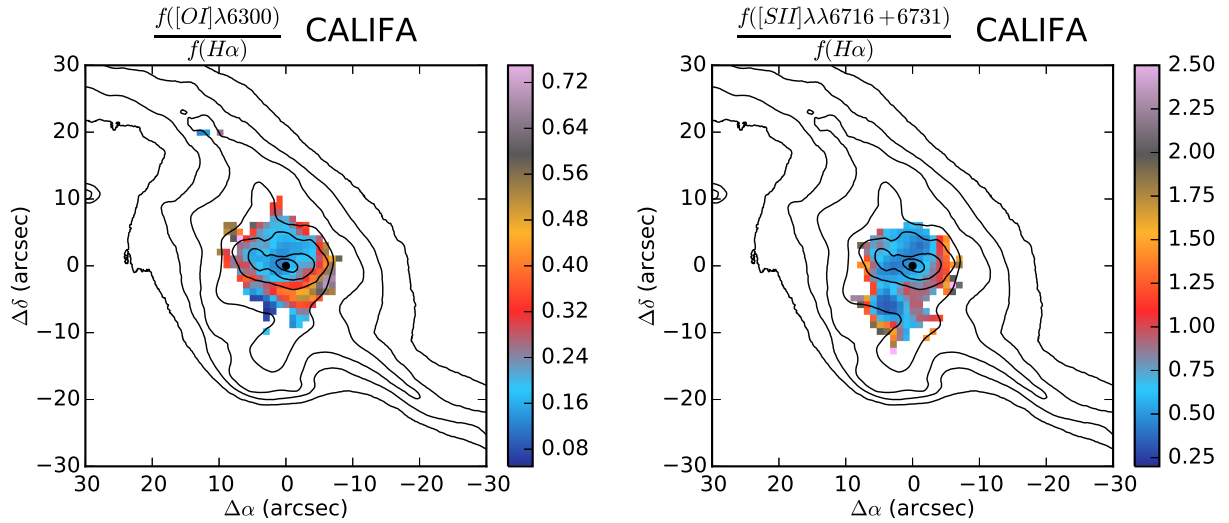


Figure 6.26 [OI] λ 6300/ $H\alpha$ (left) and [SII] $\lambda\lambda$ 6716+6731/ $H\alpha$ (right) ratio maps. Inside the L04 cone nebulae we find line ratios similar to them, of ~ 0.15 and ~ 0.5 , respectively. These values are indicative of shock heated gas of moderate velocity. The spaxels in the outskirts, however, have larger values of the ratios, up to 0.7 for [OI] λ 6300/ $H\alpha$ and 2.0 for [SII] $\lambda\lambda$ 6716+6731/ $H\alpha$, which are consistent with higher velocity shocks.

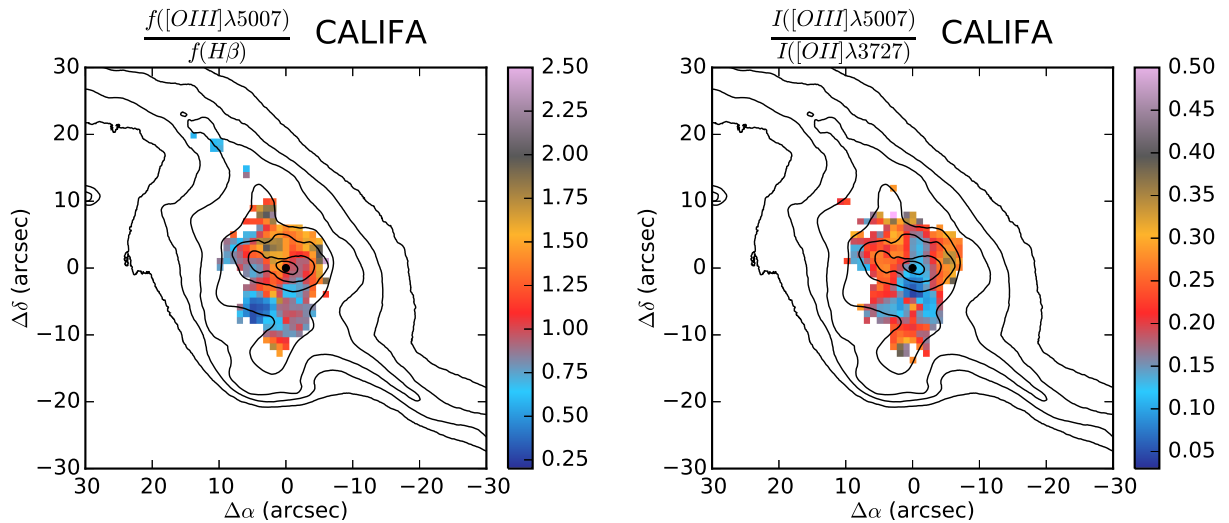


Figure 6.27 [OIII] λ 5007/ $H\beta$ ratio map (left) and [OIII] λ 5007/[OII] λ 3727 (right) ratio maps, the latter using the dust attenuation corrected fluxes. The [OIII] λ 5007/ $H\beta$ ratio map is everywhere below ~ 2 . Ratios above 3.2 would be expected for Seyfert emission, which can be discarded in NGC 2623. The lowest values of this ratio < 0.6 correspond mainly with the already known star forming regions. The dereddened ratio [OIII] λ 5007/[OII] λ 3727 is expected to have values below 1 for LINER-like emission, and above 1 for Seyferts. In NGC 2623 we found values below 0.4, consistent with softer ionization mechanisms.

mechanisms in the nuclear region of NGC 2623. In particular, inside L04 cone nebula, the nuclear knot (A) seen on OSIRIS $H\alpha$ map and some pixels at the clumpy ends of the nuclear lobe, are also consistent with high metallicity star formation ($[NII]\lambda 6583/H\alpha \sim 0.5$), while the remaining have $[NII]\lambda 6583/H\alpha$ between 1.0 - 1.2. For the pixels/spaxels at the edges of the cone nebulae, the $[NII]\lambda 6583/H\alpha$ is even larger, with values between 1 - 2, which could be mainly associated with the effects of large-scale shocks when the outflowing gas collides with the ISM (Heckman et al., 1987, 1990).

We would like to point out that our measurements are in perfect agreement with those reported by L04 inside the cone nebulae. However, outside the cone nebulae, they report very high $[NII]\lambda 6583/H\alpha > 3$ values, which we do not find. As previously mentioned, L04 $H\alpha$ flux is not corrected by the contribution of the underlying stellar absorption, and therefore, outside the cone-nebulae their $H\alpha$ flux is underestimated, leading to higher values of this ratio.

In anycase, it seems that close to the nucleus the photoionization is due to a dusty nuclear starburst, while the emission in the outskirts is more consistent with large scale shocks. The characteristics of the nucleus of NGC 2623 could be associated with a starburst related LINER. The starburst is energetic enough to generate an amount of outflowing gas that collides with the ISM, producing strong shocks (LINER emission).

In Figure 6.26 we also show $[OI]\lambda 6300/H\alpha$ (left) and $[SII]\lambda\lambda 6716+6731/H\alpha$ (right) ratio maps. Inside the cone nebulae defined by L04 we find line ratios similar to them, ~ 0.15 and ~ 0.5 , respectively. Following Heckman et al. (1990), these values are indicative of shock heated gas of moderate velocity. The spaxels in the outskirts, however, have larger ratios, up to 0.7 for $[OI]\lambda 6300/H\alpha$ and 2.0 for $[SII]\lambda\lambda 6716+6731/H\alpha$, which are consistent with higher velocity shocks (see Figure 14 of Heckman et al. 1990). In addition, the nuclear value of the $[OI]\lambda 6300/H\alpha$ ratio is in the same range as that of starburst related LINERs, i.e. 0.08 - 0.16. This is an important subclass of LINERs in which the main source of ionization is associated with the diffuse radiation field of metal rich dusty starbursts (Heckman et al., 1996). Therefore, for the nuclear region of NGC 2623, these 2D maps show results mainly consistent with ionization by a nuclear dusty starburst plus shocks (with a starburst related LINER spectrum).

In Figure 6.27 we also show $[OIII]\lambda 5007/H\beta$ (left) and $[OIII]\lambda 5007/[OII]\lambda 3727$ (right) ratio maps, the latter using the dust attenuation corrected fluxes. The $[OIII]\lambda 5007/H\beta$ ratio map is everywhere below ~ 2 . Ratios above 3.2 would be expected for Seyfert emission (Heckman et al., 1987; Veilleux et al., 1995), which can be discarded in NGC 2623, even in its nucleus. The lowest values of this ratio < 0.6 correspond mainly with the already known star forming regions. The dereddened ratio $[OIII]\lambda 5007/[OII]\lambda 3727$ is expected to have values below 1 for LINER-like emission, and above 1 for Seyferts. In NGC 2623 we found values below 0.4, consistent again with softer ionization mechanisms.

6.5.5. Diagnostic diagrams

In the left panel of Figure 6.28 we show $[NII]\lambda 6583/H\alpha$ vs $[OIII]\lambda 5007/H\beta$ diagnostic diagram. Line ratios from individual spaxels are plotted as filled circles. Overplotted as black lines are empirically and theoretically derived separations between LINERs/Seyferts and HII regions. Dotted line is from Kauffmann et al. (2003), a conservative demarcation line to separate pure star formation ionization from other ionization mechanisms; solid line is Kewley et al. (2001), which represents regions of composite ionization mechanisms, normally starbursts and shocks. Finally, the dashed-dotted line

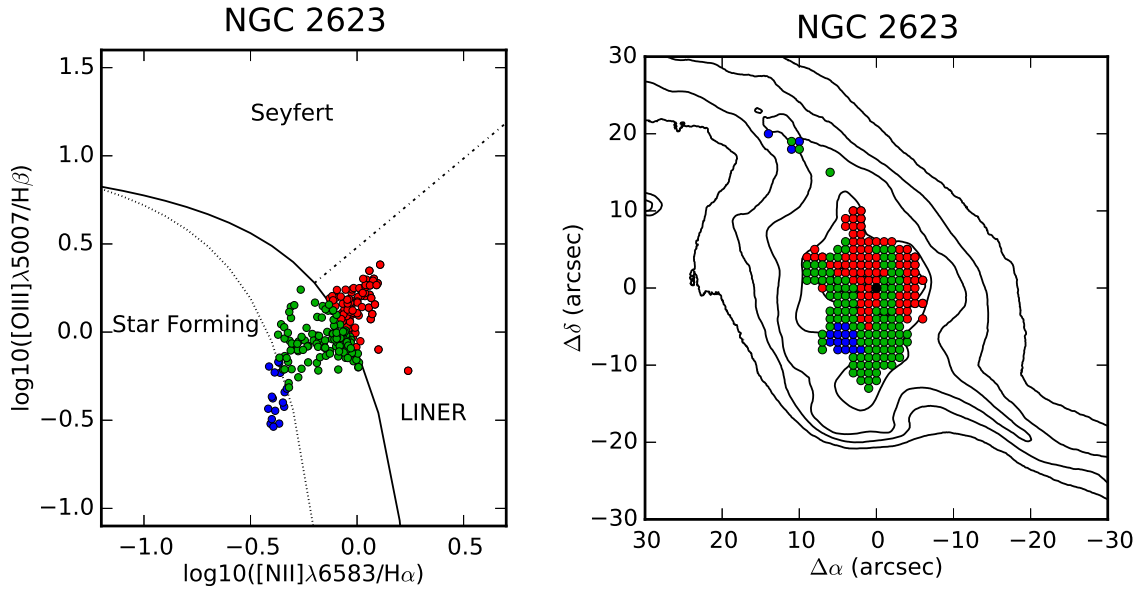


Figure 6.28 Left: $[\text{NII}]\lambda 6583/\text{H}\alpha$ vs $[\text{OIII}]\lambda 5007/\text{H}\beta$ line ratio diagnostic diagram, showing line ratios for independent spaxels in NGC 2623. Black lines are the demarcations between LINERs/Seyferts and HII regions. Dotted line is from [Kauffmann et al. \(2003\)](#), solid line is [Kewley et al. \(2001\)](#) and the dashed-dotted line is [Cid Fernandes et al. \(2010\)](#), that separates Seyferts from LINERs. Right: Map of the location in NGC 2623 of the star forming (blue), composite (green), and LINER (red) dominated spaxels.

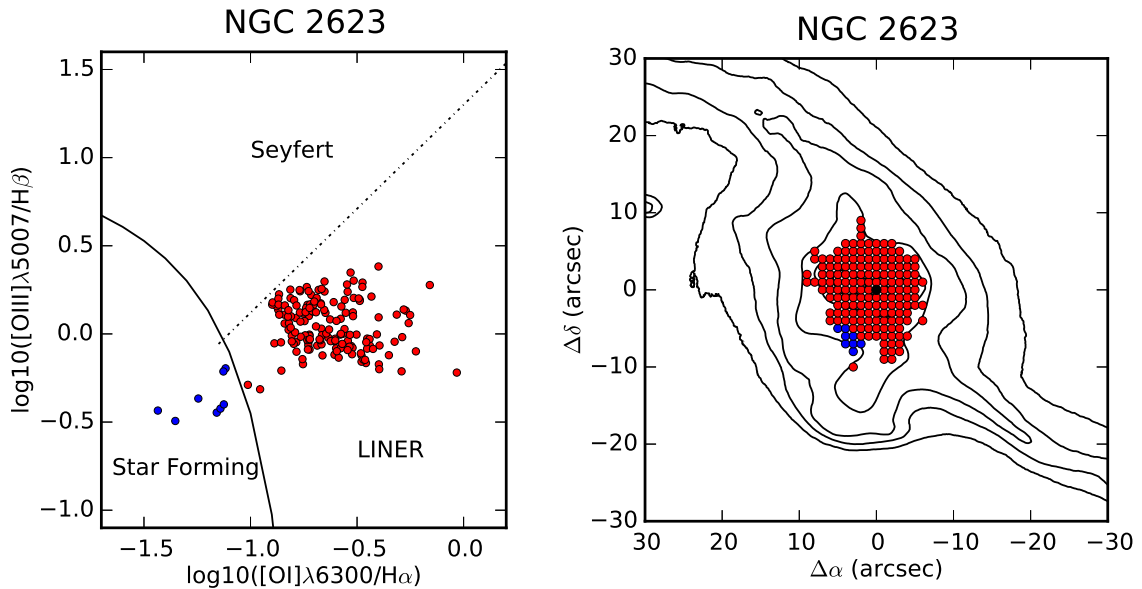


Figure 6.29 Left: $[\text{OI}]\lambda 6300/\text{H}\alpha$ vs $[\text{OIII}]\lambda 5007/\text{H}\beta$ line ratio diagnostic diagram. The solid demarcation line is [Kewley et al. \(2001\)](#), and the dashed-dotted line is [Kewley et al. \(2006\)](#). Those spaxels below [Kewley et al. \(2001\)](#) are coloured blue and are consistent with ionization due to star formation, those above [Kewley et al. \(2001\)](#) and below [Kewley et al. \(2006\)](#) are coloured red, and are LINER ionization type. Right: Map of the location in NGC 2623 of the star forming/composite and LINER dominated spaxels.

is [Cid Fernandes et al. \(2010\)](#), that separates Seyferts from LINERs. Spaxels consistent with pure star formation ionization are plotted in colour blue, those with LINER like ionization are plotted in red, and the composite regions in green. In the right panel, we show where the different ionization mechanisms are located within NGC 2623.

We found that only the gas in the north tidal tail and the brightest knot south of the nucleus is consistent with pure star formation ionization. On the other hand, the gas inside the nuclear cone defined by L04 (a bit narrower and elongated in our data), is consistent with LINER emission, together with some other spaxels to the west of the nucleus. The remaining spaxels seem to be a mixture of star formation and LINER like emission.

In Figure 6.29 we show the analogous comparison using $[\text{OI}]\lambda 6300/\text{H}\alpha$ vs $[\text{OIII}]\lambda 5007/\text{H}\beta$ diagnostic diagram. In this case, the solid demarcation line is [Kewley et al. \(2001\)](#), and the dashed-dotted line is [Kewley et al. \(2006\)](#). With this BPT, we conclude that within all the circumnuclear region of NGC 2623, the ionization mechanism is LINER type.

6.5.6. OSIRIS line emission at the edge of the SW tidal tail

The OSIRIS narrow band filter imaging data covers a very large FoV, including the whole extension of NGC 2623, beyond the tidal tails. In the OSIRIS $[\text{NII}]\lambda 6583$ map we detect four bright star forming regions, located more than 19 kpc away from the center, at the edge of the southwestern tidal tail. In Figure 6.30 we show the OSIRIS $[\text{NII}]\lambda 6583$ map, where the regions have been indicated as R1, R2, R3, and R4. The existence of these regions has been previously reported/detected by [Bournaud et al. \(2004\)](#) and [de Mello et al. \(2012\)](#).

As we mentioned in Section 3.3, the wavelength tuning is not uniform over the full field of view of OSIRIS. There is a progressive increasing shift to the blue of the central wavelength (λ_0) as the distance to the optical centre (r) increases. The wavelength (in Ångstroms) observed with the red TF relative to the optical center changes following the law reported by [González et al. \(2014\)](#):

$$\lambda = \lambda_0 - 5,04 \times r(\text{arcmin})^2 \quad (6.3)$$

Given the position of the four regions in the FoV of OSIRIS, they are emitting in wavelengths that range from 6553 to 6562 Å, consistent with the spectral region between $[\text{NII}]\lambda 6548$ and $\text{H}\alpha$. According to this, the ages of the star forming regions must be below or around 30 Myr. Stars older than this, would not be able to produce enough ionizing photons for such $\text{H}\alpha$ emission. This is consistent with [de Mello et al. \(2012\)](#) estimations. We have performed aperture photometry to derive the total fluxes of these star forming knots. Results are summarized in Table 6.1.

Attending just to their location and $\text{H}\alpha$ emission they could be compatible with the formation of a tidal dwarf galaxy in the south west tail of NGC 2623. Unfortunately, this is all the information we have about them, and we can not characterize them further, because these regions are not covered by the CALIFA datacube and we cannot estimate their precise masses, ages and metallicities. Additional spectroscopic data will be necessary to test further this hypothesis.

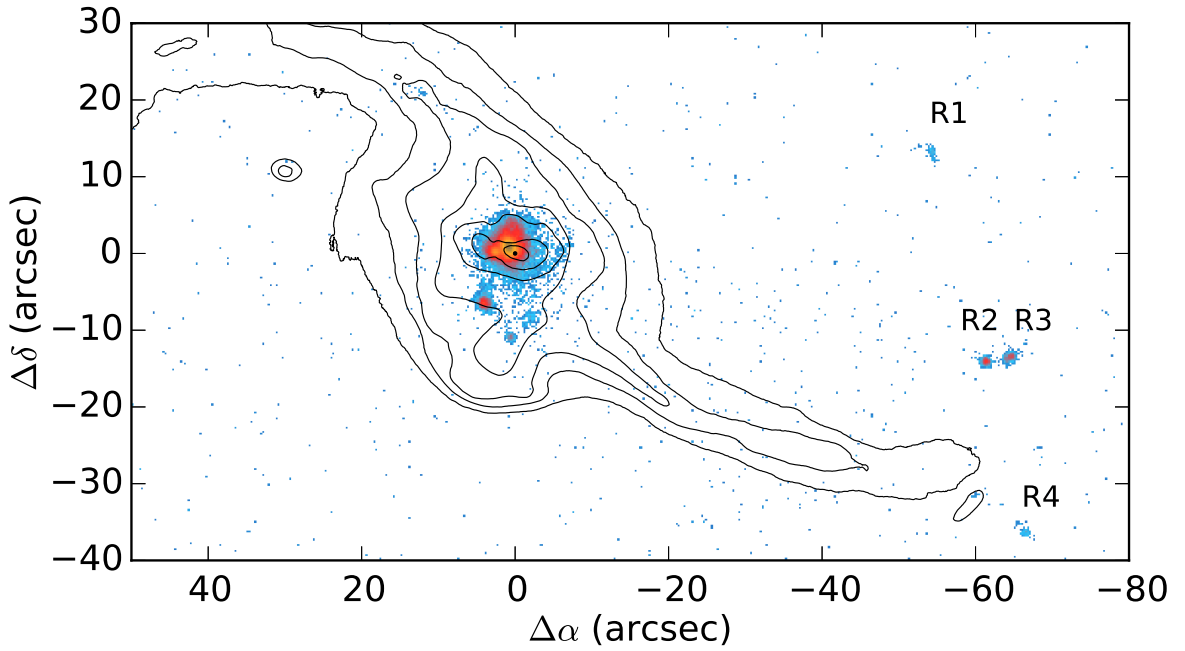


Figure 6.30 [NII] λ 6583 emission flux image from OSIRIS data. The smoothed HST F555W image has been superimposed in contours. Note the 4 regions to the west, near the end of the south tidal tail, labeled as R1, R2, R3, and R4.

Table 6.1. Fluxes of regions R1 to R4 measured in OSIRIS TF [NII] λ 6583 image.

Region	Wavelength (\AA)	Flux ($\text{erg s}^{-1} \text{cm}^{-2}$)
R1	6562	2.5×10^{-16}
R2	6558	7.6×10^{-16}
R3	6557	7.7×10^{-16}
R4	6553	2.5×10^{-16}

6.6. Kinematics

We have determined the ionized gas kinematics of NGC 2623 using $\text{H}\alpha$ and [NII] λ 6583 in order to compare to previous results from L04 and [Barrera-Ballesteros et al. \(2015\)](#). As $\text{H}\alpha$ and the [NII] $\lambda\lambda$ 6548,6583 are blended, we fitted simultaneously three Gaussians in two ways, with and without constraining the position of the nitrogens with respect to $\text{H}\alpha$. The [NII] λ 6583 velocity field is similar with both considerations and varies only smoothly. For comparison purposes with $\text{H}\alpha$, here we show the non-constrained fit. We have converted the central positions of the Gaussians to velocities using equation 5.12. Also, from the Gaussian fit to the emission lines, we derive the lines widths, which can be converted into velocity dispersions using equations 5.13 and 5.14. For CALIFA data the

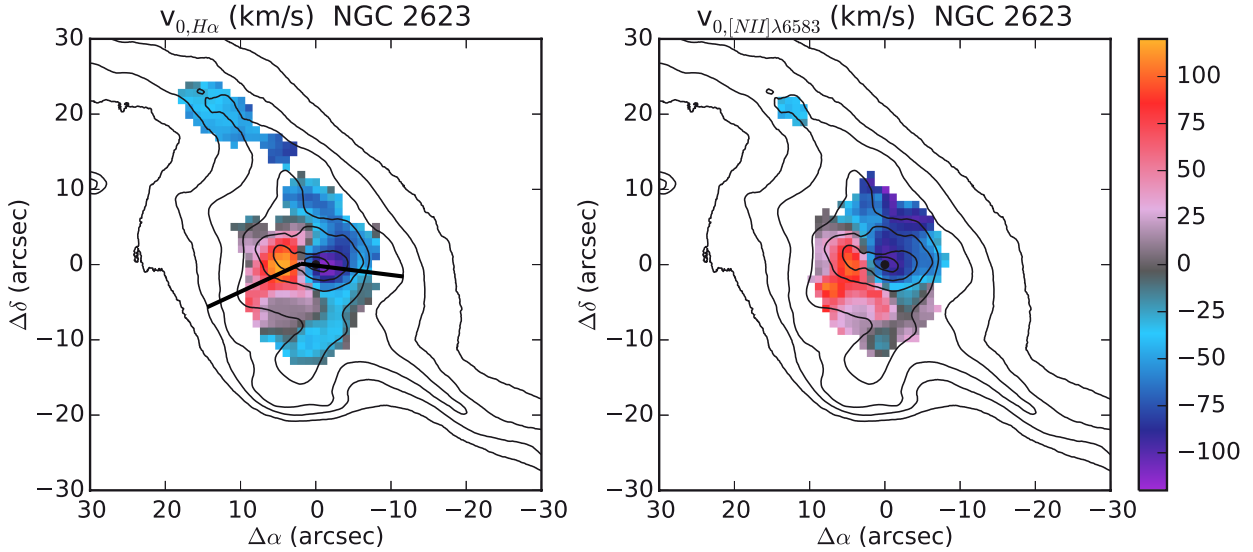


Figure 6.31 Velocity field derived from H α (left) and [NII] λ 6583 (right). A rotation pattern is preserved in the nucleus, with an amplitude of ± 120 km/s. The kinematic center is displaced 2 arcsec to the east with respect to the photometric center. The position angles of the kinematic major axis for the approaching a receding sides have been calculated by Barrera-Ballesteros et al. (2015) and shown in the figure with black solid lines. For NGC 2623, $PA_{kin}^{appro} = 83.1 \pm 5.9^\circ$ and $PA_{kin}^{reced} = 115.1 \pm 11.4^\circ$. The outflow signature can not be detected in these maps, with our spectral resolution we do not see double components in the lines. Beyond the nucleus, both the star forming regions in the north tidal tail and the material in the cluster rich region to the south are approaching to us at ~ 40 km/s.

instrumental resolution at these wavelengths is $\sigma_{inst} \sim 116$ km/s. Therefore, line widths below ~ 58 km/s are unresolved at the CALIFA resolution.

In Figure 6.31 we show the H α (left) and [NII] λ 6583 (right) velocity fields. As can be seen, a rotation pattern is preserved in the nucleus, with an amplitude of ± 120 km/s, in agreement with Barrera-Ballesteros et al. (2015). We have found that the kinematic center is displaced 2 arcsec to the east with respect to the photometric center. However, this is within our spatial resolution. The position angles of the kinematic major axis for the approaching a receding sides calculated by Barrera-Ballesteros et al. (2015) are shown in the Figure with black solid lines. For NGC 2623, $PA_{kin}^{appro} = 83.1 \pm 5.9^\circ$ and $PA_{kin}^{reced} = 115.1 \pm 11.4^\circ$.

Our results are also in agreement with L04. They also found a rotation pattern with a similar amplitude like us. They fit an axisymmetric model and a Plummer model and when subtracting they found in the residuals the signature of the outflow. Moreover, they found double [NII] components inside the cone nebulae where they report the outflow. From the bluest ones they derive the mean outflow velocity $\langle V_{OF} \rangle = -405 \pm 35$ km/s. We can not perform a similar estimate with our data, as with our spectral resolution we do not see double components but just broader emission. Beyond the nucleus, both the star forming regions in the north tidal tail and the material in the cluster-rich region to the south are approaching to us at ~ 40 km/s.

In Figure 6.32 we show the H α (left) and [NII] λ 6583 (right) velocity dispersion maps. Here we

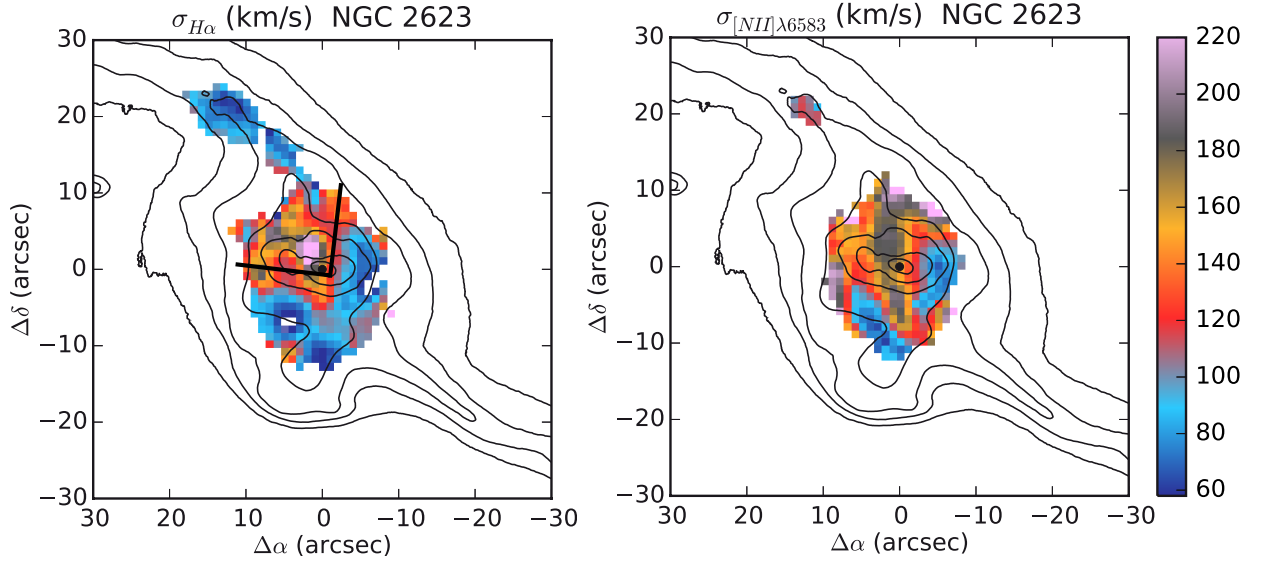


Figure 6.32 Velocity dispersion maps derived from $H\alpha$ (left) and $[NII]\lambda 6583$ (right). The instrumental resolution was subtracted from the measured line widths in quadrature ($\sigma_{instr} \sim 116$ km/s). Line widths below ~ 58 km/s are unresolved at the CALIFA resolution. We found evidence of the outflow, as the highest values of the velocity dispersion (~ 220 km/s) are reached inside the cone nebulae defined by L04 (and indicated with black solid lines in the left panel). This is specially noticeable in the $H\alpha$ map. In addition, the regions with the highest σ values are approximately coincident with pure LINER spaxels in the BPT diagram.

found evidence of the outflow, as the highest values of the velocity dispersion (~ 220 km/s) are reached inside the cone nebulae defined by L04 (and indicated with black solid lines in the left panel). This is specially noticeable in the $H\alpha$ map. In addition, the regions with the highest σ values are approximately coincident with pure LINER spaxels in the BPT diagram (right panel of Figure 6.28). In addition, we note that there is a region to the west of the nucleus with line ratios consistent with LINER ionization, although the velocity dispersion has low values in it, more typical of HII regions.

6.7. Star formation rates

From CALIFA data there are two ways to estimate the SFR, both explained in detail in Section 5.6. On the one hand, for the regions of the galaxies where the gas is photoionised by light from massive stars, we can measure the SFR from the dust attenuation corrected $H\alpha$ line luminosity, using the conversion to star formation rate provided by Lacerda et al. (private communication). They report the value of the SFR constant using BC2003 models with different IMFs (Salpeter and Chabrier) and different metallicities. The calibration for $0.4 Z_{\odot}$ (NGC 2623 mean metallicity is $\sim 0.5 Z_{\odot}$) and for Salpeter IMF is:

$$SFR(M_{\odot} yr^{-1}) = 6,6 \times 10^{-42} L(H\alpha)_{corr} (erg s^{-1}) \quad (6.4)$$

and for Chabrier IMF:

$$SFR(M_{\odot} \text{ yr}^{-1}) = 3,9 \times 10^{-42} L(H\alpha)_{corr} \text{ (erg s}^{-1}\text{)} \quad (6.5)$$

For the composite/LINER spaxels we obtain only an upper limit on the SFR, because a fraction of the $H\alpha$ flux may arise from processes unrelated to star formation, as outflow related shocks. In NGC 2623 we measure a total dust attenuation corrected $H\alpha$ luminosity of $L_{H\alpha} = 3.35 \times 10^{41}$ erg s^{-1} (spatially resolved). From the integrated spectra we derived $L_{H\alpha} = 1.96 \times 10^{41}$ erg s^{-1} . This leads to a total SFR $\leq 2.2 M_{\odot} \text{ yr}^{-1}$, which is surprisingly low, not even near the $24 M_{\odot} \text{ yr}^{-1}$ which are in principle necessary to power the observed outflow (see Section 6.8.6). The observed and dust attenuation corrected $H\alpha$ luminosities are shown in Table 6.2. The corresponding SFR are reported in Table 6.3.

On the other hand, we can also use the stellar continuum. Its decomposition provides an independent estimate of the star formation rate, uncontaminated by non-stellar photoionisation sources. For comparison purposes we estimate it for $t_{SF}=30$ Myr, which is approximately the lifetime of the ionizing populations also emitting in $H\alpha$, that is, O and early B stars, and also for $t_{SF}=140$ Myr which is more comparable to the FUV emission, tracing stellar populations dominated by up to A0 stars. We used equation 5.17.

Additionally, we have used GALEX FUV and NUV imaging to determine the SFR. First, we have measured the observed fluxes and converted them into magnitudes to calculate the extinction in the FUV, using equation 5.18. The SFR has been calculated from the dust attenuation corrected FUV luminosity, using the calibration provided by López-Fernandez et al. (private communication), derived by using CB base of models. For $Z \sim 0.4 Z_{\odot}$ this calibration is given by:

$$SFR(M_{\odot} \text{ yr}^{-1}) = 3,6 \times 10^{-44} L(FUV)_{corr} \text{ (erg s}^{-1}\text{)} \quad (6.6)$$

As can be seen in Table 6.3, there are no significant differences between the spatially resolved SFR and the SFR derived from the integrated spectra. They are comparable within a factor of ≤ 2 . Moreover, the SFR(30 Myr) is an order of magnitude (a factor ~ 7) larger than SFR($H\alpha_{corr}$), ~ 15 vs ~ 2.2 for Salpeter IMF and ~ 7 vs ~ 1.3 for Chabrier IMF. This makes no sense as the SSPs < 30 Myr are the ones expected to ionize the $H\alpha$ gas around them. The only possible explanation is that the gas is significantly more obscured than these stars, which is possible considering that the stellar winds emitted by these stars are able to clear the gas and dust in their immediate surroundings but not in the outer areas of the HII region. As discussed later in this section, when using the hybrid tracers of the SFR that combine the observed $H\alpha$ and IR or radio emission, we found that the global SFR estimated with them matches the SFR(30 Myr), therefore suggesting that a fraction of the ionizing photons is absorbed by dust and reemitted in the IR/radio wavelengths instead of ionizing the $H\alpha$ emitting gas.

The SFR(140 Myr) is more similar to the SFR(FUV), ~ 2.5 vs ~ 1.2 for Chabrier IMF, a factor 2 larger, which is within the uncertainties.

Given the heavy dust lanes observed in the HST images of NGC 2623 nucleus and the high attenuation measured in lines and continuum, we must ask whether substantial star formation is not accounted for by the Balmer decrement attenuation correction. For that, we rely on data from the

Table 6.2. Multiwavelength luminosities of NGC 2623.

Luminosities	NGC 2623	
	spatially resolved	integrated
$L(H\alpha)_{obs}$	4.06×10^{40}	4.88×10^{40}
$L(H\alpha)_{corr}$	3.35×10^{41}	1.96×10^{41}
$L(FUV)_{obs}$	4.17×10^{42}	
$L(FUV)_{corr}$	3.22×10^{43}	
$L(24)$	1.15×10^{44}	
$L(TIR)$	1.04×10^{45}	
$L(1.4GHz)$	6.6×10^{22}	

Note. — All the luminosities are in units of erg s^{-1} , except $L(1.4 \text{ GHz})$ which is in W Hz^{-1} .

IR and radio wavelengths. NGC 2623 have been observed in the mid-IR (at $24\mu\text{m}$) with the MIPS instrument on board Spitzer Telescope, in far-IR with IRAS (25, 60, and $100 \mu\text{m}$) and in radio 1.4 GHz with Very Large Array. These data provide us with three alternative SFR estimates which account for optically thick dust obscuration by direct detection of the thermal dust emission. Moreover they are very sensitive to recent star formation.

First, we combine the $24\mu\text{m}$ luminosity with the observed $H\alpha$ luminosity (not dust attenuation corrected) following the analogous calibration of Kennicutt et al. (2009), for $0.4 Z_{\odot}$ and Salpeter IMF:

$$SFR(M_{\odot} \text{ yr}^{-1}) = 6,6 \times 10^{-42} [L(H\alpha)_{obs} + 0,020 L(24)] (\text{erg s}^{-1}) \quad (6.7)$$

For a Chabrier IMF:

$$SFR(M_{\odot} \text{ yr}^{-1}) = 3,9 \times 10^{-42} [L(H\alpha)_{obs} + 0,020 L(24)] (\text{erg s}^{-1}) \quad (6.8)$$

where $L(H\alpha)_{obs}$ is the observed $H\alpha$ luminosity and $L(24) = \lambda L_{\lambda}$ at $24\mu\text{m}$.

Second, the FIR luminosity calibration analogous of Kennicutt et al. (2009), for $0.4 Z_{\odot}$ and Salpeter IMF:

$$SFR(M_{\odot} \text{ yr}^{-1}) = 6,6 \times 10^{-42} [L(H\alpha)_{obs} + 0,0024 L(TIR)] (\text{erg s}^{-1}) \quad (6.9)$$

For a Chabrier IMF:

$$SFR(M_{\odot} \text{ yr}^{-1}) = 3,9 \times 10^{-42} [L(H\alpha)_{obs} + 0,0024 L(TIR)] (\text{erg s}^{-1}) \quad (6.10)$$

where

$$L(TIR) = 2,403\nu L_{\nu}(25\mu\text{m}) - 0,2454\nu L_{\nu}(60\mu\text{m}) + 1,6381\nu L_{\nu}(100\mu\text{m}) \quad (6.11)$$

Table 6.3. Multiwavelength Star Formation Rate for NGC 2623.

SFR ($M_{\odot} \text{ yr}^{-1}$)	NGC 2623 spatially resolved	NGC 2623 integrated
Base GM Salpeter $\star < 30$ Myr	15	19
Base BC03 Salpeter $H\alpha_{corr}$	2.2	1.3
Base CB Chabrier $\star < 30$ Myr	6.9	9.9
Base BC03 Chabrier $H\alpha_{corr}$	1.3	0.8
Base CB Chabrier $\star < 140$ Myr	2.5	5.2
Base CB Chabrier GALEX FUV	1.2	
Hybrid Salpeter $H\alpha_{obs} + 24\mu\text{m}$	16	
Hybrid Salpeter $H\alpha_{obs} + \text{TIR}$	17	
Hybrid Salpeter $H\alpha_{obs} + 1.4 \text{ GHz}$	17	
Hybrid Chabrier $H\alpha_{obs} + 24\mu\text{m}$	9	
Hybrid Chabrier $H\alpha_{obs} + \text{TIR}$	10	
Hybrid Chabrier $H\alpha_{obs} + 1.4 \text{ GHz}$	10	

Note. — All the SFRs are in units of $M_{\odot} \text{ yr}^{-1}$. The SFRs derived from our optical IFS are computed for spatially resolved and integrated spectra. The first 4 rows in the table compare the continuum ($\star < 30$ Myr) and $H\alpha$ emission for the different model bases, using different IMFs. The next two rows compare the continuum ($\star < 140$ Myr) and the FUV estimates. Finally, the last six rows are the hybrid $H\alpha_{obs} + 24 \mu\text{m}$ or TIR or 1.4 GHz flux.

Finally, we determine the SFR from the 1.4 GHz luminosity. The radio continuum is dominated by nonthermal (synchrotron) emission, which presumably originates ultimately from supernova events; this interpretation forms the physical basis for using the nonthermal radio emission as a SFR tracer (Condon 1992 and references therein). The calibration for $0.4 Z_{\odot}$ and Salpeter IMF:

$$SFR(M_{\odot} \text{ yr}^{-1}) = 6,6 \times 10^{-42} [L(H\alpha)_{obs} + 0,39 \times 10^{20} L(1,4GHz [WHz^{-1}])] \text{ (erg s}^{-1}\text{)} \quad (6.12)$$

For a Chabrier IMF:

$$SFR(M_{\odot} \text{ yr}^{-1}) = 3,9 \times 10^{-42} [L(H\alpha)_{obs} + 0,39 \times 10^{20} L(1,4GHz [WHz^{-1}])] \text{ (erg s}^{-1}\text{)} \quad (6.13)$$

All the luminosities and SFRs are also provided in Tables 6.2 and 6.3 for easy comparison.

We found a strong consistency between the SFRs derived from the three multi-wavelength observations presented here. All of them point to a global average SFR $\sim 17 M_{\odot} \text{ yr}^{-1}$ (Salpeter) and SFR

$\sim 10 M_{\odot} \text{ yr}^{-1}$ (Chabrier).

This multi- λ SFR is similar to the one derived from continuum decomposition, SFR(30 Myr), and an order of magnitude larger than the SFR derived with $H\alpha$ dereddened luminosity. This result implies that some of the ionizing photons have been absorbed by dust and reemitted in the IR/radio instead of ionizing the $H\alpha$ emitting gas. According to Kennicutt et al. (2009), we can calculate the true value of the $H\alpha$ attenuation applying their equation 13:

$$A(H\alpha)(mag) = 2,5 \log \left[1 + \frac{0,020 L(24)}{L(H\alpha)_{obs}} \right] \quad (6.14)$$

We found an average $A(H\alpha) \sim 4.3$ mag. From the IFS, we measure a global average of $A(H\alpha) \sim 1.4$ mag, a factor 3 smaller than the real value. We conclude that in NGC 2623 there is substantial recent star formation which is not accounted for by the Balmer decrement attenuation correction.

Finally, we note that the average SFR in NGC 2623 is a factor 5 higher than the SFR in the Milky Way ($\langle SFR \rangle_{MW} = 1.9 \pm 0.4 M_{\odot} \text{ yr}^{-1}$, Chomiuk & Povich 2011).

6.7.1. Star formation rate densities

From the previous subsection we found that using multi-wavelength data $\langle SFR \rangle_{NGC2623} \sim 10 M_{\odot} \text{ yr}^{-1}$ with Chabrier IMF. Considering that the radius of active star formation is ~ 3 HLR (= 9.9 kpc), that implies a $\langle \Sigma SFR \rangle_{NGC2623} = 0.033 M_{\odot} \text{ yr}^{-1} \text{ kpc}^{-2}$, a factor 10 larger than the SFR density of the Milky Way ($\langle \Sigma SFR \rangle_{MW} = 3.3 \times 10^{-3} M_{\odot} \text{ yr}^{-1} \text{ kpc}^{-2}$, Kennicutt & Evans 2012).

We have also computed the star formation rate densities in NGC 2623 from $H\alpha$ and the stellar continuum in the last 30 Myr. They are shown in Figure 6.33. Comparing the left and right panels we note some similarities and differences. As expected from the previous results, the $\Sigma SFR(30 \text{ Myr})$ is higher than the $\Sigma SFR(H\alpha)$. Only in the nucleus of NGC 2623 and in the bright star forming knot C1 the star formation rate densities are similar. Everywhere else, $\Sigma SFR(30 \text{ Myr})$ is a factor between 10 - 150 higher than $\Sigma SFR(H\alpha)$. For example, in the region rich in star clusters located south of the nucleus the continuum derived star formation rate density is a factor 10 - 50 greater than the derived with $H\alpha$. However, to the west side of the nucleus it reaches a factor up to 100 - 150.

The final conclusion is that, the extinction in the nuclear regions of NGC 2623 is so high that some of the ionizing photons have been absorbed by dust and re-emitted in IR/radio wavelengths instead of ionizing the $H\alpha$ emitting gas.

On the other hand, the star formation rate density maps show that most of the recent star formation is concentrated in the nucleus, as expected for advanced mergers as a consequence of the collapse of the gas toward the galaxy nuclear region.

6.7.2. IFS-base variations over Scalo's b parameter

As stated in Cid Fernandes et al. (2013), it is often useful to consider SFR in relation to some fiducial value instead of absolute units, as for example, the Scalo's b parameter. In Section 5.7.2 we described in detail where and how the three fiducial definitions b^{loc} , b^{gal} , and c^{gal} are obtained.

In Figure 6.34 we show maps of b^{loc} (left panels), b^{gal} (middle panels), and c^{gal} (right panels) for three values of t_{SFR} : 30 Myr (top), 140 Myr (middle), and 1400 Myr (bottom). All panels are in

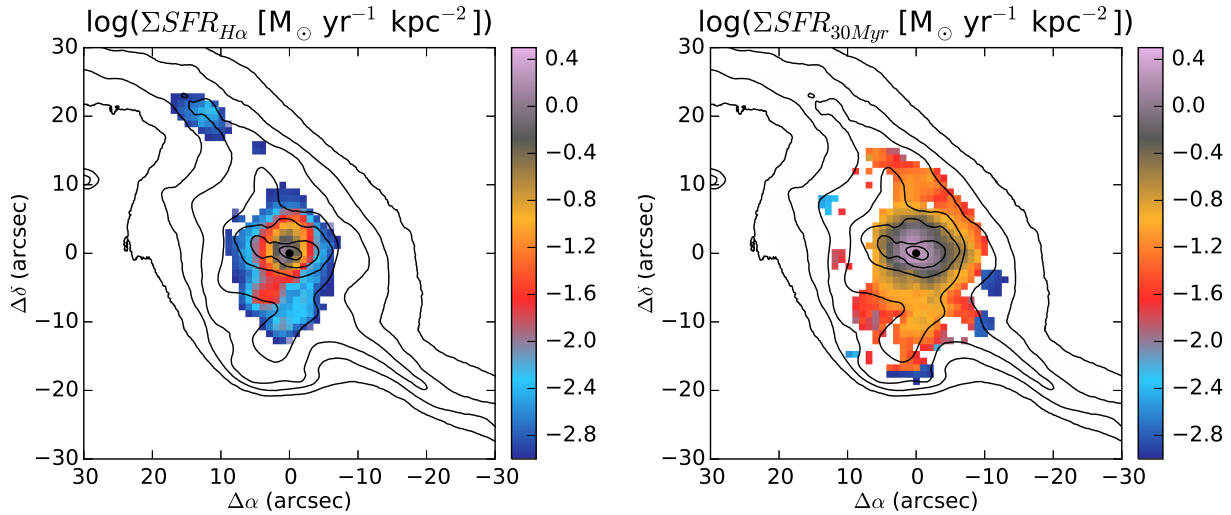


Figure 6.33 Left: Star formation rate surface density estimated from dust-attenuation corrected $H\alpha$. Right: Star formation rate surface density, averaged over the last 30 Myr, measured from the decomposition of the stellar continuum. We only plot spaxels with $\Sigma_{SFR} > 10^{-3} M_{\odot} \text{ yr}^{-1} \text{ kpc}^{-2}$. Only in the nucleus of NGC 2623 and in the bright star forming knot C1 both star formation rate densities are similar. Everywhere else, $\Sigma \text{ SFR}(30 \text{ Myr})$ it is a factor between 10 - 150 higher than $\Sigma \text{ SFR}(H\alpha)$. For example, in the region rich in star clusters located south of the nucleus the continuum derived star formation rate density is a factor 10 - 50 greater than the derived with $H\alpha$. However, to the west side of the nucleus it reaches a factor up to 100 - 150. Both maps show that most of the recent star formation is concentrated in the nucleus, as is expected for advanced mergers as a consequence of the collapse of the gas toward the galaxy nuclear region.

logarithmic scale to highlight regions where $\overline{SFR}(t_{SF})$ is larger than the chosen reference value; the dynamical range of the images goes from 1 to 100 (0 to 2 in log).

- **The first column of panels (a, d, g) shows the regions where the recent star formation on the different timescales (30 Myr, 140 Myr, 1400 Myr) is enhanced with respect to the average of these same regions over their whole lifetime:**

Before starting the description of the various panels we emphasize that this first column is the most difficult for us to interpret, given that the stellar populations inhabiting each spaxel/region have not remained static in that position throughout the whole lifetime of the system, but have changed with the dynamics of the galaxy.

In panel (a) the enhanced regions are the nucleus, and some areas to its south and north, corresponding with the beginning of the tidal tails. In this system, some of the tidal tail material has turned around and is falling back into the merger remnant (Privon et al., 2013). The morphology of the enhanced SFR in the last 30 Myr could be due to this. Considering the past 140 Myr (panel d), the regions of enhanced SFR with respect to their past average are the north tidal tail and the region rich in star clusters located south of the nucleus. On the longest time scale considered (g), we found that almost every spaxel has been more active than their lifelong average. The south tidal tail is the less active region. This distribution is consistent with our previously reported, spatially widespread intermediate age stellar populations.

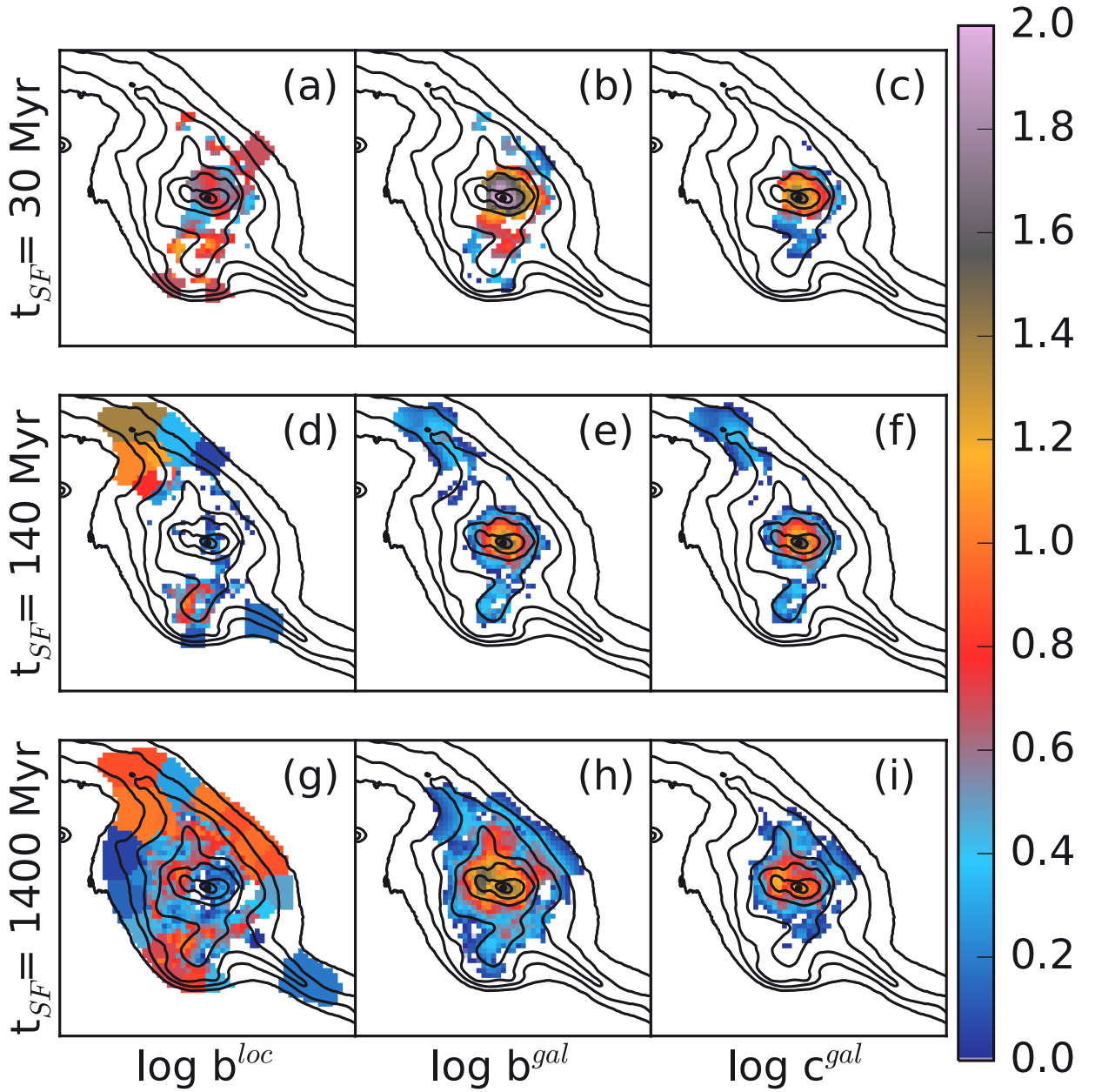


Figure 6.34 Spatially resolved SFR surface density on the last $t_{SF} = 30$ (top), 140 (middle), and 1400 (bottom) Myr in units of different reference values. The left panels compare $\overline{SFR}_{xy}(t_{SF})$ to $\overline{SFR}_{xy}(t_{\infty})$ i.e., the all-time average at xy , thus providing a local version of Scalo's b parameter (Eq. 12 of CF13). Middle panels compare the local $\overline{SFR}_{xy}(t_{SF})$ to the all-times average over the whole galaxy $\overline{SFR}_{gal}(t_{\infty})$ (Eq. 13 of CF13). Panels on the right compare $\overline{SFR}_{xy}(t_{SF})$ to that of the galaxy as a whole over the same time scale $\overline{SFR}_{gal}(t_{SF})$ (Eq. 14 of CF13). All images are in log scale from log 1 to log 100, such that only $\overline{SFR}_{xy}(t_{SF})$ values above the corresponding reference value are visible

- **In the middle column of panels (b, e, h) we can see the regions where the recent star formation on the different timescales (30 Myr, 140 Myr, 1400 Myr) is enhanced with respect to the average of the galaxy over its whole lifetime:**

From the longest timescale (h) to the shortest (b) we found that the region where the SFR is enhanced goes from almost the entire galaxy (≥ 3 HLR in panel h) to only concentrated in the nuclear region (~ 1 HLR in panel b). The 140 Myr timescale (panel e) shows something intermediate, the SFR is enhanced in the nucleus together with the region rich in star clusters located to the south and some regions in the north tidal tail.

- **The right column of panels (c, f, i) shows the regions where the recent star formation on the different timescales (30 Myr, 140 Myr, 1400 Myr) is enhanced with respect to the average of the galaxy in the same timescales:**

We found a distribution in the enhancement of the SFR very similar to the middle column of panels. Going from more extended (i, but less than h) to more concentrated (c). However, we note that in the last column we do not compare present to past in the galaxy, like in the middle column, but present to present in the galaxy. They show the location of the recent star formation in the galaxy for each timescale, so to speak.

In summary, in the advanced merger NGC 2623 we found that the SF has evolved from outside to inside. In the shortest timescale considered (30 Myr) the SF is concentrated toward the center, while in the longest timescale (1.4 Gyr) is more spatially extended, with the SFR in these regions being significantly enhanced with respect to the average past or actual SFR in the galaxy.

6.8. Discussion

6.8.1. Cluster populations tracing the merger epochs

We have used multiwavelength imaging from FUV to NIR to characterize the cluster properties in NGC 2623. Our analysis shows that NGC 2623 has experienced at least two recent major episodes of massive cluster formation, one in the innermost nuclear regions (inside 2.5 kpc) in the last ~ 50 Myr, and other around ~ 300 Myr in the off-nuclear and some clusters in the circumnuclear region (inside ~ 4.5 kpc). For the latter, and using only optical colors, [Evans et al. \(2008\)](#) derived cluster ages younger than us, between 1-100 Myr. Using their same optical color-color diagram we obtain their same result. However, we found that we can improve it including the UV data which allows us to better constrain the cluster ages. Moreover, the cluster ages derived by us are consistent with the results of the first dynamical simulation for NGC 2623 developed by [Privon et al. \(2013\)](#). They found that the first pericenter passage occurred 220 Myr ago (consistent with our intermediate age clusters), while the coalescence occurred 80 Myr ago (in agreement with our young nuclear clusters).

In anycase, the age segregation seen in the spatial distribution of the clusters suggests that the active region of cluster formation in NGC 2623 was larger ~ 300 Myr ago than it is today, with intermediate age clusters being more widespread than the younger ones. Thus, it is plausible that the earlier episode of massive cluster formation in NGC 2623 had a larger spatial extent than the current episode of cluster formation.

Something similar was found in Arp 220 by [Wilson et al. \(2006\)](#). Arp 220 is the closest ULIRG; although it is still a pre-coalescence system, it is a quite advanced pre-merger, with a very small separation between nuclei of 300pc. They found two distinct groups of clusters: a "young" population (< 10 Myr) and an intermediate age population (70 - 500 Myr). The "young" clusters are centrally concentrated, with an average radius of 1.6 kpc, while the intermediate age clusters would have formed in a region roughly twice as large if they formed in situ. NGC 7252 also shows a more compact spatial distribution for clusters younger than 10 Myr compared to the 300 Myr clusters that trace the overall light profile of the galaxy ([Miller et al., 1997](#)).

In contrast, the youngest star clusters in the pre-merger Antennae are not so centrally concentrated, distributed over a region roughly 2.5 kpc in size ([Zhang et al., 2001](#)). Also, in the pre-merger system NGC 6090 our results shown in Section 5.3 reveal widespread clusters, outside the nuclear regions and in the overlapping region whose colors are consistent with young < 300 Myr ages, but possibly even younger than < 10 Myr. In the overlapping region/bridge [Dinshaw et al. \(1999\)](#) found very young < 10 Myr cluster ages using NICMOS imaging. From FUV spectroscopy mean cluster ages ~ 5 Myr are found ([Leitherer et al., 2002](#)). Something similar is found in the pre-merger LIRG IC 1623. The clusters are extended along both components. Only in IC 1623 W they cover an area of 3.0 kpc radius. The vast majority of IC 1623 W clusters are very young (< 200 Myr), but depending on the dust extinction considered they can be younger (< 10 Myr). The only cluster we can age-date in IC 1623 E is consistent with an extinction between 2 - 3 mag and with an age below 10 Myr. This might suggest that, although hidden under large amounts of dust, some clusters in IC 1623 E are as young or more than IC 1623 W clusters.

Thus, it is plausible that the earlier episode of massive cluster formation in NGC 2623 had a larger spatial extent than the current episode of cluster formation. However, given the fact that we cannot yet estimate accurate ages for most of our cluster sample, specially those in the circumnuclear region, it is possible that massive star cluster formation in NGC 2623 has actually been more continuous over the last 300 Myr. Moreover, the cluster sample is very incomplete due to the high and variable internal reddening in NGC 2623. Spectroscopy has allow us to shed light on these issues.

6.8.2. Extended versus nuclear star formation in mergers

From the IFS we found that in NGC 2623 the young stellar populations (< 140 Myr) only dominate in the innermost (< 1 HLR ~ 3.3 kpc) nuclear regions, in some spaxels in the north tidal tail and in the three star forming knots south of the nucleus. On the other hand, the intermediate age stellar populations (between 140 Myr - 1.4 Gyr) are, in comparison, more widespread (~ 2 HLR ~ 5.4 kpc). This result reinforces what we found with photometry, and suggests that during an earlier stage of NGC 2623 the starburst process was spatially extended. However, in the current post-coalescence stage, the starburst is concentrated mainly in the nucleus.

This result would be in agreement with recent observations and state of the art numerical simulations. While for a long time simulations predicted that merger induced SF occurred only in the nuclear regions, in the last decade strong evidences of spatially extended merger-induced star formation have been found. Some examples of systems where the extended star formation is more or equally contributing to the total SFR than the nuclear star formation are: Antennae (NGC 4038 + 4039) ([Wang et al., 2004](#)), NGC2207 + IC2163 ([Elmegreen et al., 2006](#)), and NGC 7252 ([Chien & Barnes,](#)

2010). This is also the case of IC 1623 and NGC 6090 (see Chapter 5). Extended SF is also important in star forming galaxies at high redshift ($z \sim 1-3$), they present extended clumpy star formation (Förster Schreiber et al., 2009). In classical merger simulations nuclear starbursts appear naturally as a consequence of gas inflows produced by gravitational torques generated during the interaction. However, they are not able to reproduce the extended star formation. Recent simulations by Teyssier et al. (2010) and Bournaud et al. (2010), found that the extended starbursts originate from supersonic turbulence of the ISM. The ISM turbulence is increased in galaxy mergers as a consequence of the tidal interaction itself, which triggers non-circular motions, and it should arise spontaneously in hydrodynamic models capable of modeling gas below 1000 - 10000 K. Traditional SPH simulations cannot explicitly treat the supersonic turbulence that characterizes most of the mass in the real ISM (Burkert, 2006), because the limited spatial resolution translates into a minimal temperature under which gas cooling could not be modeled. This is why numerical simulations are barely starting to model merger-induced starbursts in a realistic way. The most up to date simulations use the Adaptive Mesh Refinement (AMR) technique, and have been able to reach a higher spatial resolution, modelling gas cooling down to low temperatures (below 300 K). In these models, the increased ISM turbulence is obtained without feedback, showing that it is not a consequence of the starburst activity, but is rather driven by the tidal forces in the interaction. A merger-induced nuclear starburst is also present, but the timescale is substantially longer. Therefore, they conclude that the extended star formation is important in the early stages of the merger, while the nuclear starbursts will occur in more advanced stages of the merger.

However, the timescales of the different periods of star formation still need to be observationally constrained to determine at which stage of the merger process they emerge. No extended and significant young star formation was found in the stage IIIa, post first passage Mice galaxies (Wild et al., 2014). However, in the more advanced stage IV, post coalescence merger NGC 2623, the extended star formation is already there and with ages around ~ 500 Myr. It seems like the extended star formation must appear in an interaction stage in between them, probably around stage IIIb. This is supported by our results of the IIIb stage pre-merger LIRGs IC 1623 and NGC 6090 (Chapter 5), where we found young extended stellar populations.

6.8.3. Relative importance of extended and nuclear starbursts

There is no thorough observational census of the contributions of nuclear and extended star formation to merger-induced activity, and how these contributions vary along the merger sequence. We would like to somehow quantify the relative impact of these two periods of star formation in NGC 2623, by comparing the amount of stellar mass formed in each of them. We have calculated the total mass hosted by young populations $M_*(< 140 \text{ Myr}) = 8.1 \times 10^8 M_\odot$. If we consider that most of them are inside 1 HLR (= 3.3 kpc), then the mass density of this population is $\leq 24 M_\odot \text{ pc}^{-2}$. This is an upper limit, because the young components are in fact a bit more extended. For the intermediate age stellar populations we find $M_*(140 \text{ Myr} - 1.4 \text{ Gyr}) = 1.4 \times 10^{10} M_\odot$. The intermediate burst formed 17 times more mass than the nuclear one. However, it was more widespread and the difference in mass density should not be as large. Considering that the intermediate age populations are widespread over a 2 HLR region (= 6.6 kpc), then their mass density is $\sim 102 M_\odot \text{ pc}^{-2}$, about 4 times larger than the star formation rate density of the young SSPs.

6.8.4. Ionized gas distribution in mergers

Most of the ionized gas in NGC 2623 is concentrated in the nuclear regions (inside 1 HLR or less). There are, however, some star forming regions in the north tidal tail and south of the nucleus. This reinforces the idea that the young stellar components are mostly located in the nuclear regions for the advanced post-coalescence systems. On the contrary, for pre-merger LIRGs IC 1623 and NGC 6090 the young stellar components are more widespread (see Chapter 5, Section 5.5).

This is supported by [Hattori et al. \(2004\)](#). They compare the H α emission of 22 LIRGs to study how the distribution of star forming regions in these galaxies is related to the stage of the galaxy interaction. They found that in close pairs (projected separation ranges from 4 to 20 kpc) and specially in pairs (nearby < 100 kpc companion galaxies) the contribution of extended starbursts to the emission is increasingly important and the nuclear starbursts can be > 1 kpc. On the contrary in mergers (single nucleus) the nuclear starbursts are very compact (from 100 pc - 1 kpc) with no or negligible star forming activity in the outer regions. Also, [García-Marín et al. \(2009\)](#); [Arribas et al. \(2012\)](#) study the H α emission of 26/54 local U/LIRGs, observed with IFS. They found that in the pre-coalescence systems the size of the H α emitting region is $r_{1/2}(\text{H}\alpha) > 2$ kpc and up to 7 - 8 kpc, while for the post-coalescence systems is below 2 kpc.

6.8.5. Ionization mechanism in mergers

With respect to the ionization mechanism, and thanks to the resolution of OSIRIS we found that close to the nucleus, the photoionization is due to a dusty nuclear starburst, while the emission in the outskirts is more consistent with large scale shocks. The characteristics of the nucleus of NGC 2623 could be associated with a starburst related LINER. The starburst is energetic enough to generate an amount of outflowing gas that collides with the ISM, producing shocks (LINER emission) and sweeping the dust from the nucleus. This is in agreement with previous study of NGC 2623 by L04. In the nucleus of the pre-merger systems IC 1623 and NGC 6090 we found the ionization mechanism consistent with pure star formation. No LINER emission is present in these two earlier stages of the interaction (Chapter 5, Section 5.5.6). We hypothesized that to produce a significant outflow it is necessary to have a very massive and compact starburst, like the ones produced in the central regions of galaxies in the last stages of the interaction, where a large amount of gas is concentrated into a small area.

6.8.6. Shock luminosity vs. input energy from star formation

We have determined the luminosity of the shocked regions to estimate the amount of current star formation which is necessary to power the outflow. The luminosity of the shocked regions has been calculated summing in the dust attenuation corrected H α map (right panel of Figure 6.24) the flux from all the spaxels with pure LINER ionization in the [NII]/H α vs [OIII]/H β diagram (that is, the spaxels with red dots in Figure 6.28). In this way we exclude the nuclear regions where the emission lines are strongly contaminated by star formation, like the composite ones. We find the total H α luminosity of the shocks: $L_{\text{H}\alpha}^{\text{shock}} = 2.5 \times 10^{41}$ erg s $^{-1}$, leading to a bolometric energy loss rate of $\dot{E}_{\text{shock}} \sim 2.0 \times 10^{43}$ erg s $^{-1}$, where we have taken a bolometric conversion factor of 80, appropriate for $v_{\text{shock}} \geq 140$ km s $^{-1}$ ([Rich et al., 2010](#)).

From this, we can estimate the amount of current star formation, which is necessary to power the outflow. The mechanical energy injection rate into the ISM by SNe can be estimated from evolutionary synthesis models of populations of massive stars (Leitherer et al., 1999). For Salpeter IMF, in the solar-metallicity case, and assuming a continuous SFR, the mechanical luminosity is constant beyond ~ 40 Myr and scale with SFR:

$$\dot{E}_{SNe} = 7 \times 10^{41} (\text{SFR}/M_{\odot} \text{ yr}^{-1}) \text{ erg s}^{-1} \quad (6.15)$$

We found that a SFR $\sim 29 M_{\odot} \text{ yr}^{-1}$ is at least needed to power the observed outflow in case of solar metallicity. For $0.4 Z_{\odot}$ the expected SFR would be $\sim 24 M_{\odot} \text{ yr}^{-1}$. This value is very similar to the observational one (Section 6.7) obtained from multiwavelength data, SFR $\sim 17 M_{\odot} \text{ yr}^{-1}$ for Salpeter IMF and $0.4 Z_{\odot}$.

6.8.7. Tidal Dwarf Galaxy forming in NGC 2623?

As a result of the enhancement of the star formation in galaxy mergers, SSCs are probably not the ultimate bound structures that can be created during the interaction. Condensations of large amounts of gas along the tidal tails and at the tips have been observed during the last few decades. In such condensations objects as massive and as large as the most extreme cases of SSCs and even more, within the range of the dwarf galaxy population, can be formed. Some of these structures can be bound and long-lived. They are widely known as Tidal Dwarf Galaxies (TDGs).

Numerical simulations of mergers of two gas-rich spirals show that dwarf galaxies can form at the tip of the tidal tails (Barnes & Hernquist, 1992; Yoshida et al., 1994). They consist of a chain of nebulae ionized by recently formed massive stars, which are embedded in an envelope of HI gas and low surface brightness optical emission.

Recently, TDGs have been also analysed in low- z (U)LIRGs by Monreal-Ibero et al. (2007) and Miralles-Caballero et al. (2012). Based on these observations, TDG candidates are more luminous than $B = -10.65$, typically $B = -13$, and can be as luminous as $B = -19$. Their color is typically blue ($B - I = 0.7 - 2$), indicative of young stellar population. The presence of young population is firmly proved with the detection of strong $H\alpha$ emission with an equivalent width higher than tens of \AA .

But the identification of the observed TDG candidates as real galaxies is not straightforward. They are embedded in a tidal tail and, most probably, do not have massive dark matter halos (Barnes & Hernquist 1992). Tidal forces of the parent galaxy disturb their gravitational field, strong star formation might blow away the recently accreted gas, and some of the TDGs may even fall back into the central merger (Hibbard & Mihos, 1995).

An accepted definition that tries to ensure that only those objects which called Tidal Dwarf Galaxies, deserve to be named "galaxy" is: A Tidal Dwarf Galaxy is a self-gravitating entity of dwarf-galaxy mass built from the tidal material expelled during interactions. Taking into account evaporation and fragmentation processes plus tidal disruption, Duc et al. (2004) suggested that a total mass as high as $10^9 M_{\odot}$ may be necessary for a new formed TDG to become a long-lived object. This is the typical mass of the giant HI accumulations observed near the tip of several long tidal tails. Less massive condensations may evolve, if they survive, into objects more similar to globular clusters.

In NGC 2623, most of the HI component ($M_{HI} = 3.8 \times 10^9 M_{\odot}$) is located outside the stellar main

body (Hibbard & Yun, 1996), and accumulated in both tidal tails. In Section 6.5.6 we report the detection of four bright HII regions in the southwestern tidal tail of NGC 2623, that were previously detected in the UV and H α by Bournaud et al. (2004); de Mello et al. (2012). With our data we can not characterize the properties of these HII regions and therefore, we can not ensure if a TDG is in formation in NGC 2623. de Mello et al. (2012) found that two of the HII regions are embedded near the peak of the HI emission, which is one of the requirements for a TDG candidate. Also, using FUV and NUV colors they estimate an age of ~ 30 Myr and a stellar mass of $\sim 4 \times 10^6 M_{\odot}$ for one of the regions and ~ 4 Myr old and a mass $\sim 5 \times 10^4 M_{\odot}$ for the other. They do not go into detail of whether a TDG is forming in NGC 2623. However, they conclude that "real" TDG favorably form in compact groups of galaxies rather than in other interacting systems as NGC 2623 and other U/LIRGs or mergers. The UV sources detected by them in 6 interacting galaxies (including NGC 2623) are significantly less luminous/massive than the sources in their Hickson Compact Group sample.

6.9. Summary and conclusions

In this chapter we have characterized the merger LIRG NGC 2623. Using HST multiwavelength imaging, PMAS LArr and CALIFA IFS, and OSIRIS narrow band H α and [NII] λ 6583 imaging we have analyzed the star clusters properties, the stellar population properties, the ionized gas distribution and properties, the ionization mechanism, the kinematics, and the star formation rates.

Our main results are:

1. *Star clusters properties:* The concentration of clusters south of the nucleus is consistent with not being affected by foreground extinction. They have ages ranging 100 - 500 Myr, with an average around ~ 300 Myr. Only a few of them could be younger if we consider they are affected by some extinction. On the contrary, the nuclear clusters are affected by high values of extinction, between 2 - 4 mag. Some of them, the ones less affected by extinction, are consistent with ages younger than 50 Myr. This suggests that the nuclear region of NGC 2623 is slightly younger than its surroundings. The greater scatter is in the circumnuclear clusters. They are consistent with an average extinction of around 1 mag. Given their spread in the diagrams they are compatible with having ages ranging 1 - 500 Myr. We found a large range of masses in the clusters of NGC 2623. The intermediate-age clusters in the region south of the nucleus have masses from 10^4 - $10^5 M_{\odot}$. In the circumnuclear clusters the spread is larger 10^4 - $10^7 M_{\odot}$. On the other hand, the vast majority of the inner nuclear clusters are consistent with masses between 10^6 - $10^8 M_{\odot}$. A rough estimate of the total mass in clusters in NGC 2623 is $M_{NGC2623}^{clus} \sim 6 \times 10^8 M_{\odot}$; which represents 1% of the total stellar mass.

The mass in young components derived through the IFS is comparable (only a factor ~ 1.5 less) to the mass in star clusters derived roughly from the photometry. This would agree with the hypothesis that the vast majority of stars form in clusters rather than in isolation.

2. *Stellar luminosity:* The stellar luminosity at 5635 \AA decreases uniformly from $0.1 L_{\odot} \text{ pc}^{-2} \text{ \AA}^{-1}$ in the nucleus of NGC 2623 to $0.003 L_{\odot} \text{ pc}^{-2} \text{ \AA}^{-1}$ in the outskirts. There exists a good agreement in the measured surface brightness from the LArr and CALIFA datasets.
3. *Stellar dust extinction:* Most of the dust is located in the central (inner kpc) regions, reaching values up to 2 mag. The dust content decreases with distance to the nucleus to < 1 mag outside

the inner 0.8 HLR (~ 2.2 kpc). Moreover, we found that the north tidal tail is affected by ~ 1 mag, while the south tidal tail is almost no dust obscured. The global average is $A_V \sim 0.5$ mag. Considering the dispersion of both datasets, above 0.2 HLR their results are indistinguishable from each other. Only in the nucleus itself (below 0.2 HLR) we derive slightly lower extinctions for LArr (~ 1.4 mag) than from CALIFA (~ 1.6 mag). The nuclear differences in the stellar population properties derived with PPAK and LArr are due to a combination of differences in the PSFs of PPAK and LArr, and also to the age-extinction degeneracy.

4. *Stellar ages:* The younger regions in NGC 2623 are the nucleus, the region rich in star clusters located south of the nucleus and the north tidal tail, with mean age around 250 Myr. On the other hand, the south tidal tail and the eastern region of the main body are older, with ages around 1 Gyr. In the circumnuclear regions we find a positive trend of the ages with distance, from ~ 200 Myr in the nucleus itself to ~ 500 Myr at 1 HLR. It is also interesting to note that everywhere in this system the mean stellar ages range 140 Myr to 1.4 Gyr. As a consequence of age-extinction degeneracy and differences between PPAK and LArr PSFs, below 0.2 HLR, the ages derived from LArr are 360 - 570 Myr older than CALIFA.
5. *Stellar metallicities:* Metallicity is one of the most difficult quantities to constrain. The fact that sometimes age and Z grow in the opposite sense, as in the tails of NGC 2623, could suggest that the results are affected by the age-metallicity degeneracy. The north tail is young (300 Myr) and metal rich ($1.5 Z_\odot$), while the south tail is old (1.4 Gyr) and metal poor ($0.25 Z_\odot$). Due to this, we will take the metallicity results with caution. The mean metallicity of NGC 2623 is $\sim 0.5 Z_\odot$ and its radial profile is fairly flat.
6. *Stellar mass surface density:* It follows a negative trend with distance, decreasing from $\log \mu_* \sim 3.7$ in the nucleus itself to $\log \mu_* \sim 1.5$ at ~ 3 HLR. Stellar mass surface densities from LArr data are 0.2 dex larger than CALIFA. This is due to the previously reported differences in the stellar population properties.
7. *Stellar masses:* From the spectral synthesis the total stellar mass obtained from the spatially resolved analysis is $M = 4.5 \times 10^{10} M_\odot$. This is the mass locked in stars nowadays. Counting also the mass returned by stars to the interstellar medium $M' = 6.3 \times 10^{10} M_\odot$ were involved in star formation. These are the results for GM base of models, with Salpeter IMF. With CB base (Chabrier IMF) we found $M' = 4.4 \times 10^{10} M_\odot$ and $M = 2.4 \times 10^{10} M_\odot$.
8. *Star Formation History:* We calculate and compare both the time resolved 1D SFHs and the spatially resolved SFHs, condensing the population vector into three age ranges namely young (YSP, SSPs ≤ 140 Myr), intermediate (ISP, $140 \text{ Myr} < \text{SSPs} \leq 1.4$ Gyr), and old populations (OSP, SSPs > 1.4 Gyr).
 - From the time resolved 1D SFH (in light fraction) we get a more detailed idea of when the bursts of star formation started and how many of them occurred. In NGC 2623, there could have been two relevant "young" bursts between 5 Myr to 13 Myr ago. However, the spectral differences between these 2 SSPs are not enough to distinguish (within our temporal resolution) if they were individual bursts or something more "continuous". Within

the intermediate/intermediate-old age range we found that two bursts may have occurred, the less intense peaking at 1.4 Gyr and the more intense peaking around 500 Myr but ranging from 300 Myr to 1 Gyr. The old populations formed between 14 Gyr and 4 Gyr ago for NGC 2623.

- The contribution to light of the YSP is only important in the nuclear region, the north tidal tail and the region rich in star clusters located south of the nucleus, with contributions to total light between 40 - 70 %. The ISP dominate the light almost everywhere (with contribution up to 60 - 70 %), except in the nucleus itself and the south tidal tail. It is interesting to note the presence of this widespread ISP in this merger. On the other hand, the only region which is clearly dominated by OSP is the south tidal tail, with a contribution to light of ~ 70 %. They are also responsible of 30 % of the nuclear light. From the radial profiles we found that below 1.5 kpc (0.6 HLR) the light is dominated by YSP, with contributions between 35 - 60 %. Above 1.5 kpc and up to 9 kpc the light is clearly dominated by ISP, also with contributions between 35 - 60 %.
- The fraction of stellar mass contributed by YSP is less than 5 % everywhere, except maybe in the north tidal tail, where it can be up to 30 %. Most of the mass is contained in OSP. In particular, they dominate the mass contributions below 4 kpc (1.5 HLR). Beyond, the mass contribution of the ISP is also significant, between 40 - 60 %, similar to the old stars contribution. When summing the total mass in each age bin, we found that from the total $M' = 6.3 \times 10^{10} M_{\odot}$ in NGC 2623, the mass in young $M'(Y)$, intermediate age $M'(I)$, and old $M'(O)$ stellar populations is $8.1 \times 10^8 M_{\odot}$ (1 %), $1.4 \times 10^{10} M_{\odot}$ (22 %) and $4.8 \times 10^{10} M_{\odot}$ (77 %), respectively.

9. *Ionized gas morphology:* In NGC 2623, the vast majority of the ionized gas emission comes from the nuclear regions, consistent with the outflow cone nebulae reported by L04. Outside the nuclear regions, we also found three star forming knots south of the nucleus and fainter $H\alpha$ emission in the north tidal tail, detected in both CALIFA and OSIRIS maps. Given the highest spatial resolution of OSIRIS map we are able to distinguish two substructures within the cone-nebulae, that are unresolved in the CALIFA and L04 maps. On one hand, there is a point-like source offset with respect to the nucleus by (2.7''E, 0.1''N). Its morphology is consistent with a star forming knot, also confirmed by the line ratios ($[NII]/H\alpha \sim 0.5$). Moreover, it is detected in the HST F555W continuum image. On the other hand, there is an extended, bow-shaped, lobular like emission with clumpy ends that seems to emerge from the nucleus. This kind of morphology is typical from shocked regions. From F555W image we find that the brightest $H\alpha$ emission also corresponds to several cluster aggregations. However, most of the extended $H\alpha$ emission is spatially coincident with highly dust obscured regions.
10. *Ionized gas electron density:* Using $[SII]\lambda 6716/[SII]\lambda 6731$ ratio we have determined the electron density in NGC 2623. The ratio has values around 1.25 in the nucleus, equivalent to an electron density of $\sim 200 \text{ cm}^{-3}$. To the west of the nucleus and in several spaxels to the south east we found regions with higher densities, up to $\sim 600 \text{ cm}^{-3}$ (ratios up to 1.0). Everywhere else the ratio is above 1.4, implying densities below 100 cm^{-3} .
11. *Ionized gas dust extinction:* The highest extinction is found in the nuclear regions with values up

to 4.5 magnitudes. This level of extinction is consistent with the dust lanes visible in the HST images. However, the ionized gas in the north tidal tail and in the clusters south of the nucleus has $A_V \leq 1$ mag. The global average is $A_V \sim 1.4$ mag. Compared with the stellar extinction we found an average $\langle \frac{A_{V,gas}}{A_{V,stars}} \rangle = 1.9 \pm 1.1$.

12. *Emission line ratios sensitive to ionisation source:* The star formation in the north tidal tail and the three emission knots south of the nucleus (C1, C2, and C3) is compatible with being high-metallicity star forming regions. With the greater spatial resolution of OSIRIS we see finer details of the ionization mechanisms in the nuclear region of NGC 2623. In particular, inside L04 cone nebula, the nuclear knot (A) seen on OSIRIS $H\alpha$ map and some pixels at the clumpy ends of the nuclear lobe, are also consistent with high-metallicity star formation ($[NII]\lambda 6583/H\alpha \sim 0.5$), while the remaining have $[NII]\lambda 6583/H\alpha$ between 1.0 - 1.2. For the pixels/spaxels at the edges of the cone nebulae, the $[NII]\lambda 6583/H\alpha$ is even larger, with values between 1 - 2, which could be mainly associated with the effects of large-scale shocks when the outflowing gas collides with the ISM. In anycase, it seems that close to the nucleus, the photoionization is due to a dusty nuclear starburst, while the emission in the outskirts is more consistent with large scale shocks. The characteristics of the nucleus of NGC 2623 could be associated with a starburst related LINER. Inside the cone nebulae $[OI]\lambda 6300/H\alpha$ and $[SII]\lambda\lambda 6716+6731/H\alpha$ have values ~ 0.15 and ~ 0.5 , respectively. These are indicative of shock heated gas of moderate velocity. The spaxels in the outskirts, however, have larger values of the ratios, up to 0.7 for $[OI]\lambda 6300/H\alpha$ and 2.0 for $[SII]\lambda\lambda 6716+6731/H\alpha$, which are consistent with higher velocity shocks.
13. *Diagnostic diagrams:* Only the gas in the north tidal tail and the brightest knot south of the nucleus is consistent with pure star formation ionization. On the other hand, the gas inside the nuclear cone defined by L04 (a bit narrower and elongated in our data), is consistent with LINER emission, together with some other spaxels to the west of the nucleus. The remaining spaxels seem to be composite between star formation and LINER-like emission. Using $[OI]\lambda 6300/H\alpha$ vs $[OIII]\lambda 5007/H\beta$ diagnostic diagram we derive that within all the circumnuclear region of NGC 2623, the ionization mechanism is LINER type.
14. *OSIRIS line emission at the edge of the SW tidal tail:* In OSIRIS $[NII]\lambda 6583$ map we detect four bright star forming regions, located more than 19 kpc away from the center, at the edge of the southwestern tidal tail. Given the position of these regions in OSIRIS FoV, they are emitting in wavelengths that range from 6553 to 6562 Å, consistent with the spectral region between $[NII]\lambda 6548$ and $H\alpha$. According to this, the ages of the star forming regions must be below or around 30 Myr. Their fluxes range from $2.5 - 7.7 \times 10^{-16}$ erg s $^{-1}$ cm $^{-2}$.
15. *Ionized gas velocity field:* In both $H\alpha$ and $[NII]\lambda 6583$ velocity fields the rotation pattern is preserved in the nucleus, with an amplitude of ± 120 km/s, in agreement with [Barrera-Ballesteros et al. \(2015\)](#) and L04. We have found that the kinematic center is displaced 2 arcsec to the east with respect to the photometric center. However, this is within our spatial resolution.
16. *Ionized gas velocity dispersion:* In $H\alpha$ and $[NII]\lambda 6583$ velocity dispersion maps we found evidence of the outflow, as the highest values of σ (~ 220 km/s) are reached inside the outflow nuclear

cone defined by L04. This is specially noticeable in the $H\alpha$ map. In addition, the regions with the highest σ values are approximately coincident with pure LINER spaxels in the BPT diagram.

17. *Star Formation Rates:* We have derived and compared the SFRs using multiwavelength data from UV, optical IFS (continuum and lines), MIR at $24\ \mu\text{m}$, FIR and radio 1.4 GHz.

- In NGC 2623 we measure a total dust-attenuation corrected $H\alpha$ luminosity of $L_{H\alpha} = 3.35 \times 10^{41}\ \text{erg s}^{-1}$, that lead to a total SFR $\leq 2.2\ M_{\odot}\ \text{yr}^{-1}$, which is surprisingly low, not even near the $24\ M_{\odot}\ \text{yr}^{-1}$ which are in principle necessary to power the observed outflow (see Section 6.8.6).
- From the continuum, we found that the SFR(30 Myr) is an order of magnitude (a factor between ~ 7) larger than SFR($H\alpha_{corr}$), ~ 15 vs ~ 2.2 for Salpeter IMF and ~ 7 vs ~ 1.3 for Chabrier IMF. This makes no sense as the SSPs < 30 Myr are the ones expected to ionize the $H\alpha$ gas around them. The only possible explanation is that the gas is significantly more obscured than these stars, which is possible considering that the stellar winds emitted by these stars are able to clear the gas and dust in their immediate surroundings but not in the outer areas of the HII region.
- The SFR(140 Myr) is more similar to the SFR(FUV), ~ 2.5 vs ~ 1.2 for Chabrier IMF, a factor 2 larger, which is within the uncertainties.
- The three hybrid tracers combining the observed $H\alpha$ together with $24\ \mu\text{m}$, FIR, and radio 1.4 GHz, provide us with three alternative SFR estimates which account for optically thick dust obscuration by direct detection of the thermal dust emission. We found a strong consistency between them, all pointing to a global average SFR $\sim 17\ M_{\odot}\ \text{yr}^{-1}$ (Salpeter) and SFR $\sim 10\ M_{\odot}\ \text{yr}^{-1}$ (Chabrier).
- The hybrid multi- λ SFR is similar to the one derived from continuum decomposition, SFR(30 Myr), and an order of magnitude larger than the SFR derived with $H\alpha$ dereddened luminosity. This result implies that some of the ionizing photons have been absorbed by dust and reemitted in the IR/radio instead of ionizing the $H\alpha$ emitting gas. Taking this into account, we found that the average $A(H\alpha)$ should be around 4.3 mag, instead of the ~ 1.4 mag we measure with the IFS.
- The average SFR in NGC 2623 is a factor 5 higher than the SFR in the Milky.

18. *Star Formation Rate Densities:* Considering that the radius of active star formation in NGC 2623 is ~ 3 HLR (= 9.9 kpc), that implies a $\langle \Sigma\ \text{SFR} \rangle_{NGC2623} = 0.033\ M_{\odot}\ \text{yr}^{-1}\ \text{kpc}^{-2}$, a factor 10 larger than the SFR density of the Milky Way ($\langle \Sigma\ \text{SFR} \rangle_{MW} = 3.3 \times 10^{-3}\ M_{\odot}\ \text{yr}^{-1}\ \text{kpc}^{-2}$, Kennicutt & Evans 2012).

We have also compared the star formation rate densities in NGC 2623 from $H\alpha$ and the stellar continuum in the last 30 Myr. The final conclusion is that, the extinction in the nuclear regions of NGC 2623 is so high that some of the ionizing photons have been absorbed by dust and re-emitted in IR/radio wavelengths instead of ionizing the $H\alpha$ emitting gas.

On the other hand, the $\Sigma\ \text{SFR}(30\ \text{Myr})$ and $\Sigma\ \text{SFR}(H\alpha)$ maps show that the SF in this merger is progressing inward following the collapse of gas into the nuclear region.

19. *IFS-base variations over Scalo's b parameter:* In the advanced merger NGC 2623 we found that the SF has evolved from outside to inside. In the shortest timescale considered (30 Myr) the SF is concentrated toward the center, while in the longest timescale (1.4 Gyr) is more spatially extended, with the SFR in these regions being significantly enhanced with respect to the average past or actual SFR in the galaxy.

Post-Starburst QSOs

7.1. Introduction

PSQSOs are potentially useful systems to test relations between nuclear activity and host galaxy evolution. In them, both an AGN and a post-starburst population coexist with similar bolometric luminosities. Recently, [Cales et al. \(2011, 2013\)](#) (hereafter C11 and C13) have performed an extensive study of this kind of systems, analyzing both the morphology in HST imaging and their physical properties using long slit spectroscopy. They do not find clear correlations between ages/masses of the stellar populations and the AGN properties when considering the sample as a whole. However, when classifying in morphological types, they found that PSQSOs with early type hosts have significantly higher AGN luminosities, younger starburst ages, and narrow emission-line ratios diagnostic of Seyfert when compared to their spiral counterparts. They hypothesize that early type PSQSOs are likely the result from a major merger and were likely LIRGs in the past, while spiral PSQSOs show more complex SFHs triggered by less dramatic events (harassment, bars...).

In this work we have analyzed a sample of 9 PSQSOs (all included in C13 sample), for which we have PMAS/VIMOS spectroscopy and SDSS spectroscopy. From the spectral continuum we derived the main stellar and AGN properties, while using the information from the emission lines to further unveil their characteristics. The methodology is similar to C13 work, with some improvements, and we have compared in detail our results with theirs.

7.2. Data

7.2.1. PMAS/VIMOS IFS

The IFS of the PSQSOs was described in Section 2.3 and the data reduction in Chapter 3. We find that the SNR is too low to perform an analysis in a spaxel by spaxel scheme. For this reason, we finally decided to extract and analyze the integrated and central spectra. The central aperture radius is 1.5 arcsec, identical to the fiber aperture radius of SDSS spectroscopy, described below. At the PSQSOs redshift ($z \sim 0.3$; $D_L \sim 1553.4$ Mpc) the spatial scale is 4.456 kpc/arcsec, and 1.5 arcsec corresponds to ~ 6.7 kpc. The integrated spectra have been extracted in variable apertures (all of them above the Petrosian radius aperture), in a way that it includes the whole optical extension of

each PSQSOs. The spectra of the 6 PSQSOs observed with PMAS go from 3000 - 5200 Å. We also have red spectra covering H α . In most cases, it is very noisy. We only use it to measure the H α flux, but not for continuum fitting. The spectra of the 3 PSQSOs observed with VIMOS range from 3650 - 6700 Å.

7.2.2. SDSS

The SDSS spectra were downloaded from SDSS archive Data Release 8. They were already flux- and wavelength-calibrated and cover the rest-frame spectral range from ~ 3000 to 7000 Å. The fiber aperture radius was 1.5 arcsec. As for the IFS, we have corrected SDSS spectra for Galactic extinction using the [Schlegel et al. \(1998\)](#) maps and the IRAF task `deredden` which utilizes the [Cardelli et al. \(1989\)](#) extinction curves. We converted the spectra to rest frame by using the IRAF `dopcor` task with NED redshifts.

7.3. Stellar populations synthesis and AGN component modelling

We have performed spectral synthesis with *Starlight*, similarly to how was done for the LIRGs. First, we created the necessary error spectra as explained in detail in Section 5.4.1. In summary, the error for each pixel is computed as the standard deviation of the nearest 100 pixels around the input pixel. We used these error spectra to weight spectral pixels in the fitting procedure with *Starlight*.

Our model base was formed by the solar metallicity SSPs of CB base up to 10 Gyr (the Universe age at $z \sim 0.3$) together with a power-law component that models the AGN. In this Chapter we focus on CB base results for several reasons. First, because they cover the spectral range below 912 Å and using the extrapolation of the best fit model in this range we will estimate the expected number of ionizing photons, and therefore, the expected H β and H α , which will be compared with the values directly measured from the emission lines. Second, CB base was used also in C13 work, and we plan to compare our results with theirs. Finally, we want to mention that we have also used the GM model base and found that CB base allows to better break the degeneracy between the light fraction in SSPs younger than 30 Myr and the power-law. Most of the PSQSOs spectra start around 2900 - 3000 Å, some of them with a significant slope in this range, characteristic of an AGN and / or very young stellar populations. While the GM base starts in 3540 Å, the CB base extends the fits below it, covering the whole blue range. As a consequence, CB base puts a significant contribution in light to the AGN (20 - 40%), while the GM base puts nothing and instead allocates it in the youngest stellar populations (< 30 Myr). Although here we focus on CB base results, in Section 8.3 we will also show GM results and will discuss the differences between them.

The AGN component is modeled as a composite power-law with the form $L_\lambda \propto \lambda^{\alpha_\lambda}$. Depending on the wavelength range, we fixed the spectral index α_λ to the average value previously estimated from big QSOs samples of [Telfer et al. \(2002\)](#) and [Vanden Berk et al. \(2001\)](#):

$$\alpha_\lambda = \begin{cases} -0,5 & \lambda \leq 1200\text{\AA} \\ -1,5 & 1200\text{\AA} < \lambda < 5000\text{\AA} \\ -0,5 & \lambda \geq 5000\text{\AA} \end{cases}$$

We have performed three sets of *Starlight* fits with different assumptions and have compared their quality and the consistency between them:

1. In the first set, we assume that both the stars and the AGN are affected by the same amount of dust extinction by configuring *Starlight* to use the same A_V value for the SSPs and the power-law component. This is a reasonable first approach as we expect low to no extinction in this kind of objects. Moreover, we used the total measured $H\beta$ flux as a constrain in the fits of IFS central and integrated spectra. For SDSS spectra, we used as a constrain the observed $H\alpha$ flux (see Section 7.4 for emission line measurements). In this way *Starlight* forces the $H\beta$ ($H\alpha$) flux predicted by models to equal the observed.
2. In the second set, we still assume the same extinction for stars and AGN but we did not force *Starlight* to fit the observed Balmer lines. We will refer to this as the unconstrained or non-constrained fits.
3. In the third set, we allowed *Starlight* to use different values for the extinction of stars and AGN while using the Balmer fluxes as a constrain.

With the latter set, we increase the number of free parameters and further complicate the task of unveiling the basic properties of PSQSOs. This is too ambitious given that we already have some other important degeneracies. The results obtained with this set, will not be included when calculating the global averages. However, we made it as a sanity check to confirm that the stellar and AGN properties derived do not change drastically when we allow the AGN to have a different extinction value.

Within each of these three sets of assumptions we also tried 3 different spectral bases in order to probe the presence of young ionizing components:

1. including all the SSPs down to 1 Myr,
2. excluding SSPs < 4 Myr and
3. excluding SSPs < 30 Myr.

The spectral synthesis fits, star formation histories, and stellar population results for the three sets of assumptions, each of them with the three spectral bases, are shown in Appendix A.

To discriminate the best and more reliable fits within this vast amount of information we checked by eye the fit quality and residuals and also took into account how physically meaningful they were. In particular, from *Starlight* best model fits we calculated the $H\beta$ (from IFS spectra) and $H\alpha$ (for SDSS spectra) flux expected to arise from the stellar and the power-law components by summing their flux below 912 Å to calculate the number of ionizing photons

$$Q_{H0} = \int_0^{912} \frac{i_\lambda \lambda}{hc} d\lambda \quad (7.1)$$

where i_λ is the synthetic flux emitted by the AGN or stars. For case B hydrogen recombination one out of 2.226 ionizing photons produces an $H\alpha$ photon (Osterbrock & Ferland, 2006): $Q_{H\alpha} = Q_{H0}/2,226$.

Taking this into account the expected H α flux can be calculated with

$$I_{H\alpha}(\star/AGN) = \frac{Q_{H\alpha}(\star/AGN) hc}{\lambda_{H\alpha}} \quad (7.2)$$

and the observed (dust-obscured) one will be:

$$F_{H\alpha}(\star/AGN) = I_{H\alpha}(\star/AGN) \times 10^{-0.4A_{H\alpha}^{\star/AGN}} \quad (7.3)$$

and analogously in the case of H β (these fluxes are shown for each object in the last two rows of Tables A.1 and A.2). These "expected" fluxes are compared with the H β and H α flux measured for the BLR and NLR (see Section 7.4). We considered as physically meaningful those fits which satisfied:

$$F_{H\alpha,H\beta}(AGN) \geq F_{H\alpha,H\beta}(BLR) \quad (7.4)$$

$$F_{H\alpha,H\beta}(\star) \leq F_{H\alpha,H\beta}(NLR) \quad (7.5)$$

This allow us to break some degeneracies and to discard some fitting options.

For example, we found that the spectral base including SSPs down to 1 Myr leads to results that do not satisfy Equation 7.5. Even small contributions of SSPs younger than 4 Myr shoot up the stellar H β (H α) flux well above what we measure in the NLR of some PSQSOs (J1700, J1230, J2310, J2334, J0237). Moreover, as shown is Section 7.8.1, the ionization mechanism is Seyfert for 7/9 PSQSOs, and only 2/9 are composite. Therefore, most of the narrow H α , H β do not have a stellar origin.

On the other hand, if we remove from the base all the ionizing SSPs (those with ages < 30 Myr) then Equations 7.4 and 7.5 are satisfied, but the fit quality is worst in the blue side of some spectra, specifically those of J1700, J1230, J2128 and J2310 for SDSS data and only J1230 for our IFS central spectra. This suggests that, at least in some of these systems, there could be young stellar components (between 4 - 30 Myr) contributing to the blue continuum flux. However, this may not be the case for the remaining 5/9 systems, where the fit quality is also good with this base and the young populations (when present) may not be as young.

We have found that the fits with the base excluding SSPs < 4 Myr are the best compromise between fit quality and physically meaningful results. This base gives 'average' results between those including all the ionizing stars and those excluding all of them.

In anycase, we note that most of the scatter in the results is related to the different fitting assumptions and secondarily to the spectral base used. In terms of quality fit both the constrained and unconstrained fits are equally good.

From Figures 7.1 to 7.7 we show respectively: the AGN contributions to light at 5100 Å (in percentage), the total AGN luminosity integrated from 3000 - 6000 Å ($\log L_{AGN}$ (erg s⁻¹)), contribution to light of SSPs younger than 140 Myr (in percentage), mean stellar ages ($\langle \log \text{age (yr)} \rangle_L$), mean stellar extinctions (A_V^{stars}), stellar masses ($\log M_\star$ (M_\odot)), and stellar masses in intermediate-age SSPs ($\log M_{\star < 1.5Gyr}$ (M_\odot)). In the left panels we show the results from IFS central spectra and in the right panels the results from SDSS spectra. Although not shown, the results from IFS integrated spectra follow exactly the same trends as the IFS central spectra. The circles represent the average results for the three different assumptions, with the errorbars showing the scatter associated to the spectral base choice:

- in red the average of the non constrained fits,
- in green the average of the constrained fits with the same A_V for stars and AGN and
- in blue the average of the constrained fits with different A_V for stars and AGN.

7.3.1. Comparison between constrained and unconstrained fits with a single A_V

When comparing between the constrained (green circles) and unconstrained (red circles) fits with the same A_V for stars and AGN, we find that, on average, non-constrained fits lead to AGN contributions to light 12 % (7 %) higher than constrained fits for both IFS central spectra (SDSS spectra), which imply 0.22 dex (0.10 dex) more luminous AGN (see Figure 7.1 and 7.2). Moreover, the contribution to light of SSPs younger than 140 Myr is 15 % (8 %) lower for the non-constrained fits, leading to ages 0.23 dex (0.13) dex older (see Figures 7.3 and 7.4). There are no systematic differences between the constrained and unconstrained fits in terms of the stellar extinctions, stellar masses and stellar masses in intermediate-age stellar populations (see Figures 7.5, 7.6 and 7.7).

For some reason, when not using the Balmer line fluxes as a constrain, *Starlight* gives more contribution to light for the power-law component and less contribution for the young stars. We note that there exists a degeneracy between these two. Also, from the IFS center spectra (SDSS spectra) we find that the total predicted $H\beta$ ($H\alpha$) fluxes in the unconstrained fits are, on average, a factor 1.6 (1.3) higher than the measured ones. If this 'excess' of $H\beta$ ($H\alpha$) flux is real then it would indicate that a fraction of the ionizing photons is escaping from these galaxies.

7.3.2. Comparison between constrained fits with $A_V^{AGN} = A_V^{stars}$ and $A_V^{AGN} \neq A_V^{stars}$

When comparing now between the constrained fits with a single extinction for AGN and stars (green dots) and with different extinction for AGN and the stars (blue dots), we find from our IFS that in most of the systems (6/9) the results do not significantly change, and *Starlight* continues giving almost the same amount of extinction to the AGN and the stars anyway (differences below 0.4 mag). Therefore, in these 6 systems the stellar population results derived from both assumptions are comparable.

However, for the remaining 3 systems, J0237, J1248 and J2334, *Starlight* gives significantly more extinction to the AGN than the stars by 3 mag, 0.7 mag and 1.3 mag, respectively. As a consequence, their AGN contributions to light of are ~ 10 % higher with respect to the fits with a single extinction. The contribution to light of young SSPs is only slightly lower (~ 4 %) with no significant differences in the mean stellar ages and with total stellar masses and stellar masses in intermediate age stellar populations 0.2 - 0.3 dex lower than the ones from the fits with a single extinction. In general, the variation in the average results is moderate. However, in the particular case of PSQSOs J0237, which is the PSQSO with the highest AGN extinction (~ 3 mag), we find that total predicted $H\beta$ flux is a factor 3 times higher than the measured one, in comparison with the less than 2 for both J1248 and J2334. Therefore, either the fraction of escaping ionizing photons in J0237 is very high or most probably the A_V^{AGN} is unrealistically high.

From SDSS spectra there are also 3 systems showing discrepancies (different from the IFS ones) between the fits with a single or two extinctions: J1700, J0202 and J2310, for them *Starlight* gives

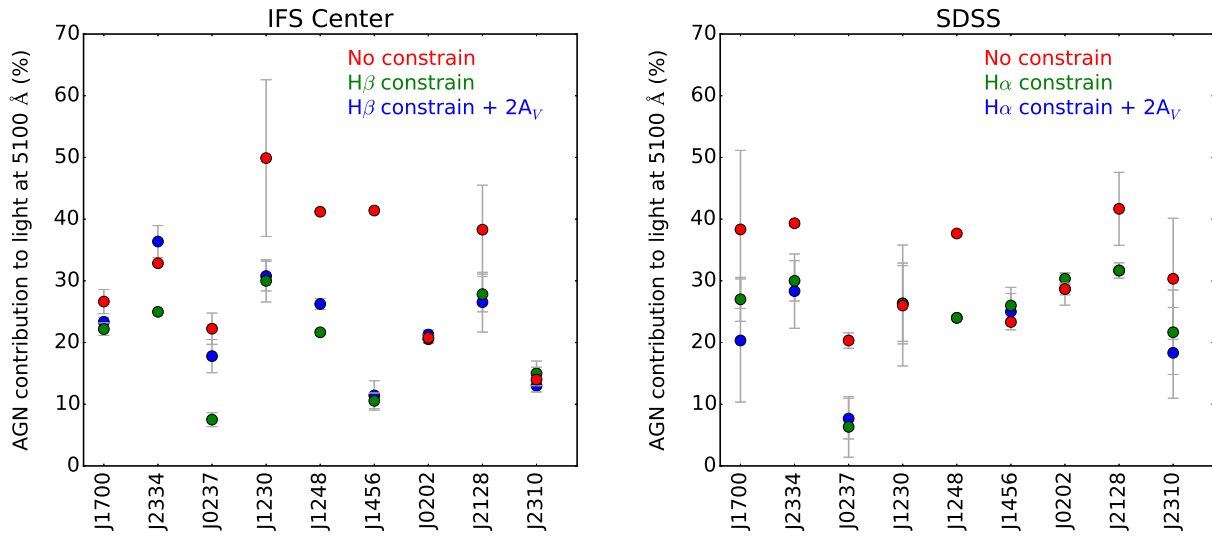


Figure 7.1 AGN contributions to light at 5100 Å for the PSQSOs under the three different assumptions. In red circles we show the average of the non constrained fits, in green the average of H β (or H α) constrained fits with the same A_V for stars and AGN, and in blue the average of the fits with different A_V for stars and AGN. Left panel: results from IFS central spectra. Right panel: results from SDSS spectra.

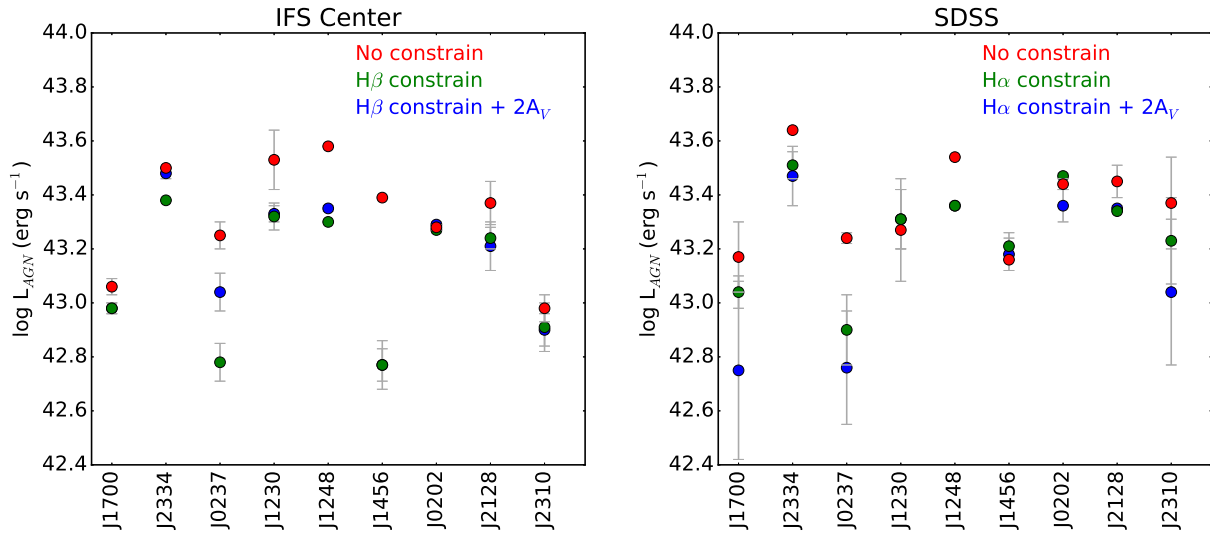


Figure 7.2 Same as Figure 7.1 for the AGN luminosities integrated from 3000 - 6000 Å, $\log L_{AGN}$. Left panel: results from IFS central spectra. Right panel: results from SDSS spectra.

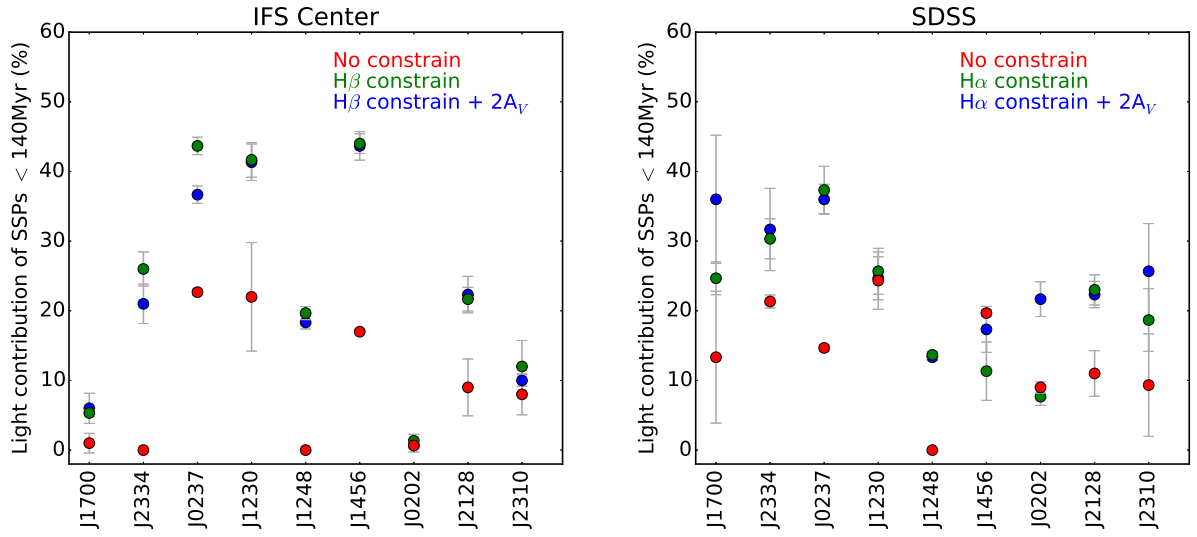


Figure 7.3 Contributions to light in percentage of SSPs younger than 140 Myr for the PSQSOs under the three different assumptions. In red circles we show the average of the non constrained fits, in green the average of constrained fits with the same A_V for stars and AGN, and in blue the average of the constrained fits with different A_V for stars and AGN. Left panel: results from IFS central spectra. Right panel: results from SDSS spectra.

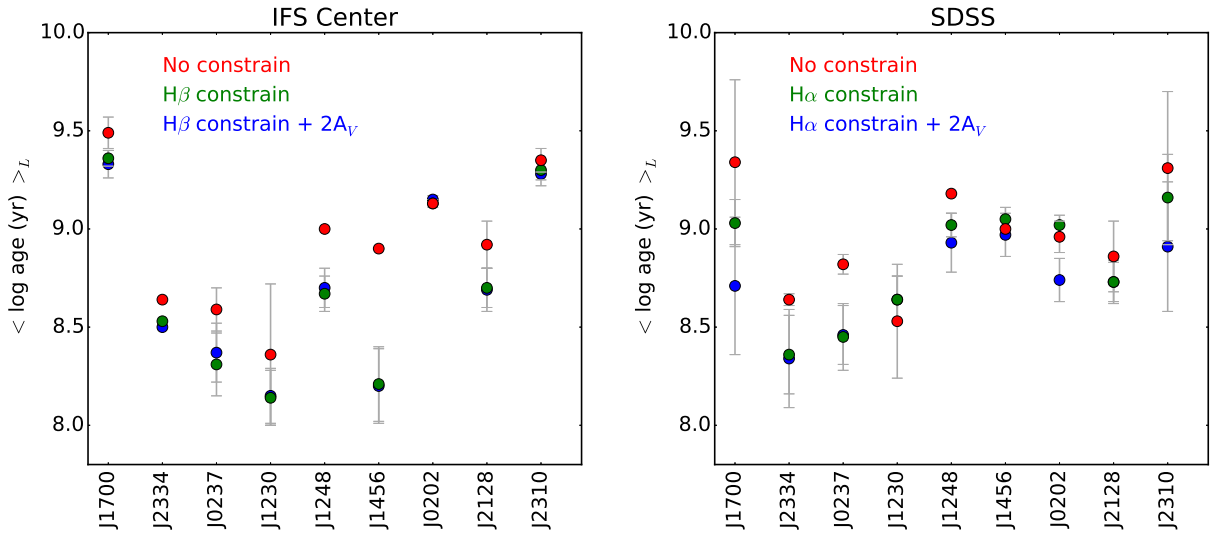


Figure 7.4 Mean light weighted stellar ages for the PSQSOs under the three different assumptions. In red circles we show the average of the non constrained fits, in green the average of constrained fits with the same A_V for stars and AGN, and in blue the average of the constrained fits with different A_V for stars and AGN. Left panel: results from IFS central spectra. Right panel: results from SDSS spectra.

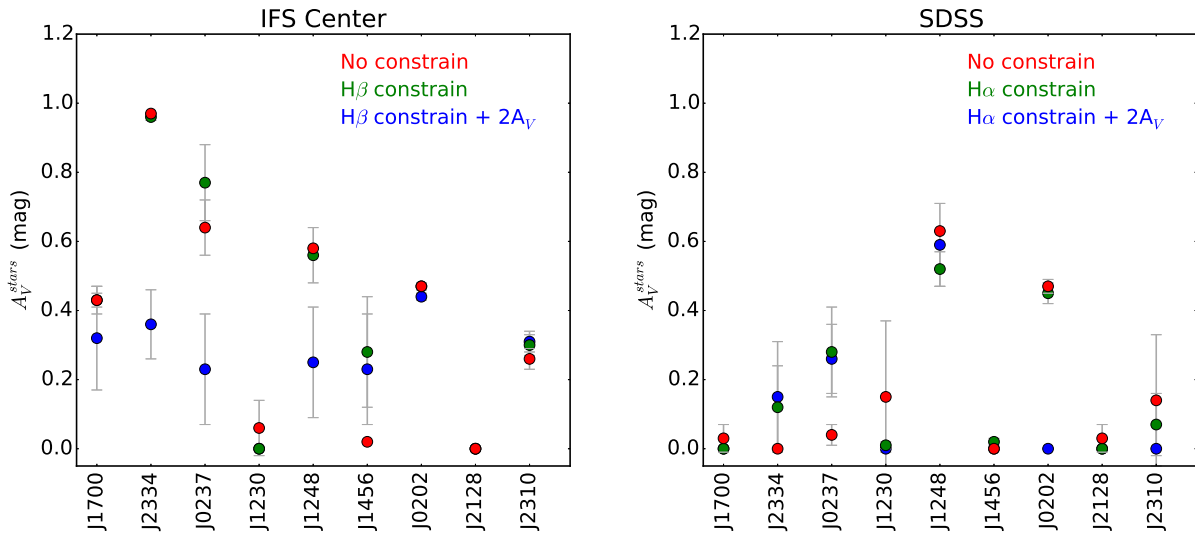


Figure 7.5 Mean stellar extinctions, A_V^{stars} , for the PSQSOs under the three different assumptions. In red circles we show the average of the non constrained fits, in green the average of constrained fits with the same A_V for stars and AGN, and in blue the average of the constrained fits with different A_V for stars and AGN. Left panel: results from IFS central spectra. Right panel: results from SDSS spectra.

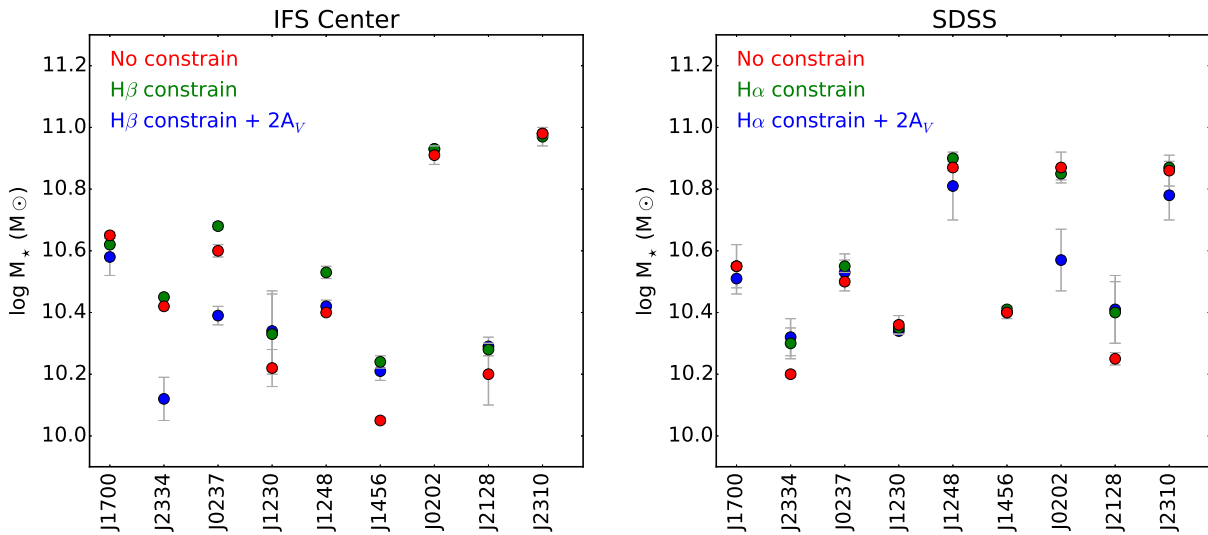


Figure 7.6 Stellar masses for the PSQSOs under the three different assumptions. In red circles we show the average of the non constrained fits, in green the average of constrained fits with the same A_V for stars and AGN, and in blue the average of the constrained fits with different A_V for stars and AGN. Left panel: results from IFS central spectra. Right panel: results from SDSS spectra.

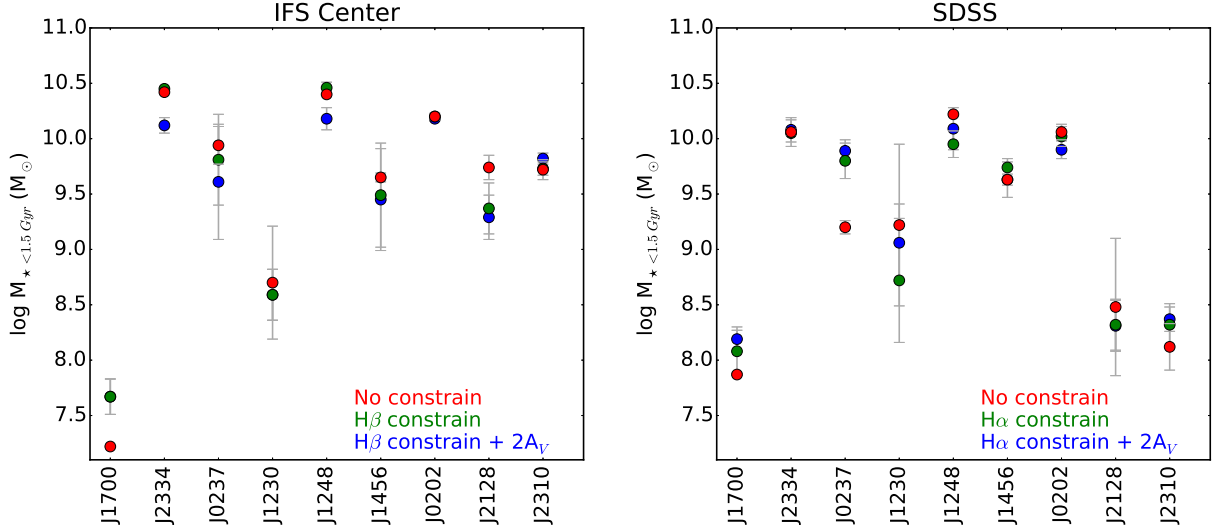


Figure 7.7 Stellar masses contained in intermediate age SSPs (< 1.5 Gyr) for the PSQSOS under the three different assumptions. In red circles we show the average of the non constrained fits, in green the average of constrained fits with the same A_V for stars and AGN, and in blue the average of the constrained fits with different A_V for stars and AGN. Left panel: results from IFS central spectra. Right panel: results from SDSS spectra.

significantly more extinction to the AGN than to the stars by 2.5 mag, 2.0 mag and 2.8 mag, respectively. Unlike to what we found from IFS data, their AGN contributions are only slightly higher ($\sim 4\%$) with respect to the fits with a single extinction, while the contribution to light of SSPs < 140 Myr is 11% higher, probably to compensate the lack of blue flux due to the 'dusty' AGN. As a consequence, in the two PSQSOS where A_V^{AGN} is greater than 2 mag, Equation 7.5 is not satisfied with the spectral base of SSPs > 4 Myr. This suggests that we can not rule out that in some cases the AGN could be more obscured than stars, yet values above 2 mag are not expected. This is also in agreement with the extinction measured from the emission lines (Section 7.4). The fits with two extinctions lead to younger stellar ages by 0.3 dex and similar stellar masses, except for J0202 which is 0.3 dex less massive. We note, however, that for most of the PSQSOS (6/9) the results are comparable and *Starlight* continues giving almost the same amount of extinction to the AGN and to the stars.

After comparing the results of the different stellar population properties with the different bases and assumptions, the final adopted values that will be used in subsequent analysis and comparisons have been obtained by averaging the constrained and unconstrained results with the same A_V for AGN and stars and for the spectral bases with SSPs > 4 Myr and SSPs > 30 Myr. From the dispersion of the averaged data we have derived the errors, calculated through the standard deviation.

The comparison between the 3 datasets (IFS center, IFS integrated and SDSS) is reported in Section 7.7.

7.3.3. Caveats about spectral modelling

We have improved C13 approach in some aspects of the modelling. In particular, they do not include in their fits SSPs younger than 56 Myr or older than 5.6 Gyr and they consider that dust is not present. Though we have addressed these issues, we have also made other simplistic considerations and their effects on our results should be considered more closely. Specifically, metallicity has been fixed to solar and the power law spectral index has been also fixed to the average expected value.

Metallicity can vary between and within galaxies and it affects the spectra of stars. If we had assumed a metallicity higher than solar we would fit younger and less massive stellar populations. Conversely, assuming a lower metallicity would result in fits with older and more massive stellar populations. In the case of the PSQSO prototype UN J1025-0040, the uncertainty in the age of the 400 Myr old stellar population was ± 50 Myr assuming a reasonable range in metallicity (Brotherton et al., 1999). Their methodology is similar to ours and therefore we expect similar uncertainties.

For the spectral index we made a secondary comparison to check if our chosen value is acceptable. The temperature of ionized gas in Sy2 and NLRGs is of the order $1 - 2 \times 10^4$ K, which is a strong observational evidence that the main source of energy input is photoionization. When collisional ionization is important, as happens in the BLR, a higher temperature would be expected ($T > 5 \times 10^4$ K). Following Osterbrock Section 13.5 we found that another check on the photoionization idea is that the total number of ionizing photons emitted by the central source must be large enough to balance the total number of recombinations in the ionized gas. Then, the $H\alpha$ luminosity could be written as:

$$L_{H\alpha} = h\nu_{H\alpha} \frac{\alpha_{H\alpha}^{eff}(H^0, T)}{\alpha_B(H^0, T)} \frac{\Omega}{4\pi} \int_{\nu_0}^{\infty} \frac{L_\nu}{h\nu} d\nu \quad (7.6)$$

where $\alpha_{H\alpha}^{eff}(H^0, T)$ is the effective recombination coefficient for the $H\alpha$ transition and $\alpha_B(H^0, T)$ is the hydrogen recombination coefficient summed over all levels above ground level. Their ratio indicates the number of $H\alpha$ photons produced per hydrogen recombination. Finally, $\frac{\Omega}{4\pi}$ is the nebular covering factor, that is, the fraction of the 4π sr that is covered by gas as viewed from the location of the central source. Observationally, it is possible to express $L_{H\alpha}$ in terms of its equivalent width $W_\lambda(H\alpha)$:

$$L_{H\alpha} = L_\lambda(\lambda 6563) W_\lambda(H\alpha) = L_\nu(\lambda 6563) \frac{d\nu}{d\lambda} W_\lambda(H\alpha) \quad (7.7)$$

where $L_\lambda(\lambda 6563)$ is the featureless continuum luminosity at $H\alpha$. We have assumed that in both $H\alpha$ and the ionizing spectral range the power law follows $L_\nu \propto \nu^{\alpha_\nu}$, where α_ν is the spectral index in frequency, equal to -1.5 in our case ($\alpha_\nu = -2 - \alpha_\lambda$). Thus, substituting the spectral shape of the power law, Equations 7.6 and 7.7 become:

$$W_\lambda(H\alpha) = \frac{3214}{\alpha_\nu} \frac{\Omega}{4\pi} (7,196)^{-\alpha_\nu} \quad (7.8)$$

which is analogous to Equation 13.5 of Osterbrock but for $H\alpha$ instead of $H\beta$. With our spectral index $\alpha_\nu = -1.5$, and considering that the ionizing continuum is fully absorbed $\frac{\Omega}{4\pi} = 1$, we found that the maximum theoretical value for the equivalent width of $H\alpha$ arising from the AGN is $W_\lambda(H\alpha) = 111\text{\AA}$. Even considering that all the NLR $H\alpha$ flux is arising from the AGN we find that for 8 out of 9 PSQSOs $W_\lambda^{NLR}(H\alpha) \leq 111\text{\AA}$, in agreement with our selected spectral index.

However, for the PSQSO J0237 we find that $W_{\lambda}^{NLR}(H\alpha) \sim 270\text{\AA}$ a factor 2.4 higher than the maximum theoretical value. This result could indicate either the presence of important collisional ionization in this system, or the other possibility, in case photoionization holds, is that the spectral index in J0237 is steeper than the one fixed by us. For example, $\alpha_{\nu} \sim -1.0$ implies a maximum theoretical value for the equivalent width of $W_{\lambda}(H\alpha) = 447\text{\AA}$.

7.4. Emission line measurements

The emission line intensities were measured in the residual spectra. The line profiles were fitted with Gaussian functions described by the amplitude of the line profile, line centroid, and FWHM. A single gaussian was used for the narrow lines: [OIII] λ 5007, [NII] λ λ ,6548,6583. However, for H α and H β two gaussians were necessary to model the broad and the narrow components. In both cases, the FWHM have been fixed to be the same for both lines. The errors in the determination of the fluxes were calculated as the product between the standard deviation in the adjacent continuum and the FWHM of the lines. The fits are shown in Appendix B. The broad and narrow emission lines measurements for IFS central spectra are summarized in Tables 7.1 and 7.2, respectively. Analogously, the broad and narrow emission lines measured in SDSS spectra are reported in Tables 7.3 and 7.4.

We have estimated, when possible, the average values of the extinction in the NLR and the BLR using these line measurements. For dereddened NLR is well established that the intrinsic $I(H\alpha)/I(H\beta)$ is larger than the recombination value 2.85. A more typical value derived for AGN is 3.1. This is the result from the additional contribution of collisional excitation of H α in the partly ionized transition region. The extinction is calculated using:

$$c(H\beta) = \frac{1}{f(H\alpha)} \times \log \frac{I(H\alpha)/I(H\beta)}{F(H\alpha)/F(H\beta)} \quad (7.9)$$

$$A_V = 2,5 [f(V) + 1] c(H\beta) \quad (7.10)$$

where $c(H\beta)$ is the so called logarithmic extinction coefficient and $f(\lambda)$ is the reddening function with $f(H\alpha) \sim -0.28$ and $f(V) \sim -0.12$ for Calzetti et al. (2000) extinction law. The derived A_V^{NLR} is shown in the last column of Tables 7.2 and 7.4.

Determining the dust extinction in the BLR is uncertain. In principle, dust is unlikely to exist within the BLR. In many BLR strong lines of Al, Ca, Si and Fe are present. These elements are strongly depleted from the gas if grains are present. Second, in BLR the gas is so close to the continuum source that solid particles would be heated above their sublimation temperature. However, we have estimated the BLR extinction using the intrinsic $I(H\alpha)/I(H\beta) = 3.1$ as for the NLR. They are shown in the last column of Tables 7.1 and 7.3. These values represent upper limits because in the BLR the collisional effects and the radiative transfer are expected to be much stronger and therefore the intrinsic H α /H β could be much larger than 3.1.

In general, we find that the extinction measured through line emission in the NLR is larger than stellar extinction derived from spectral continuum. The average A_V^{NLR} is ~ 1.65 (1.24) mag for IFS (SDSS) central spectra, while the average A_V^{stars} is ~ 0.38 (0.13) mag for IFS (SDSS) central spectra, very low in comparison. The most plausible explanation is that they are tracing different spatial regions, while the stars are distributed in a more extended region, the NLR is closer to the AGN.

Table 7.1. Central IFS Broad Emission Lines Fitting Results

Object SDSS name	Broad H β			Broad H α			A_V^{BLR*}
	Flux ^a	Error ^a	FWHM ^b	Flux	Error	FWHM	
J1700	95.79	9.47	4762	227.88	50.64	4762	-
J2334	76.07	10.25	4854	267.54	37.12	4854	< 0.43 (0.66)
J0237	-	-	-	-	-	-	-
J1230	172.85	11.91	4858	456.75	54.13	4858	-
J1248	237.33	21.53	5011	765.18	56.02	5011	< 0.13 (0.40)
J1456	35.24	5.12	4508	93.71	49.64	4508	-
J0202	64.40	4.28	2675	315.01	17.40	2675	< 1.55 (0.29)
J2128	134.04	4.08	3163	394.53	9.03	3163	-
J2310	41.25	6.19	6079	336.63	31.77	6079	< 3.30 (0.60)

Note. — (a) Scaling for the Gaussian emission lines corresponds to the integrated area under the curve in units of 10^{-17} erg s $^{-1}$ cm $^{-2}$, (b) FWHM is given in rest frame km s $^{-1}$ and (*) they represent upper limits because in the BLR the intrinsic ratio $I(H\alpha)/I(H\beta) \gtrsim 3.1$

Table 7.2. Central IFS Narrow Emission Lines Fitting Results

Object SDSS name	Narrow H β		[OIII] λ 5007		Narrow H α		[NII] λ 6583		A_V^{NLR}
	Flux ^a	Error ^a	Flux	Error	Flux	Error	Flux	Error	
J1700	15.25	1.29	61.46	1.25	77.25	6.92	42.08	4.19	1.67 (0.42)
J2334	53.90	1.14	187.20	1.55	218.39	4.14	117.10	3.95	0.91 (0.10)
J0237	48.24	0.87	83.32	1.01	166.60	3.74	110.40	3.43	0.37 (0.10)
J1230	20.43	1.38	29.86	3.00	169.27	6.25	100.10	6.04	3.35 (0.26)
J1248	-	-	97.12	6.88	-	-	-	-	-
J1456	22.09	0.74	64.73	0.67	144.16	7.19	80.25	5.40	2.54 (0.20)
J0202	54.49	0.75	137.70	2.92	215.97	3.06	149.00	3.91	0.84 (0.07)
J2128	-	-	40.83	0.96	-	-	-	-	-
J2310	18.43	0.56	54.63	0.69	99.29	2.88	50.50	2.58	1.88 (0.14)

Note. — (a) Scaling for the Gaussian emission lines corresponds to the integrated area under the curve in units of 10^{-17} erg s $^{-1}$ cm $^{-2}$.

Table 7.3. SDSS spectra Broad Emission Lines Fitting Results

Object SDSS name	Broad H β			Broad H α			A_V^{BLR*}
	Flux ^a	Error ^a	FWHM ^b	Flux	Error	FWHM	
J1700	93.7	12.4	6144	390.0	32.9	6144	<1.00 (0.53)
J2334	110.0	12.1	4034	458.0	32.1	4034	<1.00 (0.44)
J0237	-	-	-	-	-	-	-
J1230	97.1	14.5	3419	475.0	29.8	3418	<1.55 (0.55)
J1248	213.0	20.4	4944	838.0	26.3	4944	<0.81 (0.34)
J1456	65.0	12.7	5373	313.0	45.2	5373	<1.50 (0.83)
J0202	41.6	7.7	2509	517.0	59.1	2508	<4.73 (0.74)
J2128	112.0	10.0	3465	435.0	19.7	3465	<0.77 (0.34)
J2310	79.2	11.9	3799	356.0	35.3	3798	<1.27 (0.61)

Note. — (a) Scaling for the Gaussian emission lines corresponds to the integrated area under the curve in units of 10^{-17} erg s $^{-1}$ cm $^{-2}$, (b) FWHM is given in rest frame km s $^{-1}$ and (*) they represent upper limits because in the BLR the intrinsic ratio $I(\text{H}\alpha)/I(\text{H}\beta) \gtrsim 3.1$

Table 7.4. SDSS spectra Narrow Emission Lines Fitting Results

Object SDSS name	Narrow H β		[OIII] λ 5007		Narrow H α		[NII] λ 6583		A_V^{NLR}
	Flux ^a	Error ^a	Flux	Error	Flux	Error	Flux	Error	
J1700	7.51	1.09	41.20	0.91	43.30	2.89	26.50	2.35	2.11 (0.54)
J2334	45.20	1.48	161.00	2.12	223.00	3.92	125.00	4.32	1.58 (0.13)
J0237	48.30	1.19	90.40	1.27	222.00	5.11	134.00	5.23	1.34 (0.11)
J1230	29.80	1.63	42.87	1.90	164.00	3.35	87.00	3.39	1.96 (0.20)
J1248	22.30	2.15	90.70	6.06	74.50	2.77	75.70	2.80	0.25 (0.35)
J1456	25.60	0.95	73.30	0.87	113.00	3.37	61.50	3.15	1.20 (0.16)
J0202	46.60	0.90	131.40	3.84	163.00	6.85	75.80	7.19	0.41 (0.16)
J2128	8.56	1.11	44.30	1.71	33.60	2.25	39.70	2.25	0.80 (0.50)
J2310	10.70	1.12	55.67	2.39	51.30	3.32	57.80	4.24	1.49 (0.42)

Note. — (a) Scaling for the Gaussian emission lines corresponds to the integrated area under the curve in units of 10^{-17} erg s $^{-1}$ cm $^{-2}$.

In principle, what should be approximately similar is the power-law extinction derived by *Starlight* and the extinction derived in the BLR. From Section 7.3.2 we found that the power-law is not expected to be extinguished by more than ~ 2 mag relative to the stars. Here, all we can say is that, on average, A_V^{BLR} is $\lesssim 1.35$ (1.58) mag for IFS (SDSS) central spectra, which is in agreement with the previous result. Only in 2 out of the 9 PSQSOs (J0202 and J2310) we can not discard higher A_V^{BLR} values, but in anycase we are just probing upper limits.

7.5. AGN properties

The spectra of type 1 AGN, as the ones in our PSQSOs, offer important diagnostic tools to infer the properties in the very circumnuclear region, since the light of the accretion disc and the emission-lines of the BLR are visible. From the fitting results, we were able to estimate two fundamental physical AGN properties: the BH mass and the Eddington ratio.

7.5.1. Black Hole Mass

Reverberation mapping (Blandford & McKee, 1982; Peterson, 1993) is a method of measuring black hole masses in AGN that rests upon the assumption of virial motion of the BLR, that is, the motions of the gas in the BLR is dominated by the gravity of the central, supermassive black hole. Therefore, the black hole mass can be expressed as:

$$M_{BH} \propto \frac{v^2 R_{BLR}}{G} \quad (7.11)$$

where v is the velocity of the gas clouds in the BLR that can be estimated from the FWHM of broad $H\alpha$ and $H\beta$ components and R_{BLR} is the radius of the broad-line region that can be estimated from time-resolved brightness fluctuations in the continuum versus lines in the BLR. A tight correlation between R_{BLR} and the continuum luminosity of the AGN (e.g. L_{5100} at 5100 Å) could be established.

In this work we have employed the same scaling relations as C13. On the one hand, from the relation given by Vestergaard & Peterson (2006), we estimated M_{BH} based on the $H\beta$ broad line FWHM and the 5100 Å AGN monochromatic luminosity (calculated from the power-law component used in the fits):

$$\frac{M_{BH}(H\beta)}{M_{\odot}} = 10^{6,91 \pm 0,02} \left[\frac{FWHM(H\beta)}{1000 \text{ km s}^{-1}} \right]^2 \left[\frac{\lambda L_{\lambda}(5100 \text{ \AA})}{10^{44} \text{ erg s}^{-1}} \right]^{0,5} \quad (7.12)$$

The intrinsic scatter in the sample is described by 0.43 dex. On the other hand, we estimated M_{BH} based on the $H\alpha$ broad line FWHM and the 5100 Å AGN monochromatic luminosity according to the Greene et al. (2010) scaling relation:

$$\frac{M_{BH}(H\alpha)}{M_{\odot}} = (9,7 \pm 0,5) \times 10^6 \left[\frac{FWHM(H\alpha)}{1000 \text{ km s}^{-1}} \right]^{2,06 \pm 0,06} \left[\frac{\lambda L_{\lambda}(5100 \text{ \AA})}{10^{44} \text{ erg s}^{-1}} \right]^{0,519 \pm 0,07} \quad (7.13)$$

As we have fixed the FWHM to be the same for $H\alpha$ and $H\beta$, the M_{BH} derived from both are very similar. The slight differences, $< 2\%$, are due to the different prefactors and exponents in the relations

given by [Greene et al. \(2010\)](#) and [Vestergaard & Peterson \(2006\)](#) formalisms.

7.5.2. Eddington ratio

The accretion luminosity of a BH is given by,

$$L_{acc} = \eta \dot{M} c^2 \quad (7.14)$$

where η is the mass-energy efficiency conversion (typically estimated to be ~ 0.1 , but is dependent on the spin of the BH with an expected range of $\eta = 0.05 - 0.42$ ([Thorne, 1974](#)), and \dot{M} is the mass accretion rate. The theoretical upper limit on L_{acc} is called the "Eddington luminosity", that is reached when the force of gravity is equal to the radiation pressure from the accretion luminosity:

$$L_{Edd} = \frac{4\pi G m_p c}{\sigma_T} M_{BH} \quad (7.15)$$

where m_p is the proton mass, c is the speed of light, G is the gravitational constant, and σ_T is the Thomson cross-section for an electron. [Krolik \(1999\)](#) determined that $L_{Edd} = 1,51 \times 10^{38} (M_{BH}/M_{\odot}) \text{ erg s}^{-1}$.

The ratio of the observed accretion luminosity to the Eddington luminosity, the "Eddington ratio", is a useful measure for comparing BH accretion rates over a wide range of BH masses. The term "high-accretion" rate AGN is often used to refer to sources with high values of the Eddington ratio $\gtrsim 0.1$.

L_{acc} is assumed to be the radiative bolometric output of the AGN, which can be calculated for our PSQSOs. Is a common situation, as in this thesis, that AGN only have measurements in a limited range of continuum wavebands. In our case, what we have is the rest-frame flux at 5100 Å from the power-law component continuum. We have converted it into an AGN bolometric luminosity using the luminosity distances for our cosmology and an appropriate bolometric correction ($f = 8.1$; [Runnoe et al. 2012](#)):

$$L_{bol} = 4 \pi D_L^2 f (1+z) \lambda F_{\lambda}(5100 \text{ \AA}) \quad (7.16)$$

The Eddington ratios are given by L_{bol}/L_{Edd} .

In Tables 7.5 and 7.6 we report for IFS and SDSS data respectively, the AGN contribution to light at 5100 Å, the continuum flux at 5100 Å, the AGN integrated luminosity from 3000 Å to 6000 Å, the BH masses for H α and H β broad line measurements, and the Eddington ratios.

Table 7.5. AGN properties, derived from IFS center spectra

Object SDSS name	% AGN $_{\lambda 5100}$	F_{5100}	$\log L_{AGN}$	$\log M_{BH}(M_{\odot})$			L/L_{Edd}		
				H β	H α	Average	H β	H α	Average
J1700	25(2)	5.72	43.04(0.04)	7.87(0.02)	7.98(0.02)	7.92(0.06)	0.015(0.002)	0.012(0.002)	0.013(0.002)
J2334	29(4)	7.22	43.44(0.06)	8.10(0.03)	8.22(0.03)	8.16(0.06)	0.025(0.005)	0.020(0.004)	0.023(0.004)
J0237	16(8)	6.58	43.03(0.26)	-	-	-	-	-	-
J1230	43(15)	6.03	43.46(0.13)	8.10(0.07)	8.21(0.08)	8.16(0.07)	0.024(0.012)	0.019(0.010)	0.022(0.008)
J1248	31(10)	13.61	43.44(0.14)	8.13(0.07)	8.25(0.07)	8.19(0.08)	0.007(0.003)	0.006(0.003)	0.006(0.002)
J1456	26(15)	4.96	43.09(0.30)	7.89(0.13)	7.99(0.13)	7.94(0.10)	0.020(0.018)	0.016(0.014)	0.018(0.011)
J0202	21(1)	7.62	43.28(0.01)	7.50(0.01)	7.59(0.01)	7.54(0.05)	0.066(0.003)	0.053(0.002)	0.060(0.007)
J2128	36(7)	4.65	43.35(0.08)	7.66(0.04)	7.76(0.04)	7.71(0.06)	0.050(0.014)	0.033(0.010)	0.042(0.012)
J2310	16(1)	5.26	42.99(0.04)	8.06(0.02)	8.16(0.02)	8.11(0.05)	0.009(0.001)	0.007(0.001)	0.008(0.001)

Note. — Columns from left to right: (1) AGN contributions to light at 5100 Å, (2) total fluxes at 5100 Å in units of $10^{-17}(\text{erg s}^{-1} \text{cm}^{-2} \text{Å}^{-1})$, (3) logarithm of the AGN luminosities integrated from 3000 Å to 6000 Å, (4) black hole masses and (5) Eddington ratios.

Table 7.6. AGN properties, derived from SDSS spectra

Object SDSS name	% AGN $_{\lambda 5100}$	F_{5100}	$\log L_{AGN}$	$\log M_{BH}(M_{\odot})$			L/L_{Edd}		
				H β	H α	Average	H β	H α	Average
J1700	37(11)	5.06	43.16(0.11)	8.15(0.06)	8.26(0.07)	8.21(0.07)	0.010(0.005)	0.008(0.004)	0.009(0.003)
J2334	36(4)	7.37	43.59(0.05)	8.00(0.02)	8.10(0.03)	8.05(0.05)	0.041(0.007)	0.032(0.006)	0.037(0.006)
J0237	15(6)	6.55	43.07(0.20)	-	-	-	-	-	-
J1230	31(5)	6.84	43.39(0.07)	7.75(0.04)	7.85(0.04)	7.80(0.06)	0.044(0.011)	0.035(0.009)	0.040(0.008)
J1248	31(7)	13.76	43.45(0.09)	8.12(0.05)	8.23(0.05)	8.18(0.06)	0.023(0.007)	0.018(0.006)	0.020(0.006)
J1456	26(2)	5.27	43.20(0.04)	8.05(0.02)	8.16(0.02)	8.10(0.06)	0.014(0.002)	0.011(0.002)	0.013(0.002)
J0202	30(1)	7.93	43.46(0.02)	7.53(0.01)	7.62(0.01)	7.57(0.05)	0.092(0.006)	0.074(0.005)	0.083(0.010)
J2128	38(7)	5.15	43.41(0.08)	7.78(0.04)	7.88(0.04)	7.83(0.06)	0.045(0.013)	0.036(0.011)	0.040(0.009)
J2310	32(6)	5.47	43.41(0.08)	7.85(0.04)	7.96(0.05)	7.90(0.06)	0.038(0.011)	0.030(0.009)	0.034(0.008)

Table 7.7. Starburst Properties, derived from IFS central spectra

SDSS name	$\langle \log \text{age}(\text{yr}) \rangle_L$	$\log M_\star (M_\odot)$	% light $\star < 140 \text{ Myr}$	% light $\star < 1.5 \text{ Gyr}$	$\log M_\star (M_\odot)$ $\star < 1.5 \text{ Gyr}$	A_V (mag)	$\log L_{SB}^a$ (erg s^{-1})
J1700	9.47 (0.08)	10.64 (0.02)	3 (3)	3 (3)	7.73 (0.18)	0.41 (0.02)	43.36 (0.02)
J2334	8.59 (0.05)	10.43 (0.02)	13 (13)	74 (4)	10.43 (0.01)	0.96 (0.01)	43.75 (0.03)
J0237	8.49 (0.20)	10.64 (0.04)	33 (10)	48 (10)	9.76 (0.33)	0.66 (0.12)	43.75 (0.05)
J1230	8.35 (0.31)	10.32 (0.11)	32 (12)	32 (12)	8.50 (0.24)	0.00 (0.00)	43.53 (0.16)
J1248	8.85 (0.17)	10.47 (0.07)	10 (10)	68 (8)	10.42 (0.05)	0.56 (0.07)	43.69 (0.08)
J1456	8.59 (0.34)	10.14 (0.09)	30 (13)	45 (11)	9.48 (0.38)	0.12 (0.16)	43.53 (0.11)
J0202	9.14 (0.02)	10.91 (0.03)	1 (1)	54 (1)	10.20 (0.02)	0.47 (0.01)	43.74 (0.00)
J2128	8.87 (0.15)	10.21 (0.08)	14 (7)	34 (6)	9.57 (0.30)	0.00 (0.00)	43.48 (0.07)
J2310	9.36 (0.05)	10.96 (0.02)	9 (3)	30 (3)	9.70 (0.08)	0.26 (0.02)	43.69 (0.01)

Note. — (a) Total integrated luminosity of the stellar component from 3000 Å to 6000 Å. Errors between brackets.

7.6. Starburst properties

The main stellar population properties can be described using two fundamental physical parameters, starburst age and mass. The stellar mass is already an output from *Starlight* and is obtained by taking into account the M/L ratio for each SSP. The mean light weighted stellar ages have been obtained in the same way as the LIRGs, applying the Equation 5.5. The two main differences are: 1) the model bases for the PSQSOs are formed only by solar metallicity SSPs, and 2) the normalization wavelength for the PSQSOs is located at 4750 Å.

As explained in Section 7.3, for each PSQSOs we made a total of 9 *Starlight* fits (3 different assumptions and within them, 3 possible spectral bases). The mean ages and masses obtained with each of these 9 different assumptions/bases are reported in Tables A.1, A.2 and A.3. The final average values for the different properties have been obtained by averaging within the results from the 4 most reliable combinations out of the total 9, that is, the fits with and without constrain of the Balmer line fluxes, assuming a single and identical extinction for AGN and stars and for the model bases including SSPs > 4 Myr and SSPs > 30 Myr. Moreover, the errors have been estimated from the standard deviation.

Tables 7.7, 7.8, and 7.9 summarize the starburst fitting results for IFS central spectra, IFS integrated spectra and SDSS spectra, respectively. Apart from the ages and stellar masses we included in the third column the percentage of contribution to light of young stellar populations (< 140 Myr), in the fourth column the percentage of contribution to light of young intermediate age stellar populations (< 1.5 Gyr), in the fifth column the stellar mass in SSPs < 1.5 Gyr, in the sixth column the mean stellar extinction, and in the last column the integrated light of the stellar component from 3000 Å to 6000 Å.

Table 7.8. Starburst Properties, derived from IFS integrated spectra

SDSS name	$\langle \log \text{age}(\text{yr}) \rangle_L$	$\log M_*(M_\odot)$	% light ★ <140 Myr	% light ★ <1.5 Gyr	$\log M_*(M_\odot)$ ★ <1.5 Gyr	A_V (mag)	$\log L_{SB}$ (erg s ⁻¹)
J1700	9.30 (0.03)	10.73 (0.02)	0 (0)	15 (4)	9.19 (0.29)	0.57 (0.01)	43.54 (0.01)
J2334	8.59 (0.04)	10.49 (0.01)	13 (13)	77 (4)	10.49 (0.01)	0.92 (0.03)	43.83 (0.02)
J0237	8.39 (0.20)	10.80 (0.05)	41 (6)	60 (16)	9.98 (0.40)	0.64 (0.13)	43.97 (0.03)
J1230	8.45 (0.27)	10.34 (0.19)	30 (12)	30 (12)	8.56 (0.26)	0.00 (0.00)	43.63 (0.13)
J1248	9.00 (0.18)	10.82 (0.03)	10 (10)	44 (12)	10.24 (0.13)	0.37 (0.06)	43.95 (0.06)
J1456	8.54 (0.26)	10.41 (0.12)	32 (12)	53 (12)	9.77 (0.44)	0.17 (0.14)	43.80 (0.09)
J0202	9.19 (0.00)	11.08 (0.01)	0 (0)	51 (1)	10.24 (0.04)	0.45 (0.00)	43.85 (0.01)
J2128	8.93 (0.10)	10.27 (0.06)	10 (5)	45 (7)	9.88 (0.13)	0.00 (0.00)	43.56 (0.04)
J2310	9.25 (0.12)	11.14 (0.01)	9 (7)	45 (4)	10.09 (0.02)	0.27 (0.06)	43.90 (0.03)

Table 7.9. Starburst Properties, derived from SDSS spectra

SDSS name	$\langle \log \text{age}(\text{yr}) \rangle_L$	$\log M_*(M_\odot)$	% light ★ <140 Myr	% light ★ <1.5 Gyr	$\log M_*(M_\odot)$ ★ <1.5 Gyr	A_V (mag)	$\log L_{SB}$ (erg s ⁻¹)
J1700	9.31 (0.37)	10.53 (0.04)	17 (10)	17 (10)	8.05 (0.21)	0.00 (0.00)	43.27 (0.12)
J2334	8.57 (0.10)	10.24 (0.06)	25 (4)	57 (4)	10.02 (0.08)	0.02 (0.03)	43.76 (0.03)
J0237	8.70 (0.17)	10.51 (0.03)	25 (10)	41 (11)	9.47 (0.25)	0.11 (0.10)	43.76 (0.04)
J1230	8.71 (0.12)	10.35 (0.03)	23 (2)	24 (3)	8.53 (0.28)	0.00 (0.00)	43.64 (0.04)
J1248	9.12 (0.07)	10.89 (0.02)	7 (7)	39 (4)	10.04 (0.17)	0.56 (0.07)	43.69 (0.05)
J1456	9.05 (0.05)	10.40 (0.01)	14 (6)	39 (5)	9.69 (0.09)	0.01 (0.01)	43.54 (0.02)
J0202	9.02 (0.06)	10.86 (0.04)	8 (1)	42 (3)	9.99 (0.05)	0.45 (0.03)	43.71 (0.01)
J2128	8.85 (0.17)	10.34 (0.12)	18 (7)	18 (7)	8.23 (0.25)	0.00 (0.00)	43.52 (0.07)
J2310	9.43 (0.19)	10.85 (0.03)	10 (6)	10 (6)	8.17 (0.26)	0.01 (0.01)	43.61 (0.06)

7.7. Comparison between datasets

In the previous sections we described how we have obtained the stellar and AGN properties for the IFS central and integrated spectra and for SDSS spectra. In this section we are going to discuss the differences and similarities between the results derived from these three different datasets.

7.7.1. IFS central region vs SDSS

IFS central spectra and SDSS spectra traces the same region of 1.5 arcsec aperture radius around the nucleus. With this in mind, we expect the results from both datasets not to be very different. However, we must bear in mind that both datasets were observed at different times, with different instrumentation, and that PSQSOs are intrinsically variable.

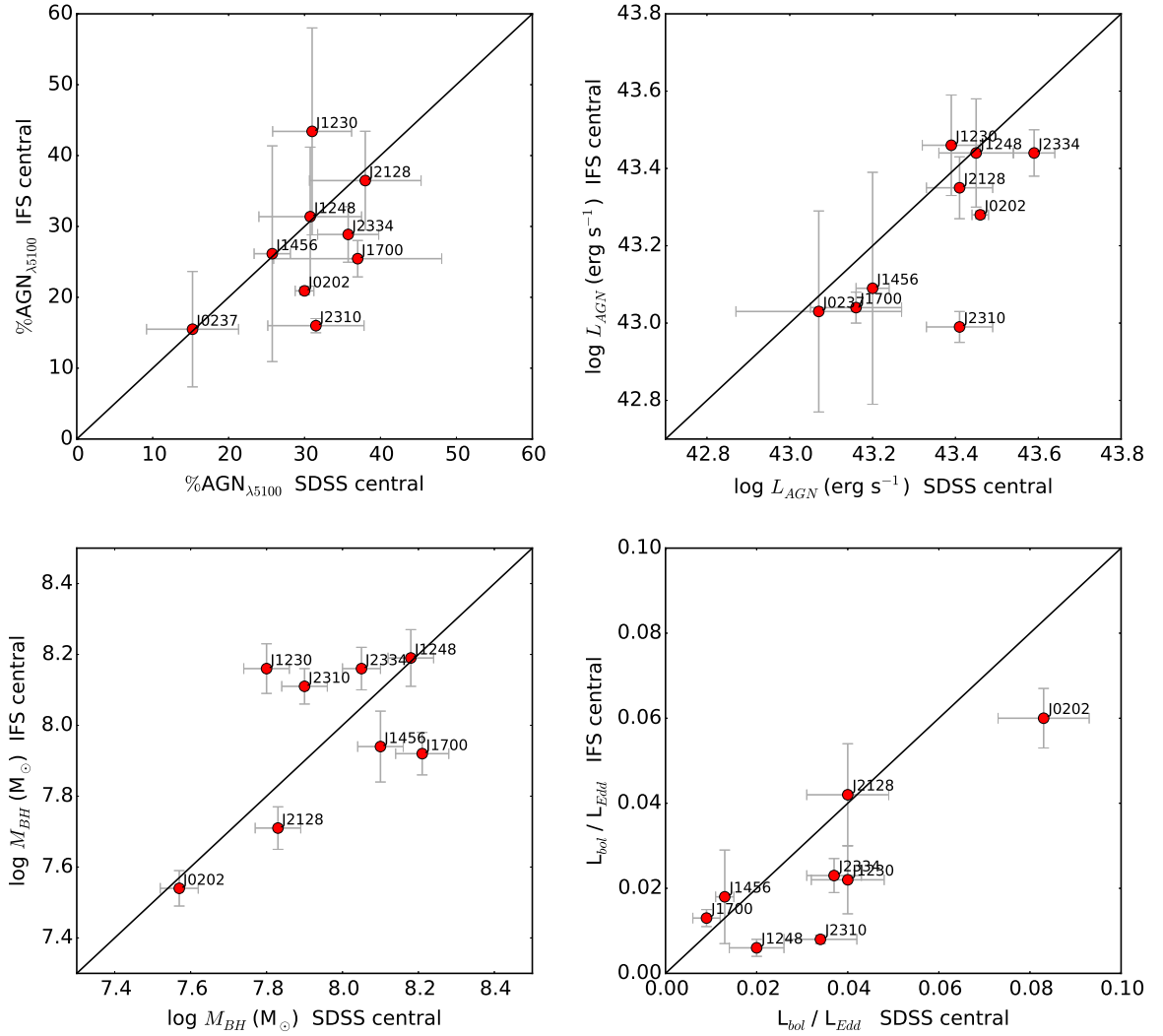


Figure 7.8 Comparison between the AGN properties derived from IFS central spectra (y axis) and SDSS central spectra (x axis). From top left to bottom right: AGN contributions to light at 5100 Å, AGN luminosities integrated from 3000 - 6000 Å, black hole masses, and Eddington ratios.

AGN properties

In Figure 7.8 we show the comparison between the AGN properties derived from IFS central spectra (y axis) and SDSS central spectra (x axis). From top left to bottom right the panels represent: AGN contributions to light at 5100 Å, AGN luminosities integrated from 3000 - 6000 Å, black hole masses, and Eddington ratios. The AGN contributions to light calculated for the IFS central spectra range from 16 - 43%, and from 15 - 38% for SDSS spectra. On average, SDSS AGN contributions are 4% higher than IFS AGN contributions. However, this is within the margin of errors (6 - 7%) and therefore, the results from both datasets can be considered equal. The object that deviates the most is J2310, for which the SDSS AGN contribution is 16% higher than IFS one. For most of the other objects the difference is less than 10%.

Analogously, the AGN luminosities are also equivalent, except for J2310. The average errorbars

are 0.15 dex, and for most of the other systems the difference between datasets is within the error.

The BH mass estimations for IFS central spectra range from $3.5 \times 10^7 - 1.5 \times 10^8 M_{\odot}$, while for SDSS spectra range from $3.7 \times 10^7 - 1.6 \times 10^8 M_{\odot}$. They are statistically similar considering the 0.4 - 0.5 dex scatter expected from the relations used to derive them. The dispersion between points is larger here, although not disproportionate.

Finally, the Eddington ratio is the property with the largest dispersion between datasets. This is expected since it is an indirect measure that depends on many variables. IFS central values range from 0.008 - 0.060, while SDSS values from 0.009 - 0.083. On average, from SDSS spectra the Eddington ratio is 0.010 larger than IFU nuclear spectra. This value is a bit larger than the average error bars 0.006 - 0.007. However, we note that in general the Eddington ratios are low (below 0.05) consistent with the PSQSOs being low accretion rate AGNs.

We emphasize that the agreement between results is quite good, considering that both datasets were observed at different times, with different instrumentations, and for intrinsically variable systems.

Stellar properties

In Figure 7.9 we show the comparison between the starburst properties derived from IFS central spectra (y axis) and SDSS central spectra (x axis). From top left to bottom right the panels represent: mean stellar ages, stellar masses, contributions to light of young-intermediate SSPs (< 1.5 Gyr), stellar mass in intermediate age SSPs (< 1.5 Gyr), mean stellar extinctions, and stellar luminosities integrated from 3000 - 6000 Å.

The mean stellar ages derived for IFS central spectra range from 220 Myr - 3 Gyr, while for SDSS between 370 Myr - 2.7 Gyr. The SDSS ages are, on average, 0.12 dex older than central IFS. However, this difference is smaller than the 0.15 dex average errorbars. Therefore, they can be considered statistically equal within the errors. The two objects which deviate most are J1456 and J1230, with SDSS ages older than central IFS by 0.46 and 0.36 dex, respectively.

The stellar masses range from $1.4 \times 10^{10} - 9.1 \times 10^{10} M_{\odot}$ for IFS central spectra, and from $1.7 \times 10^{10} - 7.8 \times 10^{10}$ for SDSS spectra. The average difference between datasets is smaller than the 0.05 dex average errorbars. J1248 is the object which deviates most from unity relation, with an SDSS stellar mass 0.42 dex higher than IFS central stellar mass. For the remaining systems, the absolute difference between the masses derived from the two datasets is below 0.20 dex.

Although not shown, the contributions to light of young stellar populations (< 140 Myr) are very uncertain, with huge errorbars that are on average $\sim 8\%$. We consider as physically valid/reliable only those contributions with percentages above 15%. The only two PSQSOs that meet this requirement for both datasets are J0237 and J1230. For them, the contributions derived by SDSS are 9% smaller than IFS contribution, a difference that is approximately within the errorbars. Only in these 2 out of the 9 PSQSOs we can ensure a significant contribution to light of young stellar populations. They are also the only two PSQSOs with composite ionization between Seyfert and star formation (see Section 7.8.1).

Analogously, the contributions to light of young-intermediate stellar populations (< 1.5 Gyr), are higher than 15% for all the PSQSOs except J1700 in the case of IFS central spectra, and J2310 for SDSS spectra. They range from 30 - 74% for IFS and from 17 - 57% for SDSS spectra. The

contributions derived from SDSS spectra are, on average, 12% smaller than central IFS contribution, which is above the average errorbars (6%).

In terms of the mass contained in intermediate age stellar populations (< 1.5 Gyr), we found very similar values for SDSS and IFS (within the 0.2 dex errorbars) for all the systems except J2310 and J2128 which are ~ 1.4 dex more massive for the central IFS than for SDSS. The values range from $0.3 \times 10^9 - 2.7 \times 10^{10} M_{\odot}$ for IFS central spectra, and from $0.1 \times 10^9 - 1.1 \times 10^{10} M_{\odot}$ for SDSS spectra. Considering the global average of the PSQSOs, the mass in intermediate age stellar populations represents a 27% (13%) of the total stellar mass for our central IFS (SDSS).

With respect to the stellar extinction, for most systems, the derived values are similar for SDSS and IFS central spectra, with differences below 0.25 mag. However, for J1700, J2334 and J0237 the stellar extinction derived from IFS is significantly higher than SDSS by 0.41 mag, 0.94 mag and 0.55 mag respectively.

The stellar luminosities derived for both datasets are remarkably similar within the margins of error. In general, the stellar population results from IFS central and SDSS spectra are in good agreement.

7.7.2. IFS Central vs IFS Integrated

The integrated spectra were obtained summing the flux over all the optical extension of the PSQSOs. When visualizing simultaneously central and integrated IFS, we found that the spectral shape of most of them are very similar. However, in terms of luminosity, the integrated spectra lie above the nuclear ones. Therefore, we expect that the extensive properties, as the stellar masses and luminosities, will be higher from integrated than from nuclear spectra, while the intensive properties as mean ages, young / intermediate stellar populations contributions, and dust extinction, remain similar. This is in fact what we found.

Stellar properties

In Figure 7.10 we show the comparison between the starburst properties derived from IFS central spectra (y axis) and IFS integrated spectra (x axis). From top left to bottom right the panels represent: mean stellar ages, stellar masses, contributions to light of young-intermediate stellar populations (< 1.5 Gyr), stellar mass in intermediate age stellar populations (< 1.5 Gyr), mean stellar extinctions, and stellar luminosities integrated from 3000 - 6000 Å.

There is no significant difference in the mean ages derived from central and integrated spectra. However, the integrated stellar masses are, on average, 0.15 dex higher than the central ones.

Although not shown, only 3 systems present a significant contribution of young SSPs < 140 Myr ($\gtrsim 15\%$); J0237, J1230 and J1456. In the previous Section we found that J0237 and J1230 had also a significant contribution of young stellar populations when derived from SDSS data. In the case of J1456, it was in the limit of detection with a contribution of $14 \pm 6\%$.

Analogously, 8/9 PSQSOs (all except J1700) have contributions of young-intermediate SSPs < 1.5 Gyr greater than 15%. The contributions are a 4% higher for integrated than central spectra. However, this is within the 7% errorbars and therefore it is not statistically significant.

For the 8 systems with reliable contributions of the young-intermediate stellar populations, the masses derived with both datasets are comparable, with an average difference within the 0.2 dex

errorbars.

There is no difference between the mean stellar extinction derived in the integrated and in the nuclear spectra.

Finally, we found that the stellar luminosity derived from the integrated spectra is 0.17 dex higher than the central one, well above the 0.05 - 0.06 dex errorbars.

7.7.3. SDSS vs C13 work

Since the only work with statistical significance studying stellar populations in PSQSOs is C13, and considering that their sample includes our sample, we compared our results with theirs for these 9 systems. We will compare with the results derived from SDSS spectra for two reasons. First, because we found that the SDSS results are in agreement with our IFS, and second, because C13 combined the SDSS spectra with their optical KPNO spectroscopy in order to increase the S/N and the wavelength coverage, and in general, they matched both their KPNO and Keck spectra to the flux calibration of the SDSS spectra (see Sections 2.2 and 2.4 of C13 for additional details). Therefore, we expect that the differences between C13 and our SDSS results are due mostly to the methodology and assumptions made in the analysis, but not to spectral differences.

AGN properties

The range of AGN contributions to the total light derived for SDSS spectra vary between 15% - 38%, with an average of 31%. This value is a factor 1.7 lower than the one obtained by C13, 53%. This could be due to several reasons. First, they do not include in their base populations younger than 56 Myr. The blue continuum characteristic of the ionizing stellar populations and the power-law blue continuum are quite similar, and there is a degeneration between them. In fact, for the fits with SSPs < 4 Myr base, the joint contribution of AGN and SSPs < 30Myr is $\sim 43\%$, more similar to C13 53%. We also see that when using the base with SSPs >30 Myr, we estimate 10% more of AGN light contribution than with the base with SSPs down to 1 Myr. If we had removed from our base all the SSPs until 56 Myr we would expect to obtain even larger AGN contributions, to counteract the lack of blue continuum flux from young SSPs. Also, and not being quite sure of the influence that could have, C13 allow the power-law spectral index to vary independently for each object, while we have fixed it.

This factor of 1.7 difference between our SDSS AGN contributions and C13 translates into our mean BH masses being on average 0.24 dex smaller than C13. However, they are still within the uncertainties, 0.4 - 0.5 dex. Also, as a consequence, our AGN luminosities are 0.25 dex lower than C13.

However, our L_{bol} / L_{Edd} are in agreement with C13 estimations, except for J2128, where there is a large difference between 0.04 (SDSS) and 0.108 (C13), most of it explained by the factor 2 of difference between the AGN luminosities.

Stellar properties

The mean ages of the PSQSOs derived from SDSS spectra oscillate between 370 Myr - 2.7 Gyr. They are within the errors similar to C13 ages, which range between 240 Myr - 2.7 Gyr. We note,

however, that C13 do not detail how they have weighted the ages. That matters because, for example, weighting in Myr instead of in logarithm would lead to older ages. Our SDSS stellar masses are also in agreement with C13 ones, within a scatter of ~ 0.2 dex. Although our spectral base includes SSPs up to 10 Gyr, we find from the SFHs that most of the PSQSOs are dominated by the SSPs younger than 3 Gyr, this could be the reason why we derive stellar masses so similar to C13. However, there is an exception, for J2334 they report a significantly lower value, $\log M_{\star} (M_{\odot}) = 9.84$ (C13) vs 10.24 (ours). We think this could be due to the significantly higher AGN light contribution they are obtaining for this PSQSO: 0.764 vs 0.36 (ours). Their large AGN contribution could lead to an underestimation of the stellar component mass, as only 24 % of the light is assigned to stars.

From SDSS spectra we obtain very low extinction values for 7/9 PSQSOs, which is in agreement with the idea of PSQSOs not being heavily extinguished by dust. Only for J1248 and J0202 we measure extinctions ~ 0.5 mag. We can not compare these results with C13 because they directly did not included dust in their modelling.

7.8. Results

Probably the most relevant result is that in 8/9 PSQSOs (all except J1700) the AGN coexists with a 30 - 77 % of SSPs younger than 1.5 Gyr. On average, the intermediate age population contribution is very important, 48 %, and coexist with an AGN which on average contributes to 27 % of the light.

Also, in 3/9 PSQSOs (J0237, J1230 and J1456) there exists an even younger stellar population < 140 Myr, contributing on average to a 32 % (34 %) in the central (integrated) spectra, however with important uncertainties around 12 % (10 %). We can not confirm the presence of young components in other systems given their low contributions < 15 % and the large uncertainties. In fact, these ‘young components’ have been proposed to be the trigger for the current AGN activity. A few of the PSQSOs in C11 have morphologies that show knots of ongoing star formation, suggesting that young stellar populations may be present. Moreover, the prototype PSQSO, UN J1025-0040 required revisiting to include a younger stellar population (~ 40 Myr) when high-resolution blue Hubble Space Telescope (HST) images were obtained (Brotherton et al., 2002).

7.8.1. BPT diagrams

As explained in Section 1.4.2, narrow emission lines can be powered by several sources of photoionizing radiation, including young ionizing stars and AGN. Comparing the relative strength of lines with high- and low-ionization potentials tells us about the shape of the photoionizing continuum and thus diagnoses the source. AGNs have harder continua (relatively more high-energy photons) while star-forming continua are softer (relatively more low-energy photons). In particular, the highly ionized [OIII] λ 5007 line is more prominent in AGN spectra, but other lines may also be diagnostic. In Figure 7.11 we show the traditional BPT diagram, [OIII] λ 5007/H β vs [NII] λ 6583/H α flux ratios for IFS central spectra (left panel, black circles) and SDSS spectra (right panel, green circles). Overplotted as black lines are empirically and theoretically derived separations between LINERs/Seyferts and HII regions. Dotted line is Kauffmann et al. (2003), solid line is Kewley et al. (2001), and dashed-dotted line is Cid Fernandes et al. (2010). Diagrams such as this help us understand the nature of relative contributions of ionizing radiation from different sources. All the PSQSOs with narrow line flux

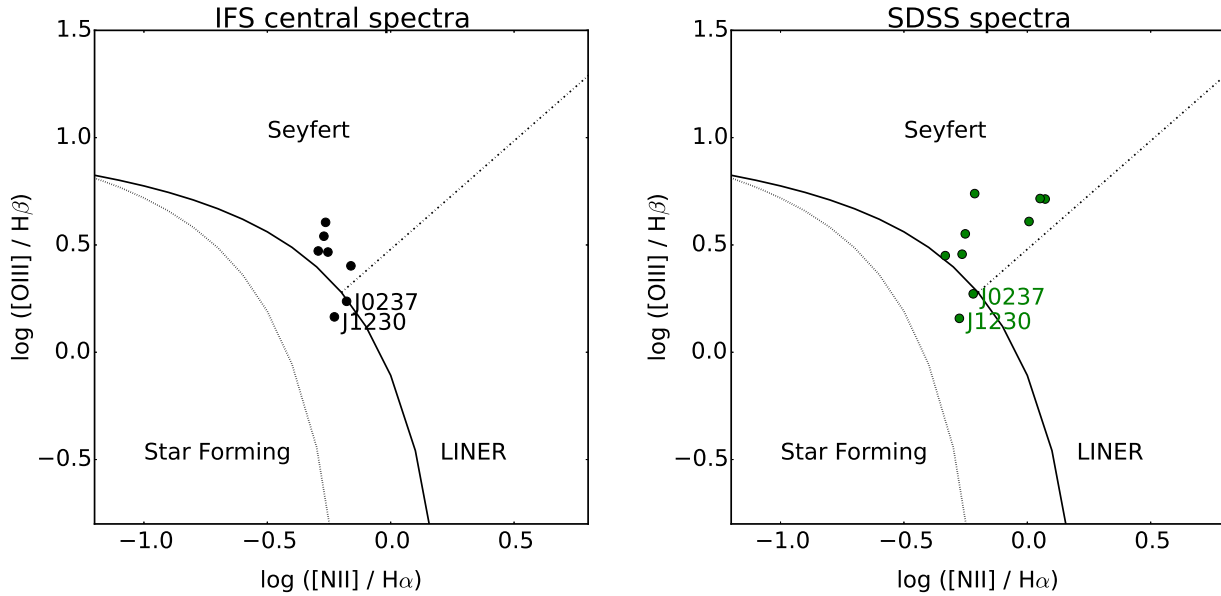


Figure 7.11 BPT diagnostic diagrams for our 9 PSQSOs for IFS central spectra (left panel, black circles) and SDSS spectra (right panel, green circles). Overplotted as black lines are empirically and theoretically derived separations between LINERs / Seyferts and HII regions. Dotted line is [Kauffmann et al. \(2003\)](#), solid line is [Kewley et al. \(2001\)](#), and dashed-dotted line is [Cid Fernandes et al. \(2010\)](#). All the PSQSOs with narrow line flux measurements fall in the Seyfert region of the BPT except two, J0237 and J1230, which fall in the composite region, suggesting that star formation is also quite important in these two systems.

measurements fall in the Seyfert region of the BPT except two, J0237 and J1230, which fall in the composite region, suggesting that recent star formation is also quite important in these two systems.

In fact, J0237 is the PSQSO in our sample with the highest contribution to light of SSPs < 140 Myr, 33%, and the only one where this contribution is higher than the AGN contribution, $\sim 16\%$. Moreover, is the only one where no broad emission is detected in either $H\alpha$ or $H\beta$. In the case of J1230, is the object with the second highest contribution to light of SSPs < 140 Myr, 32%. In all the 7 remaining systems the average contribution to light of the young SSP components is not significant and always much smaller than the AGN contribution, except for J1456 where the difference is not so clear for IFS data.

7.8.2. Correlations of AGN versus Starburst properties

In this section we have searched for correlations between the AGN and the starburst properties predicted by merger-induced evolutionary scenarios (e.g., [Di Matteo et al. 2005](#) and [Hopkins et al. 2008](#)). If there is a single mechanism driving both AGNs and starburst activity, then it will naturally lead to correlations between their properties. Specifically, AGN luminosity (and/or Eddington ratio) was predicted to decline following a merger-triggered fueling event as the age of the starburst population increases.

We find evidence of the latter. In left panel of Figure 7.12 we show how the AGN luminosity vary with the starburst age for our IFS central (black) and integrated spectra (red). In bright colors we

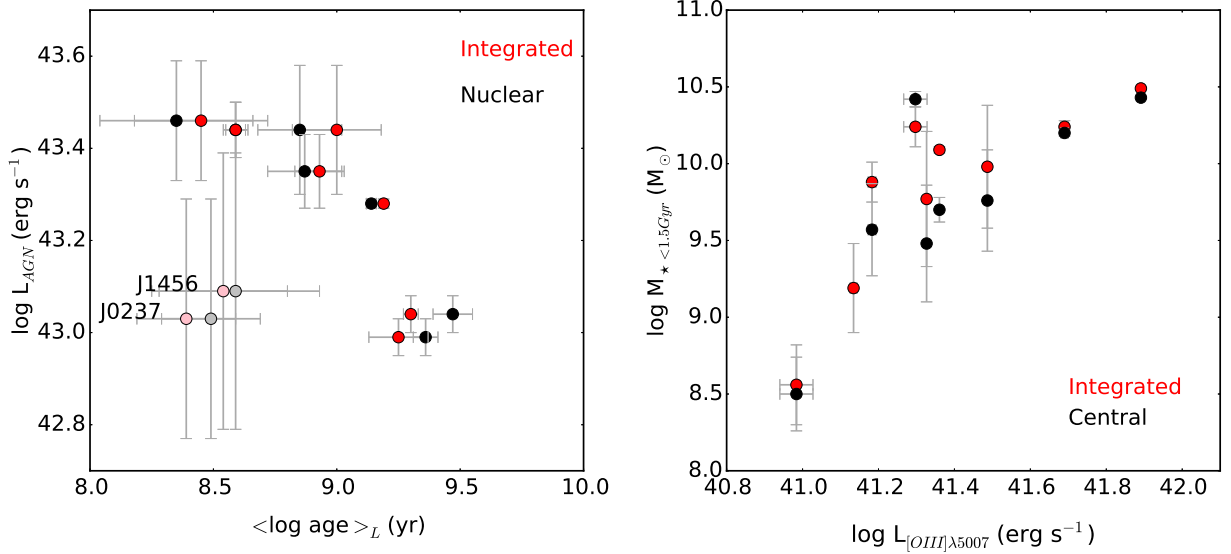


Figure 7.12 Left panel: correlation between starburst ages and AGN luminosity for our IFS central (black) and integrated (red) spectra. The two PSQSOs with an uncertain AGN contribution, smaller than 15% (J0237 and J1456), are shown in lighter colors. When not taking them into account, a declining trend of the AGN luminosity with the starburst age is seen, as predicted by merger-induced evolutionary scenarios. Right panel: correlation between [OIII] λ 5007 luminosity and the stellar mass contained in stellar populations < 1.5 Gyr for IFS central (black) and integrated (red) spectra.

show PSQSOs where the AGN contribution is unequivocally higher than 15%. In lighter shades of black and red, we show the two PSQSOs where the AGN contribution do not satisfy this requirement (J0237 and J1456). When not considering these two systems, the expected declining of the AGN luminosity with starburst age is visible. This would indicate that the gas from which the stars formed also fed the AGN. The younger the stellar age of a system the higher the contribution from recently formed young components. That requires significant gas income to the central region, part of which could also be accreted by the AGN.

It would be very interesting that we could expand the PSQSOs sample to confirm this trend, since the statistics of our current sample is not enough (only 7 objects). Apart from this, we do not find any other correlation between starburst ages or masses and the BH masses or Eddington ratios.

Additionally, we find another interesting correlation between the stellar mass in intermediate age stellar populations < 1.5 Gyr and the luminosity of [OIII] λ 5007 line, shown in the right panel of Figure 7.12. If we assume that the [OIII] λ 5007 line luminosity is tracing the intrinsic AGN luminosity (LaMassa et al., 2010), therefore, this correlation suggest that the more massive the central starburst the brighter the AGN. This could indicate that both starburst and AGN are simultaneously growing from the same gas supply, which in principle is in agreement with merger induced evolutionary scenarios. However, we note that we do not find this correlation when using directly the AGN luminosity. We have no clue about the reason why, in principle the L_{AGN} is related with the continuum which is directly emitted from the AGN, while $L_{[OIII]\lambda 5007}$ reflects somehow the influence of the AGN continuum over the gas in the more extended NLR. This work is still in progress and additional observations are necessary to further test this hypothesis.

We do not find any other correlation between the stellar mass in intermediate age stellar populations < 1.5 Gyr, neither with total stellar masses with any of the AGN properties. The small sample size, together with the limited parameter space traced could limit our ability to see correlations. In anycase, with their bigger sample, C13 neither find any correlation between stellar and AGN properties. When dividing by morphologies, they found that early type galaxies have significantly higher AGN luminosities, younger starburst ages, and narrow emission-line ratios diagnostic of Seyfert when compared to their spiral counterparts.

An extensive comparison of the SFHs of PSQSOs with LIRGs and control spiral galaxies from CALIFA is presented in the final discussion (see Chapter 8).

7.9. Conclusions

In this chapter we have characterized the AGN properties (contribution to light, luminosity, BH mass, and Eddington ratios), the stellar population properties (mean light weighted ages, total stellar masses, stellar masses in intermediate age stellar populations, stellar extinctions), and the ionization mechanism for 9 PSQSOs observed with IFS from PMAS LArr and VIMOS instruments, and also from publicly available SDSS spectra. We have characterized both the central region and the whole integrated spectra.

Our main results are:

1. Starburst properties:

- The stellar masses derived from the integrated spectra of the PSQSOs range from $1.9 \times 10^{10} M_{\odot}$ - $1.4 \times 10^{11} M_{\odot}$ (Chabrier), and the mean stellar ages from 220 Myr - 3 Gyr, both in agreement with C13. In general, the stellar extinctions are low, < 1 mag.
- In 3 out of 9 PSQSOs (J0237, J1230 and J1456) we can ensure that there is a significant contribution ($> 15\%$) of young stellar populations (< 140 Myr).
- In 8 out of 9 PSQSOs (all except J1700) we find important light contributions of intermediate-age stellar populations (< 1.5 Gyr), ranging from 30% - 77% . The stellar mass in intermediate age stellar populations range from $3.2 \times 10^8 M_{\odot}$ - $3.1 \times 10^{10} M_{\odot}$ (Chabrier). It represents, on average, a 27% of the total stellar mass formed in these systems.

2. AGN properties:

- The contribution to light (at 5100 \AA) of the AGN ranges from 16% - 43% . On average, the contributions derived by us are a factor 1.7 lower than the ones derived by C13, due to differences in the modelling assumptions. However, this does not translate in significant differences between the BH masses and Eddington ratios derived by us, which are in agreement with them.
- We find that the central black holes have masses from $3.5 \times 10^7 M_{\odot}$ - $1.5 \times 10^8 M_{\odot}$, and are low-accretion rate AGN accreting at $\lesssim 1\%$ - 6% of Eddington luminosity.

3. **Narrow line emission:** When plotted on the traditional BPT diagram, 7 out of the 9 PSQSOs fall in the Seyfert region. The other 2 systems, J0237 and J1230, fall in the composite region,

reconfirming the results from the spectral synthesis, that is, recent star formation is also quite important in some PSQSOs.

4. Starburst - AGN correlations:

- From the correlations between the AGN and the starburst properties expected by merger-induced evolutionary scenarios we find evidence of the decline in the AGN luminosity with increasing stellar ages, when considering the 7 PSQSOs with reliable AGN luminosities. This would indicate that the gas from which the stars formed also fed the AGN. The younger the stellar age of a system the higher the contribution from recently formed young components. That requires significant gas income to the central region, part of which could also be accreted by the AGN. It would be very interesting that we could expand the PSQSOs sample to confirm this trend, since the statistics of our current sample is not enough.
- We find another interesting correlation between the stellar mass in intermediate age stellar populations < 1.5 Gyr and the luminosity of $[\text{OIII}]\lambda 5007$ line. If we assume that the $[\text{OIII}]\lambda 5007$ luminosity is tracing the intrinsic AGN luminosity (LaMassa et al., 2010), therefore, this correlation suggest that the more massive the central starburst the brighter the AGN. This could also indicate that both starburst and AGN are simultaneously growing from the same gas supply, which in principle is in agreement with merger induced evolutionary scenarios. We note, however, that we do not find this correlation when using directly the AGN luminosity. This work is still in progress, and additional observations are also necessary to further test this hypothesis.

8

Overall comparison between Spirals, LIRGs and PSQSOs

In the previous chapters we have characterized the spatially resolved stellar population properties of three LIRGs, two pre-mergers (IC 1623 W and NGC 6090) and one merger (NGC 2623). Moreover, we have also studied the nuclear and integrated stellar population properties of nine PSQSOs also in different merger stages:

- Two pre-merger spiral systems, similar in morphology to our pre-merger LIRGs: J1456 and J2310.
- One undefined pre-merger system where the morphology of the main galaxy is not clear: J1230.
- Three post-merger elliptical systems: J2334, J1248, and J2128. J2128 has, in turn, another close companion of elliptical type that could end in another merger.
- Three apparently isolated but distorted spirals that could be due to past minor merging or maybe another processes: J1700, J0237 and J0202.

In this chapter we perform a global comparison between all these systems, and between them and spiral galaxies from CALIFA, whose characteristics were studied in detail in [González Delgado et al. \(2015\)](#) and in [González Delgado et al. \(in preparation\)](#). In [Section 8.1](#) I present the 2D star formation histories of our LIRGs. They are compared with spirals in [Section 8.2](#). Finally, in [Section 8.3](#) I compare the SFHs of the LIRGs with the SFHs of the PSQSOs.

8.1. Star formation histories of LIRGs

The SFHs of LIRGs have been previously analyzed by means of the 1D SFHs obtained by collapsing the spatial information, summing the SFH of every single spaxel in the datacubes ([Sections 5.4.9 and 6.4.9](#)), and also by condensing the age distribution encoded in the population vector into different age ranges to see their spatial distribution ([Sections 5.4.10 and 6.4.10](#)). Here we use the 2D SFHs to compare the differences in the evolution between the inner (0.0 - 0.5 HLR) and the outer regions

(1.0 - 1.5 HLR), whether they are dominated by different stellar populations or the mass growth and star formation rates are similar. In order to compare the radial profiles of individual galaxies on a common metric, we have expressed the distance scale in units of Half Light Radius (HLR), as was done in GD2015. As explained in [Cid Fernandes et al. \(2013\)](#), the HLR is defined as the semi-major axis length of the elliptical aperture which contains half of the total light of the galaxy at the rest-frame wavelength. In our case, the HLR, ellipticity, and position angle parameters were obtained from the continuum flux image at 5635 Å using *Pycasso* code.

We present for each LIRG several plots (see Figures 8.1 to 8.3) showing the following results:

- **Bottom panels:** Show the 2D SFH in luminosity density (left) and 2D SFH in mass surface density (right). From *Starlight* fits, we have the total stellar mass formed ($M_{ini,tot}$), the total luminosity (L_{tot}), and the population vectors expressed in terms of light fraction (x_j) and mass fraction (μ_j) for all the spaxels in the datacube. The spatially resolved SFHs are:

$$SFH_{light}(x, y, age, Z) = L_{tot}(x, y) \times x_j(x, y, age, Z)$$

$$SFH_{mass}(x, y, age, Z) = M_{ini,tot}(x, y) \times \mu_j(x, y, age, Z)$$

where x and y are the coordinates of each spaxel and age, Z are defined by the SSP models in our bases (39 ages and 4 Z in GM base and 40 ages and 4 Z in CB base). To create the 2D SFHs from them, we have followed the procedure explained in CF2013 and GD2015, first collapsing the SFH in the Z axis and then compressing xy into radial distance R , producing a radially averaged SFH(R , age) maps. Elliptical apertures 0.1 HLR in width are used to obtain the average SFH as a function of distance. The left panels show the luminosity density in units of $L_{\odot} \text{ pc}^{-2}$ at each radial position R and for each age, and the right panels show the stellar mass surface density in units of $M_{\odot} \text{ pc}^{-2}$. Both are in logarithmic scale. Therefore, the y axis represents the radial distance from the nucleus in HLR, and the x axis is the lookback time (in logarithm), that has been smoothed by a Gaussian filter with a FWHM of 0.20 dex. The smoothing was made only for visualization purposes, but the measurements were performed on the original data.

- **Middle left panels:** Show the 1D SFHs of our galaxies in different regions and as a function of lookback time in logarithmic scale. The black line is obtained by collapsing the 2D SFH_{light} (bottom left panels) over the whole radial dimension from 0.0 - 2.0 HLR, and then dividing it by the total luminosity in order to express it in light fraction units. The x axis remain unchanged. The black line represents the "average" 1D SFH in light of the galaxies. The red line is the result of collapsing the 2D SFH_{light} from 0.0 - 0.5 HLR and then dividing it by the total luminosity in that region. It represents the 1D SFH of the center (presumably related with the "bulge") of the galaxies. The blue line is the result of collapsing the 2D SFH_{light} from 1.0 - 1.5 HLR and then dividing by the total luminosity in that region. It represents the 1D SFH of the "disks" of the galaxies. In these panels we present directly the results without smoothing and the light fractions reported on the text have been measured directly from them. Although not shown, we have also computed these plots in mass fraction. The procedure is exactly the same but collapsing in the 2D SFH_{mass} map (bottom right panel) instead of in 2D SFH_{light} . The 1D SFHs in mass are analogous to light but most of the mass contribution is concentrated in the

SSPs older than 1 Gyr. The mass fraction of the younger SSPs is so low that is not possible to distinguish the differences between central region and the "disks"/outer parts. That is the reason why we have decided to show the light fractions.

- **Middle right panels:** Show the cumulative mass fraction, also called relative stellar mass growth, as a function of the lookback time in linear scale. The cumulative mass fractions have been calculated from the 1D SFHs in mass by progressively summing the mass fraction contained in all the previous (oldest) SSPs, starting from the oldest one and finishing in the youngest where the accumulated mass fraction sums up to 1. This allows us to quantify when the mass in the different regions of the galaxies formed. The color coding is the same as in the middle left panel. Because most of the mass is in the old populations, we used the linear scale in lookback time instead of logarithmic in order to better trace the old age range and to maximize the contrast between the inner and the outer regions.
- **Top left panels:** Show the radial profiles as a function of the distance (in HLR units) of the SFRs calculated by applying Equation 5.17. We have chosen four age scales that typically trace the periods of enhanced star formation in mergers: 1) 32 Myr (blue line) which represents the youngest ionizing SSPs and that is comparable to the SFR derived from H α (Lacerda et al. in prep.), 2) 300 Myr (green line) which represents young populations emitting in the UV including up to early type A stars, 3) 1.5 Gyr (orange line) which are the intermediate age populations dominated by A and early F stars, and 4) 13.5 Gyr (brown line) which represent the average over the whole Hubble time. The radial profiles of the SFR(13.5 Gyr) is equivalent to the mass surface density profiles ¹ divided by the age of the Universe.
- **Top right panels:** Show the radial profiles as a function of the distance (in HLR units) of the specific SFR (sSFR). The SFR is an extensive property (depends on the mass) and, therefore, we expect to find negative trends of the SFR with distance, given that stellar mass density is larger in the center than in the outer regions. For that reason, we have derived the sSFR by dividing the SFR radial profiles of the top left panel by the radial profiles of the stellar mass surface density (reported in Section 5.4.7 for the pre-merger LIRGs, and in Section 6.4.7 for NGC 2623). The color coding is the same as in the top left panel. As can be seen, the brown line sSFR(13.5 Gyr) is always oscillating near $\log(1/13.5) = -1.1$, the differences with respect to this value are due to the stellar mass loss. The SFR is calculated from the total stellar mass formed, while the mass surface density is obtained from the stellar mass left after some of the original mass is lost during the evolution.

8.1.1. IC 1623 W

The 2D SFH and radial profiles of the SFR of IC 1623 W (1 HLR \sim 2.8 kpc) are shown in Figure 8.1. From the bottom left and middle left panels we found that there are several periods of increased star formation, probably due to the merger. On the one hand, there is a population around 140 Myr which is important both in the center and in the "disk" (contributing to \sim 20 % of the light of both). Moreover, from 1.0 to 1.5 HLR most of the light (\sim 55 %) is dominated by populations younger than

¹Multiplied by a small factor that takes into account the mass loss due to the stellar evolution.

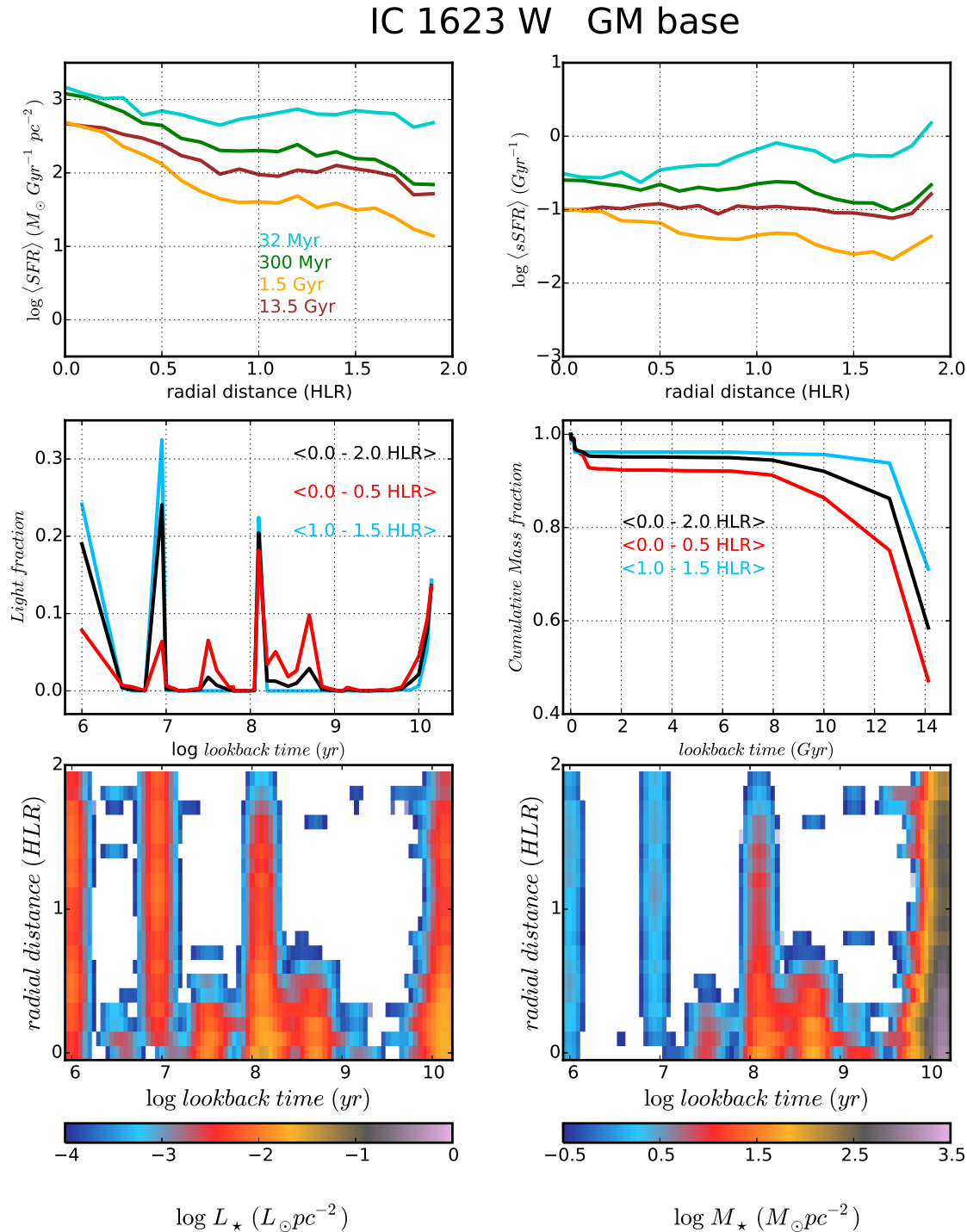


Figure 8.1 **Bottom left**: 2D SFH in light of IC 1623 W in units of surface brightness in $L_{\odot} \text{ pc}^{-2}$ and logarithmic scale. The vertical axis is the radial distance from the nucleus in HLR units. In the case of IC 1623 W, 1 HLR ~ 2.8 kpc. The horizontal axis is the SSP age (in logarithm), which has been smoothed by a Gaussian filter with a FWHM of 0.20 dex. **Bottom right**: 2D SFH in mass in units of mass surface density in $M_{\odot} \text{ pc}^{-2}$. **Middle left**: Light fraction as a function of lookback time in logarithmic scale for the inner 0.5 HLR in red, from 1.0 - 1.5 HLR in light blue and the integrated over 2 HLR in black. **Middle right**: Cumulative mass fraction as a function of the lookback time in linear scale for the inner 0.5 HLR (red line), the outer regions 1.0 - 1.5 HLR (blue line) and the integrated value (black line). **Top left**: Radial profiles of the SFRs as a function of the radial distance. The SFR calculated in the last 32 Myr is in blue, in green for the last 300 Myr, orange for the last 1.5 Gyr, and brown for the SFR along the Hubble time. **Top right**: As in the top left panel but for sSFR.

10 Myr. In the inner 0.5 HLR the SFH is more complex, the contribution of populations younger than 10 Myr is only 15 %, but the contribution of populations between 30 - 500 Myr doubles ($\sim 40\%$) with respect to the one in the "disk", showing also a more continuous star formation in that period.

From the bottom right panel we found that the contribution to stellar mass of the populations younger than 100 Myr is negligible. In fact, most of the mass is in populations older than ~ 8 Gyr. The middle right panel of this Figure shows that the mass in the outer regions formed before than the central mass. This is in contrast with the inside-out scenario found for the CALIFA galaxies (Pérez et al., 2013). In particular, 80 % of the mass of the outer regions was already there ~ 13 Gyr ago, while for the center it took around 2 Gyr more to form 80 % of its mass (11 Gyr ago). In anycase, most of the mass formed very fast both in the central part and in the "disk". At 8 Gyr, IC 1623 W had already formed 90 % of its mass everywhere. From this we conclude that as the merger is starting, the merger induced star formation has still not contributed significantly to the total stellar mass of the galaxy, most of which was already there (both in center and "disk") 8 Gyr ago. However, considering the mass formed in the last 1 Gyr as the properly "merger-induced" we found that the central part has formed 7 % of its mass in this period and the "disk" a 4 %.

From the top left panel we note that the SFRs reach their highest values in the nucleus and decrease outwards, although the SFR(32 Myr) remains significantly high in the outer parts of IC 1623 W. Moreover, in the center (< 0.5 HLR) we found that there are no significant differences between SFR(300 Myr) and SFR(32 Myr). This could indicate that the star formation has been \sim continuous in the central ~ 0.5 HLR in the last 300 Myr. On the contrary, the SFR(1.5 Gyr) is approximately 0.2 dex below SFR(300 Myr) and SFR(32 Myr), which is indicating that the SFR rate has not been continuous in this longer period up to 1.5 Gyr. Focusing now on the outer parts, from 1.0 - 1.5 HLR, we found that SFR(300 Myr) is 0.5 dex smaller than SFR(32 Myr), indicating an increase of bursty star formation in the outer parts in the last 32 Myr, while the contribution of SSPs around 300 Myr is comparatively low.

On the other hand, from the top right panel we found that the radial profiles of the sSFR flatten in the inner 0.5 HLR, indicating that the SFR per unit mass is similar in the center and in the outer parts, or even in the case of sSFR(32 Myr) is higher in the outer parts than in the center. However, as we will see in Section 8.2.4, the star formation in the last 32 Myr in the central part of these systems is still enhanced in comparison with average Sbc and Sc galaxies.

8.1.2. NGC 6090

For NGC 6090 NE the 2D SFH and SFR radial profiles are shown in Figure 8.2. The panel distribution and color coding is exactly the same as in Figure 8.1. In this case we have masked the SW component to avoid including at distances $\gtrsim 1.5$ HLR the SFH of NGC 6090 SW nucleus. For that reason and given the few spaxels available for averaging at these distances, the results beyond 1.5 HLR should be interpreted with caution. In NGC 6090 NE, 1 HLR ~ 3.7 kpc.

As can be seen in bottom left and middle left panels, the contribution of young SSPs (≤ 20 Myr) is more important in the inner 0.5 HLR (60 %) than between 1.0 - 1.5 HLR (45 %). Moreover, in the central 0.5 HLR there is a single intermediate age component of ~ 1.5 Gyr contributing to 10 % of the light, while between 1.0 - 1.5 HLR there exists, in addition to this, another intermediate age component a bit younger (~ 600 Myr) and which is also contributing to 13 % of the light of the outer

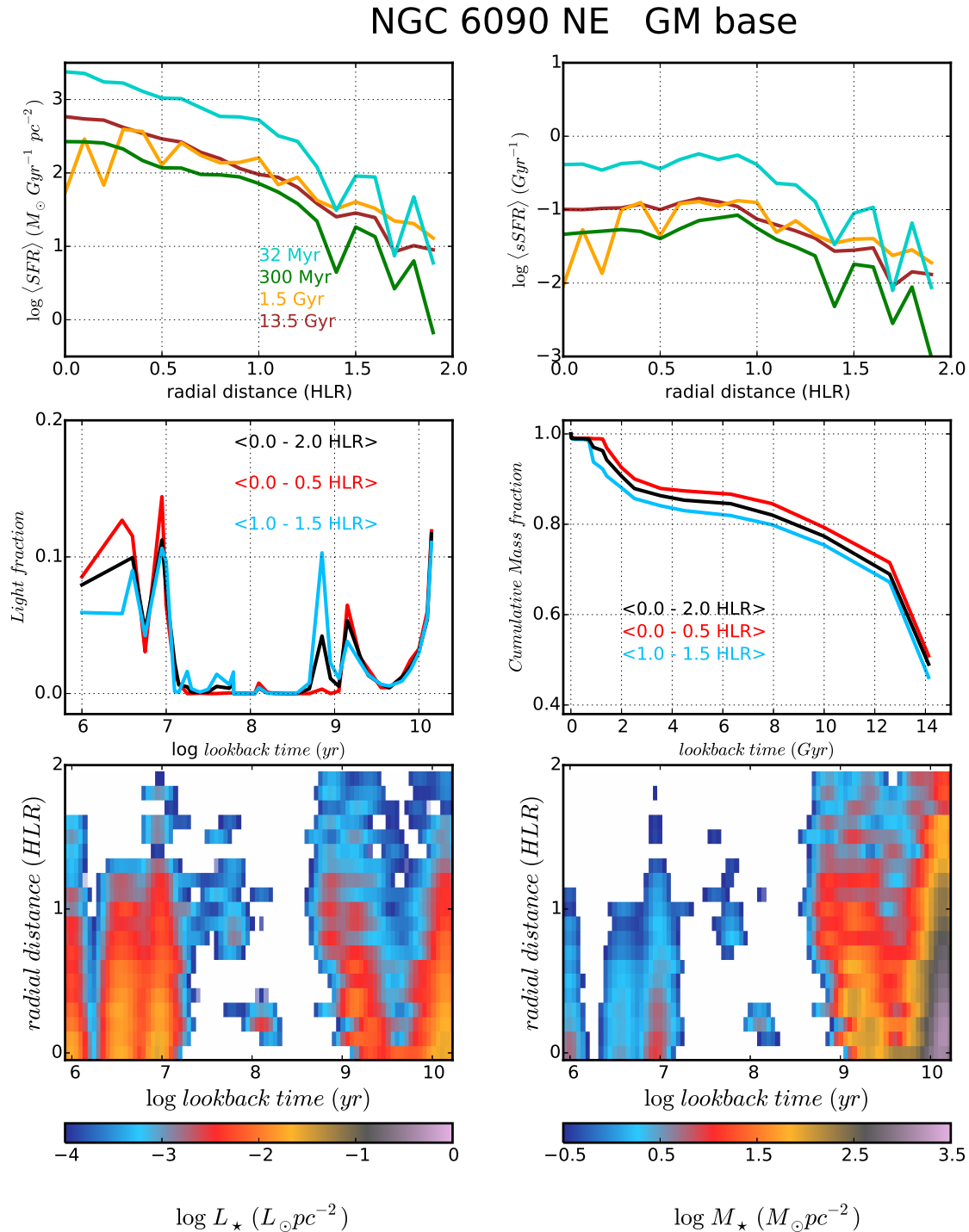


Figure 8.2 **Bottom left**: 2D SFH in light of NGC 6090 NE in units of surface brightness in $L_{\odot} \text{ pc}^{-2}$ and logarithmic scale. The vertical axis is the radial distance from the nucleus in HLR units. In the case of NGC 6090 NE, 1 HLR ~ 3.7 kpc. The horizontal axis is the SSP age (in logarithm), which has been smoothed by a Gaussian filter with a FWHM of 0.20 dex. **Bottom right**: 2D SFH in mass in units of mass surface density in $M_{\odot} \text{ pc}^{-2}$. **Middle left**: Light fraction as a function of lookback time in logarithmic scale for the inner 0.5 HLR in red, from 1.0 - 1.5 HLR in light blue and the integrated over 2 HLR in black. **Middle right**: Cumulative mass fraction as a function of the lookback time in linear scale for the inner 0.5 HLR (red line), the outer regions 1.0 - 1.5 HLR (blue line) and the integrated value (black line). **Top left**: Radial profiles of the SFRs as a function of the radial distance. The SFR calculated in the last 32 Myr is in blue, in green for the last 300 Myr, orange for the last 1.5 Gyr, and brown for the SFR along the Hubble time. **Top right**: As in the top left panel but for sSFR.

regions. While the star formation at lookback time later than 1 Gyr is similar to "isolated" spirals, recent bursts (ages < 1 Gyr) are more certainly related with the merger.

As can be seen in the bottom right panel, the mass growth in NGC 6090 NE has been more progressive than in IC 1623 W, with the mass more distributed in SSPs > 1 Gyr. Moreover, and also in contrast to IC 1623 W, from the middle right panel we found that the mass formed before in the central regions (red line) than in the outer regions (blue line). Although the difference is small. In particular, 80 % of the mass of the center was already there ~ 10 Gyr ago ($z \sim 2$), while for the outer regions is at 8 Gyr ago. It is around 2 Gyr when NGC 6090 NE formed 90 % of its mass everywhere.

In NGC 6090 there is some contribution to light of SSPs between 1 - 2 Gyr, however, we believe that SSPs above 1 Gyr are too old to have been induced by the current merger. For consistency with IC 1623 W, we will consider as merger-induced star formation everything younger than 1 Gyr. We find that the center has only increased its mass by 1 %, while the outer parts formed 7 % of its stellar mass in this same period. This is the opposite that we saw in IC 1623 W. Although both are pre-mergers, one of them has formed more mass in the central region (IC 1623 W), while the other has formed more mass in the "disk" (NGC 6090 NE).

From the top left panel, we found that all the SFRs reach their highest values in the nucleus and decrease outwards. In the inner 0.5 HLR, we found that $\text{SFR}(300 \text{ Myr}) \sim \text{SFR}(1.5 \text{ Gyr})$, while $\text{SFR}(32 \text{ Myr})$ is ~ 1 dex higher, surely due to the increased star formation in the last 32 Myr.

On the other hand, between 1.0 - 1.5 HLR, $\text{SFR}(32 \text{ Myr})$ is still 0.5 dex higher than $\text{SFR}(1.5 \text{ Gyr})$ and $\text{SFR}(300 \text{ Myr})$, indicating that youngest star formation is also relevant at these distances in comparison with star formation over longer timescales. Moreover, in comparison with IC 1623 W, the $\text{SFR}(300 \text{ Myr})$ is much less significative in NGC 6090 NE (~ 0.7 dex smaller) both in the inner 0.5 HLR and between 1.0 - 1.5 HLR. This seems to be indicating that the merger induced SF (and possibly the merger too?) is younger in NGC 6090 NE than in IC 1623 W.

Finally, from the radial profiles of the sSFR shown in the top right panel, we found that the sSFR profiles flatten below 1 HLR, as in IC 1623 W. On the contrary to IC 1623 W, the $\text{sSFR}(32 \text{ Myr})$ is still higher in the center than in the outer parts.

8.1.3. NGC 2623

From the previous results of the pre-merger LIRGs, one of the most striking findings is that star formation in the last 32 Myr is relevant not only in the central parts, but also in the outer regions up to 1.5 HLR, being the $\text{SFR}(32 \text{ Myr}) \sim 0.5 - 1$ dex higher than the SFR considering the 1.5 Gyr timescale.

The analogous results for the merger NGC 2623 (1 HLR ~ 3.3 kpc) are shown in Figure 8.3. The bottom left and middle left panels show that in the center, ~ 35 % of the light is dominated by SSPs < 20 Myr, while a similar fraction ~ 35 % is contributed by SSPs between 300 Myr - 2 Gyr. On the other hand, between 1.0 - 1.5 HLR, the contribution of SSPs < 20 Myr is significantly smaller, ~ 20 %, while the contribution of SSPs between 300 Myr - 2 Gyr is larger, ~ 45 %, than in the center.

The bottom right panel shows that the contribution to mass of the SSPs older than 1 Gyr is important, similarly to what we found in NGC 6090 NE. Moreover, the middle right panel, shows that the mass growth has been even more progressive than in NGC 6090 NE. Also, the mass formed before in the center (red line) than in the outer regions (blue line); 80 % of the mass of the center was

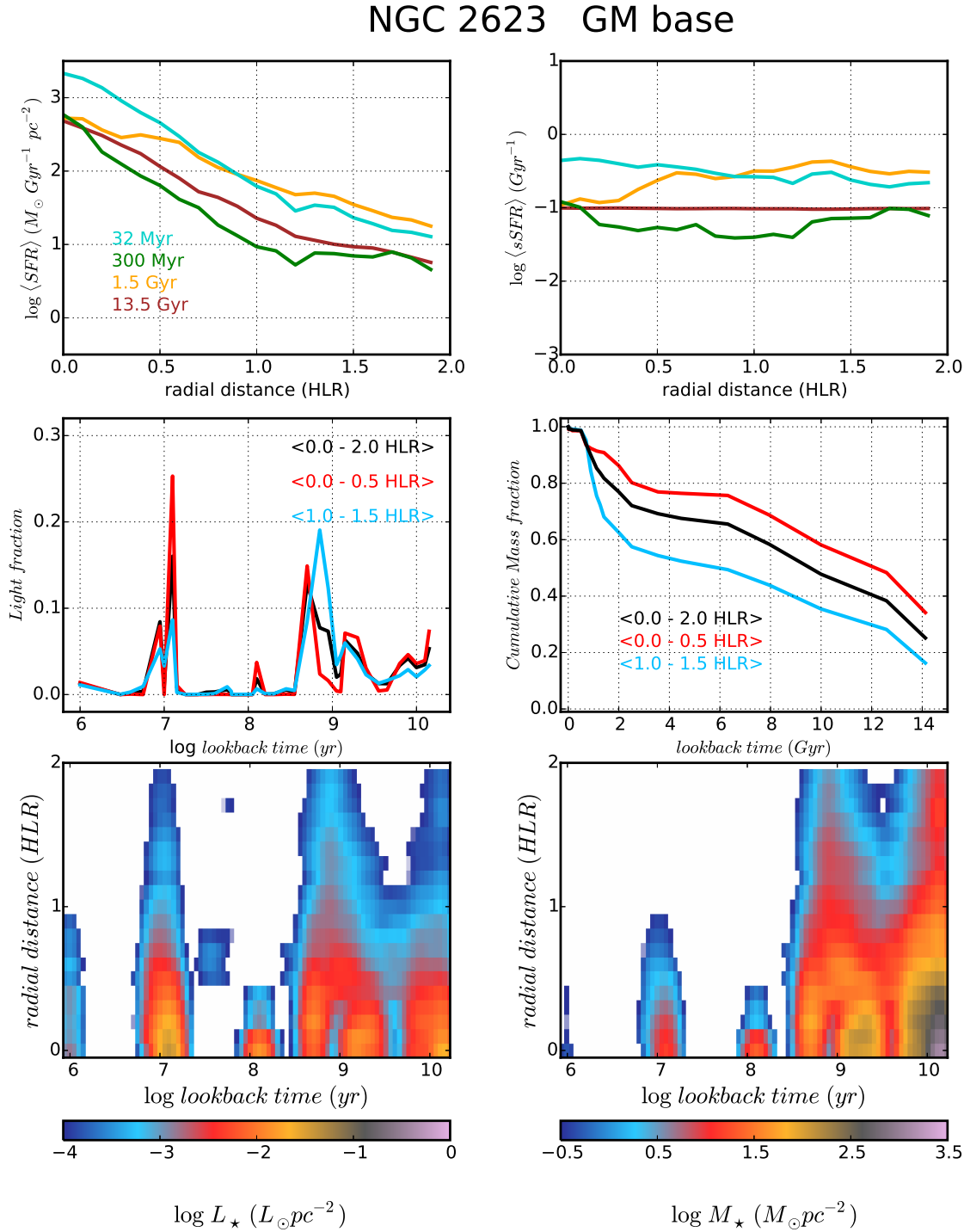


Figure 8.3 **Bottom left:** 2D SFH in light of NGC 2623 in units of surface brightness in $L_{\odot} \text{ pc}^{-2}$ and logarithmic scale. The vertical axis is the radial distance from the nucleus in HLR units. In the case of NGC 2623, 1 HLR \sim 3.3 kpc. The horizontal axis is the SSP age (in logarithm), which has been smoothed by a Gaussian filter with a FWHM of 0.20 dex. **Bottom right:** 2D SFH in mass in units of mass surface density in $M_{\odot} \text{ pc}^{-2}$. **Middle left:** Light fraction as a function of lookback time in logarithmic scale for the inner 0.5 HLR in red, from 1.0 - 1.5 HLR in light blue and the integrated over 2 HLR in black. **Middle right:** Cumulative mass fraction as a function of the lookback time in linear scale for the inner 0.5 HLR (red line), the outer regions 1.0 - 1.5 HLR (blue line), and the integrated value (black line). **Top left:** Radial profiles of the SFRs as a function of the radial distance. The SFR calculated in the last 32 Myr is in blue, in green for the last 300 Myr, orange for the last 1.5 Gyr, and brown for the SFR along the Hubble time. **Top right:** As in the top left panel but for sSFR.

there ~ 2.5 Gyr ago, while for the outer regions 1 Gyr ago. The contribution to mass of the stellar populations in the last 2 Gyr is about 13% in the center and 38% in the outer regions (in contrast to the 12% of NGC 6090 NE and the 4% of IC 1623 W). The mass growth in the outer parts of NGC 2623 in the last 2 Gyr has been 3 - 10 times more intense than the mass growth in the outer regions of the pre-merger LIRGs. In the inner 0.5 HLR, the mass growth in the last 2 Gyr has been similar (within a factor of < 2) in IC 1623 W, NGC 6090 NE, and NGC 2623.

The SFR radial profiles (top left panel) show that all the SFRs reach their highest value in the nucleus and decrease outwards. As in the pre-merger LIRGs, in the inner 0.5 HLR, the SFR(32 Myr) is significantly higher than the SFR(1.5 Gyr). On the contrary, in the outer parts (beyond 0.8 HLR) the situation is reversed, and SFR(1.5 Gyr) is a bit higher than SFR(32 Myr). This seems to be the main difference between the pre-merger LIRGs and the more advanced merger NGC 2623. Finally, from the radial profiles of the sSFR shown in the top right panel, we found that the SFRs profiles flatten below 1 HLR, as in pre-mergers. sSFRs at 32 Myr and 300 Myr are approximately flat, indicating that the SFR per unit mass at these timescales is similar in the inner and the outer regions. However, the sSFR at 1.5 Gyr increases outwards indicating that at this longer timescale the star formation has been more significant in the outer regions than in the center.

8.2. Comparison between CALIFA spirals and our LIRGs

In this Section we compare the SFHs of our LIRGs with the average SFHs of CALIFA spirals in order to quantify the degree of relevance of the merger-induced star formation and to determine when it started. We had first to apply the spectral synthesis in CALIFA sample to characterize the SFH as a function of morphological type. Part of this work was presented in [González Delgado et al. \(2015\)](#) and will be presented in a future paper in preparation.

The comparisons are made with late type spirals because the progenitor galaxies of our LIRGs are spirals without significant bulges. We have defined two possible "control galaxies". On the one hand, the average of all the Sbc galaxies in CALIFA, as they approximately cover the same mass range ($\log \langle M_{\star}^{Sbc} [M_{\odot}] \rangle = 10.70 \pm 0.34$) as our LIRGs. On the other hand, with later Sc galaxies but averaging only those in a mass range compatible with our LIRGs ($\log \langle M_{\star}^{Sc} [M_{\odot}] \rangle = 10.45 - 10.85$). There are 14 Sc galaxies in the CALIFA sample meeting this requirement and ~ 70 Sbc galaxies.

8.2.1. Radial profiles of the stellar population properties

For the LIRGs we reported the azimuthally averaged radial profiles on the following four stellar population properties: mass surface density (μ_{\star} , Sections 5.4.7 and 6.4.7), mean ages ($\langle \log age \rangle_L$, Sections 5.4.5 and 6.4.5), metallicities ($\langle \log Z_{\star} \rangle_M$, Sections 5.4.6 and 6.4.6), and extinction (A_V , Sections 5.4.4 and 6.4.4). To do the comparison we express the radial profiles presented in these Sections, using a common metric for the radial distance (HLR units).

In Figure 8.4 we show the comparison for the LIRGs and for the control Sbc and Sc galaxies. In the top left panel we show A_V , $\langle \log age \rangle_L$ in the top right panel, $\langle \log Z_{\star} \rangle_M$ in the bottom left, and μ_{\star} in the bottom right. The LIRGs are shown in colors, IC 1623 W in blue, NGC 6090 NE in orange, NGC 6090 SW in magenta, and NGC 2623 in red. The Sbc galaxies are shown in black solid lines and the Sc galaxies in black dashed lines. From the CALIFA sample we have found

that the galaxy-averaged stellar population properties are well represented by their values at 1 HLR (González Delgado et al. 2014a). For consistency, in the description of the differences we will focus first in the comparison at 1 HLR, then at the nucleus itself (or in the inner 0.5 HLR), and finally in the presence or absence of gradients both in the inner regions (from 0 - 1 HLR) and in the outer ones (from 1 - 2 HLR). The main differences are:

- A_V : At ~ 1 HLR, we found that NGC 6090 NE and NGC 2623 are, on average, 1 mag and 0.4 mag more extinguished than Sbc/Sc galaxies. On the contrary, IC 1623 W is 0.1 mag less extinguished than the control spirals. Given the low extinction in this component, the intense star formation is visible and bright in the UV, and in fact, IC 1623 W is considered as the nearest known galaxy whose basic properties are a good match to those of typical LBGs (Heckman, 2005; Grimes et al., 2006). However, in the unobserved IC 1623 E component, the level of extinction is much higher and more similar to NGC 6090 NE and NGC 2623 (see Section 5.3.2).

When focusing on the nuclear region, for the pre-merger LIRGs IC 1623 W and NGC 6090 NE the extinction values do not differ significantly from those at 1 HLR. However, for the merger LIRG NGC 2623, the nucleus is notably more extinguished (~ 1.65 mag), and there is a higher difference with respect to control spirals of ~ 1.1 mag.

With respect to the gradients, we find that the radial profiles of the pre-merger LIRGs are flat in comparison with control spirals. In Sbc and Sc galaxies there is a gradient of -0.3 mag within the inner 1 HLR, while in NGC 6090 NE and IC 1623 W there is no significant gradient. On the contrary, in the merger LIRG NGC 2623 there exists also a negative gradient with distance, but in this case it is much stronger than in the control spirals, -1 mag within the inner 1 HLR, three times higher than that of Sbc/Sc galaxies.

In the galaxies where we have information beyond 1 HLR (IC 1623 W and NGC 2623) we find outer gradients (from 1 - 2 HLR) of +0.3 mag for IC 1623 W, -0.3 dex for NGC 2623, and -0.12 dex for Sbc/Sc. The fact that IC 1623 W outer extinction gradient is positive with distance could be due to the presence of the more obscured IC 1623 E component.

If our LIRGs were originally isolated spirals, then we conclude that the merger process redistribute the gas and dust of these spirals in a way that most of it moves to the center of one of the progenitors (probably the most massive), as in IC 1623 and NGC 6090. When the galaxies finally merge, most of the dust content is already concentrated in the central regions.

- $\langle \log age \rangle_L$: At ~ 1 HLR we find that IC 1623 W, NGC 6090 NE and NGC 2623 are 1.4 dex (1.2 dex), 1.2 dex (1.0 dex), and 0.4 dex (0.2 dex) younger than Sbc (Sc) galaxies. All the LIRGs are younger than the control spirals, specially the pre-merger ones.

Analogously, at the nucleus, IC 1623 W, NGC 6090 NE, NGC 6090 SW, and NGC 2623 are 1.1 dex (0.7 dex), 1.6 dex (1.2 dex), 1.8 dex (1.4 dex), and 1.2 dex (0.8 dex) younger than Sbc (Sc) galaxies. The three LIRGs are also younger than control spirals at the nuclear regions. In the case of NGC 2623 the difference is much larger than at 1 HLR.

In the pre-merger stages the age profiles are significantly flatter than in Sbc/Sc galaxies. Even for IC 1623 W, where we find a negative gradient, the absolute variation of the age from the nucleus to 1 HLR is ~ -270 Myr, while for Sbc and Sc the variation in the inner 1 HLR is -2.4 Gyr and -665 Myr, respectively. For the merger LIRG NGC 2623 the gradient with distance is positive, inverted with respect to what happens in Sbc/Sc galaxies. The variation within the

inner 1 HLR is ~ 300 Myr.

In the galaxies where we have information beyond 1 HLR (IC 1623 W and NGC 2623) we found that the outer gradient is much flatter in all cases. From 1 to 2 HLR the variations are -24 Myr for IC 1623 W, +116 Myr for NGC 2623, -237 Myr for Sbc and -37 Myr for Sc, preserving the inner negative trends, or positive in the case of NGC 2623.

If our LIRGs were originally isolated spirals, then we conclude that the merger-induced star formation leads to a general rejuvenation of the progenitor galaxies during the pre-merger stage, that affects not only the central regions but also the "disk", as can be seen in IC 1623 W. When the galaxies finally merge, most of the gas is already in the central regions and the young star formation is therefore concentrated there. The outer parts start to evolve passively. That would explain the positive age gradient in NGC 2623.

- $\langle \log Z_{\star} \rangle_M$: At ~ 1 HLR we found $\langle \log Z_{\star} \rangle_M \sim -0.16$ for the pre-merger LIRGs NGC 6090 NE and IC 1623 W, and $\langle \log Z_{\star} \rangle_M \sim -0.37$ for NGC 2623, while for the control spirals we find $\langle \log Z_{\star} \rangle_M \sim -0.21$ for Sbc and $\langle \log Z_{\star} \rangle_M \sim -0.45$ for Sc galaxies. Pre-merger LIRGs have higher average metallicities, more similar to Sbc galaxies, while the merger LIRG NGC 2623 is less metallic, with an average value at 1 HLR more similar to Sc galaxies.

In the LIRGs we found a huge scatter in the metallicity profiles. However, in general terms, they are comparatively flat or even slightly positive in contrast to Sbc and Sc galaxies, which clearly show a negative radial gradient indicative of the inside-out growth of disks (GD2015). Inverted/flat metallicity gradients were previously found in the gas metallicity of mergers where significant gas inflows have occurred (Rich et al., 2012; Kewley et al., 2010). Here we find that beyond 0.7 HLR (1.4 HLR) in IC 1623 W (NGC 2623) the metallicities are similar to those of Sbc galaxies, but in the central regions (in the inner 0.5 HLR) the metallicities are smaller, more similar to Sc galaxies. There exist two possibilities to explain this. On the one hand, if both progenitors had similar masses (and therefore, similar metallicities) (e.g. 'Sbc'), then, merger-induced gas inflows of the lower metallicity gas located in the disks could have diminished the metallicity in the central regions, producing the observed positive gradients. On the other hand, it is also possible that one of the two progenitors was originally a less massive (with lower metallicity) galaxy (e.g. 'Sc'), which in principle would produce the same positive gradients, or even higher.

- $\log \mu_{\star}$: At ~ 1 HLR we find that the pre-merger LIRGs IC 1623 W, NGC 6090 NE, and NGC 2623 are 0.5 dex (0.8 dex), 0.6 dex (0.9 dex), and -0.02 dex (0.3 dex) more massive, respectively, than the Sbc (Sc) galaxies. The mass surface density of NGC 2623 is very similar to the one measured in Sbc galaxies, while the pre-merger LIRGs IC 1623 W and NGC 6090 NE are more massive than them.

In the nucleus, the differences between LIRGs and the control spirals are 0.06 dex (0.6 dex) for IC 1623 W, 0.14 dex (0.7 dex) for NGC 6090 NE, -0.6 dex (-0.06 dex) for NGC 6090 SW, and 0.06 dex (0.6 dex) for NGC 2623, with respect to Sbc (Sc) galaxies. That is, the central mass surface densities of IC 1623 W, NGC 6090 NE, and NGC 2623 are similar to the central density of Sbc galaxies, while the central mass surface density of NGC 6090 SW is more similar to Sc galaxies.

For the pre-merger LIRGs we find that the radial profiles are flatter than in control spirals. In

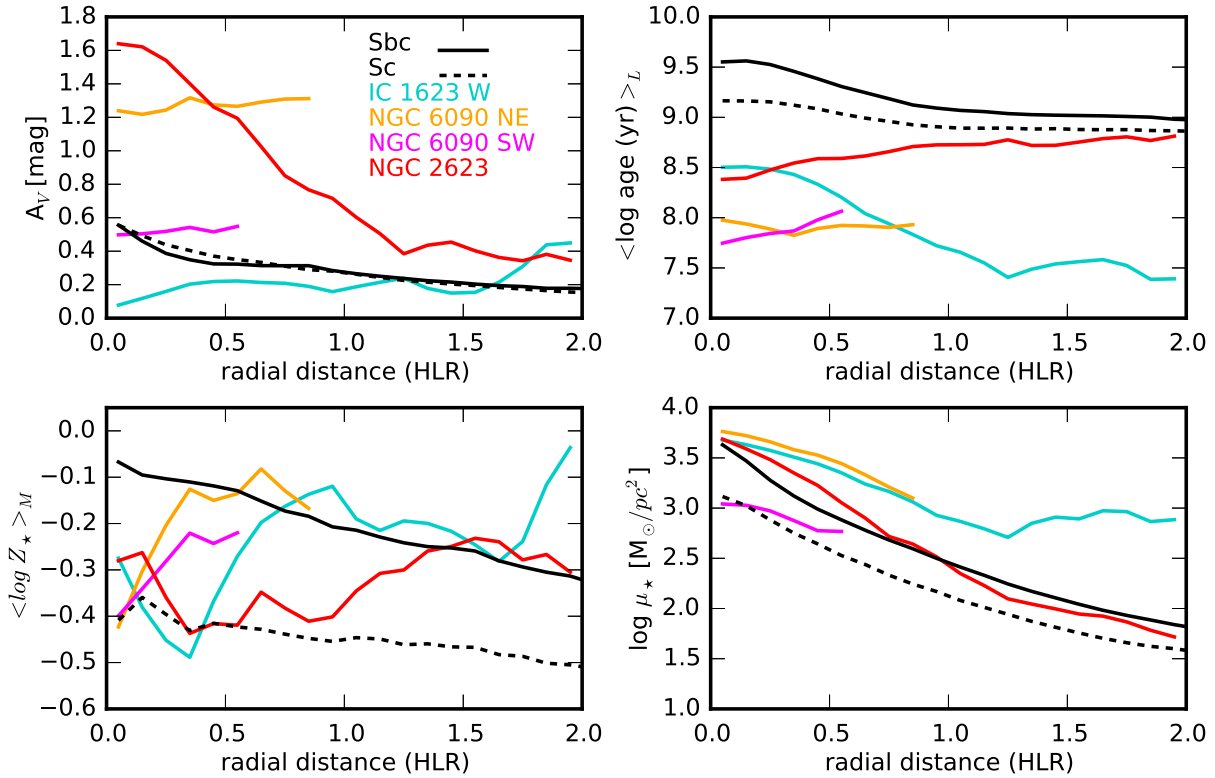


Figure 8.4 Comparison of the radial profiles of the stellar population properties for our LIRGs and the control Sbc and Sc galaxies. In top left panel we show A_V , in top right panel $\langle \log \text{age} \rangle_L$, in bottom left $\langle \log Z_* \rangle_M$, and in bottom right μ_* . LIRGs are shown in colors, IC 1623 W in blue, NGC 6090 NE in orange, NGC 6090 SW in magenta, and NGC 2623 in red. Sbc galaxies are shown in black solid lines, and Sc galaxies in black dashed lines.

the inner 1 HLR, the variations $\log \mu_*$ are -0.8 dex for IC 1623 W and -0.6 dex for NGC 6090 NE, in contrast with the steeper -1.2 dex in Sbc galaxies and -1.0 dex in Sc galaxies. The inner gradient of NGC 2623, -1.3 dex, is very similar to Sbc galaxies.

In the outer regions (from 1 - 2 HLR) we find no gradient at all in IC 1623 W, the profile is flat. In NGC 2623 the variation is -0.7 dex, not very different from the -0.6 dex of Sbc and -0.5 dex of Sc galaxies.

If our LIRGs were originally isolated spirals, we believe that the flattening of the mass density profiles in the pre-merger stages is due to the mass redistribution and/or formation during the merger. The proximity of the central regions of the two progenitor galaxies, together with the accumulation of mass toward the dynamical center lead to an increase in the mass density in a more extended region. When the galaxies finally merge most of the mass collapses in a small central region recovering the negative profile of the mass density with distance. We note, however, that if the final product of LIRGs mergers are elliptical galaxies, then NGC 2623 should be 0.7 dex more massive in order to resemble the profile of E galaxies in CALIFA (GD2015) instead of Sbc galaxies. This result would indicate that mergers such as NGC 2623 would not form massive ellipticals, but low-intermediate mass ones.

8.2.2. Central, outer, and global SFHs in light

In this section we compare the SFHs in light of our LIRGs with the ones from Sbc and Sc galaxies, in order to see if the recent star formation in the LIRGs is fully induced by the merger, or if there is significant contribution of recent star formation in late spirals. This comparison is shown in Figure 8.5, that shows the SFHs in light fraction units of our three LIRGs and the two control spirals. The color coding is the same as in Figure 8.4. The top panels are the SFHs calculated in the central regions, averaging everything inside the inner 0.5 HLR. In the middle panels we show the SFHs of the outer regions, calculated by averaging from 1.0 to 1.5 HLR, and in the bottom panels we show the global averages (from 0 to 2 HLR).

As benchmark for comparisons, we will refer to the three timescales that we already introduced in Section 8.1: 32 Myr, 300 Myr, and 1.5 Gyr. In Table 8.1 we report the light and mass contributions (in percentage) of the SSPs in these three timescales and for the 0 - 0.5 HLR region (top), 1 - 1.5 HLR (middle), and the global average from 0 - 2 HLR (bottom). In the discussion we will focus on the light contributions, because as can be noted in the Table, the mass contributions of SSPs below 300 Myr are negligible. Although they start to be significant in the 1.5 Gyr timescale, most of the mass is located in older stellar populations. The SFHs in mass fraction and mass growth will be developed in next Section.

Inner 0.5 HLR, central parts

In the central regions, we found that the contributions to light of the youngest SSPs (< 32 Myr) in IC 1623 W, NGC 6090 NE, and NGC 2623 are respectively a factor of 3 (2), 7 (5), and 5 (3) times higher than in Sbc (Sc) galaxies.

Also, the star formation over the last 300 Myr in IC 1623 W, NGC 6090 NE, and NGC 2623 is a factor of 7 (3), 8 (3), and 6 (2) times higher in light fraction than in Sbc (Sc) galaxies.

Lastly, the central star formation in the last 1.5 Gyr is also enhanced in the three LIRGs with respect to the control spirals by a factor ~ 2 , in terms of light. This is approximately a factor 2 - 3 less than what we measured for the shorter 32 Myr / 300 Myr timescales. This indicates that the star formation has not been continuous in the last 1.5 Gyr but rather in bursts.

1.0 - 1.5 HLR, outer parts

In the outer-regions of the two pre-mergers IC 1623 W and NGC 6090 NE the star formation in the last 32 Myr is a factor 3 - 4 higher in light fraction than the average of the control Sbc and Sc.

Otherwise, in the merger NGC 2623 the contribution is comparable or only slightly higher 1.2 (1.3) than in Sbc (Sc) galaxies, suggesting that the star formation in the last 32 Myr has been significantly enhanced in the central region of NGC 2623 but not in its "disk".

Again, in the outer-regions of the pre-merger LIRGs, the star formation in the last 300 Myr is a factor of 3 (for IC 1623 W) and 2 (for NGC 6090 NE) higher than in the control spirals. The contribution to light of the SSPs < 300 Myr in NGC 2623 is comparable to the one in the control spirals.

In terms of light, the star formation in the three LIRGs in the last 1.5 Gyr is not enhanced (or very slightly) with respect to the control spirals.

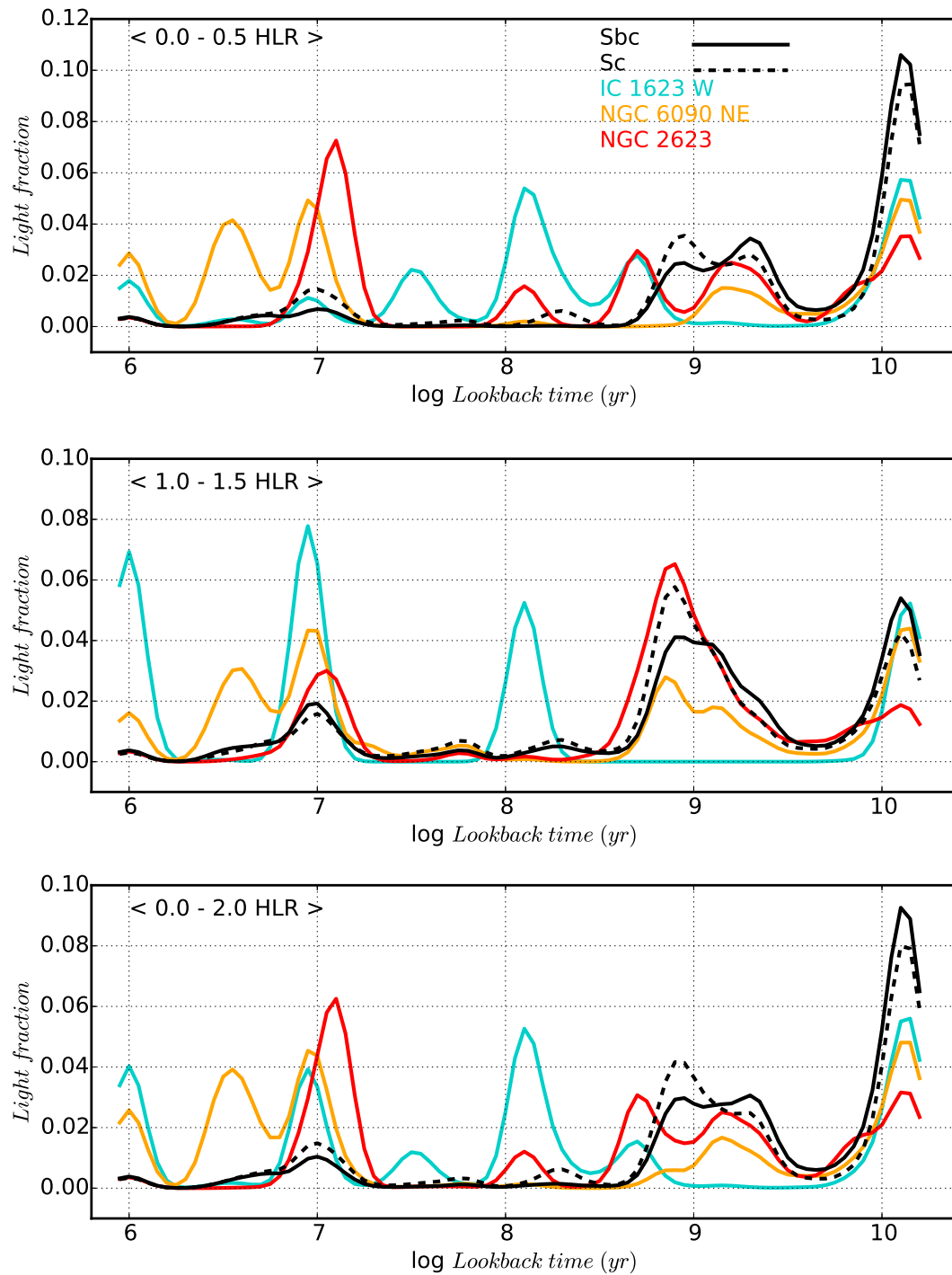


Figure 8.5 1D SFHs in light fraction of the LIRGs and of the control Sbc and Sc galaxies, calculated in the inner 0.5 HLR (top panels), between 1.0 to 1.5 HLR (middle panels), and global average from 0 to 2 HLR (bottom panels). IC 1623 W is shown in blue, NGC 6090 NE in orange, and NGC 2623 in red. The Sbc galaxies are shown in black solid lines and the Sc galaxies in black dashed lines.

Table 8.1. Light and mass contributions of SSPs over the three 32 Myr / 300 Myr / 1.5 Gyr timescales and for the three spatial regions: from 0 - 0.5 HLR (top), 1 - 1.5 HLR (middle), and 0 - 2 HLR (bottom).

0.0 - 0.5 HLR					
Light (%)	Sbc	Sc	IC 1623 W	NGC 6090 NE	NGC 2623
SSPs < 32 Myr	8	13	22	59	37
SSPs < 300 Myr	8	18	57	60	44
SSPs < 1.5 Gyr	29	43	71	66	67
Mass (%)	Sbc	Sc	IC 1623 W	NGC 6090 NE	NGC 2623
SSPs < 32 Myr	0.1	0.1	0.6	0.9	0.9
SSPs < 300 Myr	0.1	0.3	4	1.0	1.4
SSPs < 1.5 Gyr	5	8	8	7	14
1.0 - 1.5 HLR					
Light (%)	Sbc	Sc	IC 1623 W	NGC 6090 NE	NGC 2623
SSPs < 32 Myr	17	15	57	49	20
SSPs < 300 Myr	23	24	80	52	23
SSPs < 1.5 Gyr	60	69	80	74	77
Mass (%)	Sbc	Sc	IC 1623 W	NGC 6090 NE	NGC 2623
SSPs < 32 Myr	0.2	0.3	1.4	0.9	0.6
SSPs < 300 Myr	0.7	1.0	4	1.2	1.0
SSPs < 1.5 Gyr	15	21	4	12	37
0.0 - 2.0 HLR					
Light (%)	Sbc	Sc	IC 1623 W	NGC 6090 NE	NGC 2623
SSPs < 32 Myr	10	14	37	57	34
SSPs < 300 Myr	12	19	66	58	40
SSPs < 1.5 Gyr	37	50	74	68	69
Mass (%)	Sbc	Sc	IC 1623 W	NGC 6090 NE	NGC 2623
SSPs < 32 Myr	0.1	0.2	1.0	0.9	0.8
SSPs < 300 Myr	0.4	0.6	3.6	1.1	1.3
SSPs < 1.5 Gyr	10	14	5	9	23

Note. — Results from GM base.

0.0 - 2.0 HLR, global average

The global average results are somehow intermediate between the ones described above. For example, for the light contributions of the 32 Myr and 300 Myr timescales, we find similar results to what we already found in the inner 0.5 HLR. For the light contribution of populations younger than 1.5 Gyr we find intermediate numbers between what is measured in the inner 0.5 HLR and from 1 - 1.5 HLR.

In conclusion, in the two pre-merger LIRGs the star formation in the last 32 Myr, also in the last 300 Myr, is enhanced with respect to the control spirals both in the central regions and in the "disks". Yet, for the merger NGC 2623, the young star formation in the last 32 Myr or 300 Myr is significantly enhanced in the central region, while in the outer parts it is comparable to the control spirals.

8.2.3. SFHs in mass and mass growth

In the previous Section we found that most of the mass is located in stellar populations older than ~ 1 Gyr. Next we compare and quantify the mass distribution and growth of the LIRGs and the Sbc/Sc control galaxies. The 1D SFHs in mass fraction units are shown in left panels of Figure 8.6. In order to highlight the SSPs older than 1 Gyr, we have expressed the lookback time in linear scale. The upper panels were obtained by averaging in the inner 0.5 HLR, the middle panel is averaging from 1.0 - 1.5 HLR, and the bottom panel is the global average from 0 - 2 HLR. Analogously, the right column shows the cumulative mass fractions. The color coding is indicated in the top left panel and is the same as in previous figures.

Moreover, we will consider the mass contribution of SSPs < 1.5 Gyr (reported in Table 8.1) as the possibly 'merger-induced' one, as for timescales older than that we start tracing the old populations already present in the galaxies prior to the merger.

Inner 0.5 HLR, central parts

The central regions of IC 1623 W formed faster than NGC 6090 NE, this in turn formed simultaneously to Sbc (Sc) galaxies, and these faster than NGC 2623. In particular, 80 % of the mass was there 11.4 Gyr ago in IC 1623 W, 9.7 Gyr ago in NGC 6090 NE, 9.7 Gyr (10.5 Gyr) ago in Sbc (Sc) galaxies, and 2.6 Gyr ago in NGC 2623.

On the other hand, we find that the mass contribution of SSPs < 1.5 Gyr in the central regions of the two pre-mergers IC 1623 W and NGC 6090 is comparable to control spirals, while it is a factor 2 - 3 higher for the merger NGC 2623.

Note that NGC 2623 has formed a relevant mass fraction between $z = 2$ (~ 10 Gyr ago) and $z = 0.5$ (~ 4 Gyr ago) as in S0 and E galaxies in the CALIFA sample (Pérez et al., in prep.).

1.0 - 1.5 HLR, outer parts

Focusing now on the outer regions, we find that, again, IC 1623 W formed faster than NGC 6090 NE, this in turn faster than Sbc (Sc) spirals, and these faster than NGC 2623. Quantitatively, 80 % of the stellar mass was there 13.5 Gyr ago in IC 1623 W, 7.6 Gyr ago in NGC 6090 NE, 3.2 Gyr ago (1.8 Gyr ago) in Sbc (Sc), and 1 Gyr ago in NGC 2623.

Also, beyond 1 HLR, NGC 2623 formed 2 times more mass than Sbc and Sc galaxies in the last

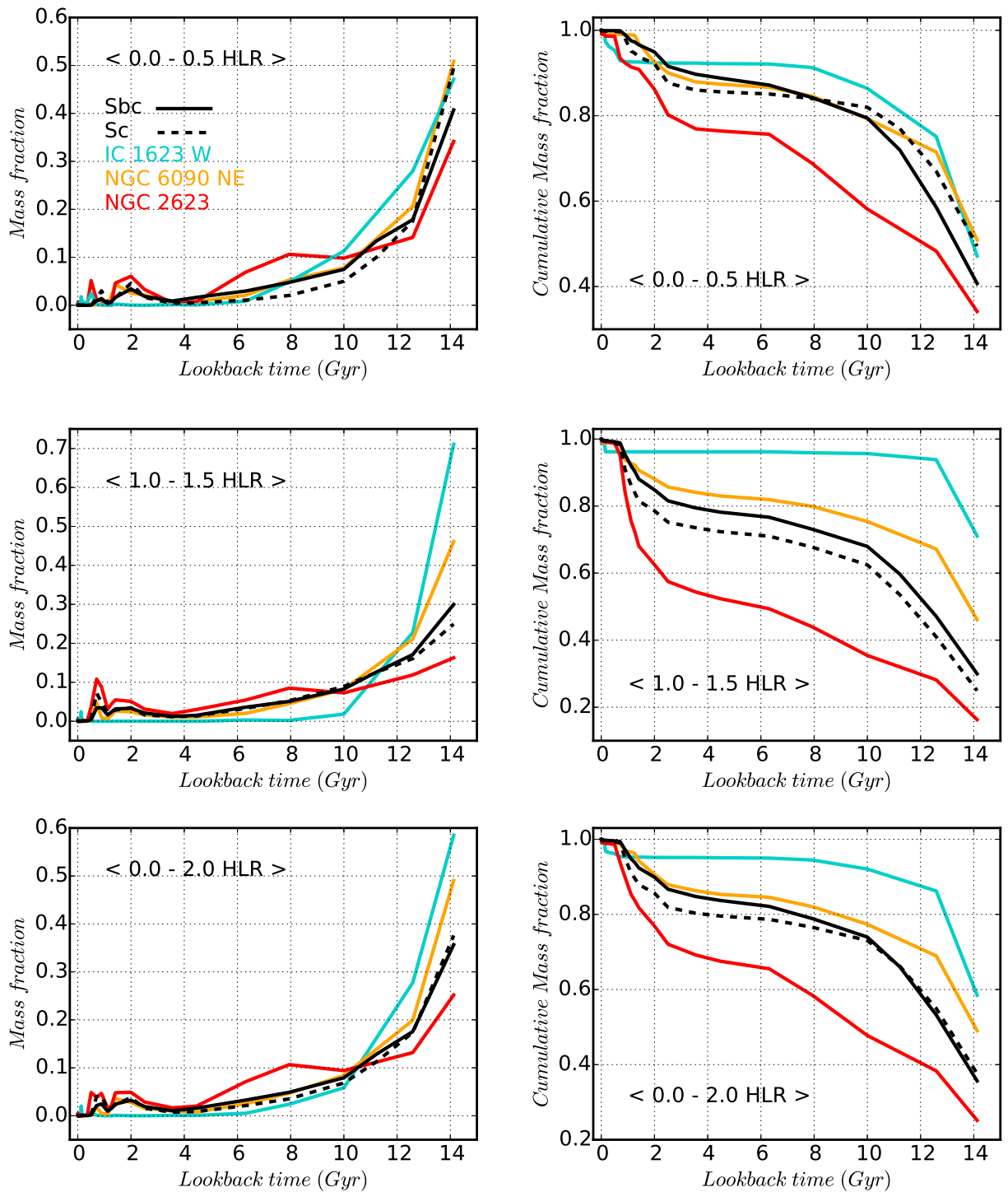


Figure 8.6 Left column shows the 1D SFHs in mass fraction as a function of the lookback time in linear scale. Right column shows the cumulative mass fractions. The top panels are averaged in the inner 0.5 HLR, the middle panels are averaged from 1.0 - 1.5 HLR, and the bottom panels show the global average from 0 - 2 HLR. The color coding is indicated in the top left panel and is the same as in previous figures.

1.5 Gyr. This increment is similar to the one found in the central part. In the pre-merger LIRG NGC 6090 the relative mass formed in the last 1.5 Gyr is comparable to Sbc spirals and in IC 1623 W it is a factor 4 less, as if the star formation would have been inhibited in this system.

0.0 - 2.0 HLR, global average

The global average results are something intermediate between the ones already derived in the central and the outer regions. IC 1623 W formed faster than NGC 6090 NE, this in turn faster than Sbc (Sc) spirals, and these faster than NGC 2623. Quantitatively, 80 % of the stellar mass was there 12.9 Gyr ago in IC 1623 W, 8.8 Gyr ago in NGC 6090 NE, 7.3 Gyr ago (3.7 Gyr ago) in Sbc (Sc), and 1.6 Gyr ago in NGC 2623.

Again, from the global averages, only NGC 2623 has formed in the last 1.5 Gyr a factor 2 more mass than the control spirals, while for the pre-merger LIRGs it is comparable or even lower.

The fact the pre-merger LIRGs seem to have formed faster than the control spirals is quite possibly an spurious effect due to the fact that the light in them is dominated by very young stellar components that may be eclipsing the underlying stellar populations older than 1.5 Gyr. To compensate the spectral fits, *Starlight* has given much weight to the oldest populations of the base ($\gtrsim 8$ Gyr), resulting in the aforementioned effect.

Hence, in the pre-merger LIRGs the mass formed in the last 1.5 Gyr is comparable to Sbc/Sc galaxies, or even lower as in the external regions of IC 1623 W. In contrast, the merger NGC 2623 has formed 2 times more mass than the control spirals in this period, both in the central and in the outer regions.

8.2.4. SFRs and specific SFRs

In this Section we compare the LIRGs SFRs and specific SFRs with respect to the ones derived in the control galaxies. The comparisons are shown in Figure 8.7. The left column represent the SFRs and the right column the sSFRs. From top to bottom what varies is the timescale traced, from 32 Myr, 300 Myr, and 1.5 Gyr. The color coding is the same as in previous figures. For consistency in the way of describing the results, we will focus first on the comparison of the SFR values in the central region (averaging in the inner 0.5 HLR), then in the outer parts (averaging from 1 - 1.5 HLR), and finally in the presence or absence of gradients in the inner 1 HLR.

32 Myr timescale, top panels

Attending to the shortest timescale, we found that in the inner 0.5 HLR, the SFRs(32 Myr) of IC 1623 W, NGC 6090 NE, and NGC 2623 are enhanced by 1.16 dex (1.07 dex), 1.40 dex (1.31 dex), and 1.20 dex (1.11 dex), respectively, with respect to the average of Sbc (Sc) galaxies. The sSFR(32 Myr) in the central 0.5 HLR of IC 1623 W, NGC 6090 NE, and NGC 2623 is respectively 0.93 dex (0.70 dex), 1.07 dex (0.83 dex), and 1.08 dex (0.85 dex) higher than in Sbc (Sc) galaxies.

Analogously, taking now as reference the outer parts from 1 - 1.5 HLR, we find differences between our LIRGs and Sbc (Sc) galaxies of 1.51 dex (1.63 dex) for IC 1623 W, 0.89 dex (1.01 dex) for NGC 6090 NE, and 0.25 dex (0.37 dex) for NGC 2623. For the sSFR(32 Myr) in the outer parts we find

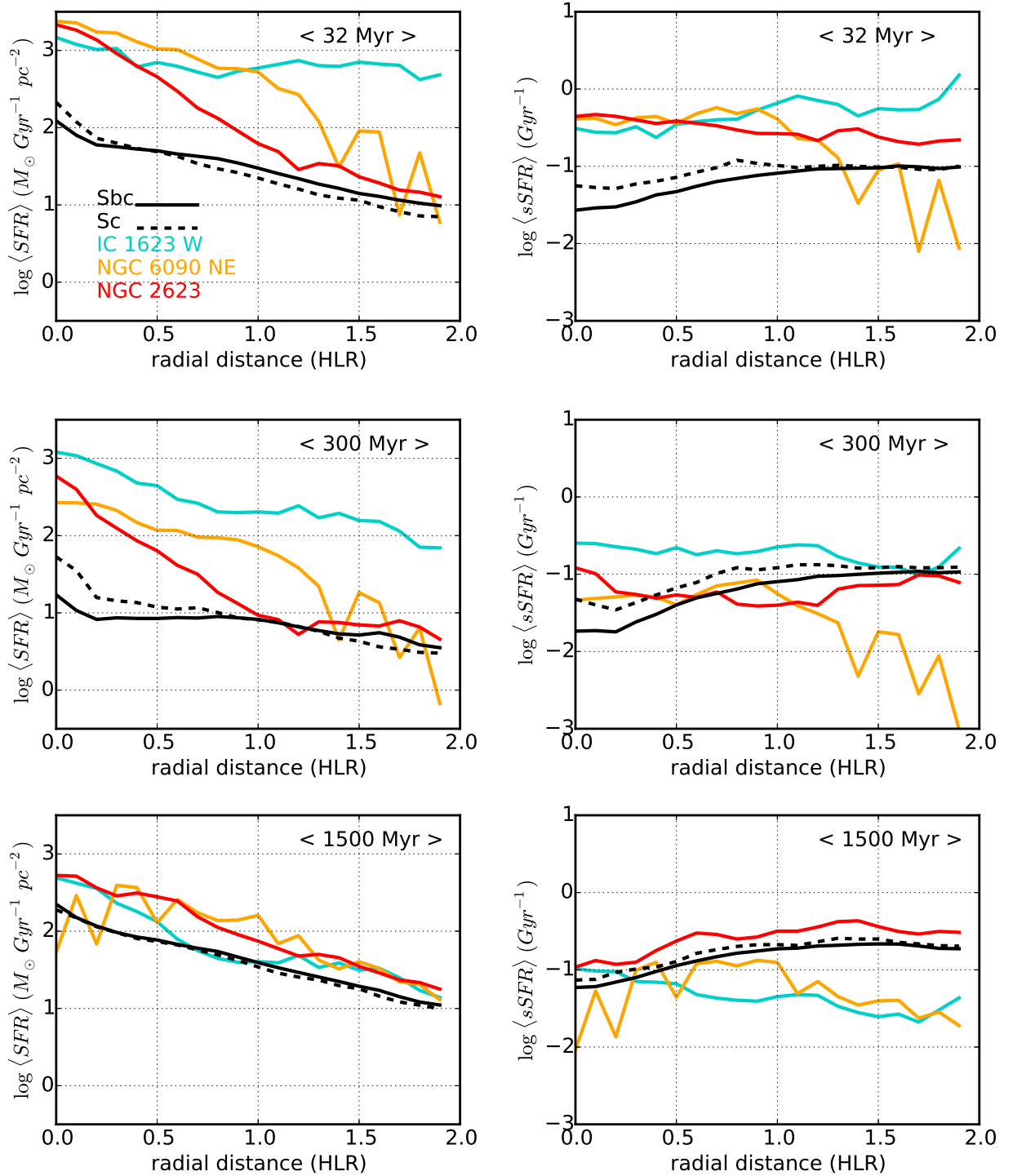


Figure 8.7 Left column represent the SFRs and the right column the sSFRs. From top to bottom what varies is the timescale traced, from 32 Myr, 300 Myr, and 1.5 Gyr. The color coding is indicated in the top left panel and is the same as in previous figures.

differences between our LIRGs and Sbc (Sc) galaxies of 0.84 dex (0.80 dex) for IC 1623 W, 0.19 dex (0.15 dex) for NGC 6090 NE, and 0.46 dex (0.42 dex) for NGC 2623.

The results for the SFR(32 Myr) are in agreement with what we found in Section 8.2.2. In the two pre-merger LIRGs the star formation in the last 32 Myr is enhanced with respect to the control spirals both in the central regions and in the "disks". Yet, for the merger NGC 2623, the young star formation in the last 32 Myr is significantly enhanced in the central region, while at the outer parts is only slightly enhanced in comparison to the control spirals.

In general, these conclusions hold when considering the sSFR(32 Myr), except for NGC 6090 NE, in which the behaviour is now more comparable to NGC 2623. That is, the star formation per unit mass sSFR(32 Myr) is significantly enhanced in the central part of NGC 6090 NE, and only slightly enhanced in the "disk".

With respect to the gradients, in the inner 1 HLR we found that for SFR(32 Myr) the gradient is negative for the three LIRGs and control spirals. The main differences are in the slope, in NGC 6090 NE is similar to Sbc galaxies, in IC 1623 the gradient is flatter, and in NGC 2623 it is even steeper than in Sc galaxies. A negative gradient indicates a central triggering of the star formation in comparison with that at 1 HLR.

On the contrary, for the sSFR(32 Myr), the gradient is positive for the control spirals, which could indicate a central quenching of the star formation in comparison with that at 1 HLR. However, for the three LIRGs the gradient is almost flat in comparison.

The sSFR allows better to compare consistently the relative star formation between different regions, as it is normalized by the amount of stellar mass. This sSFR can be interpreted as the inverse of a time scale for the SF (τ). These results in the last 32 Myr indicate that τ is much shorter in LIRGs than in spiral galaxies of similar mass. In particular, this time is ~ 2.7 Gyr for the LIRGs in the inner 1 HLR, while for the control spirals τ is above the Hubble time. That means that spiral galaxies can last a Hubble time forming stars at the current SFR without exhausting their gas reservoirs, while LIRGs can only maintain the current SFR for less than 3 Gyr.

Therefore, in the pre-merger LIRG IC 1623 W the star formation in the last 32 Myr is enhanced with respect to the control spirals both in the central regions (by a factor ~ 7) and in the "disk" (also by a factor ~ 7), while for the pre-merger NGC 6090 NE the enhancement is only important in the central region (by a factor ~ 9) while in the "disk" it is comparable to control spirals. For the merger NGC 2623, the young star formation in the last 32 Myr is significantly enhanced in the central region (by a factor ~ 9), while at the outer parts it is only slightly enhanced (by a factor ~ 3) in comparison to the control spirals.

300 Myr timescale, middle panels

In the young-intermediate scale we found that in the inner 0.5 HLR, the SFRs(300 Myr) of IC 1623 W, NGC 6090 NE, and NGC 2623 are respectively enhanced by 1.87 dex (1.56 dex), 1.31 dex (1.00 dex), and 1.25 dex (0.94 dex) with respect to Sbc (Sc) galaxies. The sSFR(300 Myr) in the central part of IC 1623 W, NGC 6090 NE, and NGC 2623 differ by 0.97 dex (0.68 dex), 0.31 dex (0.01 dex), and 0.46 dex (0.17 dex) with respect to Sbc (Sc) galaxies.

Analogously, taking now as reference the outer parts from 1 - 1.5 HLR, the SFRs(300 Myr) of IC 1623 W, NGC 6090 NE, and NGC 2623 are enhanced by 1.48 dex (1.50 dex), 0.60 dex (0.63 dex), and

0.06 dex (0.09 dex) with respect to the average of Sbc (Sc) galaxies. For the average sSFR(300 Myr) in the outer parts we find differences between our LIRGs and Sbc (Sc) galaxies of 0.29 dex (0.16 dex) for IC 1623 W, -0.61 dex (-0.74 dex) for NGC 6090 NE, and -0.24 dex (-0.38 dex) for NGC 2623.

The results of SFR(300 Myr) are in agreement with what we found in Section 8.2.2. That is, in the nuclei, the star formation in the last 300 Myr is significantly enhanced in the three LIRGs in comparison with the control spirals. However, from 1 - 1.5 HLR, only the two pre-merger LIRGs present a SFR(300 Myr) enhanced with respect to the control spirals. From 1 - 1.5 HLR, the SFR(300 Myr) of NGC 2623 is similar to the control spirals, or in other words, the star formation in the last 300 Myr is only enhanced in NGC 2623 nucleus but not in the outer regions.

In this case, not all these conclusions remain when considering the star formation per unit mass in the last 300 Myr, or sSFR(300 Myr). It remains that the sSFR(300 Myr) is enhanced in the central regions of IC 1623 W (by a factor ~ 7) and NGC 2623 (by a factor ~ 2) in comparison with the control spirals, while the central star formation in NGC 6090 is similar to them. Moreover, now, the only LIRG with significant sSFR(300 Myr) in the outer parts is IC 1623 W, twofold with respect to control spirals, much lower than the central region. The sSFR(300 Myr) in the outer parts of NGC 6090 NE and NGC 2623 is now lower than in the control spirals by a factor of 4 and 2, respectively, as if the star formation would have been slightly inhibited during this period.

With respect to the gradients, the SFR(300 Myr) gradient is negative for the three LIRGs and control spirals, as in the case of SFR(32 Myr). In IC 1623 W, the slope is very similar to Sc galaxies, and in NGC 6090 NE its value is in between Sbc and Sc galaxies. In NGC 2623, however, it is even steeper than in Sc galaxies.

On the contrary, the sSFR(300 Myr) gradient is positive for the control spirals, almost flat for the two pre-merger LIRGs and slightly negative for the merger LIRG NGC 2623. That is, compared with the LIRGs, the control spirals show a quenching of star formation to the center in the last 300 Myr.

Therefore, the star formation in the last 300 Myr is enhanced in the central regions of IC 1623 W (by a factor ~ 7) and NGC 2623 (by a factor ~ 2) in comparison with the control spirals, while the central star formation in NGC 6090 is similar to them. In the outer parts, only IC 1623 W presents a slight enhancement (by a factor $\lesssim 2$) of the star formation with respect to control spirals. On the contrary, in the outer parts of NGC 6090 NE and NGC 2623 the star formation seems to have been slightly inhibited when considering the 300 Myr period.

1.5 Gyr timescale, bottom panels

Attending to the longest, intermediate age timescale, we found that in the inner 0.5 HLR the differences in SFR(1.5 Gyr) between our LIRGs and Sbc (Sc) galaxies is 0.37 dex (0.39 dex) in IC 1623 W, 0.15 dex (0.17 dex) in NGC 6090 NE, and 0.50 dex (0.52 dex) in NGC 2623. The sSFR(1.5 Gyr) in the nuclei of IC 1623 W, NGC 6090 NE and NGC 2623 differ by 0.03 dex (-0.06 dex), -0.29 dex (-0.38 dex), and 0.27 dex (0.18 dex) with respect to Sbc (Sc) galaxies.

Analogously, taking now as reference the outer parts from 1 - 1.5 HLR, the SFRs(1.5 Gyr) of IC 1623 W, NGC 6090 NE, and NGC 2623 differ from the Sbc (Sc) galaxies by 0.14 dex (0.20 dex), 0.35 dex (0.40 dex), and 0.27 dex (0.32 dex), respectively. For the sSFR(1.5 Gyr) in the outer parts we find differences between our LIRGs and Sbc (Sc) galaxies of -0.75 dex (-0.81 dex) for IC 1623 W, -0.57 dex (-0.63 dex) for NGC 6090 NE, and 0.25 dex (0.19 dex) for NGC 2623.

Again, the results from the SFR(1.5 Gyr) are consistent with the results from Section 8.2.2. That is, the central star formation in the last 1.5 Gyr is only slightly enhanced in IC 1623 W, NGC 6090 NE, and NGC 2623 with respect to control spirals ($\lesssim 2$, much less than for the young 32 Myr and 300 Myr timescales), and in the "disks" / outer parts (1 - 1.5 HLR) of the LIRGs the star formation in the last 1.5 Gyr is not (or only slightly) enhanced with respect to the control spirals.

However, not all these conclusions remain when considering the star formation per unit mass in the last 1.5 Gyr or sSFR(1.5 Gyr). The central specific star formation in the last 1.5 Gyr is now slightly enhanced (by a factor 1.7) in NGC 2623 with respect to control spirals. In IC 1623 W it is comparable to control spirals, while in NGC 6090 NE it is significantly smaller in comparison (by a factor ~ 2). Additionally, in the outer regions, the sSFR(1.5 Gyr) is slightly enhanced in NGC 2623 (by a factor 1.7) in comparison to the control spirals, while in NGC 6090 and specially in IC 1623 W it is significantly less than in control spirals (by a factor of ~ 4 and ~ 6 , respectively), as if the sSFR(1.5 Gyr) has been inhibited in the pre-mergers.

With respect to the gradients, in the inner 1 HLR we found a negative gradient for control spirals, as well as for IC 1623 W and NGC 2623. In NGC 2623 the slope is similar to Sbc and Sc galaxies while the inner slope of IC 1623 is steeper than for the control spirals. On the contrary, in NGC 6090 NE the profile is almost flat considering the noise.

On the contrary, the sSFR(1.5 Gyr) gradient is positive for the control galaxies and NGC 6090 NE and NGC 2623. This points to a quenching in the central parts of the galaxies in comparison with the outer parts in the last 1.5 Gyr. IC 1623 W, however, presents the opposite behaviour, showing a slightly negative inner gradient.

Hence, the star formation in the last 1.5 Gyr is only slightly enhanced (by a factor 1.7) in the central regions of NGC 2623 with respect to control spirals, while in the pre-mergers it is comparable to them (IC 1623 W) or a factor 2 lower than in them (NGC 6090 NE). In the outer regions, the star formation in the last 1.5 Gyr is enhanced with respect to the control spirals by a factor 1.7 in NGC 2623, while for the pre-merger LIRGs it is a factor 4 - 6 lower than in them, as if the star formation has been inhibited in this time period.

8.3. Comparison between LIRGs and PSQSOs

In this Section we compare the SFHs of LIRGs and PSQSOs to explore a possible evolutionary connection. At the PSQSOs redshift ($z \sim 0.3$; $D_L \sim 1553.4$ Mpc) the spatial scale is 4.456 kpc/arcsec. Their central spectra were extracted in an aperture of $r = 1.5$ arcsec (to match SDSS spectra), ~ 6.7 kpc. On the other hand, 1 HLR in our LIRGs IC 1623 W, NGC 6090 NE, and NGC 2623 implies 2.8 kpc, 3.7 kpc, and 3.3 kpc, respectively. Therefore, 2 HLR in the LIRGs cover \sim the same spatial aperture in kiloparsecs as the PSQSOs central spectra. We will compare them.

Another thing we want to note, is that although the spectral synthesis for the PSQSOs was also made with both model bases (GM and CB), CB gives more credible results for the light fraction in SSPs younger than 30 Myr and the power-law. Most of the PSQSOs spectra start around 2900 - 3000 Å, some of them with a significant slope in this range, characteristic of an AGN and / or very young stellar populations. While the GM base starts in 3540 Å, the CB base extends the fits below it, covering the whole blue range. As a consequence, CB base provides better fits below 3540 Å than GM base. The result is that CB base puts a significant contribution in light to the AGN (20 - 40%),

while the GM base puts nothing and instead allocates it in the youngest stellar populations (< 30 Myr).

Given the ubiquitous presence of broad components in the Balmer lines and the fact that the narrow line ratios are Seyfert, we assume that the blue continuum is due to the AGN and not to young stars. In anycase, and given that the previous comparisons were made with the GM base, here we also show it for consistency. However, and the end we will compare and discuss the differences in the results with respect to CB base, which also serves as a general comparison between bases for spirals and LIRGs. We note, however, that as with the GM base we could not put as a constrain the Balmer lines fluxes, in this Section we compare the results between the non constrained fits and with the spectral base excluding SSPs < 4 Myr, in order to be able to compare between GM and CB results.

The GM results are summarized in Figure 8.8. The panels distribution is as follows:

- **Bottom panels:** 1D SFHs of the LIRGs and PSQSOs ordered within each group by increasing stellar mass. Although the mass of IC 1623 W is smaller than NGC 2623 we have put it above because we should also add the mass of the eastern component. The PSQSOs masses were reported in Table 7.7. The left panels are the SFHs in light fraction and the right panels in mass fraction.
- **Middle panels:** 1D SFHs of the LIRGs and PSQSOs ordered within each group by the interaction stage classification, from less to more advanced mergers. In the case of the LIRGs the order is clear, the two pre-mergers IC 1623 W and NGC 6090 go first and followed by the merger NGC 2623. The PSQSOs are a very heterogeneous group, the order we have followed is: 1) pre-merger spiral PSQSOs (J2310 and J1456), 2) undefined pre-merger system where the morphology of the main galaxy is not clear (J1230), 3) (post)merger elliptical systems (J2128, J1248 and J2334), 4) isolated but distorted spirals due to past minor merging or maybe another processes (J0202, J0237, J1700).
- **Top panels:** Comparison of the average 1D SFH of the nine PSQSOs (black) with the LIRGs (already introduced color coding). As previously, the left panels are expressed in light fraction and the right panels in mass fraction.

In principle, there is no clear or systematic evolution of the SFHs when ordering them by mass. It seems that for the PSQSOs, the higher the stellar mass the smaller the contribution to light of the SSPs < 10 Myr (see bottom left panel). However, as we previously mentioned, these young contributions are not reliable, because there exists a strong degeneracy with the AGN contribution which is not taken into account by GM base. In anycase, we note that the mass range traced is very small and almost coincident for LIRGs and PSQSOs. The LIRGs masses range from $\log M_{\star} (M_{\odot}) = 10.15$ to 10.51 , while the PSQSOs from $\log M_{\star} (M_{\odot}) = 10.14$ to 10.96 . There are only 4 PSQSOs more massive than the most massive LIRG (= NGC 6090) which are: J0237, J1700, J0202 and J2310. It is interesting to note that the first 3 of them are the isolated spirals, and the other one is a pre-merger spiral (similar in morphology to the pre-merger LIRGs). These high masses in the isolated spiral PSQSOs could indicate that they come from a previous merger. In fact, since they are morphologically distorted, we believe that it could have been a minor merger.

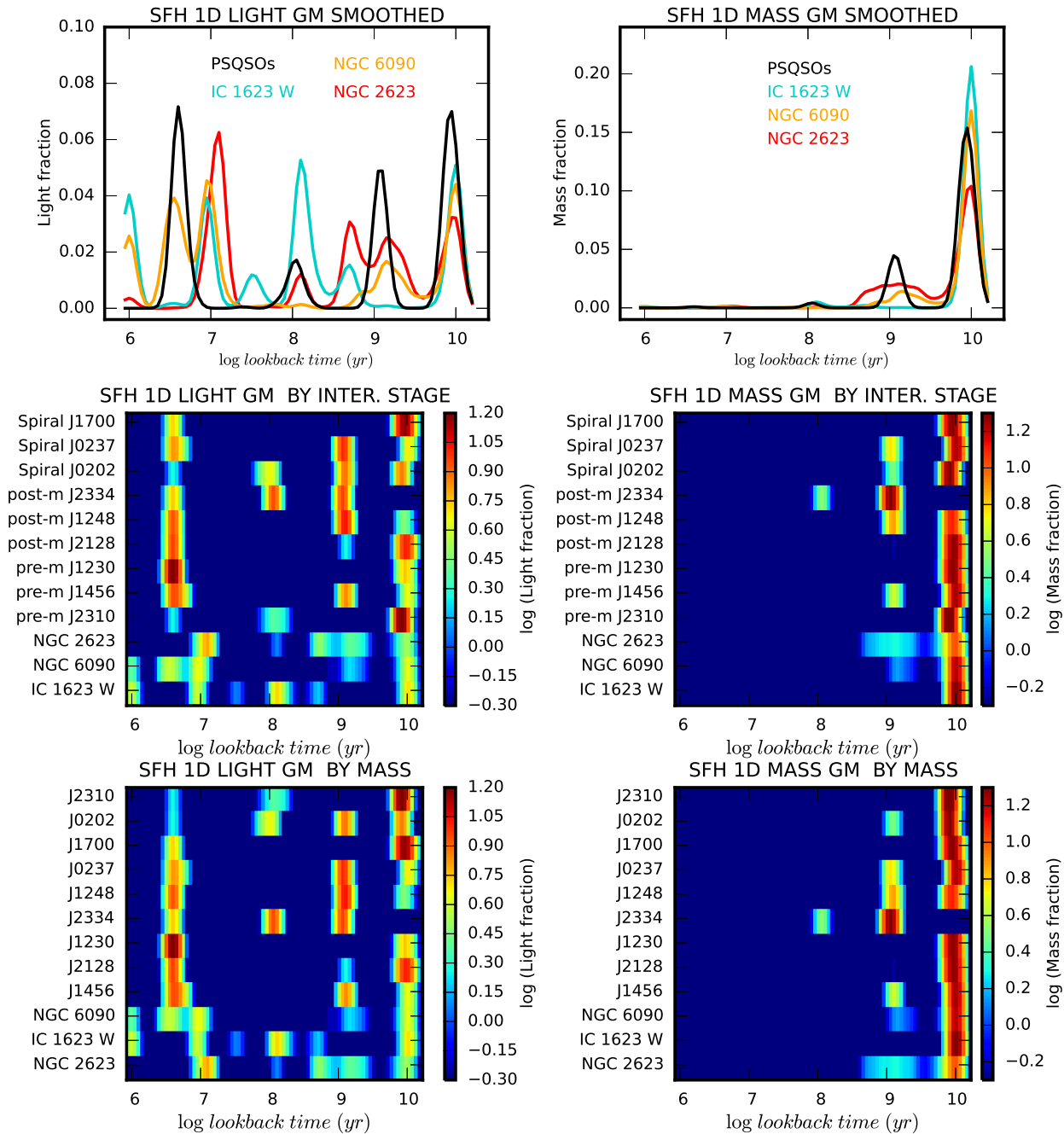


Figure 8.8 Bottom panels show the comparison of the 1D SFHs of all the LIRGs and PSQSOs. Within each group, they are ordered by increasing mass. Left panels represent SFH in light fraction and the right panels in mass fraction. Middle panels are similar but now ordered according to the interaction stage, from less to more advanced mergers. Top panels show the average SFHs of the nine PSQSOs in black, together with the LIRGs SFHs in blue, orange, and red for IC 1623 W, NGC 6090 NE, and NGC 2623, respectively. These are the results with GM base.

When ordering the systems by the interaction stage we find that, for the PSQSOs, the higher the contribution to light of the SSPs around 1 Gyr the more advanced the merger, except for J1700 (see

middle panels). The pre-merger PSQSOs have, on average, smaller contributions to light of SSPs ~ 1 Gyr than the post-merger PSQSOs, assuming that the distorted spiral PSQSOs are actually the result of a merger. This is also seen in the LIRGs, although we have no statistics, in NGC 2623 the SSPs around 1 Gyr are contributing to light more than in the pre-merger LIRGs. We also note that the intermediate age stellar populations in the PSQSOs are located ~ 1 Gyr, while in NGC 2623 there exist two bursts, one centered around ~ 1.5 Gyr, and a younger one at ~ 500 Myr.

When looking at the average SFHs of the PSQSOs (in top panels), we find, apart from the uncertain contribution of SSPs < 30 Myr, a small contribution from SSPs ~ 140 Myr, and an important contribution both to light and mass of the SSPs ~ 1 Gyr.

The results from base CB are shown in Figure 8.9, which is analogous to Figure 8.8. With this base we do not find any clear or systematic evolution of the SFHs when ordering them by mass, neither by interaction stage. The three most notable differences with respect to GM base are:

1. Lower contribution to light of SSPs < 32 Myr with CB base than with GM base. With CB base, only 4 PSQSOs have remarkable young contributions; J1230, J2128, J0237 and J2310, each belonging to a different interaction class subgroup. As we previously comment, these differences are due to the inability of the GM base to assign any contribution to the power-law. Instead, it gives the young stellar components a significant contribution.
2. The intermediate age star formation in the PSQSOs cover a wider age range from 500 Myr to 3 Gyr with CB base, apparently divided in two bursts, the most intense of them around 800 Myr, and a softer one at 2 Gyr, while in GM base there exists only one burst around 1 Gyr.
3. The light and mass contribution of the oldest populations ~ 10 Gyr is higher for GM than CB base, possibly to compensate the lack of intermediate age star formation around 2 Gyr which is present in CB base.

To compare with the LIRGs (and control spirals) we have quantified the contributions to mass and light of SSPs in the three timescales previously introduced but expressed now differentially: < 32 Myr, from 32 Myr to 300 Myr, from 300 Myr to 1.5 Gyr. Moreover, we have added a longer timescale including SSPs from 1.5 Gyr to 3 Gyr, to cover all the "probably merger induced" star formation in the PSQSOs. The contributions to light and mass in these four time ranges for all the systems are shown in Table 8.2 for GM base (top) and CB base (bottom). When comparing the numbers in the different age ranges we find:

1. Contributions of young SSPs < 32 Myr:

- As can be seen, with the base CB, the SSPs < 32 Myr contribution to light of the PSQSOs is 13%, 20% less than the contribution derived with GM base (33%), which is similar to the average percentage ($27 \pm 9\%$) attributed to the power-law by CB base.
- The contribution to light of young SSPs in the control spirals is on average, 12% (GM base) and 17.5% (CB base).

The contribution to light of young star formation in the two pre-merger LIRGs is a factor 4 (3) higher than in control spirals with GM (CB). In NGC 2623 it is also a factor 3 (2) higher than in control spirals with GM (CB). In the case of the PSQSOs the contribution is

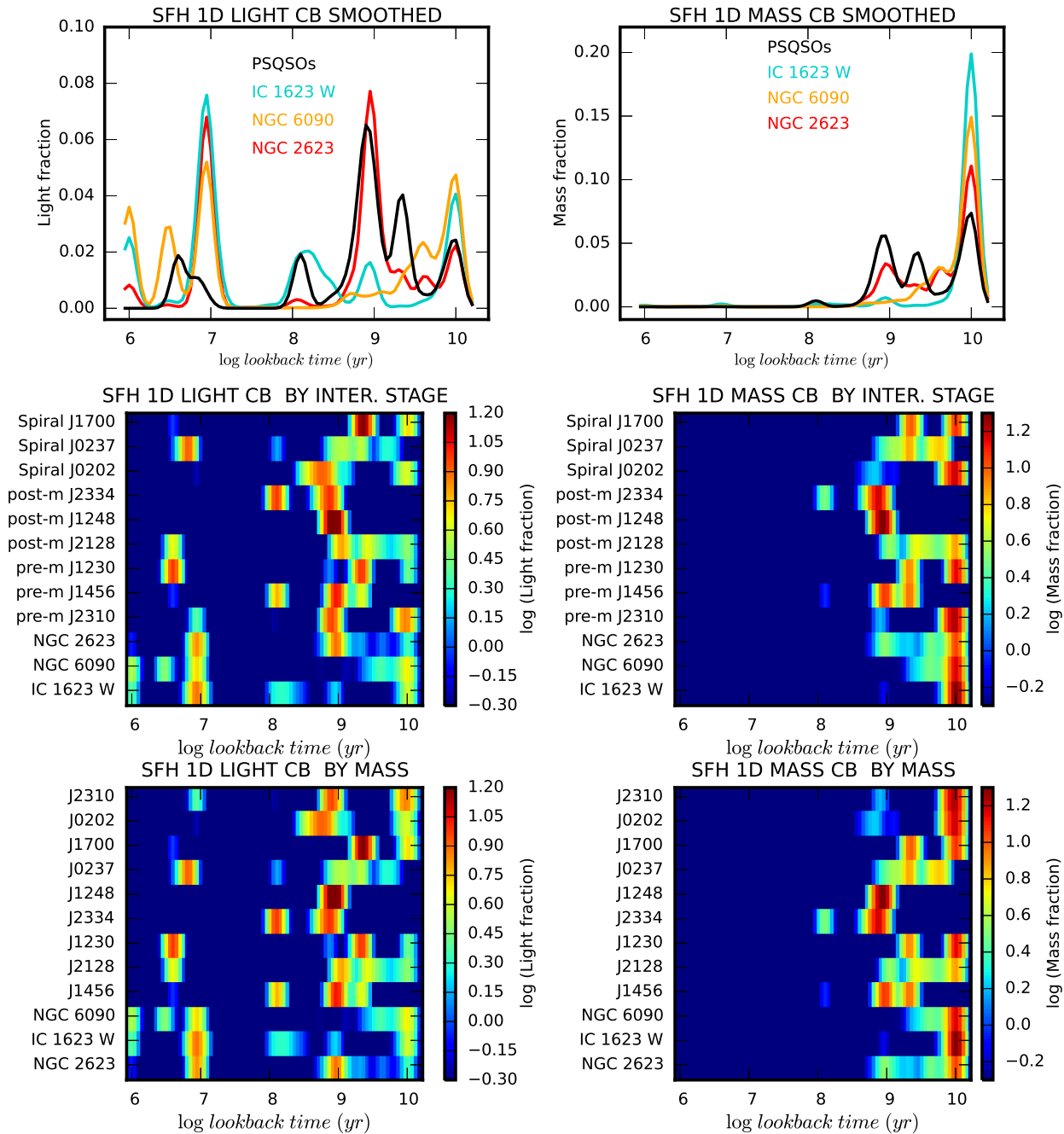


Figure 8.9 Same as Figure 8.8 but with CB base. The panel distribution is the same.

similar to control spirals with CB base, and a factor 3 higher than in them with GM base. However, in this age range the results from CB base for the PSQSOs are more reliable.

- The contributions to mass of SSPs younger than 32 Myr is below 1% for all the systems.

2. Contributions of young-intermediate SSPs from 32 Myr to 300 Myr:

- The contribution to light of young-intermediate age SSPs is low in the control spirals, with

Table 8.2. Light and mass contributions of SSPs over different time ranges with GM base (top) and CB base (bottom), calculated from the average SFHs of the control spirals and the LIRGs (from 0 - 2 HLR), and for the SFH of the central regions of the PSQSOs.

GM base results						
Light (%)	Sbc	Sc	IC 1623 W	NGC 6090 NE	NGC 2623	PSQSOs
SSPs < 32 Myr	10	14	37	57	34	33
32 Myr < SSPs < 300 Myr	2	5	29	1	6	9
300 Myr < SSPs < 1.5 Gyr	25	31	8	10	29	23
1.5 Gyr < SSPs < 3 Gyr	15	12	0	5	9	0
Mass (%)	Sbc	Sc	IC 1623 W	NGC 6090 NE	NGC 2623	PSQSOs
SSPs < 32 Myr	0.1	0.2	1.0	0.9	0.8	0.4
32 Myr < SSPs < 300 Myr	0.3	0.4	2.6	0.2	0.5	1.9
300 Myr < SSPs < 1.5 Gyr	9.6	13.4	1.4	7.9	21.7	19.7
1.5 Gyr < SSPs < 3 Gyr	6	6	0	5	9	0
CB base results						
Light (%)	Sbc	Sc	IC 1623 W	NGC 6090 NE	NGC 2623	PSQSOs
SSPs < 32 Myr	14	21	50	50	34	13
32 Myr < SSPs < 300 Myr	0	1	20	1	2	10
300 Myr < SSPs < 1.5 Gyr	28	35	8	6	42	43
1.5 Gyr < SSPs < 3 Gyr	14	12	1	8	6	19
Mass (%)	Sbc	Sc	IC 1623 W	NGC 6090 NE	NGC 2623	PSQSOs
SSPs < 32 Myr	0.2	0.3	1.6	0.7	0.6	0.1
32 Myr < SSPs < 300 Myr	0.2	0.3	2.3	0.1	0.7	2.3
300 Myr < SSPs < 1.5 Gyr	9.6	15.4	4.1	5.2	23.7	34.6
1.5 Gyr < SSPs < 3 Gyr	8	8	0	9	9	20

averages of 3.5% (GM base) and 0.5% (CB base).

From both bases, we find that in comparison with the control spirals, IC 1623 W presents enhanced young-intermediate age contributions to light by a factor of 8 (40) with GM (CB), followed by the PSQSOs which are enhanced by 3 (20) with GM (CB), and finally by NGC 2623 which is enhanced by 2 (4) with GM (CB). The light contribution of young-intermediate age SSPs in NGC 6090 NE is similar to spirals.

- In terms of mass, the SSPs in this age range only represent < 3%.

3. Contributions of intermediate age SSPs from 300 Myr to 1.5 Gyr:

- The contribution to light of intermediate age SSPs in the control spirals is on average, 28% (GM base) and 31.5% (CB base).

From both bases, we find that in comparison with the control spirals the pre-merger LIRGs present diminished intermediate age contributions to light a factor 3 (4.5) with GM (CB), as if the star formation would have been inhibited in them. On the other hand, for NGC 2623 and the PSQSOs the star formation in this age range is comparable to control spirals with GM base, and only slightly enhanced with respect to them by a factor 1.3 - 1.4 from CB results.

- This age range starts also to be important in terms of mass. The contribution to mass of intermediate age SSPs in the control spirals is on average 11.5% (GM base) and 12.5% (CB base).

From both bases, we find that in comparison with the control spirals the pre-merger LIRGs present diminished intermediate age contributions also in terms of mass by factors between 2 - 8 (2 - 3) with GM (CB). In NGC 2623 the intermediate age contribution to mass is enhanced with respect to control spirals by a factor 2 (2) with GM (CB), while for the PSQSOs is also enhanced by 2 (3) with GM (CB).

4. Contributions of intermediate-old SSPs from 1.5 Gyr to 3 Gyr:

- The contribution to light of intermediate-old SSPs in the control spirals is on average, 13.5% (GM base) and 13% (CB base).

From both bases, we find that in comparison with the control spirals the 3 LIRGs present intermediate-old contributions to light that are lower than them, almost zero for IC 1623 W, and a factor 3 (2) lower for NGC 6090 NE with GM (CB), and a factor 1.5 (2) lower for NGC 2623 with GM (CB). For the PSQSOs we find a significant difference between bases, while with GM there is no star formation in this age range, with CB base there is, and is enhanced with respect to control spirals by 1.5.

- The contribution to mass of intermediate-old SSPs in the control spirals is on average, 6% (GM base) and 8% (CB base).

From both bases, we find that in comparison with the control spirals the pre-merger LIRGs present intermediate-old contributions to mass that are similar (NGC 6090 NE) or lower (IC 1623 W). In NGC 2623 the intermediate-old SSPs contribution to mass is similar or only slightly enhanced with respect to the control spirals by 1.5 (1.1) with GM (CB). As also happens in terms of light, the PSQSOs present a significant difference between bases, while with GM there is no star formation in this age range, with CB base there is, and is enhanced in terms of mass with respect to control spirals by 2.5.

We found that the populations younger than 300 Myr do not contribute significantly to the stellar mass, but are important light contributors. *One relevant conclusion is that the global relative importance of the youngest star formation (< 32 Myr) is different in LIRGs and PSQSOs, being higher in pre-merger LIRGs (a factor between 3 - 4) than in control spirals, a bit less important in the merger NGC 2623 (but still a factor 2 - 3 higher) than in control spirals and low in the PSQSOs where it is comparable to them. However, in the young-intermediate age range from 32 Myr - 300 Myr, the PSQSOs are, after IC 1623 W, the systems with the second largest contribution to light in this range, a factor between 3 - 20 higher than in the control spirals. This seems to indicate there exists young star formation in the PSQSOs, just not so young as for the LIRGs.*

On the contrary, stellar populations above 300 Myr start to be important mass contributors. In the intermediate age range from 300 Myr to 1.5 Gyr, we find that in comparison with the control spirals the pre-merger LIRGs present diminished intermediate age contributions to mass by a factor ~ 4 on average. A possible explanation could be that the progenitors of our pre-merger LIRG were purer disks than those in Sbc / Sc galaxies, and therefore, the intermediate age mass has still not formed. In NGC 2623 the intermediate age contribution to mass is enhanced with respect to control spirals by a factor 2, while for the PSQSOs is also enhanced by a factor from 2 - 3 depending on the model base.

In the oldest age range, from 1.5 Gyr to 3 Gyr, we find similar results for the LIRGs, that is, in comparison with the control spirals the pre-merger LIRGs present intermediate-old contributions to mass that are similar or lower. In NGC 2623 the intermediate-old SSPs contribution to mass is similar or only slightly enhanced with respect to the control spirals by 1.1 - 1.5. However, the biggest difference between both bases is seen in the PSQSOs results in this age range, while with GM there is no star formation in this age range, with CB base there is, and is enhanced in terms of mass with respect to control spirals by a factor 2.5.

In NGC 2623, the contribution to mass of SSPs from 300 Myr to 1.5 Gyr is enhanced with respect to control spirals by a factor 2, while for the PSQSOs it is also enhanced by a factor from 2 - 3 depending on the model base. The PSQSOs SFHs, both in terms of light and mass, are similar to NGC 2623 ones. Attending to the average ages with CB base, we found that NGC 2623 is ~ 400 Myr, while the PSQSOs are ~ 800 Myr (both considering or not the pre-merger ones). It seems that PSQSOs are slightly more evolved, however, given the uncertainties related to the model base choice, we can not confirm to what degree.

Therefore, the conclusion we draw is that the history of formation of PSQSOs is similar to the LIRG merger NGC 2623. Both present a significant contribution to mass of SSPs younger than 1.5 Gyr, which is not present in the pre-merger LIRGs. However, we think that the current starburst seen in the pre-mergers is in fact forming the intermediate age mass that will look like NGC 2623 in $\lesssim 1.5$ Gyr. The stellar mass in stellar populations younger than 1.5 Gyr is $\sim 6.6 \times 10^9 M_{\odot}$ (Chabrier IMF) in NGC 2623 and $\sim 10^{10} M_{\odot}$ (Chabrier IMF) in the PSQSOs, we find that if the pre-merger LIRGs keep forming stars at the current rate $\sim 16 M_{\odot} \text{ yr}^{-1}$ (Chabrier IMF, see Section 5.7) during $\sim 400 - 600$ Myr, then they can account for the mass in NGC 2623 and PSQSOs. This time is approximately consistent with the 500 Myr upper limit expected for the duration of merger triggered starbursts from simulations (Di Matteo et al., 2008). Moreover, we also note that the transformation of NGC 2623 into a PSQSO should be rapid. On the one hand, it is known that NGC 2623 harbors an AGN in its dusty core (though energetically weak relative to the starburst population) given presence of the $14.3 \mu\text{m}$ [Ne V] emission line only observed in galaxies hosting AGN (Evans et al., 2008). On the other hand, we also know that the central starburst in NGC 2623 is already powering a galactic wind (Lípari et al., 2004). Recently, Herschel discovered massive molecular outflows in U/LIRGs. Although the fastest and most massive outflows are found in AGN-dominated U/LIRGs, from the three starburst dominated systems in Sturm et al. (2011) sample, they found that they are able to expel the cold gas reservoirs from the center within $\sim 2 \times 10^8$ yr. Hence, in few 100 Myr outflows like the ones in those U/LIRGs would be



Figure 8.10 Evolutionary sequence expected according to the results from our systems.

able to remove dust from the core leaving the AGN uncovered. This is consistent with the average time delay of ~ 400 Myr found by us between NGC 2623 and the PSQSOs.

8.3.1. Global evolutionary picture

With our data we find an evolutionary sequence related to the merger progression. In the initial stages the merger-induced SF is extended, while in more advanced stages it is more concentrated in the central region, in agreement with predictions from recent merger simulations Teyssier et al. (2010). The ionization conditions also change, with pre-mergers being purely dominated by star formation and shocks due to outflows being also important in more advanced mergers. If an AGN is simultaneously growing in the center, and outflows are able to remove the gas and dust in the central regions, in ~ 400 Myr, NGC 2623 could convert into a PSQSO.

Given the stellar masses measured in the LIRGs and in the PSQSOs, most of them $\lesssim 10^{11} M_{\odot}$, we propose an evolutionary sequence as shown in Figure 8.10, where they are supposed to form intermediate mass ellipticals ($\sim 10^{11} M_{\odot}$), or the core of future giant ellipticals. This is in agreement with the major-merger evolutionary scenario described in detail in Section 1.3.3.

However, these LIRGs and PSQSOs are not in agreement with the formation of the most massive ellipticals (with $M_* > 10^{11} M_{\odot}$), some of them in the CALIFA survey. In that cases the formation scenario is more probably consistent with two phases in which the "core" formed first at $z > 1$ and then further growth in mass occurs through dry mergers (see Section 1.3.2).

We hypothesize that current major-merger ellipticals in formation with $\lesssim 10^{11} M_{\odot}$, are analogous to the "cores" of the massive ellipticals that formed at $z > 1$. We can not be sure if more massive mergers, maybe those in local ULIRGs instead of LIRGs, would be able to form more massive ellipticals. In anycase, it seems that minor merging is necessary to grow ellipticals with masses well above $10^{11} M_{\odot}$, according to recent observations and cosmological simulations (Naab et al., 2009; Kormendy et al., 2009; Oser et al., 2012; Toft et al., 2014).

Conclusions

Major gas-rich mergers as those seen in U/LIRGs are thought to be responsible of a dramatic evolution of galaxies. [Sanders et al. \(1988\)](#) was the first to propose a change in the ionizing mechanism along the merger sequence from dusty starbursts in the initial stages (U/LIRGs) to unobscured QSO activity in the final ones. While it is quite clear that mergers lead to massive starburst activity, sometimes hidden by dust, and therefore, U/LIRGs ([Surace et al., 1998, 2000](#); [Veilleux et al., 2002](#); [Kim et al., 2013](#)), it is not so clear if the QSOs activity is merger-triggered and if so, when exactly during the merger it starts. Interestingly, [Brotherton et al. \(1999\)](#) identify a possible evolutionary link in the sequence, the PSQSOs. These systems show morphological disturbance typical of a past or present merger, and host bright nuclear QSOs together with a post-starburst population relic of the intense starburst activity triggered in the past, both having similar bolometric luminosities. Hence, they are ideal laboratories to study connections between the starburst and AGN phenomenon.

In this thesis we have characterized and compared the star formation histories, average stellar population properties, and ionized gas properties in two small samples of galaxies in different stages across the merger sequence, three LIRGs (the two pre-mergers IC 1623 and NGC 6090, and the merger NGC 2623) and nine PSQSOs, by analysing high quality Integral Field Spectroscopy (IFS) data in the rest-frame optical range 3700 - 7000 Å, and high resolution HST imaging. Additionally, the results from the LIRGs and PSQSOs have been compared with control Sbc and Sc galaxies from CALIFA (GD2015) in the same mass range. The methodology applied has been the same for all, a full spectral fitting analysis was performed using the *Starlight* code and a combination of SSP spectra from [González Delgado et al. \(2005\)](#), [Vazdekis et al. \(2010\)](#), or Charlot & Bruzual (2007, unpublished). The results are shown in spatially resolved maps of the stellar population properties and also in radial profiles (in units of kpc, or in HLR for comparison).

9.1. Pre-merger LIRGs IC 1623 and NGC 6090

IC 1623 and NGC 6090 are two pre-merger LIRGs in stage III of the interaction. The projected separation between the progenitors nuclei is approximately 6 kpc and 3.2 kpc, respectively. For IC 1623, only the western component is covered by our IFS, while IC 1623 E is almost totally obscured in the optical. However, we have roughly estimated its stellar population properties through the analysis

of the star cluster multiwavelength photometry. For NGC 6090, the main body is covered by our IFS, including both progenitors nuclei. The main results are:

- In IC 1623 W we determine a total current stellar mass of $3.9 \times 10^{10} M_{\odot}$ ($1.45 \times 10^{10} M_{\odot}$) with Salpeter (Chabrier) IMF. In NGC 6090 we find a total stellar mass of $6.8 \times 10^{10} M_{\odot}$ ($3.2 \times 10^{10} M_{\odot}$) with Salpeter (Chabrier) IMF. In both cases, most of the mass $\gtrsim 90\%$ is in stellar populations older than 1.4 Gyr. In the pre-merger LIRGs the intermediate age stellar populations ($140 \text{ Myr} < \text{SSPs} < 1.4 \text{ Gyr}$) contribute to less than 8% to the stellar mass.
- The mass in populations younger than 140 Myr represents only 4 - 5% of the total current stellar mass in IC 1623 W, and 1% in the case of NGC 6090. In the case of IC 1623 W the mass in young components derived through the IFS is comparable (only a factor ~ 1.3 less) to the mass in star clusters derived roughly from the photometry, which is $M_{clus}^{IC1623W} \sim 9 \times 10^8 M_{\odot}$. This would agree with the idea that the vast majority of stars form in clusters rather than in isolation. However, in NGC 6090, the mass in star clusters, $M_{clus}^{NGC6090} \sim 2 \times 10^9 M_{\odot}$, is a factor ~ 4 higher than the mass in YSP, probably due to the uncertainties in the determination of cluster ages through photometry.
- At ~ 1 HLR we find that IC 1623 W and NGC 6090 NE are 0.5 dex (0.8 dex), 0.6 dex (0.9 dex) more dense in stellar mass, respectively, than the Sbc (Sc) galaxies. In the nucleus, we find that the central mass surface densities of IC 1623 W, NGC 6090 NE are similar to the central density of Sbc galaxies, while the central mass surface density of NGC 6090 SW is more similar to Sc galaxies. For the pre-merger LIRGs we find that the radial profiles are flatter than in control spirals. In the inner 1 HLR, the variations $\log \mu_{\star}$ are -0.8 dex for IC 1623 W and -0.6 dex for NGC 6090 NE, in contrast with the steeper -1.2 dex in Sbc galaxies and -1.0 dex in Sc galaxies. If our LIRGs were originally isolated spirals, the flattening of the mass density profiles in the pre-merger stages is probably due to the mass redistribution / formation during the merger. The proximity of the central regions of the two progenitor galaxies, together with the accumulation of mass toward the dynamical center lead to an increase in the mass density in a more extended region.
- IC 1623 W and NGC 6090 NE have average light weighted ages at ~ 1 HLR of 50 Myr and 80 Myr, respectively, much younger in comparison with the 1.2 Gyr (700 Myr) old of Sbc (Sc) control galaxies. This is also true in the nuclear region (in the inner 0.2 HLR) where IC 1623 W and NGC 6090 NE have 330 Myr and 90 Myr, respectively, with respect to the 3.6 Gyr (1.4 Gyr) of Sbc (Sc) control galaxies. Moreover, in both pre-merger LIRGs the age profiles are significantly flatter than in Sbc/Sc galaxies. It seems like the merger-induced star formation leads to a general rejuvenation of the progenitor galaxies during the pre-merger stage.
- From the SFHs we find that in the two pre-merger LIRGs the contribution to light of star formation in the last 32 Myr is enhanced with respect to the control spirals both in the central regions (in the inner 0.5 HLR) and in the outskirts (from 1 - 1.5 HLR). In IC 1623 W it is a factor 2 higher than Sbc/Sc in the center and 4 times higher in the outskirts, while in NGC 6090 NE it is a factor 6 higher in the center and 3 times higher in the outskirts. This result is also valid when considering the contribution to light of SSPs < 300 Myr. The star formation in

this timescale in IC 1623 W is a factor 4 higher than Sbc/Sc in the center and 3 times higher in the outskirts, while in NGC 6090 NE it is a factor 5 higher in the center and 2 times higher in the outskirts.

- To consistently compare the relative star formation in the center and in the outer region, we have derived the specific SFRs in several timescales (32 Myr, 300 Myr, and 1.5 Gyr), normalizing by the stellar mass surface density profile:
 1. The specific star formation in the last 32 Myr in IC 1623 W is enhanced with respect to the average of control spirals by a factor 7 both at the center and in the disk. In NGC 6090 NE, the enhancement is higher in the central region (by a factor 9), still significant at one half light radius (by a factor 5), and less significant in the "disk" (only enhanced by a factor 1.5).
 2. When considering the specific star formation in the last 300 Myr, only IC 1623 W keeps presenting a significant enhancement of the sSFR(300 Myr) by a factor 7 in the nucleus and ~ 1.7 in the disk. In NGC 6090 NE, the sSFR(300 Myr) is comparable to the control spirals in the center and slightly smaller in the disk.
 3. Considering a longer timescale of 1.5 Gyr, we find that in the central regions of the pre-mergers the star formation is comparable to control spirals (within a factor 2). However, in the outer regions it is a factor 4 - 6 lower, as if the star formation has been inhibited in this time period. This could suggest that the disks of the pre-mergers progenitor galaxies formed a long time ago, being somehow more primordial than the disks in today spirals.

These results suggest that merger induced SF in these LIRGs started a few 100 Myr ago in IC 1623 W and a few 10 Myr ago in NGC 6090 NE.

- Metallicity in one of the most difficult quantities to constrain. The scatter is really huge and the fact that ages and Z grow in the opposite sense, as happens in IC 1623 W, could suggest that the results are affected somehow by the age-metallicity degeneracy. Taking the results with caution we find that the average mass weighted metallicity of the 2 pre-mergers at ~ 1 HLR is $\langle \log Z_{\star} \rangle_M \sim -0.16$ ($\sim 0.7 Z_{\odot}$) similar to the one measured in Sbc galaxies, $\langle \log Z_{\star} \rangle_M \sim -0.21$ ($\sim 0.6 Z_{\odot}$). Although we found a huge scatter in the metallicity profiles, in general terms, they are comparatively flat or even slightly positive in contrast to Sbc and Sc galaxies. We find that beyond 0.7 HLR in IC 1623 W the metallicities are similar to those of Sbc galaxies, but in the central regions (in the inner 0.5 HLR) the metallicities are smaller, more similar to Sc galaxies. Flat gradients were previously found in the gas metallicity of mergers due to the effect of large gas inflows (Kewley et al., 2010; Rupke et al., 2010; Rich et al., 2012). Therefore, merger-induced gas inflows could also be the explanation for the inverted/flat stellar metallicities.
- With respect to the dust distribution we find that in both pre-mergers one of the progenitors is remarkably more extinguished than the other. From star clusters photometry we find that IC 1623 E could be affected by more than $A_V \gtrsim 2$ mag (and in extreme cases up to 6 mag), in contrast with the almost no obscured IC 1623 W. In NGC 6090 the contrast between the progenitors is not so severe, still NGC 6090 NE is 0.8 - 1.0 mag more extinguished than the SW component.

- From the IFS, we found that at 1 HLR, IC 1623 W is extinguished by $A_V = 0.2$ mag, which is 0.1 mag less extinguished than Sbc/Sc galaxies. It is worth mentioning that IC 1623 W is considered the nearest local Lyman Break Galaxy Analog (Grimes et al., 2006). On the contrary, NGC 6090 NE has $A_V = 1.3$ mag, which is 1 mag more extinguished than the control spirals. With respect to the gradients, we find that the radial profiles of the pre-merger LIRGs in the inner 1 HLR are flat in comparison with control spirals. We hypothesize that if our LIRGs were originally spirals, then the merger process redistribute the gas and dust of these spirals in a way that most of it moves to the center of one of the progenitors (probably the most massive one), as happens in IC 1623 and NGC 6090.
- With respect to the ionization mechanism, from the $[\text{NII}]\lambda 6583/\text{H}\alpha$ vs $[\text{OIII}]\lambda 5007/\text{H}\beta$ diagnostic diagram we find that both IC 1623 W and NGC 6090 are dominated by star formation in the region mapped by us. There are also some spaxels with composite ionization. Given the proximity of the vast majority of the composite spaxels to the Kauffmann demarcation line, we do not believe that the ionization source is different for them, and is therefore quite possible that they are also star forming regions.

However, for a few spaxels we can not discard a truly composite photoionization which we believe it should be due to ISM shocks that would occur naturally as a result of the increase of the supersonic turbulence in mergers (Bournaud et al., 2010) or also possibly to stellar winds and outflows from star forming regions (Heckman et al., 1990).

- A few spaxels at the edges of IC 1623 W line ratio maps are consistent with starburst-related LINER ionization. Moreover, from the $\text{H}\alpha$ velocity dispersion map we find $\sigma_{\text{H}\alpha} > 140$ km/s in several outermost spaxels, with a region to the north west of the nucleus where $\sigma_{\text{H}\alpha}$ reaches up to 170 km/s. We interpret this result as a consequence of shocks being more important in the outskirts, producing a broadening of the emission lines. This is in agreement with Rich et al. (2011), who found widespread shocks in the outskirts of IC 1623, beyond the region traced by us.
- In a few spaxels to the south of NGC 6090 SW component we find a $[\text{OI}]\lambda 5007/\text{H}\alpha$ line ratios consistent with starburst-related LINER ionization and enhanced $[\text{OIII}]\lambda 5007/\text{H}\beta$ ratios. Interestingly, the highest values of the velocity dispersion map ($\sigma_{\text{H}\alpha} > 200$ km/s) are also reached to the south of the SW component. We believe that this could be due to the presence of shocks induced by the interaction itself, although there also exists the possibility that we are simultaneously observing several gas components moving at different velocities as a consequence of the interaction.
- We do not have clear evidences of outflows in neither of the two galaxies. In the non-rotating face on spiral NGC 6090 NE, the only spaxels approaching to us in the $\text{H}\alpha$ velocity field are the ones located to the north of the nucleus. We hypothesize that there could be an outflow, however, we can not resolve it with our spectral resolution. We note, however, the velocity dispersion is relatively low in this region ($\sigma_{\text{H}\alpha} \sim 140$ km/s).
- The SFRs calculated from both the very young stellar populations (SSPs < 30 Myr) and $\text{H}\alpha$ are in very good agreement, with average values of $14 \pm 1 M_{\odot} \text{ yr}^{-1}$ for IC 1623 W and $20 \pm 3 M_{\odot}$

yr^{-1} for NGC 6090 (with Chabrier IMF). Analogously, the SFRs calculated from populations younger than 140 Myr and FUV also agree, with an average of $\text{SFR} = 5 \pm 1 \text{ M}_{\odot} \text{ yr}^{-1}$ for both systems (Chabrier IMF), and a factor 3 - 4 smaller than the one from very young components and $\text{H}\alpha$, indicating that recent SFR is more concentrated in instantaneous bursts occurred in the last few 10 Myr rather than as a continuum SFR.

- From MIR at $24\mu\text{m}$ we found hybrid $\text{SFR} = 15 \text{ M}_{\odot} \text{ yr}^{-1}$ and $17 \text{ M}_{\odot} \text{ yr}^{-1}$ for IC 1623 W and NGC 6090, respectively (Chabrier IMF). They are very similar to the ones derived from dust-attenuation corrected $\text{H}\alpha$ and $\text{SFR}(30 \text{ Myr})$. We can conclude that for IC 1623 W and NGC 6090 there is no substantial star formation which is not accounted for by the Balmer decrement attenuation correction.
- We find that the average SFR in our two pre-merger LIRGs is enhanced by a factor 8 - 9 with respect to the Milky Way ($\langle \text{SFR} \rangle_{\text{MW}} = 1.9 \pm 0.4 \text{ M}_{\odot} \text{ yr}^{-1}$, Chomiuk & Povich 2011).
- We find an average value of the star formation rate density measured from the stellar continuum emitted by stellar populations $< 30 \text{ Myr}$ and $\text{H}\alpha$ of $\sim 500 \text{ M}_{\odot} \text{ Gyr}^{-1} \text{ pc}^{-2}$ for both IC 1623 W and NGC 6090 NE. Compared with the $\langle \Sigma_{\text{SFR}} \rangle = 3.3 \text{ M}_{\odot} \text{ Gyr}^{-1} \text{ pc}^{-2}$ of the Milky Way (Kennicutt & Evans, 2012), the star formation rate density of our pre-merger LIRGs is ~ 150 times higher than in it.

9.2. Merger LIRG NGC 2623

NGC 2623 is a merger LIRG in stage IV of the interaction. The nuclei have already coalesced and two tidal tails are still visible. Except the outer parts of the tails, the main body of NGC 2623 is covered by our IFS. The main results are:

- In NGC 2623 we determine a total current stellar mass of $4.6 \times 10^{10} \text{ M}_{\odot}$ ($2.4 \times 10^{10} \text{ M}_{\odot}$) with Salpeter (Chabrier) IMF. 70 - 75 % of the stellar mass is in stellar populations older than 1.4 Gyr. The intermediate age stellar populations ($140 \text{ Myr} < \text{SSPs} < 1.4 \text{ Gyr}$) are important in NGC 2623, contributing by 23 - 28 % to the total the stellar mass.
- The mass in populations younger than 140 Myr represents only 1 - 2 % of the total current stellar mass in NGC 2623. The mass in young components derived through the IFS is comparable (only a factor ~ 1.5 less) to the mass in star clusters derived roughly from the photometry, which is $M_{\text{clus}}^{\text{NGC}2623} \sim 6 \times 10^8 \text{ M}_{\odot}$. This would agree with the hypothesis that the vast majority of stars form in clusters rather than in isolation.
- The mass surface density of NGC 2623 is very similar to the one measured in Sbc galaxies both in the nucleus and at 1 HLR. Therefore, the gradient in the inner 1 HLR of NGC 2623, -1.3 dex, is very similar to Sbc galaxies. According to this, when the progenitor galaxies finally merge most of the mass collapses in a small central region recovering the negative profile of the mass density with distance. We note, however, that if the final product of LIRGs mergers are elliptical galaxies, then NGC 2623 should be 0.7 dex more massive in order to resemble the profile of E galaxies in CALIFA (GD2015) instead of Sbc galaxies. This result would indicate

that mergers such as NGC 2623 would not form massive ellipticals, but low-intermediate mass elliptical systems.

- The average light weighted age of NGC 2623 at ~ 1 HLR is 540 Myr, younger than Sbc (Sc) galaxies which are 1.2 Gyr (700 Myr) old. The contrast is much higher in the nuclear region (in the inner 0.2 HLR) where NGC 2623 has 250 Myr old, with respect to the 3.6 Gyr (1.4 Gyr) of Sbc (Sc) control galaxies. For the merger LIRG NGC 2623 the gradient with distance is positive, inverted with respect to what happens in Sbc/Sc galaxies. The variation within the inner 1 HLR is 300 Myr, in comparison with the -2.4 Gyr (-665 Myr) of Sbc (Sc) galaxies. The positive age gradient in NGC 2623 would be explained if in advanced mergers most of the gas and the young star formation is concentrated in the central region (in the inner 1 HLR), while the outer parts start to evolve passively.
- For the merger NGC 2623, the contribution to light of the young star formation in the last 32 Myr or 300 Myr, is only significantly enhanced with respect to Sbc (Sc) galaxies in the central region by a factor of ~ 6 (3), while in the outskirts it is comparable.
- To consistently compare the relative star formation in the center and in the outer regions, we have derived the specific SFRs in several timescales (32 Myr, 300 Myr and 1.5 Gyr), normalizing by the stellar mass surface density profile:
 1. The specific SFRs in the last 32 Myr is significantly enhanced in the central region of NGC 2623 (by a factor ~ 9), while at the outer parts it is only slightly enhanced (by a factor ~ 3) in comparison to the control spirals.
 2. Although the sSFR in the last 300 Myr is only enhanced in the center (by a factor ~ 2) with respect to control spirals, the sSFR in the last 1.5 Gyr is enhanced by a factor 1.7 with respect to control spirals in the center and in the outer parts. This is in agreement with the fact that NGC 2623 has formed 2 times more mass than the control spirals in the last 1.5 Gyr, both in the central and the outer regions.
- The average mass weighted metallicity of NGC 2623 at ~ 1 HLR is $\langle \log Z_{\star} \rangle_M \sim -0.37$ ($\sim 0.4 Z_{\odot}$) similar to the one measured in Sc galaxies, $\langle \log Z_{\star} \rangle_M \sim -0.45$ ($\sim 0.4 Z_{\odot}$). As for the pre-mergers, metallicity is one of the most difficult properties to characterize through spectral synthesis in these kind of systems. We find that beyond 1.4 HLR the metallicity of NGC 2623 is similar to those of Sbc galaxies, but in the inner 0.5 HLR it is smaller, more similar to Sc galaxies. As for the pre-merger LIRGs, merger-induced gas inflows could be the explanation for the inverted/flat stellar metallicities. Flat gradients were previously found in the gas metallicity of mergers due to the effect of large gas inflows (Rupke et al., 2010; Kewley et al., 2010).
- From the IFS, we found that at 1 HLR, NGC 2623 is extinguished by $A_V = 0.7$ mag, which is 0.4 mag more extinguished than Sbc/Sc galaxies. The contrast is higher in the inner 0.2 HLR, where NGC 2623 is affected by $A_V = 1.6$ mag, approximately 1.1 mag more extinguished than Sbc/Sc galaxies. In the inner 1 HLR there exists a negative A_V gradient which is much steeper in NGC 2623 (-1 mag) than in Sbc/Sc galaxies (-0.3 mag). This is consistent with the idea that in mergers with coalesced nuclei most of the dust content is already concentrated in the central regions.

- With respect to the ionization mechanism, we find that only the gas in the north tidal tail and the brightest knot south of the nucleus are ionized by pure star formation. On the other hand, there is LINER ionization in the nuclear region of NGC 2623, consistent with the existence of an outflow as previously reported by [Lípari et al. \(2004\)](#). Further evidence of the outflow come from the high values of the gas velocity dispersion, $\sigma \sim 220$ km/s, that are coincident with the LINER spaxels in the BPT diagram, which are, in turn, approximately inside the outflow cone nebulae defined by [Lípari et al. \(2004\)](#). With our spectral resolution we can not conduct a thorough characterization of the outflow. We note, however, that no pure LINER emission is present in the nucleus of the pre-merger systems IC 1623 W and NGC 6090. We hypothesized that to produce a significant nuclear outflow it is necessary to have a very massive and compact starburst, like the ones produced in the central regions of galaxies in the last stages of the interaction, where a large amount of gas is concentrated into a small area.
- We have estimated the amount of current star formation which is necessary to power the outflow from the luminosity of the shocked regions. We find the total $H\alpha$ luminosity of the shocks $L_{H\alpha}^{shock} = 2.5 \times 10^{41}$ erg s⁻¹, leading to a bolometric energy loss rate of $\dot{E}_{shock} \sim 2.0 \times 10^{43}$ erg s⁻¹, where we have taken a bolometric conversion factor of 80, assuming that $v_{shock} \geq 140$ km s⁻¹ ([Rich et al., 2010](#)). The mechanical energy injection rate into the ISM by SNe can be estimated from evolutionary synthesis models of populations of massive stars ([Leitherer et al., 1999](#)). For Salpeter IMF, in the 0.4 Z_{\odot} case, and assuming a continuous SFR in the last 40 Myr, the expected SFR would be $\sim 24 M_{\odot} \text{ yr}^{-1}$, very similar to the observational one obtained from multiwavelength data.
- We find a strong consistency in the SFR derived with three hybrid tracers combining the observed $H\alpha$ together with $24\mu\text{m}$, FIR and radio 1.4 GHz. All point to a global average SFR $\sim 17 M_{\odot} \text{ yr}^{-1}$ (with Salpeter IMF) and SFR $\sim 10 M_{\odot} \text{ yr}^{-1}$ (with Chabrier IMF). The hybrid multi- λ SFR is similar to the one derived from continuum decomposition, SFR(30 Myr), and an order of magnitude larger than the SFR derived with $H\alpha$ dereddened luminosity ($< 2.2 M_{\odot} \text{ yr}^{-1}$, Salpeter IMF). As the hybrid multi- λ SFRs account for optically thick dust obscuration by direct detection of the thermal dust emission, we find that some of the ionizing photons have been absorbed by dust and reemitted in the IR/radio instead of ionizing the $H\alpha$ emitting gas. Taking this into account, we found that the average $A(H\alpha) \sim 4.3$ mag, instead of the ~ 1.4 mag we measure with the IFS.
- The average SFR in NGC 2623 is comparable to the pre-merger LIRGs, and a factor 5 higher than the SFR in the Milky Way ($\langle SFR \rangle_{MW} = 1.9 \pm 0.4 M_{\odot} \text{ yr}^{-1}$, [Chomiuk & Povich 2011](#)).
- In the advanced merger NGC 2623 we found that the SF has evolved from outside to inside. In the shortest timescale considered (30 Myr) the SF is concentrated toward the center, while in the longest timescale (1.4 Gyr) it is more spatially extended, with the SFR in these regions being significantly enhanced with respect to the average past or actual SFR in the galaxy. This is in agreement with recent merger simulations which find that the first merger induced SF episode is spatially extended ([Teyssier et al., 2010](#)), while the second burst later on during coalescence is more centrally concentrated, as predicted by classical merger simulations ([Mihos & Hernquist, 1996](#); [Di Matteo et al., 2008](#)).

9.3. PSQSOs

Our PSQSO sample is quite heterogeneous, comprising 9 systems with different morphologies and in different evolutionary stages. Given the low SNR of their IFS, we have analysed the stellar population properties in integrated and central spectra. The integrated spectra have been extracted in variable apertures (all of them above the Petrosian radius given by SDSS DR7), in a way that they include the whole optical extension of each PSQSOs in ACS F606W image. The companion galaxies (when present) have not been included. The spectra of the central regions have been extracted using an aperture radius of 1.5 arcsec, identical to the fiber aperture radius of SDSS spectroscopy, with which we have compared. For the comparison with the LIRGs we have used the central spectra of the PSQSOs. At their redshift ($z \sim 0.3$; $D_L \sim 1553.4$ Mpc) the spatial scale is 4.46 kpc/arcsec. Therefore, the central spectra aperture radius correspond to ~ 6.7 kpc, similar to a 2 HLR aperture in our three LIRGs. The main results:

- The stellar masses derived from the integrated spectra of the PSQSOs range from $1.9 \times 10^{10} M_\odot$ - $1.4 \times 10^{11} M_\odot$ (Chabrier), and the mean stellar ages from 220 Myr - 3 Gyr. In general, the stellar extinctions are low, < 1 mag.
- In 8 out of 9 PSQSOs (all except J1700) we find important light contributions of intermediate-age stellar populations (< 1.5 Gyr), ranging from 30 % - 77 %. The stellar mass in intermediate age stellar populations range from $3.2 \times 10^8 M_\odot$ - $3.1 \times 10^{10} M_\odot$ (Chabrier IMF). With an average of $\sim 1 \times 10^{10} M_\odot$, it represents 27 % of the total stellar mass formed in these systems.
- The contribution to light (at 5100 Å) of the AGN ranges from 16 % - 43 %. We find that the central black holes have masses from $3.5 \times 10^7 M_\odot$ - $1.5 \times 10^8 M_\odot$, and are low-accretion rate AGN accreting at $\lesssim 1\%$ - 6 % of Eddington luminosity.
- When plotted on the traditional BPT diagram, 7 out of the 9 PSQSOs fall in the Seyfert region. The other 2 systems, J0237 and J1230, fall in the composite region, confirming the results from the spectral synthesis, which indicate that recent star formation (SSPs < 140 Myr) is also quite important in some PSQSOs (at least in J0237, J1230 and J1456).
- We find evidence of a decline in the AGN luminosity with increasing stellar ages, as expected by merger-induced evolutionary scenarios. This would indicate that the gas from which the stars formed also fed the AGN. The younger the stellar age of a system the higher the contribution from recently formed young components. That requires significant gas income to the central region, part of which could also be accreted by the AGN. A larger sample is necessary to confirm this result.
- We also find an increase of the stellar mass in intermediate age SSPs < 1.5 Gyr with increasing [OIII] λ 5007 line luminosity. If we assume that the [OIII] λ 5007 luminosity is tracing the intrinsic AGN luminosity (LaMassa et al., 2010), this correlation suggests that the more massive the central starburst the brighter the AGN. This could also indicate that both starburst and AGN are simultaneously growing from the same gas supply, which in principle is in agreement with merger induced evolutionary scenarios. However, we note that we do not find this correlation

when using directly the AGN luminosity and additional observations are also necessary to further test this hypothesis.

9.4. Global evolutionary picture

With our data we find an evolutionary sequence related to the merger progression. In the initial stages (pre-mergers) the induced SF in the last 32 Myr is extended (in agreement with recent merger simulations by [Teyssier et al. 2010](#)), and enhanced, on average, by a factor ~ 4 with respect to the control spirals. When we resolve it spatially, we find that for IC 1623 W the enhancement is the same in the central region and in the disk (by a factor 7), while for NGC 6090 NE the enhancement is higher in the central region (by a factor 9), still significant at one half light radius (by a factor 5) and less significant in the "disk" (only enhanced by a factor 1.5). Attending to the importance of stellar populations ~ 300 Myr, we find that the merger-induced star formation started earlier in IC 1623 W than in NGC 6090 NE.

In more advanced mergers, as NGC 2623, we find that most of the young SF (in the last 32 Myr) is concentrated in the central region, enhanced by a factor 9 with respect to control spirals. However, there exists also low level star formation in the disk, enhanced by $\lesssim 3$ in comparison to spirals. From the global average across the whole galaxy we find a factor ~ 3 higher than in spirals. In addition, in NGC 2623 we detect fossil emission of an extended merger-induced burst occurred ~ 1.5 Gyr ago, probably when it was at the pre-merger stage. The mass formed during this first burst is enhanced by a factor 2, both in the center and in the outer parts, with respect to the mass formed in the same period in isolated spirals.

From the average of the nine PSQSOs we find that, both in terms of light and mass, the SFH is comparable to NGC 2623. Attending to the average age, we found that PSQSOs are ~ 400 Myr older than NGC 2623. It seems that they are slightly more evolved, however, given the uncertainties related to the model base choice, and the heterogeneity of the sample, we can not confirm exactly to what degree. We note that both present a significant contribution to mass of stellar populations younger than 1.5 Gyr, which is not present in the pre-merger LIRGs. However, we think that the current starburst seen in the pre-mergers is in fact forming the intermediate age mass that will look like NGC 2623 in $\lesssim 1.5$ Gyr. The stellar mass in stellar populations younger than 1.5 Gyr is $\sim 6.6 \times 10^9 M_{\odot}$ (Chabrier IMF) in NGC 2623 and $\sim 10^{10} M_{\odot}$ (Chabrier IMF) in the PSQSOs, hence, we find that if the pre-merger LIRGs keep forming stars at the current rate $\sim 16 M_{\odot} \text{ yr}^{-1}$ (Chabrier IMF) during $\sim 400 - 600$ Myr, then they can account for the mass in NGC 2623 and PSQSOs. This time is approximately consistent with the 500 Myr upper limit expected for the duration of merger triggered starbursts from simulations ([Di Matteo et al., 2008](#)). Moreover, we also note that the transformation of NGC 2623 into a PSQSO should be rapid. On the one hand, it is known that NGC 2623 harbors an AGN in its dusty core (though energetically weak relative to the starburst population) given the presence of the $14.3 \mu\text{m}$ [Ne V] emission line only observed in galaxies hosting AGN ([Evans et al., 2008](#)). On the other hand, we also know that the central starburst in NGC 2623 is already powering a galactic wind ([Lípari et al., 2004](#)). Recently, Herschel discovered massive molecular outflows in U/LIRGs. Although the fastest and most massive outflows are found in AGN-dominated U/LIRGs, from the three starburst dominated systems in [Sturm et al. \(2011\)](#) sample, they found that they are able to expel the cold gas reservoirs from the center within $\sim 2 \times 10^8$ yr. Hence, in few 100 Myr

outflows like the ones in those U/LIRGs would be able to remove dust from the core leaving the AGN uncovered. This is consistent with the average time delay of ~ 400 Myr found by us between NGC 2623 and the PSQSOs.

Finally, given the stellar masses measured in the LIRGs and in the PSQSOs, most of them $\lesssim 10^{11} M_{\odot}$, we find that they can only form intermediate mass ellipticals ($\sim 10^{11} M_{\odot}$), or the core of future massive ellipticals, in agreement with the major-merger evolutionary scenario. They are not in agreement with the formation of the most massive ellipticals (with $M_{\star} > 10^{11} M_{\odot}$) which have been observed by the CALIFA survey. In those cases the formation scenario is more probably consistent with two phases in which the "core" formed first at $z > 1$ and then further growth in mass occurs through dry mergers.

We hypothesize that current major-merger ellipticals in formation with $\lesssim 10^{11} M_{\odot}$, are analogous to the "cores" of the massive ellipticals that formed at $z > 1$. We can not be sure if more massive mergers, maybe those in local ULIRGs instead of LIRGs, would be able to form more massive ellipticals. In anycase, it seems that minor merging is necessary to grow ellipticals with masses well above $10^{11} M_{\odot}$, according to recent observations and cosmological simulations (Naab et al., 2009; Kormendy et al., 2009; Oser et al., 2012; Toft et al., 2014).

A

PSQSOs: Spectral synthesis results

The main results from the 9 different spectral fits are summarized in Tables A.1, A.2 and A.3 for IFS central, integrated and SDSS spectra, respectively. For each galaxy we report: (a) the χ^2 of the fitting, (b) the deviation (in percentage) from the best model fit to the observed spectra expressed as Δ , (c) the average age in logarithm, (d) the stellar mass in logarithm, (e) the percentage of contribution to light of the SSPs younger than 140 Myr, (f) the percentage of contribution to light of the SSPs younger than 1.5 Gyr, (g) the stellar mass contained in SSPs younger than 1.5 Gyr, (h) the stellar luminosity in logarithm calculated by integrating the stellar component from 3000 - 6000Å, (i) the stellar dust extinction in magnitudes, (j) the AGN dust extinction in magnitudes, (k) the contribution to light of the AGN in percentage, (l) the AGN luminosity in logarithm calculated by integrating the power-law component from 3000 - 6000Å, (m) the H β or H α flux expected from the stellar component in units of 10^{-17} erg s $^{-1}$ cm $^{-2}$, (n) the H β or H α flux expected from the AGN component in units of 10^{-17} erg s $^{-1}$ cm $^{-2}$.

We want to note that for integrated spectra we are only interested in the stellar properties, since the AGN properties from IFS data, will be derived from the central spectra. That is why in Table A.2 we only report results from (a) to (i).

In addition, Figures A.1, A.2 and A.3 present the spectral fits for the base with SSPs > 4 Myr for central IFS, SDSS and integrated spectra, respectively. These are the fits using H β (H α for SDSS) as constrain and a single extinction value for stars and AGN. In the upper panels we show the observed spectra (in black) and the best *Starlight* fit (in red). The stellar component contribution is shown in blue and the AGN contribution in orange. In the bottom panels we show the residuals in red.

Moreover, Figures A.4 and A.5 show the star formation histories of the PSQSOs for IFS central spectra for the constrained and unconstrained fits, respectively. In colors, we show the SFH obtained with the different bases: in red the base including only SSPs > 30 Myr, in green the base including only SSPs > 4 Myr and in blue the base including all the SSPs down to 1 Myr. Analogously, in Figures A.6 and A.7 we show the star formation histories of the PSQSOs for SDSS central spectra for constrained and unconstrained fits, respectively, and the same in Figures A.8 and A.9 for integrated IFS spectra.

Table A.1. Summary of the central IFS spectral modelling results for the three different configurations, each of them with the three different spectral bases.

		Single $A_V + H\beta$ constrain			Single $A_V + \text{No constrain}$			$2A_V + H\beta$ constrain		
		All	>4Myr	>30Myr	All	>4Myr	>30Myr	All	>4Myr	>30Myr
J1700	$\chi^2 a$	1.41	1.40	1.42	1.39	1.39	1.39	1.43	1.40	1.42
	Δ^b	8.97	8.94	8.87	5.50	8.89	8.89	8.97	8.95	8.87
	$\langle \log \text{age (yr)} \rangle_L^c$	9.30	9.36	9.41	9.38	9.54	9.56	9.23	9.36	9.40
	$\log M_\star^d$	10.62	10.63	10.62	10.65	10.64	10.67	10.50	10.64	10.60
	% $\star < 140\text{Myr}^e$	6	5	5	3	0	0	9	5	4
	% $\star < 1.5\text{Gyr}^f$	6	5	5	3	0	0	9	5	4
	$\log M(\star < 1.5\text{Gyr})^g$	7.55	7.55	7.90	7.22	-	-	7.58	7.53	7.89
	$\log L_{SB}^h$	43.40	43.38	43.38	43.38	43.34	43.34	43.40	43.38	43.38
	$A_V^{stars\ i}$	0.45	0.45	0.41	0.48	0.40	0.40	0.12	0.45	0.40
	$A_V^{AGN\ j}$	0.45	0.45	0.41	0.48	0.40	0.40	1.81	0.45	0.40
	% $AGN_{\lambda 5100}^k$	21	23	23	24	28	28	24	23	23
	$\log L_{AGN}^l$	42.95	42.99	43.00	43.01	43.08	43.08	42.95	42.99	43.00
$F(H\beta)^{stars\ m}$	12.97	1.54	0.65	94.52	0.74	0.82	31.61	2.04	0.61	
$F(H\beta)^{AGN\ n}$	108.06	119.35	118.71	124.52	144.84	145.48	140.32	119.35	118.39	
J2334	χ^2	1.38	1.38	1.41	1.38	1.39	1.38	1.37	1.36	1.36
	Δ	5.50	5.50	5.53	5.50	5.50	5.50	5.44	5.47	5.48
	$\langle \log \text{age (yr)} \rangle_L$	8.53	8.53	8.53	8.64	8.64	8.64	8.51	8.49	8.50
	$\log M_\star$	10.45	10.45	10.44	10.42	10.42	10.42	10.22	10.08	10.07
	% $\star < 140\text{Myr}$	26	23	29	0	0	0	25	19	19
	% $\star < 1.5\text{Gyr}$	78	78	78	70	70	70	72	68	68
	$\log M(\star < 1.5\text{Gyr})$	10.45	10.45	10.44	10.42	10.42	10.42	10.22	10.08	10.07
	$\log L_{SB}$	43.78	43.78	43.78	43.72	43.73	43.72	43.75	43.73	43.73
	A_V^{stars}	0.96	0.96	0.94	0.97	0.97	0.97	0.50	0.30	0.28
	A_V^{AGN}	0.96	0.96	0.94	0.97	0.97	0.97	1.95	2.45	2.47
	% $AGN_{\lambda 5100}$	25	25	25	33	33	33	33	38	38
	$\log L_{AGN}$	43.38	43.38	43.38	43.50	43.50	43.50	43.45	43.50	43.50
$F(H\beta)^{stars}$	0.15	0.15	0.15	0.14	0.14	0.14	2.41	0.31	0.12	
$F(H\beta)^{AGN}$	170.32	170.00	169.03	225.81	223.87	224.84	240.32	292.90	295.48	
J0237	χ^2	1.56	1.56	1.63	1.50	1.50	1.52	1.51	1.52	1.53
	Δ	6.44	6.44	6.47	6.43	6.37	6.43	6.49	6.51	6.48
	$\langle \log \text{age (yr)} \rangle_L$	8.20	8.18	8.54	8.52	8.50	8.74	8.27	8.26	8.58
	$\log M_\star$	10.67	10.68	10.69	10.62	10.62	10.58	10.42	10.40	10.35
	% $\star < 140\text{Myr}$	44	45	42	22	23	23	38	37	35
	% $\star < 1.5\text{Gyr}$	64	64	42	56	48	37	63	66	35
	$\log M(\star < 1.5\text{Gyr})$	10.11	10.09	9.23	10.13	9.99	9.71	9.94	10.01	8.88
	$\log L_{SB}$	43.80	43.81	43.79	43.73	43.72	43.69	43.78	43.78	43.75
	A_V^{stars}	0.84	0.85	0.61	0.71	0.66	0.53	0.35	0.35	0.00
	A_V^{AGN}	0.84	0.85	0.61	0.71	0.66	0.53	3.64	4.34	3.63
	% $AGN_{\lambda 5100}$	7	6	9	20	21	26	16	16	22
	$\log L_{AGN}$	42.76	42.69	42.86	43.20	43.23	43.32	43.00	42.98	43.13
$F(H\beta)^{stars}$	14.65	21.52	0.64	212.26	56.13	0.46	13.16	20.74	0.50	
$F(H\beta)^{AGN}$	45.16	38.39	54.19	121.29	127.74	154.52	122.58	125.48	163.55	

Note. — (a) the χ^2 of the fitting, (b) the deviation (in percentage) from the best model fit to the observed spectra expressed as Δ , (c) average stellar age in logarithm, (d) the stellar mass in M_\odot in logarithm, (e) the percentage of contribution to light of the SSPs younger than 140 Myr, (f) the percentage of contribution to light of the SSPs younger than 1.5 Gyr, (g) the stellar mass in M_\odot and in log, in SSPs younger than 1.5 Gyr, (h) the stellar luminosity in erg s^{-1} in logarithm, (i) the stellar dust extinction in magnitudes, (j) the AGN dust extinction in magnitudes, (k) the contribution to light of the AGN in percentage, (l) the AGN luminosity in erg s^{-1} in logarithm, (m) the $H\beta$ flux expected from the stellar component in units of $10^{-17} \text{ erg s}^{-1} \text{ cm}^{-2}$, (n) the $H\beta$ flux expected from the AGN component in units of $10^{-17} \text{ erg s}^{-1} \text{ cm}^{-2}$.

Table A.1. Continued

	Single $A_V + H\beta$ constrain			Single $A_V + \text{No}$ constrain			$2A_V + H\beta$ constrain			
	All	>4Myr	>30Myr	All	>4Myr	>30Myr	All	>4Myr	>30Myr	
J1230	χ^2	2.11	2.08	4.11	1.84	2.05	2.70	2.09	2.08	4.11
	Δ	3.80	3.75	5.54	3.64	3.72	4.33	3.78	3.75	5.54
	$\langle \log \text{age (yr)} \rangle_L$	8.04	8.06	8.34	8.07	8.14	8.86	8.04	8.05	8.34
	$\log M_\star$	10.23	10.26	10.51	10.15	10.22	10.29	10.24	10.25	10.51
	% $\star < 140\text{Myr}$	41	39	45	23	31	12	40	39	45
	% $\star < 1.5\text{Gyr}$	41	39	45	34	31	12	40	39	45
	$\log M(\star < 1.5\text{Gyr})$	8.43	8.42	8.91	9.42	8.32	8.36	8.44	8.42	8.91
	$\log L_{SB}$	43.68	43.65	43.62	43.58	43.57	43.26	43.67	43.65	43.62
	A_V^{stars}	0.00	0.00	0.00	0.17	0.00	0.00	0.00	0.00	0.00
	A_V^{AGN}	0.00	0.00	0.00	0.17	0.00	0.00	0.00	0.00	0.00
	% $\text{AGN}_{\lambda 5100}$	25	31	34	41	41	68	28	31	34
	$\log L_{AGN}$	43.25	43.34	43.37	43.45	43.46	43.68	43.29	43.34	43.37
$F(H\beta)^{stars}$	43.23	13.94	0.74	790.32	11.10	0.39	30.90	13.90	0.74	
$F(H\beta)^{AGN}$	134.19	163.55	177.42	220.32	218.06	361.29	146.45	163.55	177.42	
J1248	χ^2	2.08	2.08	2.14	1.67	1.67	1.67	2.04	2.04	2.08
	Δ	4.21	4.21	4.24	3.61	3.61	3.61	4.12	4.13	4.08
	$\langle \log \text{age (yr)} \rangle_L$	8.62	8.59	8.80	9.00	9.00	9.00	8.64	8.63	8.85
	$\log M_\star$	10.51	10.52	10.56	10.39	10.40	10.40	10.43	10.44	10.40
	% $\star < 140\text{Myr}$	19	21	19	0	0	0	19	19	17
	% $\star < 1.5\text{Gyr}$	80	80	69	61	61	61	67	64	54
	$\log M(\star < 1.5\text{Gyr})$	10.49	10.50	10.38	10.39	10.40	10.40	10.28	10.23	10.04
	$\log L_{SB}$	43.77	43.77	43.77	43.61	43.61	43.61	43.76	43.75	43.75
	A_V^{stars}	0.59	0.63	0.45	0.58	0.59	0.57	0.36	0.37	0.02
	A_V^{AGN}	0.59	0.63	0.45	0.58	0.59	0.57	1.14	1.15	1.36
	% $\text{AGN}_{\lambda 5100}$	22	22	21	41	41	41	26	26	28
	$\log L_{AGN}$	43.30	43.31	43.30	43.58	43.58	43.58	43.34	43.34	43.37
$F(H\beta)^{stars}$	4.06	4.42	1.07	0.49	0.49	0.51	3.84	4.10	1.03	
$F(H\beta)^{AGN}$	272.90	276.45	262.26	509.68	512.90	506.45	332.26	335.48	364.52	
J1456	χ^2	1.56	1.56	1.63	1.23	1.23	1.23	1.56	1.57	1.64
	Δ	3.44	3.45	3.52	3.10	3.10	3.10	3.44	3.46	3.51
	$\langle \log \text{age (yr)} \rangle_L$	8.07	8.07	8.48	8.90	8.89	8.90	8.08	8.05	8.46
	$\log M_\star$	10.25	10.26	10.22	10.05	10.04	10.06	10.22	10.25	10.17
	% $\star < 140\text{Myr}$	45	45	42	17	17	17	44	46	41
	% $\star < 1.5\text{Gyr}$	68	64	42	36	39	34	65	64	41
	$\log M(\star < 1.5\text{Gyr})$	9.87	9.78	8.83	9.65	9.71	9.60	9.80	9.75	8.80
	$\log L_{SB}$	43.65	43.65	43.63	43.42	43.42	43.42	43.65	43.66	43.63
	A_V^{stars}	0.40	0.40	0.06	0.01	0.02	0.01	0.33	0.35	0.00
	A_V^{AGN}	0.40	0.40	0.06	0.01	0.02	0.01	0.81	0.85	0.62
	% $\text{AGN}_{\lambda 5100}$	10	10	12	41	42	41	11	9	15
	$\log L_{AGN}$	42.73	42.73	42.85	43.39	43.39	43.38	42.76	42.66	42.89
$F(H\beta)^{stars}$	17.65	18.19	0.41	0.19	0.18	0.19	17.06	26.42	0.40	
$F(H\beta)^{AGN}$	43.55	42.90	53.55	180.65	181.29	179.03	50.65	40.65	65.81	

Table A.1. Continued

	Single $A_V + H\beta$ constrain			Single $A_V + \text{No}$ constrain			$2A_V + H\beta$ constrain			
	All	>4Myr	>30Myr	All	>4Myr	>30Myr	All	>4Myr	>30Myr	
J0202	χ^2	1.52	1.52	1.52	1.52	1.52	1.52	1.52	1.52	
	Δ	3.86	3.85	3.85	3.85	3.85	3.85	3.86	3.85	
	$\langle \log \text{ age (yr)} \rangle_L$	9.11	9.11	9.16	9.11	9.14	9.13	9.13	9.17	9.16
	$\log M_\star$	10.94	10.93	10.92	10.92	10.93	10.87	10.95	10.93	10.92
	% $\star < 140\text{Myr}$	2	2	0	1	1	0	2	0	0
	% $\star < 1.5\text{Gyr}$	54	56	54	56	55	52	55	56	53
	$\log M(\star < 1.5\text{Gyr})$	10.16	10.22	10.21	10.22	10.20	10.17	10.20	10.16	10.18
	$\log L_{SB}$	43.75	43.75	43.74	43.75	43.74	43.74	43.74	43.73	43.73
	A_V^{stars}	0.48	0.48	0.46	0.48	0.47	0.48	0.46	0.44	0.43
	A_V^{AGN}	0.48	0.48	0.46	0.48	0.47	0.48	0.50	0.52	0.54
	% $\text{AGN}_{\lambda 5100}$	20	20	21	20	21	21	20	22	22
$\log L_{AGN}$	43.27	43.26	43.29	43.26	43.28	43.29	43.27	43.30	43.30	
$F(H\beta)^{stars}$	1.73	1.51	0.79	1.36	1.15	0.52	1.66	0.86	0.83	
$F(H\beta)^{AGN}$	140.00	139.03	148.06	139.03	144.52	148.39	140.97	151.94	151.94	
J2128	χ^2	1.74	1.73	1.86	1.59	1.67	1.72	1.76	1.73	1.87
	Δ	4.15	4.16	4.29	4.02	4.14	4.21	4.15	4.16	4.30
	$\langle \log \text{ age (yr)} \rangle_L$	8.60	8.66	8.83	8.77	8.90	9.07	8.56	8.67	8.83
	$\log M_\star$	10.30	10.26	10.29	10.32	10.20	10.09	10.33	10.26	10.29
	% $\star < 140\text{Myr}$	24	20	21	14	9	4	26	20	21
	% $\star < 1.5\text{Gyr}$	35	39	25	36	30	40	35	34	24
	$\log M(\star < 1.5\text{Gyr})$	9.39	9.64	9.08	9.65	9.67	9.89	9.32	9.51	9.03
	$\log L_{SB}$	43.59	43.55	43.54	43.56	43.45	43.39	43.62	43.55	43.54
	A_V^{stars}	0.00	0.00	0.00	0.00	0.00	0.00	0.00	0.00	0.00
	A_V^{AGN}	0.00	0.00	0.00	0.00	0.00	0.00	0.00	0.00	0.00
	% $\text{AGN}_{\lambda 5100}$	24	29	30	29	40	46	20	30	30
	$\log L_{AGN}$	43.18	43.27	43.28	43.26	43.40	43.46	43.09	43.27	43.28
	$F(H\beta)^{stars}$	27.29	4.81	0.38	172.90	13.16	0.23	44.19	3.94	0.37
$F(H\beta)^{AGN}$	97.42	120.00	124.52	118.39	163.87	187.42	80.65	120.65	124.52	
J2310	χ^2	1.90	1.90	1.88	1.88	1.88	1.88	1.89	1.90	1.88
	Δ	3.88	3.89	3.87	3.88	3.88	3.87	3.89	3.89	3.87
	$\langle \log \text{ age (yr)} \rangle_L$	9.22	9.32	9.35	9.31	9.32	9.43	9.23	9.25	9.36
	$\log M_\star$	11.01	10.94	10.96	10.99	10.98	10.97	10.98	10.98	10.97
	% $\star < 140\text{Myr}$	17	8	11	9	11	4	11	10	9
	% $\star < 1.5\text{Gyr}$	37	31	29	33	34	25	36	37	31
	$\log M(\star < 1.5\text{Gyr})$	9.81	9.73	9.66	9.74	9.81	9.60	9.84	9.87	9.76
	$\log L_{SB}$	43.73	43.70	43.69	43.70	43.70	43.68	43.72	43.71	43.69
	A_V^{stars}	0.34	0.29	0.27	0.29	0.28	0.22	0.34	0.32	0.26
	A_V^{AGN}	0.34	0.29	0.27	0.29	0.28	0.22	0.34	0.32	0.26
	% $\text{AGN}_{\lambda 5100}$	12	16	16	11	14	16	12	13	15
	$\log L_{AGN}$	42.78	42.98	42.98	42.94	42.95	43.05	42.84	42.88	42.98
	$F(H\beta)^{stars}$	24.06	1.84	0.85	2.54	2.26	1.02	17.84	14.16	0.86
$F(H\beta)^{AGN}$	37.42	53.39	59.03	54.19	54.84	68.06	43.55	46.77	59.03	

Table A.2. Summary of the integrated IFS spectral modelling results for the three different configurations, each of them with the three different spectral bases

		Single $A_V + H\beta$ constrain			Single $A_V + \text{No}$ constrain			$2A_V + H\beta$ constrain		
		All	>4Myr	>30Myr	All	>4Myr	>30Myr	All	>4Myr	>30Myr
J1700	χ^2	1.67	1.67	1.67	1.66	1.66	1.66	1.65	1.65	1.65
	Δ	23.59	23.71	23.74	23.24	23.23	23.24	22.36	22.21	22.32
	$\langle \log \text{age (yr)} \rangle_L$	9.28	9.33	9.32	9.27	9.28	9.27	9.38	9.39	9.38
	$\log M_\star$	10.76	10.76	10.72	10.70	10.71	10.71	10.54	10.57	10.59
	% $\star < 140\text{Myr}$	2	0	0	4	0	1	2	1	1
	% $\star < 1.5\text{Gyr}$	22	21	14	11	11	11	10	10	9
	$\log M(\star < 1.5\text{Gyr})$	9.67	9.64	9.27	8.87	8.93	8.93	8.67	8.72	8.74
	$\log L_{SB}$	43.55	43.53	43.53	43.56	43.55	43.55	43.50	43.50	43.50
A_V^{stars}	0.59	0.58	0.57	0.53	0.56	0.55	0.05	0.10	0.16	
J2334	χ^2	1.50	1.51	1.53	1.47	1.47	1.47	1.46	1.47	1.45
	Δ	7.31	7.34	7.34	7.23	7.23	7.23	7.15	7.18	7.19
	$\langle \log \text{age (yr)} \rangle_L$	8.54	8.54	8.56	8.62	8.62	8.62	8.53	8.53	8.55
	$\log M_\star$	10.49	10.50	10.49	10.47	10.48	10.48	10.21	10.20	10.05
	% $\star < 140\text{Myr}$	21	22	28	0	0	0	22	21	17
	% $\star < 1.5\text{Gyr}$	80	80	81	73	73	73	73	73	69
	$\log M(\star < 1.5\text{Gyr})$	10.49	10.50	10.49	10.47	10.48	10.48	10.21	10.20	10.05
	$\log L_{SB}$	43.85	43.85	43.85	43.80	43.80	43.80	43.81	43.81	43.79
A_V^{stars}	0.89	0.90	0.87	0.95	0.95	0.95	0.38	0.36	0.06	
J0237	χ^2	1.71	1.71	1.78	1.65	1.69	1.75	1.62	1.61	1.66
	Δ	7.68	7.69	7.84	7.59	7.69	7.88	7.55	7.54	7.65
	$\langle \log \text{age (yr)} \rangle_L$	8.14	8.14	8.54	8.30	8.25	8.61	8.26	8.28	8.55
	$\log M_\star$	10.82	10.84	10.85	10.75	10.74	10.75	10.48	10.45	10.59
	% $\star < 140\text{Myr}$	49	49	45	34	37	34	38	40	40
	% $\star < 1.5\text{Gyr}$	76	71	45	85	80	45	77	76	42
	$\log M(\star < 1.5\text{Gyr})$	10.34	10.22	9.38	10.60	10.45	9.85	10.21	10.18	9.35
	$\log L_{SB}$	44.01	44.01	43.98	43.97	43.97	43.92	43.96	43.96	43.95
A_V^{stars}	0.81	0.80	0.51	0.83	0.73	0.51	0.27	0.25	0.06	
J1230	χ^2	1.99	1.99	3.36	1.81	1.91	2.16	1.98	1.98	3.36
	Δ	4.10	4.13	5.32	4.04	4.03	4.38	4.11	4.13	5.33
	$\langle \log \text{age (yr)} \rangle_L$	8.14	8.14	8.47	8.46	8.31	8.86	8.14	8.14	8.46
	$\log M_\star$	10.25	10.27	10.66	10.34	10.17	10.25	10.24	10.24	10.65
	% $\star < 140\text{Myr}$	38	38	44	15	25	12	38	38	44
	% $\star < 1.5\text{Gyr}$	38	38	44	34	25	12	38	38	44
	$\log M(\star < 1.5\text{Gyr})$	8.50	8.51	8.99	9.57	8.31	8.42	8.49	8.50	8.99
	$\log L_{SB}$	43.76	43.75	43.73	43.62	43.63	43.42	43.75	43.75	43.73
A_V^{stars}	0.00	0.00	0.00	0.00	0.00	0.00	0.00	0.00	0.00	
J1248	χ^2	2.30	2.29	2.31	2.05	2.06	2.05	2.26	2.25	2.26
	Δ	4.54	4.55	4.59	4.16	4.17	4.17	4.46	4.46	4.49
	$\langle \log \text{age (yr)} \rangle_L$	8.78	8.74	8.92	9.18	9.16	9.16	8.79	8.79	8.94
	$\log M_\star$	10.85	10.83	10.86	10.82	10.79	10.80	10.75	10.76	10.76
	% $\star < 140\text{Myr}$	18	19	20	0	0	0	17	18	18

Table A.2. Continued

		Single $A_V + H\beta$ constrain			Single $A_V + \text{No}$ constrain			$2A_V + H\beta$ constrain		
		All	>4Myr	>30Myr	All	>4Myr	>30Myr	All	>4Myr	>30Myr
J1248	$\% \star < 1.5\text{Gyr}$	58	63	45	30	35	34	56	52	37
	$\log M(\star < 1.5\text{Gyr})$	10.40	10.46	10.20	10.04	10.16	10.13	10.31	10.22	9.99
	$\log L_{SB}$	44.01	44.00	44.01	43.89	43.89	43.89	43.99	43.99	43.99
	A_V^{stars}	0.43	0.47	0.30	0.34	0.35	0.34	0.24	0.25	0.08
J1456	χ^2	1.48	1.54	1.57	1.31	1.31	1.31	1.48	1.48	1.58
	Δ	3.68	3.74	3.73	3.43	3.44	3.44	3.68	3.68	3.73
	$\langle \log \text{age (yr)} \rangle_L$	8.17	8.12	8.57	8.71	8.70	8.78	8.17	8.18	8.54
	$\log M_\star$	10.48	10.55	10.51	10.33	10.29	10.30	10.47	10.45	10.47
	$\% \star < 140\text{Myr}$	43	47	41	20	20	19	43	42	41
	$\% \star < 1.5\text{Gyr}$	84	71	41	56	57	44	74	79	41
	$\log M(\star < 1.5\text{Gyr})$	10.31	10.08	9.02	10.14	10.10	9.87	10.17	10.23	9.01
	$\log L_{SB}$	43.89	43.91	43.87	43.72	43.72	43.70	43.89	43.89	43.87
A_V^{stars}	0.38	0.41	0.03	0.18	0.13	0.10	0.34	0.31	0.00	
J0202	χ^2	1.46	1.46	1.47	1.47	1.46	1.46	1.46	1.46	1.46
	Δ	4.43	4.43	4.44	4.43	4.42	4.43	4.43	4.43	4.44
	$\langle \log \text{age (yr)} \rangle_L$	9.19	9.19	9.18	9.18	9.19	9.19	9.19	9.18	9.21
	$\log M_\star$	11.09	11.08	11.07	11.06	11.08	11.09	11.08	11.07	11.07
	$\% \star < 140\text{Myr}$	0	0	0	0	0	0	0	0	0
	$\% \star < 1.5\text{Gyr}$	50	52	49	49	52	51	50	52	48
	$\log M(\star < 1.5\text{Gyr})$	10.20	10.27	10.18	10.21	10.27	10.24	10.22	10.27	10.13
	$\log L_{SB}$	43.84	43.85	43.84	43.85	43.85	43.84	43.84	43.85	43.84
A_V^{stars}	0.45	0.45	0.46	0.46	0.45	0.45	0.43	0.43	0.38	
J2128	χ^2	1.67	1.65	1.71	1.57	1.63	1.66	1.68	1.65	1.71
	Δ	4.69	4.70	4.75	4.60	4.70	4.74	4.66	4.69	4.75
	$\langle \log \text{age (yr)} \rangle_L$	8.72	8.79	8.91	8.84	8.95	9.07	8.68	8.78	8.91
	$\log M_\star$	10.36	10.30	10.33	10.34	10.27	10.17	10.38	10.32	10.33
	$\% \star < 140\text{Myr}$	20	15	16	11	7	3	22	16	16
	$\% \star < 1.5\text{Gyr}$	46	47	35	49	42	54	46	44	38
	$\log M(\star < 1.5\text{Gyr})$	9.80	9.87	9.69	9.91	9.90	10.05	9.77	9.82	9.76
	$\log L_{SB}$	43.64	43.60	43.59	43.62	43.54	43.49	43.67	43.61	43.59
A_V^{stars}	0.00	0.00	0.00	0.00	0.00	0.00	0.00	0.00	0.00	
J2310	χ^2	1.61	1.58	1.61	1.55	1.55	1.56	1.60	1.58	1.61
	Δ	3.94	3.93	3.93	3.91	3.91	3.96	3.94	3.92	3.93
	$\langle \log \text{age (yr)} \rangle_L$	9.04	9.09	9.18	9.30	9.31	9.41	9.06	9.10	9.18
	$\log M_\star$	11.15	11.13	11.15	11.14	11.15	11.14	11.12	11.15	11.15
	$\% \star < 140\text{Myr}$	16	12	18	4	4	0	15	14	19
	$\% \star < 1.5\text{Gyr}$	55	50	46	44	44	39	51	51	45
	$\log M(\star < 1.5\text{Gyr})$	10.21	10.11	10.08	10.09	10.11	10.06	10.13	10.13	10.05
	$\log L_{SB}$	43.94	43.93	43.92	43.88	43.88	43.86	43.93	43.93	43.92
A_V^{stars}	0.36	0.34	0.30	0.23	0.23	0.20	0.36	0.32	0.29	

Table A.3. Summary of the SDSS spectral modelling results for the three different configurations, each of them with the three different spectral bases

		Single $A_V + H\alpha$ constrain			Single $A_V + \text{No constrain}$			$2A_V + H\alpha$ constrain		
		All	>4Myr	>30Myr	All	>4Myr	>30Myr	All	>4Myr	>30Myr
J1700	χ^2 ^a	1.50	1.49	1.86	1.41	1.48	1.61	1.51	1.76	1.85
	Δ ^b	6.02	6.00	7.04	5.91	5.95	6.14	6.06	6.38	7.01
	$\langle \log \text{age (yr)} \rangle_L$ ^c	8.90	9.01	9.19	9.00	9.09	9.93	8.56	8.38	9.19
	$\log M_\star^d$	10.57	10.54	10.55	10.63	10.57	10.46	10.54	10.44	10.54
	% $\star < 140\text{Myr}$ ^e	28	23	23	19	21	0	43	42	23
	% $\star < 1.5\text{Gyr}$ ^f	28	23	23	19	21	0	43	42	23
	$\log M(\star < 1.5\text{Gyr})$ ^g	7.98	7.92	8.35	7.85	7.88	-	8.14	8.09	8.34
	$\log L_{\text{SEB}}$ ^h	43.41	43.35	43.34	43.38	43.33	43.07	43.51	43.43	43.33
	$A_V^{\text{stars } i}$	0.00	0.00	0.00	0.08	0.00	0.00	0.00	0.00	0.00
	$A_V^{\text{AGN } j}$	0.00	0.00	0.00	0.08	0.00	0.00	4.00	2.46	0.00
	% $\text{AGN}_{\lambda 5100}$ ^k	22	29	30	26	33	56	7	23	31
	$\log L_{\text{AGN}}^l$	42.95	43.07	43.09	43.03	43.12	43.35	42.30	42.84	43.10
$F(H\alpha)^{\text{stars } m}$	120.00	21.80	2.76	1830.00	20.30	1.89	337.00	125.00	2.55	
$F(H\alpha)^{\text{AGN } n}$	303.00	402.0	422.00	367.00	449.00	767.00	131.00	370.00	432.00	
J2334	χ^2	1.39	1.39	1.38	1.37	1.37	1.37	1.40	1.38	1.38
	Δ	6.93	6.90	6.89	6.86	6.86	6.86	6.96	6.90	6.89
	$\langle \log \text{age (yr)} \rangle_L$	8.10	8.40	8.59	8.62	8.62	8.68	8.01	8.40	8.60
	$\log M_\star$	10.33	10.33	10.23	10.20	10.21	10.19	10.40	10.28	10.28
	% $\star < 140\text{Myr}$	34	30	27	22	20	22	40	27	28
	% $\star < 1.5\text{Gyr}$	72	52	62	58	54	58	75	60	55
	$\log M(\star < 1.5\text{Gyr})$	10.18	9.88	10.08	10.09	10.02	10.08	10.23	10.03	9.98
	$\log L_{\text{SEB}}$	43.84	43.80	43.77	43.73	43.73	43.72	43.88	43.80	43.77
	A_V^{stars}	0.29	0.07	0.00	0.00	0.00	0.00	0.37	0.07	0.0
	A_V^{AGN}	0.29	0.07	0.00	0.00	0.00	0.00	0.37	0.08	0.00
	% $\text{AGN}_{\lambda 5100}$	26	30	34	39	39	40	20	31	34
	$\log L_{\text{AGN}}$	43.44	43.52	43.57	43.63	43.64	43.64	43.32	43.53	43.57
	$F(H\alpha)^{\text{stars}}$	165.00	78.40	1.20	55.80	56.40	1.16	288.00	65.00	1.23
	$F(H\alpha)^{\text{AGN}}$	532.00	607.00	680.00	780.00	782.00	798.00	414.00	621.00	680.00
J0237	χ^2	1.33	1.32	1.33	1.31	1.31	1.31	1.33	1.32	1.32
	Δ	7.18	7.35	7.07	7.05	7.05	7.03	7.14	7.12	7.07
	$\langle \log \text{age (yr)} \rangle_L$	8.24	8.44	8.66	8.78	8.79	8.89	8.31	8.42	8.66
	$\log M_\star$	10.59	10.56	10.50	10.53	10.52	10.46	10.57	10.54	10.47
	% $\star < 140\text{Myr}$	42	36	34	14	15	15	38	37	33
	% $\star < 1.5\text{Gyr}$	66	56	45	30	32	30	65	60	52
	$\log M(\star < 1.5\text{Gyr})$	9.97	9.83	9.59	9.13	9.27	9.20	10.00	9.92	9.75
	$\log L_{\text{SEB}}$	43.85	43.81	43.78	43.74	43.73	43.72	43.83	43.82	43.78
	A_V^{stars}	0.45	0.27	0.13	0.06	0.05	0.00	0.38	0.27	0.12
	A_V^{AGN}	0.45	0.27	0.13	0.06	0.05	0.00	0.41	0.34	0.12
	% $\text{AGN}_{\lambda 5100}$	0	7	12	19	20	22	4	7	12
	$\log L_{\text{AGN}}$	-	42.77	43.02	43.22	43.23	43.27	42.51	42.74	43.02
	$F(H\alpha)^{\text{stars}}$	230.00	99.70	1.60	95.80	112.00	1.64	156.00	105.00	1.76
	$F(H\alpha)^{\text{AGN}}$	0.00	127.00	223.00	346.00	351.00	385.00	73.10	122.00	222.00

Note. — (a) the χ^2 of the fitting, (b) the deviation (in percentage) from the best model fit to the observed spectra expressed as Δ , (c) average stellar age in logarithm, (d) the stellar mass in M_\odot in logarithm, (e) the percentage of contribution to light of the SSPs younger than 140 Myr, (f) the percentage of contribution to light of the SSPs younger than 1.5 Gyr, (g) the stellar mass in M_\odot and in log, in SSPs younger than 1.5 Gyr, (h) the stellar luminosity in erg s^{-1} in logarithm, (i) the stellar dust extinction in magnitudes, (j) the AGN dust extinction in magnitudes, (k) the contribution to light of the AGN in percentage, (l) the AGN luminosity in erg s^{-1} in logarithm, (m) the $H\alpha$ flux expected from the stellar component in units of $10^{-17} \text{ erg s}^{-1} \text{ cm}^{-2}$, (n) the $H\alpha$ flux expected from the AGN component in units of $10^{-17} \text{ erg s}^{-1} \text{ cm}^{-2}$.

Table A.3. Continued

		Single $A_V + H\alpha$ constrain			Single $A_V + \text{No}$ constrain			$2A_V + H\alpha$ constrain		
		All	>4Myr	>30Myr	All	>4Myr	>30Myr	All	>4Myr	>30Myr
J1230	χ^2	1.82	1.83	1.90	1.72	1.83	1.89	1.82	1.83	1.90
	Δ	7.33	7.35	7.57	7.11	7.33	7.54	7.31	7.35	7.56
	$\langle \log \text{age (yr)} \rangle_L$	8.51	8.60	8.80	8.15	8.59	8.85	8.51	8.60	8.80
	$\log M_\star$	10.35	10.38	10.33	10.40	10.38	10.32	10.36	10.34	10.33
	% $\star < 140\text{Myr}$	30	25	22	29	25	19	29	23	22
	% $\star < 1.5\text{Gyr}$	43	25	22	84	28	19	44	30	22
	$\log M(\star < 1.5\text{Gyr})$	9.45	8.09	8.61	10.24	8.88	8.55	9.48	9.09	8.62
	$\log L_{SB}$	43.73	43.68	43.61	43.76	43.68	43.58	43.73	43.67	43.61
	A_V^{stars}	0.02	0.00	0.00	0.46	0.00	0.00	0.01	0.00	0.00
	A_V^{AGN}	0.02	0.00	0.00	0.46	0.00	0.00	0.01	0.00	0.00
	% $AGN_{\lambda 5100}$	19	26	34	14	26	38	18	27	34
	$\log L_{AGN}$	43.17	43.32	43.43	43.02	43.32	43.48	43.17	43.34	43.43
	$F(H\alpha)^{stars}$	290.00	153.00	1.44	4480.00	132.00	1.45	293.00	128.00	1.50
$F(H\alpha)^{AGN}$	347.00	483.00	635.00	271.00	484.00	698.00	345.00	508.00	635.00	
J1248	χ^2	2.72	2.72	2.72	2.57	2.57	2.57	2.74	2.73	2.72
	Δ	7.07	7.06	7.03	7.06	7.06	7.06	7.07	7.07	7.04
	$\langle \log \text{age (yr)} \rangle_L$	8.95	9.01	9.10	9.18	9.18	9.19	8.78	8.86	9.13
	$\log M_\star$	10.89	10.91	10.91	10.87	10.86	10.88	10.68	10.78	10.95
	% $\star < 140\text{Myr}$	13	14	14	0	0	0	13	13	14
	% $\star < 1.5\text{Gyr}$	46	37	33	46	43	43	54	44	35
	$\log M(\star < 1.5\text{Gyr})$	10.12	9.92	9.82	10.25	10.20	10.20	10.32	10.09	9.85
	$\log L_{SB}$	43.74	43.74	43.74	43.64	43.64	43.64	43.75	43.75	43.74
	A_V^{stars}	0.58	0.52	0.45	0.63	0.63	0.62	0.71	0.64	0.42
	A_V^{AGN}	0.58	0.52	0.45	0.63	0.63	0.62	0.71	0.64	0.42
	% $AGN_{\lambda 5100}$	24	24	24	38	38	37	24	24	24
	$\log L_{AGN}$	43.35	43.36	43.37	43.54	43.54	43.54	43.35	43.35	43.37
	$F(H\alpha)^{stars}$	13.30	10.50	3.80	3.39	3.35	3.51	18.20	14.70	4.76
$F(H\alpha)^{AGN}$	946.00	945.00	946.00	1470.00	1460.00	1460.00	951.00	949.00	943.00	
J1456	χ^2	1.42	1.42	1.42	1.41	1.41	1.41	1.42	1.41	1.42
	Δ	7.54	7.52	7.51	7.51	7.51	7.50	7.52	7.50	7.50
	$\langle \log \text{age (yr)} \rangle_L$	8.98	9.04	9.13	8.99	9.00	9.02	8.86	8.92	9.12
	$\log M_\star$	10.41	10.41	10.40	10.38	10.39	10.41	10.39	10.43	10.39
	% $\star < 140\text{Myr}$	17	7	10	20	19	20	21	18	
13	% $\star < 1.5\text{Gyr}$	44	46	34	37	40	35	45	44	28
$\log M(\star < 1.5\text{Gyr})$	9.75	9.83	9.64	9.62	9.69	9.58	9.75	9.73	9.41	
$\log L_{SB}$	43.57	43.53	43.51	43.56	43.56	43.56	43.58	43.56	43.51	
A_V^{stars}	0.03	0.02	0.00	0.00	0.00	0.00	0.00	0.00	0.00	
A_V^{AGN}	0.03	0.02	0.00	0.00	0.00	0.00	0.47	0.33	0.02	
% $AGN_{\lambda 5100}$	22	27	29	23	23	24	22	24	29	
$\log L_{AGN}$	43.14	43.22	43.26	43.16	43.16	43.17	43.11	43.16	43.26	
$F(H\alpha)^{stars}$	107.00	39.20	1.06	3.78	4.56	1.18	110.00	73.00	1.11	
$F(H\alpha)^{AGN}$	317.00	385.00	422.00	329.00	332.00	340.00	324.00	359.00	423.00	

Table A.3. Continued

		Single $A_V + H\alpha$ constrain			Single $A_V + \text{No}$ constrain			$2A_V + H\alpha$ constrain		
		All	>4Myr	>30Myr	All	>4Myr	>30Myr	All	>4Myr	>30Myr
J0202	χ^2	1.43	1.43	1.43	1.43	1.42	1.43	1.43	1.42	1.44
	Δ	7.30	7.30	7.30	7.30	7.30	7.30	7.31	7.30	7.28
	$\langle \log \text{age (yr)} \rangle_L$	8.97	9.01	9.08	8.90	8.92	9.07	8.65	8.69	8.89
	$\log M_\star$	10.88	10.83	10.85	10.82	10.85	10.93	10.54	10.47	10.70
	% $\star < 140\text{Myr}$	8	6	9	9	8	10	25	19	21
	% $\star < 1.5\text{Gyr}$	48	41	38	49	47	41	61	48	46
	$\log M(\star < 1.5\text{Gyr})$	10.13	10.00	9.92	10.13	10.07	9.97	10.02	9.84	9.84
	$\log L_{SB}$	43.72	43.71	43.70	43.73	43.73	43.71	43.79	43.75	43.73
	A_V^{stars}	0.47	0.46	0.41	0.49	0.49	0.44	0.00	0.00	0.00
	A_V^{AGN}	0.47	0.46	0.41	0.49	0.49	0.44	2.44	1.97	1.56
	% $AGN_{\lambda 5100}$	29	31	31	28	28	30	25	30	31
	$\log L_{AGN}$	43.45	43.47	43.48	43.42	43.43	43.46	43.28	43.38	43.42
$F(H\alpha)^{stars}$	44.60	8.78	1.71	14.60	14.10	2.38	153.00	36.00	2.67	
$F(H\alpha)^{AGN}$	658.00	693.00	698.00	627.00	628.00	677.00	632.00	746.00	760.00	
J2128	χ^2	1.59	1.59	1.72	1.54	1.57	1.61	1.58	1.57	1.71
	Δ	8.26	8.26	8.45	8.21	8.23	8.32	8.26	8.24	8.43
	$\langle \log \text{age (yr)} \rangle_L$	8.65	8.66	8.87	8.71	8.75	9.12	8.65	8.67	8.89
	$\log M_\star$	10.31	10.34	10.53	10.27	10.23	10.25	10.31	10.34	10.57
	% $\star < 140\text{Myr}$	21	22	26	11	15	7	21	21	25
	% $\star < 1.5\text{Gyr}$	21	22	26	20	15	7	21	21	25
	$\log M(\star < 1.5\text{Gyr})$	8.15	8.17	8.65	9.35	8.00	8.08	8.15	8.15	8.64
	$\log L_{SB}$	43.58	43.58	43.57	43.55	43.53	43.40	43.59	43.58	43.57
	A_V^{stars}	0.00	0.00	0.00	0.09	0.00	0.00	0.00	0.00	0.00
	A_V^{AGN}	0.00	0.00	0.00	0.09	0.00	0.00	0.00	0.00	0.00
	% $AGN_{\lambda 5100}$	31	32	32	37	38	50	30	32	33
	$\log L_{AGN}$	43.34	43.34	43.35	43.40	43.42	43.54	43.33	43.35	43.36
$F(H\alpha)^{stars}$	17.90	14.40	1.43	1330.00	14.40	0.83	41.10	15.60	1.72	
$F(H\alpha)^{AGN}$	440.00	443.00	457.00	518.00	529.00	701.00	427.00	453.00	467.00	
J2310	χ^2	1.31	1.31	1.35	1.27	1.30	1.31	1.30	1.36	1.35
	Δ	12.13	12.10	12.23	12.10	12.09	12.15	12.21	12.15	12.23
	$\langle \log \text{age (yr)} \rangle_L$	8.86	9.23	9.38	8.80	9.37	9.75	8.70	8.65	9.38
	$\log M_\star$	10.87	10.85	10.89	10.92	10.87	10.81	10.72	10.74	10.89
	% $\star < 140\text{Myr}$	25	15	16	18	10	0	30	31	16
	% $\star < 1.5\text{Gyr}$	25	15	16	18	10	0	30	31	16
	$\log M(\star < 1.5\text{Gyr})$	8.36	8.07	8.52	8.33	7.91	-	8.33	8.25	8.52
	$\log L_{SB}$	43.76	43.66	43.65	43.72	43.62	43.51	43.79	43.74	43.65
	A_V^{stars}	0.20	0.02	0.00	0.41	0.02	0.00	0.00	0.00	0.00
	A_V^{AGN}	0.20	0.02	0.00	0.41	0.02	0.00	4.00	2.79	0.00
	% $AGN_{\lambda 5100}$	12	26	27	18	31	42	9	19	27
	$\log L_{AGN}$	43.00	43.34	43.35	43.15	43.41	43.55	42.70	43.06	43.35
$F(H\alpha)^{stars}$	226.00	16.60	2.75	2320.00	12.70	2.51	279.00	132.00	2.67	
$F(H\alpha)^{AGN}$	188.00	391.00	404.00	281.00	465.00	634.00	173.00	339.00	404.00	

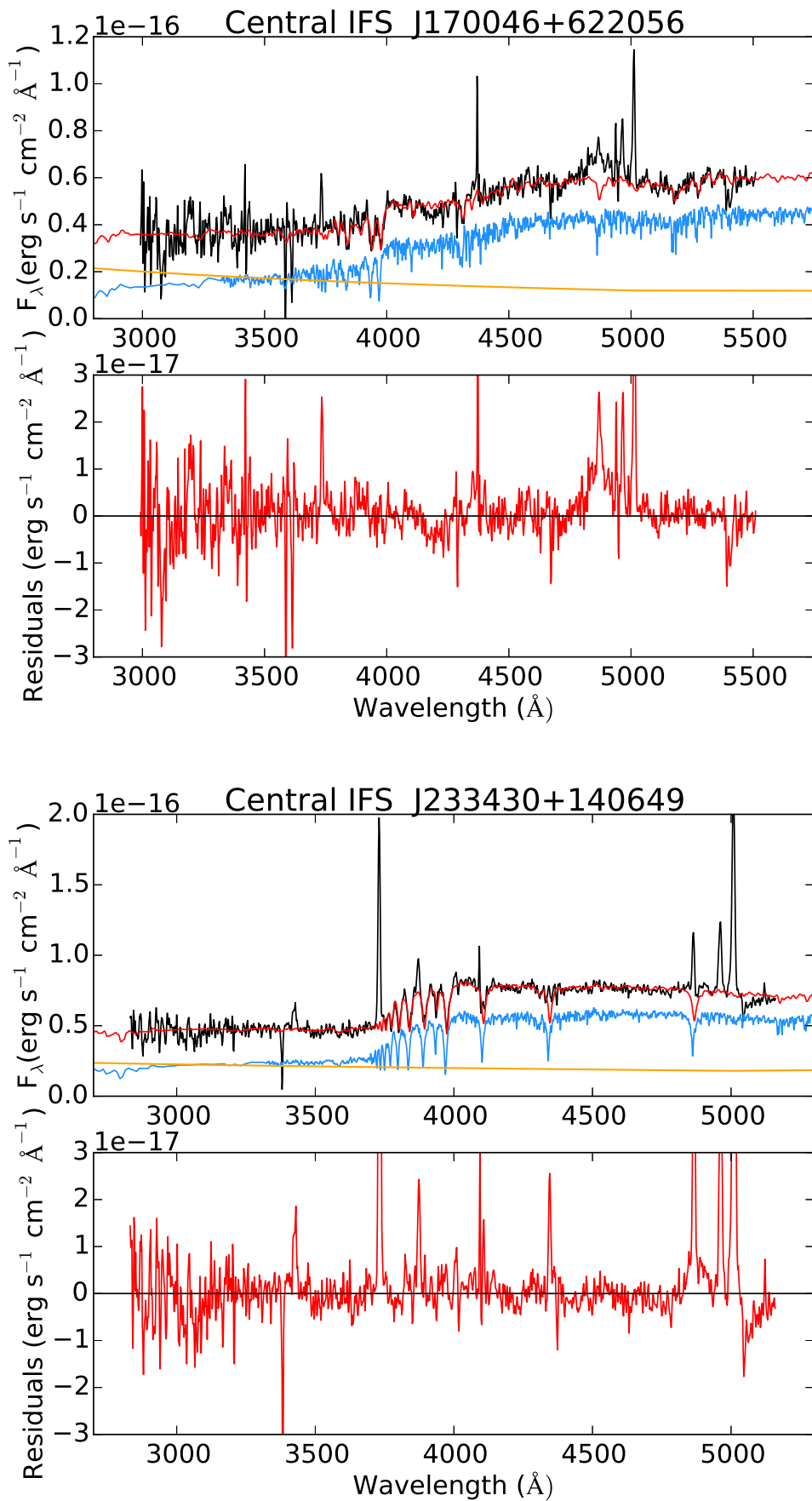


Figure A.1 Spectral fits of the central IFS for the base with SSPs $> 4\text{Myr}$, using $\text{H}\beta$ constrain and a single extinction value for star and AGN. In the upper panels we show the observed spectra (in black) and the best *Starlight* fit (in red). The stellar component contribution is shown in blue and the AGN contribution in orange. In the bottom panels we show the residuals in red.

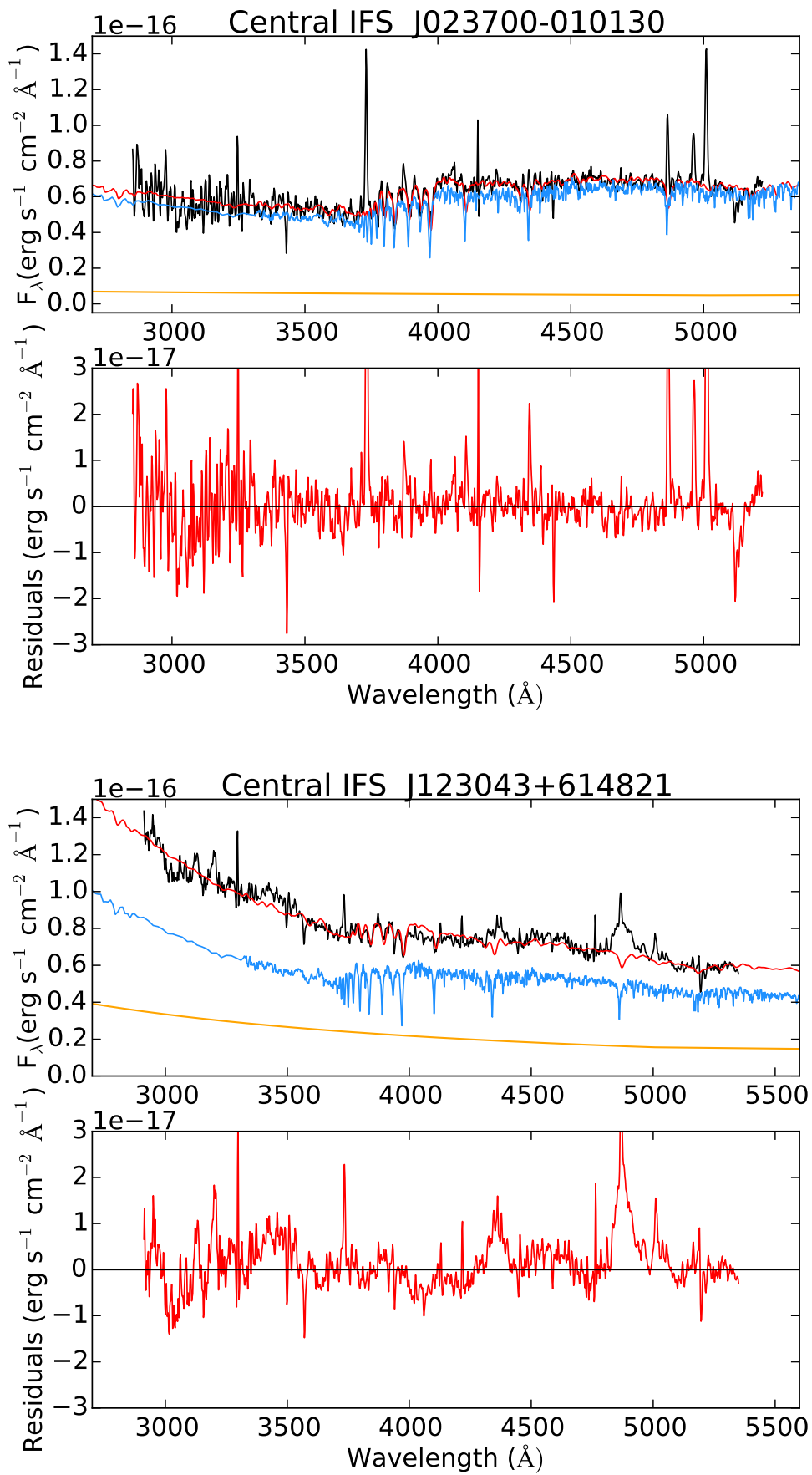


Figure A.1 Continued

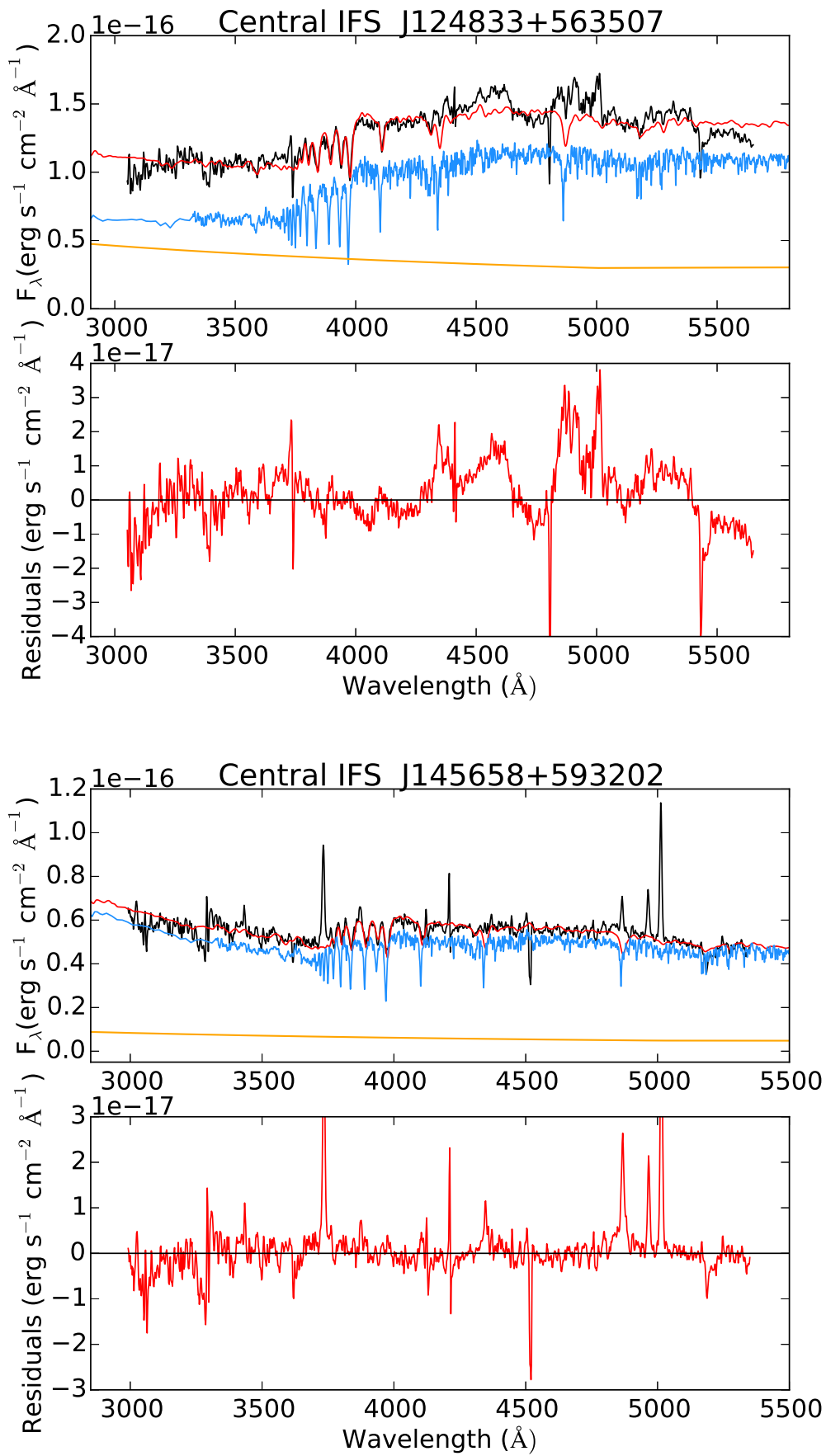


Figure A.1 Continued

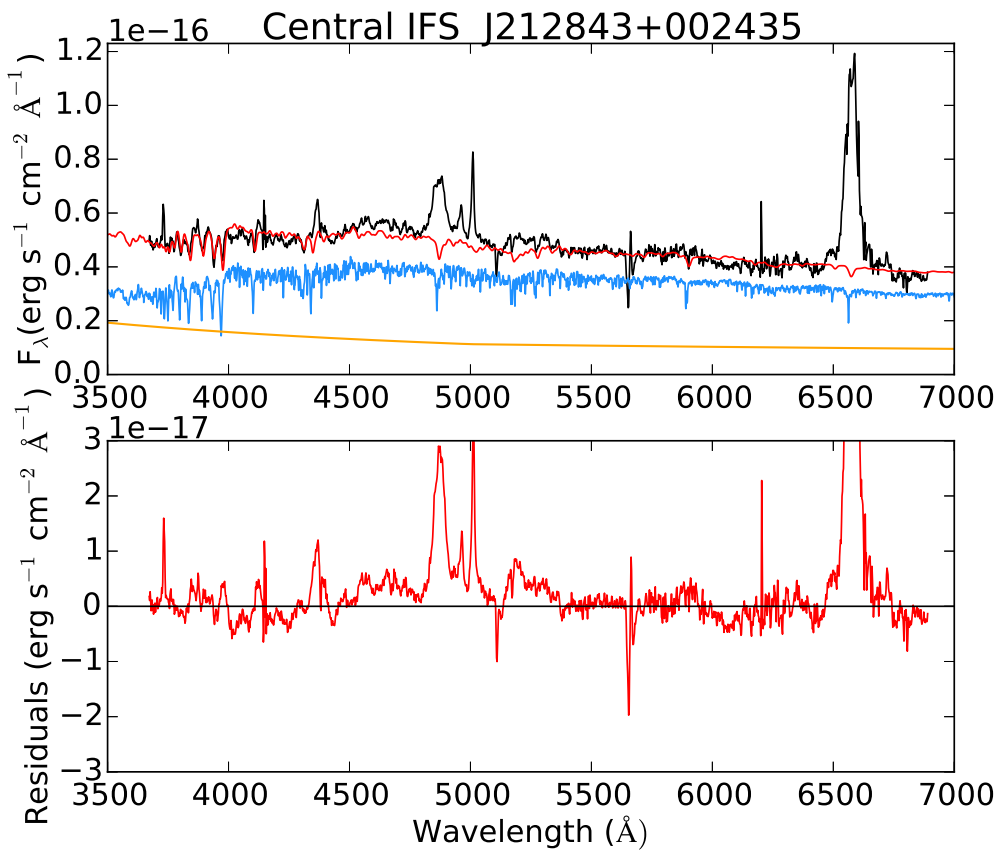
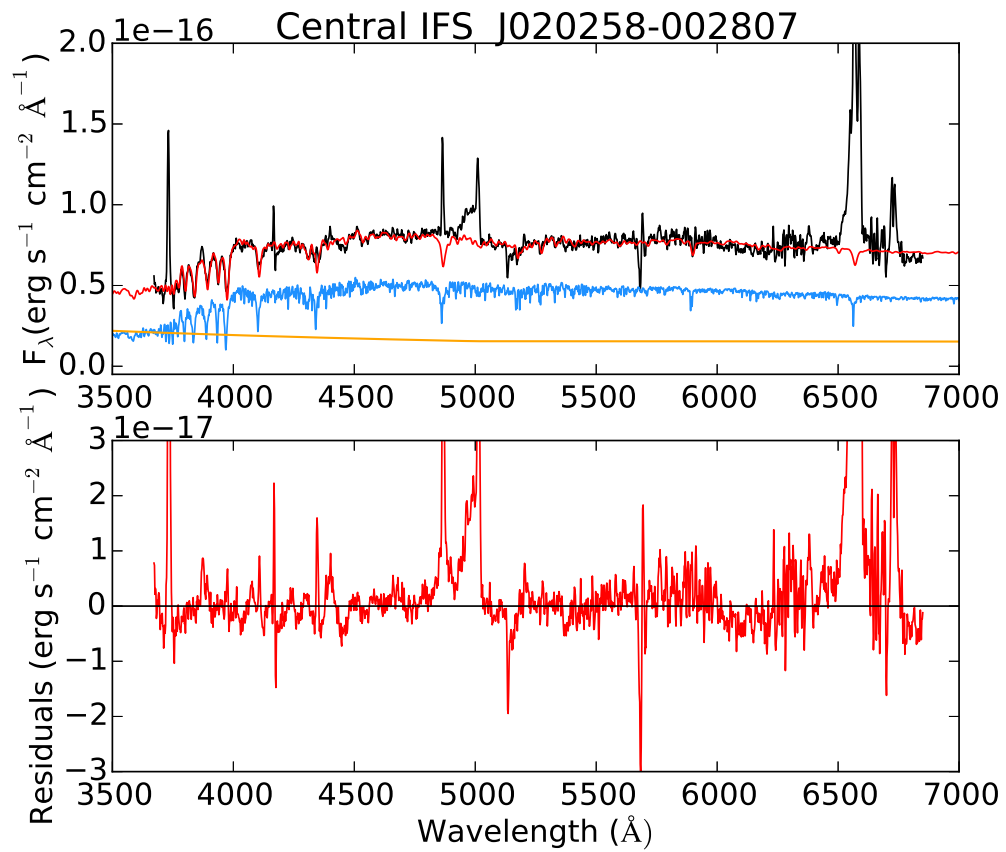


Figure A.1 Continued

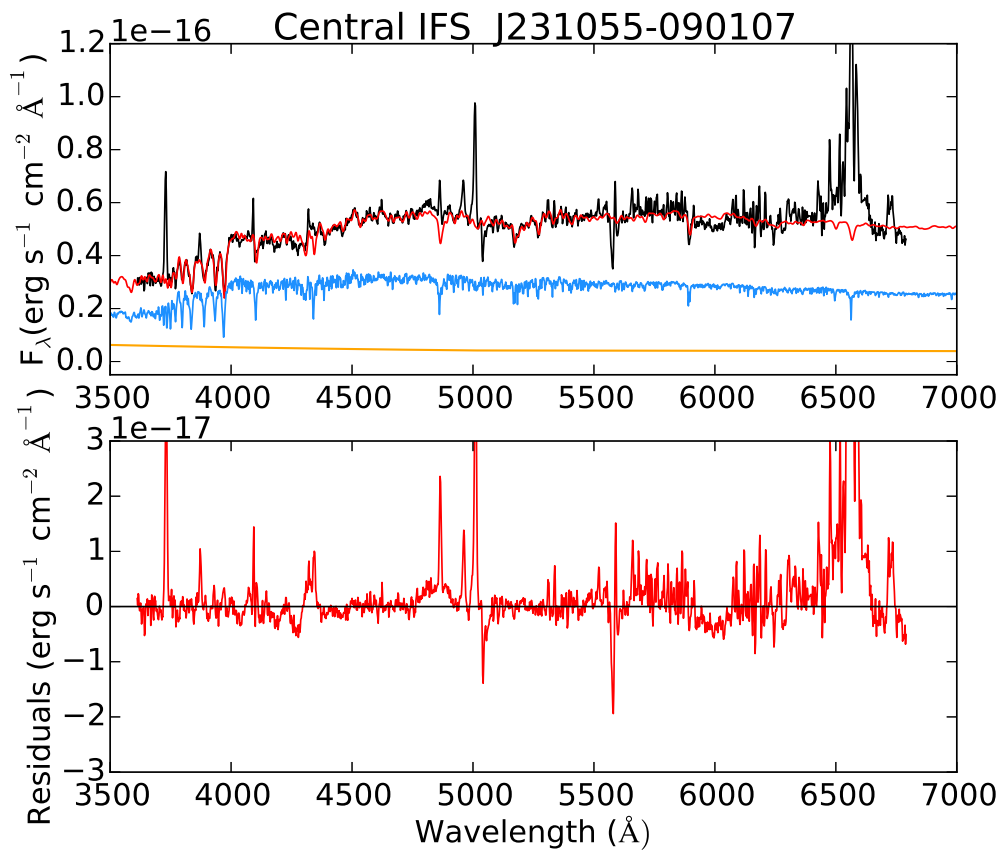


Figure A.1 Continued

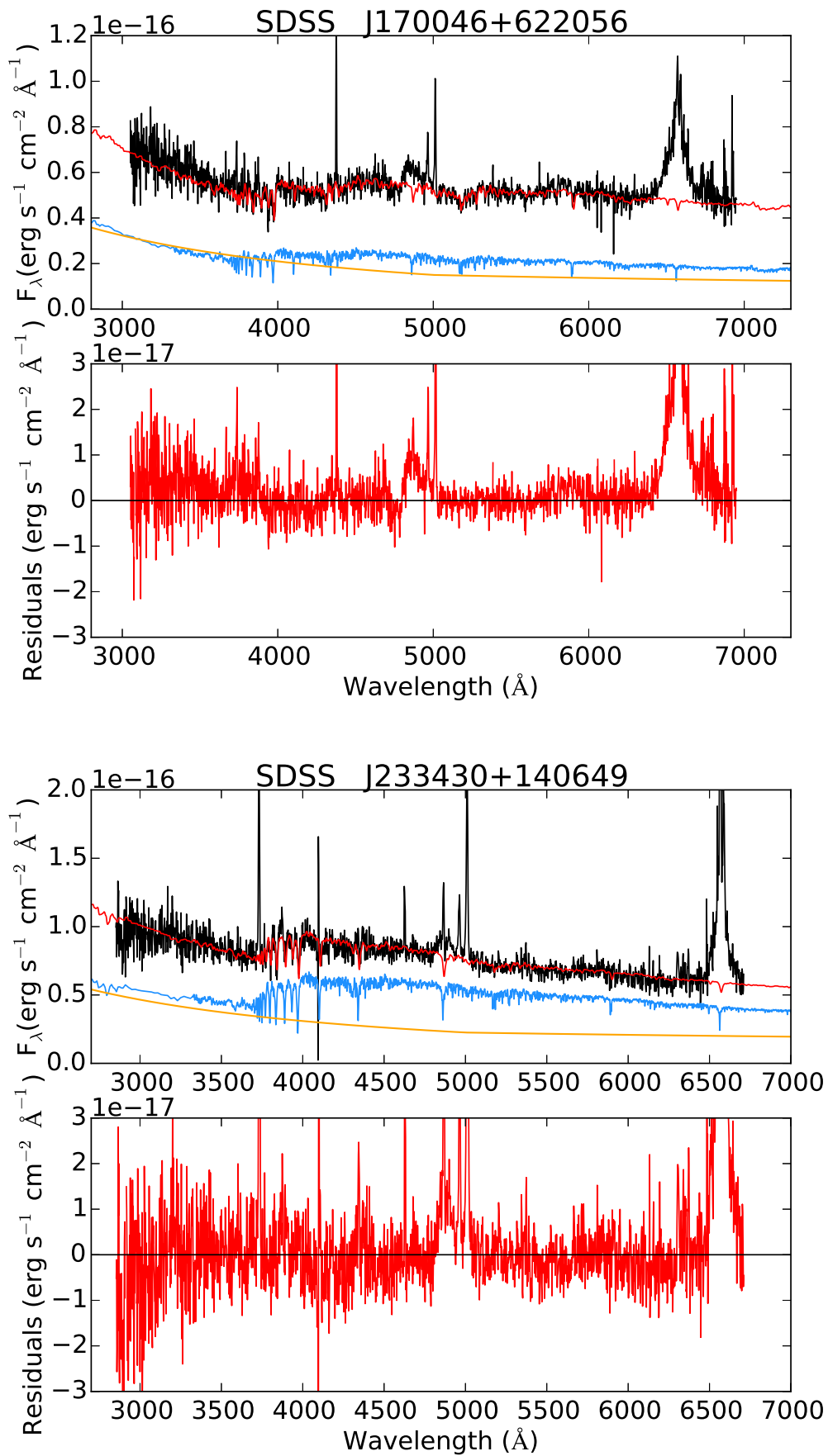


Figure A.2 Spectral fits of SDSS spectra for the base with SSPs $> 4\text{Myr}$, using $\text{H}\alpha$ constrain and a single extinction value for star and AGN. In the upper panels we show the observed spectra (in black) and the best *Starlight* fit (in red). The stellar component contribution is shown in blue and the AGN contribution in orange. In the bottom panels we show the residuals in red.

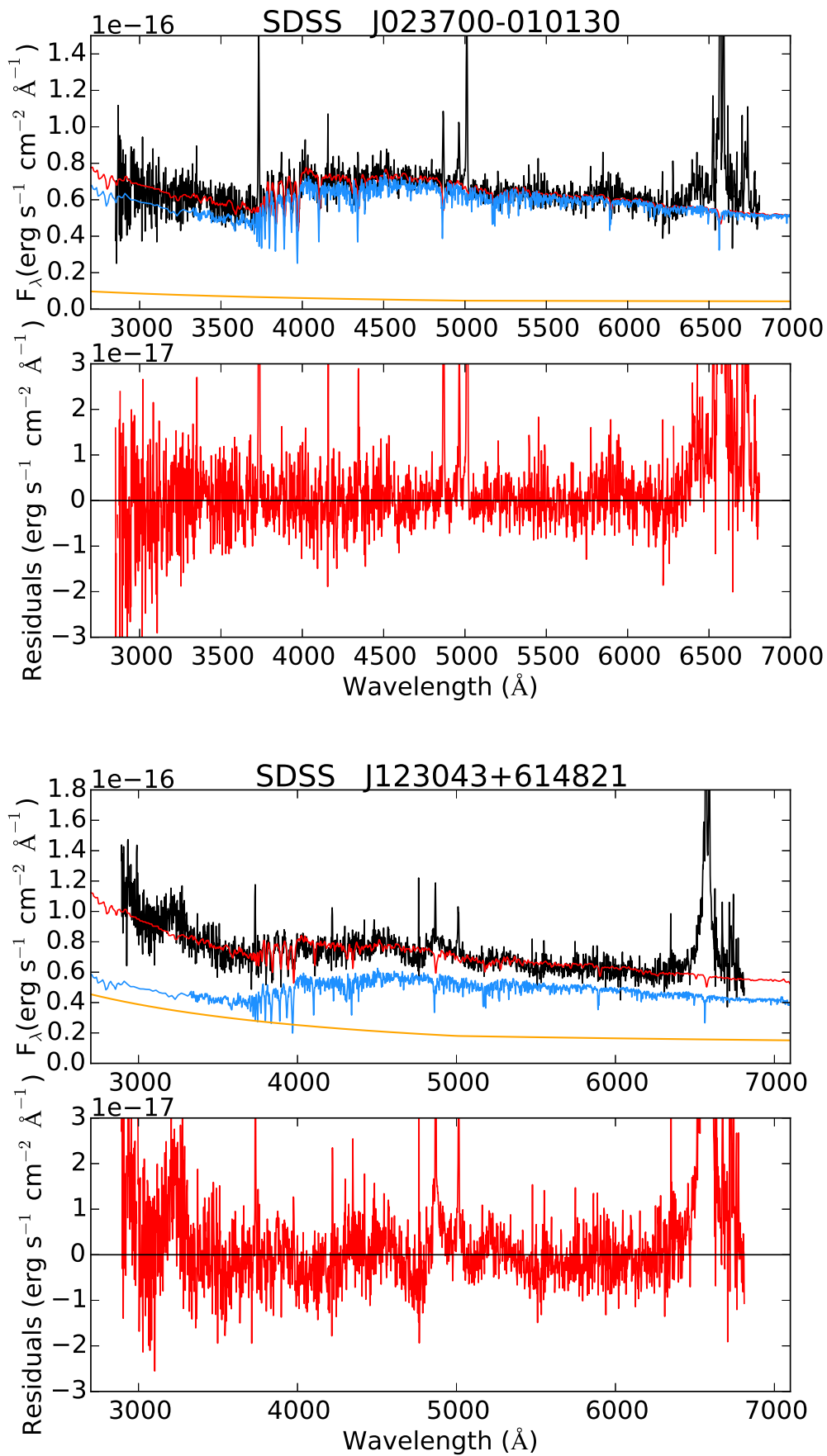


Figure A.2 Continued

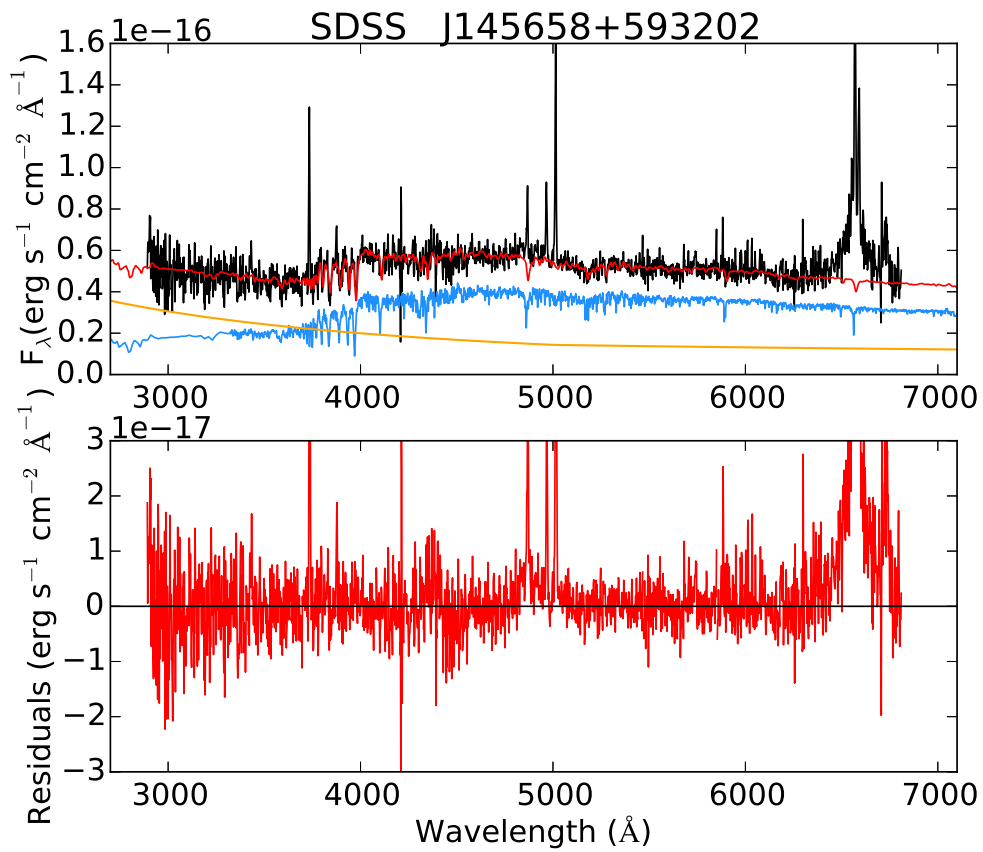
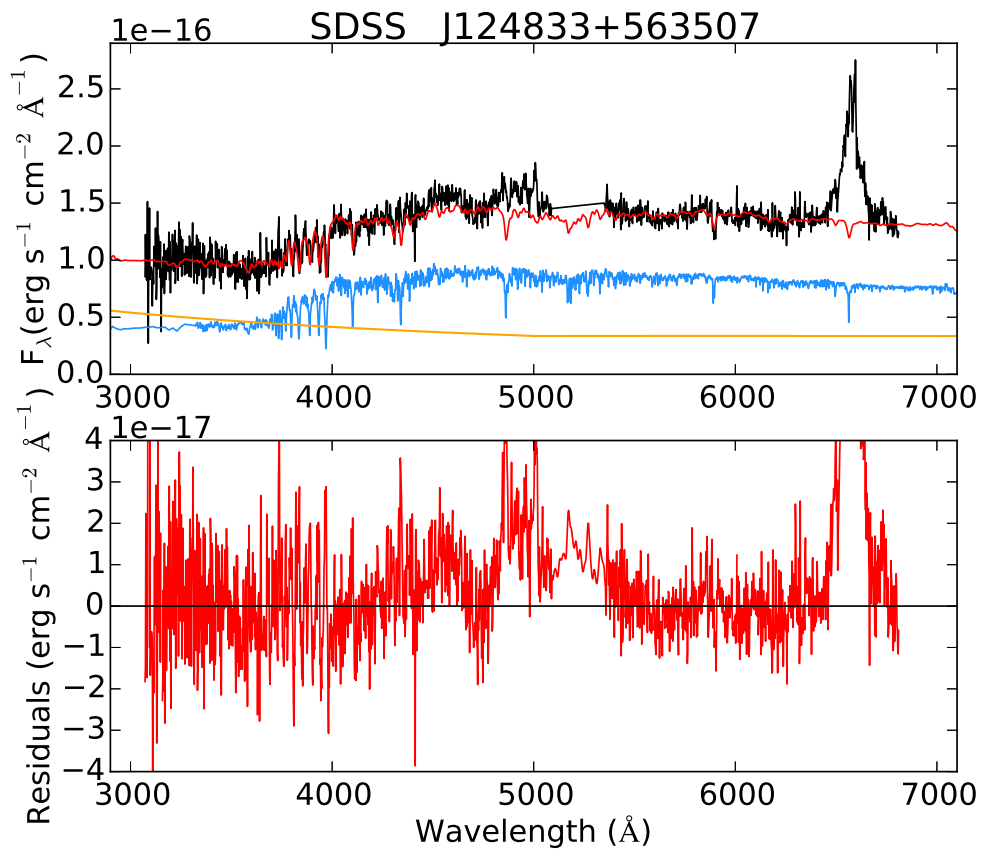


Figure A.2 Continued

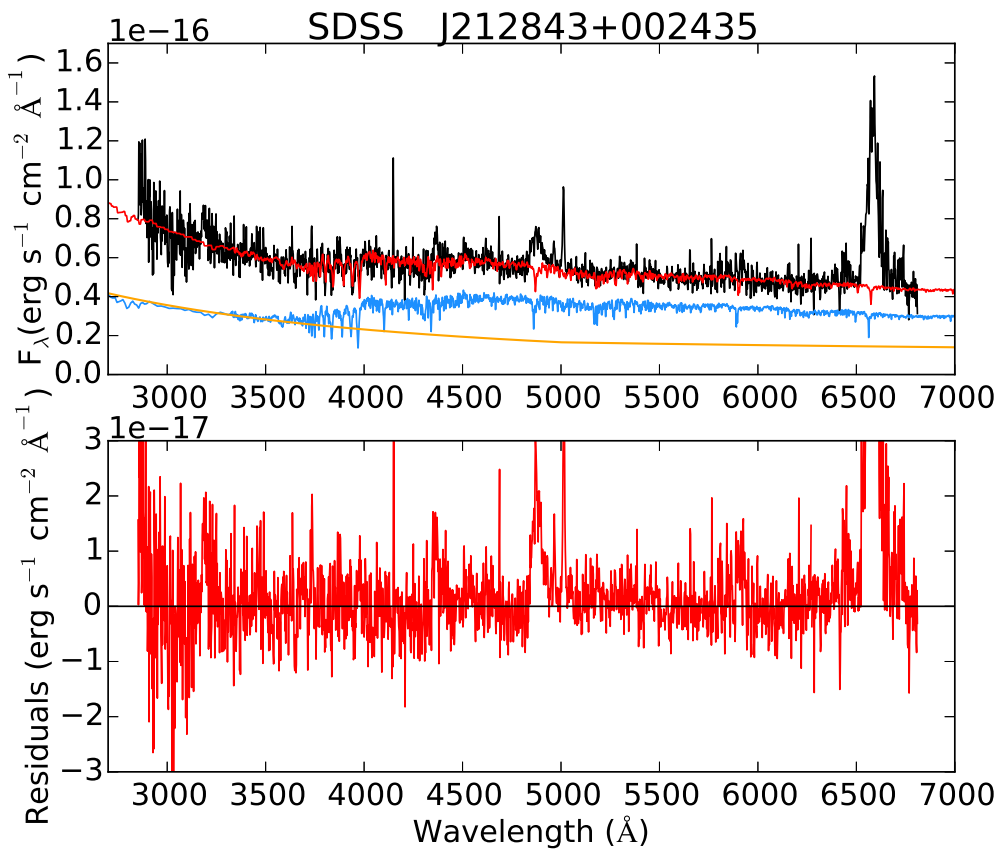
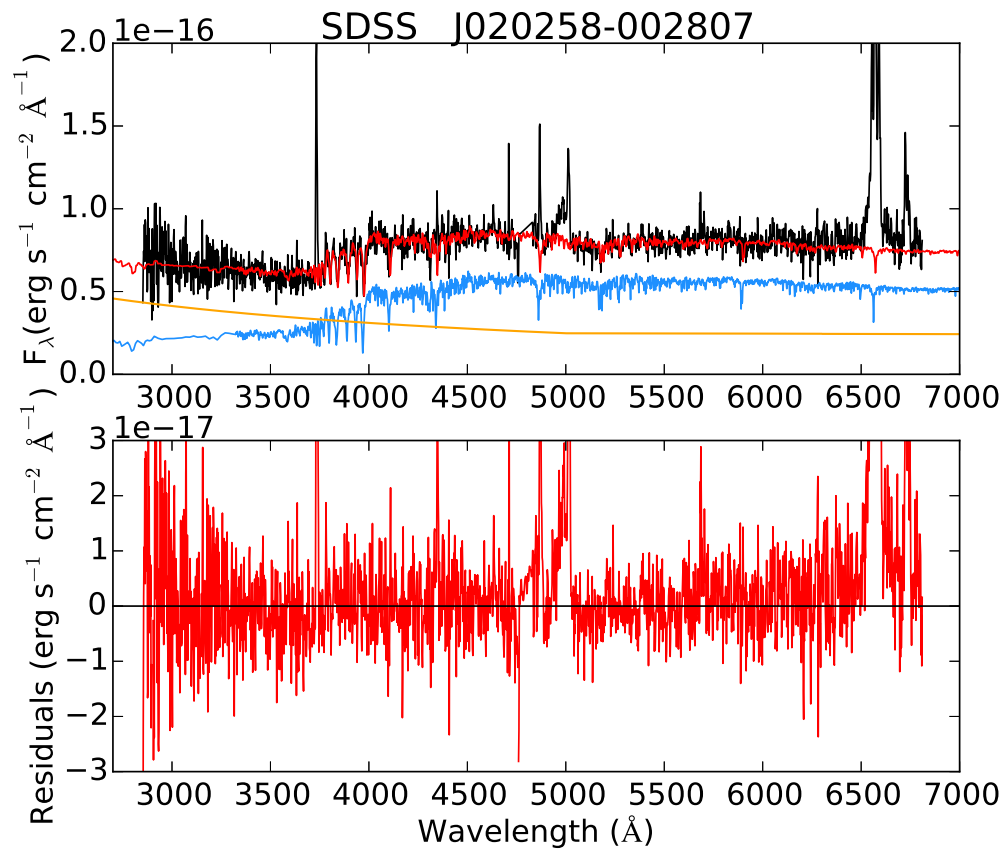


Figure A.2 Continued

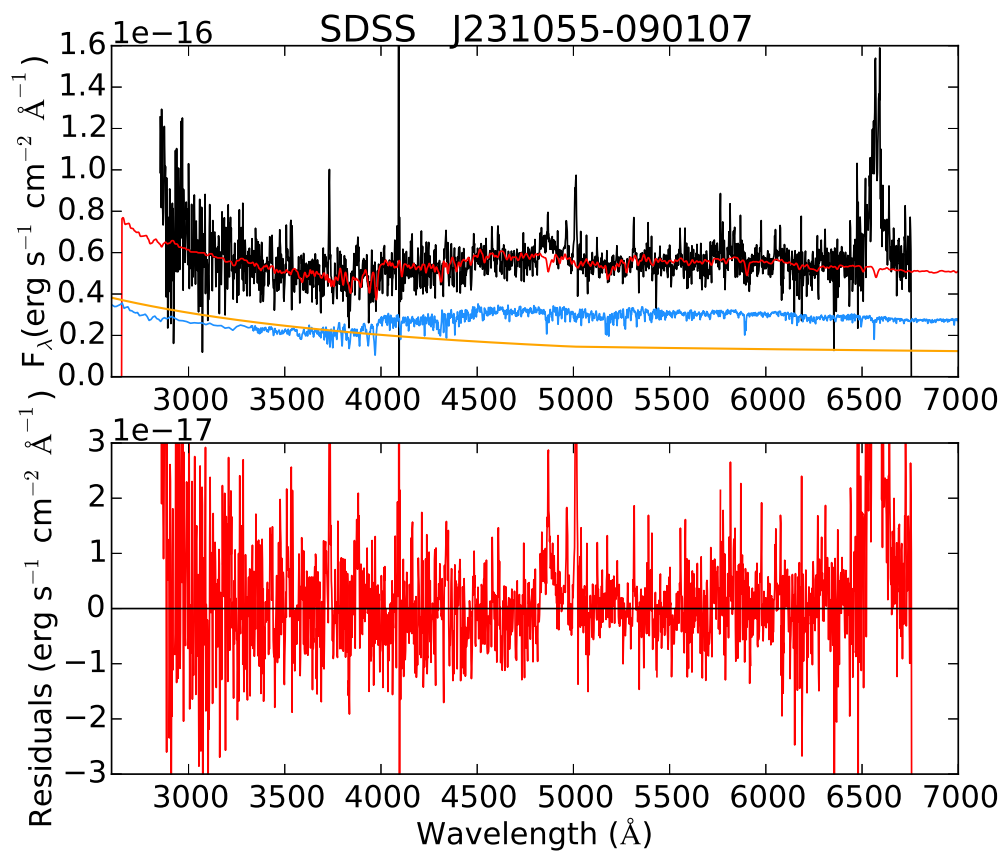


Figure A.2 Continued

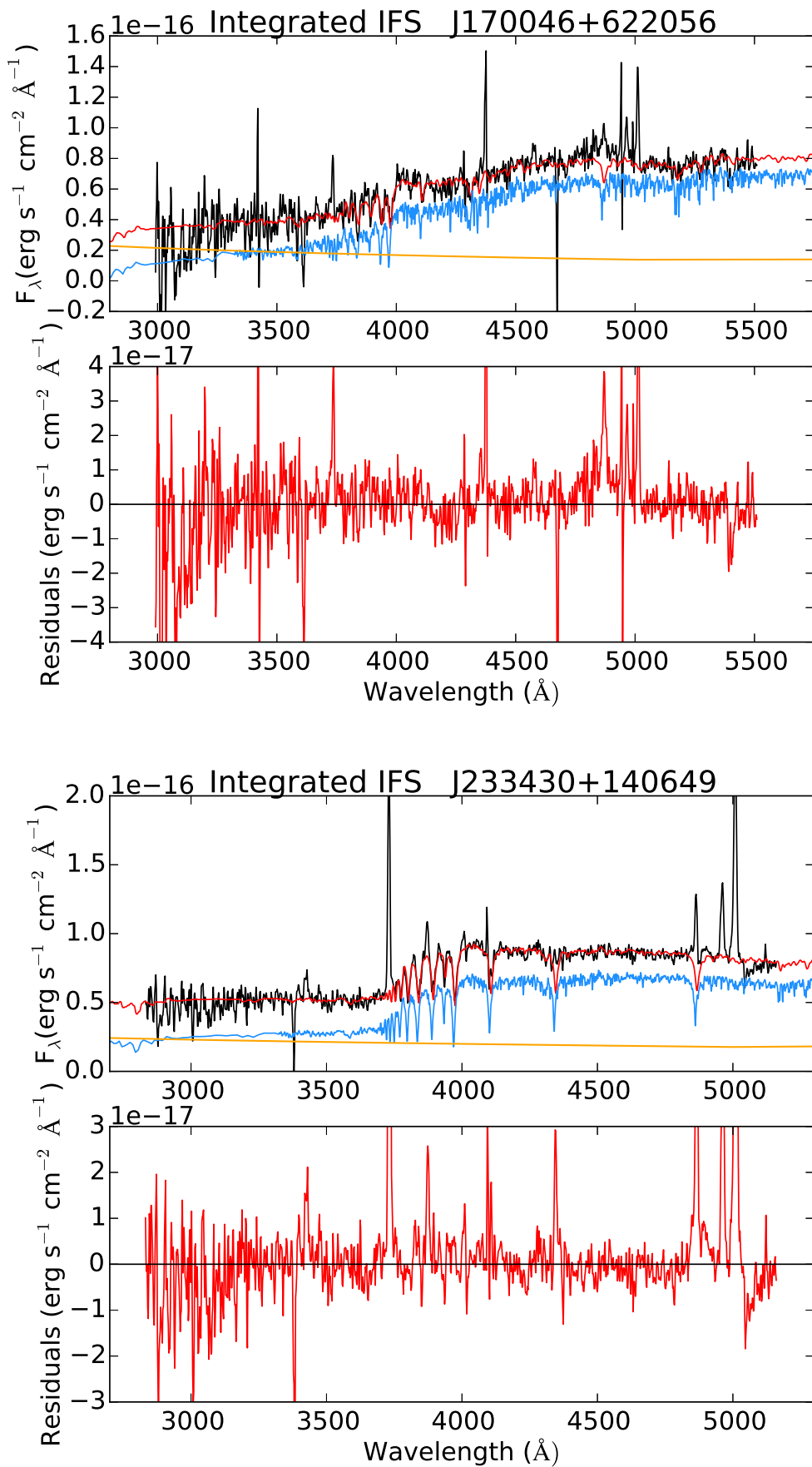


Figure A.3 Spectral fits of integrated IFS with the base with SSPs > 4Myr, using $H\beta$ constrain and a single extinction value for star and AGN. In the upper panels we show the observed spectra (in black) and the best *Starlight* fit (in red). The stellar component contribution is shown in blue and the AGN contribution in orange. In the bottom panels we show the residuals in red.

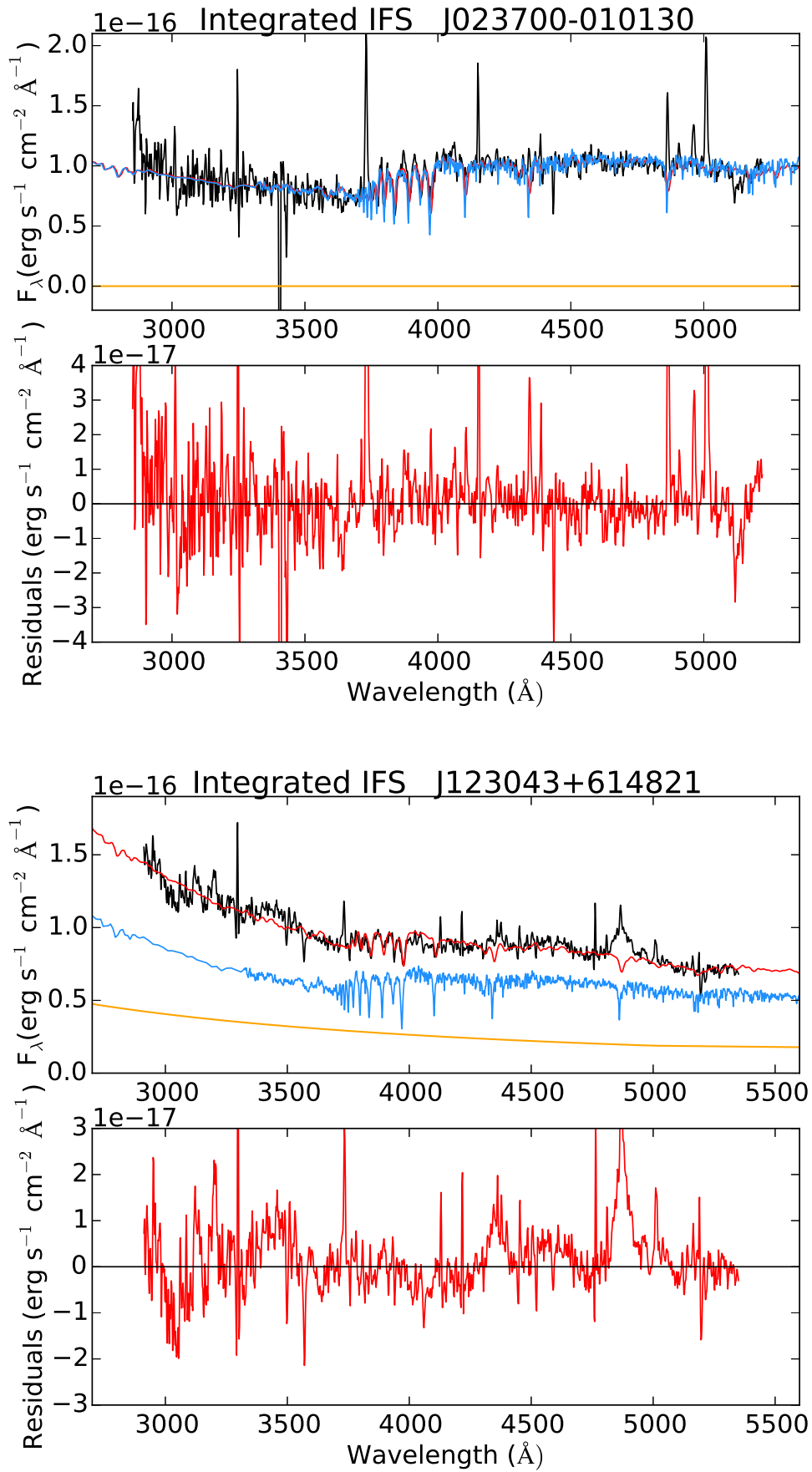


Figure A.3 Continued

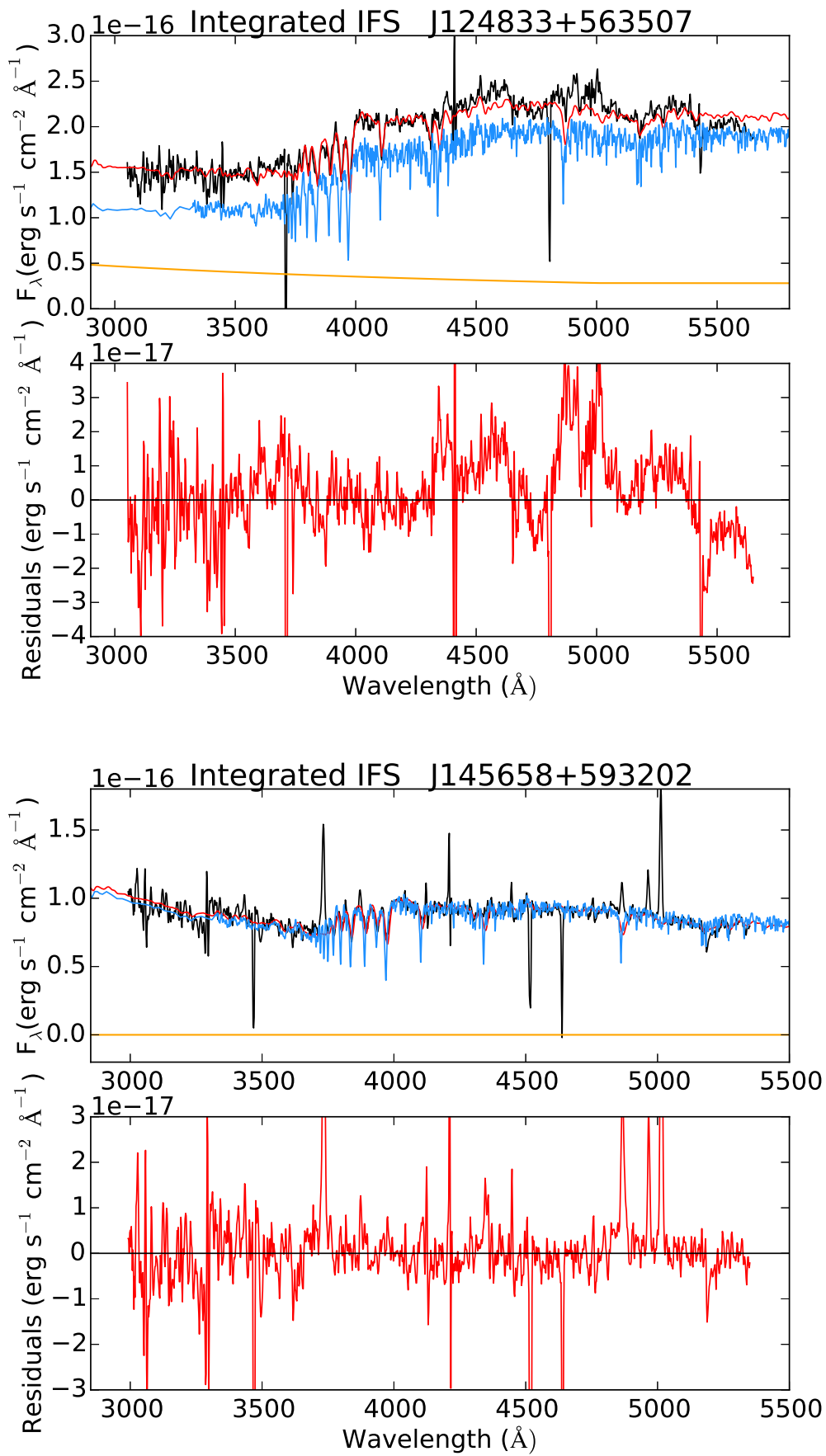


Figure A.3 Continued

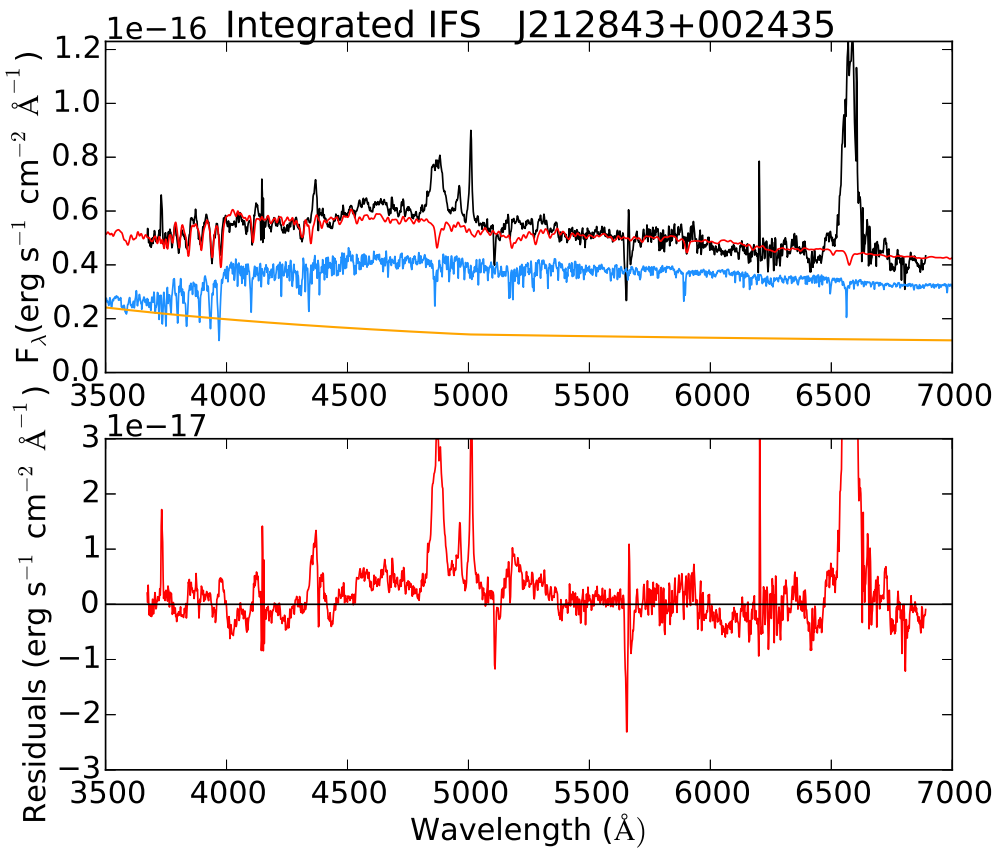
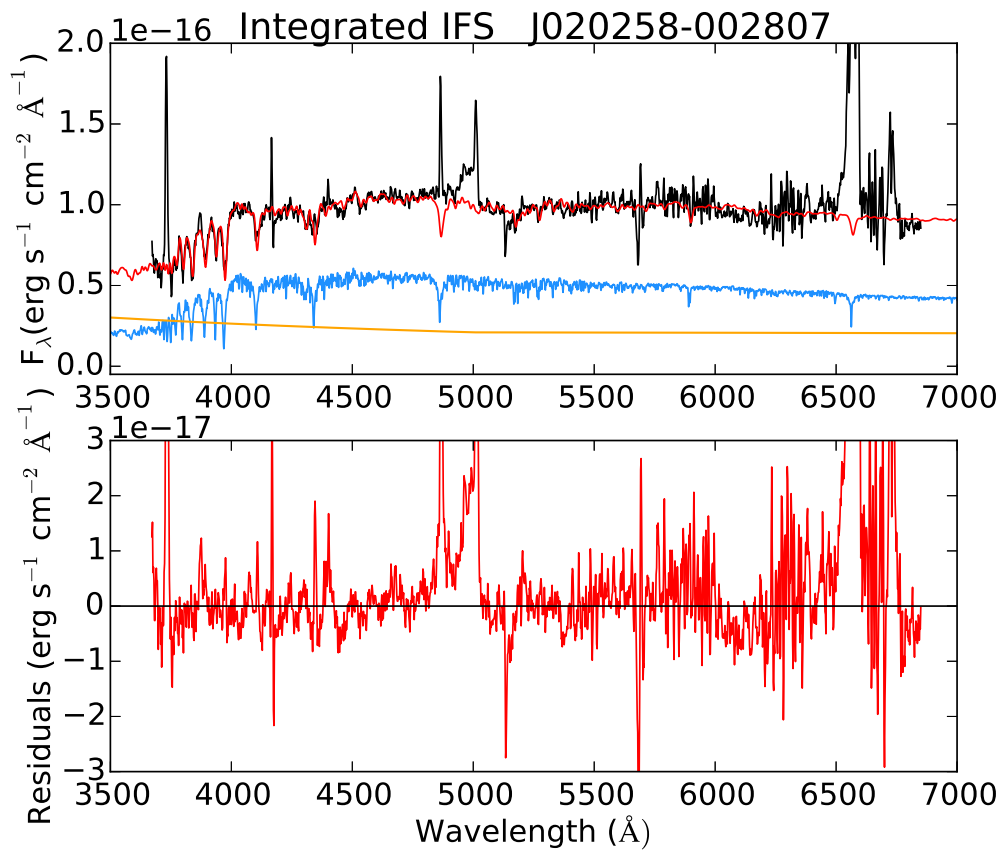


Figure A.3 Continued

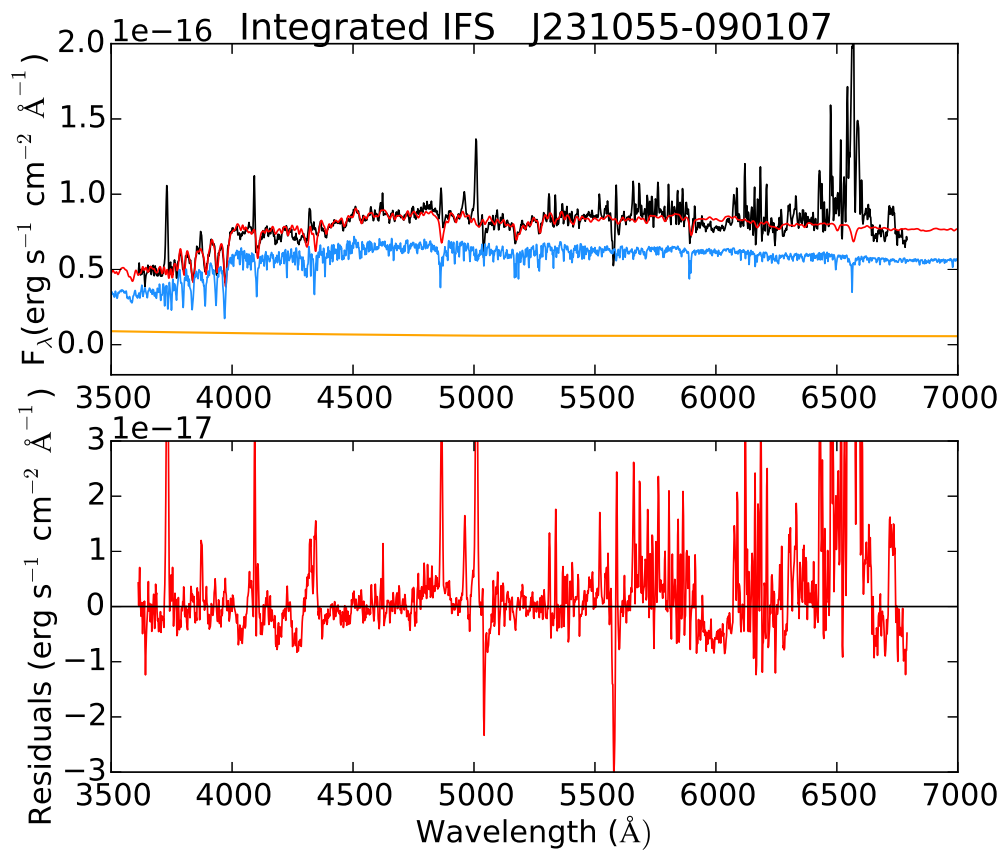


Figure A.3 Continued

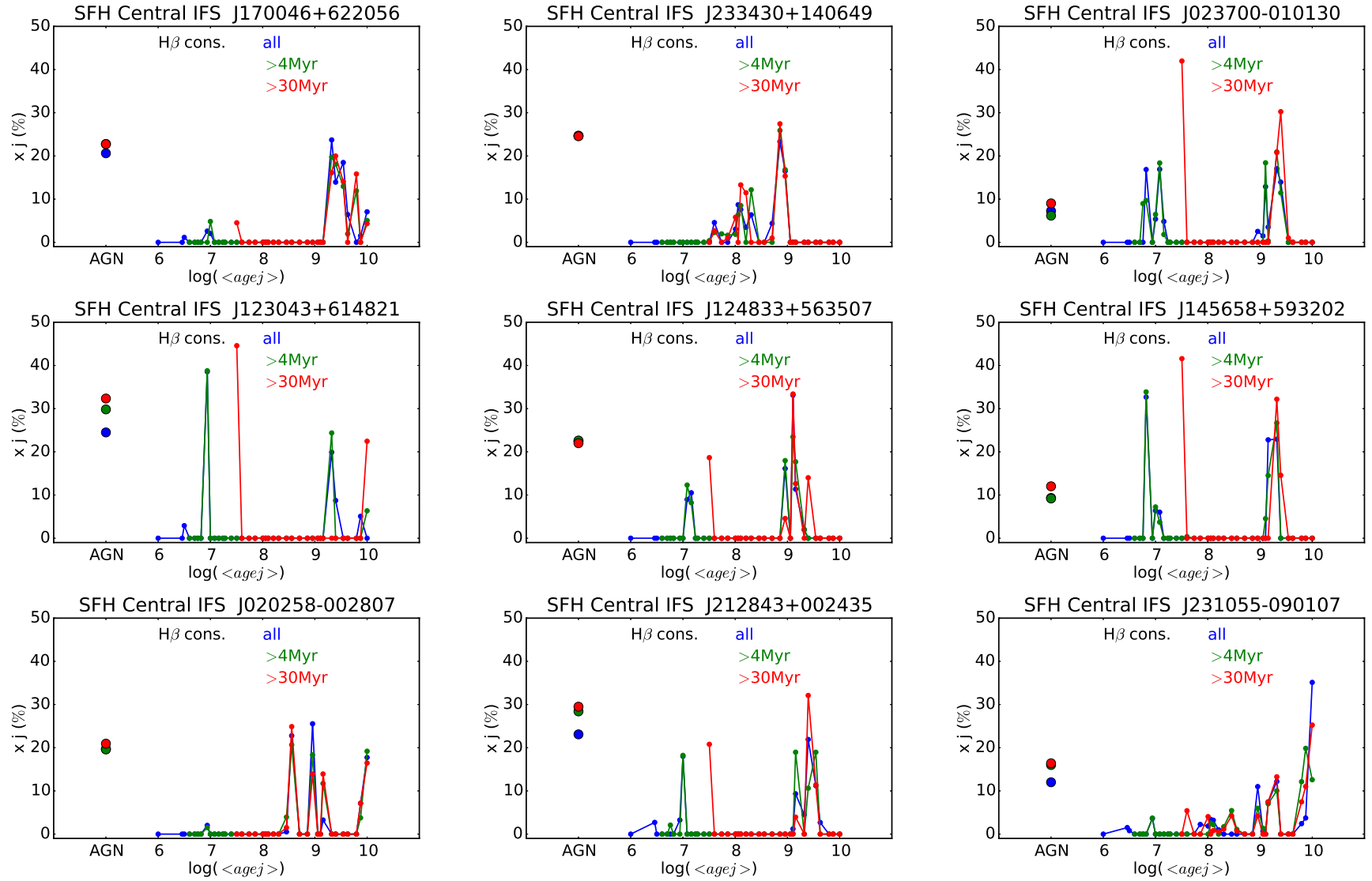


Figure A.4 Average SFHs for all the PSQSOs derived from central IFS fits with $H\beta$ constrain. The first tick in the x-axis indicate the AGN contribution, while the remaining is the logarithm of the ages of the SSPs used in the fits. The y-axis is the contribution in percentage to the total luminosity. The name of the PSQSO is indicated in the title of the figures.

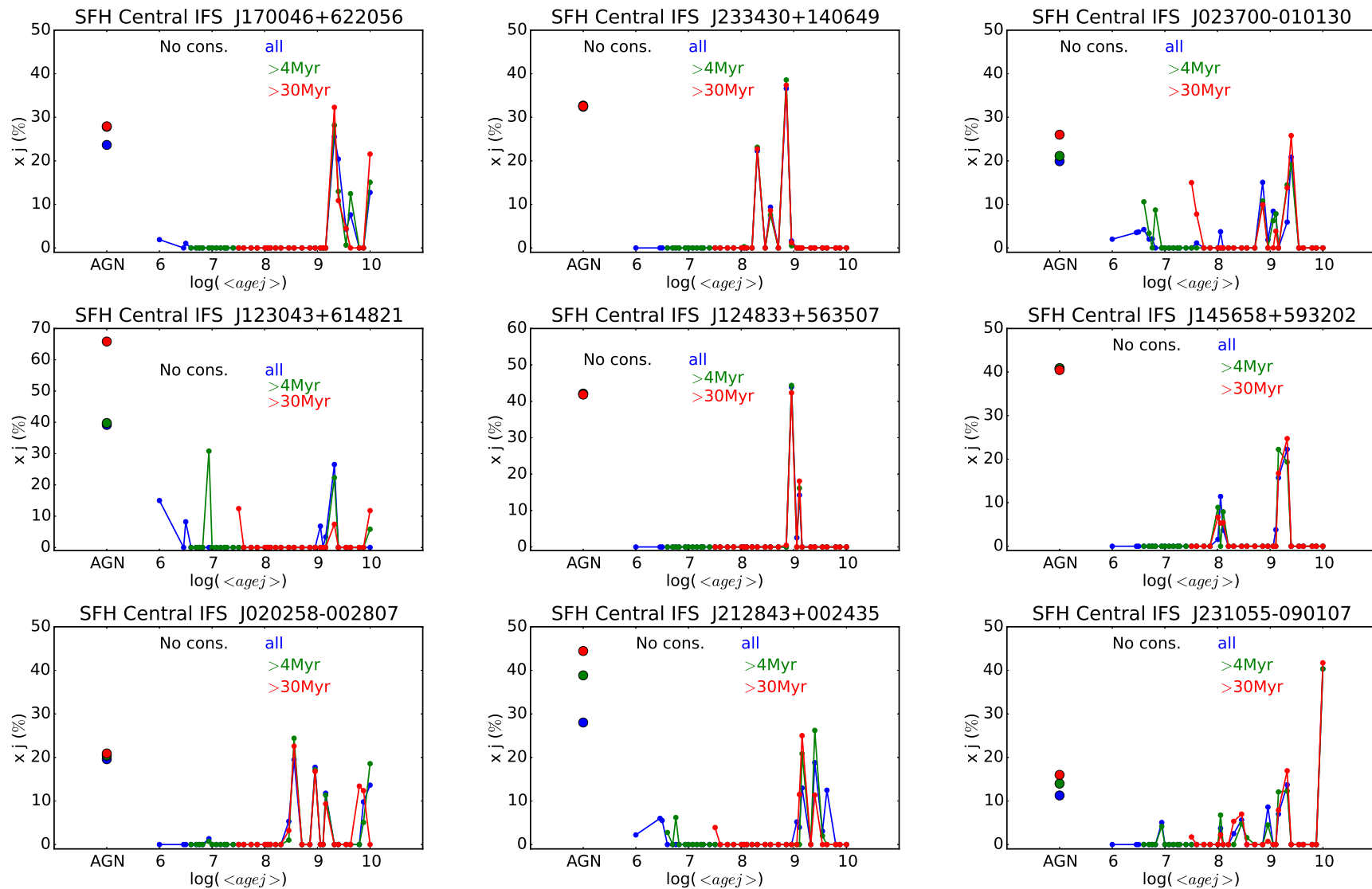


Figure A.5 Average SFHs for all the PSQSOs derived from central IFS without constrain. The first tick in the x-axis indicate the AGN contribution, while the remaining is the logarithm of the ages of the SSPs used in the fits. The y-axis is the contribution in percentage to the total luminosity. The name of the PSQSO is indicated in the title of the figures.

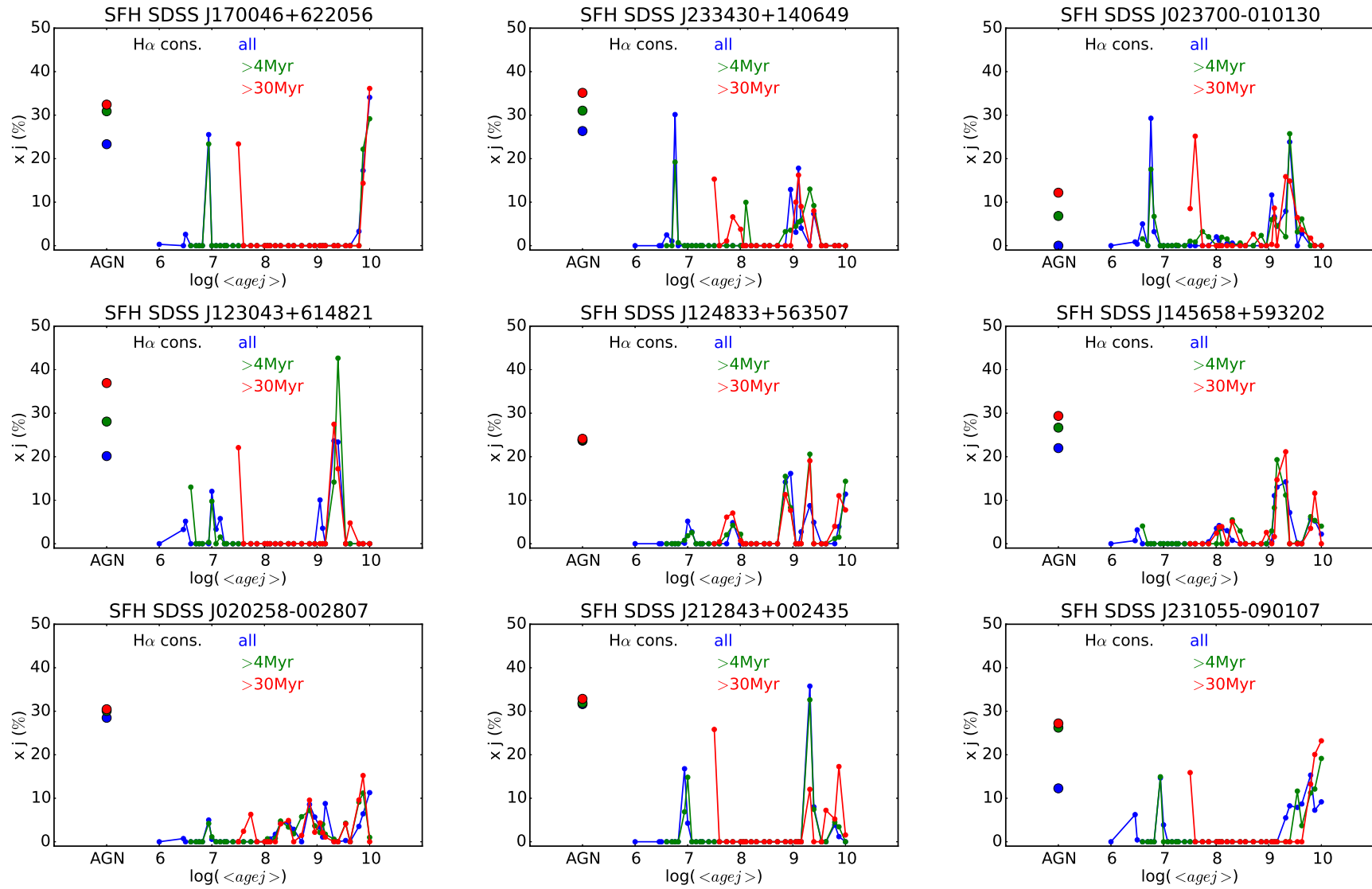


Figure A.6 Average SFHs for all the PSQSOs using SDSS spectra for the fits with H α constrain. The first tick in the x-axis indicate the AGN contribution, while the remaining is the logarithm of the ages of the SSPs used in the fits. The y-axis is the contribution in percentage to the total luminosity. The name of the PSQSO is indicated in the title of the figures.

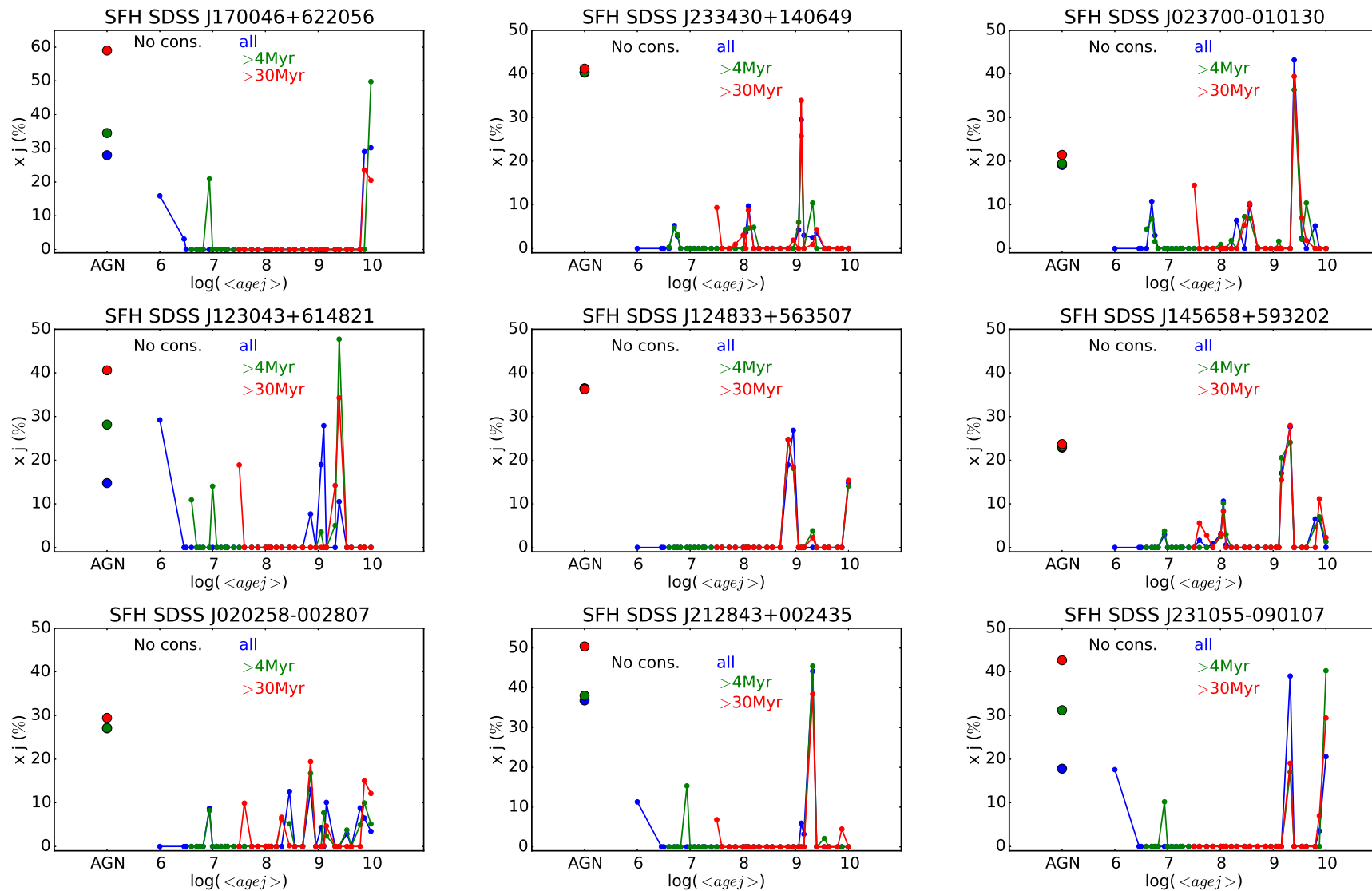


Figure A.7 Average SFHs for all the PSQSOS using SDSS spectra for the fits without constrain. The first tick in the x-axis indicate the AGN contribution, while the remaining is the logarithm of the ages of the SSPs used in the fits. The y-axis is the contribution in percentage to the total luminosity. The name of the PSQSO is indicated in the title of the figures.

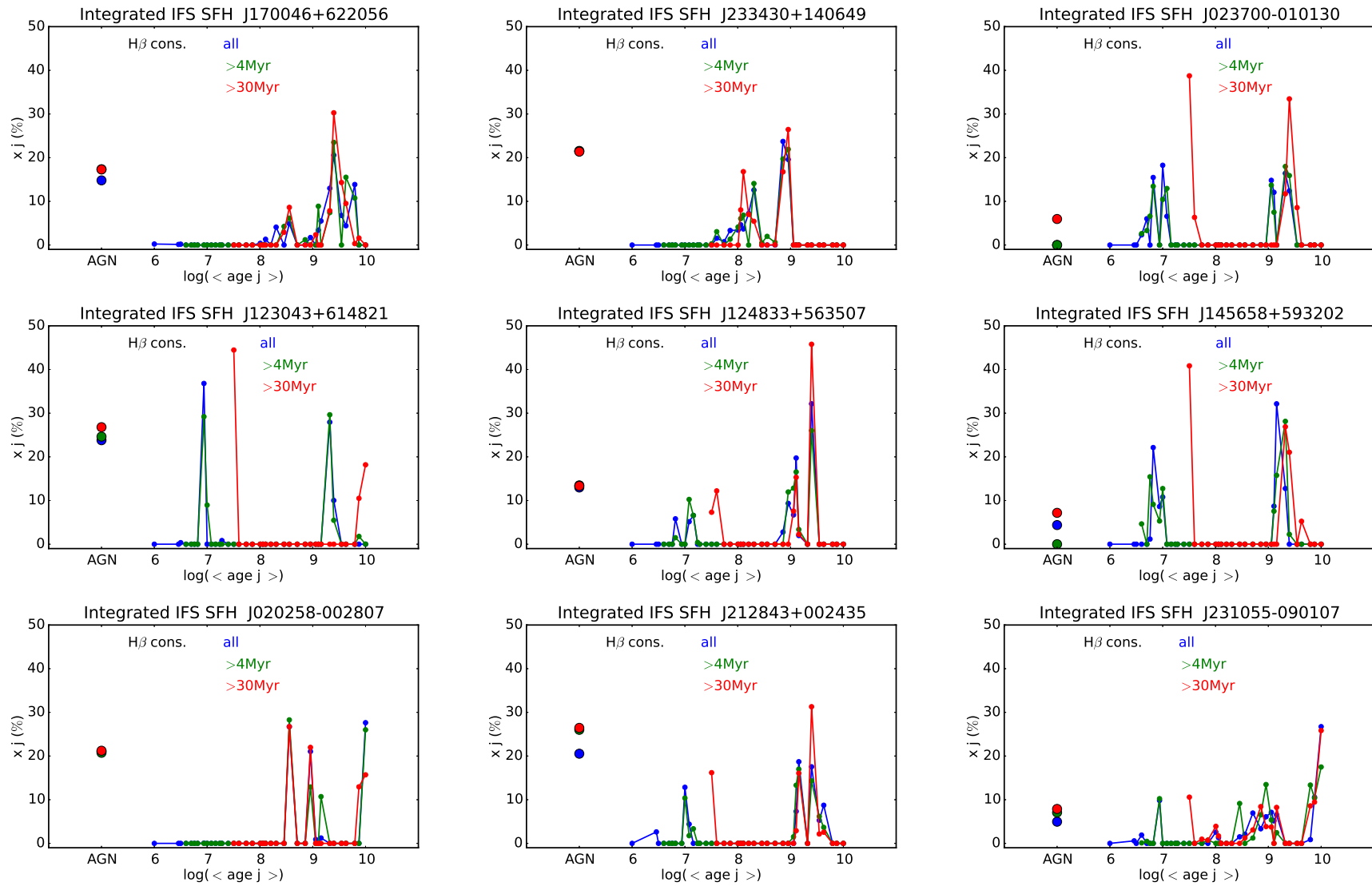


Figure A.8 Average SFH for all the PSQSOs from integrated IFS fits with $H\beta$ constrain. The first tick in the x-axis indicate the AGN contribution, while the remaining is the logarithm of the ages of the SSPs used in the fits. The y-axis is the contribution in percentage to the total luminosity. The name of the PSQSO is indicated in the title of the figures.

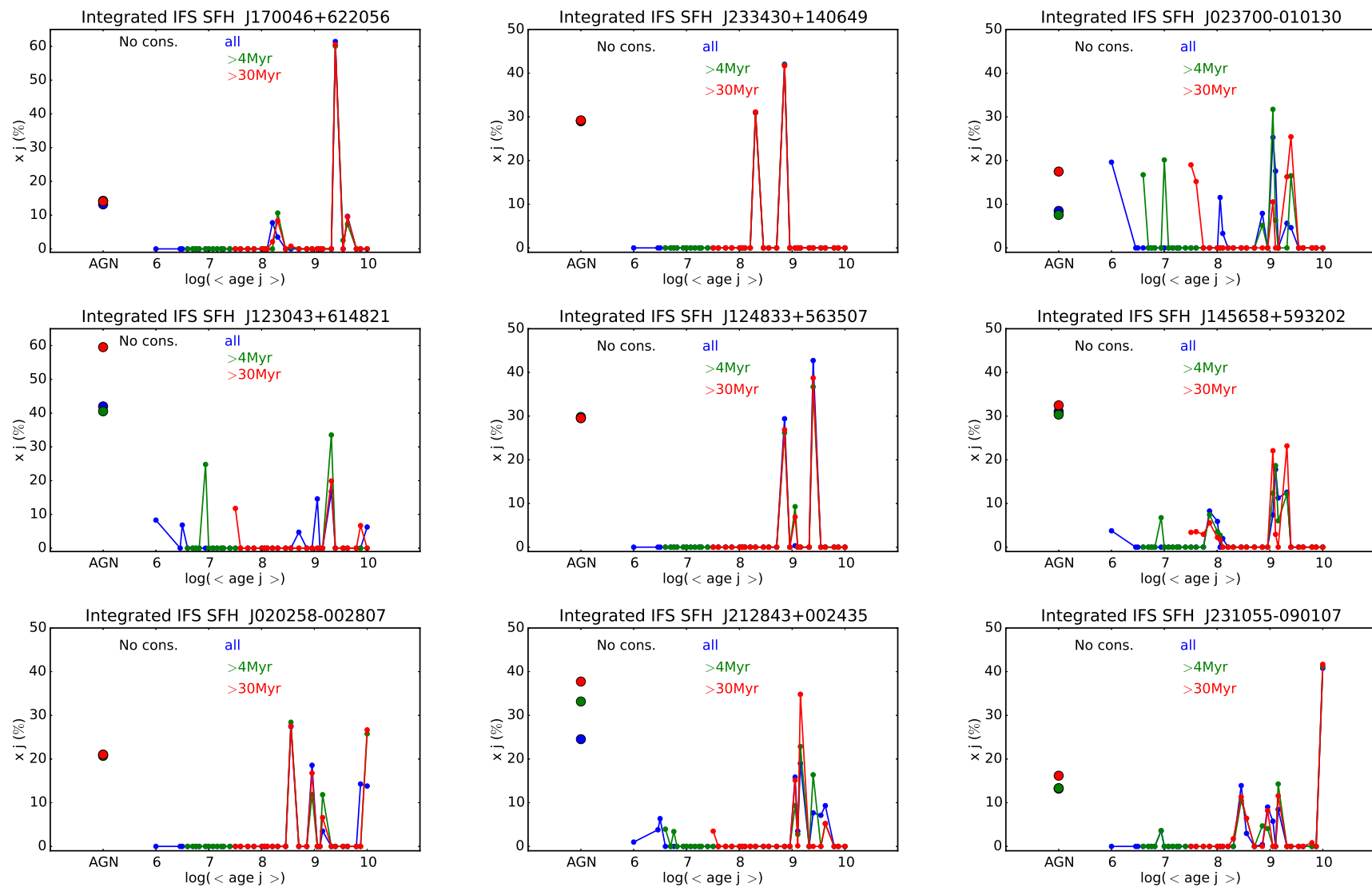


Figure A.9 Average SFH for all the PSQSOs from integrated IFS fits without constrain. The first tick in the x-axis indicate the AGN contribution, while the remaining is the logarithm of the ages of the SSPs used in the fits. The y-axis is the contribution in percentage to the total luminosity. The name of the PSQSO is indicated in the title of the figures.

B

PSQSOs: Emission line fits

In Figures B.1 and B.2 we show the the gaussian line fitting of the PSQSOs for central IFS and SDSS, respectively. In the left panels, we show the $H\beta$ region and in the right panel the $H\alpha$ region for the same PSQSO. The emission line spectra, obtained from *Starlight* residual spectra, is shown in black, the narrow components of $H\alpha$ and $H\beta$, $[\text{NII}]\lambda 6548$, $[\text{NII}]\lambda 6583$ and $[\text{OIII}]\lambda 5007$, are shown in blue, the broad components of $H\alpha$ and $H\beta$ in orange and the global fit in red dashed lines.

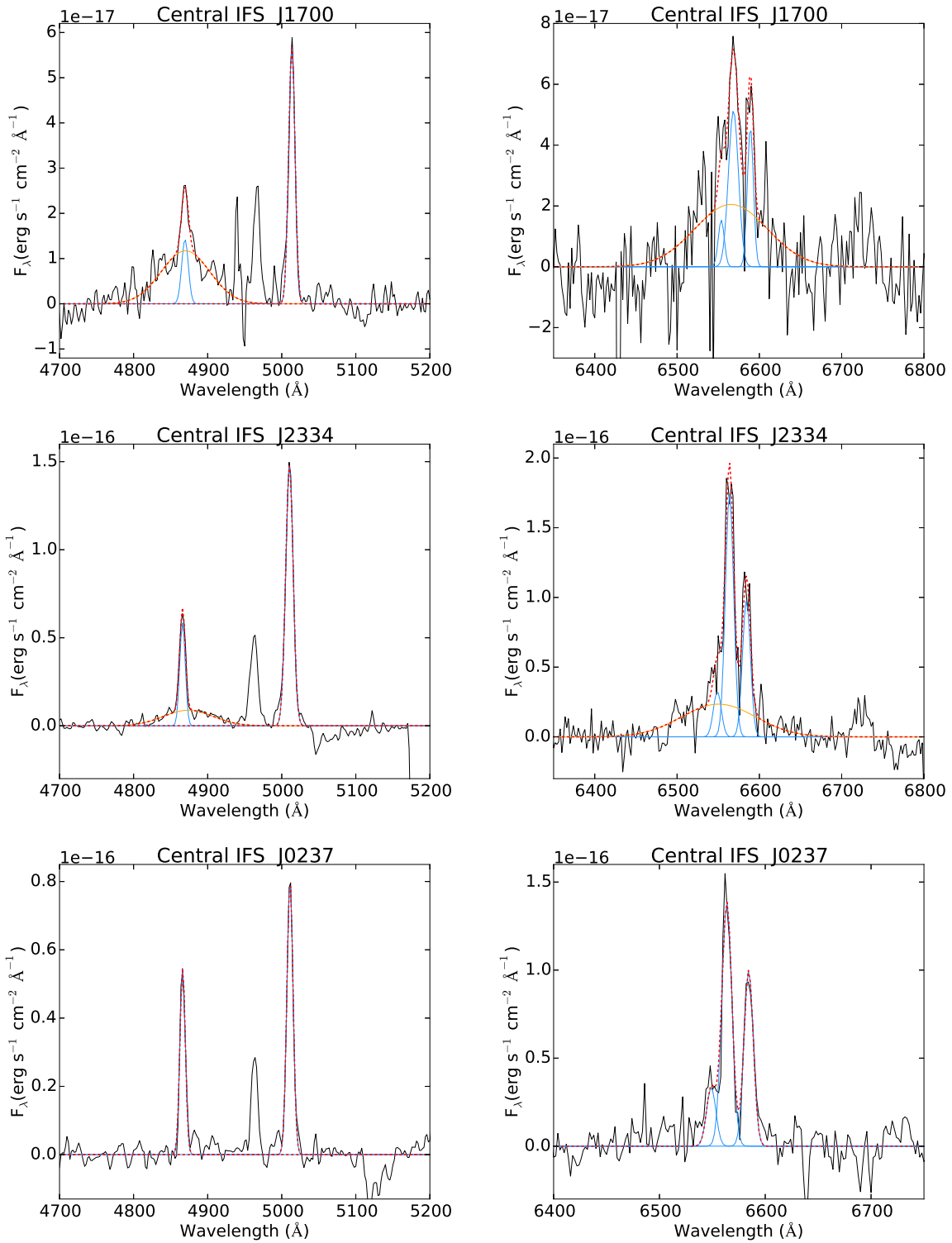


Figure B.1 Gaussian line fitting for all the PSQSOs for central IFS. In the left panels, we show the H β region, in the right panel the H α region for the same PSQSO. The emission line spectra is shown in black, the narrow components of H α and H β , [NII] λ 6548, [NII] λ 6583 and [OIII] λ 5007, are shown in blue, the broad H α and H β in orange and the global fit in red dashed lines.

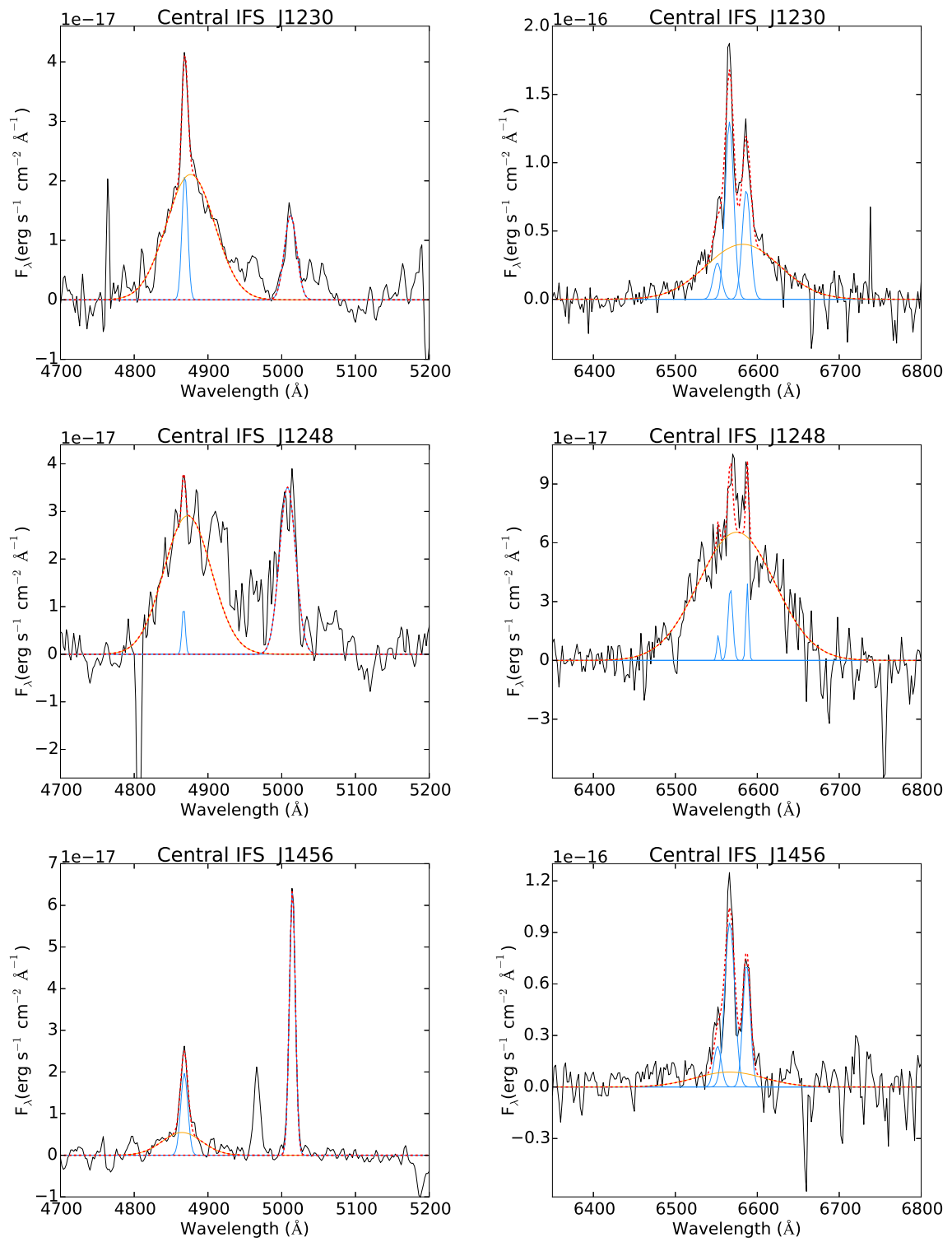


Figure B.1 Continued

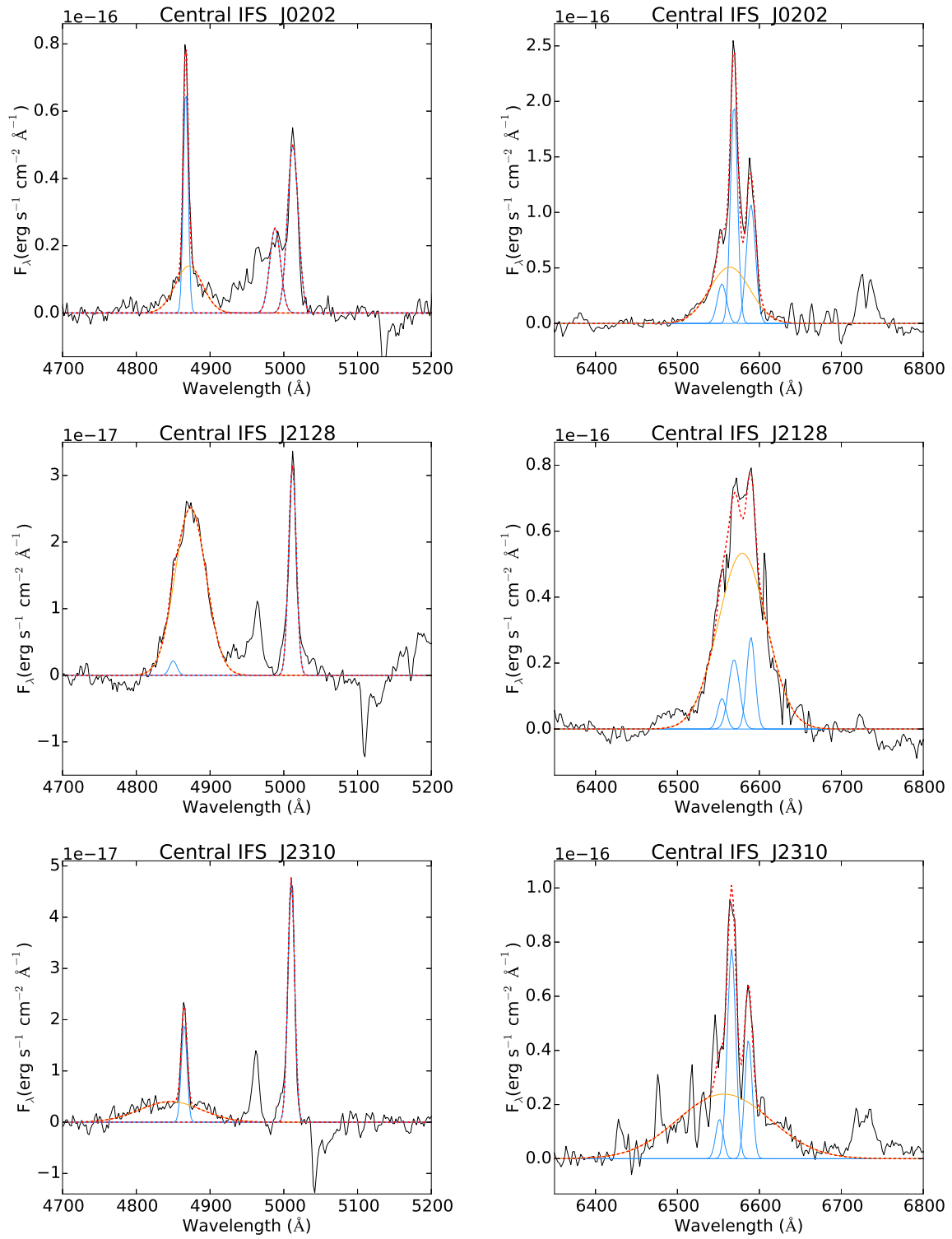


Figure B.1 Continued

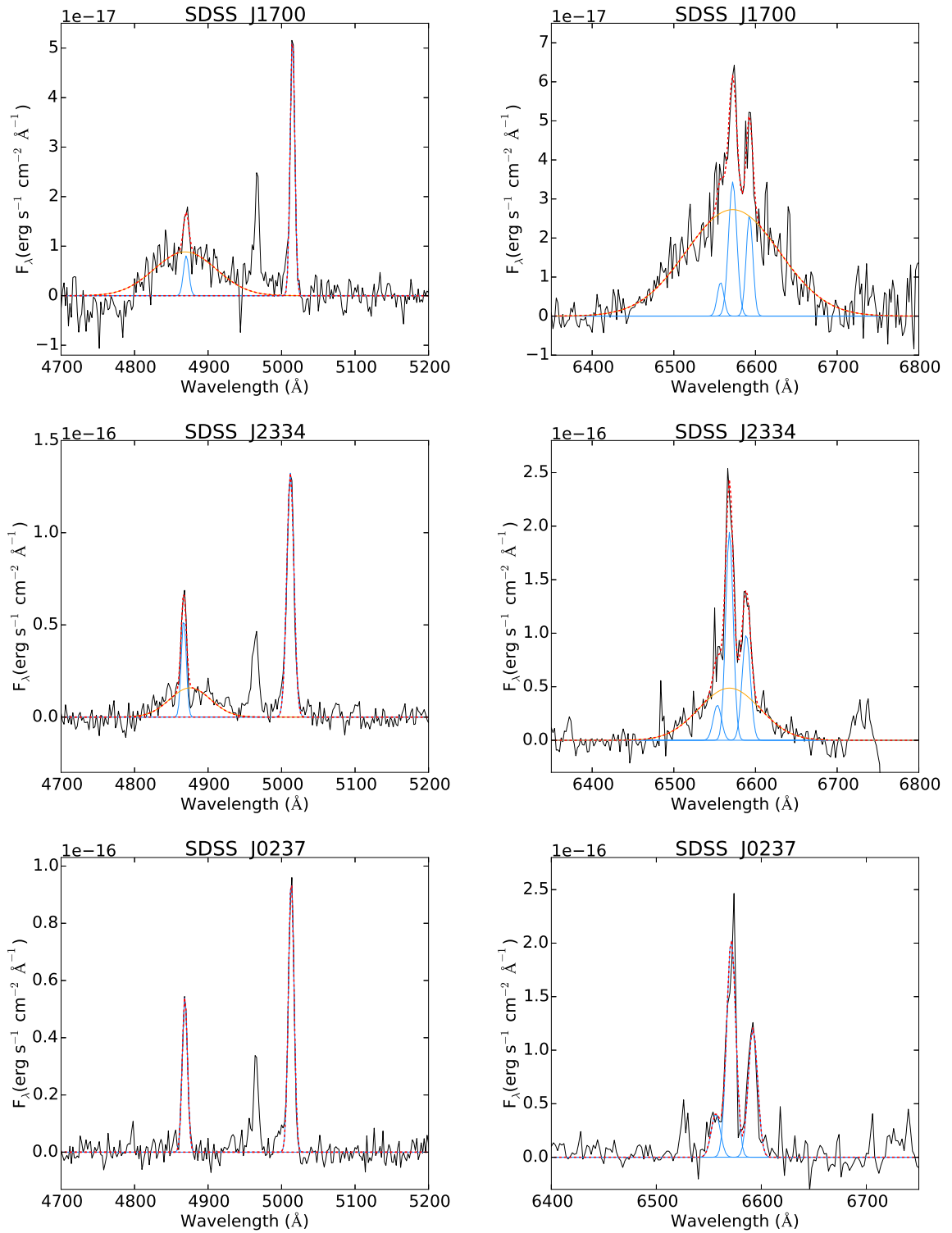


Figure B.2 Gaussian line fitting for all the PSQSOs for SDSS spectra. In the left panels, we show the H β region, in the right panel the H α region for the same PSQSO. The emission line spectra is shown in black, the narrow components of H α and H β , [NII] λ 6548, [NII] λ 6583 and [OIII] λ 5007, are shown in blue, the broad H α and H β in orange and the global fit in red dashed lines.

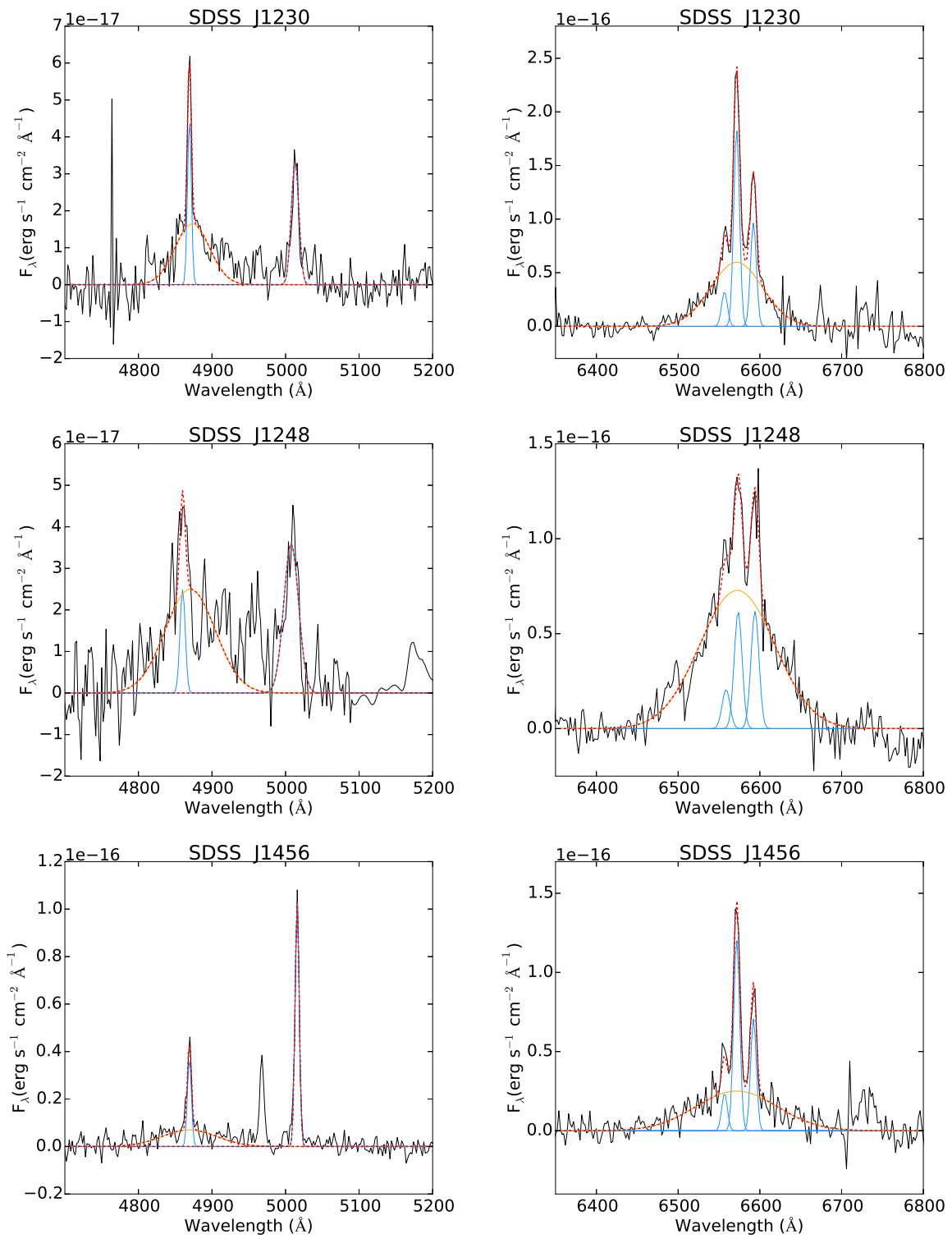


Figure B.2 Continued

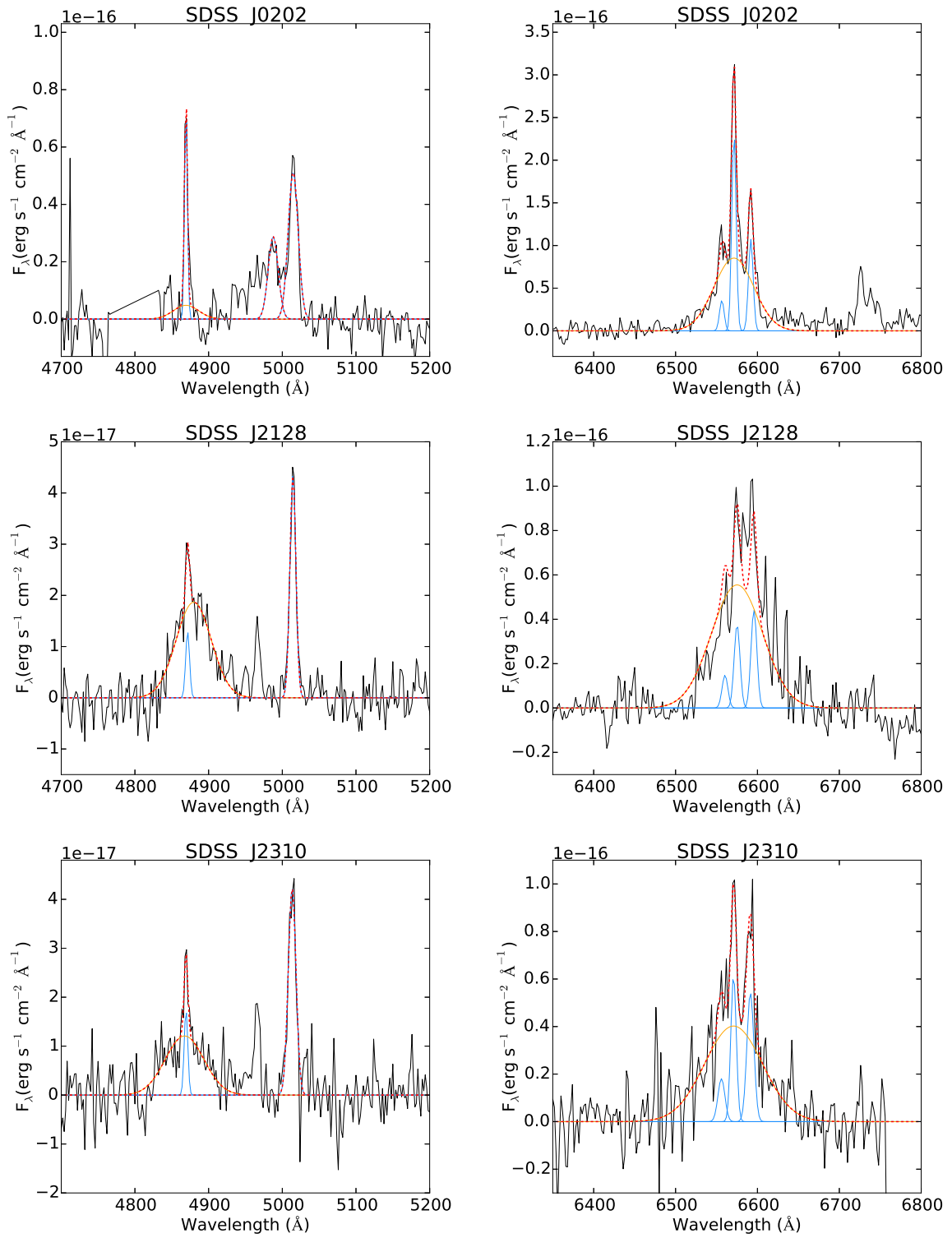


Figure B.2 Continued

Bibliography

- Aird, J., Nandra, K., Laird, E. S., et al. 2010, MNRAS, 401, 2531
- Alexander, D. M., & Hickox, R. C. 2012, , 56, 93
- Allington-Smith, J. R. 2007, Revista Mexicana de Astronomia y Astrofisica Conference Series, 28, 17
- Alonso-Herrero, A., Rieke, G. H., Rieke, M. J., et al. 2006, ApJ, 650, 835
- Alonso-Herrero, A., Pereira-Santaella, M., Rieke, G. H., & Rigopoulou, D. 2012, ApJ, 744, 2
- Alvensleben, U. F. 2004, The Formation and Evolution of Massive Young Star Clusters, 322, 91
- Antonucci, R. 1993, ARA&A, 31, 473
- Armus, L., Heckman, T. M., & Miley, G. K. 1989, ApJ, 347, 727
- Armus, L., Mazzarella, J. M., Evans, A. S., et al. 2009, PASP, 121, 559
- Arnouts, S., Walcher, C. J., Le Fèvre, O., et al. 2007, A&A, 476, 137
- Arribas, S., Bushouse, H., Lucas, R. A., Colina, L., & Borne, K. D. 2004, AJ, 127, 2522
- Arribas, S., Colina, L., Alonso-Herrero, A., et al. 2012, A&A, 541, A20
- Bahcall, J.Ñ., Kirhakos, S., Saxe, D. H., & Schneider, D. P. 1997, ApJ, 479, 642
- Baldry, I. K., Glazebrook, K., Brinkmann, J., et al. 2004, ApJ, 600, 681
- Baldry, I. K., Balogh, M. L., Bower, R. G., et al. 2006, MNRAS, 373, 469
- Baldwin, J. A., Phillips, M. M., & Terlevich, R. 1981, PASP, 93, 5
- Barnes, J. E., & Hernquist, L. E. 1991, ApJ, 370, L65
- Barnes, J. E., & Hernquist, L. 1992, Nature, 360, 715
- Barnes, J. E. 2004, MNRAS, 350, 798
- Barrera-Ballesteros, J. K., García-Lorenzo, B., Falcón-Barroso, J., et al. 2015, A&A, 582, A21
- Bastian, N., Emsellem, E., Kissler-Patig, M., & Maraston, C. 2006, A&A, 445, 471

- Bastian, N., Saglia, R. P., Goudfrooij, P., et al. 2006, *A&A*, 448, 881
- Bastian, N., Covey, K. R., & Meyer, M. R. 2010, *ARA&A*, 48, 339
- Bekki, K., Couch, W. J., Shioya, Y., & Vazdekis, A. 2005, *MNRAS*, 359, 949
- Bell, E. F., Zheng, X. Z., Papovich, C., et al. 2007, *ApJ*, 663, 834
- Bellochi, E., Arribas, S., Colina, L., & Miralles-Caballero, D. 2013, *A&A*, 557, A59
- Bender, R., Doebereiner, S., & Moellenhoff, C. 1988, *A&AS*, 74, 385
- Bennert, N., Canalizo, G., Jungwiert, B., et al. 2008, *ApJ*, 677, 846
- Benson, A. J., Bower, R. G., Frenk, C. S., et al. 2003, *ApJ*, 599, 38
- Bernloehr, K. 1993, *A&A*, 268, 25
- Bessiere, P. S., Tadhunter, C.Ñ., Ramos Almeida, C., & Villar Martín, M. 2014, *MNRAS*, 438, 1839
- Béthermin, M., Dole, H., Lagache, G., Le Borgne, D., & Penin, A. 2011, *A&A*, 529, A4
- Bica, E., Arimoto, N., & Alloin, D. 1988, *A&A*, 202, 8
- Blandford, R. D., & McKee, C. F. 1982, *ApJ*, 255, 419
- Bournaud, F., Duc, P.-A., Amram, P., Combes, F., & Gach, J.-L. 2004, *A&A*, 425, 813
- Bournaud, F., Elmegreen, B. G., Teyssier, R., Block, D. L., & Puerari, I. 2010, *MNRAS*, 409, 1088
- Bower, R. G., McCarthy, I. G., & Benson, A. J. 2008, *MNRAS*, 390, 1399
- Brammer, G. B., Whitaker, K. E., van Dokkum, P. G., et al. 2009, *ApJ*, 706, L173
- Brotherton, M. S., van Breugel, W., Stanford, S. A., et al. 1999, *ApJ*, 520, L87
- Brotherton, M. S., Grabelsky, M., Canalizo, G., et al. 2002, *PASP*, 114, 593
- Brotherton, M. S., Stoll, R., Paul, C., et al. 2007, *Bulletin of the American Astronomical Society*, 39, 95
- Brotherton, M. S., Cales, S., Ganguly, R., Shang, Z., & Canalizo, G. 2008, *Bulletin of the American Astronomical Society*, 40, 217
- Bruzual, G., & Charlot, S. 2003, *MNRAS*, 344, 1000
- Bryant, P. M., & Scoville, N. Z. 1999, *AJ*, 117, 2632
- Burkert, A. 2006, *Comptes Rendus Physique*, 7, 433
- Cales, S. L., Brotherton, M. S., Shang, Z., et al. 2011, *ApJ*, 741, 106
- Cales, S. L., Brotherton, M. S., Shang, Z., et al. 2013, *ApJ*, 762, 90

- Cales, S. L., & Brotherton, M. S. 2015, *MNRAS*, 449, 2374
- Calzetti, D., Kinney, A. L., & Storchi-Bergmann, T. 1994, *ApJ*, 429, 582
- Calzetti, D., Armus, L., Bohlin, R. C., et al. 2000, *ApJ*, 533, 682
- Calzetti, D. 2013, *Secular Evolution of Galaxies*, 419
- Canalizo, G., Stockton, A., Brotherton, M. S., & van Breugel, W. 2000, *AJ*, 119, 59
- Canalizo, G., & Stockton, A. 2000, *ApJ*, 528, 201
- Canalizo, G., & Stockton, A. 2001, *ApJ*, 555, 719
- Canalizo, G., & Stockton, A. 2013, *ApJ*, 772, 132
- Cappellari, M., Emsellem, E., Krajnović, D., et al. 2011, *MNRAS*, 413, 813
- Cappellari, M., Emsellem, E., Krajnović, D., et al. 2011, *MNRAS*, 416, 1680
- Cardelli, J. A., Clayton, G. C., & Mathis, J. S. 1989, *ApJ*, 345, 245
- Catalán-Torrecilla, C., Gil de Paz, A., Castillo-Morales, A., et al. 2015, arXiv:1507.03801
- Cattaneo, A., Dekel, A., Devriendt, J., Guiderdoni, B., & Blaizot, J. 2006, *MNRAS*, 370, 1651
- Cattaneo, A., & Best, P.Ñ. 2009, *MNRAS*, 395, 518
- Chabrier, G. 2003, *PASP*, 115, 763
- Charbonnel, C., Meynet, G., Maeder, A., Schaller, G., & Schaerer, D. 1993, *A&AS*, 101, 415
- Chien, L. 2010, *Galaxy Wars: Stellar Populations and Star Formation in Interacting Galaxies*, 423, 197
- Chien, L.-H., & Barnes, J. E. 2010, *MNRAS*, 407, 43
- Chiosi, C., & Carraro, G. 2002, *MNRAS*, 335, 335
- Chomiuk, L., & Povich, M. S. 2011, *AJ*, 142, 197
- Cid Fernandes, R., Mateus, A., Sodré, L., Stasińska, G., & Gomes, J. M. 2005, *MNRAS*, 358, 363
- Cid Fernandes, R., Stasińska, G., Schlickmann, M. S., et al. 2010, *MNRAS*, 403, 1036
- Cid Fernandes, R., & González Delgado, R. M. 2010, *MNRAS*, 403, 780
- Cid Fernandes, R., Pérez, E., García Benito, R., et al. 2013, *A&A*, 557, A86
- Cid Fernandes, R., González Delgado, R. M., García Benito, R., et al. 2014, *A&A*, 561, A130
- Colina, L., Arribas, S., & Clements, D. 2004, *ApJ*, 602, 181
- Colina, L., Arribas, S., & Monreal-Ibero, A. 2005, *ApJ*, 621, 725

- Condon, J. J. 1992, *ARA&A*, 30, 575
- Conroy, C., Gunn, J. E., & White, M. 2009, *ApJ*, 699, 486
- Cox, T. J., Jonsson, P., Somerville, R. S., Primack, J. R., & Dekel, A. 2008, *MNRAS*, 384, 386
- Croton, D. J., Springel, V., White, S. D. M., et al. 2006, *MNRAS*, 365, 11
- Dasyra, K. M., Tacconi, L. J., Davies, R. I., et al. 2006, *ApJ*, 651, 835
- Davies, R. I., Müller Sánchez, F., Genzel, R., et al. 2007, *ApJ*, 671, 1388
- de Grijs, R., Parmentier, G., & Lamers, H. J. G. L. M. 2005, *MNRAS*, 364, 1054
- de Mello, D. F., Urrutia-Viscarra, F., Mendes de Oliveira, C., et al. 2012, *MNRAS*, 426, 2441
- De Propriis, R., & Melnick, J. 2014, *MNRAS*, 439, 2837
- de Vaucouleurs, G. 1948, *Annales d'Astrophysique*, 11, 247
- de Zeeuw, P. T., Bureau, M., Emsellem, E., et al. 2002, *MNRAS*, 329, 513
- Delvecchio, I., Gruppioni, C., Pozzi, F., et al. 2014, *MNRAS*, 439, 2736
- Di Matteo, T., Springel, V., & Hernquist, L. 2005, *Nature*, 433, 604
- Di Matteo, P., Combes, F., Melchior, A.-L., & Semelin, B. 2007, *A&A*, 468, 61
- Di Matteo, P., Bournaud, F., Martig, M., et al. 2008, *A&A*, 492, 31
- Dinshaw, N., Evans, A. S., Epps, H., Scoville, N. Z., & Rieke, M. 1999, *ApJ*, 525, 702
- Djorgovski, S., & Davis, M. 1987, *ApJ*, 313, 59
- Downes, D., & Solomon, P. M. 1998, *ApJ*, 507, 615
- Dressler, A., Lynden-Bell, D., Burstein, D., et al. 1987, *ApJ*, 313, 42
- Dressler, A., & Gunn, J. E. 1983, *ApJ*, 270, 7
- Driver, S. P., Allen, P. D., Graham, A. W., et al. 2006, *MNRAS*, 368, 414
- Duc, P.-A., Bournaud, F., & Masset, F. 2004, *A&A*, 427, 803
- Elmegreen, D. M., Elmegreen, B. G., Kaufman, M., et al. 2006, *ApJ*, 642, 158
- Elson, R. A. W., & Fall, S. M. 1985, *ApJ*, 299, 211
- Emsellem, E., Cappellari, M., Krajnović, D., et al. 2007, *MNRAS*, 379, 401
- Emsellem, E., Cappellari, M., Krajnović, D., et al. 2011, *MNRAS*, 414, 888
- Evans, A. S., Vavilkin, T., Pizagno, J., et al. 2008, *ApJ*, 675, L69
- Faber, S. M., Willmer, C.Ñ. A., Wolf, C., et al. 2007, *ApJ*, 665, 265

- Fabian, A. C. 2012, *ARA&A*, 50, 455
- Fagotto, F., Bressan, A., Bertelli, G., & Chiosi, C. 1994, *A&AS*, 104, 365
- Fagotto, F., Bressan, A., Bertelli, G., & Chiosi, C. 1994, *A&AS*, 105, 29
- Fath, E. A. 1909, Ph.D. Thesis,
- Fathi, K., Lundgren, A. A., Kohno, K., et al. 2013, *ApJ*, 770, L27
- Fernandes, R. C., Leão, J. R. S., & Lacerda, R. R. 2003, *MNRAS*, 340, 29
- Ferrarese, L., & Merritt, D. 2000, *ApJ*, 539, L9
- Feruglio, C., Maiolino, R., Piconcelli, E., et al. 2010, *A&A*, 518, L155
- Filippenko, A. V. 1982, *PASP*, 94, 715
- Fischer, J., Sturm, E., González-Alfonso, E., et al. 2010, *A&A*, 518, L41
- Förster Schreiber, N. M., Genzel, R., Bouché, N., et al. 2009, *ApJ*, 706, 1364
- Franzetti, P., Scodreggio, M., Garilli, B., et al. 2007, *A&A*, 465, 711
- Frayer, D. T., Ivison, R. J., Smail, I., Yun, M. S., & Armus, L. 1999, *AJ*, 118, 139
- García-Benito, R., Zibetti, S., Sánchez, S. F., et al. 2015, *A&A*, 576, A135
- García-Marín, M., Colina, L., Arribas, S., & Monreal-Ibero, A. 2009, *A&A*, 505, 1319
- Gebhardt, K., Bender, R., Bower, G., et al. 2000, *ApJ*, 539, L13
- Genzel, R., Lutz, D., Sturm, E., et al. 1998, *ApJ*, 498, 579
- Genzel, R., Tacconi, L. J., Rigopoulou, D., Lutz, D., & Tecza, M. 2001, *ApJ*, 563, 527
- Girardi, L., Bressan, A., Bertelli, G., & Chiosi, C. 2000, *A&AS*, 141, 371
- Goldader, J. D., Meurer, G., Heckman, T. M., et al. 2002, *ApJ*, 568, 651
- Gonçalves, T. S., Martin, D. C., Menéndez-Delmestre, K., Wyder, T. K., & Koekemoer, A. 2012, *ApJ*, 759, 67
- González, J. J., Cepa, J., González-Serrano, J. I., & Sánchez-Portal, M. 2014, *MNRAS*, 443, 3289
- González Delgado, R. M., Leitherer, C., Heckman, T., et al. 1998, *ApJ*, 495, 698
- González Delgado, R. M., Cid Fernandes, R., Pérez, E., et al. 2004, *ApJ*, 605, 127
- González Delgado, R. M., Cerviño, M., Martins, L. P., Leitherer, C., & Hauschildt, P. H. 2005, *MNRAS*, 357, 945
- González Delgado, R. M. 2008, *Pathways Through an Eclectic Universe*, 390, 205

- González Delgado, R. M. 2009, *Ap&SS*, 324, 231
- González Delgado, R. M., & Cid Fernandes, R. 2010, *MNRAS*, 403, 797
- González Delgado, R. M., Pérez, E., Cid Fernandes, R., et al. 2014, *A&A*, 562, A47
- González Delgado, R. M., Cid Fernandes, R., García-Benito, R., et al. 2014, *ApJ*, 791, L16
- González Delgado, R. M., García-Benito, R., Pérez, E., et al. 2015, *A&A*, 581, A103
- Greene, J. E., Peng, C. Y., Kim, M., et al. 2010, *ApJ*, 721, 26
- Greene, J. E., Murphy, J. D., Comerford, J. M., Gebhardt, K., & Adams, J. J. 2012, *ApJ*, 750, 32
- Greenstein, J. L. 1963, *Nature*, 197, 1041
- Grimes, J. P., Heckman, T., Hoopes, C., et al. 2006, *ApJ*, 648, 310
- Gültekin, K., Richstone, D. O., Gebhardt, K., et al. 2009, *ApJ*, 698, 198
- Haan, S., Surace, J. A., Armus, L., et al. 2011, *AJ*, 141, 100
- Hattori, T., Yoshida, M., Ohtani, H., et al. 2004, *AJ*, 127, 736
- Hauschildt, P. H., Allard, F., & Baron, E. 1999, *ApJ*, 512, 377
- Heavens, A. F., Jimenez, R., & Lahav, O. 2000, *MNRAS*, 317, 965
- Heckman, T. M., Armus, L., & Miley, G. K. 1987, *AJ*, 93, 276
- Heckman, T. M., Armus, L., & Miley, G. K. 1990, *ApJS*, 74, 833
- Heckman, T. M., Dahlem, M., Eales, S. A., Fabbiano, G., & Weaver, K. 1996, *ApJ*, 457, 616
- Heckman, T. 2005, *Chandra Proposal*, 2053
- Heckman, T. M., & Best, P.Ñ. 2014, *ARA&A*, 52, 589
- Heger, A., & Langer, N. 2000, *ApJ*, 544, 1016
- Hibbard, J. E., & Mihos, J. C. 1995, *AJ*, 110, 140
- Hibbard, J. E., & Yun, M. S. 1996, *Cold Gas at High Redshift*, 206, 47
- Hibbard, J. E., Vacca, W. D., & Yun, M. S. 2000, *AJ*, 119, 1130
- Holtzman, J. A., Faber, S. M., Shaya, E. J., et al. 1992, *AJ*, 103, 691
- Holtzman, J. A., Watson, A. M., Mould, J. R., et al. 1996, *AJ*, 112, 416
- Hönig, S. F., Beckert, T., Ohnaka, K., & Weigelt, G. 2006, *A&A*, 452, 459
- Hopkins, P. F., Hernquist, L., Cox, T. J., & Kereš, D. 2008, *ApJS*, 175, 356
- Hopkins, P. F., Cox, T. J., Kereš, D., & Hernquist, L. 2008, *ApJS*, 175, 390

- Hopkins, P. F., & Hernquist, L. 2009, *ApJ*, 694, 599
- Houck, J. R., Soifer, B. T., Neugebauer, G., et al. 1984, *ApJ*, 278, L63
- Howard, S., Keel, W. C., Byrd, G., & Burkey, J. 1993, *ApJ*, 417, 502
- Husemann, B., Jahnke, K., Sánchez, S. F., et al. 2013, *A&A*, 549, A87
- Iono, D., Saito, T., Yun, M. S., et al. 2013, *PASJ*, 65, L7
- Jarosik, N., Bennett, C. L., Dunkley, J., et al. 2011, *ApJS*, 192, 14
- Jarrett, T. H., Masci, F., Tsai, C. W., et al. 2013, *AJ*, 145, 6
- Jog, C. J., & Solomon, P. M. 1992, *ApJ*, 387, 152
- Jogee, S. 2006, *Physics of Active Galactic Nuclei at all Scales*, 693, 143
- Joseph, R. D., & Wright, G. S. 1985, *MNRAS*, 214, 87
- Joy, M., & Harvey, P. M. 1987, *ApJ*, 315, 480
- Kauffmann, G., Heckman, T. M., Tremonti, C., et al. 2003, *MNRAS*, 346, 1055
- Kaviraj, S., Ting, Y.-S., Bureau, M., et al. 2012, *MNRAS*, 423, 49
- Kelz, A., Verheijen, M. A. W., Roth, M. M., et al. 2006, *PASP*, 118, 129
- Kennicutt, R. C., Jr. 1998, *ARA&A*, 36, 189
- Kennicutt, R. C., Jr. 1998, *ApJ*, 498, 541
- Kennicutt, R. C., Jr., Hao, C.-N., Calzetti, D., et al. 2009, *ApJ*, 703, 1672
- Kennicutt, R. C., & Evans, N. J. 2012, *ARA&A*, 50, 531
- Kewley, L. J., Heisler, C. A., Dopita, M. A., & Lumsden, S. 2001, *ApJS*, 132, 37
- Kewley, L. J., Groves, B., Kauffmann, G., & Heckman, T. 2006, *MNRAS*, 372, 961
- Kewley, L. J., Rupke, D., Zahid, H. J., Geller, M. J., & Barton, E. J. 2010, *ApJ*, 721, L48
- Khalatyan, A., Cattaneo, A., Schramm, M., et al. 2008, *MNRAS*, 387, 13
- Kim, D.-C., Veilleux, S., & Sanders, D. B. 1998, *ApJ*, 508, 627
- Kim, D.-C., Evans, A. S., Vavilkin, T., et al. 2013, *ApJ*, 768, 102
- Knierman, K. A., Gallagher, S. C., Charlton, J. C., et al. 2003, *AJ*, 126, 1227
- Knop, R. A., Soifer, B. T., Graham, J. R., et al. 1994, *AJ*, 107, 920
- Koleva, M., Prugniel, P., Ocvirk, P., Le Borgne, D., & Soubiran, C. 2008, *MNRAS*, 385, 1998
- Komatsu, E., Smith, K. M., Dunkley, J., et al. 2011, *ApJS*, 192, 18

- Kormendy, J., & Bender, R. 1996, *ApJ*, 464, L119
- Kormendy, J., & Sanders, D. B. 1992, *ApJ*, 390, L53
- Kormendy, J., Fisher, D. B., Cornell, M. E., & Bender, R. 2009, *ApJS*, 182, 216
- Kormendy, J., & Ho, L. C. 2013, *ARA&A*, 51, 511
- Koss, M., Mushotzky, R., Baumgartner, W., et al. 2013, *ApJ*, 765, L26
- Krajnović, D., Emsellem, E., Cappellari, M., et al. 2011, *MNRAS*, 414, 2923
- Krist, J. E., Hook, R.Ñ., & Stoehr, F. 2011, *Proc. SPIE*, 8127, 81270J
- Krolik, J. H. 1999, *Active galactic nuclei : from the central black hole to the galactic environment* /Julian H. Krolik. Princeton, N. J. : Princeton University Press, c1999.,
- Kroupa, P. 2001, *MNRAS*, 322, 231
- Kurucz, R. L. 1993, *VizieR Online Data Catalog*, 6039, 0
- LaMassa, S. M., Heckman, T. M., Ptak, A., et al. 2010, *ApJ*, 720, 786
- Lançon, A., & Mouhcine, M. 2002, *A&A*, 393, 167
- Lanz, T., & Hubeny, I. 2003, *ApJS*, 146, 417
- Larsen, S. S. 2004, *The Formation and Evolution of Massive Young Star Clusters*, 322, 19
- Larsen, S. S., & Brodie, J. P. 2000, *AJ*, 120, 2938
- Larson, R. B. 1969, *MNRAS*, 145, 405
- Larson, R. B. 1975, *MNRAS*, 173, 671
- Le Borgne, J.-F., Bruzual, G., Pelló, R., et al. 2003, *A&A*, 402, 433
- Le Fèvre, O., Saisse, M., Mancini, D., et al. 2003, *Proc. SPIE*, 4841, 1670
- Le Floch, E., Charmandaris, V., Laurent, O., et al. 2002, *A&A*, 391, 417
- Leitherer, C., Schaerer, D., Goldader, J. D., et al. 1999, *ApJS*, 123, 3
- Leitherer, C., Li, I.-H., Calzetti, D., & Heckman, T. M. 2002, *ApJS*, 140, 303
- Leitherer, C., Ekström, S., Meynet, G., et al. 2014, *ApJS*, 212, 14
- Lípari, S., Mediavilla, E., Díaz, R. J., et al. 2004, *MNRAS*, 348, 369
- Liu, C. T., & Kennicutt, R. C., Jr. 1995, *ApJ*, 450, 547
- Lonsdale, C. J., Farrah, D., & Smith, H. E. 2006, *Astrophysics Update* 2, 285
- Lotz, J. M., Jonsson, P., Cox, T. J., & Primack, J. R. 2010, *MNRAS*, 404, 590

- Madau, P., & Dickinson, M. 2014, *ARA&A*, 52, 415
- Magnelli, B., Elbaz, D., Chary, R. R., et al. 2011, *A&A*, 528, A35
- Magorrian, J., Tremaine, S., Richstone, D., et al. 1998, *AJ*, 115, 2285
- Maiolino, R., Comastri, A., Gilli, R., et al. 2003, *MNRAS*, 344, L59
- Maraston, C., Kissler-Patig, M., Brodie, J. P., Barmby, P., & Huchra, J. P. 2001, *A&A*, 370, 176
- Maraston, C., Bastian, N., Saglia, R. P., et al. 2004, *A&A*, 416, 467
- Maraston, C. 2005, *MNRAS*, 362, 799
- Marino, R. A., Gil de Paz, A., Sánchez, S. F., et al. 2015, arXiv:1509.07878
- Martin, D. C., Wyder, T. K., Schiminovich, D., et al. 2007, *ApJS*, 173, 342
- Martins, L. P., González Delgado, R. M., Leitherer, C., Cerviño, M., & Hauschildt, P. 2005, *MNRAS*, 358, 49
- Martins, L. P., & Coelho, P. 2007, *MNRAS*, 381, 1329
- Mateus, A., Sodr e, L., Cid Fernandes, R., et al. 2006, *MNRAS*, 370, 721
- Matthews, T. A., & Sandage, A. R. 1963, *ApJ*, 138, 30
- McCarthy, I. G., Schaye, J., Ponman, T. J., et al. 2010, *MNRAS*, 406, 822
- McNamara, B. R., & Nulsen, P. E. J. 2012, *New Journal of Physics*, 14, 055023
- Meidt, S. E., Schinnerer, E., Knapen, J. H., et al. 2012, *ApJ*, 744, 17
- Meidt, S. E., Schinnerer, E., van de Ven, G., et al. 2014, *ApJ*, 788, 144
- Mihos, J. C., & Hernquist, L. 1996, *ApJ*, 464, 641
- Miller, B. W., Whitmore, B. C., Schweizer, F., & Fall, S. M. 1997, *AJ*, 114, 2381
- Miralles-Caballero, D., Colina, L., Arribas, S., & Duc, P.-A. 2011, *AJ*, 142, 79
- Miralles-Caballero, D., Colina, L., & Arribas, S. 2012, *A&A*, 538, A61
- Monreal-Ibero, A., Colina, L., Arribas, S., & Garc a-Mar n, M. 2007, *A&A*, 472, 421
- Monreal-Ibero, A., V lchez, J. M., Walsh, J. R., & Mu oz-Tu n n, C. 2010, *A&A*, 517, A27
- Moster, B. P., Somerville, R. S., Maubetsch, C., et al. 2010, *ApJ*, 710, 903
- Mullan, B., Konstantopoulos, I. S., Kepley, A. A., et al. 2011, *ApJ*, 731, 93
- Naab, T., Johansson, P. H., & Ostriker, J. P. 2009, *ApJ*, 699, L178
- Neugebauer, G., Habing, H. J., van Duinen, R., et al. 1984, *ApJ*, 278, L1

- Ocvirk, P., Pichon, C., Lançon, A., & Thiébaud, E. 2006, *MNRAS*, 365, 46
- Oke, J. B. 1990, *AJ*, 99, 1621
- Oser, L., Naab, T., Ostriker, J. P., & Johansson, P. H. 2012, *ApJ*, 744, 63
- Osterbrock, D. E., & Ferland, G. J. 2006, *Astrophysics of gaseous nebulae and active galactic nuclei*, 2nd. ed. by D.E. Osterbrock and G.J. Ferland. Sausalito, CA: University Science Books, 2006,
- Panter, B., Jimenez, R., Heavens, A. F., & Charlot, S. 2007, *MNRAS*, 378, 1550
- Patel, S. G., van Dokkum, P. G., Franx, M., et al. 2013, *ApJ*, 766, 15
- Pérez, E., Cid Fernandes, R., González Delgado, R. M., et al. 2013, *ApJ*, 764, L1
- Pérez-González, P. G., Rieke, G. H., Egami, E., et al. 2005, *ApJ*, 630, 82
- Perlmutter, S., Aldering, G., Goldhaber, G., et al. 1999, *ApJ*, 517, 565
- Peterson, B. M. 1993, *PASP*, 105, 247
- Peterson, B. M., Ferrarese, L., Gilbert, K. M., et al. 2004, *ApJ*, 613, 682
- Peterson, B. W., Struck, C., Smith, B. J., & Hancock, M. 2009, *MNRAS*, 400, 1208
- Petric, A. O., Armus, L., Howell, J., et al. 2011, *ApJ*, 730, 28
- Portegies Zwart, S. F., McMillan, S. L. W., & Gieles, M. 2010, *ARA&A*, 48, 431
- Privon, G. C., Barnes, J. E., Evans, A. S., et al. 2013, *ApJ*, 771, 120
- Renaud, F. 2010, Ph.D. Thesis,
- Rich, J. A., Dopita, M. A., Kewley, L. J., & Rupke, D. S.Ñ. 2010, *ApJ*, 721, 505
- Rich, J. A., Kewley, L. J., & Dopita, M. A. 2011, *ApJ*, 734, 87
- Rich, J. A., Torrey, P., Kewley, L. J., Dopita, M. A., & Rupke, D. S.Ñ. 2012, *ApJ*, 753, 5
- Richards, G. T., Lacy, M., Storrie-Lombardi, L. J., et al. 2006, *ApJS*, 166, 470
- Riess, A. G., Filippenko, A. V., Challis, P., et al. 1998, *AJ*, 116, 1009
- Robaina, A. R., & Cepa, J. 2007, *A&A*, 464, 465
- Rosales-Ortega, F. F. 2009, Ph.D. Thesis,
- Rosales-Ortega, F. F., Kennicutt, R. C., Sánchez, S. F., et al. 2010, *MNRAS*, 405, 735
- Roth, M. M., Kelz, A., Fechner, T., et al. 2005, *PASP*, 117, 620
- Roth, M. M., Fechner, T., Wolter, D., et al. 2010, *Proc. SPIE*, 7742, 774209
- Rothberg, B., & Joseph, R. D. 2004, *AJ*, 128, 2098

- Rothberg, B., Fischer, J., Rodrigues, M., & Sanders, D. B. 2013, *ApJ*, 767, 72
- Runnoe, J. C., Brotherton, M. S., & Shang, Z. 2012, *MNRAS*, 422, 478
- Rupke, D. S., Veilleux, S., & Sanders, D. B. 2005, *ApJS*, 160, 115
- Rupke, D. S.Ñ., Veilleux, S., & Baker, A. J. 2008, *ApJ*, 674, 172
- Rupke, D. S.Ñ., Kewley, L. J., & Chien, L.-H. 2010, *ApJ*, 723, 1255
- Rupke, D. S.Ñ., & Veilleux, S. 2011, *ApJ*, 729, L27
- Rupke, D. S.Ñ., & Veilleux, S. 2013, *ApJ*, 768, 75
- Salim, S., Rich, R. M., Charlot, S., et al. 2007, *ApJS*, 173, 267
- Salpeter, E. E. 1955, *ApJ*, 121, 161
- Sánchez, S. F. 2004, *Astronomical Data Analysis Software and Systems (ADASS) XIII*, 314, 517
- Sánchez, S. F., Jahnke, K., Wisotzki, L., et al. 2004, *ApJ*, 614, 586
- Sánchez, S. F. 2006, *Astronomische Nachrichten*, 327, 850
- Sánchez, S. F., Rosales-Ortega, F. F., Kennicutt, R. C., et al. 2011, *MNRAS*, 410, 313
- Sánchez, S. F., Kennicutt, R. C., Gil de Paz, A., et al. 2012, *A&A*, 538, A8
- Sánchez, S. F., Pérez, E., Rosales-Ortega, F. F., et al. 2015, *A&A*, 574, A47
- Sánchez-Blázquez, P., Peletier, R. F., Jiménez-Vicente, J., et al. 2006, *MNRAS*, 371, 703
- Sánchez-Blázquez, P., Courty, S., Gibson, B. K., & Brook, C. B. 2009, *MNRAS*, 398, 591
- Sánchez-Blázquez, P., Ocvirk, P., Gibson, B. K., Pérez, I., & Peletier, R. F. 2011, *MNRAS*, 415, 709
- Sanders, D. B., Soifer, B. T., Elias, J. H., et al. 1988, *ApJ*, 325, 74
- Sanders, D. B., Soifer, B. T., Elias, J. H., Neugebauer, G., & Matthews, K. 1988, *ApJ*, 328, L35
- Sanders, D. B., & Mirabel, I. F. 1996, *ARA&A*, 34, 749
- Sanders, D. B., Mazzarella, J. M., Kim, D.-C., Surace, J. A., & Soifer, B. T. 2003, *AJ*, 126, 1607
- Sandin, C., Schönberner, D., Roth, M. M., et al. 2008, *A&A*, 486, 545
- Schaerer, D., Meynet, G., Maeder, A., & Schaller, G. 1993, *A&AS*, 98, 523
- Schaerer, D., Charbonnel, C., Meynet, G., Maeder, A., & Schaller, G. 1993, *A&AS*, 102, 339
- Schawinski, K., Urry, C. M., Virani, S., et al. 2010, *ApJ*, 711, 284
- Schawinski, K., Dowlin, N., Thomas, D., Urry, C. M., & Edmondson, E. 2010, *ApJ*, 714, L108
- Schawinski, K., Urry, C. M., Simmons, B. D., et al. 2014, *MNRAS*, 440, 889

- Schlegel, D. J., Finkbeiner, D. P., & Davis, M. 1998, *ApJ*, 500, 525
- Schmidt, M. 1959, *ApJ*, 129, 243
- Schmidt, M. 1963, *Nature*, 197, 1040
- Scoville, N. Z., Sanders, D. B., & Clemens, D. P. 1986, *ApJ*, 310, L77
- Scoville, N. Z., Evans, A. S., Dinshaw, N., et al. 1998, *ApJ*, 492, L107
- Scoville, N. Z., Evans, A. S., Thompson, R., et al. 2000, *AJ*, 119, 991
- Sérsic, J. L. 1963, *Boletín de la Asociación Argentina de Astronomía La Plata Argentina*, 6, 41
- Seyfert, C. K. 1943, *ApJ*, 97, 28
- Shankar, F., Bernardi, M., & Haiman, Z. 2009, *ApJ*, 694, 867
- Shier, L. M., Rieke, M. J., & Rieke, G. H. 1996, *ApJ*, 470, 222
- Silk, J., & Rees, M. J. 1998, *A&A*, 331, L1
- Sirianni, M., Jee, M. J., Benítez, N., et al. 2005, *PASP*, 117, 1049
- Snyder, G. F., Cox, T. J., Hayward, C. C., Hernquist, L., & Jonsson, P. 2011, *ApJ*, 741, 77
- Soifer, B. T., Neugebauer, G., Helou, G., et al. 1984, *ApJ*, 283, L1
- Soifer, B. T., Rowan-Robinson, M., Houck, J. R., et al. 1984, *ApJ*, 278, L71
- Spergel, D.Ñ., Bean, R., Doré, O., et al. 2007, *ApJS*, 170, 377
- Springel, V., Di Matteo, T., & Hernquist, L. 2005, *ApJ*, 620, L79
- Springel, V., White, S. D. M., Jenkins, A., et al. 2005, *Nature*, 435, 629
- Springel, V., Di Matteo, T., & Hernquist, L. 2005, *MNRAS*, 361, 776
- Sturm, E., González-Alfonso, E., Veilleux, S., et al. 2011, *ApJ*, 733, L16
- Sugai, H., Hattori, T., Kawai, A., et al. 2004, *ApJ*, 615, L89
- Surace, J. A., Sanders, D. B., Vacca, W. D., Veilleux, S., & Mazzarella, J. M. 1998, *ApJ*, 492, 116
- Surace, J. A., Sanders, D. B., & Evans, A. S. 2000, *ApJ*, 529, 170
- Strateva, I., Ivezić, Ž., Knapp, G. R., et al. 2001, *AJ*, 122, 1861
- Tacconi, L. J., Genzel, R., Lutz, D., et al. 2002, *ApJ*, 580, 73
- Telfer, R. C., Zheng, W., Kriss, G. A., & Davidsen, A. F. 2002, *ApJ*, 565, 773
- Teyssier, R., Chapon, D., & Bournaud, F. 2010, *ApJ*, 720, L149
- Thomas, D., Maraston, C., Bender, R., & Mendes de Oliveira, C. 2005, *ApJ*, 621, 673

- Thorne, K. S. 1974, *ApJ*, 191, 507
- Tinsley, B. M. 1968, *ApJ*, 151, 547
- Toft, S., Smolčić, V., Magnelli, B., et al. 2014, *ApJ*, 782, 68
- Toomre, A., & Toomre, J. 1972, *ApJ*, 178, 623
- Toomre, A. 1977, *Evolution of Galaxies and Stellar Populations*, 401
- Trager, S. C., Faber, S. M., Worthey, G., & González, J. J. 2000, *AJ*, 119, 1645
- Trancho, G., Bastian, N., Miller, B. W., & Schweizer, F. 2007, *ApJ*, 664, 284
- Urry, C. M., & Padovani, P. 1995, *PASP*, 107, 803
- van Dokkum, P. G. 2001, *PASP*, 113, 1420
- van Dokkum, P. G., Whitaker, K. E., Brammer, G., et al. 2010, *ApJ*, 709, 1018
- Van Wassenhove, S., Volonteri, M., Mayer, L., et al. 2012, *ApJ*, 748, L7
- Vanden Berk, D. E., Richards, G. T., Bauer, A., et al. 2001, *AJ*, 122, 549
- Vazdekis, A., Sánchez-Blázquez, P., Falcón-Barroso, J., et al. 2010, *MNRAS*, 404, 1639
- Veilleux, S., Kim, D.-C., Sanders, D. B., Mazzarella, J. M., & Soifer, B. T. 1995, *ApJS*, 98, 171
- Veilleux, S., Kim, D.-C., & Sanders, D. B. 1999, *ApJ*, 522, 113
- Veilleux, S., Sanders, D. B., & Kim, D.-C. 1999, *ApJ*, 522, 139
- Veilleux, S., Kim, D.-C., & Sanders, D. B. 2002, *ApJS*, 143, 315
- Veilleux, S., Kim, D.-C., Peng, C. Y., et al. 2006, *ApJ*, 643, 707
- Veilleux, S., Cecil, G., & Bland-Hawthorn, J. 2005, *ARA&A*, 43, 769
- Veilleux, S., Meléndez, M., Sturm, E., et al. 2013, *ApJ*, 776, 27
- Véron-Cetty, M.-P., & Véron, P. 2006, *A&A*, 455, 773
- Vestergaard, M., & Peterson, B. M. 2006, *ApJ*, 641, 689
- Walcher, C. J., Lamareille, F., Vergani, D., et al. 2008, *A&A*, 491, 713
- Walcher, C. J., Wisotzki, L., Bekeraité, S., et al. 2014, *A&A*, 569, A1
- Wang, Z., Fazio, G. G., Ashby, M. L.Ñ., et al. 2004, *ApJS*, 154, 193
- Weedman, D. W. 1977, *ARA&A*, 15, 69
- Wei, P., Shang, Z., Brotherton, M. S., et al. 2013, *ApJ*, 772, 28
- Westmoquette, M. S., Clements, D. L., Bendo, G. J., & Khan, S. A. 2012, *MNRAS*, 424, 416

- Whitmore, B. C., Schweizer, F., Leitherer, C., Borne, K., & Robert, C. 1993, *AJ*, 106, 1354
- Whitmore, B. C., Zhang, Q., Leitherer, C., et al. 1999, *AJ*, 118, 1551
- Whitmore, B. C., Chandar, R., Schweizer, F., et al. 2010, *AJ*, 140, 75
- Wild, V., Kauffmann, G., Heckman, T., et al. 2007, *MNRAS*, 381, 543
- Wild, V., Rosales-Ortega, F., Falcón-Barroso, J., et al. 2014, *A&A*, 567, A132
- Wilson, C. D., Harris, W. E., Longden, R., & Scoville, N. Z. 2006, *ApJ*, 641, 763
- Wong, O. I., Schawinski, K., Kaviraj, S., et al. 2012, *MNRAS*, 420, 1684
- Wright, G. S., James, P. A., Joseph, R. D., & McLean, I. S. 1990, *Nature*, 344, 417
- Yesuf, H. M., Faber, S. M., Trump, J. R., et al. 2014, *ApJ*, 792, 84
- Yoshida, M., Taniguchi, Y., & Murayama, T. 1994, *PASJ*, 46, L195
- Yuan, T.-T., Kewley, L. J., & Sanders, D. B. 2010, *ApJ*, 709, 884
- Yun, M. S., Scoville, N. Z., & Knop, R. A. 1994, *ApJ*, 430, L109
- Zakamska, N. L., Strauss, M. A., Krolik, J. H., et al. 2006, *AJ*, 132, 1496
- Zepf, S. E., Ashman, K. M., English, J., Freeman, K. C., & Sharples, R. M. 1999, *AJ*, 118, 752
- Zhang, Q., Fall, S. M., & Whitmore, B. C. 2001, *ApJ*, 561, 727

Future work

We aim to perform a statistical study of the SFHs of interacting galaxies (not necessarily U/LIRGs). We find that 152 out of 939 (16%) of the galaxies in the CALIFA mother sample are interactions/mergers (Walcher et al., 2014) in all the different merger stages from first approach to post-mergers. Moreover, for the systems where the two progenitors have still not coalesced, we have complementary data from Barrera-Ballesteros et al. (in prep.) covering the progenitor which was not included in CALIFA observations. We expect to have ~ 80 galaxies in our interacting sample. One of these systems is NGC 5394, whose morphology is shown in Figure 1 (left) and whose 2D SFHs are shown in Figure 2, with the same set of plots that we have already studied in our three LIRGs.

Additionally, we also plan to analyze well known mergers as the Mice (Figure 1, middle) and Arp 220 (Figure 1, right). The Mice is a famous gas-rich major merger between first passage and coalescence with sub-LIRG infrared luminosity that was already studied by Wild et al. (2014). They found that star formation induced by the recent close passage has not contributed significantly to the total star formation rate or stellar mass of the galaxies. This probes that not all the major-mergers have a significant enhancement of the star formation when compare to isolated galaxies, as was also found from simulations (Di Matteo et al., 2008). On the other hand, Arp 220 is the closest ULIRG to Earth, and was initially included in the sample of this thesis. This is also a well studied system. However, in this case the extinction is so high that even affects the red optical wavelengths (see Figure 2.8). We note that it is necessary to take care of the extinction modelling and confirm that the analysis in the optical is consistent with infrared observations. We note that in the thesis we have assumed a Calzetti et al. (2000) extinction law, as it has been proven to perform better in starburst galaxies. However, the plots shown here are based on Cardelli extinction law. We will compare between both laws in detail. In Figures 3, 4 and 5, we show the 2D SFHs for the Mice A, Mice B and Arp 220, respectively.

Some preliminar results:

1. NGC 5394 is the less massive progenitor in the first interacting system. The contribution to mass of the SSPs younger than 1.5 Gyr is more important in the outer parts than in the nucleus, as we also found in the pre-merger NGC 6090 NE and NGC 2623. In the inner 0.5 HLR the SFR is dominated by the youngest stellar populations (< 32 Myr), indicative of a nuclear starburst. Beyond 1 HLR the star formation is dominated by the intermediate age stellar populations (< 1.5 Gyr). Paradoxically, this is similar to what we found in the more advanced merger NGC 2623.
2. In the Mice A, we find that the contribution to mass of the SSPs younger than 1.5 Gyr is negligible both in the central region and in the "disk", suggesting that there is no significant merger induced star formation in this component. In the inner 0.5 HLR the SFR is dominated by the oldest stellar populations computed over the Hubble time, indicating that star formation is more recent times is not relevant. Only in the nucleus itself the contribution of the younger

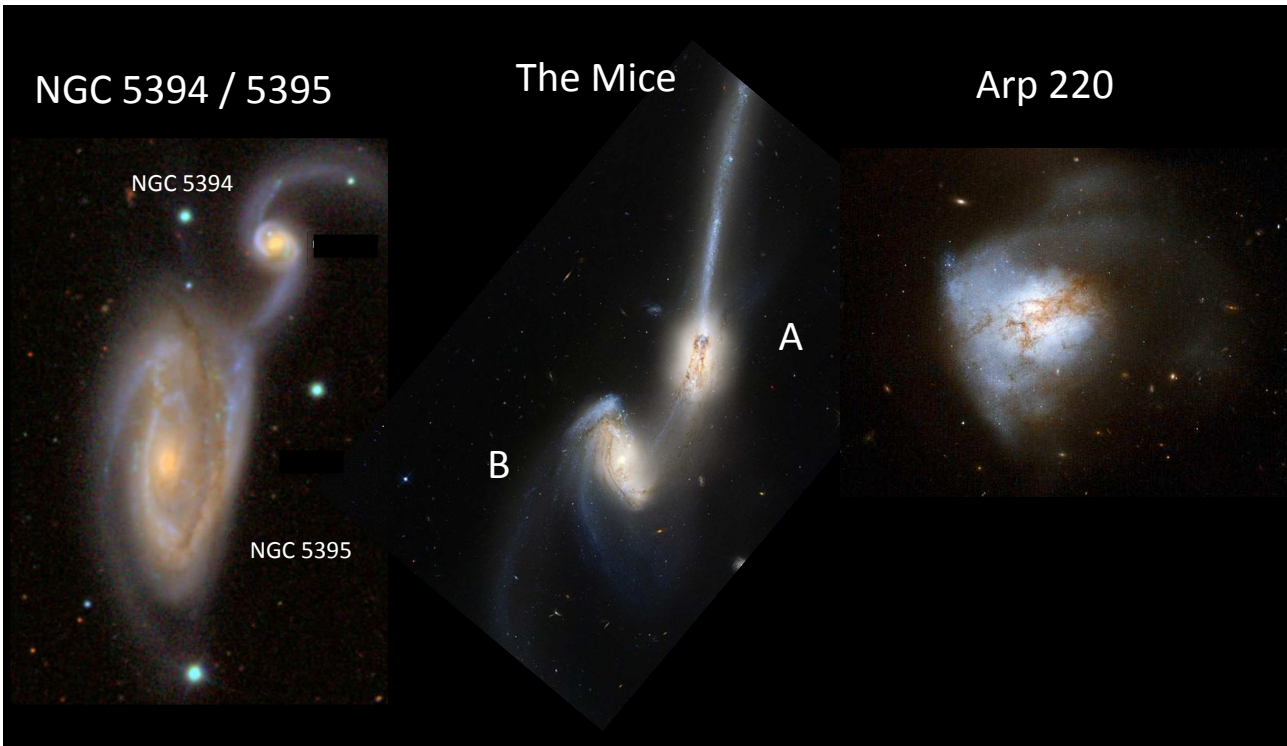


Figure 1 From left to right, images of NGC 5394/5395, The Mice and Arp 220.

components is comparable to the SFR(13.5 Gyr). In the outer parts, SFR(1.5 Gyr) is similar to the SFR(13.5 Gyr) computed over the Hubble time, with the SFR(32 Myr) and SFR(300 Myr) being irrelevant in comparison.

3. In the Mice B, we find similar results to Mice A. The contribution to mass of the SSPs younger than 1.5 Gyr is negligible both in the central region and in the "disk", suggesting that there is no significant merger induced star formation in this component. Both in the inner 0.5 HLR and in the "disk", the SFR is dominated by the oldest stellar populations computed over the Hubble time, indicating that star formation is more recent times is not relevant. This results are in agreement with [Wild et al. \(2014\)](#).
4. In Arp 220 we find that the contribution to mass of the SSPs younger than 1.5 Gyr is more important in the outer parts (30 %) than in the nucleus (10 %), similar to what we found in the also merger LIRG NGC 2623. In the inner 0.5 HLR, both the young SFRs(32 Myr, 300 Myr) and the old SFRs(1.5 Gyr, 3 Gyr) are similar, indicating an approximately continuum star formation along the Hubble time. However, the outer parts are clearly dominated by the intermediate age stellar populations (< 1.5 Gyr), with the younger components being irrelevant in comparison. The results for this system are similar to the ones for NGC 2623, with the difference that in NGC 2623 the star formation in the last 32 Myr is much more important both in the nucleus and in the outer parts.

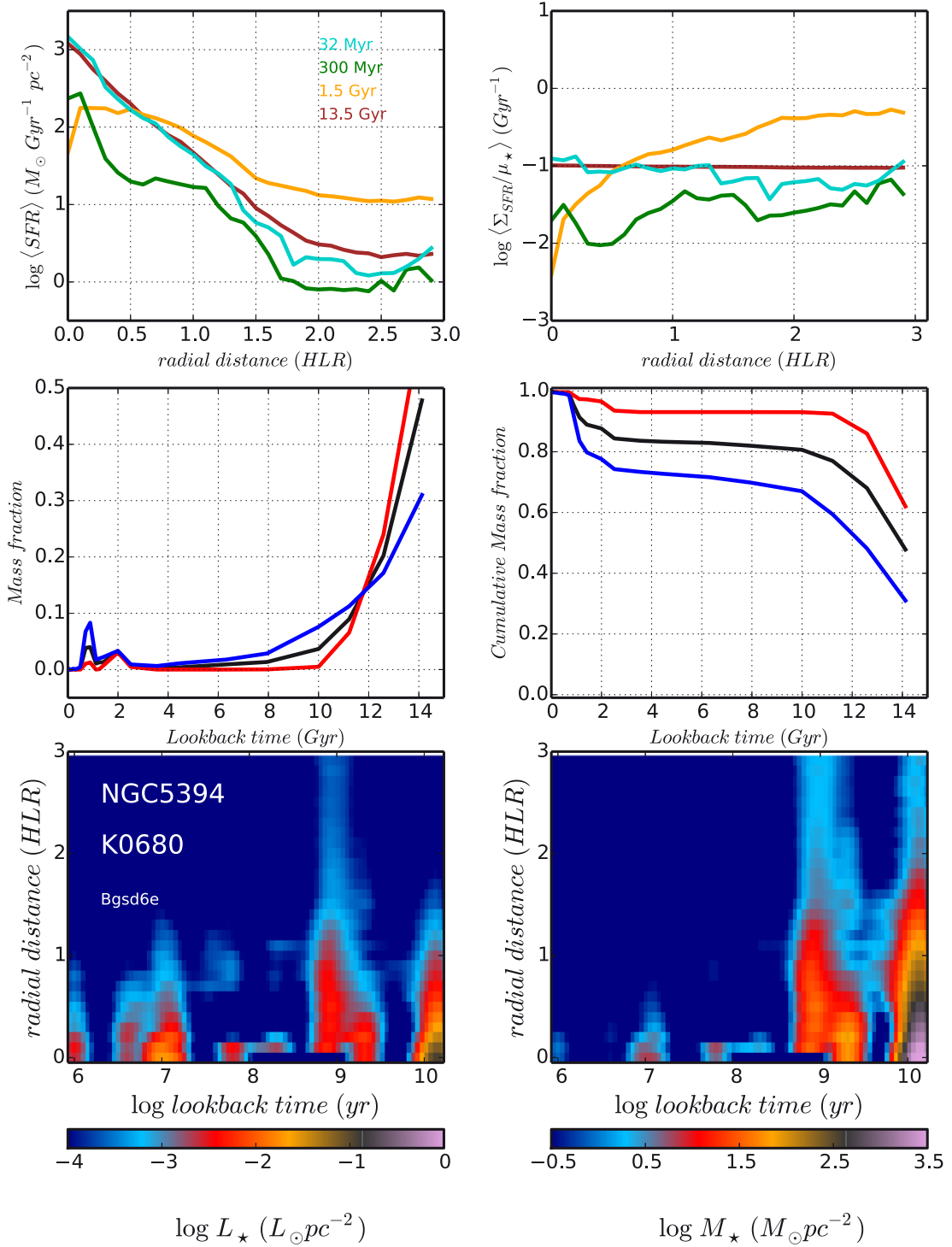


Figure 2 **Bottom left:** 2D SFH in light of NGC 5394 in units of surface brightness in $L_{\odot} \text{ pc}^{-2}$ and logarithmic scale. The vertical axis is the radial distance from the nucleus in HLR units. The horizontal axis is the SSP age (in logarithm), which has been smoothed by a Gaussian filter with a FWHM of 0.20 dex. **Bottom right:** 2D SFH in mass in units of mass surface density in $M_{\odot} \text{ pc}^{-2}$. **Middle left:** Mass fraction as a function of lookback time in logarithmic scale for the inner 0.5 HLR in red, from 1.0 - 1.5 HLR in blue and the integrated over 2 HLR in black. **Middle right:** Cumulative mass fraction as a function of the lookback time in linear scale for the inner 0.5 HLR (red line), the outer regions 1.0 - 1.5 HLR (blue line) and the integrated value (black line). **Top left:** Radial profiles of the SFRs as a function of the radial distance. The SFR calculated in the last 32 Myr is in blue, in green for the last 300 Myr, orange for the last 1.5 Gyr and brown for the SFR along the Hubble time. **Top right:** As in the top left panel but for sSFR.

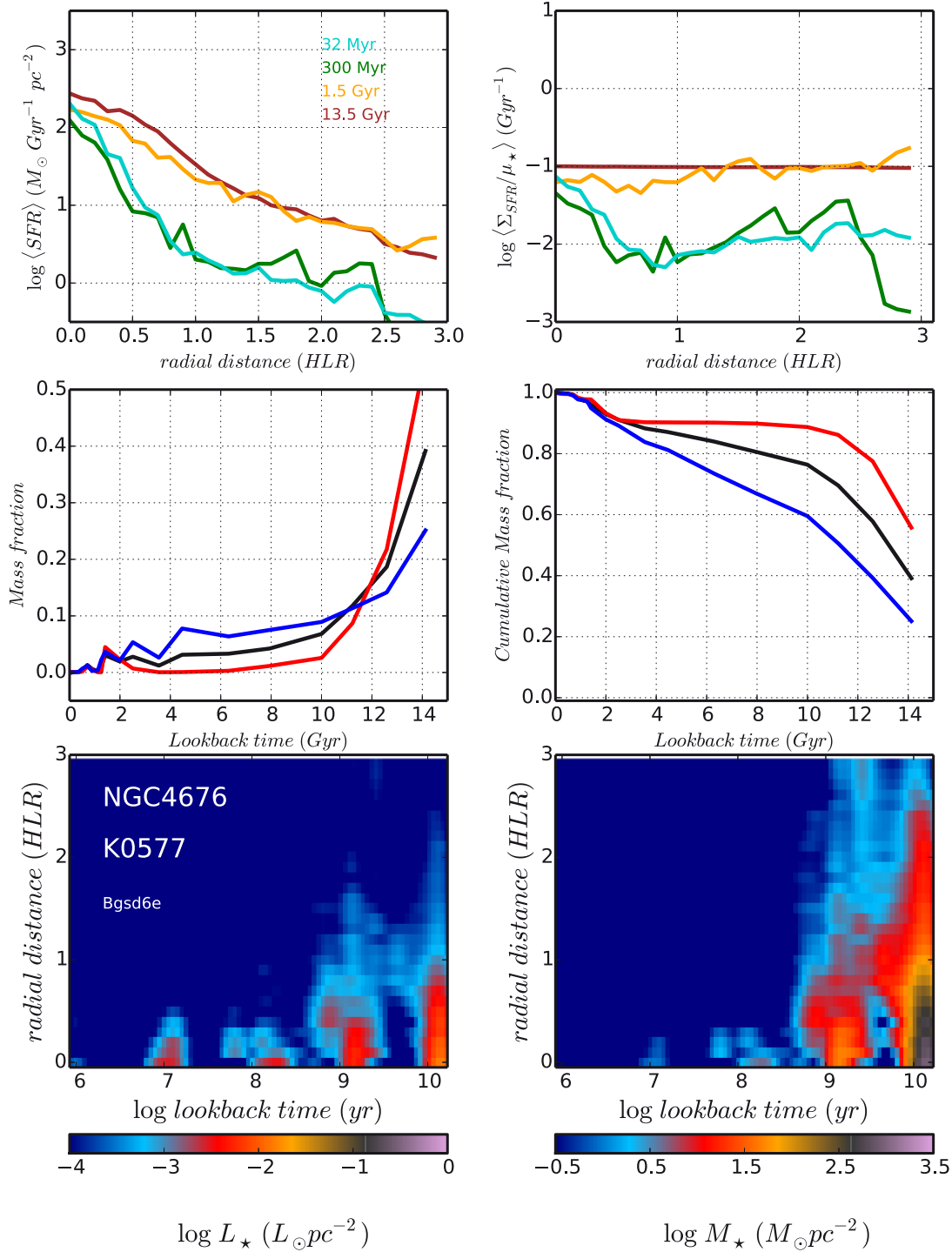


Figure 3 **Bottom left**: 2D SFH in light of Mice A in units of surface brightness in $L_{\odot} \text{ pc}^{-2}$ and logarithmic scale. The vertical axis is the radial distance from the nucleus in HLR units. The horizontal axis is the SSP age (in logarithm), which has been smoothed by a Gaussian filter with a FWHM of 0.20 dex. **Bottom right**: 2D SFH in mass in units of mass surface density in $M_{\odot} \text{ pc}^{-2}$. **Middle left**: Mass fraction as a function of lookback time in logarithmic scale for the inner 0.5 HLR in red, from 1.0 - 1.5 HLR in blue and the integrated over 2 HLR in black. **Middle right**: Cumulative mass fraction as a function of the lookback time in linear scale for the inner 0.5 HLR (red line), the outer regions 1.0 - 1.5 HLR (blue line) and the integrated value (black line). **Top left**: Radial profiles of the SFRs as a function of the radial distance. The SFR calculated in the last 32 Myr is in blue, in green for the last 300 Myr, orange for the last 1.5 Gyr and brown for the SFR along the Hubble time. **Top right**: As in the top left panel but for sSFR.

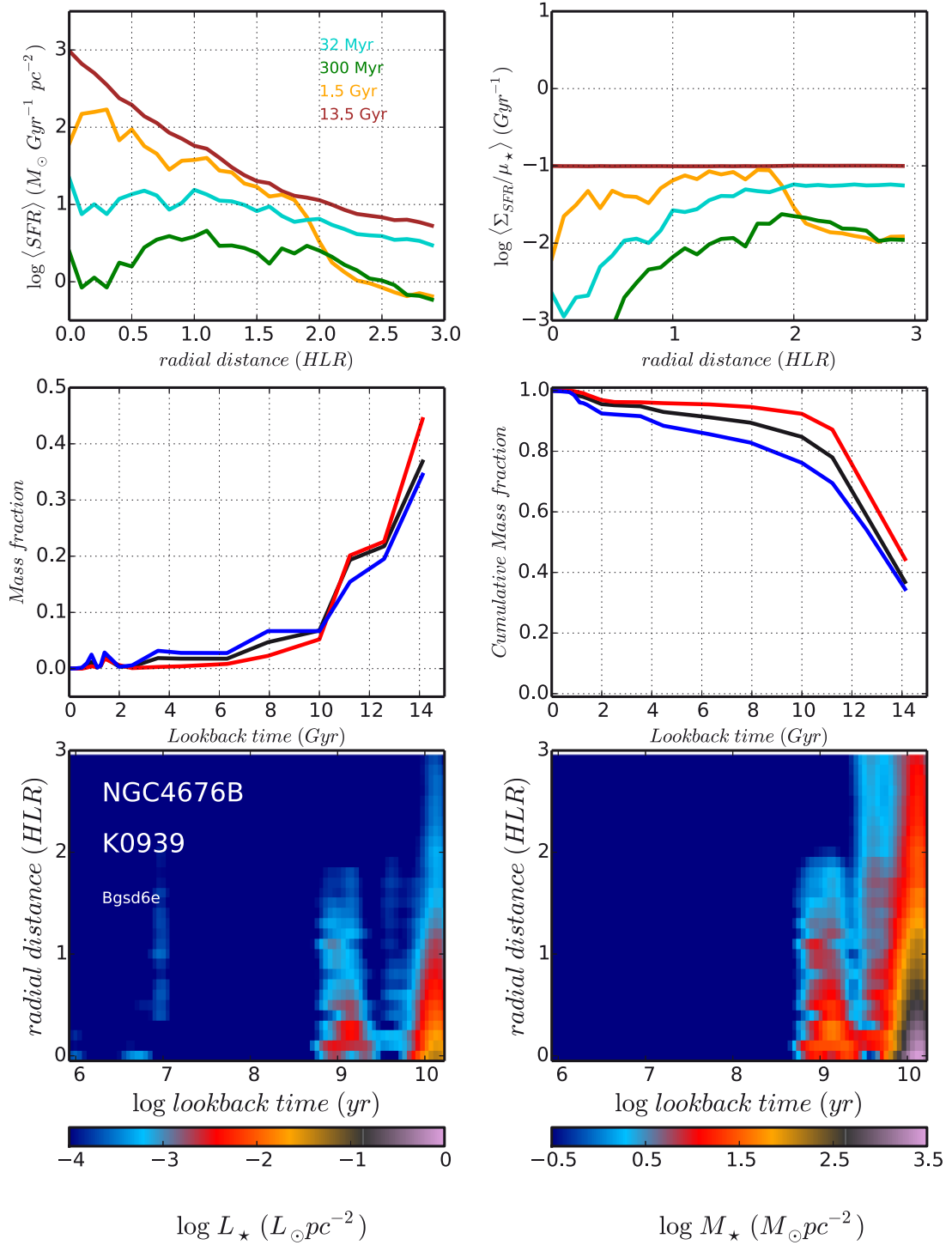


Figure 4 **Bottom left:** 2D SFH in light of Mice B in units of surface brightness in $L_{\odot} \text{ pc}^{-2}$ and logarithmic scale. The vertical axis is the radial distance from the nucleus in HLR units. The horizontal axis is the SSP age (in logarithm), which has been smoothed by a Gaussian filter with a FWHM of 0.20 dex. **Bottom right:** 2D SFH in mass in units of mass surface density in $M_{\odot} \text{ pc}^{-2}$. **Middle left:** Mass fraction as a function of lookback time in logarithmic scale for the inner 0.5 HLR in red, from 1.0 - 1.5 HLR in blue and the integrated over 2 HLR in black. **Middle right:** Cumulative mass fraction as a function of the lookback time in linear scale for the inner 0.5 HLR (red line), the outer regions 1.0 - 1.5 HLR (blue line) and the integrated value (black line). **Top left:** Radial profiles of the SFRs as a function of the radial distance. The SFR calculated in the last 32 Myr is in blue, in green for the last 300 Myr, orange for the last 1.5 Gyr and brown for the SFR along the Hubble time. **Top right:** As in the top left panel but for sSFR.

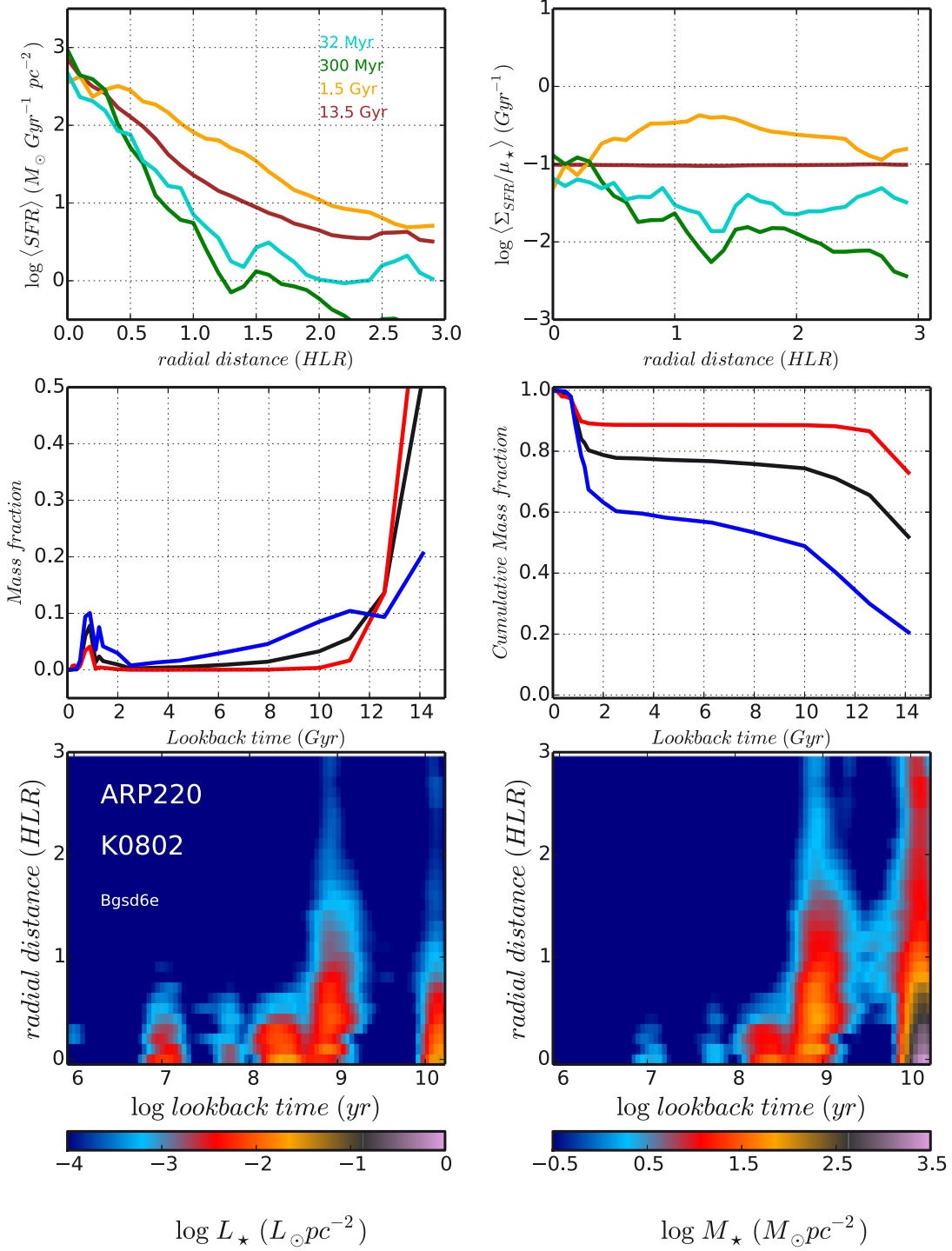


Figure 5 **Bottom left:** 2D SFH in light of Arp 220 in units of surface brightness in $L_{\odot} \text{ pc}^{-2}$ and logarithmic scale. The vertical axis is the radial distance from the nucleus in HLR units. The horizontal axis is the SSP age (in logarithm), which has been smoothed by a Gaussian filter with a FWHM of 0.20 dex. **Bottom right:** 2D SFH in mass in units of mass surface density in $M_{\odot} \text{ pc}^{-2}$. **Middle left:** Mass fraction as a function of lookback time in logarithmic scale for the inner 0.5 HLR in red, from 1.0 - 1.5 HLR in blue and the integrated over 2 HLR in black. **Middle right:** Cumulative mass fraction as a function of the lookback time in linear scale for the inner 0.5 HLR (red line), the outer regions 1.0 - 1.5 HLR (blue line) and the integrated value (black line). **Top left:** Radial profiles of the SFRs as a function of the radial distance. The SFR calculated in the last 32 Myr is in blue, in green for the last 300 Myr, orange for the last 1.5 Gyr and brown for the SFR along the Hubble time. **Top right:** As in the top left panel but for sSFR.

*Y me niego a creer que tras el Big Bang
todo será lo mismo.*

- en Big Bang, Aeropuertos, Txanxu -

